transactions of the ASME

Published Quarterly by
The American Society of
Mechanical Engineers
Volume 94 • Series C • Number 4
NOVEMBER 1972

journal of heat transfer



**EDITED and PUBLISHED** quarterly at the offices of The American Society of Mechanical Engineers, United Engineering Center, 345 E. 47th St., New York, N.Y. 10017. Cable address, "Mechaneer," New York. Second-class postage paid at New York, N. Y., and at additional mailing offices.

**CHANGES OF ADDRESS** must be received at Society headquarters seven weeks before they are to be effective. Please send old label and new address.

**PRICES:** To members, $15.00, annually; to nonmembers, $30.00. Single copies, $10.00 each. Add $1.50 for postage to countries outside the United States and Canada.



INDEXED by the Engineering Index, Inc.



**(Contents continued on page 346)**

# CONTENTS
## (CONTINUED)

DOUGLAS G. FOX
J. W. DEARDORFF
National Center for Atmospheric Research,[1] Boulder, Colo.

# Computer Methods for Simulation of Multidimensional, Nonlinear, Subsonic, Incompressible Flow

*This review attempts to summarize the current state of fluid flow simulations with particular regard to numerical discretization techniques, treatment of large Reynolds numbers, and past and future accomplishments of the simulation methodology. Three alternative mathematical representations of the flow are presented and compared for an idealized two-dimensional flow, namely, use of the velocity and pressure as dependent variables (primitive equation), use of vorticity and stream function as dependent variables, and expansion of either of these in a truncated set of orthogonal eigenfunctions of the boundary-value problem (whose coefficients become the dependent variables). Various classes of finite-difference algorithms are discussed with regard to their conditional stability as well as their ability to preserve invariants of the continuous equations. Methods of removing aliasing of high-frequency solutions are discussed. Parameterization and other techniques for dealing with the high-Reynolds-number regime in which solutions exhibit a wide range of scales are considered in depth. We conclude that certain types of information can be better obtained by numerical simulation than by other techniques.*

## I Introduction

This paper presents a rather partial review of fluid dynamic simulations of the type suggested by the title. In particular we wish to discuss solutions of the Navier–Stokes equations within the Boussinesq approximation. We therefore wish to contrast our approach from the vast literature dealing with solutions of boundary-layer equations.

Our aim is to simulate from as basic a state as is possible the development and evolution of a fluid flow. Inasmuch as this is not generally possible in complicated geometries, we restrict our discussion to regular boundaries and will generally assume at least one of the dimensions can be extended by the artifice of assuming periodic boundary conditions. Implicit in our approach is the availability of large powerful computers. In fact, in the past the approach we espouse has been pursued most successfully at such locations as NCAR, Los Alamos and the Lawrence Radiation Laboratories of the University of California, and NOAA's Geophysical Fluid Dynamics Laboratory. However, computers are continuously improving and their availability seems based mainly on need. A main theme of the present paper will be to present methods which we feel are the best within the constraints of both economy and accuracy.

The main section of the paper is broken into two parts, in the first of which we outline the equations of motion and present three alternate forms for performing the types of calculation envisioned. In the second we discuss numerical approximations for the substantial derivative dealing mainly with prescriptions for the nonlinear terms and secondarily for the linear aspects of the problem. The next section (III) discusses the treatment of turbulence and its parameterization as a subgrid scale phenomena. Finally, we conclude with a somewhat philosophical note regarding the usefulness and relevance of the numerical simulation of fluid flows.

## II General Approach

**Primitive Equations.** The incompressible Navier–Stokes equations within the Boussinesq approximation can be written as:

$$\frac{d}{dt}u_i = B\delta_{i3} + \nu\frac{\partial^2}{\partial x_j{}^2}u_i - \frac{\partial \pi}{\partial x_i} = R_i - \partial\pi/\partial x_i \qquad (2.1)$$

$$\frac{\partial u_i}{\partial x_i} = 0 \qquad (2.2)$$

$$\frac{d}{dt}B = \kappa\frac{\partial^2}{\partial x_j{}^2}B \qquad (2.3)$$

[1] The National Center for Atmospheric Research is sponsored by the National Science Foundation.

Contributed by the Heat Transfer Division of The American Society of Mechanical Engineers and presented at the AIChE-ASME Heat Transfer Conference, Denver, Colo., August 6–9, 1972. Manuscript received by the Heat Transfer Division June 19, 1972. Paper No. 72-HT-61.

where $\frac{d}{dt} = \frac{\partial}{\partial t} + u_j \frac{\partial}{\partial x_j}$ is the substantial derivative and $B = g\alpha(T - T_0)$ is a buoyancy force based upon temperature perturbation from a specified state (although other density-related scalars or the density itself could replace temperature with no mathematical changes). Here $u_i$ are the velocities in the $x_i$ coordinate directions, $\pi$ is the pressure per unit density, $\nu$ and $\kappa$ are molecular coefficients of kinematic viscosity and thermal conductivity respectively, $g$ is the acceleration of gravity oppositely directed from the $x_3$ coordinate, $\alpha$ is the thermal-expansion coefficient, and $T_0$ is a specified reference (not necessarily spatially constant) temperature. The system represents what are generally called the primitive equations, although that term sometimes includes use of the hydrostatic assumption which is not made here. Numerical procedures are based somewhat upon the form of equations (2.1)–(2.3). We shall first present the approach used in solving equations (2.1)–(2.3) and then discuss two alternative equation sets and the approach used in solving each of these.

The presence of pressure in equation (2.1) of course represents a major difficulty in solving for $u_i$. It has been found, therefore (Harlow and Welch [1],[2] Williams [2]) that the most efficient procedure involves formation of an equation for the pressure. Philosophically this can be looked upon as turning the incompressibility condition (2.2) into a predictive equation for this condition. Taking the divergence of equation (2.1) results in

$$\frac{\partial}{\partial t}\left(\frac{\partial u_i}{\partial x_i}\right) + \frac{\partial}{\partial x_i}\left(u_j \frac{\partial u_i}{\partial x_j}\right) = \frac{\partial B}{\partial x_3} - \frac{\partial^2 \pi}{\partial x_i{}^2} + \nu \frac{\partial^2}{\partial x_j{}^2}\left(\frac{\partial u_i}{\partial x_i}\right)$$

In order to predict zero divergence we set $\left(\frac{\partial u_i}{\partial x_i}\right)^{n+1} \equiv 0$ (where we indicate discrete time in the superscript such that time is approximated as $t = n\Delta t$) and the following Poisson-type equation results:

$$\frac{\partial^2 \pi^n}{\partial x_i{}^2} = \left(\frac{\partial B}{\partial x_3}\right)^n - \frac{\partial}{\partial x_i}\left(u_j \frac{\partial u_i}{\partial x_j}\right)^n + \frac{1}{2\Delta t}\left(\frac{\partial u_i}{\partial x_i}\right)^{n-1} + \nu \frac{\partial^2}{\partial x_j{}^2}\left(\frac{\partial u_i}{\partial x_j}\right)^{n-1} \quad (2.4)$$

where we have assumed that the time-stepping procedure used is of a centered variety (see the ensuing paragraphs) and the viscous term (nearly zero) is set at the $n - 1$ time level. Clearly a solution to equation (2.4) of the form

$$\pi^n = \nabla^{-2}\left[\frac{\partial B^n}{\partial x_3} - \frac{\partial}{\partial x_i}\left(u_j \frac{\partial u_i}{\partial x_j}\right)^n + \frac{1}{2\Delta t}\left(\frac{\partial u_i}{\partial x_i}\right)^{n-1} + \nu \frac{\partial^2}{\partial x_j{}^2}\left(\frac{\partial u_i}{\partial x_i}\right)^{n-1}\right]$$

enforces zero divergence and hence satisfies equation (2.2).

Calculation proceeds from given initial conditions, say $u_i(0)$ and $B(0)$ by calculating $B(1)$ from equation (2.3) and then the right-hand side of equation (2.1) without the pressure, i.e., $R_i(0)$; taking the divergence of $R_i(0)$ and forming therefrom the forcing function for the Poisson equation (2.4); inverting the Poisson equation and using the value of $\pi(0)$ obtained to calculate $u_i(1)$ from equation (2.1). The procedure is continued in this manner. Boundary conditions are required on the velocities $u_i$ and buoyancy as well as on the pressure $\pi$. The former are stated as necessary conditions in specifying the problem while the latter are determined by requiring equation (2.1) to hold at boundary points, hence supplying a value for the pressure gradient at these points.

**The Vorticity Vector-Potential Approach.** A vorticity equation can be formulated by taking the curl of equation (2.1) resulting in

$$\frac{\partial}{\partial t}\omega_i + u_j \frac{\partial \omega_i}{\partial x_j} - \omega_j \frac{\partial u_i}{\partial x_j} = \nu \frac{\partial^2}{\partial x_k{}^2}\omega_i - \frac{\partial B}{\partial x_j}\epsilon_{ij3} \quad (2.5)$$

where $\omega_i = \epsilon_{ijk}\frac{\partial u_j}{\partial x_k}$ and where $\epsilon_{ijk}$ is the unit alternating tensor which is 0 if any of the indices repeat, +1 when in cyclic order, and −1 when in noncyclic order. Equation (2.5) has the obvious benefit of the absence of the pressure variable. Expression of the velocity in terms of a vector potential $\psi_i$ such that $u_i = \epsilon_{ijk}\frac{\partial \psi_j}{\partial x_k}$ insures incompressibility since $\frac{\partial}{\partial x_i}u_i = \frac{\partial}{\partial x_i}\epsilon_{ijk}\frac{\partial \psi_j}{\partial x_k} \equiv 0$. The vorticity can then be specified in terms of $\psi_i$ as

$$\omega_i = \epsilon_{ijk}\frac{\partial}{\partial x_k}\epsilon_{j\beta\gamma}\frac{\partial \psi_\beta}{\partial x_\gamma} = -\frac{\partial^2}{\partial x_k{}^2}\psi_i \quad (2.6)$$

In three dimensions, Aziz and Hellums [3] have presented computations and discussed the proper boundary conditions for this formulation. The methods of solution of equations (2.5) and (2.6) are about the same for (2.1)–(2.4) with the exception that the vorticity is defined initially and potential is calculated by inverting the Poisson equation (2.6) and so on. It seems difficult to justify the use of this system in three dimensions since it involves more nonlinear terms in (2.5) and two more inversions of the Poisson equation at each time step. This approach, however, has been used extensively in two dimensions where $\omega_i = (0, 0, \omega)$ and the velocity potential becomes the stream function, so that (2.5) and (2.6) reduce to scalar equations. In this case there is one less marching equation to solve for than for equations (2.1)–(2.4).

***Galerkin* Approach.** To effect solution of either set of equations, some method of discretization is required. The most common method in the past has been through the use of finite differences wherein a grid of points is defined for each variable and the variable is treated only at these grid points. This procedure allows the partial differential equations to be transformed into sets of simultaneous equations. An alternative approach, and one which is a rather conventional method of solving linear partial differential equations, is to expand the dependent variables in a set of orthogonal functions which satisfy the boundary conditions (eigenfunctions) and introduce these expansions into the original equations, thereby rendering them ordinary differential equations. Numerically these ODE's are much simpler to solve. To be precise, expansion in a truncated set of orthogonal functions, i.e., Galerkin's method, is most efficient for computations.

To illustrate, we assume that we can expand in a finite Fourier series such that

$$\begin{Bmatrix} u_i(\mathbf{x}, t) \\ \pi(\mathbf{x}, t) \\ B(\mathbf{x}, t) \end{Bmatrix} = \sum_{\mathbf{k}=-\mathbf{K}}^{\mathbf{K}'} \begin{Bmatrix} u_i(\mathbf{k}, t) \\ \pi(\mathbf{k}, t) \\ B(\mathbf{k}, t) \end{Bmatrix} e^{i\mathbf{k}\cdot\mathbf{x}}$$

where we assume $\mathbf{u}(0, t) = 0$ (no mean flow); $\mathbf{k} = (2\pi/L)\mathbf{n}$; $\mathbf{n} = n_1, n_2, n_3$; $n_i = 0, \pm 1, \pm 2, \ldots$. For simplicity we shall limit $L$ to be $2\pi$. $\mathbf{K}$ is the cutoff wave number, while $\mathbf{K}'$ corresponds to $\mathbf{n}$ one less in magnitude than the cutoff value. Since the velocities $u_i(\mathbf{x}, t)$ are real, the Fourier coefficients are half complex,

$$u_\alpha(\mathbf{k}) = u_\alpha(-\mathbf{k})^*$$

Introducing this discretization into equations (2.1), (2.2), and (2.3) gives

$$\left[\frac{\partial}{\partial t} + \nu k^2\right] u_\alpha(\mathbf{k}) = -\frac{i}{2}P_{\alpha\beta\gamma}(\mathbf{k}) \sum_{\mathbf{p}=-\mathbf{K}}^{\mathbf{K}'} u_\beta(\mathbf{p})u_\gamma(\mathbf{k} - \mathbf{p}) - i\frac{k_\alpha k_3}{k^2}B(\mathbf{k}) \quad (2.7)$$

[2] Numbers in brackets designate References at end of paper.

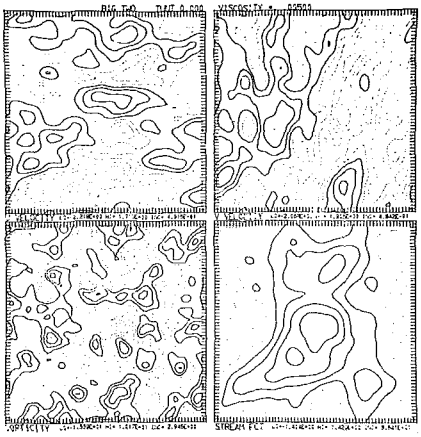

**Fig. 1(a) Initial conditions—contours of velocity, vorticity, and stream function for all the calculations reported in this paper; the generating mechanism is discussed in [7]; solid lines represent positive values and dotted negative values; maxima, minima, and contour intervals are recorded under each individual picture**

$$k_\alpha u_\alpha(\mathbf{k}) = 0 \tag{2.8}$$

$$\left[\frac{\partial}{\partial t} + \kappa k^2\right] B(\mathbf{k}) = -i \sum_{\mathbf{p}=-K}^{K'} p_\alpha u_\alpha(\mathbf{k} - \mathbf{p}) B(\mathbf{p}) \tag{2.9}$$

where

$$P_{\alpha\beta\gamma}(\mathbf{k}) = k_\beta\left(\delta_{\alpha\gamma} - \frac{k_\alpha k_\gamma}{k^2}\right) + k_\gamma\left(\delta_{\alpha\beta} - \frac{k_\alpha k_\beta}{k^2}\right) \tag{2.7a}$$

The pressure has been eliminated from equation (2.7) by solution of the equivalent of (2.4) (explicit in Fourier space). There are a great many advantages to seeking solutions in Fourier space and essentially one disadvantage. Considering the latter first, the difficulty which has in the past prevented use of equations like (2.7)–(2.9) with large cutoff wave numbers $K$ is the nonlocal character of the convolution sums which require a sum over approximately $2K$ wave vectors for each nonlinear component and for each $2K$ wave vector. The amount of arithmetic required to augment a solution of equation (2.7) is therefore approximately $2K$ times the amount required for finite-difference solutions of either equation (2.1) or (2.5) (Orszag [4]). Orszag [5] showed that this disparity can be removed by judicious use of the fast Fourier transform, implementing the convolution sums in part in physical space and in part in Fourier space. Orszag [4, 6] has established the substantially greater accuracy of Galerkin techniques over, say, fourth-order-accurate finite differences, for a wide class of linear problems; Fox and Orszag [7] are currently undertaking an extensive study of numerical solutions of the Navier–Stokes equations by both Galerkin and finite-difference techniques.

Reasons for expecting better results with equation (2.7) are based upon elimination of differencing errors (derivatives in function space are exact up to the cutoff wave number), preservation of invariance properties of the continuous equations (also a characteristic of the finite-difference schemes we recommend), exact removal of aliasing interactions, and more proper satisfaction of boundary conditions (especially for rigid boundaries, Orszag [8]). We feel that if time-differencing errors are kept to a minimum and only flows treated for which the smallest scales present are well within the resolution range of the computation, the Galerkin (Fourier) methods are capable of producing for all practical purposes the correct solution to the Navier–Stokes equations. For this reason we will briefly outline the methods used and present the results of the solution of a particular problem. This solution will then serve as a control with which to compare finite-difference approximations of equations (2.1) and (2.5) for accuracy. As well, various forms of the finite-difference approximations will be tested and presented.

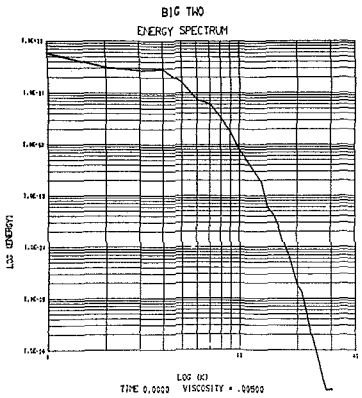


**Fig. 1(b) Energy spectrum for these initial conditions**

## III Numerical Approximations

Much has been written concerning the relative advantages and disadvantages of numerical schemes for solving fluid dynamic problems, a conclusion from which might be that different methods are appropriate for different problems. Our title indicates some of the conditions we apply to our simulations. Our primary purpose is in developing methods which work best on flows possessing many scales of motion, i.e., turbulence. Inasmuch as turbulence is strongly coupled with the dissipation mechanism present in the flow, we have sought numerical schemes which are free from numerical damping (diffusion) (Fox and Lilly [9]). For this reason we emphasize the invariance properties of equations (2.1) and (2.3). A semiconservative (in the absence of viscous terms and time-differencing errors) scheme guarantees that nonlinear numerical instability will not occur. We will therefore discuss various schemes with regard to their stability and conservative properties as well as present results of their solutions and comparative accuracy.

**The Problem and Its Galerkin Solution.** We will consider decaying two-dimensional isothermal turbulence (cf. Lilly [10]). An initial stream function consisting of a set of numbers which are random among themselves but constrained to produce a particular spectrum is chosen. A contour plot of this stream function, along with derived velocity and vorticity fields, is shown in Fig. 1. The same stream function will serve as the initial condition for all the examples.

The calculation proceeds by methods discussed in detail in Fox and Orszag [7]. For efficiency, instead of solving equation (2.7) we use the Galerkin form of equation (2.5) which requires expansion of the stream function in a Fourier series such that

$$\psi(\mathbf{x}, t) = \sum_{|\mathbf{k}|<\mathbf{K}} \hat{\psi}(\mathbf{k}, t) e^{i\mathbf{k}\cdot\mathbf{x}} \tag{3.1}$$

and the equivalent of equation (2.5) becomes

$$\left[\frac{\partial}{\partial t} + \nu k^2\right] k^2\hat{\psi}(\mathbf{k}) = \sum_{\substack{\mathbf{p}+\mathbf{q}=\mathbf{k} \\ |\mathbf{p}|,|\mathbf{k}|<\mathbf{K}}} (p_1 q_2 - p_2 q_1) q_2 \hat{\psi}(\mathbf{p})\hat{\psi}(\mathbf{q}) = r(\mathbf{k}) \tag{3.2}$$

Solution is obtained by calculating $r(k)$ as

$$\begin{aligned} r(k) &= F\left\{\frac{\partial}{\partial x_1} u_1\omega + \frac{\partial}{\partial x_2} u_2\omega\right\} \\ &= F\left\{\frac{\partial}{\partial x_1}\left(\frac{\partial\psi}{\partial x_2}\nabla^2\psi\right) - \frac{\partial}{\partial x_2}\left(\frac{\partial\psi}{\partial x_1}\nabla^2\psi\right)\right\} \\ &= ik_1 F\left(\frac{\partial\psi}{\partial x_2}\nabla^2\psi\right) - ik_2 F\left(\frac{\partial\psi}{\partial x}\nabla^2\psi\right) \\ &= ik_1 F[F^{-1}(ik_2\hat{\psi})F^{-1}(-k^2\hat{\psi})] - ik_2 F[F^{-1}(ik_1\hat{\psi})F^{-1}(-k^2\hat{\psi})] \end{aligned}$$

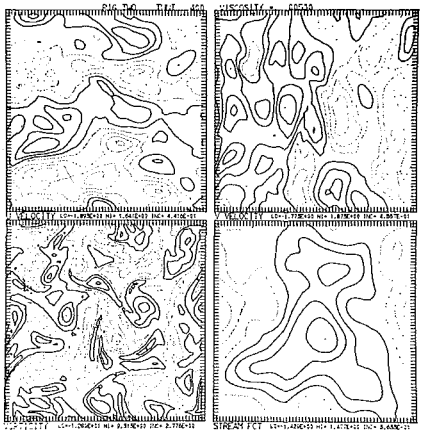

**Fig. 2 Spectral calculation contours at $t = 0.4$ (100 time steps); otherwise the same as Fig. 1**

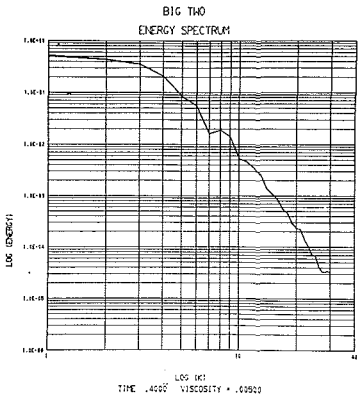


**Fig. 3(*a*) Energy spectrum at $t = 0.4$ for the spherical calculation (see [7] regarding details of spectral computation)**

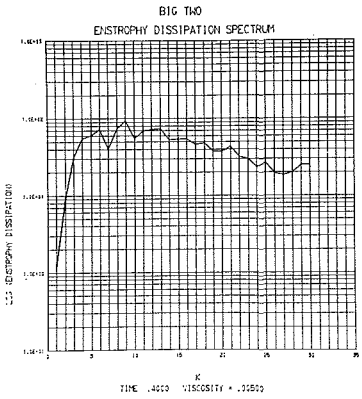


**Fig. 3(*b*) Vorticity gradient squared or enstrophy dissipation spectrum at $t = 0.4$ for the spectral code [7]**

where $F$ indicates a Fourier transform and $F^{-1}$ its inverse transform. It should be noted that calculation of nonlinear products as outlined above will be fully aliased (see Orszag [4, 6] for a discussion of aliasing and its control). This aliasing has been removed in our calculation by essentially repeating the procedure with an $F'$ (a differently phased Fourier transform) such that the sum of $r$ and $r'$ is unaliased (Patterson and Orszag [11]). The solution proceeds by discretizing equation (3.2) as

$$\frac{\hat{\psi}^{n+1}(\mathbf{k}) - \hat{\psi}^{n-1}(\mathbf{k})}{2\Delta t} + \frac{\nu k^2}{2}\left[\hat{\psi}^{n+1}(\mathbf{k}) + \hat{\psi}^{n-1}(\mathbf{k})\right] = r^n(\mathbf{k}) \quad (3.3)$$

and solving for $\hat{\psi}^{n+1}$. This is a so-called leapfrog (centered) treatment of the time derivative and a Crank–Nicholson treatment of the viscous terms. In configuration space a Crank–Nicholson scheme would be fully implicit and require relaxation to implement.

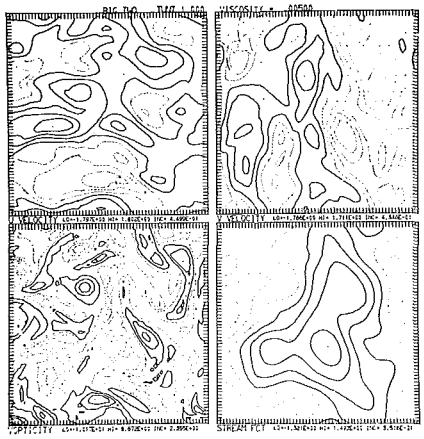

**Fig. 4 Spectral calculation contours at $t = 1.0$**

The boundary conditions are periodic, and there are approximately $64 \times 64$ wave vectors ($K = 32$) included in the calculation. The initial energy spectrum is given by Fig. 1(*b*),

$$E(k) = \frac{2k}{3} e^{-2k/3}$$

where $k = \sqrt{k_1^2 + k_2^2}$ and the viscosity is specified as $\nu = 0.005$. Figs. 2, 3, and 4 show the results of the calculation at time 0.4 (2 and 3) and 1.0 (4). Fig. 2 shows contours of the two velocity components, stream function and vorticity, while Fig. 3 shows the energy spectrum and the enstrophy dissipation spectrum.[3] Fig. 4 shows the contours at a later time.

**Primitive Equations.** The methods we chose for discretizing equations (2.1)–(2.4) follow from work of Lilly [12], Arakawa [13], Harlow and Welch [1], Williams [2], Deardorff [14], and Fox [16]. In the absence of viscosity and buoyancy, integration of equation (2.1) over the physical domain yields

$$\int u_i d \text{ vol.} = \text{const.} \quad (3.4a)$$

since boundary conditions are cyclic. An energy equation (inner product of $u_i$ with equation (2.1) integrated over the same domain) yields

$$\int u_i^2 d \text{ vol.} = \text{const.} \quad (3.4b)$$

as do the buoyancy and buoyancy-variance equations ($B$ times equation (2.3))

$$\int B d \text{ vol.} = \text{const.}, \qquad \int B^2 d \text{ vol.} = \text{const.} \quad (3.4c)$$

In two dimensions, equation (2.5) becomes a scalar equation and yields a class of integrals of the form

$$\int \omega^n d \text{ vol.} = \text{const.} \quad (3.4d)$$

where $n$ is any positive number, indeed any $f(\omega)$ will be conserved. For reasons suggested above, it is essential to preserve these invariants as well as possible by numerical schemes. The Galerkin technique in the preceding section preserves equations (3.4*a*), (3.4*b*), and (3.4*d*) for $n = 0, 1, 2$. This conservation is exact for continuous time and only approximate for the leapfrog time scheme used. In fact, the leapfrog scheme admits a well-known weak instability (Lilly [12]) which can be suppressed by occasional averaging of adjacent time steps. The reason for using the leapfrog method in spite of this is because it is the only one-step technique to our knowledge which has neutral error growth (i.e., neither amplifying nor decaying). The time-step size is adjusted to the maximum value for which results are essentially independent of $\Delta t$. We find that this value is considerably

[3] Enstrophy ($\equiv {}^1/_2\langle\omega^2\rangle$) is conserved in two dimensions so that enstrophy dissipation $\nu\langle(\nabla\omega)^2\rangle$ becomes the relevant driving quantity generated by the decaying turbulence (Batchelor [15]).

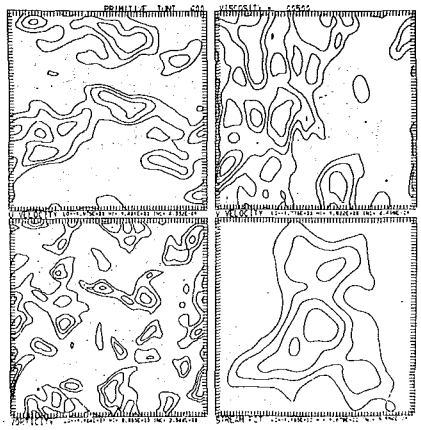

**Fig. 5 Primitive-equations (3.5) calculation contours at $t = 0.4$**

smaller than the maximum value allowable to maintain computational stability and energy semi-conservation. The leapfrog time scheme is used for all our problems.

The most difficult task facing the numerical modeler in fluid dynamics is finding the proper way of handling the nonlinear terms. In order to treat these with a minimum of truncation error, we stagger the finite-difference mesh points on which the dependent variables are defined. In two dimensions [$u_i = (u, v)$] this becomes

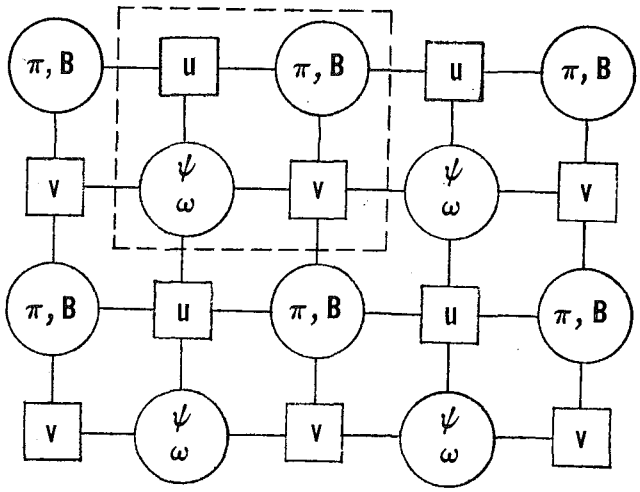


where all the variables within the dashed-line square are designated by the discrete coordinates of the pressure buoyancy points, i.e., $x = I\Delta x$, $y = J\Delta y$.

Using a finite-difference operator notation of the form

$$\delta_x A = \frac{A(x + \Delta x/2) - A(x - \Delta x/2)}{\Delta x}$$

$$\bar{A}^x = \frac{A(x + \Delta x/2) + A(x - \Delta x/2)}{2}$$

the nonlinear portions of equation (2.1) for $u$ can be discretized as

$$\overline{\bar{u}^x \delta_x u}^x + \overline{\bar{v}^x \delta_y u}^y \equiv \delta_x \overline{u^2}^x + \delta_y(\bar{v}^x \bar{u}^y) \tag{3.5a}$$

with the equivalent expression for the same terms in $v$,

$$\overline{\bar{u}^y \delta_x v}^x + \overline{\bar{v}^y \delta_y v}^y \equiv \delta_x(\bar{v}^x \bar{u}^y) + \delta_y \overline{v^2}^y \tag{3.5b}$$

Lilly [17] has shown that this system and an equivalent system for buoyancy variables conserve equations (3.4*a*, *b*, *c*, *d*). It does not, in general, conserve equation (3.4*d*) for $n > 1$.

Treatment of the viscous terms ($\nu\nabla^2 u_i$, $\kappa\nabla^2 B$) in equations (2.1) and (2.3) requires some care. A centered (leapfrog) time

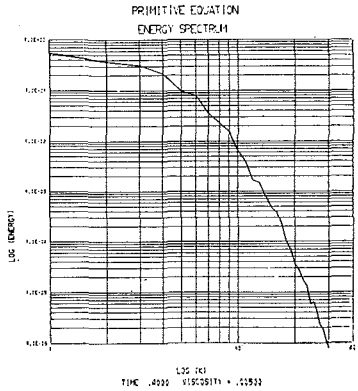


**Fig. 6(*a*) Energy spectrum from primitive-equation calculation at $t = 0.4$**

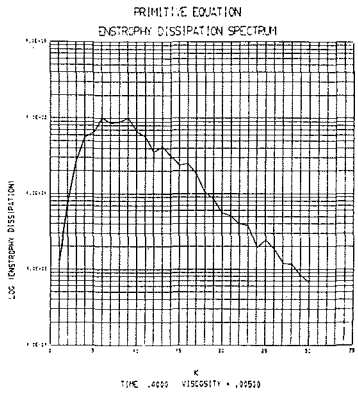


**Fig. 6(*b*) Enstrophy dissipation spectrum from primitive-equation calculation at $t = 0.4$**

difference coupled with the viscous terms is unstable. (This is a well-known instability of parabolic equations.) To correct this, various techniques have been developed. One popular scheme is to use a Dufort–Frankel [18] difference so that $\nu\nabla^2 u^n$ is approximated by

$$\frac{\nu}{\Delta^2}[u^n(I + 1, J) + u^n(I - 1, J) + u^n(I, J + 1) + u^n(I, J - 1) - 2u^{n+1}(I, J) - 2u^{n-1}(I, J)]$$

which is easily made explicit. This scheme can become rather complicated if the viscosity coefficient is not constant but is assumed to be a flow-property-dependent function like a nonlinear eddy viscosity (see section IV). For this reason our calculations are generally done by simply lagging the entire term shown in the brackets one time step (i.e., all superscripts become $n - 1$). It has never seemed necessary in our experience to use more involved approximations for the viscous terms although we certainly recognize that for large $\nu$ computations the time-step size limitation on our viscous terms (roughly $\Delta t < (\Delta x)^2/4\nu$) can become quite stringent. In this case a number of implicit and semi-implicit schemes are available and recommended (cf. Israeli [19], Chorin [20]).

The solution of the finite-difference elliptic equation (2.4) can be found in a number of ways. Although the conceptually simplest of these is to use an iteration with either an over-relaxation factor (SOR) or an alternating directional technique to organize and optimize the iteration, it seems for our applications much more efficient to use a direct (exact) method. The method used in the calculations reported here is Hockney's [21]. Essentially this performs a one-dimensional Fourier transform converting the partial difference equation set into a tri-diagonal or nearly tri-diagonal matrix problem. A rather rapid technique for inverting this matrix is included in Hockney's algorithm. On the NCAR CDC-7600 computer, inversion of the finite-

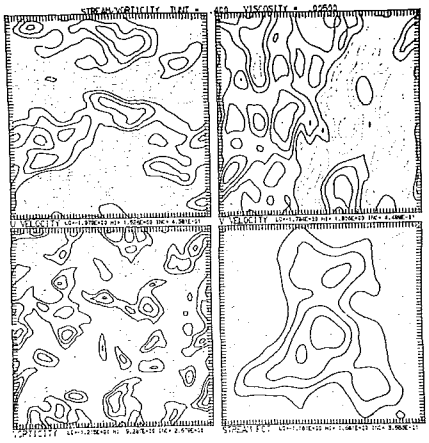

**Fig. 7 Stream-function–vorticity-equations (3.9) calculation contours at $t = 0.4$**

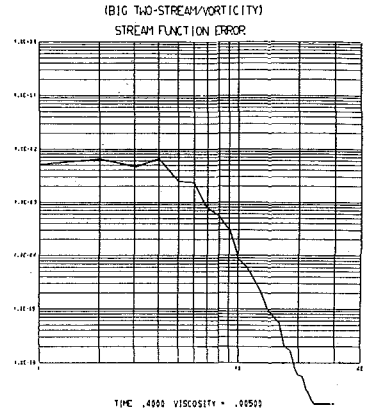


**Fig. 8(a) Error stream-function variance spectrum formed from the field of the spectral stream function minus the finite-difference stream function of Fig. 7**

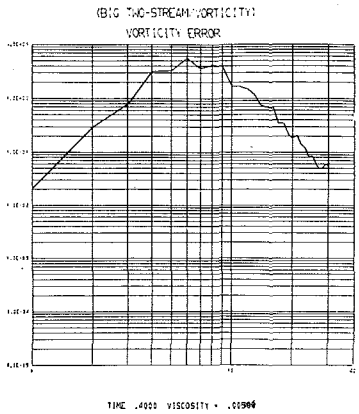


**Fig. 8(b) Error vorticity-variance spectrum formed from the field of the spectral vorticity minus the finite-difference vorticity of Fig. 7**

difference Poisson equation requires less than 0.09 sec for a 64 × 64 array. A complete time step requires 0.175 sec on the same machine.

Results of the computations are shown in Figs. 5 and 6. Fig. 5 shows contours of the velocity stream function and vorticity fields at a time equivalent to Fig. 2 for the spectral calculation, and Fig. 6 presents spectra. As can be easily seen the small scales are somewhat different; however, there is relatively less error in the large scales. The finite-difference calculation is subject to errors due to finite representation of a derivative. Essentially this amounts to introduction of factors like $\sin(k\Delta x)/k\Delta x$ in the differential equations. Thus one expects relatively larger errors at higher wave numbers $k$. This error is such that *it manifests itself most in higher order terms, so one typically* sees a decreased amount of dissipation in the early stages of a finite-difference calculation. The differences between the two calculations will be analyzed in more detail following the next section.

**Stream-Function–Vorticity Equations.** The stream-function–vorticity calculation is performed in essentially the same manner as the primitive-equation calculation. In particular, the only differences are in that we solve one marching equation for the vorticity instead of two for the velocity components. A single Poisson equation for the stream function is inverted. The solution of the Poisson equation and the treatment of time differencing and of viscous terms are done in the same manner in both calculations. Equation (2.5) in two-dimensional flow can be written as

$$\frac{\partial}{\partial t}\omega + J(\omega, \psi) = \nu\nabla^2\omega \tag{3.6}$$

$$\omega = \nabla^2\psi \tag{3.7}$$

where $J(\omega, \psi)$ is the Jacobian of $\omega(x, y)$ and $\psi(x, y)$.

We have compared the results of discretizing the nonlinear terms in three different ways. We have considered the following three types:

Second-Order Centered Differences.

$$J(\omega, \psi) = \delta_x\bar{\omega}^x\delta_y\bar{\psi}^y - \delta_y\bar{\omega}^y\delta_x\bar{\psi}^x \tag{3.8}$$

There was no substantial difference between the results of the second-order centered difference of equation (3.8) and results to be presented later. The discretized version of the Jacobian did not preserve any of the quadratic invariants preserved by the Arakawa Jacobian; however, for the viscous calculation considered here, this did not seem to have much effect on the results. In fact, flow patterns observed for a similar set of initial conditions but with $\nu \equiv 0$ also did not seem to deviate substantially from the Arakawa results. The energy and enstrophy in this inviscid case were increasing with time and aliasing interactions would eventually lead to instability. However, in the short times we observed the flows, only very minor details were not the same as either the Arakawa results or the primitive results.

Arakawa Differencing Schemes. Equations (3.6) and (3.7) also preserve the appropriate invariants in equation (3.4). In particular it can be shown that conservation of vorticity requires

$$\overline{J(\omega, \psi)} = 0$$

conservation of energy requires

$$\overline{\psi J(\omega, \psi)} = 0$$

and conservation of square vorticity (enstrophy) requires

$$\overline{\omega J(\omega, \psi)} = 0$$

where the overbar indicates an average over all space. The following difference scheme due to Arakawa [13] preserves all of these properties:

$$J(\omega, \psi) = \tfrac{1}{3}\Big[(\delta_x\bar{\omega}^x\delta_y\bar{\psi}^y - \delta_x\bar{\psi}^x\delta_y\bar{\omega}^y) + \Big(\delta_x\overline{(\omega\delta_y\bar{\psi}^y)}^x - \delta_y\overline{(\omega\delta_x\bar{\psi}^x)}^y\Big) + \Big(-\delta_x\overline{(\psi\delta_y\bar{\omega}^y)}^x + \delta_y\overline{(\psi\delta_x\bar{\omega}^x)}^y\Big)\Big] \tag{3.9}$$

The first bracketed term in equation (3.9) is just the second-order centered difference of equation (3.8). It only maintains the first of the invariants. The second term conserves vorticity and its square (the first and third invariants) and the last term preserves vorticity and energy (the first and second invariants). The last term can be shown to be exactly equivalent to the discretized nonlinear terms in the primitive equations of the previous section. The averaged Jacobian preserves all three of these invariants.

Fig. 7 shows the results of our computation with the averaged

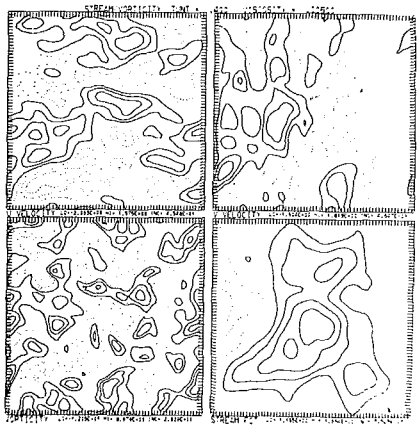

**Fig. 9 Stream-function–vorticity-equations (using fourth-order differencing equation (3.10)) calculation contours at $t = 0.4$**

Jacobian equation (3.9). As we have said (at this point in time for these particular fields), equation (3.8) and (3.9) results are nearly identical. Nor was there substantial difference in the inviscid results between these two cases. Obviously there is little, if any, difference between computations performed with primitive equations and with vorticity–stream-function equations.

Fig. 8 shows a comparison of the difference between the results of the spectral calculation and a calculation using equation (3.9). Plotted in Fig. 8($a$) is the spectrum of the variance of the stream function, and in Fig. 8($b$) the spectrum of the variance of the vorticity. Both are shown at the same time of $t = 0.4$. These spectra are calculated by transforming the physical-space stream function and vorticity into Fourier space, and subtracting them from their spectrally calculated counterparts to produce difference or "error" stream function and vorticity. The spectra are band-averaged over discrete approximations to concentric circles of thickness $|\Delta \mathbf{k}| = 0.5$ and represent

$$\sum_{k-\Delta k}^{k+\Delta k} \psi_e \psi_e^* \quad \text{and} \quad \sum_{k-\Delta k}^{k+\Delta k} \omega_e \omega_e^*$$

where the subscript $e$ denotes the error quantities. Some interpretation of these errors is necessary. First, as we have said, finite-difference errors can be expected to be greatest at the largest values of $k$. The reason these error spectra fall off so rapidly with $k > 10$ is because the spectra of energy ($\sim k^2\psi^2$) and enstrophy ($\sim k^4\psi^2$) themselves fall off very rapidly. Thus, while the difference between two results may be a larger percentage of, say, the mean value as $k$ increases, this mean value itself decreases very sharply. Notice that the finite-difference schemes tend to produce a uniform stream-function error in wave bands 1–4 with maximum errors at $k \approx 2$ and $k \approx 4$, while the vorticity error is concentrated at somewhat higher wave numbers ($k = 6$) with a significant decrease in low-wave-number bands. The time development of these errors is of some interest. The shape of the vorticity error remains about the same and simply grows from a very small (three orders of magnitude smaller) initial value due to the initial truncation error in calculating a vorticity by finite-difference approximations. The stream-function errors first develop the most between wave bands 6 and 10 and the larger wave-number spectrum remains relatively stationary as the errors in the small scales develop. The error spectra for the difference between spectral and second-order Jacobian and between spectral and the primitive equations are very similar to those shown.

**Fourth-Order Centered.** There has been increasing discussion of late concerning the accuracy and utility of using fourth-order differences (i.e., approximations of the derivatives in which errors up to the fourth order in the grid interval are not present). The centered fourth-order scheme can be written as

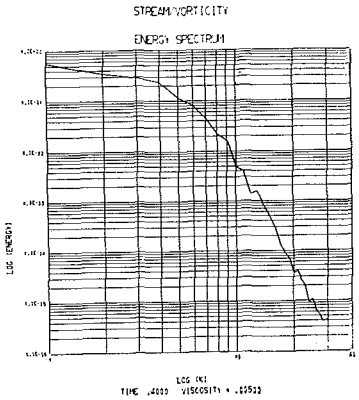


**Fig. 10($a$) Energy spectrum for calculation shown in Fig. 9**

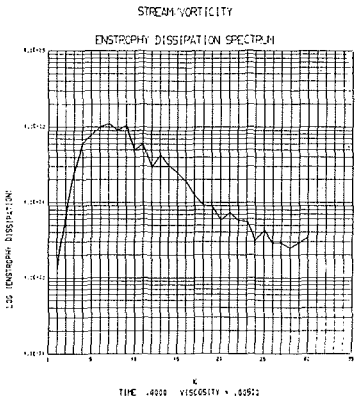


**Fig. 10($b$) Enstrophy dissipation spectrum for calculation shown in Fig. 9**

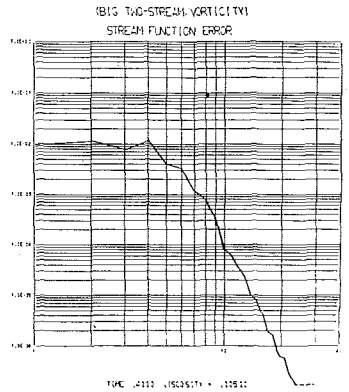


**Fig. 11($a$) Error stream-function variance spectrum from spectral stream function minus finite-difference (fourth-order) stream function of Fig. 9**

$$J(\omega, \psi) = \tfrac{4}{3}\,[\delta_x \bar{\omega}^x \delta_y \bar{\psi}^y - \delta_y \bar{\omega}^y \delta_x \bar{\psi}^x]$$

$$- \tfrac{1}{3}\,[\delta_{2x} \bar{\omega}^{2x} \delta_{2y} \bar{\psi}^{2y} - \delta_{2y} \bar{\omega}^{2y} \delta_{2x} \bar{\psi}^{2x}] \quad (3.10)$$

While this scheme neither preserves energy nor enstrophy, it theoretically reduces discretization error substantially. It is, however, quite significant that the fourth-order-scheme results were not at all the same as the spectral-technique results. Figs. 9 and 10 present these results, and Fig. 11 shows error spectra between spectral and the fourth-order results.

In order to establish that the differences between Fig. 2 and Fig. 9 were not due to inaccurate treatment of the viscous terms, we present some results of the inviscid calculation discussed above. Figs. 12 and 13 show the spectral and fourth-order calculations the same time as Figs. 2, 5, 7, and 9. Fig. 14 presents the results of an Arakawa-method, equation (3.9), simula-

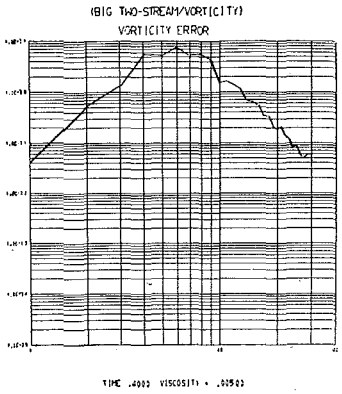


**Fig. 11(b) Error vorticity-variance spectrum from spectral vorticity minus finite-difference (fourth-order) vorticity of Fig. 9**

tion. It is obvious but quite surprising that the fourth-order scheme is no better than the second-order method and far inferior to the spectral calculation. We have no explanation for this behavior.

## iV Extension to Large Reynolds Number (Re)

If the spectra of either energy or enstrophy dissipation obtained from numerical integration of the Navier–Stokes equations exhibit more intensity at the largest wave number $k = \pi/\Delta x$ than at intermediate $k$, then it is apparent that Re is too large for the available numerical resolution. That is, significant amounts of energy are then implied to exist on the subgrid scale. The method of handling this situation involves the problem of turbulence closure.

The governing equations are averaged everywhere over small volumes comparable in size to the grid volume, i.e., the incompressible Navier–Stokes equation (2.1) in flux form becomes

$$\frac{\overline{\partial u_i}}{\partial t} = -\overline{\frac{\partial}{\partial x_j}(u_i u_j)} - \overline{\frac{\partial \pi}{\partial x_i}} + \delta_{i3}\overline{B} + \nu\,\overline{\nabla^2 u_i} \tag{4.1}$$

where the overbar is defined by

$$\bar{u}_i(\mathbf{x}, t) \equiv \frac{1}{\Delta x'\Delta y'\Delta z'} \int_{z-1/2\Delta z'}^{z+1/2\Delta z'} \int_{y-1/2\Delta y'}^{y+1/2\Delta y'} \int_{x-1/2\Delta x'}^{x+1/2\Delta x'} \times u_i(\xi, \eta, \zeta, t)\,d\xi d\eta d\zeta \tag{4.2}$$

where $\Delta x'$, $\Delta y'$, and $\Delta z'$ are averaging increments and $\xi$, $\eta$, $\zeta$ are dummy space variables. Thus, each averaged dependent variable at any point in space is centered within the averaging volume $\Delta x' \cdot \Delta y' \cdot \Delta z'$. Equation (4.2) is equivalent to

$$\bar{u}_i(\mathbf{x}, t) \equiv \frac{1}{\Delta x'\Delta y'\Delta z'} \int_{-1/2\Delta z'}^{1/2\Delta z'} \int_{-1/2\Delta y'}^{1/2\Delta y'} \int_{-1/2\Delta x'}^{1/2\Delta x'} \times u_i(x - \xi, y - \eta, z - \zeta)\,d\xi d\eta d\zeta \tag{4.3}$$

By differentiating both sides of equation (4.3) we see that

$$\frac{\partial \bar{u}_i}{\partial t} = \overline{\frac{\partial u_i}{\partial t}}; \qquad \frac{\partial \bar{u}_i}{\partial x_j} = \overline{\frac{\partial u_i}{\partial x_j}} \tag{4.4}$$

Therefore the averaged Navier–Stokes equation becomes

$$\frac{\partial \bar{u}_i}{\partial t} = -\frac{\partial}{\partial x_j}\overline{(u_i u_j)} - \frac{\partial \bar{\pi}}{\partial x_j} + \delta_{i3}\overline{B} + \nu\nabla^2 \bar{u}_i \tag{4.5}$$

The quantity $\overline{u_i u_j}$ constitutes a set of six additional unknowns, but is usually considered to bear some resemblance to the known quantity $\bar{u}_i\bar{u}_j$. Therefore the former is expressed as

$$\overline{u_i u_j} \equiv \bar{u}_i\bar{u}_j + \overline{(u_i u_j - \bar{u}_i\bar{u}_j)} \tag{4.6}$$

where the second quantity on the right involves the Reynolds stresses and is sometimes abbreviated $\overline{u_i' u_j'}$. However, following Lilly [22], it will not be assumed here that this quantity is the same as $\overline{u_i' u_j'}$, and therefore Reynolds averaging assumptions need not be made. Substitution of equation (4.6) into (4.5) gives us

$$\frac{\partial \bar{u}_i}{\partial t} = -\frac{\partial}{\partial x_j}\bar{u}_i\bar{u}_j - \frac{\partial}{\partial x_j}\overline{(u_i u_j - \bar{u}_i\bar{u}_j)} - \frac{\partial \bar{\pi}}{\partial x_j} + \delta_{i3}\overline{B} + \nu\nabla^2 \bar{u}_i \tag{4.7}$$

Since the calculations are now made with respect to an averaged variable such as $\bar{u}_i$, using $\Delta x' \approx \Delta x$, etc., only insignificant amounts of calculated energy can be expected to spill over onto

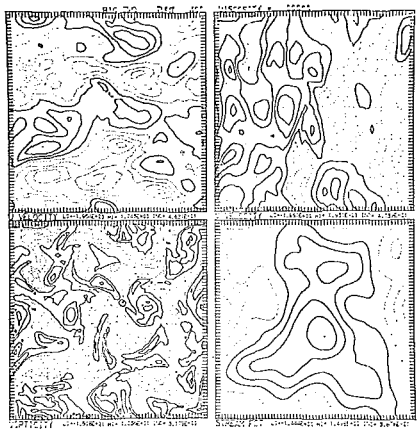

**Fig. 12 Inviscid ($\nu \equiv 0$) spectral calculation contours at $t = 0.4$**

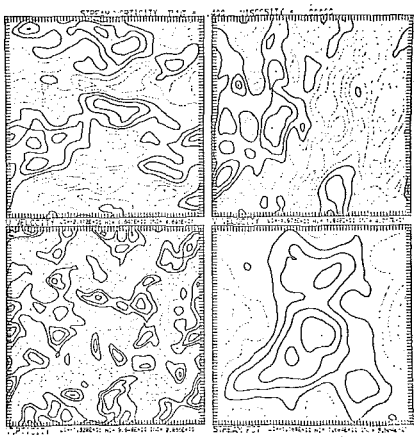

**Fig. 13 Inviscid ($\nu \equiv 0$) fourth-order stream-function–vorticity-equations calculation contours at $t = 0.4$**

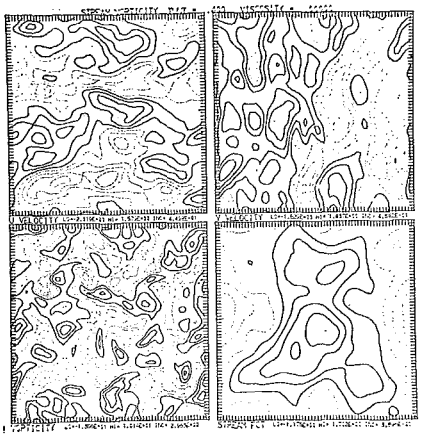

**Fig. 14 Inviscid ($\nu \equiv 0$) Arakawa differencing stream-function–vorticity-equations calculation contours at $t = 0.4$**

the subgrid scale. Therefore, calculated values of $\bar{u}_i$ should exhibit no more small-scale irregularity or truncation error than would $u_i$ in a laminar calculation at small Re.

The turbulence closure problem consists of finding a reasonable approximation to the quantity $\overline{u_i u_j} - \bar{u}_i \bar{u}_j$. The simplest, or first-order, closure approximation which has been frequently used is

$$\overline{u_i u_j} - \bar{u}_i \bar{u}_j = -K_m \left( \frac{\partial \bar{u}_i}{\partial x_j} + \frac{\partial \bar{u}_j}{\partial x_i} \right) \tag{4.8}$$

where $K_m$ is a subgrid-scale eddy coefficient for momentum.

In two dimensions, Leith [23] has shown that, consistent with the inertial cascade and dissipation of enstrophy, $K_m$ should be given by

$$K_m = \gamma_2 \left| \frac{\partial \bar{\omega}}{\partial x_i} \right| (\Delta x)^3 \tag{4.9}$$

where $\gamma_2$ is an as yet undetermined constant. Presumably equation (4.9) is applicable to numerical studies of the large-scale atmospheric or oceanic circulations in which the flow is quasi-two-dimensional.

In three dimensions, Leith [23] has shown that the formulation of Smagorinsky [24] and Lilly [22] is applicable:

$$K_m = \frac{(c\Delta)^2}{2^{1/2}} \left[ \left( \frac{\partial \bar{u}_i}{\partial x_j} + \frac{\partial \bar{u}_j}{\partial x_i} \right) \left( \frac{\partial \bar{u}_i}{\partial x_j} + \frac{\partial \bar{u}_j}{\partial x_i} \right) \right]^{1/2} \tag{4.10}$$

in which $\Delta$ has been defined as

$$\Delta = (\Delta x \Delta y \Delta z)^{1/3} \tag{4.11}$$

The primary purpose of $K_m$ as it occurs in equations (4.7) and (4.8) is to simulate the transfer (removal) of kinetic energy as it cascades from resolvable scales to the subgrid scale. The constant $c$ depends upon the size of the small-scale averaging volume relative to the grid volume. When the two are equal it has been predicted by Lilly [22] to have a value near 0.2. Essentially nothing is yet known about the dependence of $c$ upon the grid ratios $\Delta y/\Delta x$, $\Delta z/\Delta x$ when these differ from unity.

The method above was tested by Deardorff [14] for channel shear-flow turbulence at large Re using $24 \times 14 \times 20$ grid intervals in the respective downstream ($x$), lateral ($y$), and normal ($z$) directions, and using $c = 0.13$ in equation (4.10). The volume treated was of size $3h \times 0.7h \times h$, where $h$ is the channel depth. This volume was translated downstream at approximately the speed of the mean flow. Finite-difference methods were for the most part as recommended by Williams [2]. Results for turbulence intensities, mean flow profile, and velocity correlation functions were surprisingly satisfactory in comparison with measurements of Laufer [25] and Comte-Bellot [26]. However, the limited numerical resolution did not permit eddies on a small scale, or their associated statistics, to be calculated or examined.

The above calculations did not utilize rigid-wall boundary conditions for the tangential velocity components. Instead, conditions were placed on those tangential components located one-half grid interval from the wall and designed to be consistent with the "law of the wall" on the average. Such boundary conditions constitute an assumption because the law of the wall holds only on the average and not at each point in time. It may be mentioned that since this method avoids numerical resolution of the laminar sublayer, and since it is usually found that $K_m \gg \nu$, the molecular term in equation (4.7) is usually neglected altogether.

Similar numerical integrations have been performed for the planetary boundary layer (Deardorff [27, 28]) under conditions of either neutral thermal stability or for various degrees of unstable stratification. In all latter cases it was found that $c = 0.21$ in equation (4.10) gave most realistic results. This value could be extended to the case of neutral stability as well if any overall mean shear at a given level were removed from the velocity deformation in (4.10). However, the validity of the procedure is open to question. One result of numerical interest is the finding (Deardorff [29]) that, for apparently most realistic results,

$$K_h/K_m = 3 \tag{4.12}$$

where $K_h$ is the subgrid eddy coefficient for heat or for a passive scalar.

More recent attempts to apply these methods to problems containing stable stratification have run into serious difficulties. It is found that equation (4.12) gives too much smoothing of the mean thermal structure; yet a significant reduction in the ratio $K_h/K_m$ apparently gives insufficient rate of transfer of thermal variance to the subgrid scale in selected regions. For the subgrid-scale heat fluxes, at least, a more complicated formulation of the nature

$$\overline{u_i T} - \bar{u}_i \bar{T} = -K_{ij} \frac{\partial \bar{T}}{\partial x_j} + \delta_{i3} g \alpha \overline{T'^2} \left( \frac{c' \Delta}{E^{1/2}} \right) \tag{4.13}$$

may therefore be necessary to account for sources of anisotropy. Here $E$ is the subgrid turbulence energy and $c'$ another constant of order unity. For their evaluations, see Lilly [22]. Expression (4.13) is actually a crude approximation to the time-dependent heat-flux equation as has been used recently by Donaldson [30]. When applied to subgrid-scale turbulence, with the grid scale taking the place of an assumed mixing length, that approach becomes the same as Lilly's [22] second-order theory. It might prove necessary to use this approach for all the subgrid Reynolds fluxes and stresses, in which case 10 additional space–time-dependent variables enter into a problem containing thermal effects, and four more for any additional scalar quantity.

Generally speaking, a subgrid-turbulence-closure assumption which may be reasonable for large Re is usually poor at moderately small Re. Therefore, we regard the problem of the onset and development of turbulence in three dimensions at modest Re to be perhaps the most demanding in terms of both theory and computer time. Turbulence occurring at large Re but with stable stratification appears to fall into this same classification of difficulty because the turbulence may then be damped out on resolvable scales but should rightfully appear on the subgrid scale.

## V Lessons from the Past and Prospects for the Future

There is no question that numerical simulation holds a place in science and engineering. As we are all aware, the nature of most realistic physical systems is a nonlinear one. This nonlinearity manifests itself in what might be called "nongenerality." Thus, obtaining a solution for a nonlinear system subject to a set of parameters does not necessarily tell you very much about the same system under a slightly different set of parameters. Therefore one major argument in favor of, say, analysis (meaning analytical solutions of the equations) doesn't really hold for nonlinear systems. Certainly the most successful methods of dealing with nonlinear systems have been statistical and numerical. A major criticism of numerical simulations in the past has been that there has been lacking any guarantee that solutions of the difference equations converge to solutions of the differential equations. While much of this criticism has been valid, the use of Fourier techniques goes a long way toward providing such a guarantee. As our sophistication in performing simulations improves, so does our credibility.

Another related criticism of numerical simulations is that they are literally simulations, namely, they include parameters—indeed parameterized processes—which are adjusted to give the proper results for known situations. In some instances, however, a parameterization may be tested against a well-known situation and the information so obtained used to extrapolate

to a physically more complicated situation. Perhaps the most persuasive argument in favor of this procedure is that it provides some information where none existed before. The final justification of a simulation must come from a careful analysis of each assumption and check of the computer programming, and then careful comparison with available knowledge concerning the problem being simulated.

## Acknowledgment

Cheryl Kingry programmed most of the calculations reported in this work. Her assistance and diligence were an essential part of its completion. The spectral code used herein was developed by Prof. S. A. Orszag of M.I.T. We thank Dr. D. K. Lilly for reading the manuscript and offering many suggestions for its improvement.

## References

1 Harlow, F. W., and Welch, J. E., "Numerical Calculation of Time-Dependent Viscous Incompressible Flow of Fluid with Free Surface," *Phys. Fluids*, Vol. 8, 1965, pp. 2182–2189.

2 Williams, G. P., "Numerical Integration of the Three-Dimensional Navier–Stokes Equations for Incompressible Flow," *J. Fluid Mech.*, Vol. 37, 1969, pp. 727–750.

3 Aziz, K., and Hellums, J. D., "Numerical Solution of the Three-Dimensional Equations of Motion for Laminar Natural Convection," *Phys. Fluids*, Vol. 10, 1967, pp. 314–324.

4 Orszag, S. A., "Numerical Simulation of Incompressible Flows within Simple Boundaries. I. Galerkin (Spectral Representation)," *Studies in Applied Math.*, Vol. 50, 1971, pp. 293–327.

5 Orszag, S. A., "Numerical Methods for the Simulation of Turbulence," *Phys. Fluids*, Suppl. II, 1969, pp. 250–257.

6 Orszag, S. A., "Numerical Simulation of Incompressible Flows within Simple Boundaries. II. Accuracy," *J. Fluid Mech.*, Vol. 49, 1971, pp. 75–112.

7 Fox, D. G., and Orszag, S. A., "Spectral Simulations of Homogeneous Isotropic Two-Dimensional Turbulence," to be published.

8 Orszag, S. A., "Galerkin Approximations to Flows within Slabs, Spheres, and Cylinders," *Phys. Rev. Lett.*, Vol. 26, 1971, pp. 1100–1103.

9 Fox, D. G., and Lilly, D. K., "Numerical Simulation of Turbulent Flows," *Rev. Geophys. & Space Phys.*, Vol. 10, 1972, pp. 51–72.

10 Lilly, D. K., "Numerical Simulation of Developing and Decaying Two-Dimensional Turbulence," *J. Fluid Mech.*, Vol. 45, 1971, pp. 395–415.

11 Patterson, G. S., and Orszag, S. A., "Spectral Calculations of Isotropic Turbulence: Efficient Removal of Aliasing Interactions," *Phys. Fluids*, Vol. 14, 1971, pp. 2538–2541.

12 Lilly, D. K., "On the Computational Stability of Numerical Solutions of Time-Dependent Non-Linear Geophysical Fluid Dynamics Problems," *Mon. Wea. Rev.*, Vol. 93, 1965, pp. 11–26.

13 Arakawa, A., "Computational Design for Long-Term Numerical Integration of the Equations of Fluid Motion: Two-Dimensional Incompressible Flow. Part 1," *J. Comp. Phys.*, Vol. 1, 1966, pp. 119–143.

14 Deardorff, J. W., "A Numerical Study of Three-Dimensional Turbulent Channel Flow at Large Reynolds Numbers," *J. Fluid Mech.*, Vol. 41, 1970, pp. 453–480.

15 Batchelor, G. K., "Computation of the Energy Spectrum in Homogeneous Two-Dimensional Turbulence. High-Speed Computing in Fluid Dynamics," *Phys. Fluids*, Suppl. II, 1969, pp. 223–239.

16 Fox, D. G., "Numerical Simulation of Three-Dimensional, Shape-Preserving Convective Elements," *J. Atmos. Sci.*, Vol. 29, 1972, pp. 322–341.

17 Lilly, D. K., "Numerical Solutions for the Shape-Preserving, Two-Dimensional Thermal Convection Element," *J. Atmos. Sci.*, Vol. 21, 1964, pp. 83–98.

18 Dufort, E. C., and Frankel, S. P., *Stability Conditions in the Numerical Treatment of Parabolic Differential Equations*, Vol. 7, Interscience, New York, N. Y., 1953.

19 Israeli, M., "A Fast Implicit Numerical Method for Time Dependent Viscous Flows," *Studies in Applied Math.*, Vol. 49, 1970, pp. 327–349.

20 Chorin, A. J., "Numerical Solution of Incompressible Flow Problems," *Studies in Num. Anal.*, Vol. 2, 1968, pp. 64–71.

21 Hockney, R. W., *Methods in Computational Physics*, Vol. 9, Academic Press, New York, N. Y., 1971.

22 Lilly, D. K., "The Representation of Small-Scale Turbulence in Numerical Simulation Experiments," in: *Proceedings of the IBM Scientific Computing Symposium on Environmental Sciences*, White Plains, N. Y., 1967, pp. 195–210.

23 Leith, C. E., "Two Dimensional Eddy Viscosity Coefficients," in: *Proceedings of the WMO–IUGG Symposium on Numerical Weather Prediction*, Tokyo, Japan, Nov. 1968.

24 Smagorinsky, J., "General Circulation Experiments with the Primitive Equations. I. The Basic Experiment," *Mon. Wea. Rev.*, Vol. 91, 1963, pp. 99–164.

25 Laufer, J., "Investigation of Turbulent Flow in a Two-Dimensional Channel," NASA Technical Note 2123, 1950.

26 Comte-Bellot, G., "Ecoulement turbulent entre deux parois paralleles," *Publications Scientifiques et Techniques du Ministere de l'Air*, No. 419, 1965.

27 Deardorff, J. W., "A Three-dimensional Numerical Investigation of the Idealized Planetary Boundary Layer," *Geophys. Fluid Dynamics*, Vol. 1, pp. 377–410.

28 Deardorff, J. W., "Numerical Investigation of Neutral and Unstable Planetary Boundary Layers," *J. Atmos. Sci.*, Vol. 29, 1972, pp. 91–115.

29 Deardorff, J. W., "On the Magnitude of the Subgrid Scale Eddy Coefficient," *J. Comp. Physics*, Vol. 7, 1971, pp. 120–133.

30 Donaldson, C. DuP., "Calculations of Turbulent Shear Flows for Atmospheric and Vortex Motions," *AIAA Journal*, Vol. 10, 1972, pp. 4–12.

BARRY L. CLARK[1]
NSF Trainee,
Cornell University,
Ithaca, N. Y.

# A Parametric Study of the Transient Ablation of Teflon

*An analytical and experimental investigation was performed to simultaneously determine 18 ablation heat-transfer parameters for Teflon by the method of nonlinear estimation. A transient one-dimensional ablation model solved numerically was utilized to represent the thermal response of Teflon samples that were instrumented in-depth with thermocouples. The nonlinear estimation computer program was based on a modified version of Marquardt's algorithm. A matching of the predicted and measured temperatures was effected and the results for the parameter values were in accord with available information in the literature. It was concluded that the ablation model accurately predicted the transient thermal response and surface recession of ablating Teflon.*

## Introduction

MANY NEW materials are being created today at an increasing rate, and conventional materials are being subjected to more demanding thermal conditions. Many such examples can be cited in the space program and in cryogenic laboratories. Conventional methods of property evaluation and phenomena investigation consequently often fail to keep pace with the demands placed upon them. The method of nonlinear estimation promises to alleviate some of these problems. Utilizing today's high-speed second- and third-generation digital computers and relatively general experimental designs and analytical models, nonlinear estimation offers its users a rapid, powerful, and economically competitive approach to keep pace with the requirements of the times.

Complex physical systems, even with coupled phenomena, can usually be modeled mathematically to any degree of completeness desired once the physical processes are identified. With fast digital computers, solution of such models becomes a practical reality. The mathematical model may be sufficiently detailed to describe the phenomena involved, but often it is difficult to find property data in the literature to adequately fit the needs of the model. If this is the case, the complex mathematical model ceases to justify its use. If the phenomena are coupled, it is often impossible to separate properties for conventional experimental determination. Nonlinear estimation offers the experimentalist a simultaneous method of determining properties and at the same time demonstrates if the mathematics correctly describe the phenomena. If the system response is accurately described, then more practical objectives can be satisfied, such as finding optimum operating conditions.

Ablation phenomena are ideal for study by nonlinear estimation. In fact, nonlinear estimation may be the only method to measure properties of materials that are subjected to severe thermal conditions. The transient one-dimensional ablation of Teflon, which melts and depolymerizes when subjected to a severe heat flux, is considered in this investigation. The purpose is to describe, in a rather complete manner, the ablation processes and then simultaneously determine all the parameters of importance experimentally.

## Ablation Analysis

**High-Temperature Behavior of Teflon.** Since the phenomena involved in ablation processes are dependent primarily upon the type of material involved, it would be best to first consider the behavior of Teflon when subjected to various thermal conditions. Polytetrafluoroethylene, herein referred to by one of its trademarks as Teflon (DuPont), is a white, partially crystalline material below 1080 deg R. At this temperature (called $T_m$) Teflon undergoes a phase transition, commonly called the "melting point," where the heat of transition $H_m = 25.2$ Btu/lb$_m$. Above $T_m$, Teflon is clear and amorphous [1].[2] It should be pointed out that molten Teflon is not particularly fluid, as the viscosity remains very high. The author [2] applied a simple melting-ablation theory to estimate the lateral flow of Teflon when subjected to stagnation-point ablative environments typical of the conditions in the experiments and found that the lateral velocity was several orders of magnitude (perhaps 9) less than the ablation velocity. It is therefore concluded that no treatment of the flow of molten Teflon is necessary. However, the effect of the melt plane on the temperature distribution must

[1] Presently, Mechanical Engineer, Naval Weapons Laboratory, Dahlgren, Va.

Contributed by the Heat Transfer Division of THE AMERICAN SOCIETY OF MECHANICAL ENGINEERS and presented at the AIChE-ASME Heat Transfer Conference, Denver, Colo., August 6–9, 1972. Manuscript received by the Heat Transfer Division May 14, 1971. Paper No. 72-HT-32.

[2] Numbers in brackets designate References at end of paper.

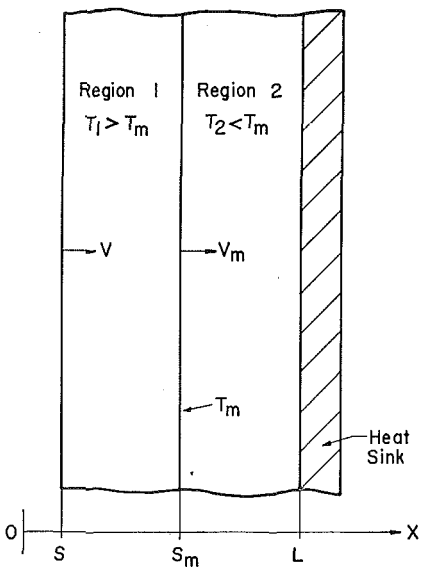


**Fig. 1 Coordinate system for ablation model**

be included since the energy wave and property discontinuity produce a flux discontinuity.

As the temperature of Teflon is raised well above $T_m$, the polymer depolymerizes into a monomer. Whereas the monomer has a very high vapor pressure (e.g., 1 atm at 1585 deg R), the monomer will under most conditions flash directly into vapor. The lumped depolymerization and vaporization processes absorb approximately $H_p \approx 750$ Btu/lb$_m$. Although $H_p$ is essentially a thermodynamic property, under ablative (nonequilibrium) conditions the reaction may be carried out at very high temperatures, and it is possible for some polymers to diffuse through the surface and thus escape before being completely depolymerized. It is possible to take this factor into consideration by estimating $H_p$ parametrically as a function of temperature.

$$H_p = H_{p0} - H_{p1}T \tag{1}$$

The depolymerization of Teflon is generally regarded to be governed by a first-order reaction of the type

$$\dot{w}_{\text{TFE}} = \hat{k}\rho \tag{2}$$

where $\dot{w}_{\text{TFE}}$ is the mass rate of monomer production and $\hat{k}$ is the reaction-rate constant of the Arrhenius form, i.e.,

$$\hat{k} = A_p \exp(-B_p/T) \tag{3}$$

so that

$$\dot{w}_{\text{TFE}} = A_p\rho \exp(-B_p/T) \tag{4}$$

This information can be used to describe the distribution of energy absorbed per unit volume by the action of Teflon depolymerization.

$$Q_p(T) = -\dot{w}_{\text{TFE}}(T)H_p(T) = -A_p\rho H_p(T) \exp(-B_p/T) \tag{5}$$

$Q_p(T)$ will appear as a source term in the heat-transfer equation.

The behavior of the thermal conductivity, specific heat, and density is assumed linear with respect to temperature but with discontinuities at the phase-transition temperature $T_m$. Accordingly, four parameters are required to specify each of the three properties under consideration.

**Mathematical Treatment of the Transient Ablation of Teflon.** With this information about the high-temperature behavior of Teflon, one can now consider the mathematical treatment of the ablation process. A transient one-dimensional ablation model was chosen to represent the thermal response of a Teflon slab exposed to an impinging subsonic argon plasma jet in the stagnation region. The phase transition is represented by a melt plane receding into the material. Thermal expansion is neglected.

Consider a finite slab of Teflon (see Fig. 1) with the exposed surface at $x = s$ receding at the ablation velocity $v$ and the phase transition plane at $x = s_m$ receding at velocity $v_m$. A heat sink is located at $x = L$. The melt plane divides the slab into two regions as shown: Region 1 between $s$ and $s_m$ where $T_1 > T_m$, and Region 2 between $s_m$ and $L$ where $T_2 < T_m$.

The thermal response is governed by one-dimensional Fourier equations, i.e.,

$$\frac{\partial}{\partial x}\left(k\frac{\partial T_1}{\partial x}\right) + Q_p(T_1) = \rho c\frac{\partial T_1}{\partial t} \tag{6}$$

$$\frac{\partial}{\partial x}\left(k\frac{\partial T_2}{\partial x}\right) = \rho c\frac{\partial T_2}{\partial t} \tag{7}$$

The sink term is negligibly small in Region 2, since $T_2 < T_m$, and is deleted. The total mass rate of production of gaseous products is obtained by integrating equation (4) over Region 1 where all appreciable depolymerization occurs.

$$\dot{m}_{\text{TFE}}(t) = \int_{s(t)}^{s_m(t)} \dot{w}_{\text{TFE}}dx = A_p\int_s^{s_m} \rho(x', t) \exp[-B_p/T_1(x', t)]dx' \tag{8}$$

## Nomenclature

$A_p, B_p$ = Arrhenius constants, sec$^{-1}$, deg R
$c$ = specific heat, Btu/lb$_m$-deg R
$C_{\text{hs}}$ = volumetric specific heat of heat sink, Btu/ft$^3$-deg R
$E$ = experimental values
$F$ = sum-of-squares function
$h$ = heat-transfer coefficient, lb$_m$/ft$^2$-sec
$H$ = argon enthalpy, Btu/lb$_m$
$H_m$ = heat of transition (or fusion), Btu/lb$_m$
$H_p$ = lumped depolymerization and vaporization energy, Btu/lb$_m$
$H_{p0}, H_{p1}$ = defined by equation (1)
$k$ = thermal conductivity, Btu/ft-sec-deg R
$\hat{k}$ = reaction-rate constant, sec$^{-1}$
$L$ = thickness of ablation sample, ft
$M$ = predicted values
$\dot{m}_{\text{TFE}}$ = mass rate of ablation, lb$_m$/ft$^2$-sec
$P$ = parameters
$q$ = number of parameters
$q_0$ = heat flux, Btu/ft$^2$-sec
$Q_p$ = depolymerization energy per unit volume, Btu/ft$^3$
$R_1, R_2$ = stretching factors, equation (25)
$s$ = ablation surface location, ft
$s_m$ = phase-transition-plane location, ft
$t$ = time, sec
$T$ = temperature, deg R
$T_m$ = phase-transition temperature, deg R
$v$ = ablation velocity, ft/sec
$v_m$ = phase-transition velocity, ft/sec
$\dot{w}$ = mass rate of production of products, lb$_m$/ft$^3$-sec
$x$ = spatial coordinate, ft
$\delta$ = region size, ft
$\epsilon$ = emissivity
$\eta$ = mass-transfer cooling coefficient
$\xi$ = transformed spatial coordinate, equation (25)
$\rho$ = density, lb$_m$/ft$^3$
$\sigma$ = Stefan–Boltzmann constant, $4.761 \times 10^{-13}$ Btu/ft$^2$-sec-deg R$^4$
$\psi$ = transformed spatial coordinate, equations (23) and (24)

**Subscripts**

$m$ = at the phase transition
TFE = tetrafluoroethylene
1, 2 = regions, see Fig. 1

To obtain an expression for the ablation-surface location, an arbitrary definition of this surface must be made, since there does not exist a clearly discernible interface between a solid and a gas, but only a gradual transition from a solid polymer to a gaseous monomer. The use of a simple mass balance provides a reasonable and direct approach to this situation. By defining the surface recession rate $v(t)$ by the relation

$$\rho_{\text{ref}} v(t) \equiv \dot{m}_{\text{TFE}}(t) \tag{9}$$

the surface location after a specified time can be obtained from

$$s(t) = \int_0^t v(t')dt' \tag{10}$$

where

$$v(t) = \int_s^{s_m} A_p \frac{\rho}{\rho_{\text{ref}}} \exp(-B_p/T_1)dx' \tag{11}$$

and $\rho_{\text{ref}}$ is some parametric reference density to be determined. An alternate approach might be to define the surface as that plane at which the fraction of material depolymerized is some specified arbitrary value.

The expression for the phase-transition velocity is obtained from an energy balance at $x = s_m$.

$$\left(-k\frac{\partial T_1}{\partial x}\right)_{s_m} - \left(-k\frac{\partial T_2}{\partial x}\right)_{s_m} = \rho_m H_m v_m(t) \tag{12}$$

where

$$\rho_m \equiv (\rho_{m1} + \rho_{m2})/2 \tag{13}$$

and so

$$s_m(t) = \int_0^t v_m(t')dt' \tag{14}$$

The flux boundary condition at the exposed surface $x = s$ is

$$\left(-k\frac{\partial T_1}{\partial x}\right)_s = h(H_e - H_s) - \sigma\epsilon T_s^4 - \dot{m}_{\text{TFE}}[\eta(H_e - H_s) - c_s T_s] \tag{15}$$

where the combined convective–radiative heat-transfer coefficient $h$ is defined in terms of the total applied heat flux $q_0$ and the enthalpy difference $H_e - H_s$ between the adiabatic and nonadiabatic wall. The term $\sigma\epsilon T_s^4$, the re-radiation from the surface $x = s$, is usually negligible compared to $q_0$. The ablation term, proportional to the total depolymerization rate $\dot{m}_{\text{TFE}}$, contains the mass-transfer cooling effect (where $\eta$ is the heat-blocking coefficient) and the energy stored in the ablated material. For a laminar boundary layer the factor $\eta$ is generally considered a function of the molecular-weight ratio of the decomposition products and the boundary-layer gases.

The boundary condition at the phase transition $x = s_m$ is simply the definition

$$T_1(s_m, t) = T_2(s_m, t) \equiv T_m \tag{16}$$

The thermal diffusivity of the heat sink is considered to be sufficiently high, relative to that of Teflon, as to be infinite. Therefore no conduction equation for the heat sink is required and the temperature of the heat sink is a constant, the same as that of the Teflon at $x = L$. An energy balance on the heat sink then furnishes the last boundary condition

$$\left(-k\frac{\partial T_2}{\partial x}\right)_L = C_{\text{hs}}\left(\frac{\partial T_2}{\partial t}\right)_L \tag{17}$$

The initial conditions are a prescribed initial temperature profile

$$T_2(x, 0) = T_i(x) < T_m \tag{18}$$

and no initial melting or ablation

$$v(0) = v_m(0) = s(0) = s_m(0) = 0 \tag{19}$$

Since Region 1 does not initially exist, one must consider the conditions prior to the establishment of the melt layer. At time $t = 0+$, the surface $x = 0$ is exposed to the applied flux and initial heating is governed by the boundary condition

$$\left(-k\frac{\partial T_2}{\partial x}\right)_{x=0} = q_0 - \sigma\epsilon T_{2_{x=0}}^4 \tag{20}$$

until such time (say $t_m$) that the melt temperature $T_m$ is attained at the surface. At that instant the boundary condition changes to

$$T_2(0, t_m) = T_m \tag{21}$$

and the surface energy balance can be solved for the initial melting velocity

$$v_m(t_m) = \frac{1}{\rho_{m2} H_m}\left[q_0 - \sigma\epsilon T_m^4 - \left(-k\frac{\partial T_2}{\partial x}\right)_0\right] \tag{22}$$

The value of $v_m(t_m)$ is usually very large because the phase-transition plane "sees" the applied flux $q_0$ as a driving force instead of as merely the difference in conductive flux. Once a finite thickness $s_m$ is realized, then the regular equations apply.

The main difficulty in obtaining a reasonable analytical solution to this set of equations is the appearance of several nonlinear features. Besides the apparent nonlinearities of the energy-absorption term and temperature-variable properties, additional nonlinearities are concealed in the moving boundaries. The moving boundaries can be eliminated under the transformations for Region 1, $s(t) \leq x \leq s_m(t)$

$$\psi_1 = \frac{x - s}{\delta_1} \qquad \delta_1 = s_m - s \tag{23}$$

and for Region 2, $s_m(t) \leq x \leq L$

$$\psi_2 = \frac{x - s_m}{\delta_2} \qquad \delta_2 = L - s_m \tag{24}$$

The nonlinearity of the moving boundaries becomes evident now by the appearance of additional terms in the heat-transfer equation. For example, equation (6) becomes

$$\frac{1}{\delta_1^2}\frac{\partial}{\partial \psi_1}\left(k\frac{\partial T_1}{\partial \psi_1}\right) + \rho c\left[\frac{v(1 - \psi_1) + v_m\psi_1}{\delta_1}\right]\frac{\partial T_1}{\partial \psi_1} - A_p\rho H_p(T_1)\exp(-B_p/T_1) = \rho c\frac{\partial T_1}{\partial t}$$

**Numerical Solution.** A numerical approach provides a direct modus operandi for the solution of this set of equations. An implicit finite-difference approximation of the type suggested by Crank and Nicolson [3] was originally tried in an attempt to take advantage of the inherent stability and efficiency of that method over the explicit method. This attempt failed, however, due to a boundary-condition instability that the Crank–Nicolson scheme was unable to alleviate. Since short time increments were required to satisfy the boundary instability, it was therefore felt that an explicit finite-difference method, if it could be effected economically, would be the best approach.

Another transformation was first applied to the equations to provide more grid points in the regions of higher gradients, i.e., near the outer surfaces of each region. The stretching transformations are given implicitly as

$$\psi_j = \frac{2\xi_j + (R_j - 1)\xi_j^2}{R_j + 1} \qquad j = 1, 2 \tag{25}$$

where $R_1$ and $R_2$ are the stretching factors for Regions 1 and 2

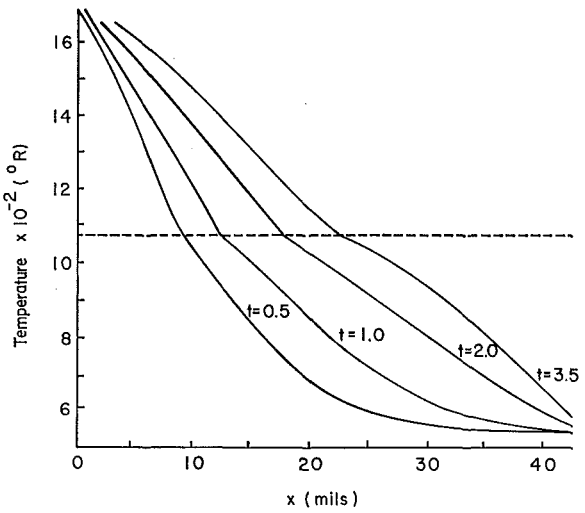


**Fig. 2 Typical predicted temperature distributions of prescribed times for transient ablation**

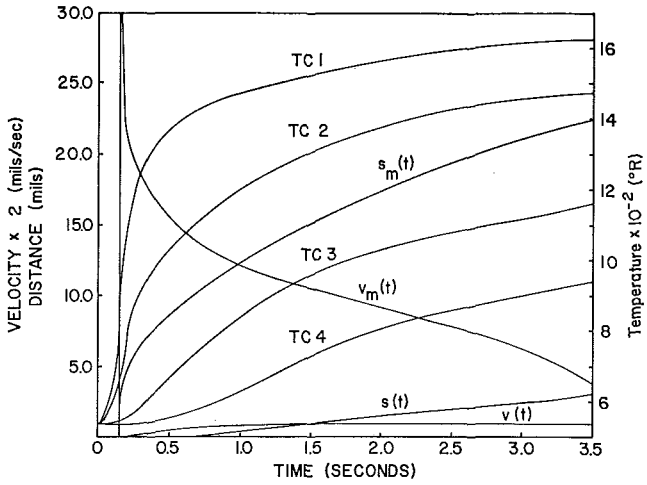


**Fig. 3 Typical solution for the velocities and locations of the ablation and melting surfaces and predicted thermocouple response**

respectively. The complete set of equations in the transformed variables is reproduced in the Appendix.

The equations for each region are of the form

$$A\frac{\partial}{\partial\xi}\left(D\frac{\partial T}{\partial\xi}\right)+B\frac{\partial T}{\partial\xi}+Q=C\frac{\partial T}{\partial t}$$

When one divides the region into $n-1$ equal sections of length $\Delta\xi$, the coordinate $\xi$ at the $i$th grid point is

$$\xi_i=(i-1)/(n-1)$$

and

$$\Delta\xi=1/(n-1)$$

The first (conduction) term, now written in conservative form, was approximated by centered differences, and the second (ablation) term and fourth (storage) term by forward differences. This arrangement was implemented to avoid unnecessary and costly stability requirements. Letting the prime denote values at time $t+\Delta t$, the finite-difference approximation for the equation above is then simply

$$T_i'=U_iT_i+V_iT_{i+1}+W_iT_{i-1}+Q_i\Delta t/C_i$$

where

$$U_i=1-(n-1)\Delta t[(n-1)A_i(D_{i+1}+D_{i-1})/2-B_i]/C_i$$

$$V_i=(n-1)\Delta t(A_iD_{i+1}/2+B_i)/C_i$$

$$W_i=(n-1)^2\Delta tA_iD_{i-1}/2C_i$$

The exponential term, given explicitly, posed no unusual problems. The flux boundary condition at $x=s$ was treated by using equation (15) to generate a fictitious temperature outside the boundary for use in the finite-difference equation for $i=1$. Equation (11) for $v(t)$ was integrated assuming a linear temperature distribution between adjacent grid points. Backward and forward temperature differences for Regions 1 and 2 were used to calculate the fluxes required to compute $v_m(t)$ in equation (12).

The criterion for stability was based on the condition that the solution at time $t+\Delta t$ should be a weighted spatial average of the solution at time $t$. The only requirement is that the weighting factors be non-negative and bounded, a condition that yielded information about the maximum permissible time step.

$$\Delta t\leq\min_{i=1,n}\left\{\frac{C_i}{(n-1)[(n-1)A_i(D_{i+1}+D_{i-1})/2+B_i]}\right\}$$

As mentioned previously, the boundary condition at the exposed surface proved very troublesome from a stability standpoint. The principal difficulty arises due to the strong exponential coupling between the flux boundary condition, with its corresponding effect on the temperature field, and the ablation rate $\dot{m}_{\mathrm{TFE}}$, which is a function of that temperature field. If the time increments were too large, an unstable oscillatory coupling of the ablation rate and temperature field developed. Various implicit methods, which in effect introduce algebraic damping, were found to be impotent against the exponential strength of the instability. A criterion was found [2] that eliminated the instability, but the required time increments were not large enough to warrant the use of implicit methods. No noticeable effect, however, was observed on the amount of calculation needed by the explicit method upon introduction of this criterion.

The criterion was based on the supposition that as the computation proceeds through time and the steady state is being approached, the surface temperature (indeed the whole temperature field) should be changing at a decreasing rate, thus disallowing any growing unstable behavior. It was found that if, for point 1 of Region 1, one requires

$$|T_1(t+\Delta t)-T_1(t)|\leq|T_1(t)-T_1(t-\Delta t)|=|\Delta T_{\mathrm{old}}|$$

then

$$\Delta t\leq\frac{C_1|\Delta T_{\mathrm{old}}|}{|(n_1-1)^2A_1D_1(T_0+T_2-2T_1)/2|}$$

This criterion was found to completely eliminate the coupling instability while imposing no noticeable computation time penalty for the explicit method.

Figures 2 and 3 display the sample results, obtained numerically from the computer program, corresponding to typical conditions encountered in the experimental study. A fictitious ablation sample, of thickness $L=42.5$ mil, was exposed for 3.5 sec to a "cold-wall" heat flux $q_0=100$ Btu/ft²-sec (with $H_e=2000$ Btu/lb$_m$ and $h=0.05$ lb$_m$/ft²-sec). Four thermocouples, labeled TC 1 to TC 4, are located at $x=5$, 10, 20, and 30 mil, respectively, and register an initial temperature of 540 deg R. The parameter values used here were obtained from the best data available in the literature for Teflon.

Figure 2 displays temperature distributions at times 0.5, 1.0, 2.0, and 3.5 sec. Notice the aforementioned "kinks" in the distributions at the phase-transition plane ($T=1080$ deg R). They are sharper near the origin $t=0$ when the higher difference in gradient across the melt plane gives rise to a higher value of $v_m(t)$ [see equation (12)]. This is evident from Fig. 3, showing the melting and ablation velocities, because the melt plane travels slower as it recedes farther from the outer surface. Recall also that the initial melting velocity at $t=t_m$ [equation (22)] is very high due to the fact that the melt plane "sees" the applied flux $q_0$ at the exposed surface. The ablation velocity, on the other

hand, increases gradually as the temperature in Region 1 increases, and approaches an almost constant value, increasing only slightly as the temperature penetration slowly reduces the gradient under the surface at $x = s$. If the medium and time were infinite ($L$ and $t \rightarrow \infty$) and the quasi steady state were obtained, then $v(t)$ and $v_m(t)$ would be equal. Perhaps their values might be a good indication of how closely one approaches this condition. Figure 3 also indicates the time integrations of the velocities, i.e., the surface locations. Notice the sharp rise in melt-layer thickness due to the high initial melting rate. Included in Fig. 3 is the theoretical response for the four embedded thermocouples. Thermocouple response is the actual part of the solution used for comparison with the experimental data, and therefore plays a most important role. Although not occurring in this situation, it is also possible for the exposed surface $x = s$ to pass a thermocouple location, thus exposing the thermocouple to the hot gases. When this occurs, the thermocouple is immediately destroyed.

The finite-difference approximation for the transformed equations and boundary conditions can be found in reference [2] along with the development of the stability criteria and FORTRAN IV computer-program listing.

## Nonlinear Estimation

Nonlinear estimation (NLE) is a procedure for calculating the parameters that appear in a mathematical model hypothesized for a physical process. The approach of NLE is to minimize, in a least-squares sense, the difference between the experimental and theoretical system response. NLE requires, therefore, experimental observations and the mathematical model, in solution form, as input. Used as a statistical tool, NLE has been found to be a powerful and extremely useful method for the combined study of properties and model identification. It is basically a method used for the experimental determination of parametric properties. NLE, however, is not subject to many of the restrictions commonly placed upon conventional property-measuring methods, and, as such, can be considered to be the most general of all available methods.

The method of NLE seeks to minimize the sum-of-squares error function $F$, defined as

$$F = \sum_{j=1}^{m} (E_j - M_j)^2$$

in such a way as to determine selected parameters of the mathematical model. The $E_j$ are a set of measured or experimental values of the dependent variable(s) taken at $m$ various selected discrete values of the independent variable(s), and the $M_j$ are the corresponding set of analytically predicted dependent variables. Since the model is an analytical conception of a physical process, it is a function of a set of $q$ parameters as well as the independent variables, i.e.,

$$M = M(X_1, X_2, \ldots ; \quad P_1, P_2, \ldots, P_q)$$

If a minimum of $F$ exists in parameter space, then the gradient of $F$ must vanish, i.e.,

$$\frac{\partial F}{\partial P_k} = -2 \sum_{j=1}^{m} \left[ (E_j - M_j) \frac{\partial M_j}{\partial P_k} \right] = 0 \qquad k = 1, 2, \ldots, q$$

These equations represent a set of $q$ nonlinear equations in $q$ unknowns (the $P_k$) where the $M_j$ and $\partial M_j/\partial P_k$ are, in general, nonlinear functions of the $P_k$.

There are a number of iterative numerical methods available for the solution of the nonlinear estimation equations. The classical method, suggested originally by Gauss [5], employs a first-order Taylor series expansion in parameter space to locally linearize the equations. Box and Coutie [6] suggested a steepest-descent method. Marquardt [7] suggested an algorithm that essentially interpolates in an optimum sense between the Taylor method, with its rapid convergence within a limited range of validity, and the steepest-descent method, with its guaranteed convergence. A modified version of this algorithm was used in this investigation.

Lapidus and Peterson [8] suggested a method called "cyclic parameter estimation," a simple method of grouping parameters for separate estimation which proved extremely valuable for the simultaneous estimation of many parameters. Pfahl [9], in an excellent state-of-the-art paper, presented a new measurement of convergence, called $T_{\text{norm}}$, which was quite useful in determining when the NLE procedure had reached a point where the iterations could be terminated. Box and Lucas [10] provided suggestions for the optimum design of the experiment for determination of the parameters. The author [2] developed a method to estimate the maximum error that one might expect for the parameters after the application of NLE.

The modified version of Marquardt's algorithm, with the equations and discussion of the various aspects of nonlinear estimation as related to this problem, and the FORTRAN IV computer programs and description are found in reference [2].

## Experiments

**Test Facilities.** A plasma-arc jet, originally built by Avco RAD, was used as a heat source for the experimental simulation of heat fluxes of the severity necessary for ablation studies. The arc is classified as a stick-and-cylinder configuration where the cathode (the "stick") is made of thoriated tungsten and the anode (the "cylinder") is made of copper and is water-cooled. The plasma arc produces a subsonic laminar free atmospheric jet of lightly ionized argon and is useful for simulating a high-pressure ballistic-missile environment. The arc is powered by a 20-kw motor–generator set capable of supplying more than 900 amp. The arc is started by imposing a high-frequency voltage across the electrodes, causing the argon to ionize and thus complete the circuit. Once started, the Joulean heating of the argon maintains the ionization level and the high-frequency unit shuts off automatically. The arc is extinguished with a simple remotely activated shorting circuit.

The heat flux applied to the ablation sample was measured using a water-cooled guarded-ring copper calorimeter. Once the heat flux is determined, knowing the enthalpy from an energy balance of the arc, one can infer the value of the combined convective and radiative heat-transfer coefficient. The value of $h$ calculated from the calorimeter, however, is only approximate (within 20 percent), and this value is used only as an initial guess in the nonlinear-estimation calculations.

The calorimeter is mounted on a motorized table that can be moved into and out of position as required by remote control. After steady-state operation of the arc is achieved and heat-flux measurements taken, the sample is dropped into place by a guillotine device. This is simply a gravity-driven sample holder dropped between two grooved uprights and controlled remotely by a choke cable. A microswitch on the sample dropping mechanism signals the recorder that a test has begun.

**Sample Design and Construction.** A transient-ablation test was required in order to estimate all the parameters for Teflon ablation heat transfer. Since quasi-steady ablation is realized very quickly for Teflon, very short testing times (less than 5 sec) were necessary. In order to achieve good thermal penetration in such a short time, the ablation samples had to be rather thin (say of the order of 50 mil). Parameter-correlation considerations also dictate that the thermocouples be located close together and near flux boundary conditions. The practical considerations of sample construction seemed best served by locating 1-mil thermocouples 5 or 10 mil apart.

The manufacture of the samples was conceived as a sandwich construction where layers of Teflon are stacked up with thermocouples located between the layers. The Teflon layers were cut from DuPont Teflon tape of two thicknesses (5 and 10 mil).

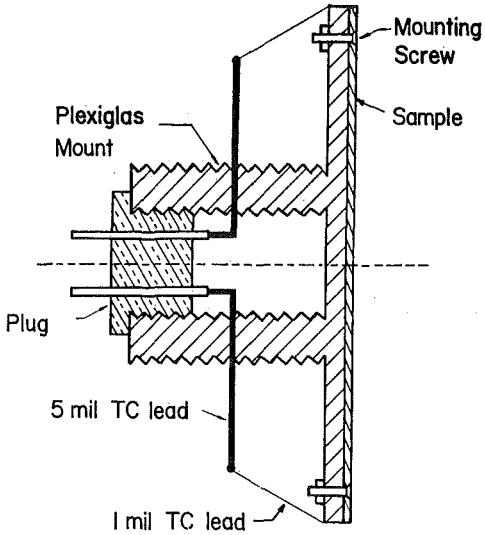


Fig. 4 Sample assembly

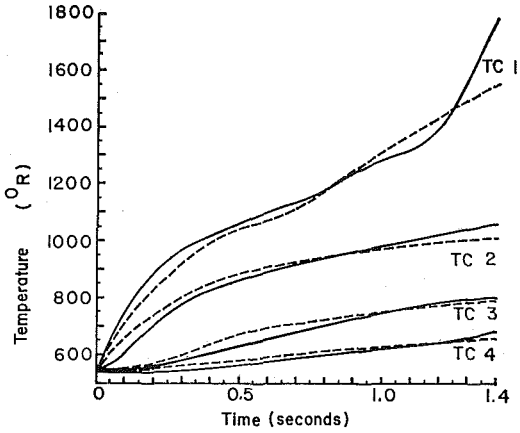


Fig. 5 Comparison of experimental and predicted thermocouple response

The heat sinks were cut from stainless-steel shim stock. The total diameter of the samples, 2.5 in., was more than sufficient to insure one-dimensional heat transfer.

The layers of Teflon, with 1-mil chromel–alumel thermocouples placed in between, were molded together under high temperature and moderate pressure in a compression cell. The compression cell with the sample was placed in an oven and the cell temperature monitored until the Teflon temperature was above the melting point (about 700 deg F). The cell and sample were then removed from the oven and quenched in water. A sample of continuous Teflon was produced and the layers became indistinguishable. Very little change in sample thickness was observed. The stainless-steel heat sink was cemented to the sample back with a special epoxy, Chemplast high-temperature grade (fluorocarbon-based) epoxy. This epoxy is rated at 700 deg F for short durations and no failure of this epoxy was encountered during any of the ablation tests. The layer of epoxy was generally less than 1 mil thick.

The thermocouples were staggered over an area $^1/_8$ in. in diameter (an arbitrarily selected area) so that no thermocouple was directly beneath another one. It was noted that the thermocouple bead tended to center itself perfectly between the two adjacent Teflon layers. The Teflon simply yielded and flowed around the bead and wire in such a way that each bead penetrated the two layers equally. The location of the thermocouple bead could therefore be assumed to be centered between the layers, thus insuring the accurate positioning of the thermocouple. It is also felt that this method produced a very intimate contact between the thermocouple and the adjacent Teflon, thus insuring low thermal-contact resistance and good thermocouple response. The thermocouple wires had an angular spacing of about 10 deg.

The sample was then bolted to a $^1/_8$-in-thick Plexiglas disk to provide mechanical support and hold the sample flat (see Fig. 4). Attached to the back of the disk was a Plexiglas mount designed to protect the delicate thermocouple wires and to serve as a mount and wire conduit. The entire assembly was then screwed into the guillotine sample holder and plugged into the recording system ready for testing.

The problem of sensor disturbance was studied to determine if the perturbation of the thermocouple on the temperature field it was trying to measure was serious. Such a disturbance can occur when the thermocouple thermal properties differ greatly from the surrounding material, as in this situation. Pfahl [11] investigated the case of a sensor placed parallel to the heated surface, and the use of his analysis indicated that no serious temperature perturbations could be expected for this sample design. The thermocouple recording equipment had to have a fast response and a relatively high and variable sensitivity. This requirement was well satisfied with the use of a calibrated four-channel Beckman Offner Type R dynograph.

## Results

This section summarizes the results of the application of NLE to the ablation model discussed previously and the experimental results. A total of 20 samples, 19 of the author's (with a range in heat flux of 28.73 to 342 Btu/ft$^2$) plus a data set obtained from Avco Space Systems, were studied. Approximately 25 hr of computer time on Cornell University's IBM Systems 360/65 was consumed in this study. The thermal-matching and parameter results for each sample can be found in reference [2]. The parameter results in the following paragraphs represent averages over all the samples. Upper and lower root-mean-square values were also calculated to give an idea of the spread and bias of the results. The 18 parameters estimated are thermal conductivity, specific heat, and density, each at temperatures of 532, 1080 (crystalline), 1080 (amorphous), and 1600 deg R, the Arrhenius constants $A_p$ and $B_p$, the depolymerization energy parameters $H_{p0}$ and $H_{p1}$, the mass-transfer cooling coefficient $\eta$, and the heat-transfer coefficient in the absence of mass transfer $h$.

**Thermal-Matching Results.** The achievement of a close match between the experimental and predicted thermocouple responses was a prime objective in this investigation. Figure 5 shows the thermal-matching results for a typical sample with a cold-wall heat flux of 68.45 Btu/ft$^2$-sec, an arc enthalpy of 1773 Btu/lb$_m$, and a thickness of 40 mil. The thermocouples were located at 5, 10, 20, and 30 mil for TC 1 through TC 4 respectively. The test duration was 1.4 sec. The solid lines represent the experimental results and the dashed lines represent the best fit obtained.

In general the first thermocouple (closest to the exposed surface) was the most difficult to fit. This of course is only natural since this thermocouple undergoes the most severe gradients and transients and achieves the highest temperatures compared with the other thermocouples with more material protection. The thermocouples that were ablated away display a characteristic "tail" (a rapid upward time response) in the experimental response that could not be described by the ablation model. However, the graph illustrates the relatively good fit of the predicted response to the experimental data.

**Arrhenius Constants.** The exponential form of the reaction rate, given by equation (3), dictates a strong temperature-dependence. It remains difficult, however, to determine both $A_p$ and $B_p$ from one ablation test. The reason for this stems from the fact that Teflon depolymerization takes place in such a relatively narrow temperature range under ablation conditions that the temperature-dependence of the reaction rate is difficult to resolve. The classical method of obtaining kinetic parameters is by vacuum pyrolysis in a thermogravimetric apparatus, a situation much

different than the severe transient condition encountered here. There is, however, an apparently unresolved data spread in the literature (see Table 1) and all the values for $A_p$ and $B_p$, as predicted by the application of nonlinear estimation to the experimental data, are within this range of these values.

**Thermal Conductivity, Specific Heat and Density.** The parametric results for the thermal properties generally conform to the values that might be expected based on prior information available from the literature (see Table 1). It is obvious that few data are available from other sources on the high-temperature behavior of these properties. This can be explained by the difficulty of phenomena isolation encountered by Teflon at these temperatures, and further substantiates the need for nonlinear-estimation studies. The specific-heat results were generally good except for an unexpectedly low value of the specific heat at 532 deg R. The parametric reference (ablation) density was estimated at

$$\rho_{ref} = 120.7 \begin{cases} +20.0 \\ -30.9 \end{cases} \text{lb}_m/\text{ft}^3$$

**Other Parameters.** The linearized parametric-depolymerization-energy results (Table 1) were quite good, as the leading term fell in the middle of the values found in the literature and there are not enough data available for comparison purposes for the temperature-variable term. The mass-transfer cooling coefficient is primarily a function of the ratio of the molecular weights of the boundary-layer gases to the injected gases for laminar boundary layers. All theories found in the literature [26–29] develop formulae of the form

$$\eta = C_1 \left[ \frac{\text{molecular weight of boundary-layer gases}}{\text{molecular weight of injected gases}} \right]^{C_2}$$

It is not possible to infer the values of both $C_1$ and $C_2$ from this study. Comparison with the theoretical values (Table 1) shows very good agreement. The results of the application of NLE to the heat-transfer coefficient were within an average 6.82 percent of the measured values. Since the heat-transfer coefficient varied from one sample to the next according to conditions, the detailed results for every sample will not be presented but can be found in reference [2].

## References


1 Wentink, T., Jr., "High Temperature Behavior of Teflon," Avco-Everett Research Report 55, July 1959.

2 Clark, B. L., "An Experimental and Analytical Investigation of Teflon Ablation Heat Transfer Parameters by the Method of Nonlinear Estimation," PhD thesis, Cornell University, Ithaca, N. Y., 1971.

3 Crank, J., and Nicolson, P., "A Practical Method for Numerical Evaluation of Solutions of Partial Differential Equations of the Heat-Conduction Type," *Proc. Cambridge Philos. Soc.*, Vol. 43, 1947, pp. 50–67.

4 Beck, J. V., "The Optimum Analytical Design of Transient Experiments for Simultaneous Determinations of Thermal Conductivity and Specific Heat," PhD thesis, Michigan State University, East Lansing, Mich., 1964.

5 Gauss, K. F., "Theoria Motus Corporum Coelestium," *Werke*, Vol. 7, 1809, p. 240; English translation: "Theory of Least Squares," H. F. Trotter, Princeton University, Stat. Tech. Research Group, Tech. Report No. 5.

6 Box, G. E. P., and Coutie, G. A., "Application of Digital Computers to the Exploration of Functional Relationships," *Proceedings of The Institution of Electrical Engineers*, Vol. 103, 1956, pp. 100–107.

7 Marquardt, D. W., "An Algorithm for Least-Squares Estimation of Nonlinear Parameters," *Journal of the Society for Industrial and Applied Mathematics*, Vol. 11, June 1963, pp. 431–441.

8 Lapidus, L., and Peterson, T. I., "Analysis of Heterogeneous Catalytic Reactions by Nonlinear Estimation," *AIChE Journal*, Vol. 11, 1965, pp. 891–897.

9 Pfahl, R. C., Jr., and Mitchel, B. J., "A General Method for Simultaneous Measurement of Thermal Properties," AIAA Paper No. 69-602, June 1969.

10 Box, G. E. P., and Lucas, H. L., "Design of Experiments in Nonlinear Situations," *Biometrika*, Vol. 46, 1959, pp. 77–90.

11 Pfahl, R. C., Jr., "An Experimental and Analytical Investigation of the Internal Mechanisms of Ablative Heat Transfer in Charring Cork," PhD thesis, Cornell University, Ithaca, N. Y., 1965.

12 Settlage, P. H., and Siegel, J. C., "Behavior of 'Teflon' Fluorocarbon Resins at Elevated Temperatures," *Physical Chemistry in Aerodynamics and Space Flight*, Pergamon Press, New York, N. Y., 1961.

13 Schultz, A. W., and Wong, A. K., "Thermal Conductivity of Teflon, Kel-F and Duroid-5600 at Elevated Temperatures," WAL Report No. TR-397/10, March 1958.

14 Milek, J. T., "A Survey Materials Report on Tetrafluoroethylene (TFE) Plastics," Hughes Electronic Information Center EPIC Report No. S-3, Sept. 1964.

15 Nagler, R. G., Blizzard, E. M., and Jirka, R. J., "Transient Techniques for Determining the Thermal Conductivity of Homogeneous Polymeric Materials of Elevated Temperatures," *Journal of Applied Polymer Science*, Vol. 9, 1965, pp. 801–819.

16 Loser, J. B., Moeller, C. E., and Thomson, M. B., "Thermophysical Properties of Thermal Insulating Materials," Air Force Materials Laboratory ML-TDR-64-5, Apr. 1964.

17 Kemp, N. H., "Surface Recession Rate of an Ablation Polymer," *AIAA Journal*, Vol. 6, Sept. 1968, pp. 1790–1791.

18 Marx, P., and Dole, M., *Journal of American Chemical Society*, Vol. 77, 1955, p. 4771.

19 Hurwicz, H., "Aerothermochemistry Studies in Ablation," *Combustion and Propulsion*, Fifth AGARD Colloquium on High-Temperature Phenomena, 1963, pp. 403–455.

20 Scala, S., "A Study of Hypersonic Ablation," Conference on the Behavior of Plastics in Advanced Flight Vehicle Environments, WADD TR 60-101, Sept. 1960; also General Electric Report R59SD438.

21 Reich, L., "Estimation of Kinetic Parameters during Teflon


**Table 1 Summary of parametric results and comparison with literature**

| Parameter | Values from Literature | +RMS | -RMS | NLE |
|---|---|---|---|---|
| $A_p$ ($10^{18}$sec$^{-1}$) | 30.0[17],4.70[19],9.40[20],50.0[22] | 12.18 | 5.96 | 12.90 |
| $B_p$ (°R) | 75200[16],72900[19],73800[20],55300[21],70700[22] | 610 | 820 | 67200 |
| $k_r$($10^{-5}$ Btu/ft sec °R) | 2.69[1],4.26[12],4.30[13],4.17[14],2.27[15],3.41[16],3.89[19] | 2.39 | 1.17 | 3.99 |
| $k_{m2}$($10^{-5}$ Btu/ft sec °R) | 5.37[1],7.62[12],6.60[13],6.60[14],4.37[16] | 2.40 | 1.21 | 5.81 |
| $k_{m1}$($10^{-5}$ Btu/ft sec °R) | 4,03[1] | 3.00 | 1.53 | 3.94 |
| $k_h$($10^{-5}$ Btu/ft sec °R) | | 0.57 | 0.91 | 3.97 |
| $c_r$(Btu/lb$_m$ °R) | 0.222[1],0.230[14],0.200[17],0.230[18] | 0.047 | 0.057 | 0.169 |
| $c_{m2}$(Btu/lb$_m$ °R) | 0.285[1],0.290[14],0.305[17],0.295[18] | 0.094 | 0.102 | 0.291 |
| $c_{m1}$(Btu/lb$_m$ °R) | 0.310[1],0.350[17] | 0.111 | 0.086 | 0.353 |
| $c_h$(Btu/lb$_m$ °R) | 0.450[17] | 0.247 | 0.064 | 0.367 |
| $\rho_r$(lb$_m$/ft$^3$) | 144.7[12],138.0[16],144.1[17],137.3[19] | -- | -- | 137.5[2] |
| $\rho_{m2}$(lb$_m$/ft$^3$) | 130.3[12] | 14.6 | 8.4 | 135.7 |
| $\rho_{m1}$(lb$_m$/ft$^3$) | 96.0[12] | 26.3 | 15.1 | 108.6 |
| $\rho_h$(lb$_m$/ft$^3$) | | 8.3 | 9.9 | 67.8 |
| $H_{po}$ (Btu/lb$_m$) | 670[1],763[17],680[19],600[23],750[24],750[25] | 94 | 133 | 678 |
| $H_{p1}$ (Btu/lb$_m$ °R) | 66.7[17] | 0.51 | 0.27 | 1.10 |
| $\eta$ | 0.430[23],0.563[26],0.492[27],0.536[28] | 0.229 | 0.149 | 0.504 |

[1]Values in literature, if not available in this form, were estimated from data (graphs, equations, etc.) presented.
[2]$\rho_{ref}$ was estimated in lieu of $\rho_r$.

Note:
±RMS refer to upper and lower root-mean-square deviations.
Subscripts r, m2, m1, and h refer to values at 532°R, 1080°R(crystalline), 1080°R(amorphous), and 1600°R.

Degradation from Linearized Differential TGA Traces," *Journal of Applied Polymer Science*, Vol. 11, No. 5, 1967, pp. 699–703.
22 Newman, R. L., "A Kinetic Treatment of Ablation," *Journal of Spacecraft and Rockets*, Vol. 2, May–June 1965, pp. 449–452.
23 John, R. R., and Recesso, J., "Ablation Characteristics of a Subliming Material Using Arc Heated Air," *ARS Journal*, Vol. 29, Sept. 1959, pp. 663–665.
24 Diaconis, N. S., Fanucci, J. B., and Sutton, G. W., "The Heat Protection Potential of Several Ablation Materials for Satellite and Ballistic Re-entry Into the Earth's Atmosphere," General Electric Report R59SD423, Sept. 1959.
25 Steg, L., and Lew, H., "Hypersonic Ablation," in: *The High Temperature Aspects of Hypersonic Flow*, W. C. Nelson, ed., Pergamon Press, 1964, pp. 629–680; also General Electric Report R62SD55, May 1962.
26 Kreith, F., *Principles of Heat Transfer*, 2nd ed., International Textbook Co., 1965, pp. 538–545.
27 Freedman, S. I., "Ablation," in: *Developments in Heat Transfer*, W. M. Rohsenow, ed., M.I.T. Press, Cambridge, Mass., 1964, pp. 87–106.
28 Bethe, H. A., and Adams, M. C., "A Theory for the Ablation of Glassy Materials," *Journal Aerospace Sci.*, Vol. 26, June 1959, pp. 321–328; also Avco Research Report 38, Nov. 1958.
29 Gross, J. J., Masson, D. J., and Gazley, C., Jr., "General Characteristics of Binary Boundary Layers with Applications to Sublimation Cooling," Rand Report P-1371, May 8, 1958.

# APPENDIX

## Transformed Equations and Boundary Conditions

The transformed heat-transfer equations for Region $j$ (equal to 1 or 2) are

$$\frac{(R_j+1)^2}{4\delta_j^2[1+(R_j-1)\xi_j]}\frac{\partial}{\partial\xi_j}\left\{\frac{k}{[1+(R_j-1)\xi_j]}\frac{\partial T_j}{\partial\xi_j}\right\}+Q_{pj}$$

$$=\rho c\left\{\frac{\partial T_j}{\partial t}-\frac{(R_j+1)V_j^*}{2\delta_j[1+(R_j-1)\xi_j]}\frac{\partial T_j}{\partial\xi_j}\right\} \quad (26)$$

where

$$V_1^*=V+(V_m-V)\psi_1 \qquad V_2^*=V_m(1-\psi_2)$$

The velocities are

$$V(t)=\frac{A_p\delta_1}{\rho_{\text{ref}}}\int_0^1\rho(\xi_1,t)\exp\left[-B_p/T_1(\xi_1,t)\right]d\psi_1 \quad (27)$$

and

$$V_m(t)=\frac{1}{\rho_m H_m}\left[\frac{(R_1+1)}{2R_1\delta_1}\left(-k\frac{\partial T_1}{\partial\xi_1}\right)_{\xi_1=1}-\frac{(R_2+1)}{2\delta_2}\left(-k\frac{\partial T_2}{\partial\xi_2}\right)_{\xi_2=0}\right] \quad (28)$$

The boundary conditions are

$$\frac{(R_1+1)}{2\delta_1}\left(-k\frac{\partial T_1}{\partial\xi_1}\right)_{\xi_1=0}=\dot{q}_0-\sigma\epsilon[T_1(1,t)]^4-\dot{m}_{\text{TFE}}[\eta(H_e-H_s)-c_sT_1(1,t)] \quad (29)$$

$$T_1(1,t)=T_2(0,t)=T_m \quad (30)$$

$$\frac{(R_2+1)}{2\delta_2}\left(-k\frac{\partial T_2}{\partial\xi_2}\right)_{\xi_2=1}=C_{\text{hs}}\left(\frac{\partial T_2}{\partial t}\right)_{\xi_2=1} \quad (31)$$

E. O. STOFFEL
Professor,
Department of Mechanical Engineering,
California Polytechnic State University,
San Luis Obispo, Calif.
Mem. ASME

J. R. WELTY
Head,
Department of Mechanical and
Nuclear Engineering,
Oregon State University,
Corvallis, Ore.
Mem. ASME

# The Effect of Entrance Configuration on Local Heat-transfer Coefficients in Subsonic Diffusers

*The effects of square and reentrant entrances on flow regimes (no "appreciable" separation, large transitory stall, and fully developed two-dimensional stall) and local heat-transfer coefficients were determined with air flowing through a symmetrical, plane-wall, two-dimensional subsonic diffuser with one of the diverging walls heated and maintained isothermal. Flow and heat-transfer studies were made for the following ranges: $2\theta = 0$ to 45 deg, $L/W = 6$ to 18, and $\mathrm{Re}_{x_{tot}} = 4 \times 10^4$ to $3 \times 10^5$. Results indicated that $2\theta$, $L/W$, and entrance configuration greatly affected the flow regime and heat transfer. Equations relating $U_m'$ to $U_t$, $U_r$ to $U_t$, and equations of the type $\mathrm{Nu} = C\,\mathrm{Pr}^{0.6}\,\mathrm{Re}_x^{0.8}$ are presented. For the configurations tested, heat-transfer rates were greater for reentrant than for square entrances.*

## Introduction

THE DIFFUSER is used in a myriad of engineering applications where dynamic pressure is converted to static pressure. Examples include space vehicles, turbomachinery, nuclear-reactor components, and acoustic generators. Factors which complicate the analysis of diffusers are separation, entrance conditions, and heat transfer.

A review of the literature reveals that much has been written about separation [1, 2],[1] some about the effects of inlet conditions [3, 4], and little about heat transfer [5, 6] in two-dimensional subsonic diffusers.

The present study involves a symmetrical, plane-wall, two-dimensional subsonic diffuser with one of the diverging walls isothermally heated. Local heat-transfer coefficients were evaluated for three types of flow (unseparated, transient separated, and fully separated). Provision was made for flow visualization during all tests and velocities were measured in regions of fully developed stall (separation).

Kline [1] has established the flow regimes for two-dimensional subsonic diffusers. These are illustrated in Fig. 1.

Velocities and heat-transfer coefficients determined by experimentation can be accurate and dependable. However, experiments are very time-consuming and expensive. Thus, on practical grounds, it is desirable to analyze empirical data with equations based on theoretical considerations. VanSant

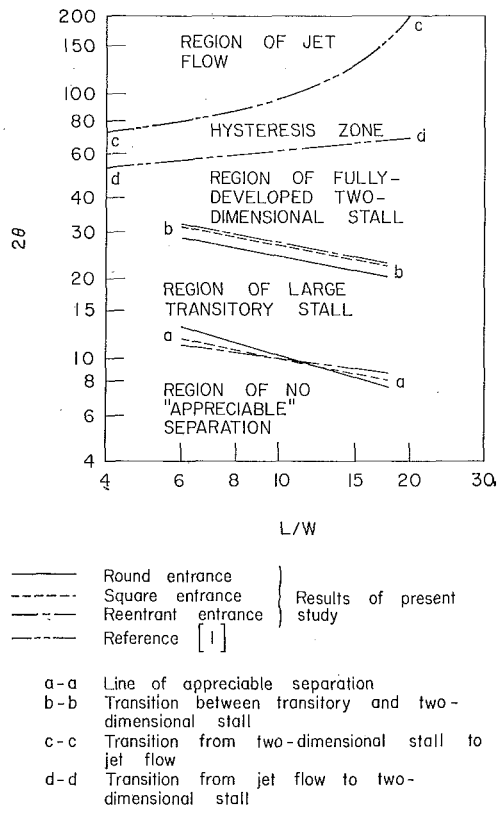


**Fig. 1 Flow regimes in two-dimensional straight-wall diffusers; round, square, and reentrant entrances**

[1] Numbers in brackets designate References at end of paper.

Contributed by the Heat Transfer Division of THE AMERICAN SOCIETY OF MECHANICAL ENGINEERS and presented at the AIChE-ASME Heat Transfer Conference, Denver, Colo., August 6–9, 1972. Manuscript received by the Heat Transfer Division August 24, 1971. Paper No. 72-HT-34.

[5] has had some success in predicting heat transfer for conditions of no "appreciable" separation and fully developed two-dimensional stall for turbulent flow in round-entranced subsonic diffusers. The present investigation confirmed the findings of VanSant [5] and extended the heat-transfer investigations to consider diffusers with square and reentrant entrances. A brief summary of the equations used will now be given.

**Equations Pertaining to Two-dimensional Subsonic Diffusers.** For turbulent flow, a number of analyses for the step wall-temperature distribution have been made. Reynolds, Kays, and Kline [7] have developed the equation which was used here; their equation is

$$\mathrm{Nu}_{x_t}(T_w/T_\infty)^{0.4}[1 - (\xi_t/X_t)^{0.9}]^{1/9} = 0.0296\ \mathrm{Pr}^{0.6}\mathrm{Re}_x^{0.8} \quad (1)$$

The velocity used in equation (1) is the mean local velocity.

The entrances of the diffuser used in the present investigation were adiabatic. Thus, an estimate of the unheated entrance length $\xi_t$ was required for equation (1). This length was determined by equating an estimated value of momentum thickness that occurred at the diffuser throat to $0.037\ \xi_t^{0.8}\ (\nu/U_t)^{0.2}$ (an expression for the momentum thickness of a turbulent boundary layer at position $\xi_t$ on a flat plate having a $1/7$-power velocity profile and a mainstream velocity $U_t$). An estimate of the momentum thickness at the diffuser throat was determined with an integral equation (reference [8]). The free-stream velocity along curved inlet surfaces was estimated using the flow net technique.

Myers, Schauer, and Eustis [9] developed the equation for $U_m$ as

$$U_m/U_t = \begin{Bmatrix} 1 \quad \text{for} \quad l/W < 7 \\ [1 + 0.381(l/7W - 1)]^{-1/2} \quad \text{for} \quad l/W > 7 \end{Bmatrix} \quad (2)$$

Using the approach of VanSant [5], it was found that

$$U_r/U_t = f(W/L, \theta) \quad (3)$$

$$\frac{U_r}{U_t} = \frac{0.04161\left[1 + 0.381\left(\frac{L}{7W} - 1\right)\right]^{-1/2}}{\left\{\frac{W}{L} + \left[1 + \left(0.182 + 0.8233\,\frac{W}{L}\right)\tan\theta\right] 2\sin\theta\right\}\cos\theta - 0.182 - 0.8233\,\frac{W}{L}} \quad \text{for} \quad \frac{L}{W} > 7$$

$$\frac{U_r}{U_t} = \frac{0.04161}{\left\{\frac{W}{L} + \left[1 + \left(0.1096 + 1.33\,\frac{W}{L}\right)\tan\theta\right] 2\sin\theta\right\}\cos\theta - 0.1096 - 1.33\,\frac{W}{L}} \quad \text{for} \quad \frac{L}{W} < 7 \quad (4)$$

Derivation of equation (4) is found in [10]; $U_m$ and $U_r$ are shown graphically in Fig. 2.

## Experimental Program

**Experimental Apparatus.** The experimental apparatus was first used by VanSant [5]. It was modified to incorporate variable inlet conditions for the present study.

Entrance details are shown in Fig. 3. Sand grains were attached to the round entrance for flow stability but were not attached to the square and reentrant entrances. The throat width $W$ could be varied from 2 to 6 in. and $2\theta$ from 0 to 45 deg.

Wool tufts and smoke streamers were used to observe flow regimes.

## Nomenclature

$C$ = constant in equation, $\mathrm{Nu} = C\mathrm{Pr}^{0.6}\mathrm{Re}_x^{0.8}$

$c_p$ = constant-pressure specific heat, Btu/lb$_m$-deg F

$f(W/L, \theta)$ = a functional relation for predicting $U_t/U_r$, see equation (4)

$h$ = heat-transfer film coefficient, Btu/hr-sq ft-deg F

$k$ = thermal conductivity, Btu/hr-ft-deg F

$l$ = distance from the upstream edge of the plane section forming one of the two diverging walls in a direction parallel to the wall, ft

$l_b$ = distance from the downstream edge of the plane section forming one of the two diverging walls in a direction parallel to the wall, ft

$L$ = length of a plane section forming one of the two diverging walls, ft

$\mathrm{Nu}_x$ = Nusselt number, $hX/k$, dimensionless

$\mathrm{Nu}_{xb_c}$ = Nusselt number including the equivalent distance from the diffuser exhaust, $X_b$, and corrected for unheated starting length and variation of fluid properties, $(hX_b/k)[1 - (\xi_b/X_b)^{0.9}]^{1/9}(T_w/T_\infty)^{0.4}$, dimensionless

$\mathrm{Nu}_{x_{t_c}}$ = Nusselt number including the equivalent distance from the diffuser throat, $X_t$, and corrected for the unheated starting length and variation of fluid properties, $(hX_t/k)[1 - (\xi_t/X_t)^{0.9}]^{1/9}(T_w/T_\infty)^{0.4}$, dimensionless

Pr = Prandtl number, $\rho\nu c_p/k$, dimensionless

$\mathrm{Re}_x$ = Reynolds number, $UX/\nu$, dimensionless

$\mathrm{Re}_{x_{bu_t}} = U_tX_b/\nu$, dimensionless

$\mathrm{Re}_{x_t} = \dfrac{X_t}{\nu} \cdot \dfrac{U_t}{1 + 2(l/W)\sin\theta}$, dimensionless

$\mathrm{Re}_{x_{tu_{m'}}} = U_m'X_t/\nu$, dimensionless

$\mathrm{Re}_{x_{tu_t}} = U_tX_t/\nu$, dimensionless

$T_w$ = temperature of heated wall, deg R

$T_\infty$ = free-stream gas temperature, deg R

$U$ = local velocity, fph

$U_m$ = maximum velocity in a plane turbulent wall jet, see equation (2), fph

$U_m'$ = measured maximum velocity in the wall jet during fully developed two-dimensional stall, fph

$U_r$ = velocity of the reversed-flow region during fully developed two-dimensional stall, fph

$U_t$ = throat velocity, fph

$W$ = throat width, ft

$X$ = distance from the beginning of entrance surface, ft

$X_b$ = the equivalent distance from the diffuser exhaust, $\xi_b + l_b$, ft

$X_t$ = the equivalent distance from the diffuser throat, $\xi_t + l$, ft

$\theta$ = one-half the total divergence angle, deg

$\nu$ = kinematic viscosity, sq ft/hr

$\xi_b$ = unheated starting length for the exhaust end of a diffuser wall subjected to reversed flow, ft

$\xi_t$ = unheated starting length for boundary-layer development on the diffuser entrance surface, ft

$\rho$ = fluid density, lb$_m$/cu ft

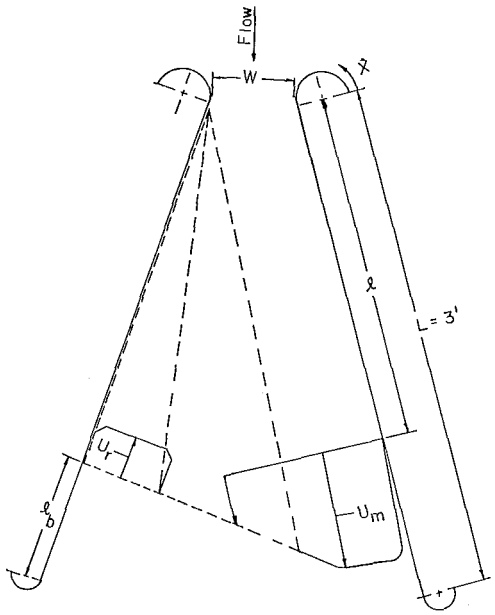


**Fig. 2 An illustration of velocity profiles in a subsonic diffuser during fully developed two-dimensional stall**

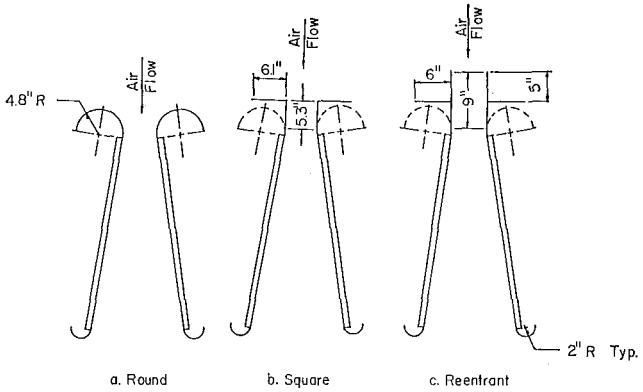


**Fig. 3 Schematic of wall showing entrance and exit details**

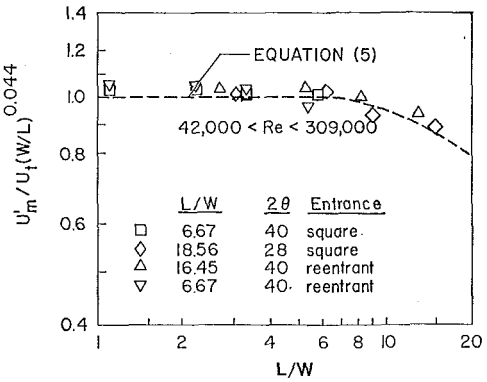


**Fig. 4 Correlation of the maximum velocity along the "wall of jet flow" during fully developed two-dimensional stall**

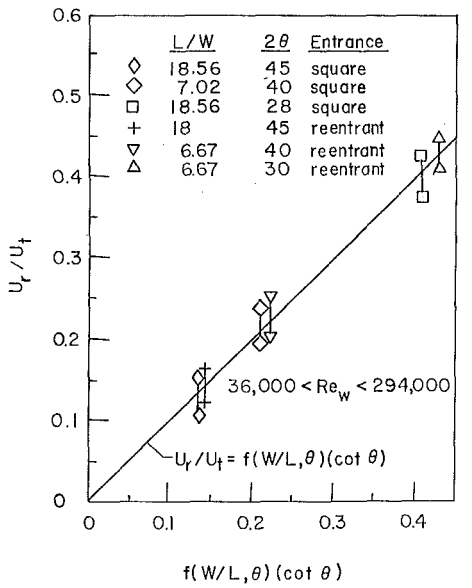


**Fig. 5 Correlation of measured reversed-flow velocities in fully developed two-dimensional stall**

Twenty-three spot heaters were used in the determination of local heat-transfer rates.

**Experimental Procedures.** After throat width, wall divergence angle, and flow were adjusted, the flow regime was determined. Velocity measurements were made during fully developed two-dimensional stall.

After the heated wall was brought to an isothermal condition, local heat-transfer rates were determined from the measured electrical power to each spot heater.

Forty-eight test runs were made. Sixteen tests using round entrances were conducted to confirm the flow and heat-transfer results of VanSant [5].

Thirty-two tests were made on square and reentrant entrances. Each test took an average of 3 hr to complete.

A more complete description of experimental apparatus and procedures, including calibration and computing techniques, has been presented in [10].

## Results

**Flow Studies.** Results of flow studies for round entrances agreed substantially with those of VanSant [5].

The line of appreciable separation (a-a in Fig. 1) has smaller negative slopes for the square and reentrant entrances, respectively, than for the round entrance. These three lines intersected at a value of $L/W = 11$. This agreed generally with the findings of Waitman, Reneau, and Kline [3].

The line b-b in Fig. 1 for the square and reentrant entrances was above that for the round entrance. Except for very large values of $2\theta(2\theta = 40$ to 45 deg), the region of fully developed two-dimensional stall was not as clearly defined for square and reentrant entrances. It appeared that some sort of unsteady "transient zone" was present between the large transitory stall and fully developed two-dimensional stall regions.

Correlation of the maximum velocity along the "wall of jet flow" is shown in Fig. 4. Data points agreed to within ±6 and ±7 percent for the square and reentrant entrances respectively with the values determined by

$$U_m'/U_t(W/L)^{0.044} = \begin{Bmatrix} 1 & \text{for} \quad l/W < 7 \\ [1 + 0.381\,(l/7W - 1)]^{-1/2} & \text{for} \quad l/W > 7 \end{Bmatrix} \quad (5)$$

The difference between equation (5) and equation (2) is the empirical constant $(W/L)^{0.044}$.

The fluid velocities in the region of reversed flow during fully developed two-dimensional stall did not correlate well with those of equation (4).

For square and reentrant entrances, correlations of $U_r/U_t$ are given in Fig. 5. A new function which was within ±50 percent of the true velocity was obtained by multiplying $f(W/L, \theta)$ by cot $\theta$. The improvement afforded by this empirical correction cannot be presently explained.

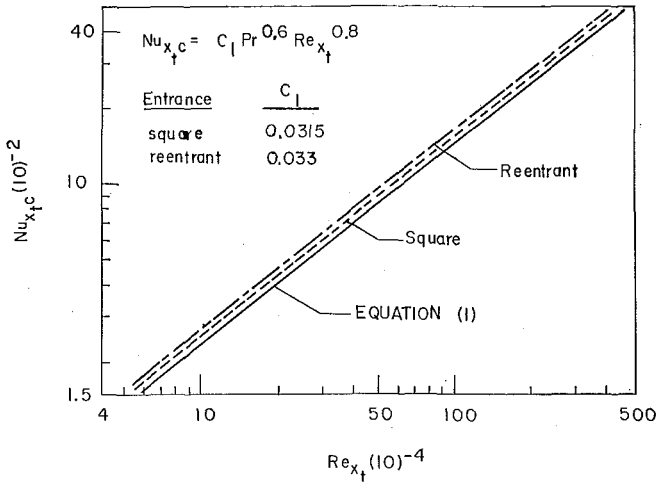


Fig. 6 Results of heat-transfer measurements during no "appreciable" separation

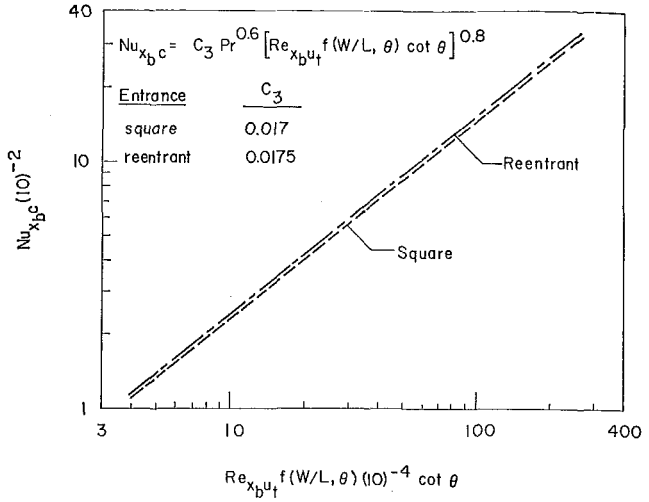


Fig. 8 Correlation of heat-transfer data from the "wall of reversed flow" during fully developed two-dimensional stall

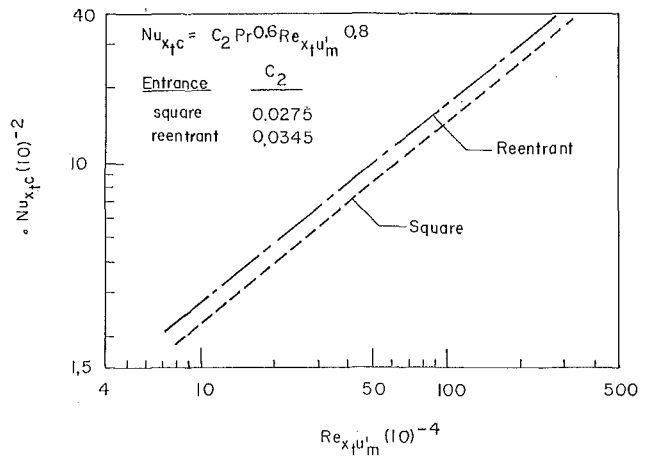


Fig. 7 Results of heat-transfer measurements on the "wall of jet flow" during fully developed two-dimensional stall; $U_m'$ determined from a correlation of experimental measurements, equation (5)

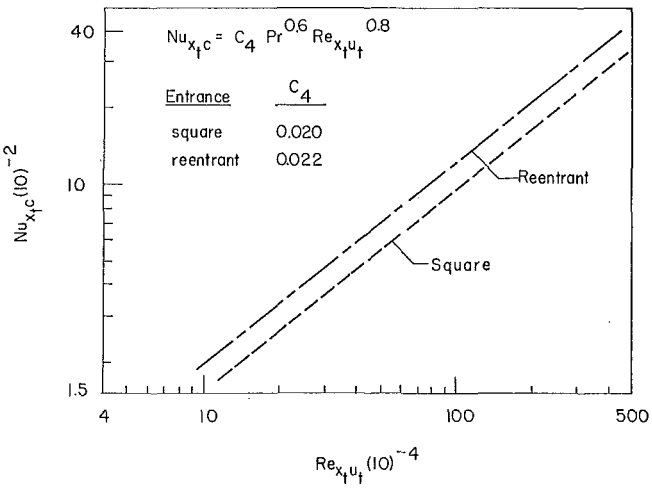


Fig. 9 Results of heat-transfer measurements during large transitory stall

### Heat Transfer

**Round Entrances.** Heat transfer for round entrances in the no-"appreciable"-separation, wall-of-jet-flow, wall-of-reversed-flow, and large-transitory-stall regimes agreed substantially with the findings of VanSant [5]. Detailed results are presented in [10].

**No-"Appreciable"-Separation Regime.** Heat-transfer data taken in the no-"appreciable"-separation regime (indicated by the area under a-a in Fig. 1) are presented in Fig. 6 for square and reentrant entrances. These data were correlated by the relation

$$(hX_t/k)[1 - (\xi_t/X_t)^{0.9}]^{1/9}(T_w/T_\infty)^{0.4} = C_1 \mathrm{Pr}^{0.6}\left[\frac{X_t}{\nu} \cdot \frac{U_t}{1 + 2(l/W)\sin\theta}\right]^{0.8} \quad (6)$$

For square entrances, approximately 90 percent of the data points lie within ±20 percent of the line predicted by equation (1). With $C_1 = 0.0315$, equation (6) departs by less than ±15 percent.

For reentrant entrances, approximately 90 percent of the data lie within ±30 percent of the line predicted by equation (1). With $C_1 = 0.033$ equation (6) departs by less than ±19 percent.

**Wall of Jet Flow.** Heat-transfer data in the wall-of-jet-flow regime are presented in Fig. 7. Experimental correlations were expressed in terms of

$$(hX_t/k)[1 - (\xi_t/X_t)^{0.9}]^{1/9}(T_w/T_\infty)^{0.4} = C_2 \mathrm{Pr}^{0.6}(X_t U_m'/\nu)^{0.8} \quad (7)$$

For square entrances, with $C_2 = 0.0275$, equation (7) holds for 90 percent of all data within ±30 percent.

For the reentrant entrance, with $C_2 = 0.0345$, equation (7) holds for 90 percent of all data within ±24 percent.

**Wall of Reversed Flow.** Heat-transfer data for the wall-of-reversed-flow regime are presented in Fig. 8. Experimental correlations were expressed in terms of

$$(hX_b/k)[1 - (\xi_b/X_b)^{0.9}]^{1/9}(T_w/T_\infty)^{0.4} = C_3 \mathrm{Pr}^{0.6}\{(X_b U_t/\nu) f(W/L, \theta) \cot\theta\}^{0.8} \quad (8)$$

For square entrances, with $C_3 = 0.017$, equation (8) departs by less than ±25 percent for 90 percent of the data.

For reentrant entrances, with $C_3 = 0.0175$, equation (8) departs by less than ±57 percent for 90 percent of the data.

**Large Transitory Stall.** Heat-transfer measurements in this regime could not be estimated by theoretical equations. The best empirical correlation was found by plotting Nusselt number against Reynolds number based on length $X_t$ and throat velocity.

Results are presented in Fig. 9. Experimental correlations were expressed as

$$(hX_t/k)[1 - (\xi_t/X_t)^{0.9}]^{1/9}(T_w/T_\infty)^{0.4} = C_4 \mathrm{Pr}^{0.6}(X_t U_t/\nu)^{0.8} \quad (9)$$

For square entrances, with $C_4 = 0.020$, equation (9) departs by less than ±34 percent for 90 percent of the data.

Finally, for reentrant entrances, with $C_4 = 0.022$, equation (9) departs by less than ±40 percent for 90 percent of the data.

## Conclusions

**Flow Studies.** (*a*) Diffuser flow regimes closely agree with those of Waitman, Reneau, and Kline [3]. (*b*) The magnitude of the measured velocity in flow past the wall of jet flow during fully developed two-dimensional stall can be determined from equation (5). (*c*) The fluid velocity in the region of reversed flow is not repeatable from test to test. Equation (4), when multiplied by cot $\theta$, predicts reversed-flow velocities within $\pm 50$ percent for square and reentrant entrances.

**Heat Transfer.** (*a*) For no "appreciable" separation, the best experimental correlation is

$$\mathrm{Nu}_{x_{tc}} = C_1 \mathrm{Pr}^{0.6} \mathrm{Re}_{x_t}{}^{0.8} \tag{10}$$

where suggested values of $C_1$ are 0.0315 and 0.033 for square and reentrant entrances respectively. (*b*) For the wall of jet flow

$$\mathrm{Nu}_{x_{tc}} = C_2 \mathrm{Pr}^{0.6} \mathrm{Re}_{x_{tu_m}}{}^{0.8} \tag{11}$$

where the suggested values of $C_2$ are 0.0275 and 0.0345 for square and reentrant respectively. (*c*) For the wall of reversed flow

$$\mathrm{Nu}_{x_{bc}} = C_3 \mathrm{Pr}^{0.6} \{(\mathrm{Re}_{x_{bu_t}}) f(W/L, \theta) \cot \theta\}^{0.8} \tag{12}$$

where the suggested values of $C_3$ are 0.017 and 0.0175 for square and reentrant respectively. (*d*) For large transitory stall

$$\mathrm{Nu}_{x_{tc}} = C_4 \mathrm{Pr}^{0.6} \mathrm{Re}_{x_{tu_t}}{}^{0.8} \tag{13}$$

where suggested values of $C_4$ are 0.020 and 0.022 for square and reentrant entrances. (*e*) Heat-transfer rates from the plane-wall two-dimensional diffusers are greatest when the angle of divergence is 0 deg. When the angle is increased, the heat-transfer rates decrease. (*f*) For the configurations tested, heat-transfer rates are greater for reentrant than for square entrances.

## References


1 Kline, S. J., "On the Nature of Stall," *Journal of Basic Engineering*, TRANS. ASME, Series D, Vol. 81, No. 3, Sept. 1959, pp. 305–320.

2 Dean, R. C., Jr., "Separation and Stall," *Handbook of Fluids*, ed. by V. L. Streeter, McGraw-Hill, New York, N. Y., 1961, pp. 11–1 to 11–40.

3 Waitman, B. A., Reneau, L. R., and Kline, S. J., "Effect of Inlet Conditions on Performance of Two-Dimensional Subsonic Diffusers," *Journal of Basic Engineering*, TRANS. ASME, Series D, Vol. 83, No. 3, Sept. 1961, pp. 349–360.

4 Robertson, J. M., and Ross, D., "Effect of Entrance Conditions on Diffuser Flow," *Trans. ASCE*, Vol. 118, 1953, pp. 1068–1097.

5 VanSant, J. H., Jr., "Convection Heat Transfer in Separated Regions Subsonic Diffusers," PhD thesis, Oregon State University, Corvallis, Ore., 1964 (microfilm).

6 VanSant, J. H., Jr., and Larson, M. B., "Convection Heat Transfer for Turbulent Flow in Subsonic Diffusers," JOURNAL OF HEAT TRANSFER, TRANS. ASME, Series C, Vol. 88, No. 4, Nov. 1966, pp. 391–398.

7 Reynolds, W. C., Kays, W. M., and Kline, S. J., "A Summary of Experiments on Turbulent Heat Transfer From a Nonisothermal Flat Plate," JOURNAL OF HEAT TRANSFER, TRANS. ASME, Series C, Vol. 82, No. 4, Nov. 1960, pp. 341–348.

8 Kutateladze, S. S., and Leont'ev, A. I., *Turbulent Boundary Layers in Compressible Gases*, Academic Press, New York, N. Y., 1964, p. 107.

9 Myers, G. E., Schauer, J. J., and Eustis, R. H., "Plane Turbulent Wall Jet Flow Development and Friction Factor," *Journal of Basic Engineering*, TRANS. ASME, Series D, Vol. 85, No. 1, Mar. 1963, pp. 47–54.

10 Stoffel, E. O., "The Effect of Entrance Configuration on Local Heat Transfer Coefficients in Subsonic Diffusers," MS thesis, Oregon State University, Corvallis, Ore., 1968.

H. G. WHITLEY III[1]
R. I. VACHON
Alumni Professor.
Mem. ASME

Department of Mechanical Engineering,
Auburn University,
Auburn, Ala.

# Transient Laminar Free Convection in Closed Spherical Containers

*The transient laminar free-convection heat and mass transfer of fluids in closed spherical containers is studied analytically. The coupled nonlinear partial differential equations for conservation of mass, energy, and momentum are solved simultaneously. Finite-difference approximations of the governing equations are organized for an iterative numerical-integration scheme which yields temperature and mass flux as a function of time and space. A computational procedure is given and results from application of the model are presented.*

## Introduction

THIS ANALYSIS attempts to determine the effects of external disturbances on a mass of fluid contained in a spherical container. Such disturbances might include charging or discharging operations, a change in the ambient condition surrounding a system, an energy transfer across the boundary of the vessel, or a variation of gravitational forces acting on the system. Results are presented for transient, axisymmetric, and natural convection resulting from a step change in the uniform temperature of the container wall.

Formulated from the conservation equations of mass, momentum, and energy, the model describes temporal and spatial variations in the system as changes occur in the attainment of new conditions of equilibrium. Simplifications include neglecting the effects of viscous heating and treating all fluid properties as constants, with the exception of density variations which result from temperature changes which are the driving potential for natural convection. The resultant governing relationships are transformed into simpler forms through the use of a stream function and the $\phi$ component of the vorticity vector.

Finite-difference equations are formed in such a manner that their solution converges to the solution of the simultaneous partial differential equations governing the system. Convergence and stability of the numerical-integration technique is obtained through the use of implicit central-difference approximations for partial differentials in the iterative routine.

## Related Studies

Previous approaches to convection analyses have included large experimental programs to augment analysis by lumped-parameter methods in which mean properties of the system are determined not as functions of position within the space but as functions of time only. At the other end of the information spectrum are distributed-systems analyses in which properties such as temperature, pressure, and velocity are determined as functions of time and position within the space of the system. Obviously the latter type provides much more information, but in terms of time and financial investment the latter approach is often considerably more expensive.

The analyses by Tanger et al. [1],[2] in which mean properties of the gas receiver on the gas-pressure feed system of a large space vehicle are studied, is typical of the lumped-parameter analyses. Refinements to the model based upon experiment enabled Tatom et al. [2] to obtain results that agree with the unreported experimental work of investigators at the Marshall Space Flight Center, although the initial goals of including effects of stratification of the gas in the model were never realized.

Distributed-systems analyses, formulated from the rate-type equations of conservation of mass, momentum, and energy, provide a complete description of the system including temporal and spatial variations. The work Mack and Hardee [3] describes the steady axisymmetric natural convection between isothermal concentric spheres. In simplifying their analysis, the authors, who rely somewhat heavily upon the experimental work of Scanlan et al. [4], expand the dependent variables (temperature and stream function) in power series of the Rayleigh number and substitute the resulting relationships into the conservation equations governing the system to obtain an infinite set of uncoupled linear differential equations.

Numerical solutions to convection problems have increased in number and complexity since the work of Blair et al. [5]. Their studies were confined to the two-dimensional motion of two incompressible fluids subject to gravitational and hydrodynamic forces. One of the most important developments established in [5] was that in an explicit scheme the convective-transport terms in the conservation equations must be formed according to whether the sign of the velocity in the direction under consideration is negative or positive.

[1] Presently, Chief of Operations Research Branch, Scientific Systems Division, U. S. Army Management Systems Support Agency, Washington, D. C.

Contributed by the Heat Transfer Division of THE AMERICAN SOCIETY OF MECHANICAL ENGINEERS and presented at the AIChE-*ASME Heat Transfer Conference*, Denver, Colo., August 6–9, 1972. Manuscript received by the Heat Transfer Division December 14, 1970. Paper No. 72-HT-37.

[2] Numbers in brackets designate References at end of paper.

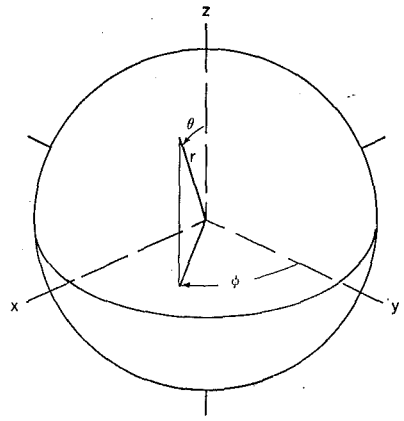


**Fig. 1(a) Storage vessel and coordinate system**

Approximate numerical solutions of free convection in closed containers include the works of Wilkes and Churchill [6], Barakat [7], and Clark and Barakat [8]. These analyses are similar, with the primary differences being in the geometry and in the addition of distributed heat sources in [7]. Viscous heating is neglected and the properties of the fluid are assumed to remain constant. Density variations resulting from temperature changes (the driving potential for free convection) are used in the buoyancy term of the momentum equation. The equations of energy and momentum are transformed into relationships for temperature and vorticity through the use of a stream function satisfying the mass-conservation relationship. The complexity of determining boundary conditions for vorticity is bypassed through the use of the defining equation for vorticity in terms of the stream function. The resulting boundary-value problem is one in which the gradients are specified, rather than actual values as in the case of the stream function.

## Analysis

**Formulation.** The problem involves a closed spherical vessel containing a gas at uniform temperature with pressure, density, and velocity at hydrostatic conditions. The external forces acting on the fluid create potentials for convection of varying magnitude throughout the container. To adjust to the disturbance the system passes through a sequence of nonequilibrium conditions and attains a new condition of equilibrium at some subsequent time.

Problem formulation is based on studying the transport phenomena in a control volume, the spherical container. The resulting differential equations, which satisfy the conservation of mass, momentum, and energy, permit a detailed study of the action of the fluid throughout the period of interest.

Simplifications are introduced to obtain results by available techniques within a reasonable length of time and with a minimum loss of generality. The governing differential equations are rewritten in terms of finite differences. These equations are programmed for digital computation.

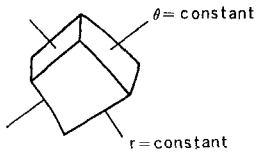


**Fig. 1(b) Elemental volume**

**General Model.** To facilitate the writing of the boundary conditions and the mathematical description of the gravitational forces acting on the fluid, the spherical coordinate system, Fig. 1(*a*), with its origin at the center of the container was chosen. An obvious advantage of this coordinate system is the compensation for change in the volume of the elemental control, Fig. 1(*b*), as its location varies throughout the container.

The governing equations for the system are [10]

Conservation of mass

$$\frac{D\rho}{Dt} + \rho(\nabla \cdot V) = 0 \tag{1}$$

Conservation of momentum

$$\rho \frac{DV}{Dt} - \nabla P + \nabla \cdot \sigma - \rho g = 0 \tag{2}$$

Conservation of energy

$$\rho C_v \frac{DT}{Dt} - \nabla \cdot (\kappa \nabla T) + P(\nabla \cdot V) + \sigma : \nabla V = 0 \tag{3}$$

Equation of state

$$F(\rho, P, T) = 0$$

Equations of state for most gaseous substances are quite complex, and in only a few instances have relationships been developed which are applicable to a wide range of temperatures and pressures. The ideal-gas equation of state can be used for gases of relatively low molecular weight at low pressures and moderate temperatures. However, the model is designed in such a manner that this is not a restriction.

A no-slip condition at the wall along with zero mass generation (or degradation) at the wall requires that all components of velocity be zero at the wall. Geometrical symmetry requires that the angular components of velocity vanish along the vertical axis of the sphere and prohibits angular variation of the radial component of velocity along this axis.

The wall of the container is at a uniform initial temperature $T_0$, and any change will result in a new wall temperature $T_{R,\theta}$ which is not necessarily uniform. The gas, which is assumed to conform to the relationships governing Newtonian fluids, is assumed to have constant viscosity, thermal diffusivity, and specific heat.

## Nomenclature

$C_v$ = constant-volume specific heat, Btu/lb$_m$-deg R
$d$ = diameter, ft
Gr = Grashof modulus ($\beta g d^3 \Delta T/\nu^2$)
$g$ = gravitational acceleration, ft/sec$^2$
$P$ = pressure, lb$_f$/ft$^2$
Pr = Prandtl modulus ($\nu/\alpha$)
$R$ = radius of sphere, ft
$R_g$ = gas constant, ft-lb$_f$/lb$_m$-deg R
Ra = Rayleigh modulus (Gr Pr)
$r, \theta, \phi$ = spherical coordinates, rad
$T$ = temperature, deg R
$t$ = time, sec
$V$ = velocity, ft/sec
$x, y, z$ = rectangular cartesian coordinates, ft
$\alpha$ = thermal diffusivity, ft$^2$/sec
$\beta$ = coefficient of volumetric expansion, 1/deg R
$\Delta$ = difference operator
$\delta$ = central difference operator
$\zeta$ = $\phi$ component of vorticity, rad/sec
$\kappa$ = thermal conductivity, Btu/sec-ft-deg R
$\lambda$ = iteration parameter
$\mu$ = viscosity, lb$_m$/ft-sec
$\nu$ = kinematic viscosity, ft$^2$/sec
$\pi$ = 3.1415927
$\rho$ = density, lb$_m$/ft$^3$
$\sigma$ = stress tensor, lb$_f$/ft$^2$
$\tau$ = dimensionless time
$\psi$ = stream function, ft$^3$/sec
$\omega$ = relaxation parameter

**Subscripts**

0 = initial condition
$\infty$ = shock condition

**Superscripts**

* = dimensionless variable
— = reference condition

Actual variations of these properties over the range of temperatures considered are negligible.

**Simplified Model.** The velocity component and all variations of the dependent variables in the $\phi$ direction are assumed to be zero (or negligible). This assumption of axisymmetric motion is based primarily on the absence of a component of gravitational force in the $\phi$ direction and on the fact that the external excitation will be applied in such a way that no variations will be induced in this direction.

The transient-convection conditions considered are those which occur as the fluid temperature varies from an initial temperature distribution $\bar{T}_{r,\theta}$. For zero initial velocity the pressure gradient in the system is given from the momentum-conservation equation as

$$\nabla P_{r,\theta} = \bar{\rho}_{r,\theta} g$$

in which $\bar{\rho}_{r,\theta}$ is the density which corresponds to the initial conditions of temperature $\bar{T}_{r,\theta}$. When velocity gradients are induced, they are usually quite small, and the above relation is a good approximation for the pressure gradient in the moving fluid. As the temperature varies from the initial (reference) temperature, the density variation can be expressed in terms of the temperature variation by a Taylor expansion about the reference condition as

$$\rho_{r,\theta} = \bar{\rho}_{r,\theta} + (T_{r,\theta} - \bar{T}_{r,\theta}) \frac{\partial \bar{\rho}}{\partial T}$$

where second- and higher-order terms have been neglected and $\partial\bar{\rho}/\partial T$ indicates that the differential is to be evaluated at the reference conditions. Introducing the coefficient of volumetric expansion $\bar{\beta}$ which corresponds to the reference condition and using this with the previous result, one obtains

$$\rho \frac{DV}{Dt} + \rho\beta g(T - \bar{T}) + \nabla \cdot \sigma = 0$$

as the relationship governing momentum conservation for this problem.

The effects of viscous heating and compressibility have been shown to be negligible when compared with conduction and convection for low-velocity fluid motion, as in the case under consideration; thus this simplification will be applied to the energy relationship governing the model. The effect of compressibility on the deformation of a fluid element and the resulting shear and normal forces were neglected in the momentum-conservation equations. The maximum percentage change in density is approximately 2 percent; thus the substantial derivative of density can be neglected in the continuity equation. Introducing the simplifications described above into equations (1)–(3) and rendering the equations in dimensionless form using

$$\begin{aligned} T^* &= (T - \bar{T})/(T_\infty - T) \\ \tau &= \alpha t/R^2 \\ V_r^* &= RV_r/\alpha \\ V_\theta^* &= RV_\theta/\alpha \\ r^* &= r/R \end{aligned} \tag{4}$$

and simplifying computational requirements by introducing a dimensionless stream function $\psi$ and vorticity $\zeta$ given by

$$\begin{aligned} V_r^* &= \frac{1}{r^{*2} \sin\theta} \frac{\partial \psi^*}{\partial \theta} \\ V_\theta^* &= \frac{1}{r^* \sin\theta} \frac{\partial \psi^*}{\partial r} \end{aligned} \tag{5}$$

$$\zeta^* = \frac{1}{r^* \sin\theta} \left( \frac{\partial^2 \psi^*}{\partial r^{*2}} + \frac{1}{r^{*2}} \frac{\partial^2 \psi^*}{\partial \theta^2} - \frac{\cot\theta}{r^{*2}} \frac{\partial \psi^*}{\partial \theta} \right) \tag{6}$$

gives the following equations for dimensionless temperature $T^*$, vorticity $\zeta^*$, and stream function $\psi^*$:

Energy transfer

$$\frac{\partial T^*}{\partial \tau} - \frac{1}{r^{*2} \sin\theta} \frac{\partial \psi^*}{\partial \theta} \frac{\partial T^*}{\partial r^*} + \frac{1}{r^{*2} \sin\theta} \frac{\partial \psi^*}{\partial r^*} \frac{\partial T^*}{\partial \theta} - \frac{\partial^2 T^*}{\partial r^{*2}} - \frac{2}{r^*} \frac{\partial T^*}{\partial r^*} - \frac{1}{r^{*2}} \frac{\partial^2 T^*}{\partial \theta^2} - \frac{\cot\theta}{r^{*2}} \frac{\partial T^*}{\partial \theta} = 0 \tag{7}$$

Vorticity transfer

$$\frac{\partial \zeta^*}{\partial \tau} + \frac{1}{r^{*2} \sin\theta} \frac{\partial \psi^*}{\partial r^*} \left( \frac{\partial \zeta^*}{\partial \theta} - \cot\theta \zeta^* \right) - \frac{1}{r^{*2} \sin\theta} \frac{\partial \psi^*}{\partial \theta} \left( \frac{\partial \zeta^*}{\partial r^*} - \frac{\zeta^*}{r^*} \right) + \frac{\mathrm{Gr}\,\mathrm{Pr}}{8} \left( \sin\theta \frac{\partial T^*}{\partial r^*} + \frac{\cos\theta}{r^*} \frac{\partial T^*}{\partial \theta} \right) + \mathrm{Pr} \left( \frac{\partial^2 \zeta^*}{\partial r^{*2}} + \frac{2}{r^*} \frac{\partial \zeta^*}{\partial r^*} + \frac{1}{r^{*2}} \frac{\partial^2 \zeta^*}{\partial \theta^2} + \frac{\cot\theta}{r^{*2}} \frac{\partial \zeta^*}{\partial \theta} - \frac{\csc^2\theta \zeta^*}{r^{*2}} \right) = 0 \tag{8}$$

Stream function

$$\frac{\partial^2 \psi^*}{\partial r^{*2}} + \frac{1}{r^{*2}} \frac{\partial^2 \psi^*}{\partial \theta^2} - \frac{\cot\theta}{r^{*2}} \frac{\partial \psi^*}{\partial \theta} - r^* \sin\theta \, \zeta^* = 0 \tag{9}$$

The transformation of the equations requires that the boundary and initial conditions be prescribed in terms of the variables $T^*$, $\zeta^*$, and $\psi^*$ rather than in terms of temperature and velocity components. It can be shown in a straightforward manner that the initial conditions for this problem are

$$T_{r,\theta}^* = 0 \quad \text{for} \quad \tau = 0 \tag{10}$$

$$\zeta_{r,\theta}^* = 0 \quad \text{for} \quad \tau = 0 \tag{11}$$

and

$$\psi_{r,\theta}^* = 0 \quad \text{for} \quad \tau = 0 \tag{12}$$

The boundary conditions for the dimensionless temperature are

$$T_{R,\theta}^* = 1 \quad \text{for} \quad \tau > 0 \tag{13}$$

$$\left. \frac{\partial T^*}{\partial \theta} \right|_{r,0} = 0 \quad \text{for} \quad \tau > 0 \tag{14}$$

and

$$\left. \frac{\partial T^*}{\partial \theta} \right|_{r,\pi} = 0 \quad \text{for} \quad \tau > 0 \tag{15}$$

The initial dimensionless stream function is chosen as zero; this choice dictates the following prescribed boundary conditions:

$$\psi_{R,\theta}^* = 0 \quad \text{for} \quad \tau > 0 \tag{16}$$

$$\psi_{r,0}^* = 0 \quad \text{for} \quad \tau > 0 \tag{17}$$

and

$$\psi_{r,\pi}^* = 0 \quad \text{for} \quad \tau > 0 \tag{18}$$

The boundary conditions for dimensionless vorticity are derived from the defining equation (6) in terms of the stream function and the velocity components. From equation (6), with the boundary conditions for $\psi^*$ prescribed by equation (16), it is seen, noting $r^* = 1$, that

$$\zeta_{R,\theta}^* = \frac{1}{r^* \sin\theta} \frac{\partial^2 \psi_{R,\theta}^*}{\partial r^{*2}} \quad \text{for} \quad \tau > 0 \tag{19}$$

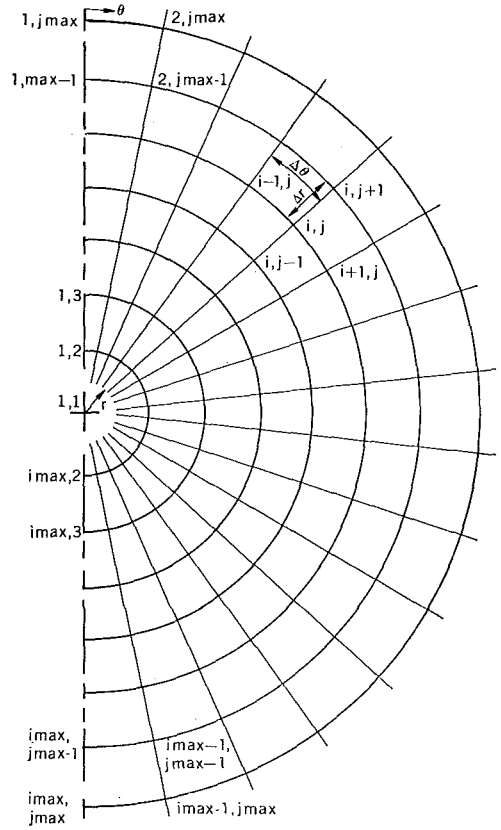


**Fig. 1(c) Finite-difference grid for a sphere**

From the description of the general model and

$$\zeta^* = \frac{\partial V_\theta^*}{\partial r^*} + \frac{V_\theta^*}{r^*} - \frac{1}{r^*}\frac{\partial V_r^*}{\partial \theta}$$

it is evident that one must require for boundary conditions that

$$\zeta_{r,0}^* = 0 \qquad \text{for} \qquad \tau > 0 \tag{20}$$

and

$$\zeta_{r,\pi}^* = 0 \qquad \text{for} \qquad \tau > 0 \tag{21}$$

If equations (7), (8), and (9), along with the boundary and initial conditions (10)–(21), are used in a computational procedure, then the energy and mass flux during the transition period from the disruption of equilibrium to the reestablishment of steady-state conditions may be described in detail.

## Computational Procedure

The coupled nonlinear partial differential equations (7), (8), and (9) are transformed into simultaneous difference equations through the use of central-difference relationships which can be found by several methods [11].

A difference form is required to calculate vorticity at the boundary where the gradient is specified. Equation (12) is transformed into a difference equation through the use of a second-order approximation to the second derivative with respect to the independent variable with backward differences. The resulting equation for (19) is

$$\zeta_{R,\theta}{}^{*\tau} = \frac{1}{R\sin\theta}\,\frac{b^{\delta^2}\psi^{*\tau}}{(\Delta r)_{R,\theta^2}}$$

where

$$b^{\delta^2}\psi^* = 2\psi_R{}^* - 5\psi_{R-\Delta r}{}^* + 4\psi_{R-2\Delta r}{}^* - \psi_{R-3\Delta r}{}^* \tag{22}$$

The combination of the above equation with equation (29) yields

$$\zeta_{ij}{}^{*\tau} \approx \frac{1}{R\sin\theta(\Delta r)^2}\,(2\psi_{ij}{}^* - 5\psi_{ij-1}{}^* + 4\psi_{ij-2}{}^* - \psi_{ij-3}{}^*) \tag{23}$$

as the relationship for calculating vorticity at the solid boundary.

The difference equations employ subscripts $i$ and $j$ to refer to angular and radial positions, respectively, on the finite-difference grid as shown in Fig. 1($c$).

An implicit formulation is used to avoid the restrictions common to explicit systems [12]. As an example to clarify the particular form used, if

$$\frac{\partial T}{\partial \tau} = F(T)$$

is to be set up in an implicit form with central differences in time, one uses

$$\frac{T^{\tau+\Delta\tau} - T^\tau}{\Delta\tau} = F^1(T^{\tau+\lambda\Delta\tau})$$

where $F^1$ denotes the approximation to $F$ in spatial finite differences and

$$T^{\tau+\lambda\Delta\tau} \equiv \lambda T^{\tau+\Delta\tau} + (1-\lambda)T^\tau$$

$\lambda$ being a parameter of the implicit formulation. For $\lambda = 0$, the system is explicit, and for $0 < \lambda \leq 1$, the system is implicit.

Several investigators [6, 7, 8] have found that using $\psi^*$ as explicit in approximations for energy and vorticity transfer greatly facilitates the computation of linear-difference relationships for temperature and vorticity with a minimum degree of error. That is, one uses $\psi^{*\tau}$ in equations for $T^{*\tau+\Delta\tau}$ and $\zeta^{*\tau+\Delta\tau}$, and $\psi^{*\tau+\lambda\Delta\tau}$ or $\psi^{*\tau+\Delta\tau}$ is substituted for $\psi^*$ in equation (14) once the new temperature and vorticity have been computed.

Thus one obtains the following as the difference equations governing the problem (the * notation is omitted here with the understanding that all quantities are dimensionless):

Energy transfer

$$\frac{T_{ij}{}^{\tau+\Delta\tau} - T_{ij}{}^\tau}{\Delta\tau} - \frac{1}{r_j{}^2\sin\theta_i}\left(\frac{\delta\theta\psi^\tau}{2\Delta\theta}\right)_{ij}\left(\frac{\delta r T^{\tau+\lambda\Delta\tau}}{2\Delta r}\right)_{ij} + \frac{1}{r_j{}^2\sin\theta_i}\left(\frac{\delta r\psi}{2\Delta r}\right)_{ij}^{\tau}\left(\frac{\delta\theta T^{\tau+\lambda\Delta\tau}}{2\Delta\theta}\right)_{ij} - \left(\frac{\delta^2 r T^{\tau+\lambda\Delta\tau}}{(\Delta r)^2}\right)_{ij} - \frac{2}{r_j}\left(\frac{\delta r T^{\tau+\lambda\Delta\tau}}{2\Delta r}\right)_{ij} - \frac{1}{r_j{}^2}\left(\frac{\delta\theta^2 T^{\tau+\lambda\Delta\tau}}{(\Delta\theta)^2}\right)_{ij} - \frac{\cot\theta_i}{r_j{}^2}\left(\frac{\delta\theta T^{\tau+\lambda\Delta\tau}}{2\Delta\theta}\right)_{ij} = 0 \tag{24}$$

Vorticity transfer

$$\frac{\zeta_{ij}{}^{\tau+\Delta\tau} - \zeta_{ij}{}^\tau}{\Delta\tau} - \frac{1}{r_j{}^2\sin\theta_i}\left(\frac{\delta\theta\psi}{2\Delta\theta}\right)^{\tau}_{ij} \times\left[\left(\frac{\delta r\zeta^{\tau+\lambda\Delta\tau}}{2\Delta r_{ij}}\right) - \frac{\zeta_{ij}{}^{\tau+\lambda\Delta\tau}}{r_j}\right] + \frac{1}{r_j{}^2\sin\theta_i}\left(\frac{\delta r\psi^\tau}{2\Delta r}\right)_{ij} \times\left[\left(\frac{\delta\theta\zeta^{\tau+\lambda\Delta\tau}}{2\Delta\theta}\right)_{ij} - \cot\theta_i\zeta_{ij}{}^{\tau+\lambda\Delta\tau}\right] + \frac{\mathrm{Gr}\,\mathrm{Pr}^2}{8} \times\left[\sin\theta_i\left(\frac{\delta r T^{\tau+\lambda\Delta\tau}}{2\Delta r}\right)_{ij} + \frac{\cos\theta_i}{r_j}\left(\frac{\delta\theta T^{\tau+\lambda\Delta\tau}}{2\Delta\theta}\right)_{ij}\right] - \mathrm{Pr}\left[\left(\frac{\delta^2 r\zeta^{\tau+\lambda\Delta\tau}}{(\Delta r)^2}\right)_{ij} + \frac{2}{r_j}\left(\frac{\delta r\zeta^{\tau+\lambda\Delta\tau}}{2\Delta r}\right)_{ij} + \frac{1}{r_j{}^2}\left(\frac{\delta^2\theta\zeta^{\tau+\lambda\Delta\tau}}{(\Delta\theta)^2}\right)_{ij} + \frac{\cot\theta_i}{r_j{}^2}\left(\frac{\delta\theta\zeta^{\tau+\lambda\Delta\tau}}{2\Delta\theta}\right)_{ij} - \frac{\csc^2\theta_i}{r_j{}^2}\zeta_{ij}{}^{\tau+\lambda\Delta\tau}\right] = 0 \tag{25}$$

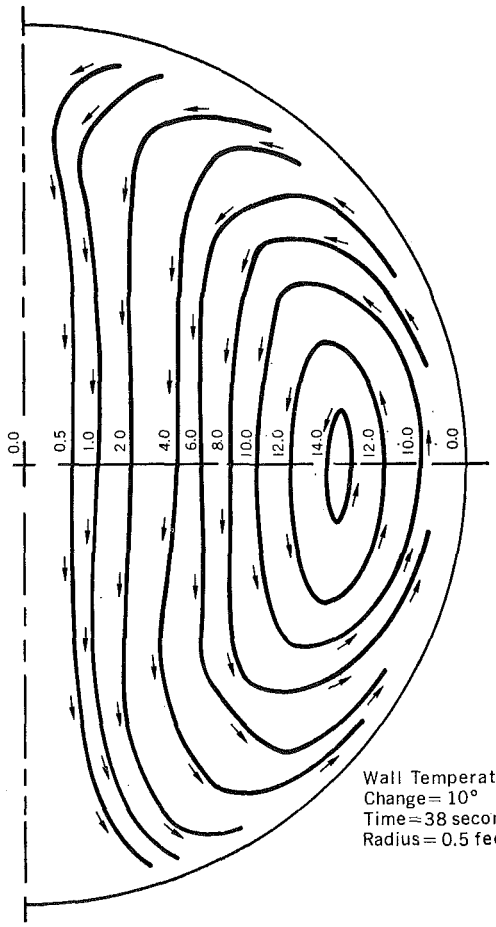


Fig. 2(a) Dimensionless streamlines at $\tau = 0.030$ in a sphere

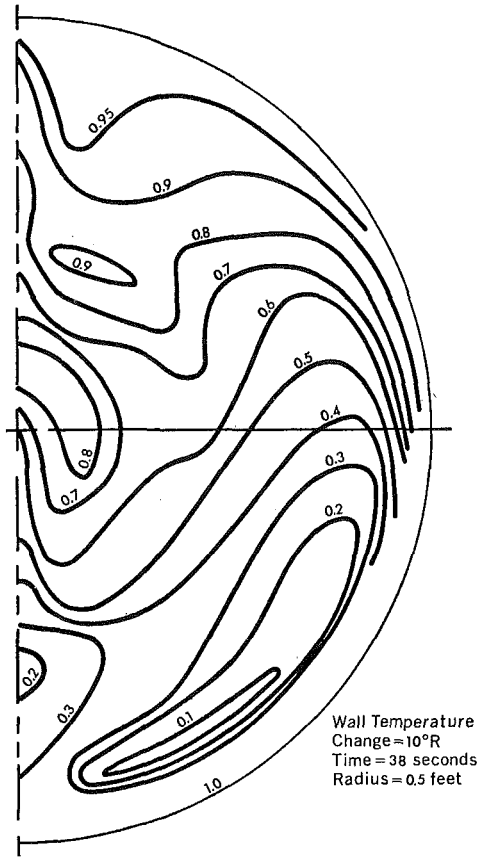


Fig. 2(b) Dimensionless isotherms at $\tau = 0.030$ in a sphere

Stream function

$$\left(\frac{\delta^2 r \psi^{\tau+\Delta\tau}}{(\Delta r)^2}\right)_{ij} + \frac{1}{r_j^2}\left(\frac{\delta^2\theta\psi^{\tau+\Delta\tau}}{(\Delta\theta)^2}\right)_{ij} - \frac{\cot\theta_i}{r_j^2} \times \left(\frac{\delta\theta\psi^{\tau+\Delta\tau}}{2\Delta\theta}\right)_{ij} - r_j \sin\theta_i \zeta_{ij}^{\tau+\Delta\tau} = 0 \quad (26)$$

When the iterative process converges sufficiently, the new values of $T^*$ and $\zeta^*$ are used for first approximations in computing for $\tau + 2\Delta\tau$ and the new $\psi^*$ is considered constant over the next set of computations. The matrix equation is solved using a block iterative method which is a successive approximation to a specified degree of convergence. All variables for each particular point are recomputed simultaneously, each point in turn one at a time.

## Results

Figures 2 and 3 show typical results as obtained from computer solutions for air at atmospheric pressure in a 1-ft-dia container initially at 492 deg R subjected to a 10 deg increase in the wall temperature. Mass flux at selected times is indicated in Figs. 2(*a*) and 3(*a*) by the use of dimensionless streamlines. As expected, mass is transferred in an upward direction, with higher velocities being indicated in the regions near the wall. A semicircular flow pattern is given, indicating the upward flow of the heated fluid which forces the cooler fluid to the lower regions of the spherical container. The dimensionless isotherms in Figs. 2(*b*) and 3(*b*) indicate that heat transfer by convection dominates conduction effects, with overall heating occurring from the top to the bottom of the container. Temperature transients at various locations in the container are indicated in Fig. 4. The most rapidly increasing temperatures are for the positions in the upper portion of the container. In and near the bottom, oscillations occur in the temperatures initially, but as the system ap-

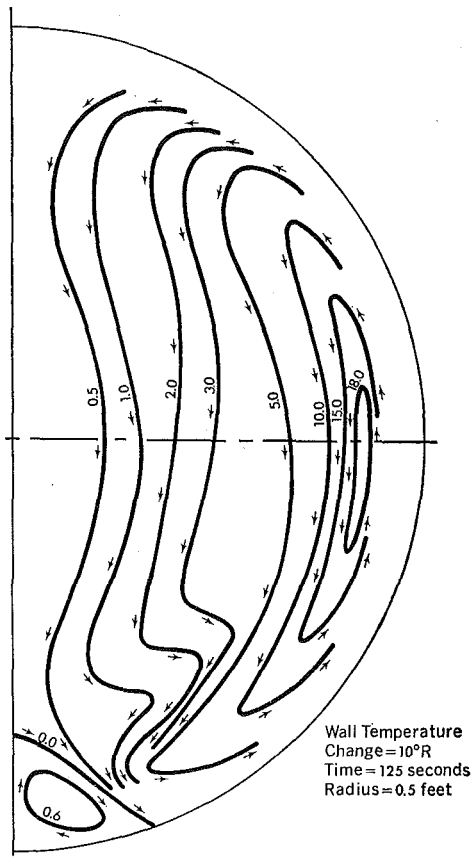


Fig. 3(a) Dimensionless streamlines at $\tau = 0.10$ in a sphere

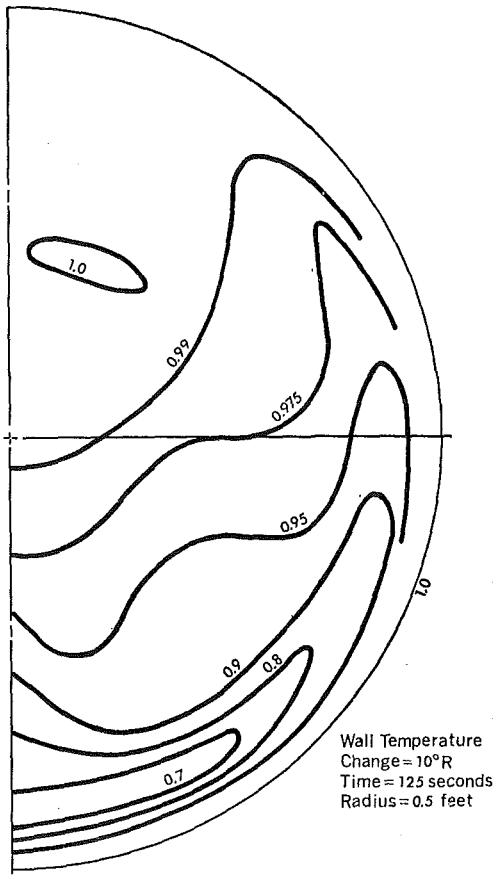


**Fig. 3(b) Dimensionless isotherms at $\tau = 0.100$ in a sphere**

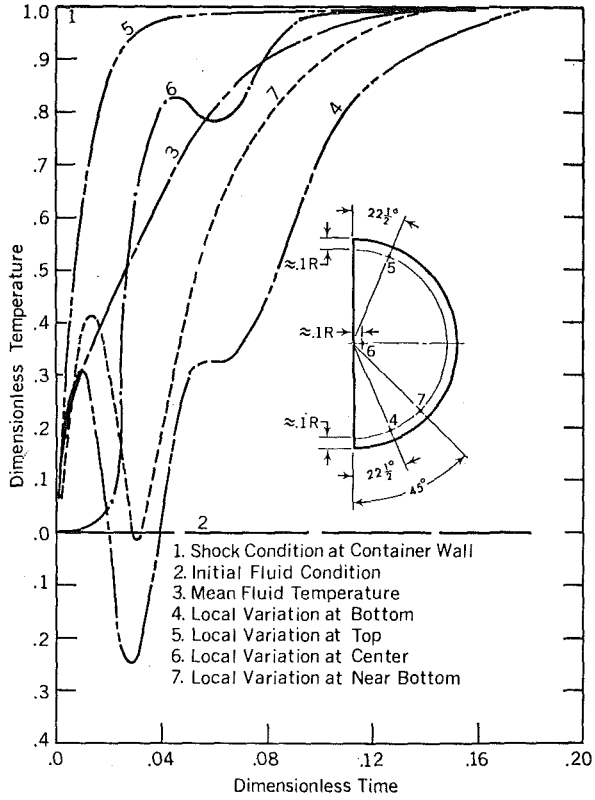


**Fig. 4 Temperature transients at selected points**

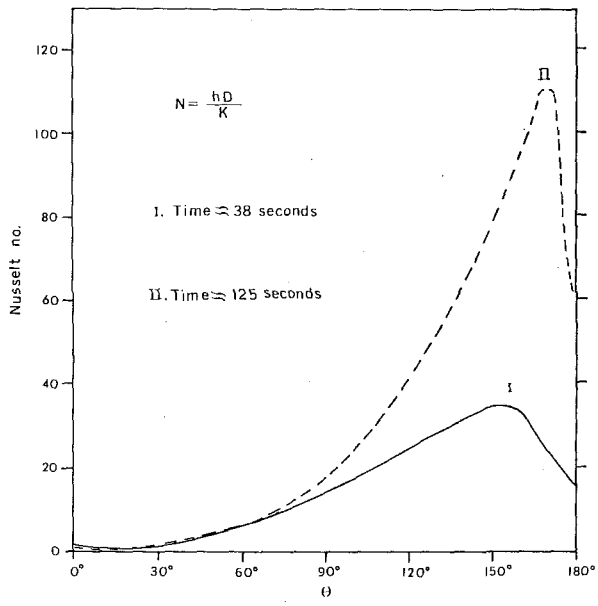


**Fig. 5 Nusselt number vs. $\theta$**

proaches the new equilibrium condition the temperatures at the low positions rise steadily to the equilibrium temperature of the system. The average fluid temperature indicated in Fig. 4 agrees with the mean fluid-temperature-transient pattern obtained from a lumped-parameter analysis of the problem taking into account the variation of the mean heat-transfer coefficient. This result

$$T_{\text{mean}} = T_\infty + (T_0 - T_\infty)e^{-\frac{A}{\rho C_v}\Sigma h_i \Delta t_i}$$

was obtained from a modification of the general energy equation for a control volume. Kinetic- and potential-energy effects were neglected and Newton's law of cooling was used for an expression of the rate of heat transfer to the system. As indicated previously, a prior knowledge of certain information is required for such an analysis and the resultant relationships to be useful. In the above, the mean-heat-transfer-coefficient variation with respect to time is required. In the absence of such data, one normally would not be able to use the result. The model developed for the analysis of this problem produces local and average heat-transfer coefficients based on the temperature distributions at each time step. These data were used in the above equation to obtain a crude estimate of the error bound during the development of the computational procedure of the model.

The streamline and isotherm patterns indicate a boundary-layer-type flow near the wall of the container in the lower and middle regions. This result was obtained without any assumptions regarding boundary-layer flow near the wall.

The appearance of a recirculation pattern after a short period of time at the bottom is a result of the opposing conduction and convection heat-transfer trends in this region. During this period of time, the point of maximum heat transfer to the fluid occurs near $\theta = 180$ deg. As the heated fluid rises, it loses energy by conduction and is partially cooled by the downward flow of cold fluid from the upper part of the container. The strong variations in temperature are due to the coupled interaction of these two effects.

The computer results, obtained by applications of the model to the problem stated above, indicate acceptable trends for the period of time presented in the figures.

Convergence and stability of the computational procedure were obtained by decreasing the spatial increments until a point was reached where no changes in the results were obtained as a result of a further decrease in the increments. As expected, an increased amount of computing time was required as the spatial increments were decreased. It was necessary to distinguish between changes due to convergence and the greater amount of detail given for

small grid sizes as compared with coarse grids. The smaller the grid size, the more detail is obtained at the expense of considerably more computer time.

The computer used in this study was the IBM 360/50. The convergence and stability of implicit central-difference schemes having been discussed in a number of mathematical and engineering papers and textbooks, it is sufficient here to state that as many as 1300 points were used to determine the values of temperature vorticity and stream function for each point in time. Carrying this procedure to equilibrium would have required many hours of computer time which from an economic standpoint was unavailable. It is anticipated that a faster computer system would permit carrying the procedure to equilibrium.

Local Nusselt number versus $\theta$ is displayed in Fig. 5 at 38 and 125 sec to give a representative indication of Nusselt-number values.

## Conclusion

The main shortcoming of the model is that the procedure is slow and no experimental results have been found with which to compare the analysis. However, this analysis should be helpful to the experimentalist, and the reader is referred to [13] for a more detailed presentation of the study.

## References


1 Tanger, G. E., Phillips, B. R., Vachon, R. I., Soileau, J. F., Hofer, R. G., and Tatom, F. B., "Theoretical Studies of Transient Heat Transfer between a Gas and Spherical Container," Progress Report I, NASA Contract Number NAS8-2411, Auburn Research Foundation, 1961.

2 Tatom, F. B., Lytle, J. H., Nix, G. H., and Pollard, R. B., "Analytical Studies in Heat Transfer and Thermodynamics," Report VII, NASA Contract Number NAS8-2411, Auburn Research Foundation, 1963.

3 Mack, L. R., and Hardee, H. C., "Natural Convection between Concentric Spheres at Low Rayleigh Numbers," *International Journal of Heat and Mass Transfer*, Vol. 11, 1968.

4 Bishop, E. H., Mack, L. R., and Scanlan, J. A., "Heat Transfer by Natural Convection between Concentric Spheres," *International Journal of Heat and Mass Transfer*, Vol. 9, 1966.

5 Blair, A., Metropolis, N., von Newmann, J., Taub, A. H., and Tsingou, H., "A Study of a Numerical Solution to a Two-Dimensional Hydrodynamical Problem," Report LA-2165, Los Alamos Scientific Laboratory, 1959.

6 Wilkes, J. O., and Churchill, S. W., "Finite Difference Computation of Natural Convection in a Rectangular Enclosure," *AIChE Journal*, Vol. 12, No. 1, 1966.

7 Barakat, H. Z., "Transient Laminar Free-Convection Heat and Mass Transfer in Two-Dimensional Closed Containers Containing Distributed Heat Source," *Proceedings of the Conference on Propellant Tank Pressurization and Stratification*, Marshall Space Flight Center, Huntsville, Ala., 1965.

8 Clark, J. A., and Barakat, H. Z., "Transient Laminar Free-Convection Heat and Mass Transfer in Closed, Partially Filled, Liquid Containers," Technical Report 1, NASA Contract Number NAS8-825, University of Michigan, Ann Arbor, Mich., 1964.

9 Churchill, S. W., "The Present Limits of Our Ability to Predict Natural Circulation and Radiation," *Proceedings of the Second Southeastern Seminar on Thermal Sciences*, Oak Ridge National Laboratory, Oak Ridge, Tenn., 1966.

10 Bird, R. B., Stewart, W. E., and Lightfoot, E. N., *Transport Phenomena*, John Wiley & Sons, New York, N. Y., 1960.

11 Scarborough, J. B., *Numerical Mathematical Analysis*, 5th ed., The Johns Hopkins Press, Baltimore, Md., 1962.

12 Crandall, S. H., *Engineering Analysis*, McGraw-Hill, New York, N. Y., 1956.

13 Whitley, H. G., III, "Transient Laminar Free Convection Heat and Mass Transfer in Closed Spherical Containers," unpublished MS thesis, Auburn University, Auburn, Ala., 1968.

D. P. WEHMEYER[1]
Senior Engineer,
McDonnell Aircraft Co.

T. W. JACKSON[2]
Professor,
School of Mechanical Engineering,
Georgia Institute of Technology,
Atlanta, Ga.

# Transient Film Boiling of Carbon Tetrachloride and Freon-113 on a Horizontal Cylindrical Surface

*This paper presents an experimental and analytical investigation to determine the film growth during the initial regimes of transient film boiling from a horizontal wire for carbon tetrachloride and Freon-113. The wire was subjected to a step change in temperature by a rapid discharge of energy from an electrical capacitor. Constant wire temperature was assumed in the analytical model, and heat transfer through the vapor phase was assumed to be by radiation and conduction. All radiation from the wire was determined to pass through the vapor and to be absorbed in depth within the liquid phase. Convection heat transfer to the liquid pool was considered to take place at the vapor–liquid interface. Heat-transfer rates within the vapor phase were calculated, as was the growth rate of the vapor–liquid interface.*

## Introduction

A SMALL-VOLUME periodic fluid flow could conceivably be obtained by electrical energy discharges into a small-diameter wire that is located within a confined space with a liquid in contact with the wire surface. With each discharge of energy a small volume of vapor would be formed and this in turn could displace a slightly smaller volume of liquid from the confining space. An initial example of this phenomenon was studied by Richards [1],[3] who investigated transient film boiling in a horizontal annulus filled with saturated water.

Pitts [2] obtained experimental values of vapor growth rates for transient film boiling from a horizontal wire in a pool of saturated water. He compared his experimental data to an analytical theory.

Yen [3] also studied the film formation on a horizontal wire for the subcooled-liquid case. His experiments indicated a definite reduction in final film thickness with increased subcooling of the liquid pool. Again, water was the liquid under investigation.

Thus, prior to the present research, there appear to be no published results of experimental studies for liquids other than water. The results reported here are for transient film boiling of carbon tetrachloride and Freon-113 on a submerged horizontal cylindrical surface.

## Analysis

**The Analytical Model.** Consider a horizontal cylindrical wire submerged in a liquid pool and subjected to a sudden step change in temperature which is sufficiently large to result in film boiling, Fig. 1. Some initial radius $R_0$ is reached by the vapor film in a time that is short compared to the total transient time. The initial temperature of the vapor is assumed to be equal to that of the saturation temperature of the liquid at the system pressure, which is 1 atm for this investigation. The film is considered to be cylindrical, with no axial variation in thickness. The wire temperature is considered to be constant with negligible axial or radial variation.

Heat transfer through the vapor is by conduction, convection, and radiation. It is shown in reference [4] that the vapor film is optically thin and thus absorbs and emits radiation negligibly due to its low extinction coefficient. Also in reference [4], the convective-heat-transfer effect within the vapor phase is shown to be negligible when compared to the conductive heat transfer.

Heat transfer to the liquid from the vapor–liquid interface is approximated by the formula for the heat-transfer coefficient at the stagnation point of a solid cylinder in forced transverse flow. This approximation is somewhat arbitrary but was used because the flow field relative to and around the vapor cylinder resembles locally the stagnation conditions at a cylinder. It is recognized, however, that it is a transient process and the Reynolds number does depend on time.

The pressure variation within the vapor and the buoyancy force on the vapor are negligible and the temperature of the

[1] Formerly, Graduate Student, School of Mechanical Engineering, Georgia Institute of Technology, Atlanta, Ga.

[2] Currently on leave as Technical Director, NIPCC, U. S. Department of Commerce, Washington, D. C.

[3] Numbers in brackets designate References at end of paper.

Contributed by the Heat Transfer Division of THE AMERICAN SOCIETY OF MECHANICAL ENGINEERS and presented at the AIChE-ASME Heat Transfer Conference, Denver, Colo., August 6–9, 1972. Manuscript received by the Heat Transfer Division October 19, 1971. Paper No. 72-HT-35.

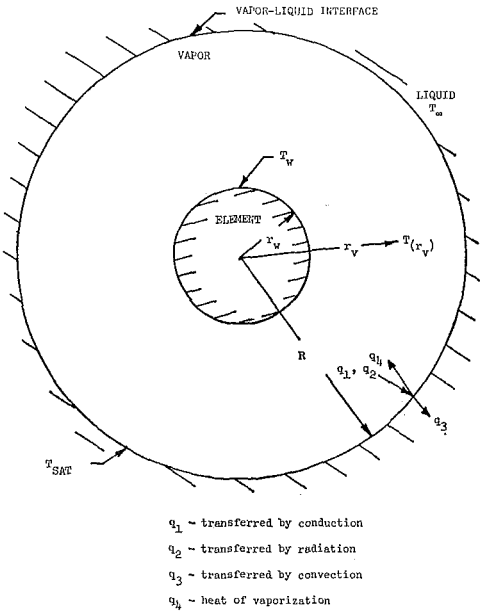


**Fig. 1 Physical model of transient film boiling from a cylindrical surface**

liquid at the vapor–liquid interface varies negligibly from that of the saturation temperature of the liquid, as is shown in reference [4].

**Temperature Distribution in Vapor Phase.** The temperature distribution within the vapor phase was determined for the case of negligible vapor-convection effects by using the energy equation

$$\frac{\partial T}{\partial \theta} - \alpha_v \left( \frac{\partial^2 T}{\partial r^2} + \frac{1}{r} \frac{\partial T}{\partial r} \right) = 0 \tag{1}$$

The initial condition is

$$T(r, 0) = T_{SAT} \qquad r_w < r \leq R \tag{2}$$

and the boundary conditions are

$$T(r_w, \theta) = T_w \qquad \theta > 0 \tag{3}$$

and

$$T(R, \theta) = T_{SAT} \qquad \theta > 0 \tag{4}$$

Using standard techniques as given in Carslaw and Jaeger (see reference [4] for details), the temperature distribution in the vapor was determined to be

$$T = T_w + \frac{(T_{SAT} - T_w)\left[ E_1\left(\frac{r^2}{4\alpha_v\theta}\right) - E_1\left(\frac{r_w^2}{4\alpha_v\theta}\right)\right]}{E_1\left(\frac{R^2}{4\alpha_v\theta}\right) - E_1\left(\frac{r_w^2}{4\alpha_v\theta}\right)} \tag{5}$$

Partial differentiation of equation (5) with respect to $r$ yields

**Table 1 Experimental vapor-cylinder-radius study**

| No. | $\Delta T$ $(T_w - T_{SAT})$ (°F) | $T_\infty$ (°F) | Wire Diameter (inches) | Vapor Cylinder Radius at 9 Millisec. (inches) |
|---|---|---|---|---|
| Fluid: | Carbon Tetrachloride | | | |
| 1 | 1775 | 170.0 | 0.010 | 0.0235 |
| 2 | 1802 | 157.7 | 0.010 | 0.0180 |
| 3 | 1768 | 153.9 | 0.010 | 0.0190 |
| 4 | 1744 | 168.9 | 0.010 | 0.0255 |
| 5 | 1180 | 168.9 | 0.010 | 0.0165 |
| 6 | 1315 | 169.0 | 0.010 | 0.0230 |
| 7 | 1382 | 169.0 | 0.010 | 0.0250 |
| 8 | 1325 | 164.6 | 0.010 | 0.0210 |
| 9 | 1350 | 163.2 | 0.010 | 0.0185 |
| Fluid: | Water | | | |
| 10 | 1263 | 212.0 | 0.010 | 0.0275 |
| (5) | *1265 | 210.9 | 0.0098 | 0.0255 |
| (9) | *1468 | 210.9 | 0.0098 | 0.0335 |
| (8) | **1343 | 194.0 | 0.0098 | 0.0125 |
| (20) | **1108 | 205.0 | 0.0126 | 0.0165 |
| Fluid: | Freon 113 | | | |
| 11 | 1253 | 111.2 | 0.010 | 0.0185 |
| 12 | 1302 | 111.2 | 0.010 | 0.0170 |
| 13 | 1306 | 104.3 | 0.010 | 0.0165 |
| 14 | 1432 | 116.7 | 0.010 | 0.0235 |
| 15 | 1458 | 117.1 | 0.010 | 0.0235 |
| 16 | 1462 | 103.4 | 0.010 | 0.0190 |
| 17 | 1403 | 102.6 | 0.010 | 0.0170 |
| 18 | 1463 | 110.5 | 0.010 | 0.0185 |

* Reference 2
** Reference 3

$$\frac{\partial T}{\partial r} = \frac{(T_{SAT} - T_w)}{E_1\left(\frac{R^2}{4\alpha_v\theta}\right) - E_1\left(\frac{r_w^2}{4\alpha_v\theta}\right)} \cdot \frac{-2e^{-\frac{r^2}{4\alpha_v\theta}}}{r} \tag{6}$$

This result is used later in the conduction equation to represent the conductive heat flux arriving at the vapor–liquid interface.

**Convection Energy Transfer within the Liquid Phase.** The convective-heat-transfer coefficient from the vapor cylinder to the liquid phase is taken as that of the stagnation point of a cylinder in forced transverse flow and is computed from the Nusselt number

$$\mathrm{Nu} = c\,\mathrm{Re}^n \mathrm{Pr}^m \tag{7}$$

where $n$, $m$, and $c$ may tentatively be taken from Jacob [5] to be

$$n = 0.5$$
$$m = 0.31 \tag{8}$$

and

$$c = 1.20$$

and where Re and Pr represent, respectively, the Reynolds and Prandtl numbers.

In computer calculations the value of $c$ was varied for the vapor-film growth rate to see if better agreement between theory and experiment could be obtained. The velocity of the interface is given by

$$v = \frac{dR}{d\theta} \tag{9}$$

## Nomenclature

$h_{fg}$ = heat of vaporization, Btu/lb
$h_{lm}$ = convection-heat-transfer coefficient, Btu/sec-in²-deg F
$k$ = thermal conductivity, Btu/sec-in-deg F
$R$ = vapor–liquid interfacial radius, in.
$r$ = radius, in.
$T$ = temperature, deg F
$v$ = velocity, in./sec
$x$ = argument for exponential integral
$Z$ = variable of integration
$\alpha$ = thermal diffusivity, in.²/sec
$\nu$ = kinematic viscosity, in.²/sec
$\rho$ = density, lb/in.³
$\theta$ = time, sec
$\phi$ = dummy function in solution of energy equation, deg F
$\eta$ = dummy function in solution of energy equation

**Subscripts**

$l$ = refers to liquid phase
$m$ = refers to evaluation at mean temperature of liquid phase, $(T_\infty + T_{SAT})/2$
SAT = refers to saturation conditions
$v$ = refers to vapor phase
$w$ = refers to wire condition
$\infty$ = refers to pool conditions
0 = initial condition

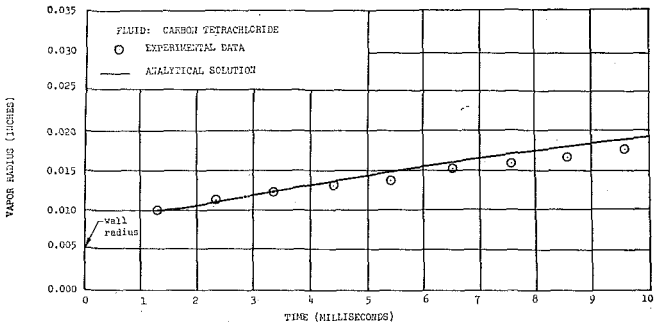


**Fig. 2 Plot of vapor radius as a function of time for No. 5; $T_w$ = 1350 deg F, $T_\infty$ = 168.9 deg F**

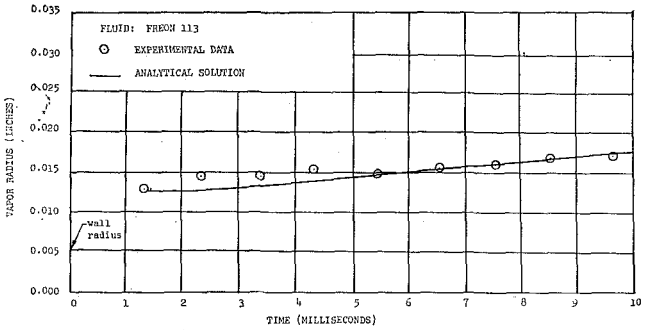


**Fig. 3 Plot of vapor radius as a function of time for No. 17; $T_w$ = 1520 deg F, $T_\infty$ = 102.6 deg F**

Substitution of equations (8) and (9) into equation (7) gives

$$\frac{h_{lm}2R}{k_{lm}} = 1.20\left(\frac{\frac{dR}{d\theta}2R}{\nu_{lm}}\right)^{0.5} \mathrm{Pr}_{lm}{}^{0.31} \qquad (10)$$

which is an expression for the convective-heat-transfer coefficient $h_{lm}$ in terms of fluid properties, vapor-film radius, and vapor-film velocity.

**Energy Balance at the Vapor–Liquid Interface.** The energy balance at the vapor–liquid interface of the vapor film is

$$q_1 + q_2 = q_3 + q_4 \qquad \text{(see Fig. 1)}$$

Radiation from the wire was considered to be absorbed in depth within the liquid pool and not at the liquid–vapor interface. This assumption, which is discussed in detail in reference [4], makes $q_2$ equal to zero. Therefore,

$$-k_v \left.\frac{\partial T}{\partial r}\right|_{r=R} = h_{lm}(T_{\mathrm{SAT}} - T_\infty) + \rho_v h_{fg}\dot{R} \qquad (11)$$

Substitution of equations (6) and (10) into equation (11) gives

$$\rho_v h_{fg} R\dot{R} = \frac{2k_v(T_{\mathrm{SAT}} - T_w)e^{-\frac{R^2}{4\alpha_v\theta}}}{E_1\left(\frac{R^2}{4\alpha_v\theta}\right) - E_1\left(\frac{r_w{}^2}{4\alpha_v\theta}\right)} - \frac{0.60k_{lm}\mathrm{Pr}_{lm}{}^{0.31}(T_{\mathrm{SAT}} - T_\infty)\sqrt{2R}\sqrt{\dot{R}}}{\sqrt{\nu_{lm}}} \qquad (12)$$

Equation (12), subject to the initial condition

$$R = R_0 \quad \text{at} \quad \theta = 0$$

constitutes an initial-value problem the solution of which should yield the vapor–liquid interface radius as a function of time.

## Discussion of Results

The heating-element temperature and vapor-film growth rate were determined for the fluids used. Both the conductive heat transfer through the vapor phase into the vapor–liquid interface and the convective heat transfer from the vapor–liquid interface into the liquid phase were calculated numerically.

**Temperature Determination.** A Wheatstone bridge and oscilloscope system (reference [4], Chapter IV) provided a means for determining the heating-element temperature as a function of time. A typical plot of heating-element temperature versus time is presented in reference [4], and proved to be linear during the transient boiling period. The element temperature change was initiated by the capacitor discharge and was better than 99 percent complete at the end of 145 microsec.

Since the transient-film-boiling period was approximately 10 millisec, the mean temperature was defined as the element temperature at 5 millisec following capacitor discharge. In 10 millisec the typical wire at a temperature of 1950 deg F changed its temperature only 30 deg F. The mean element temperature was used in the vapor-growth-rate calculations reported herein.

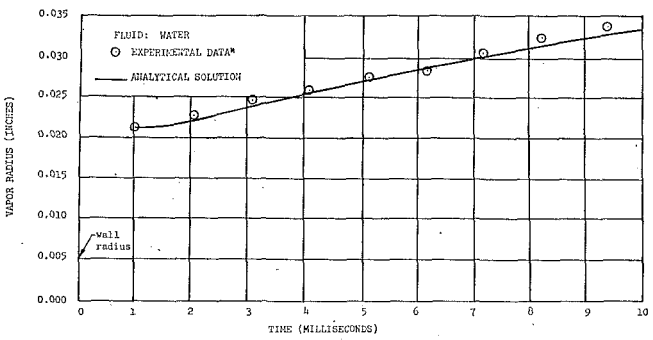


**Fig. 4 Plot of vapor radius as a function of time for water; $T_w$ = 1680 deg F, $T_\infty$ = 210.9 deg F; * reference [2]**

**Experimental Vapor Growth Data.** The experimental vapor formation data are summarized in Table 1. The vapor cylinder radius at 9 millisec is given for each of 18 film boiling experiments. The vapor-film growth was obtained from measurements on selected photographic frames of the phenomena, which were recorded by a Hycam camera connected into the initiation circuit. The camera operated at approximately 4000 frames per sec.

An initial burst of vapor was observed at the beginning of each of the filmed tests. This vapor was nucleate in character and somewhat opaque, while the vapor found later was transparent. It was thus seen that during the initial period, which was microseconds in duration, nucleate boiling took place. The first frame that showed a transparent vapor was considered to be the start of the transient-film-boiling process, and all numerical calculations were started using the corresponding value of time and vapor radius.

As indicated in Table 1, tests were made to verify the repeatability of the experimental results under approximately the same conditions. Representative runs were selected to be analytically verified and the comparisons are presented graphically in Figs. 2 and 3. A test result for water from reference [2] is shown in Fig. 4.

**Nusselt Relation for Convection and Its Effect on Vapor Growth.** Equation (12) was programmed for a Burrough 5500 digital computer and solved by means of Runge–Kutta integration for each run of this investigation.

At the start of the numerical-solution process the value of $c$, the coefficient in the Nusselt relationship of equation (7), was varied to determine if some other value besides $c$ = 1.2 would yield better agreement between the proposed theory and experimental data. It was determined that the final value of the vapor-film radius at 10 millisec depended on the value of $c$ used. To approach the limiting value of saturated pool temperature, where the convective heat transferred reduces to zero, it was found that better agreement between the theory and the experi-

mental data could be obtained if a value of $c$ equal to 2.2 were used. Therefore, this value was used for all the comparisons. The mean deviation between the theory and experimental data was calculated to be approximately 9 percent.

**Thermal Decomposition of Test Fluid.** Thermal decomposition was minimal under the conditions encountered in this investigation. The extremely short time period during which the vapor was at its elevated temperature was not long enough to produce the thermal decompositions shown in references [6, 7]. The total time that the heating-element temperature was higher than the pool temperature was approximately $^9/_{10}$ sec for a test run.

To check for possible deposits that may have been left on the wire due to possible decomposition of the fluid, a "Steroscan" Mark II scanning electron microscope (Cambridge Instrument Co.) was used to photograph calibrated wire elements. No noticeable deposits could be detected.

## Conclusions

1 It is not possible to obtain film boiling immediately upon a step change in wire temperature. Initially nucleate-type bubbles are formed which quickly unite to form a vapor film. It requires approximately 1 millisec for a clear vapor film to form.

2 The transient-film-boiling process occurs in thermal equilibrium. The vapor–liquid interface is at the saturation temperature corresponding to the external pressure that is present.

3 The analytical model presented here gives agreement within 9 percent of the experimental data from Freon-113, carbon tetrachloride, and water if the coefficient $c = 2.2$ is used in the Nusselt relationship, equation (22). However, the analytical model is hypothetical in other respects (arbitrary starting conditions), and the Nusselt relationship cannot be inferred with confidence, nor can it be proved to have constant exponents and coefficients.

## References


1 Richards, E. L., "Transient Film Boiling in a Horizontal Annulus Filled with a Saturated Liquid," PhD thesis, School of Mechanical Engineering, Georgia Institute of Technology, Atlanta, Ga., June 1969.

2 Pitts, D. R., "Transient Film Boiling on a Horizontal Cylindrical Surface," PhD thesis, School of Mechanical Engineering, Georgia Institute of Technology, Atlanta, Ga., Aug. 1967.

3 Yen, H. H., "Transient Film Boiling on a Horizontal Cylindrical Surface in a Subcooled Liquid," PhD thesis, School of Mechanical Engineering, Georgia Institute of Technology, Atlanta, Ga., July 1968.

4 Wehmeyer, D. P., "The Effect of Radiation and Fluid Properties on Transient Film Boiling on a Horizontal Cylindrical Surface," PhD thesis, School of Mechanical Engineering, Georgia Institute of Technology, Atlanta, Ga., June 1970.

5 Jacob, M., *Heat Transfer*, John Wiley & Sons, New York, N. Y., Vol. 1, 1949, p. 563.

6 "Stability at High Temperatures," E. I. du Pont de Nemours and Co., Technical Bulletin X-13.

7 Bromley, L. A., "Heat Transfer in Stable Film Boiling," *Chemical Engineering Progress 46*, No. 5, 1950, p. 221.

J. KLEPPE
Graduate Assistant.

W. J. MARNER
Assistant Professor.
Mem. ASME

Department of Mechanical Engineering,
South Dakota School of
Mines and Technology,
Rapid City, S. D.

# Transient Free Convection in a Bingham Plastic on a Vertical Flat Plate

*A theoretical investigation of transient free convection in a Bingham plastic on a vertical flat plate with constant wall temperature is presented. Except for a linear variation of density with temperature in the body force term, all fluid properties are assumed to be constants. The parameters of the problem are the Prandtl number* Pr *and a dimensionless group involving the Hedstrom and Grashof numbers,* $\mathrm{He}/\mathrm{Gr}_L^{3/4}$. *Solutions to the governing boundary-layer equations are obtained using an explicit finite-difference procedure. Mean Nusselt numbers* $\overline{\mathrm{Nu}}_L$ *are presented for a range of the parameters, along with representative velocity profiles, temperature profiles, and friction coefficients. Flow in the Bingham plastic does not start until the buoyancy forces become sufficiently large to cause a shear stress in the material which exceeds the yield stress. Thus, for short times heat is transferred by one-dimensional transient conduction, which has the well-known solution expressed in terms of the complementary error function. A temporal minimum, which becomes more pronounced with increasing* $\mathrm{He}/\mathrm{Gr}_L^{3/4}$, *is noted in the mean Nusselt number. Steady-state* $\overline{\mathrm{Nu}}_L$ *values are higher for Bingham plastics than for Newtonian fluids, but the maximum increase, which decreases with increasing* Pr, *is noted to be less than 15 percent. Due to the behavior of the velocity gradient at the wall, which reaches a maximum before steady-state conditions are reached, a temporal maximum is observed in the mean friction coefficient. Bingham-plastic friction coefficients are significantly higher than for Newtonian fluids; however, this increase is due primarily to the yield stress rather than as a consequence of a steeper velocity gradient at the wall.*

## Introduction

Considerable attention has been devoted to convective heat transfer in non-Newtonian liquids during the past few years, primarily because of the increasing importance of these fluids in various chemical, processing, and nuclear industries.

A Bingham plastic is a non-Newtonian fluid which has a linear relationship between shear stress and velocity gradient, but which is characterized by a yield stress $\tau_0$. If the shear stress exceeds the yield stress, the material flows as a viscous liquid; however, if the converse is true, it behaves as a solid. Thus, Bingham-plastic velocity profiles typically consist of two regions: a viscous region where $|\tau_{xy}| > \tau_0$, and a plug-flow region of uniform velocity where $|\tau_{xy}| < \tau_0$. Representative fluids which have been found to exhibit at least approximate Bingham-plastic behavior include thorium and uranium oxide slurries, certain plastic melts, oil-well drilling muds, cement, oil paints, paper pulp, toothpaste, catsup, and grain–water suspensions.

The classical problem of laminar free convection on a vertical flat plate has been the subject of a rather large number of investigations, including both transient and steady-state situations. Most of the work in this area has been concerned with Newtonian fluids and is summarized in review articles by Ede [1][1] and Gebhart [2] and in a bibliography by Julian and Akins [3]. A few investigations dealing with non-Newtonian fluids, all limited to steady-state conditions, have been reported, and these studies are of particular interest here.

Acrivos [4] considered free convection in a power-law fluid for different geometrical configurations, including the isothermal vertical flat plate. By neglecting the inertia terms in the momentum equation, he was able to derive an expression for the Nusselt number which is valid for large Prandtl numbers. Acrivos' analysis was later verified by Reilly, Tien, and Adelman [5] who used moderately pseudoplastic 0.5 and 1.0 percent aqueous Carbopol solutions in their experimental work. Tien [6] followed with an integral solution for a power-law fluid, also for large Prandtl numbers, which included uniform wall temperature, arbitrary wall temperature, and uniform-wall-heat-flux boundary conditions. His results were in excellent agreement with the experimental data of Reilly, Tien, and Adelman. In a

Contributed by the Heat Transfer Division of The American Society of Mechanical Engineers and presented at the AIChE-ASME Heat Transfer Conference, Denver, Colo., August 6–9, 1972. Manuscript received by the Heat Transfer Division July 8, 1971. Paper No. 72-HT-36.

[1] Numbers in brackets designate References at end of paper.

similar analysis for the three-parameter Ellis fluid, however, Tien and Tsuei [7] noted deviations of up to 40 percent from the experimental data. Soundalgekar [8], using an integral method, and Na and Hansen [9], using the group-theory method, investigated the possibility of similarity solutions for free convection in power-law fluids. Sharma and Adelman [10] extended the experimental work of Reilly, Tien, and Adelman to highly pseudoplastic non-Newtonian fluids by using 1.25, 1.50, and 1.75 percent aqueous Carbopol solutions. In a recent study Dale [11] found excellent agreement between a uniform-wall-heat-flux numerical solution and experimental data obtained for aqueous CMC and Carbopol solutions. Mishra [12, 13] and Amato and Tien [14] have carried out analytical studies of free convection in second-order and Oldroyd viscoelastic fluids, respectively. In a study involving fully developed Bingham-plastic free convection between vertical parallel plates at different temperatures, Yang and Yeh [15] found that flow ceases whenever the dimensionless yield stress is equal to or exceeds one-fourth of the Grashof–Prandtl-number product.

The purpose of the present investigation is to extend the problem of transient free convection on a vertical flat plate to an important non-Newtonian fluid, the Bingham plastic.

## Analysis

Consider a vertical flat plate of length $L$ located in a large quiescent body of Bingham plastic. Initially the plate and fluid are at the same temperature $T_\infty$. At time $t = 0$, the plate is suddenly heated to a higher uniform temperature $T_w$, thus causing temperature gradients in the fluid near the wall. The resultant density gradients create buoyancy forces and hence shear stresses in the Bingham plastic. Once the yield stress is exceeded, the fluid moves upward in the vicinity of the plate.

For unsteady laminar flow and heat transfer, constant properties except for density in the body force term in the momentum equation, no viscous dissipation, no viscoelastic effects, and making the usual boundary-layer assumptions, the continuity, momentum, and energy equations become

$$\frac{\partial u}{\partial x} + \frac{\partial v}{\partial y} = 0 \tag{1}$$

$$\rho\left(\frac{\partial u}{\partial t} + u\frac{\partial u}{\partial x} + v\frac{\partial u}{\partial y}\right) = -\frac{\partial \tau_{xy}}{\partial y} + \rho g\beta_\infty(T - T_\infty) \tag{2}$$

$$\rho c_p\left(\frac{\partial T}{\partial t} + u\frac{\partial T}{\partial x} + v\frac{\partial T}{\partial y}\right) = k\frac{\partial^2 T}{\partial y^2} \tag{3}$$

where the $x$ coordinate is directed upward along the plate and the $y$ coordinate outward from the plate. The shear stress $\tau_{xy}$ is given by the Bingham-plastic constitutive equation [16]

$$\tau_{xy} = \pm\tau_0 - \mu_B\frac{\partial u}{\partial y} \qquad |\tau_{xy}| > \tau_0 \tag{4a}$$

$$\frac{\partial u}{\partial y} = 0 \qquad |\tau_{xy}| < \tau_0 \tag{4b}$$

where, in equation (4$a$), the $-$ sign holds for a positive velocity gradient and the $+$ sign for a negative velocity gradient.

The initial and boundary conditions are

$$\begin{aligned} &t = 0: && u = v = 0 && T = T_\infty \\ &x = 0: && u = v = 0 && T = T_\infty \\ &y = 0: && u = v = 0 && T = T_w \\ &y = \infty: && u = 0 && T = T_\infty \end{aligned} \tag{5}$$

Making use of equation (4), the conservation equations may be expressed in dimensionless form as

$$\frac{\partial U}{\partial X} + \frac{\partial V}{\partial Y} = 0 \tag{6}$$

$$\frac{\partial U}{\partial t^*} + U\frac{\partial U}{\partial X} + V\frac{\partial U}{\partial Y} = \frac{\partial^2 U}{\partial Y^2} + \theta \qquad |\tau^*| > 1 \tag{7}$$

$$\frac{\partial U}{\partial t^*} + U\frac{\partial U}{\partial X} = -\frac{\mathrm{He}}{\mathrm{Gr}_L^{3/4}}\frac{\partial \tau^*}{\partial Y} + \theta \qquad |\tau^*| < 1 \tag{8}$$

$$\frac{\partial \theta}{\partial t^*} + U\frac{\partial \theta}{\partial X} + V\frac{\partial \theta}{\partial Y} = \frac{1}{\mathrm{Pr}}\frac{\partial^2 \theta}{\partial Y^2} \tag{9}$$

while the initial and boundary conditions, equation (5), in dimensionless form become

$$\begin{aligned} &t^* = 0: && U = V = \theta = 0 \\ &X = 0: && U = V = \theta = 0 \\ &Y = 0: && U = V = 0 && \theta = 1 \\ &Y = \infty: && U = \theta = 0 \end{aligned} \tag{10}$$

From equations (6)–(9) it is seen that the dependent variables are functions of the dimensionless independent variables $X$, $Y$, and $t^*$ and the parameters Pr and $\mathrm{He}/\mathrm{Gr}_L^{3/4}$. The significance of the Prandtl and Grashof numbers is well known and need not be elaborated on here. The Hedstrom number is a dimensionless group which indicates the importance of Bingham-plastic be-

## Nomenclature

$C_f$ = local friction coefficient, $\tau_w/{}^1\!/_2\rho u_0^2$
$\bar{C}_f$ = mean friction coefficient, $\frac{1}{L}\int_0^L C_f dx$
$c_p$ = constant-pressure specific heat
$g$ = acceleration due to gravity
$\mathrm{Gr}_L$ = Grashof number, $\rho^2 g\beta_\infty(T_w - T_\infty)L^3/\mu_B^2$
$h$ = local convective heat-transfer coefficient, $-k(\partial T/\partial y)_w/(T_w - T_\infty)$
$\bar{h}$ = mean convective heat-transfer coefficient, $\frac{1}{L}\int_0^L h dx$
He = Hedstrom number, $\rho\tau_0 L^2/\mu_B^2$
$k$ = thermal conductivity
$L$ = length of plate
$\mathrm{Nu}_x$ = local Nusselt number, $hx/k$
$\overline{\mathrm{Nu}}_L$ = mean Nusselt number, $\bar{h}L/k$
Pr = Prandtl number, $c_p\mu_B/k$
$t$ = time
$t^*$ = dimensionless time, $(t\nu/L^2)\,\mathrm{Gr}_L^{1/2}$
$T$ = temperature
$u$ = velocity component parallel to plate
$u_0$ = characteristic velocity, $[\beta_\infty g L(T_w - T_\infty)]^{1/2}$
$U$ = dimensionless velocity component parallel to plate, $(uL/\nu)\mathrm{Gr}_L^{-1/2}$
$v$ = velocity component normal to plate
$V$ = dimensionless velocity component normal to plate, $(vL/\nu)\mathrm{Gr}_L^{-1/4}$
$x$ = coordinate along plate
$X$ = dimensionless coordinate along plate, $x/L$
$y$ = coordinate normal to plate
$Y$ = dimensionless coordinate normal to plate, $(y/L)\mathrm{Gr}_L^{1/4}$
$\beta$ = coefficient of volumetric expansion
$\theta$ = dimensionless temperature, $(T - T_\infty)/(T_w - T_\infty)$
$\mu_B$ = Bingham plastic viscosity
$\nu$ = kinematic viscosity, $\mu_B/\rho$
$\rho$ = density
$\tau_{xy}$ = shear stress
$\tau_0$ = yield stress
$\tau^*$ = dimensionless shear stress, $\tau_{xy}/\tau_0$

### Subscripts

$w$ = wall
$\infty$ = far from the wall

havior. As He $\rightarrow$ 0, the plug-flow region becomes smaller, and Newtonian fluid behavior is approached. By observing the dimensionless energy equation, it is apparent that the right-hand side of equation (9) will vanish as Pr $\rightarrow \infty$. Thus, it may be concluded that the importance of the Prandtl number as a parameter decreases as Pr increases.

Equation (4) indicates that there will be no flow along the plate until the yield stress of the fluid is exceeded. Thus, there will be an initial no-flow period during which the heat transfer is due entirely to conduction. During this initial period equation (8) reduces to

$$\frac{\partial \tau^*}{\partial Y} = \frac{\mathrm{Gr}_L^{3/4}}{\mathrm{He}}\,\theta \tag{11}$$

and equation (9) becomes

$$\frac{\partial \theta}{\partial t^*} = \frac{1}{\mathrm{Pr}}\frac{\partial^2 \theta}{\partial Y^2} \tag{12}$$

Equation (12) is the one-dimensional transient heat-conduction equation which, for a step-change in the temperature $\theta$ at $Y = 0$, has the solution [17]

$$\theta = \mathrm{erfc}\left[\frac{Y}{2}\,(\mathrm{Pr}/t^*)^{1/2}\right] \tag{13}$$

where erfc is the complementary error function. Substituting equation (13) into equation (11) and integrating between the limits $Y = 0$ where $\tau^* = \tau_w^*$ and $Y = \infty$ where $\tau^* = 0$ yields

$$\tau_w^* = 2\,\frac{\mathrm{Gr}_L^{3/4}}{\mathrm{He}}\,(t^*/\pi\mathrm{Pr})^{1/2} \tag{14}$$

By substituting the value $\tau_w^* = 1$, the length of the initial period is

$$t^* = \frac{\pi}{4}\,\mathrm{Pr}(\mathrm{He}/\mathrm{Gr}_L^{3/4})^2 \tag{15}$$

and the temperature distribution when the flow starts is

$$\theta = \mathrm{erfc}\left[\frac{Y}{\pi^{1/2}}\,\frac{\mathrm{Gr}_L^{3/4}}{\mathrm{He}}\right] \tag{16}$$

The phenomenon of an initial period without flow is unique for free convection in fluids with a yield stress. Due to the presence of a temperature distribution within the fluid when the flow starts, the time required to reach steady state, from the time the flow starts, will be shorter for Bingham plastics than for fluids without a yield stress.

Results of primary interest in this study include the Nusselt number and friction coefficient. The local Nusselt number $\mathrm{Nu}_x$ is defined by

$$\mathrm{Nu}_x = hx/k \tag{17}$$

or, in terms of dimensionless variables,

$$\mathrm{Nu}_x = -(\partial\theta/\partial Y)_w X \mathrm{Gr}_L^{1/4} \tag{18}$$

The mean, or average, Nusselt number $\overline{\mathrm{Nu}}_L$ is defined by

$$\overline{\mathrm{Nu}}_L = \bar{h}L/k \tag{19}$$

or, in terms of dimensionless variables,

$$\overline{\mathrm{Nu}}_L = -\mathrm{Gr}_L^{1/4}\int_0^1 (\partial\theta/\partial Y)_w dX \tag{20}$$

The local friction coefficient $C_f$ is defined by

$$C_f = \tau_w/{}^1\!/_2\rho u_0^2 \tag{21}$$

where $u_0$ is a characteristic velocity and $\tau_w$ is the wall shear stress. In this analysis $u_0$ is chosen to be the group $[\beta_\infty g L(T_w - T_\infty)]^{1/2}$. Making use of equation (4*a*), evaluated at the wall, the local friction coefficient in dimensionless form is

$$C_f = 2\mathrm{Gr}_L^{-1/4}[\mathrm{He}/\mathrm{Gr}_L^{3/4} + (\partial U/\partial Y)_w] \tag{22}$$

and the mean, or average, friction coefficient $\bar{C}_f$ is calculated using

$$\bar{C}_f = \int_0^1 C_f dX \tag{23}$$

## Method of Solution

Solutions to the governing equations (6)–(9), subject to the boundary conditions (10), were obtained using an explicit finite-difference method. Only an outline of the approach used will be given here. Additional details of the numerical procedure, including a listing of the computer program, may be found in [18].

The temperature distribution in the Bingham plastic at the time when flow starts was determined from equation (16) and the corresponding time from equation (15). The velocity and temperature distributions from that point on were calculated step by step in both space and time, always checking to see whether the flow was viscous or plug, i.e., whether equation (7) or (8) was applicable.

Velocity and temperature gradients at the wall, required for the determination of the local Nusselt numbers and friction coefficients, were evaluated using a five-point formula. Integrals involved in mean values of these quantities, $\overline{\mathrm{Nu}}_L$ and $\bar{C}_f$, were evaluated using Simpson's rule.

In order to obtain adequate convergence it was necessary to use very small $X$-mesh sizes near the leading edge of the plate as well as very small $Y$-mesh sizes near the wall. As a consequence of a thinner thermal boundary layer, convergence became more difficult with increasing Prandtl number. However, convergence was checked numerically for each value of Pr by doubling the mesh sizes and then comparing changes in the dependent variables. In all cases the changes were less than 5 percent, which was considered adequate.

Following the stability analysis of Carnahan, Luther, and Wilkes [19], the present finite-difference procedure was stable for all Pr $\geq$ 1 provided that the relation

$$\frac{U}{\Delta X} + \frac{|V|}{\Delta Y} + \frac{2}{(\Delta Y)^2} \leq \frac{1}{\Delta t^*} \tag{24}$$

was satisfied at all points in the flow field.

As a partial check on the accuracy of the numerical procedure, comparisons of steady-state local Nusselt numbers were made with the tabulated solutions of Ostrach [20] for Newtonian fluids. For Pr = 1 the deviations in $\mathrm{Nu}_x/\mathrm{Gr}_x^{1/4}$ ranged from 1.8 percent near the leading edge to 0.10 percent at the upper end of the plate, while for Pr = 100 the differences were 3.7 and 1.3 percent, respectively. Since a substantially smaller error is involved in the mean Nusselt number, which is of greater interest here than the local value, and in order to keep the computing-time requirements within reasonable limits, this error level was considered acceptable.

## Results

**Velocity and Temperature Profiles.** Representative transient velocity and temperature profiles for Pr = 1 and $\mathrm{He}/\mathrm{Gr}_L^{3/4} = 1.0$ are shown in Figs. 1 and 2, respectively. It is seen that for these values of the parameters the flow starts at $t^* = 0.785$ and that both the velocity and temperature profiles reach a transient maximum—at approximately $t^* = 2.660$ as shown in Figs. 1 and 2—and then decrease to their steady-state values at $t^* \doteq 3.785$. The condition of a maximum velocity at $t^* \doteq 2.660$ evidently corresponds to the time at which buoyancy forces in the Bingham plastic are largest. However, it should be pointed out that this behavior is not unique for Bingham plastics since a

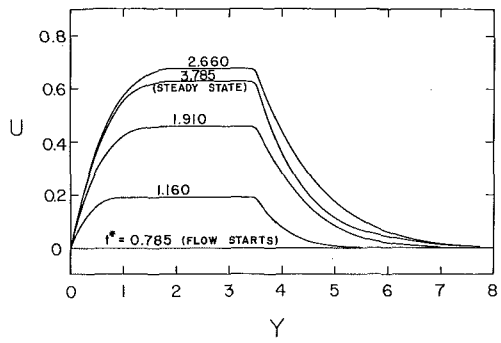


Fig. 1 Representative transient velocity profiles for Pr = 1, $He/Gr_L^{3/4}$ = 1.0, and $X$ = 1.0

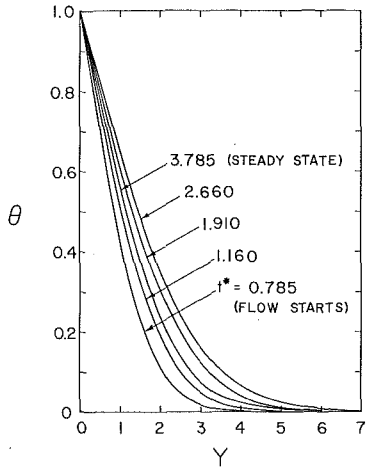


Fig. 2 Representative transient temperature profiles for Pr = 1, $He/Gr_L^{3/4}$ = 1.0, and $X$ = 1.0

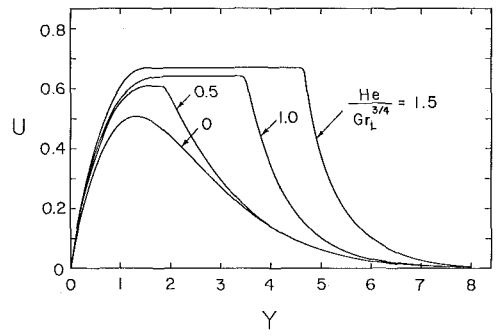


Fig. 3 Representative steady-state velocity profiles for Pr = 1 and $X$ = 1.0

temporal maximum in the velocity profile was also observed for Newtonian fluids.

In Figs. 3 and 4, respectively, representative steady-state velocity and temperature profiles are shown for Pr = 1 and $X$ = 1.0 as a function of $He/Gr_L^{3/4}$. Both the plug-flow thickness as well as the maximum velocity are observed to increase with $He/Gr_L^{3/4}$, the former very significantly. However, very little change in the velocity profiles near the wall, the region which controls the heat-transfer process, is noted. Consequently, for Pr = 1 a further increase in $He/Gr_L^{3/4}$ above values of 1.5 had very little influence on the steady-state temperature profiles. Although not shown, for a fixed value of $He/Gr_L^{3/4}$, an increase in the Prandtl number Pr resulted in an increase in the plug-flow thickness, a decrease in the magnitude of the maximum velocity, and a decrease in the slope of the velocity profile at the wall.

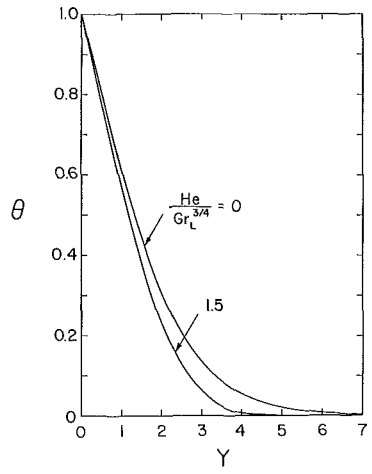


Fig. 4 Representative steady-state temperature profiles for Pr = 1 and $X$ = 1.0

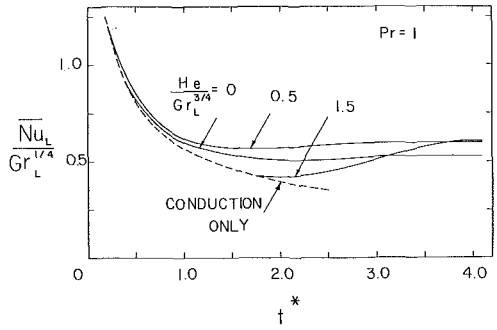


Fig. 5 Transient mean Nusselt numbers for Pr = 1

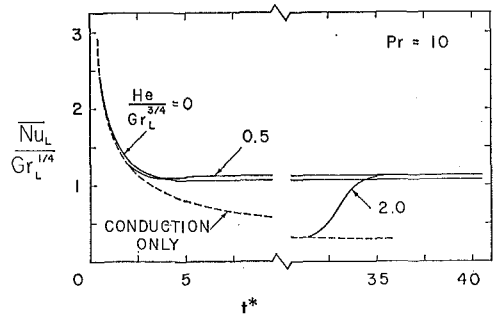


Fig. 6 Transient mean Nusselt numbers for Pr = 10

**Nusselt Number.** Figs. 5, 6, and 7 show the transient mean Nusselt number in the form $\overline{Nu}_L/Gr_L^{1/4}$ as a function of $He/Gr_L^{3/4}$ for Pr = 1, 10, and 100, respectively. During the initial heat-transfer period the mean Nusselt number lies along the dotted line which represents the one-dimensional transient heat-conduction solution. For $He/Gr_L^{3/4} > 0$ the fully drawn curves arising from the dotted line represent the mean Nusselt numbers after the yield stress of the Bingham plastic is exceeded. Thus, the distance from the origin to the starting point for any of these curves represents the length of the initial period, which increases with $He/Gr_L^{3/4}$ for a given value of Pr.

A temporal minimum in the mean Nusselt number is noted for all values of $He/Gr_L^{3/4}$, as first reported by Siegel [21] for Newtonian fluids. However, due to a longer period of pure conduction as a consequence of the yield stress, the temporal minimum is more pronounced for Bingham plastics than for Newtonian fluids.

The general trend in $\overline{Nu}_L/Gr_L^{1/4}$, except for Pr = 1 and $He/Gr_L^{3/4}$ = 0.5, is for the Bingham-plastic Nusselt number to be lower than the corresponding Newtonian-fluid value during the

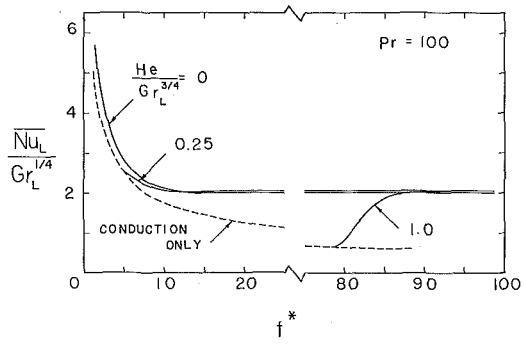


Fig. 7 Transient mean Nusselt numbers for Pr = 100

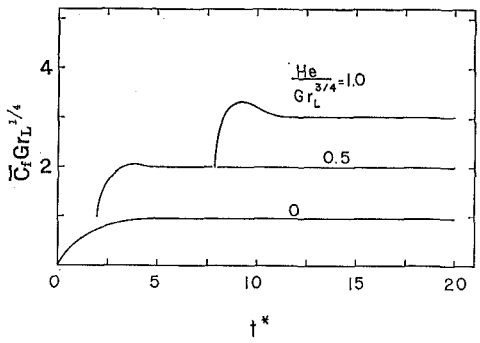


Fig. 8 Representative transient mean friction coefficients for Pr = 10

initial conduction period. However, as movement of the fluid increases due to buoyancy effects, $\overline{Nu}_L/Gr_L^{1/4}$ increases such that in all cases the steady-state Bingham-plastic Nusselt number $\overline{Nu}_L$ is larger than for a Newtonian fluid. Also, it is noted that for a given Pr, the Nusselt number approaches a finite upper limit as $He/Gr_L^{3/4}$ increases. For Pr = 10 and 100 this maximum value was achieved; however, for Pr = 1 a value of $He/Gr_L^{3/4} = 1.5$ was not quite large enough to reach the upper limit. The maximum increases in $\overline{Nu}_L/Gr_L^{1/4}$ due to Bingham-plastic behavior, for the parameters used in this investigation, were observed to be 14.8, 5.1, and 2.5 percent for Pr = 1, 10, and 100, respectively. This behavior may be attributed to the very small Bingham-plastic effects on the velocity profile near the wall for large values of the Prandtl number.

The time required to reach steady-state conditions from $t^* = 0$ is noted to increase sharply with Pr for Bingham plastics as well as for Newtonian fluids. This effect is due to a decrease in the rate of energy diffusion in the fluid as the Prandtl number increases.

**Friction Coefficient.** Representative transient mean friction coefficients are shown in Fig. 8 for Pr = 10 and $He/Gr_L^{3/4} = 0$, 0.5, and 1.0. Steady-state local friction coefficients for the same values of the parameters are shown in Fig. 9.

In Fig. 8 it is noted that for Bingham plastics the flow does not start at $t^* = 0$ because of the yield stress; thus, during the initial period $\bar{C}_f$ is undefined. At the yield point—from equations (21), (22), and (23)—it may be deduced that $C_f = \tau_0/{}^1/_2\rho u_0^2$, $C_f Gr_L^{1/4} = 2He/Gr_L^{3/4}$, and $\bar{C}_f Gr_L^{1/4} = 2He/Gr_L^{3/4}$. Thus, when the flow starts the mean friction coefficient $\bar{C}_f Gr_L^{1/4} = 0$, 1.0, and 2.0 for $He/Gr_L^{3/4} = 0$, 0.5, and 1.0, respectively. In Fig. 8 it may also be observed that the transient-mean-friction-coefficient curves are shifted to the right with increasing $He/Gr_L^{3/4}$, i.e., as Bingham-plastic behavior becomes more important a longer period of time is required to reach the yield point.

Once the flow starts the transient mean friction coefficient increases sharply, overshoots the steady-state value, and then decreases fairly rapidly to the steady-state value as shown in Fig. 8. This overshoot, which increases with $He/Gr_L^{3/4}$, is a consequence of the fact that the maximum velocity gradient at the wall occurs before steady-state conditions are reached.

Since the yield stress is added directly to the Newtonian wall shear stress in the expression for $\tau_w$, there is a significant increase in the friction coefficient due to Bingham-plastic behavior. An additional, but smaller, contribution to the Bingham-plastic friction coefficients is due to a steeper velocity gradient at the wall. Thus, the vertical displacements of the curves in Fig. 8, which are equal to $2\ He/Gr_L^{3/4}$ at the yield point, exceed only slightly the value $2\ He/Gr_L^{3/4}$ after yielding has taken place. A similar argument for steady-state local friction coefficients may be used to account for the vertical displacements of the curves in Fig. 9.

Due to a decrease in $(dU/dY)_w$ with increasing Prandtl number, it was observed that both the local and mean friction coefficients decrease with increasing Pr for fixed values of $He/Gr_L^{3/4}$.

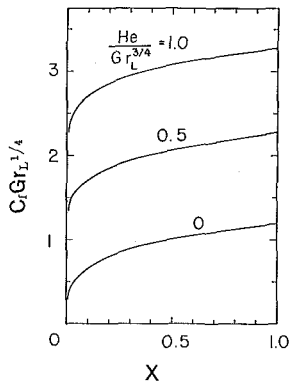


Fig. 9 Representative steady-state local friction coefficients for Pr = 10

## Concluding Remarks

A numerical solution for the problem of transient free convection in a Bingham plastic on a vertical isothermal flat plate has been carried out. Except for a linear variation of density with temperature in the body force term, all properties were taken to be constants. The most important results and conclusions may be summarized as follows:

1 The parameters of the problem are $He/Gr_L^{3/4}$ and Pr. The Hedstrom number He, which is a dimensionless yield stress, is a characteristic of Bingham plastics.

2 Flow does not start in the Bingham plastic until the buoyancy forces are sufficiently large to cause shear stresses in the material which exceed the yield stress.

3 For short times the results are given by the well-known solution for transient heat conduction in a semi-infinite solid.

4 After flow starts both the velocity and temperature profiles reach a transient maximum and then decrease to their steady-state values.

5 Both transient and steady-state velocity profiles show strong Bingham-plastic effects away from the wall, but very weak effects near the wall.

6 A temporal minimum is noted in the mean Nusselt number $\overline{Nu}_L$ which becomes more pronounced with increasing $He/Gr_L^{3/4}$. The time required to reach steady-state conditions increases sharply with Pr.

7 Due to the very small change in the velocity profile near the wall, the increase in steady-state $\overline{Nu}_L$ due to Bingham-plastic behavior is quite small and is noted to decrease as Pr increases.

8 A temporal maximum is noted in the mean friction coefficient due to the fact that the maximum velocity gradient at the wall occurs before steady-state conditions are reached.

9 Both transient and steady-state friction coefficients are significantly larger for Bingham plastics than for Newtonian fluids. However, this increase is due primarily to the Bingham-plastic yield stress, with only a relatively small contribution resulting from a steeper velocity gradient at the wall.

## References


1 Ede, A. J., "Advances in Free Convection," in: *Advances in Transfer*, Hartnett, J. P., and Irvine, T. F., eds., Vol. 4, Academic Press, New York, N. Y., 1967.

2 Gebhart, B., "External Natural Convection Flows," *Applied Mechanics Reviews*, Vol. 22, 1969, pp. 691–701.

3 Julian, D. V., and Akins, R. G., "Bibliography of Natural Convection Heat Transfer from a Vertical Flat Plate," *Kansas State University Bulletin*, Special Report No. 77, Vol. 51, 1967.

4 Acrivos, A., "A Theoretical Analysis of Laminar Natural Convection Heat Transfer to Non-Newtonian Fluids," *AIChE Journal*, Vol. 6, 1960, pp. 584–590.

5 Reilly, I. G., Tien, C., and Adelman, M., "Experimental Study of Natural Convective Heat Transfer from a Vertical Plate in a Non-Newtonian Fluid," *Canadian Journal of Chemical Engineering*, Vol. 43, 1965, pp. 157–160.

6 Tien, C., "Laminar Natural Convection Heat Transfer from Vertical Plate to Power-Law Fluid," *Applied Scientific Research*, Vol. 17, 1967, pp. 233–248.

7 Tien, C., and Tsuei, H. S., "Laminar Natural Convection Heat Transfer in Ellis Fluids," *Applied Scientific Research*, Vol. 20, 1969, pp. 131–147.

8 Soundalgekar, V. M., "Laminar Free Convection Flow of a Power-law Fluid from a Vertical Plate with Variable Wall Temperature," *Indian Journal of Pure and Applied Physics*, Vol. 2, 1964, pp. 360–361.

9 Na, T. Y., and Hansen, A. G., "Possible Similarity Solutions of the Laminar Natural Convection Flow of Non-Newtonian Fluids," *International Journal of Heat and Mass Transfer*, Vol. 9, 1966, pp. 261–262.

10 Sharma, K. K., and Adelman, M., "Experimental Study of Natural Convection Heat Transfer from a Vertical Plate in a Non-Newtonian Fluid," *Canadian Journal of Chemical Engineering*, Vol. 47, 1969, pp. 553–555.

11 Dale, J. D., "Laminar Free Convection of Non-Newtonian Fluids from a Vertical Flat Plate with Uniform Heat Flux," PhD dissertation, University of Washington, Seattle, Wash., 1969.

12 Mishra, S. P., "Free Convection Elastico-Viscous Flow Past a Porous Flat Plate," *Indian Journal of Pure and Applied Physics*, Vol. 3, 1965, pp. 111–113.

13 Mishra, S. P., "Free Convection of a Second-order Fluid Past a Hot Vertical Plate," *Proceedings of the Indian Academy of Sciences*, Vol. 64, Section A, 1966, pp. 291–303.

14 Amato, W. S., and Tien, C., "Natural Convection Heat Transfer from a Vertical Plate to an Oldroyd Fluid," *Chemical Engineering Progress Symposium Series*, Vol. 66, No. 102, 1970, pp. 92–99.

15 Yang, W.-J., and Yeh, H.-C., "Free Convective Flow of Bingham Plastic Between Two Vertical Plates," JOURNAL OF HEAT TRANSFER, TRANS. ASME, Series C, Vol. 87, No. 2, May 1965, pp. 319–320.

16 Bird, R. B., Stewart, W. E., and Lightfoot, E. N., *Transport Phenomena*, John Wiley & Sons, New York, N. Y., 1960.

17 Carslaw, H. S., and Jaeger, J. C., *Conduction of Heat in Solids*, 2nd ed., Oxford University Press, London, 1959.

18 Kleppe, J., "Free and Combined Free and Forced Laminar Convection in a Bingham Plastic on a Vertical Flat Plate," MS thesis, South Dakota School of Mines and Technology, Rapid City, S. D., 1971.

19 Carnahan, B., Luther, H. A., and Wilkes, J. O., *Applied Numerical Methods*, John Wiley & Sons, New York, N. Y., 1969.

20 Ostrach, S., "An Analysis of Laminar Free Convection Flow and Heat Transfer about a Flat Plate Parallel to the Direction of the Generating Body Force," National Advisory Committee for Aeronautics, Report 1111, 1953, pp. 63–79.

21 Siegel, R., "Transient Free Convection From a Vertical Flat Plate," TRANS. ASME, Vol. 80, 1958, pp. 347–359.

**N. V. SURYANARAYANA**
Visiting Assistant Professor of Mechanical Engineering, Michigan Technological University, Houghton, Mich.

**H. MERTE, JR.**
Professor of Mechanical Engineering and Professor-in-Charge, Heat Transfer Laboratory, University of Michigan, Ann Arbor, Mich.

# Film Boiling on Vertical Surfaces

*Film boiling of a saturated liquid on a vertical surface is analyzed to determine the local heat-transfer rates as a function of height and heater-surface superheat. Experiments show that the laminar-flow model is inadequate. A turbulent-vapor-flow model is used, and the influence of the interfacial oscillations is incorporated on a semiempirical basis. Measurements of local film boiling were obtained with a transient technique using saturated liquid nitrogen.*

## Introduction

Bromley [1][1] assumed a model for laminar-film boiling on vertical surfaces similar to that of Nusselt [2] for condensation and supported his correlations with experimental data obtained from horizontal tubes of relatively small diameters. Improvements to this simple model were made employing boundary-layer-type equations with different boundary conditions by McFadden and Grosh [3], Cess [4], and Koh [5] for saturated liquids and by Sparrow and Cess [6] and Nishikawa and Ito [7] for subcooled liquids; integral methods were employed by Frederking [8], Frederking and Hopenfield [9], and Tachinaba and Fukaui [10]. All the above analyses are for laminar vapor film.

It has been recognized that laminar-film boiling occurs rather infrequently as compared with turbulent-film boiling. Hsu [11] reported analytical and experimental studies on turbulent-film boiling on vertical surfaces. He postulated a two-layer model with a smooth, steady vapor–liquid interface. Recently a more sophisticated velocity and temperature profile was adopted by Coury and Dukler [12], who have also attempted to take into account the effect of interfacial oscillations.

Laminar analyses with a steady interface predict that heat flux continuously decreases with height. However, there is experimental evidence [11–13] to indicate that this is not the case in practice. Visual observations in the present work reveal interfacial oscillations of relatively large amplitudes, of the same order as the mean vapor-film thickness. Thus there is evidence to indicate that the mechanism of heat transport undergoes a change with height, probably due to the onset of turbulence and interfacial waves. So far, no attempt seems to have been made to find the local heat-transfer rates. The purpose of the present study was to experimentally determine the local heat-transfer rates in film boiling on a vertical surface and analyze the phenomenon on the basis of a gradual onset of turbulence, taking into account the effect of interfacial oscillations.

## Analysis

A vertical isothermal surface at $T_w$ is immersed in a saturated liquid at $T_s$ such that film boiling takes place. To find the local heat flux, the following assumptions were made:

($a$) Liquid and vapor are incompressible.

($b$) Vapor properties, including density, are constant, evaluated at film temperature.

($c$) Liquid is uniformly at its saturation temperature.

($d$) Heat flux across the vapor film at any given height is constant. To compensate for the vapor superheat, the enthalpy of vaporization is replaced by the difference in enthalpies of the vapor at the film temperature and saturated liquid [14].

($e$) Velocity profile and shear-stress distribution are not influenced by vaporization.

($f$) The eddy diffusivities for heat and momentum are equal.

($g$) Heat transfer by radiation is negligible.

($h$) The vapor–liquid interfacial velocity is zero. For a laminar vapor film with a smooth interface, it has been shown [5] that this is a reasonable assumption if $[(\rho\mu)_v/(\rho\mu)_l]^{1/2}$ is much less than 1. For most common fluids, this condition is satisfied. On a qualitative basis, neglecting the interfacial velocity may be a reasonable approximation when the vapor film becomes turbulent even though there will be an increase in the interfacial velocity due to the increased shear stress in turbulent flows.

($i$) Other researchers [11, 12] have attempted to seek a parameter to define the transition from laminar to turbulent region. However, it is known that such transition is not sudden but gradual. In a related problem on condensation [22] an attempt was made to account for this gradual transition by using portions of von Karman's 3-layer model as appropriate to the value of the dimensionless thickness $y^+$. Several complications must be considered in specifying the transition of the laminar vapor flow to turbulent flow in the absence of any definitive experimental data. In general, both vaporization at the interface

[1] Numbers in brackets designate References at end of paper.

Contributed by the Heat Transfer Division of The American Society of Mechanical Engineers and presented at the AIChE-ASME Heat Transfer Conference, Denver, Colo., August 6–9, 1972. Manuscript received by the Heat Transfer Division March 22, 1971. Paper No. 72-HT-38.

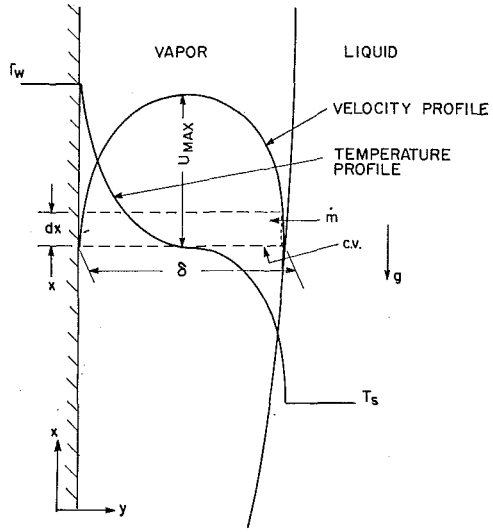


**Fig. 1 Velocity and temperature profiles in vapor film**

and heat transfer to the vapor film have a destabilizing effect, and one can expect turbulence effects to become evident much closer to the leading edge than in the case of flow in a channel. In the present approximate analysis no critical Reynolds number for the onset of turbulence is specified. Instead, it is hypothesized that the universal velocity profile proposed by Spalding [15] for single-phase flows is also valid for the vapor film in film boiling; it is assumed that this profile is valid for half the vapor-film thickness, and its mirror image for the other half, Fig. 1. This yields an approximately linear velocity profile for small vapor-film thickness and a logarithmic velocity profile for large values of vapor-film thickness. The velocity profile used has the form

$$Y^+ = U^+ + \frac{1}{E}\left[e^{KU^+} - 1 - KU^+ - \frac{(KU^+)^2}{2!} - \frac{(KU^+)^3}{3!} - \frac{(KU^+)^4}{4!}\right] \quad (1)$$

where $K = 0.407$ and $1/E = 0.0991$.

On the basis of equality of eddy diffusivities for heat and momentum, for vapors having $\mathrm{Pr} \simeq 1$, turbulence effects begin to be significant in heat-transfer rates for values of $Y^+ \simeq 10$. Defining the Reynolds number by $\Gamma/\mu$, this gives a value of $\mathrm{Re}_\delta = 100$, which may be inferred as representing the condition where turbulence becomes significant.

(*j*) To account for the effect of large-amplitude interfacial oscillations which were observed to be present with vertical surfaces at standard gravity conditions, the following approach is adopted. It is assumed that these oscillations are sinusoidal, and that the dimensionless temperature profile $\phi = f(\eta)$ is unaffected by the oscillations. Therefore

$$q'' = -k\left.\frac{dT}{dy}\right|_{y=0} = k\Delta T f'(0)\left.\frac{d\eta}{dy}\right|_{y=0} \quad (2)$$

Taking the time-averaged value of the heat flux by integrating equation (2) over one period, the ratio of the mean heat flux with an oscillating film to that with a steady film is given by

$$\frac{\overline{q''(t)}}{q''(s)} = \frac{1}{\sqrt{1-b^2}} = C \quad (3)$$

where $b$ is the dimensionless amplitude of oscillation, the ratio of the actual amplitude to the mean vapor-film thickness. The coefficient $C$ is a measure of the increase in heat transfer due to the oscillations and may be termed the heat-transfer-enhancement coefficient. A similar approach was made by Coury and Dukler [12].

Regarding the onset of these interfacial instabilities, it may be expected that it will be a function of the velocity of the vapor, the densities of the vapor and liquid, surface tension, gravity, and other parameters. Frederking [16] has given a linear analysis to predict the onset of the interfacial waves on a plane interface and concludes that for all values of $\mathrm{Re}_\delta$ there is a finite range of unstable wave numbers such that the flow is never completely stable. However, with film boiling on a vertical surface the vapor-film thickness increases with height, giving rise to a finite curvature of the interface. The curvature is particularly significant near the leading edge, as can be seen in the photographs of film boiling of liquid nitrogen in Fig. 2. Analysis of the parallel flow of two fluids of different densities with a relative velocity $u$ [17] shows that the critical wavelengths for small velocities are large. Hence, the onset of instability is indicated by the appearance of growing waves of long wavelengths. Near the leading edge with film boiling the velocity of the vapor is small, being zero at the leading edge, and hence the critical wave-

## Nomenclature

$A$ = area, ft²
$a$ = amplitude of interfacial oscillations, ft
$b$ = amplitude of interfacial oscillations, $a/\delta(s)$, dimensionless
$C$ = heat-transfer enhancement coefficient, equation (3)
$C_p$ = specific heat, Btu/lb$_m$-deg R
$g$ = gravitational acceleration, ft/sec²
$h_{fg}$ = enthalpy of vaporization, Btu/lb$_m$
$h_{fg}'$ = modified enthalpy of vaporization, $h_{fg} + 0.5C_p\Delta T$, Btu/lb$_m$
$h$ = heat-transfer coefficient, Btu/hr-ft²-deg R
$h_x$ = local heat-transfer coefficient at height $x$, Btu/hr-ft²-deg R
$k$ = thermal conductivity, Btu/hr-ft-deg R
$K$ = wave number or constant
$m$ = mass, lb$_m$
$\mathrm{Nu}_x$ = local Nusselt number
$n$ = integer
$P$ = pressure, psi
Pr = Prandtl number
$q$ = heat-transfer rate, Btu/hr
$q''$ = heat flux, $q/A$, Btu/hr-ft²
Re = Reynolds number, $\Gamma/\mu$
$T$ = vapor temperature, deg R
$T_w$ = heater-surface temperature, deg R
$T_s$ = liquid saturation temperature, deg R
$t$ = time, hr
$u$ = velocity, ft/hr
$U^*$ = friction velocity, $\tau_w/\rho$, ft/hr
$U^+$ = velocity, $u/u^*$, dimensionless
$v$ = velocity, ft/hr
$w$ = rate of vaporization, lb$_m$/hr-ft²
$x$ = height along heater surface, ft
$y$ = distance perpendicular to heater surface, ft
$y^+$ = distance, $yu^*/\nu$, dimensionless
$\Gamma$ = mass rate of flow per unit width, lb$_m$/hr-ft
$\delta$ = vapor-film thickness, ft
$\Delta T$ = surface superheat, $T_w - T_s$, deg R
$\eta$ = vapor-film thickness, $y/\delta$, dimensionless
$\theta^+ = \dfrac{\rho cU^*(T_w - T)}{q_w''}$, dimensionless
$\lambda$ = wavelength, ft
$\mu$ = viscosity, lb$_m$/hr-ft
$\nu$ = kinematic viscosity, $\mu/\rho$, ft²-hr
$\rho$ = density, lb$_m$/ft³
$\sigma$ = surface tension, lb$_f$/ft
$\tau$ = shear stress, lb$_f$/ft²
$\epsilon$ = eddy diffusivity

**Subscripts**

$c$ = critical
$l$ = liquid
$s$ = saturation
$v$ = vapor
$w$ = heater surface

When there is no subscript the quantities refer to the vapor.

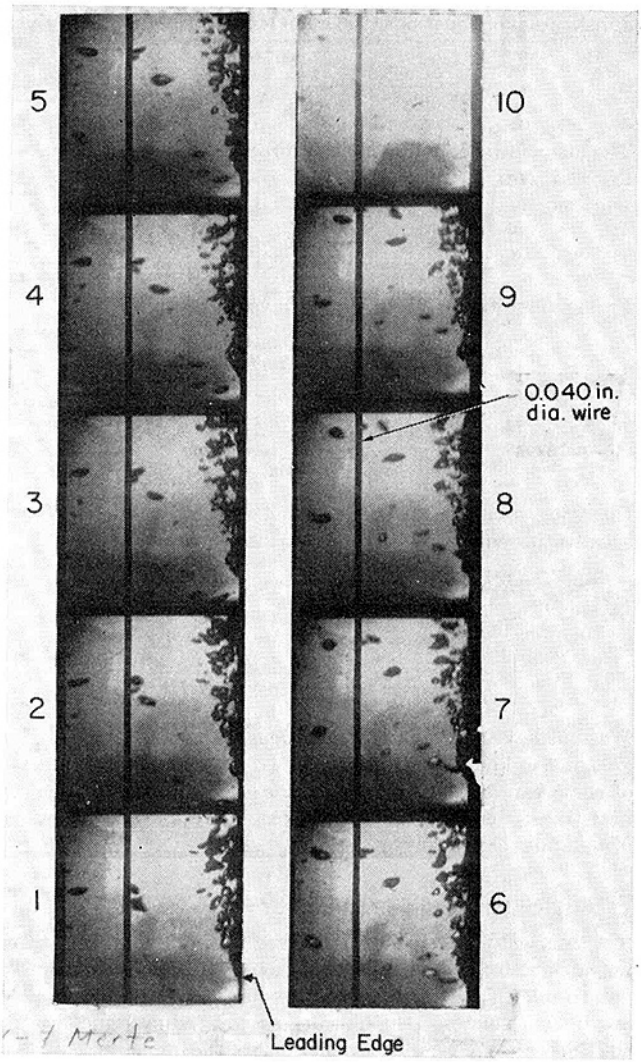


Fig. 2 Film boiling, $LN_2$; $\Delta T = 315$ deg R, $x = 0$–1 in., 104 frames/sec

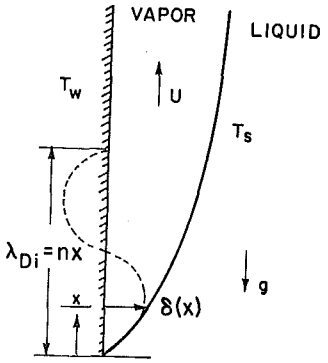


Fig. 3 Model for predicting instability of interface

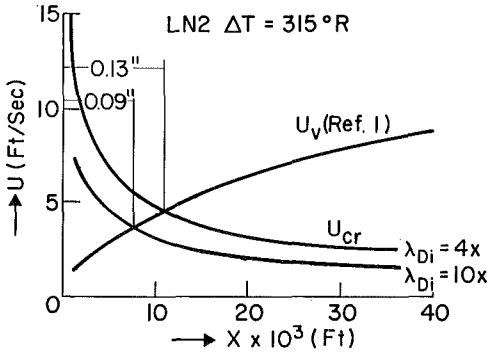


Fig. 4 Critical velocity vs. height for interfacial instability, $a/g = 1$

lengths are large in this region, while the relatively large curvature of the interface near the leading edge would correspond to waves of small wavelength. Hence the interface remains stable. However, as the vapor proceeds up the surface the relative velocity between the phases increases, decreasing the minimum unstable or critical wavelength, and the curvature decreases, increasing the wavelength of waves corresponding to this curvature. At some point these two wavelengths become equal, and this is taken as the point at which oscillation of the liquid–vapor interface begins. To estimate this point the model of Fig. 3 is used. As an approximation the curved interface up to distance $X$ from the leading edge can be considered to be a part of a wave of wavelength $\lambda_{Di} = nx$, where $n$ is an integer. This wave is considered as a disturbance on the interface. Whether this disturbance is damped or whether it grows, resulting in oscillations, depends on the relation between the critical wavelength $\lambda_c$ and the wavelength of this disturbance $\lambda_{Di}$. If $\lambda_c > \lambda_{Di}$, the configuration is stable, while when $\lambda_c \leq \lambda_{Di}$ interfacial oscillation is considered to begin. The vapor-film thickness $\delta$ is increasing with $x$ because of the vaporization at the liquid–vapor interface. Hence $d\delta/dx$ is positive at every $x$ so that $n$ cannot be less than 4, while an arbitrary upper limit of $n = 10$ would appear reasonable. At a given height $x$ the vapor velocity is $u$. From reference [17], for parallel flows in a vertical plane with one fluid (liquid in the present case) stationary, the condition for the critical velocity giving rise to instability of the interface, referred to as Kelvin–Helmholtz instability, is given by

$$u_c^2 = \frac{\rho_v + \rho_l}{\rho_v \rho_l} K \tag{4}$$

where $K$ is the wave number designated by $K = 2\pi/\lambda$. Every height $x$ is associated with a wave of wavelength $\lambda_{Di} = nx$; corresponding to the wavelength $\lambda_{Di}$ there is a critical velocity $u_c$ given by equation (4). If at $x$ the velocity of the vapor $u_v > u_c$, instabilities are expected to set in.

Figure 4 is a plot of $u_v$ and $u_c$ vs. $x$ for liquid nitrogen at $\Delta T = 315$ deg R; $u_v$ was calculated as the maximum vapor velocity from reference [1]; $u_c$ is computed for values of $n = 4$ and $n = 10$; $X_c$ is the critical height where $u_v = u_c$. From Fig. 4 this is relatively insensitive to $n$, being on the order of 0.12 in. From these approximate calculations, supported by linearized analysis and photographic studies, it can be concluded that a steady interface, if it exists, will be limited to an extremely small region near the leading edge.

The heat-transfer-enhancement coefficient, being a function of the interface oscillation amplitude in equation (3), may be expected to be a function of $x$, being small near the leading edge where the surface waves have small amplitudes, and increasing with height owing to the large-amplitude waves resulting when both the vapor velocity and vapor-film thickness increase.

($k$) For the vapor film, $P = P(x)$; in particular $P \neq P(y)$.

With these assumptions, we proceed with the analysis. From assumption ($i$)

$$Y^+ = U^+ + \frac{1}{E}\left[e^{KU^+} - 1 - (KU^+) - \frac{(KU^+)^2}{2!} - \frac{(KU^+)^3}{3!} - \frac{(KU^+)^4}{4!}\right] = F_1(U^+) \tag{1}^2$$

From assumption ($f$)

$$\frac{\epsilon_H}{\nu} = \frac{\epsilon_M}{\nu} = \frac{dy^+}{du^+} - 1 = F_2(U^+) \tag{5}$$

[2] See Appendix for functional forms of $F_1(U^+)$ etc.

Define

$$\theta^+ = \frac{\rho C_p U^*(T_w - T)}{q''(s)} \quad \text{in} \quad 0 \le y \le \delta/2 \tag{6}$$

$$\theta^+ = \frac{\rho C_p U^*(T - T_s)}{q''(s)} \quad \text{in} \quad \frac{\delta}{2} \le y \le \delta \tag{6a}$$

and

$$\theta_w{}^+ = \frac{\rho C_p U^*(T_w - T_s)}{q''(s)} \tag{6b}$$

With assumption $(d)$, the energy equation becomes

$$\frac{\overline{q''(t)}}{\rho C_p} = \frac{q_w{}''}{\rho C_p} = -\nu \left(\frac{\epsilon_H}{\nu} + \frac{1}{\mathrm{Pr}}\right) \frac{dT}{dy} \tag{7}$$

Substitution of (6) in (7) yields

$$\frac{d\theta^+}{dy^+} = \frac{1}{\dfrac{\epsilon_H}{\nu} + \dfrac{1}{\mathrm{Pr}}} \tag{8}$$

Noting that

$$dy^+ = F_3(U^+)dU^+ \tag{9}$$

we obtain

$$\frac{d\theta^+}{dU^+} = \frac{F_3(U^+)}{F_2(U^+) + \dfrac{1}{\mathrm{Pr}}} \tag{10}$$

Assumptions $(e)$ and $(h)$ lead to a symmetric velocity profile, the velocity in $\delta/2 \le y \le \delta$ being the mirror image of that in $0 \le y \le \delta/2$. Similarly from equations (6a) and (10), the temperature profile for $\theta^+$ in $\delta/2 \le y \le \delta$ is the inverted mirror image of that in $0 \le y \le \delta/2$. These profiles are sketched in Fig. 1. Thus

$$\theta_w{}^+ = 2\int_0^{U_M{}^+} \frac{F_3(U^+)}{F_2(U^+) + \dfrac{1}{\mathrm{Pr}}}\, dU^+ \tag{11}$$

It may be noted, since $F_3(U^+) = F_2(U^+) + 1$, that for $\mathrm{Pr} = 1$ the nondimensional temperature profile $\theta^+$ is identical to the velocity profile.

From conservation of mass for the control volume

$$\frac{d}{dx}\int_0^\delta \rho u dy = w \tag{12}$$

where $w$ is the rate of vaporization at the liquid–vapor interface. To evaluate $w$, the energy equation for a steady flow gives

$$q_w{}'' = wh_{fg} + \frac{d}{dx}\int_0^\delta \rho u C_p T dy \tag{13}$$

The last term in equation (13) represents the increase in enthalpy of the vapor that enters the control volume at $x$ and the increase in enthalpy of $w$ above that of saturated vapor in crossing the control volume. A correction to take this into account has been made by using the modified value $h_{fg}'$ in place of $h_{fg}$, so that equation (13) takes the form

$$w = \frac{q_w{}''}{h_{fg}'} = \frac{\overline{q''(t)}}{h_{fg}'} \tag{14}$$

After changing variables, the left-hand side of equation (12) yields

$$\frac{d}{dx}\int_0^\delta \rho u dy = 2\rho\nu F_4(U_M{}^+)\frac{dU_M{}^+}{dx} \tag{15}$$

Substitution of equations (15) and (14) into equation (12) gives

$$\frac{dU_M{}^+}{dx} = \frac{1}{F_4(U_M{}^+)} \frac{\overline{q''(t)}}{2h_{fg}'\rho\nu} \tag{16}$$

The momentum equation in the $x$ direction integrated over $y = 0$ to $y = \delta$ gives

$$\frac{d}{dx}\int_0^\delta \rho u^2 dy = -\frac{dP}{dx}\,\delta - \tau_i - \tau_w - \rho g\delta \tag{17}$$

From assumptions $(e)$ and $(k)$ we have, respectively,

$$\frac{\tau_i}{\rho} = \frac{\tau_w}{\rho} = U^{*2} \tag{18}$$

$$\left.\frac{dP}{dx}\right|_{\mathrm{vap}} = \left.\frac{dP}{dx}\right|_{\mathrm{liq}} = -\rho_l g \tag{19}$$

Changing variables on the left-hand side of equation (17) and substituting equations (18) and (19) into equation (17),

$$F_5(U_M{}^+)\frac{dU^*}{dx} + U^* F_6(U_M{}^+)\frac{dU_M{}^+}{dx} = \frac{\rho_l - \rho}{\rho} g \frac{F_1(U_M{}^+)}{U^*} - \frac{U^{*2}}{\nu} \tag{20}$$

We thus have a system of 5 equations, (3), (6b), (11), (16), and (20), in 5 unknowns $\overline{q''(t)}$, $q''(s)$, $\theta_w{}^+$, $U_M{}^+$, and $U^*$. If the value of these variables at some location $x = x_0$ and the value of the heat-transfer-enhancement coefficient $C$ are known, the system of equations can be solved.

## Experimental Technique and Setup

A transient technique was employed to obtain local heat-transfer rates with film boiling. The general nature of the technique was to immerse a relatively warm body in a saturated liquid of low boiling point so that film boiling was induced and measure the time rate of change of temperature of the immersed body. If the spatial temperature distribution in the body is known as a function of time, the rate of change of enthalpy of the body gives the heat-transfer rate to the fluid. This transient technique was successfully employed in earlier works [18, 19]. The validity of the transient technique in the present study was confirmed by $(a)$ computed values of nondimensional rate of temperature changes, which were very small, of the order of 0.001 and $(b)$ by comparing the heat-flux values obtained under transient conditions to those obtained under steady-state conditions in liquid nitrogen [20].

To determine the local heat-flux values on a vertical surface as a function of temperature, a test surface with thermally isolated test sections, Fig. 5, to which thermocouples were attached was used. The test surfaces were made of OFHC copper whose properties at low temperatures are well documented. To avoid edge effects in finite flat surfaces, cylindrical test surfaces were employed. The test sections were insulated from the adjoining spacer pieces with 0.005-in. Teflon washers; heat leakage to the adjoining sections was further reduced by cutting a recess in the spacer pieces such that a circular section of a relatively small radial width would bear in between the sections. Boiling from the top and bottom ends was prevented by mounting hollow end pieces of very low heat capacity, made of 0.001-in. s.s. shimstock. The sections were held together by $^3/_{32}$-in-dia s.s. bolts appropriately insulated from the test surface. The test surface was given a smooth polish after assembly. Copper–constantan thermocouples were attached to a tapered pin of OFHC copper which was driven into the test section as shown in Fig. 5. Three test surfaces of 1-in. diameter and two of $2^1/_4$-in. diameter were constructed and test sections of $^1/_4$-in. thickness were located at 11 positions in a height of 6 in. Each test surface had three test sec-

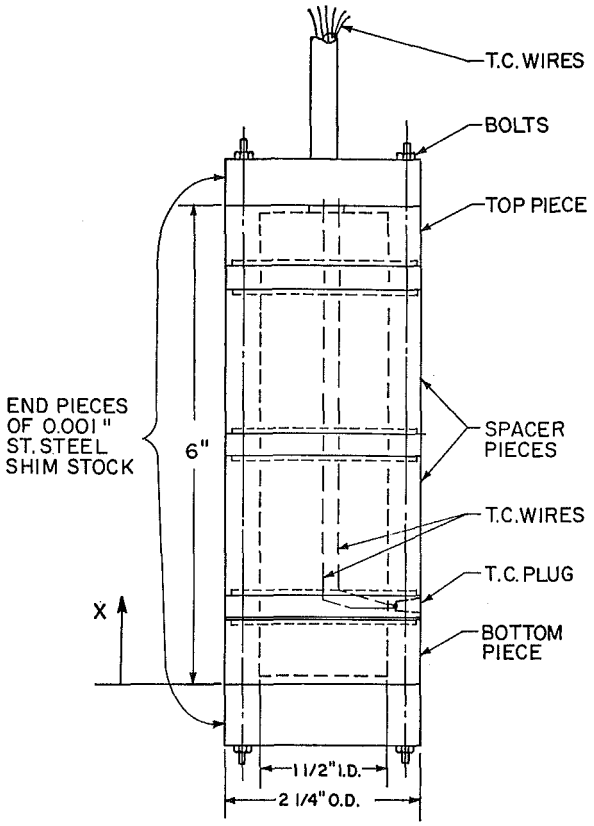


**Fig. 5 Test surface**

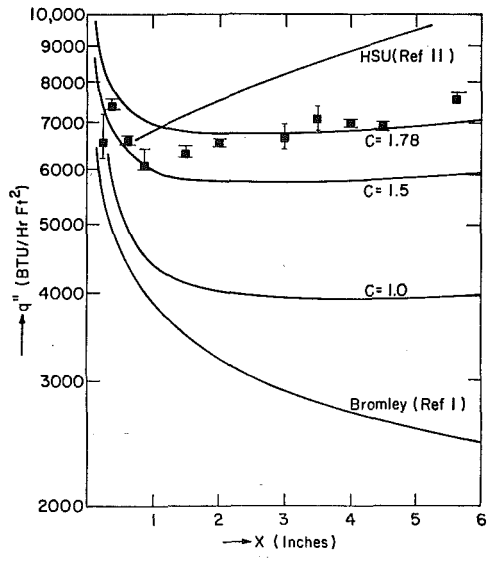


**Fig. 6 Film boiling, height vs. heat flux, saturated $LN_2$; $P = 14.9$ psia, $\Delta T = 315$ deg R**

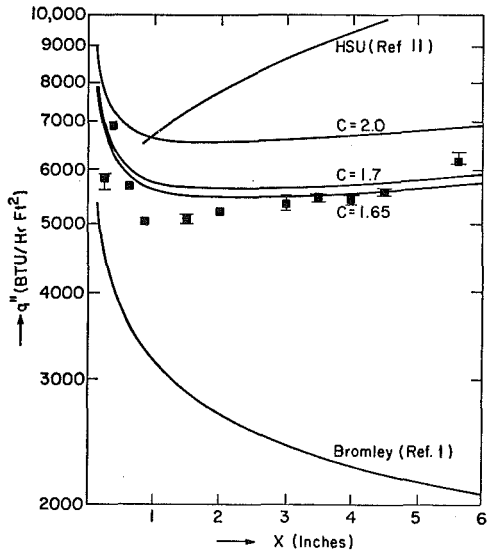


**Fig. 7 Film boiling, height vs. heat flux, saturated $LN_2$; $P = 14.9$ psia, $\Delta T = 251$ deg R**

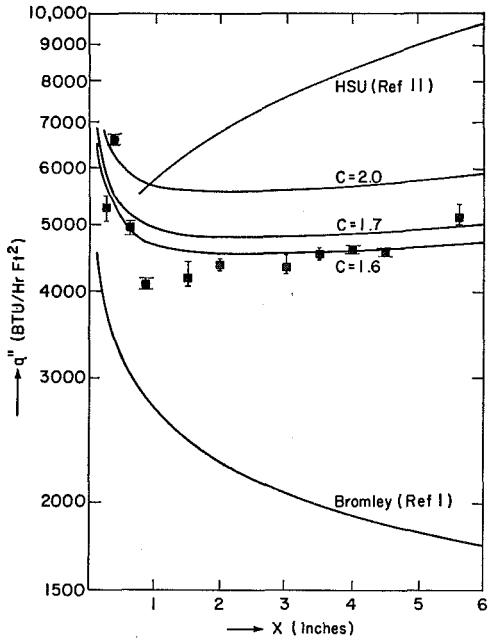


**Fig. 8 Film boiling, height vs. heat flux, saturated $LN_2$; $P = 14.9$ psia, $\Delta T = 204$ deg R**

tions with one section located at the same height in all the test surfaces so that data obtained with the different test surfaces could be compared for consistency.

Starting with an initially uniform temperature, the test surface was immersed in liquid nitrogen, inducing film boiling, and the outputs of the thermocouples attached to the different test sections located at different heights were recorded on an 8-channel recorder. The time rate of thermocouple output computed from the recorder output was then translated to time rate of change of temperature of the corresponding test section at the corresponding temperature of the test section. From an analytical solution it was established that lumped analysis gives acceptable accuracy in the computation of heat flux in the present case, the error being less than 0.1 percent. Hence, if the time rate of change of temperature at any one location in the test section is known, the heat flux is given by

$$\overline{q''(t)} = q_w'' = \frac{mC_p(T)}{A}\frac{dT}{dt} \tag{21}$$

Employing this technique, heat-flux values at 11 locations and four levels of $(T_w - T_s)$ in liquid nitrogen were determined. Heat transfer from the surfaces by radiation was negligible.

## Results

Figures 6–9 are plots of experimental values of $q''$ vs. height above the leading edge for four different values of $\Delta T$. Each of these figures includes:

($a$) Experimental data for one value of $\Delta T$. The data point is the mean of several runs under the same conditions, with the vertical line through each point showing the range of experimental values obtained.

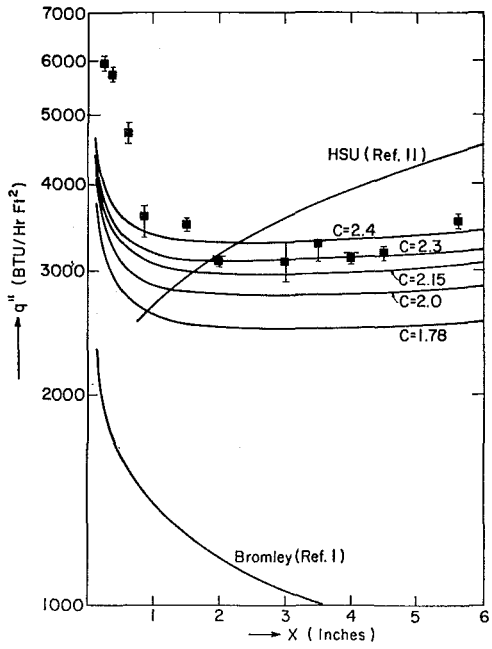


**Fig. 9 Film boiling, height vs. heat flux, saturated $LN_2$; $P$ = 14.9 psia, $\Delta T$ = 100 deg R**

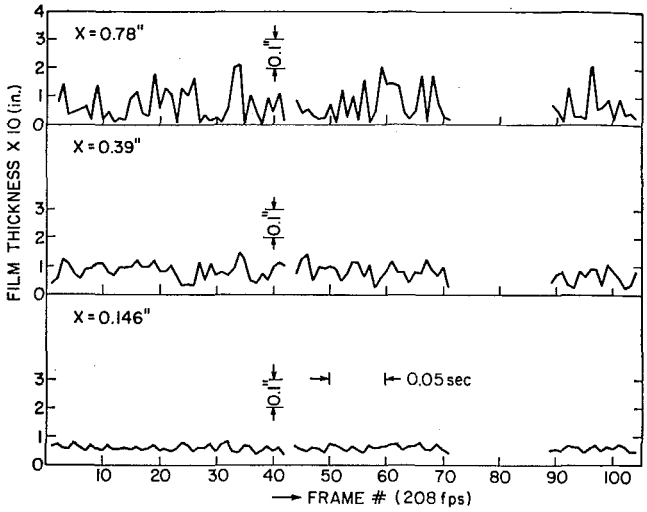


**Fig. 10 Variation of vapor-film thickness with time, saturated $LN_2$; $\Delta T$ = 100 deg R**

($b$) Several curves showing variation of heat flux with height as predicted from the present analysis for various constant values of the heat-transfer-enhancement coefficient $C$, which indicates the influence of interfacial oscillations. The set of equations (3), (6$b$), (11), (16), and (20) was solved in a computer, employing the Runge–Kutta procedure. The values of the various variables were initialized using the laminar solution [1] at $Y^+ = 2$, appropriately recast for use in the present analysis.

($c$) Predictions from the laminar analysis of Bromley [1] and the turbulent analysis of Hsu [11].

## Discussion

It is clearly seen that the predictions of the laminar analysis are quantitatively much lower than those obtained experimentally, and also predict the heat flux as continuously decreasing with height, whereas experimental data show an initial rapid decrease, a minimum, and then a gradual increase. The turbulent model of Hsu [11] also shows a considerable deviation from the experimental data. The prediction from the present analysis assuming a steady interface ($C = 1$) is shown in Fig. 6. While this prediction is substantially higher than that by laminar analysis [1] and qualitatively follows the same trends as observed experimentally, the difference from experimental data is still considerable. It has been suggested by some researchers that the eddy diffusivity for heat is higher than the eddy diffusivity for momentum. Using a ratio of 1.4 for $\epsilon_H/\epsilon_M$, computations from the present analysis with $C = 1.0$ showed a marginal increase in the predictions of heat-flux values as compared with the assumption of equality of eddy diffusivities for heat and momentum. It is evident that some mechanism other than turbulence causes an increase in the heat-transfer rates with height.

Both visual observations and linearized analysis [16] confirm the presence of interfacial oscillations of amplitudes of the order of the vapor-film thickness quite near to the leading edge. Under the assumption of constant temperature profile it has already been established that the heat-transfer-enhancement coefficient $C$ due to the interfacial oscillations is given by

$$C = \frac{1}{\sqrt{1 - b^2}} \qquad \text{where} \qquad b = \frac{a}{\delta(s)} \tag{3}$$

As there is no known way of predicting $a$ and hence $C$, the set of equations resulting from the present analysis was solved for different values of $C$ assumed constant over the entire height. These results are included in Figs. 6–9. Even with a $C$ value independent of the height, the present analysis comes closer to the experimental values both qualitatively and quantitatively than either of the two other predictions plotted [1, 11], if an appropriate value of $C$ is used. This ana ysis shows the greatest deviation near the leading edge. The elxtent of departure from the predictions is within ±23 percent, except in one case when it is −50 percent at $\Delta T$ = 100 deg R and $x$ = 1/4 in. However, the surface superheat is quite close to the second boiling crisis, which is around 40–50 deg R [19], and it is possible that the effects of transition boiling are beginning to show up. If the first 1 in. of the surface from the leading edge is excluded, the experimental values are within ±13.5 percent of the predicted values using $C$ constant for each $\Delta T$ but varying from 1.8 to 2.4 with $\Delta T$.

It is to be expected that the amplitude of interfacial oscillations will be a function of height, being very small or even zero at the leading edge and increasing with height. Thus, it would be unlikely that $C$ remains constant, but rather increases with height in some way. This variation cannot be determined directly from the plots of Figs. 6–9, since the computational procedure involves a marching process in the direction of increasing $x$. It was considered possible that the experimental observations of the variation of the amplitude of the interfacial oscillations might provide insight on the variation of $C$ with height. In order to study the nature of these interfacial oscillations, high-speed motion pictures where taken and analyzed.

To obtain motion pictures a steady-state technique was employed. A cartridge heater was installed in a vertical, hollow, cylindrical copper test surface 1 in. in diameter and 7 in. long. A double-walled rectangular dewar of stainless steel with plane windows of Pyrex glass was fabricated. A Beckman and Whitley drum-type camera (model 326) was used to obtain the motion pictures at a framing rate of approximately 200 frames per second. Other details are given in reference [20]. Motion pictures were obtained for three values of surface superheat in liquid nitrogen at four different heights. The films were projected on a ground-glass screen with a linear magnification corresponding to 10 times the actual size, and the vapor-film thickness was measured frame by frame at different heights. A typical diagram is shown in Fig. 10. This clearly shows the growth of the interfacial oscillations with distance from the leading edge. It can be seen that the oscillations do not appear to show a regular sinusoidal pattern and do not have a "minimum" or a "maximum" value for vapor-film thickness. A calculation of the heat-transfer-enhancement coefficient $C$ directly from these plots with equation (3) becomes difficult for the following reasons:

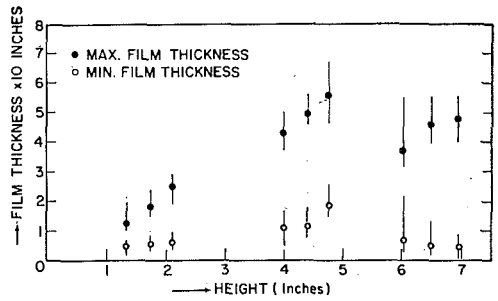


**Fig. 11 Variation of vapor-film thickness with height, saturated $LN_2$; $\Delta T = 315$ deg R**

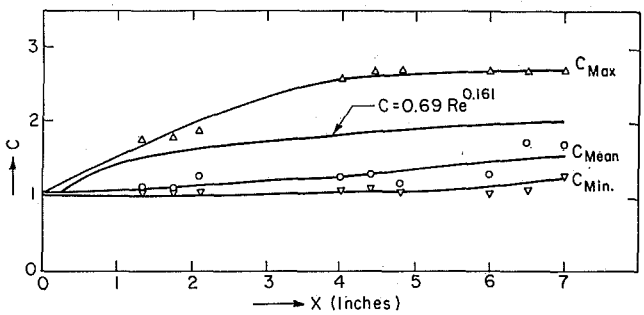


**Fig. 12 Variation of C with x, saturated $LN_2$; $\Delta T = 315$ deg R**

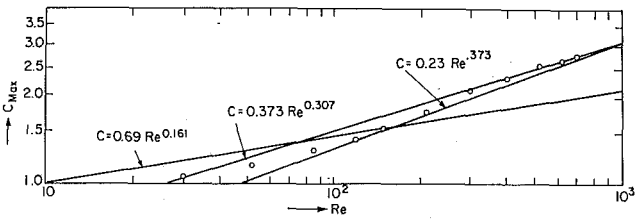


**Fig. 13 Variation of $C_{max}$ with Re, saturated $LN_2$; $\Delta T = 315$ deg R**

($a$) The amplitude of oscillations is a function of time, and hence $C$ is also a function of time.

($b$) The amplitude of oscillations is of the same order of magnitude as the vapor-film thickness, and for such large amplitudes the value of the heat-transfer-enhancement coefficient $C$ is very sensitive to changes in values of the amplitude. A measurement of the vapor-film thickness and amplitude of oscillation to the degree of precision required was not possible with the photographic equipment employed in the present study.

($c$) It is also doubtful if the assumption of constant temperature profile is valid when the vapor-film thickness becomes very small. In such situations it is likely that due to the high heat-transfer rates possible under such circumstances, local quenching may take place leading to local suppression of surface superheat which, in turn, causes a reduction in the heat-transfer rates.

With these things in mind, instead of attempting to determine one value of $C$ at a given location, data such as those in Fig. 10 were replotted as shown in Fig. 11. Each darkened circle represents the mean "maximum" vapor-film thickness, the vertical line through this representing the range of the "maximum" values. Similarly, values of "minimum" vapor-film thickness are represented by blank circles. From such plots as Fig. 11, three possible values of $C$ were determined at a given location: a maximum value obtained from the upper limit of the maximum vapor-film thickness and the lower limit of the minimum vapor-film thickness, a minimum value obtained from the lower limit of the maximum and the upper limit of the minimum vapor-film thicknesses, and a mean value obtained from the mean maximum and the mean minimum values of vapor-film thickness. Such a plot is shown in Fig. 12 for a nominal surface superheat of 315 deg R. The mechanism of these oscillations is not completely understood, but the value of $C$ may be expected to depend on the velocity of the vapor, vapor-film thickness, surface tension, gravity, densities of vapor and liquid, etc. As a simplification it is hypothesized that the local Reynolds number is an indication of the amplitude of such oscillations. The values of $C_{max}$ in Fig. 12 were replotted against local Reynolds number in Fig. 13. Two lines represented by $C = 0.373\ Re^{0.307}$ and $C = 0.23\ Re^{0.373}$ are shown plotted in Fig. 13 and can be said to encompass the values of $C_{max}$ for a surface superheat of 315 deg R. $C_{min}$ is close to 1.0, being less than 1.1 to a height of 5 in. and thereafter increasing to 1.15 at a height of 6 in. Because of these low values $C_{min}$ was set equal to 1.0, and the predictions from present analysis, using $C_{min} = 1.0$, $C_{max} = 0.373\ Re^{0.307}$, and $C_{max} = 0.23\ Re^{0.373}$, are shown plotted in Fig. 14. The best fit of experimental data, both qualitatively and quantitatively, is obtained by using $C = 0.69\ Re^{0.161}$ (which is also shown plotted in Figs. 12 and 13). However, while this functional form for $C$ gives the best fit for experimental data for a surface superheat of 315 deg R, the functional form for $C$ that gives the best fit for the four levels of surface superheat for which experimental data were obtained in liquid nitrogen is $C = 0.548\ Re^{0.187}$. With this functional form, the experimental values are within ±30 percent over the entire height for which the data were obtained and within ±15 percent if the values within 1/4 in. of the leading edge are ignored. It is possible that a functional form of $C$ that includes the surface superheat as a variable would be more successful, but this requires further work.

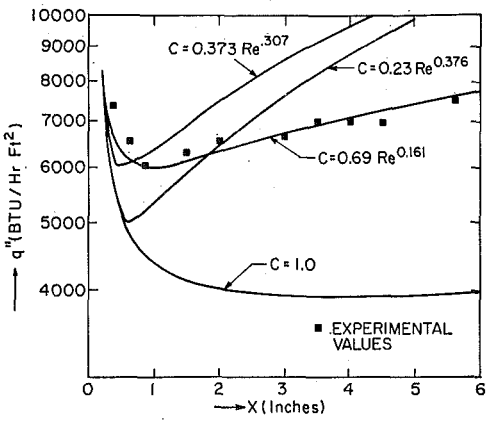


**Fig. 14 Effect of varying C with x, saturated $LN_2$; $\Delta T = 315$ deg R**

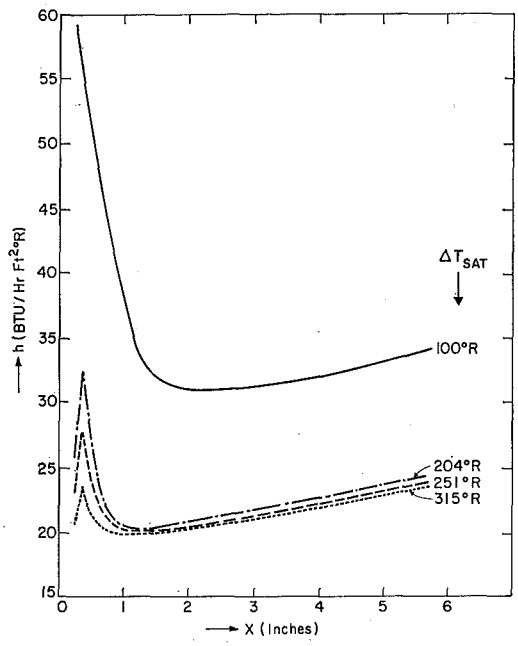


**Fig. 15 Effect of height on h, saturated $LN_2$; $P = 14.9$ psia**

The data obtained in the present study are replotted in Fig. 15 showing $h$ vs. $x$. The following conclusions can be drawn:

($a$) Initially there is a rapid decrease in $h$.

($b$) For the three higher values of surface superheat, approximately the same minimum value of $h$ is reached, and at approximately the same height of 1 in.

($c$) At a given height $x$, the value of $h$ is higher for lower values of surface superheat.

Trends similar to each of the above were also observed by Breen and Westwater [13] in their experiments with horizontal tubes in isopropanol, where the diameter of the tube was varied. For a surface superheat of 100 deg R, trends similar to the above are observed, but the value of $h$ is significantly higher. This value of surface superheat is close to the surface superheat for minimum heat flux which is around 40 to 50 deg R [18], and it is possible that transition effects are beginning to show.

One interesting feature of the variation of heat-transfer coefficient with height is that near the leading edge, where for $\Delta T$ = 315, 250, and 204 deg R a maximum in $h$ occurs. This is contrary to the trend predicted by laminar analysis. End effects would tend to make $h$ increase as $x$ approaches zero. This anomalous behavior is as yet unexplained.

## Conclusions

From the data obtained in the present study of film boiling on a vertical surface, both in regard to local heat-flux values and amplitude of interfacial oscillations, it appears that laminar vapor film with a steady interface is confined to a very short distance from the leading edge, and effects of interfacial oscillations and turbulence must be included even at short distances away from the leading edge. Even close to the leading edge where laminar analysis may be expected to be valid, experimental heat-flux values are considerably higher than predicted by laminar analysis.

## Acknowledgment

This study was supported, in part, by George C. Marshall Space Flight Center, NASA, under Contract No. NAS8-20228, and the support is gratefully acknowledged.

## References

1 Bromley, L. A., "Heat Transfer in Stable Film Boiling," *Chem. Eng. Progr.*, Vol. 46, 1950, p. 221.

2 Nusselt, W., "Die Oberflachenkondensation des Wasserdampfes," *VDI Z.*, Vol. 60, 1916, p. 541.

3 McFadden, P. W., and Grosh, R. J., "High Heat Flux Heat Transfer Studies—An Analytical Investigation of Laminar Film Boiling," *AEC Res. and Dev. Rep.*, ANL-6060, 1959.

4 Cess, R. D., "Analysis of Laminar Film Boiling from a Vertical Plate," Research Report 405 FF 340-R2-X, Westinghouse Research Lab., 1959.

5 Koh, J. C. Y., "Analysis of Film Boiling on Vertical Surfaces," JOURNAL OF HEAT TRANSFER, TRANS. ASME, Series C, Vol. 84, No. 1, Feb. 1962, pp. 55–62.

6 Sparrow, E. M., and Cess, R. D., "The Effect of Subcooled Liquid on Laminar Film Boiling," JOURNAL OF HEAT TRANSFER, TRANS. ASME, Series C, Vol. 84, No. 2, May 1962, pp. 149–156.

7 Nishikawa, K., and Ito, T., "Two-Phase Boundary Layer Treatment of Free Convective Film Boiling," *International Journal of Heat and Mass Transfer*, Vol. 9, 1966, pp. 103–115.

8 Frederking, T. H. K., "Laminar Two-Phase Boundary Layers in Natural Convection Film Boiling," *ZAMP*, Vol. 14, 1963, pp. 207–218.

9 Frederking, T. H. K., and Hopenfield, J., "Laminar Two-Phase Boundary Layers in Natural Convection Film Boiling of Subcooled Liquids," *ZAMP*, Vol. 15, 1964, pp. 388–399.

10 Tachinaba, F., and Fukaui, S., "Heat Transfer in Film Boiling to Subcooled Liquids," *International Developments in Heat Transfer*, Proceedings International Heat Transfer Conference, Boulder, Colo., 1961, Part II, ASME, New York, N. Y.

11 Hsu, Y. Y., and Westwater, J. W., "Film Boiling from a Vertical Surface," *AIChE Journal*, Vol. 4, 1958, pp. 58–62.

12 Coury, G. E., and Dukler, A. E., "Turbulent Film Boiling on Vertical Surface—A Study Including the Influence of Interfacial Waves," Paper B.3.6, Proceedings International Heat Transfer Conference, Paris, 1970.

13 Breen, B. P., and Westwater, J. W., "Effect of Diameter of Horizontal Tubes on Film Boiling Heat Transfer," *Chem. Eng. Progr.*, Vol. 58, No. 7, 1962, pp. 67–72.

14 Dougall, R. P., and Rohsenow, W. H., "Film Boiling on the Inside of Vertical Tubes with Upward Flow of the Fluid at Low Qualities," Tech. Rep. No. 9079-26, Department of Mechanical Engineering, M.I.T., Cambridge, Mass.

15 Spalding, D. B., "Heat Transfer to a Turbulent Stream from a Surface with a Stepwise Discontinuity in Wall Temperature," *International Developments in Heat Transfer*, Proceedings International Heat Transfer Conference, Boulder, Colo., 1961, Part III, ASME, New York, N. Y.

16 Frederking, T. H. K., "Stability of Film Boiling Two-Phase Flow in Cryogenic Systems," Report NSG-237-62, Department of Engineering, UCLA, Los Angeles, Calif.

17 Chandrasekhar, S., *Hydrodynamic and Hydromagnetic Stability, The International Series of Monographs in Physics*, Oxford University Press, 1961, pp. 485.

18 Merte, H., Jr., and Clark, J. A., "Boiling Heat Transfer With Cryogenic Fluids at Standard, Fractional, and Near-Zero Gravity," JOURNAL OF HEAT TRANSFER, TRANS. ASME, Series C, Vol. 86, No. 3, Aug. 1964, pp. 351–359.

19 Lewis, Eugene W., "Boiling of Liquid Nitrogen in Reduced Gravity Fields with Subcooling," PhD thesis, University of Michigan, Ann Arbor, Mich., 1967.

20 Suryanarayana, N. V., "Film Boiling on Vertical Surfaces in Turbulent Regime," PhD thesis, University of Michigan, Ann Arbor, Mich., 1970.

21 Frederking, T. H. K., and Clark, J. A., "Natural Convection Film Boiling on a Sphere," *Advances in Cryogenic Engineering*, Vol. 8, 1963, pp. 501–506.

22 Rohsenow, W. M., Webber, J. H., and Ling, A. T., "Effect of Vapor Velocity on Laminar and Turbulent-Film Condensation," TRANS. ASME, Vol. 78, 1956, pp. 1637–1643.

## APPENDIX

Definitions of functions used in equations:

$$F_1(x) = x + \frac{1}{E}\left[e^{kx} - 1 - kx - \frac{(kx)^2}{2!} - \frac{(kx)^3}{3!} - \frac{(kx)^4}{4!}\right]$$

$$F_2(x) = \frac{k}{E}\left[e^{kx} - 1 - kx - \frac{(kx)^2}{2!} - \frac{(kx)^3}{3!}\right]$$

$$F_3(x) = 1 + F_2(x)$$

$$F_4(x) = x + \frac{1}{E}\left[kxe^{kx} - kx - (kx)^2 - \frac{(kx)^3}{2!} - \frac{(kx)^4}{4!}\right]$$

$$F_5(x) = \frac{x^3}{3} + \frac{1}{k^2E}\left[(kx)^2e^{kx} - 2kxe^{kx} + 2e^{kx} - 2 - \frac{(kx)^3}{3} - \frac{(kx)^4}{4} - \frac{(kx)^5}{10} - \frac{(kx)^6}{36}\right]$$

$$F_6(x) = x^2F_3(x)$$

$$k = 0.407 \qquad \frac{1}{E} = 0.0991$$

L. L. DEBRUGE
Aerospace Engineer,
Wright–Patterson Air Force Base,
Dayton, Ohio

L. S. HAN
Professor,
Department of Mechanical Engineering,
Ohio State University,
Columbus, Ohio.
Assoc. Mem. ASME

# Heat Transfer in a Channel with a Porous Wall for Turbine Cooling Application

*A method of cooling turbine blades internally by continuous injection through an interior baffle is analyzed. The analytical model consists of a two-dimensional channel formed by a solid wall (blade surface) and a porous plate (injection source). Based on incompressible- and laminar-flow assumptions, the velocity and the temperature fields are determined. The Nussell numbers for a power-law surface-temperature variation are obtained and expressed in terms of the Prandtl and the Reynolds numbers. A related problem of cooling the turbine disk is also solved.*

## Introduction

Parallel to the research for better heat-resistant materials for gas-turbine applications, the search for a practicable scheme of thermal protection against high-temperature effects for existing materials continues to play a major role in improving the performance of gas-turbine engines. Transpiration cooling is effective in principle, but its adaptation to production engines is still years away because of the numerous difficulties yet to be resolved. These include the diminished fatigue life occasioned by the fine porous structure of the blade surface, the possible clogging of the coolant openings, reduced impact strength, etc. Consequently, recent interests have been directed to non-transpiration types which offer a more immediate return. The non-transpiration types consist of (*a*) internal ducting and (*b*) local impingement.

The former relies on the flow of a coolant along a pre-designed path inside a turbine blade to remove the heat originating from the external gas stream. From a heat-transfer viewpoint it is based on the well-established channel-flow theory, but is complicated by bends and turns. Its overall performance as measured by the heat-transfer rate balanced by the required pumping power appears to warrant further improvement. On the other hand, the impingement method utilizes the localized jet effect which reduces the thermal boundary layer, thus enhancing the heat-removal rate. The recent heat-transfer literature records a number of such investigations as exemplified by the work of Metzger [1].[1]

It is a well-known fact that for a turbine blade in a high-temperature stream the external flow-field characteristics are such that there is a region around and in the vicinity of the stagnation point where the external heat-transfer coefficient is highest relative to the downstream region of the blade surface. This region of high heat transfer extends approximately 30 deg or about one-half of the nose radius of curvature. In order to cool this region, the cross section of the internal air jet is to be of the same order of magnitude as the nose radius, and in the meantime the downstream region of the blade will be left unprotected or at least "unprogrammed" in the cooling-design stage. All this is not to say that impingement cooling is ineffective. However, in a certain combination of circumstances it is worthwhile to examine a third alternative, which in essence is a combination of the internal-ducting method and the local-impingement method.

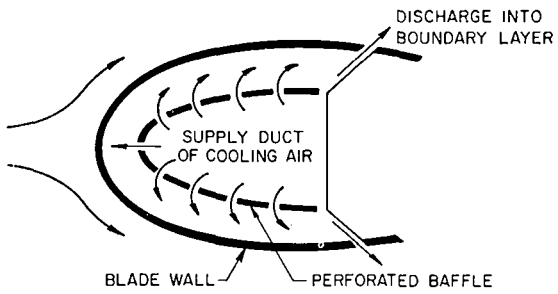


**Fig. 1 Cooling of turbine blade by continuous injection**

Basically the proposed method of blade cooling is a continuous-injection concept from a series of perforations on an internal baffle. The essential components are embodied in Fig. 1, which shows an internal perforated baffle hugging the contour of the blade profile. Cooling air is fed from a central cavity or supply chamber through the perforations. The cooling air accumulating from the continuous injection flows along the ducted passages until discharged overboard. The scope of the present investigation is to determine the heat transfer from the blade surface to the injected fluid. The first phase of the investigation is a theoretical analysis concerned with the velocity and temperature analyses based on a laminar-flow model. The next phase will deal with the experimental aspects and will be reported subsequently.

[1] Numbers in brackets designate References at end of paper.

Contributed by the Heat Transfer Division of The American Society of Mechanical Engineers and presented at the AIChE-ASME Heat Transfer Conference, Denver, Colo., August 6–9, 1972. Manuscript received by the Heat Transfer Division November 24, 1971. Paper No. 72-HT-39.

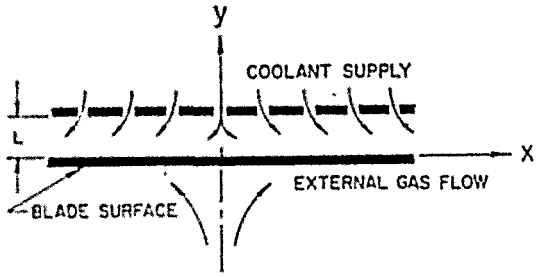


Fig. 2 Analytical model of channel flow

From a practical viewpoint, the density of the perforation on the baffle plate (Fig. 1) may be varied so as to permit a controlled rate of coolant injection toward the hot surface. Furthermore, the spacing or clearance may be altered or made variable along its passage so that the location of the flow streamline division becomes coincident with the external flow stagnation point. There are, of course, other engineering refinements to be implemented in the actual development of this scheme of cooling. However, for the sake of arriving at a magnitude of the heat-transfer value, the schematic model shown in Fig. 2 was adopted to represent the engineering model of Fig. 1. To simplify the analysis, two general assumptions were made: (*a*) The flow between the baffle and the inner surface of the turbine blade is laminar and steady and (*b*) the clearance $L$ is small compared to the radius of curvature, and consequently two-dimensional flow representation in Fig. 2 is justified. In addition, constant physical properties were assumed for the fluid, and the rate of fluid injection was assumed uniform along the length.

The overall fluid-dynamic picture of the problem depicted in Fig. 2 has the general feature of a flow field defined by a porous surface with injection. This type of problem has been treated by Yuan [2], White [3], and Terrill [4]. The main feature of the problem they studied consisted of the determination of the flow field resulting from peripheral injection with an initial entry profile (which cannot be arbitrarily set). Yuan's approach was a perturbation method and White used an exact series expansion to solve the problem. The method used in this paper, however, resembles that of Terrill in the sense that a coordinate stretching and a direct numerical-integration scheme were adopted.

## Two-dimensional Flow Analysis

With the assumptions of steady flow of an incompressible fluid with constant physical properties, the pertinent flow equations (with $u$ and $v$ as the $x$, $y$ velocities and with variable subscripts denoting differentiation) are as follows:

$$uu_x + vu_y = -P_x/\rho + \nu(\nabla^2 u) \tag{1}$$

$$uv_x + vv_y = -P_y/\rho + \nu(\nabla^2 v) \tag{2}$$

$$u_x + v_y = 0 \tag{3}$$

The boundary conditions are

$$u = v = 0 \qquad y = 0 \tag{4}$$

$$u = 0 \qquad y = L \tag{5}$$

$$v = -V \qquad y = L \tag{6}$$

where the last condition signifies a uniform rate $V$ of downward (see Fig. 2) injection of coolant. The origin of Fig. 2 has been placed at the dividing point as has been previously discussed. As is done in previous work, we use the stream function $\psi$ in the form

$$\psi = xVf(y/L) \tag{7}$$

with the standard convention $u = \psi_y$ and $v = -\psi_x$.

The resulting velocities and the two equations of motion are

$$u = V(x/L)f'(y/L) \tag{8}$$

$$v = -Vf(y/L) \tag{9}$$

$$f'^2 - ff'' = -(L^2P_x/\rho V^2 x) + f'''/\mathrm{Re} \tag{10}$$

$$ff' = -(LP_y/\rho V^2) - f''/\mathrm{Re} \tag{11}$$

where the injection Reynolds number is $\mathrm{Re} = VL/\nu$. It is apparent from equation (11) that $P_y$ is independent of $x$. Then $P_x$ must be independent of $y$. Consequently, the pressure-gradient term in (10) is a constant, i.e., independent of $y$ but nonetheless an unknown constant. Calling this constant $K$, equation (10) is now cast as

$$f'^2 - ff'' = K + f'''/\mathrm{Re} \tag{10a}$$

$$K = -L^2P_x/\rho V^2 x \tag{10b}$$

Now, in principle, equation (10*a*) can be solved as follows: Fix a value for the injection Reynolds number; start the numerical integration stepwise with $f(0) = 0, f'(0) = 0$, and two more trial values, one for $f''(0)$ and the other for $K$. The integration will proceed from $y/L = 0$ until $y/L = 1$ at which $f(1)$ and $f'(1)$ should be 1 and 0 respectively. If this should not be the case a searching procedure for the correct combination of $K$ and $f''(0)$ will have to be followed until the following four conditions are met:

$$f(0) = f'(0) = f'(1) = 1 - f(1) = 0 \qquad (12a; b, c)$$

The fact that there are four boundary conditions associated with a third-order equation (10*a*) determines the value of the pressure-gradient parameter $K$. Once this is accomplished, equation (11) can be used to determine $P_y$ directly.

**Solution of Equation (10*a*).** The integration of equation (10*a*) subject to the boundary conditions of (12) is best accomplished by a numerical method and through a coordinate stretching method utilizing the following transformations:

$$\text{let} \quad f(y/L) = aF(\eta) \quad \text{with} \quad \eta = by/L \tag{13}$$

where $a$ and $b$ are undetermined constants. Substitution of (13) into (10*a*) and (12) gives the new equations as

$$F'^2 - FF'' - (b/a\ \mathrm{Re})F''' = K/a^2b^2$$

An optimum choice is of course

## Nomenclature

$a, b$ = transformation coefficients, equation (13*a*)
$C$ = blade-wall temperature coefficients, equations (18) and (28)
$e$ = subscript for "external"
$f, F$ = velocity functions, equations (7) and (13)
$h$ = heat-transfer coefficient
$k$ = fluid thermal conductivity
$K$ = pressure-gradient parameter, equations (10*b*) and (25)
$L$ = clearance
$m, n$ = integer indexes
Nu = Nusselt number
$P$ = fluid pressure
Pr = Prandtl number
$q$ = heat flux
Re = injection Reynolds number ($VL/\nu$)
$T$ = temperature
$x, y$ = coordinates parallel and transverse to surface
$u, v$ = fluid velocities in the $x$, $y$ directions
$V$ = injection velocity
$w$ = subscript for blade wall
$\alpha$ = thermal diffusivity
$\eta$ = transformed coordinate ($by/L$)
$\nu$ = kinematic viscosity
$\rho$ = density
$\phi$ = temperature function

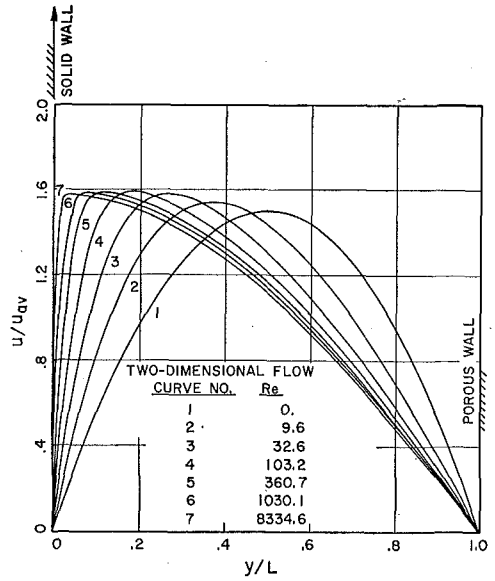


Fig. 3(*a*) Velocity distribution in two-dimensional channel

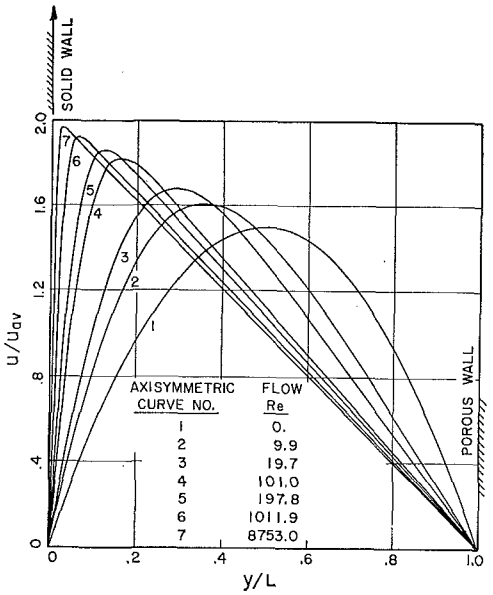


Fig. 3(*b*) Velocity distribution in axisymmetric channel

$$a^4 = K/\mathrm{Re} \qquad b = a\,\mathrm{Re} \tag{13a}$$

such that the new equation becomes

$$F'^2 - FF'' - F''' = 1 \tag{14}$$

and the new boundary conditions become

$$F(0) = F'(0) = F'(b) = F(b) - 1/a = 0 \tag{15}$$

The advantage of the transformations (13) is apparent because the scheme of integrating equation (14) is now a simple straightforward process: By assuming $F''(0)$ equals, say , 0.5 and with $F'(0) = F(0) = 0$, equation (14) can be integrated starting from $\eta = 0$ by any sensible method until $F'$ returns to zero. When it does the value of $\eta$ is set as $b$ and the value of $F$ as $1/a$. The use of (13*a*) produces the value of $K$ and the injection Reynolds number. Equation (14) is of course the familiar Fage–Skan equation [5] for boundary-layer flow near the stagnation point; its behavior is well known, and in particular with $F(0) = F'(0) = 0$ and $F''(0) = 1.2326$ the asymptotic value of $F' \to 1$ as $\eta \to \infty$. In the present scheme, the value of $F''(0) = 1.2326$ corresponds to an infinite Reynolds number. For $F''(0) > 1.2326$, $F'(\eta)$ is increasing without bound, and for $F''(0) < 1.2326$, $F'(\eta)$ starting from zero returns to zero at a finite value of $\eta$. Thus the task of integrating equation (14) is simplified to selecting a value of $F''(0) < 1.2326$. In this way, the values of $K$ and Re are the output. Some of the pertinent numerical values of $f''(0)$, $K$, and $f''(0)/\mathrm{Re}^{1/2}$ resulting from the aforementioned integration procedure are tabulated in Table 1. Table 1 also contains the corresponding values for the axisymmetric case discussed later. The normalized velocity in the channel direction, i.e., $(u/u_{av}) = f'(y/L)$, is shown in Fig. 3.

Two interesting observations can be made. At lower Reynolds numbers, the velocity profiles exhibit centerline symmetry indicating a Poiseuille flow. At higher Reynolds numbers the maximum-velocity point is shifted to the solid wall where the shear stress becomes larger as the Reynolds number grows. In fact, a boundary layer now exists near the solid wall as a result of injection from the perforated baffle, as is confirmed by the asymptotic relations for $\mathrm{Re} > 20$, i.e., $f''(0)/\mathrm{Re}^{1/2} \to$ constant.

**Asymptotic Analysis of Equation (10*a*).** For a very small rate of injection corresponding to a vanishingly small Reynolds number, equation (10*a*) can be reduced by dropping the terms on the right-hand side, thus becoming $f''' = -K\,\mathrm{Re}$. The four boundary conditions are $f(0) = f'(0) = f'(1) = 1 - f(1) = 0$. Its solution is simply

$$f = -2(y/L)^3 + 3(y/L)^2 \qquad f' = 6(y/L)[1 - (y/L)]$$

$$K\,\mathrm{Re} = 12$$

and is consistent with the numerical results in Table 1 for low Reynolds numbers. This is of course the Poiseuille flow.

On the other hand, for large Reynolds numbers equation (10*a*) can be simplified by dropping the term $f'''/\mathrm{Re}$ and the equation becomes $f'^2 - ff'' = K$. Because of the reduced order of the truncated equation, not all four boundary conditions can be satisfied. The appearance of an extra parameter $K$ therefore allows the fulfillment of three conditions, which are now $f(0) = 0$, $f(1) = 1$, $f'(1) = 0$. These conditions satisfy the mass conservation at both walls and the no-slip requirement on the porous wall ($y = L$). The result is

$$f = \sin\,[(y/L)\sqrt{K}] \qquad \text{and} \qquad K = \pi^2/4$$

The value of $K$ in Table 1 is seen to approach $\pi^2/4$ as the Reynolds number increases, and the shape of the velocity closely parallels the cosine distribution except near the solid wall $y \approx 0$ where a boundary layer exists.

In the boundary layer itself, the solution of the velocity is given by equation (14) for $\mathrm{Re} \to \infty$. In other words,

$$f = aF(\eta) \qquad f' = abF'(\eta) \qquad f'' = ab^2F''(\eta)$$

For asymptotically large Reynolds numbers, $F''(0) = 1.2326$ and

**Table 1 Shear stresses and pressure gradient *K* for two-dimensional flow and axisymmetric flow**

| Two-dimensional case | | | | Axisymmetric case | | | |
|---|---|---|---|---|---|---|---|
| Re | K | f"(0) | f"(0)/√Re | Re | K | f"(0) | f"(0)/√Re |
| 1.391 | 11.01 | 6.63 | 5.62 | 10.15 | 6.33 | 9.93 | 3.12 |
| 2.968 | 6.494 | 7.32 | 4.25 | 19.99 | 5.40 | 13.0 | 2.92 |
| 4.806 | 5.524 | 8.10 | 3.69 | 56.58 | 4.72 | 20.9 | 2.77 |
| 6.901 | 4.300 | 8.92 | 3.40 | 72.12 | 4.62 | 23.4 | 2.75 |
| 9.494 | 3.855 | 9.86 | 3.20 | 101.0 | 4.51 | 27.4 | 2.73 |
| 32.62 | 3.045 | 15.9 | 2.79 | 310.8 | 4.28 | 47.3 | 2.68 |
| 59.36 | 2.863 | 20.7 | 2.69 | 505.6 | 4.20 | 59.9 | 2.67 |
| 103.2 | 2.753 | 26.6 | 2.62 | 680.3 | 4.18 | 69.4 | 2.66 |
| 291.4 | 2.629 | 43.4 | 2.54 | 1012. | 4.15 | 84.4 | 2.65 |
| 361.1 | 2.610 | 48.0 | 2.53 | 1663. | 4.11 | 108. | 2.65 |
| 692.0 | 2.568 | 65.7 | 2.50 | 1892. | 4.11 | 115. | 2.65 |
| 1033. | 2.548 | 79.9 | 2.49 | 2173. | 4.10 | 123. | 2.65 |
| ∞ | $\pi^2/4$ | ∞ | 2.43 | ∞ | 4 | ∞ | 2.6240 |

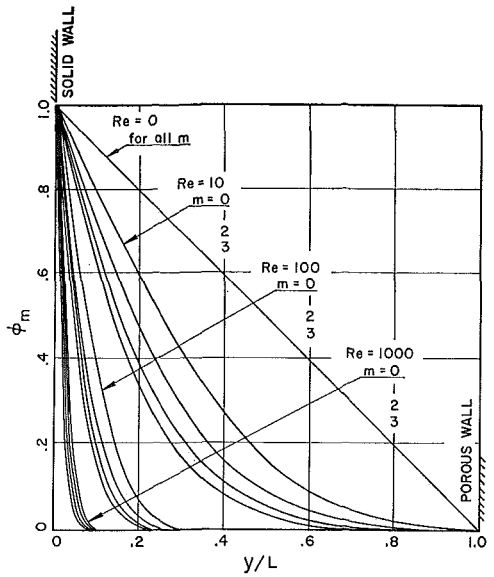


Fig. 4(a) Temperature profiles across the cooling gap for two-dimensional flow, Pr = 0.7

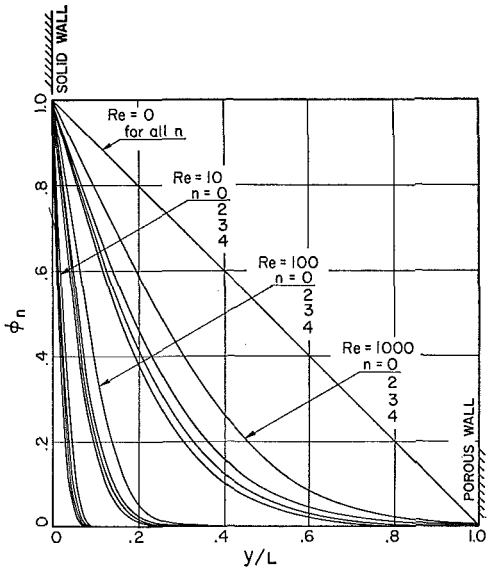


Fig. 4(b) Temperature profiles across the cooling gap for axisymmetric flow, Pr = 0.7

$$f''(0) = K^{3/4}1.2326\sqrt{\mathrm{Re}} = (\pi^2/4)^{3/4}1.2326\sqrt{\mathrm{Re}} = 2.43\sqrt{\mathrm{Re}}$$

where 2.43 is the exact asymptotic value in Table 1 for two-dimensional flow.

## Two-dimensional Temperature Analysis

For studying the effectiveness of the proposed cooling scheme, the perforated baffle or the porous plate ($y = L$) is assumed to have the same temperature $T_0$ as that of the incoming coolant. The blade wall ($y = 0$) is assumed to have a polynomial variation (symmetrical about $x = 0$) in the form

$$T_w = T_0 + \sum_{m=0} C_m(x/L)^m \tag{16}$$

For a uniform blade-wall temperature, equation (16) is reduced to $T_w = T_0 + C_0$, where $C_0$ represents the temperature difference. Neglecting the dissipation effects[2] and the conduction flux along the $x$ direction, the equation for determining the temperature is

$$uT_x + vT_y = \alpha T_{yy} \tag{17}$$

Assuming the fluid temperature to have the form

$$T = T_0 + \sum_{m=0} C_m(x/L)^m\phi_m(y/L) \tag{18}$$

and introducing (8), (9), and (18) into (17), there results an equation containing terms of various powers of $x$. Separating those terms gives the following equations for $m = 0, 1, 2, \ldots$

$$\mathrm{Pr\ Re}(mf'\phi_m - f\phi_m') = \phi_m'' \tag{19}$$

The boundary conditions on $\phi_m$'s are

$$\phi_m(1) = 0 \qquad \phi_m(0) = 1 \tag{20}$$

Equation (19) of course admits a simple solution $\phi_m = 1 - (y/L)$ for zero Reynolds number representing the case of pure conduction. For other values, however, a standard numerical-integration procedure together with known $f$ and $f'$ from the velocity analysis gives the desired distributions and the gradients at the solid wall $y = 0$.

Fig. 4 exhibits the temperature profiles across the "cooling gap" for Pr = 0.7 and Re = 10, 100, and 1000. For each Reynolds number, the values of $m$ are 0, 1, 2, and 3. For the high-Reynolds-number case, the large temperature gradient near the solid wall is again indicative of the boundary-layer characteristics.

**Heat-Transfer Coefficients and Correlation.** It is not possible to obtain a single value for the heat-transfer coefficient applicable for all $x$ if the blade surface temperature follows a polynomial variation, unless the temperature profile along the blade surface is a power law as expressed by a *single* term in (16), i.e., $T_w = T_0 + C_m(x/L)^m$. For such a power-law blade-surface-temperature variation, a heat-transfer coefficient $h_m$ can be defined as

$$h_m(T_w - T_0) = -k(\partial T/\partial y)$$

and the nondimensional Nusselt number $\mathrm{Nu}_m$ is then

[2] The viscous dissipation effects were analyzed in [6], which also contains more detailed numerical tabulations than in this paper. The viscous effects were found negligible.

Table 2(a) Numerical tabulations of power-law Nusselt numbers $\mathrm{Nu}_m$ for two-dimensional flow, Pr = 0.7, 1

| Re | m = 0 | m = 1 | m = 2 | m = 3 |
|---|---|---|---|---|
| 1.391 | 1.15 (1.21) | 1.40 (1.55) | 1.61 (1.81) | 1.80 (2.04) |
| 2.968 | 1.33 (1.46) | 1.78 (2.03) | 2.13 (2.44) | 2.42 (2.77) |
| 4.806 | 1.54 (1.74) | 2.16 (2.48) | 2.61 (3.00) | 2.97 (3.40) |
| 6.901 | 1.77 (2.03) | 2.54 (2.92) | 3.07 (3.52) | 3.48 (3.98) |
| 9.494 | 2.03 (2.35) | 2.94 (3.38) | 3.55 (4.07) | 4.02 (4.60) |
| 32.62 | 3.68 (4.24) | 5.28 (6.05) | 6.36 (7.27) | 7.19 (8.20) |
| 59.36 | 4.93 (5.68) | 7.06 (8.08) | 9.49 (9.70) | 9.60 (10.9) |
| 103.2 | 6.46 (7.43) | 9.24 (10.6) | 11.1 (12.7) | 12.6 (14.3) |
| 291.4 | 10.8 (12.4) | 15.4 (17.6) | 18.5 (21.1) | 20.9 (23.8) |
| 361.1 | 12.0 (13.8) | 17.1 (19.6) | 20.6 (23.5) | 23.2 (26.5) |
| 692.0 | 16.5 (19.0) | 23.6 (27.0) | 28.4 (32.4) | 32.1 (36.5) |
| 1033. | 20.1 (23.2) | 28.8 (32.9) | 34.6 (39.5) | 39.1 (44.5) |

Table 2(b) Numerical tabulations of power-law Nusselt numbers $\mathrm{Nu}_n$ for axisymmetric flow, Pr = 0.7, 1

| Re | n = 0 | n = 2 | n = 3 | n = 4 |
|---|---|---|---|---|
| 10.15 | 2.12 (2.45) | 3.06 (3.52) | 3.40 (3.90) | 3.70 (4.23) |
| 19.99 | 2.97 (3.43) | 4.26 (4.88) | 4.73 (5.40) | 5.13 (5.85) |
| 56.58 | 5.00 (5.75) | 7.13 (8.15) | 7.90 (9.01) | 8.55 (9.75) |
| 72.12 | 5.65 (6.49) | 8.05 (9.19) | 8.91 (10.2) | 9.65 (11.0) |
| 101.0 | 6.68 (7.68) | 9.51 (10.9) | 10.5 (12.0) | 11.4 (13.0) |
| 310.8 | 11.7 (13.5) | 16.7 (19.0) | 18.4 (21.0) | 19.9 (22.7) |
| 505.6 | 15.0 (17.2) | 21.2 (24.2) | 23.5 (26.8) | 25.4 (28.9) |
| 680.3 | 17.4 (19.9) | 24.6 (28.1) | 27.2 (31.0) | 29.5 (33.5) |
| 1012. | 21.2 (24.3) | 30.0 (34.2) | 33.2 (37.8) | 35.9 (40.9) |
| 1663. | 27.1 (31.1) | 38.5 (43.9) | 42.5 (48.5) | 46.0 (52.4) |
| 1892. | 28.9 (33.2) | 41.0 (46.8) | 45.4 (51.7) | 49.1 (55.9) |
| 2173. | 31.0 (35.6) | 44.0 (50.2) | 48.6 (55.4) | 52.6 (59.9) |

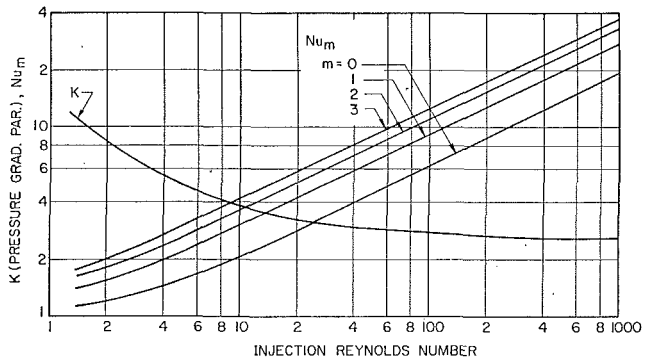


**Fig. 5(a) Pressure-gradient parameter $K$ and power-law Nusselt numbers for two-dimensional flow, Pr = 0.7**

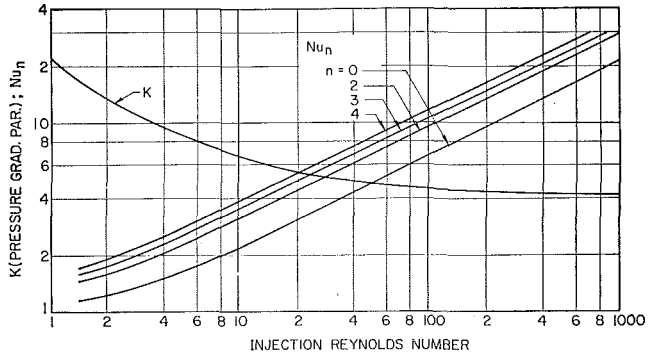


**Fig. 5(b) Pressure-gradient parameter $K$ and power-law Nusselt numbers for axisymmetric flow, Pr = 0.7**

**Table 3 Correlation constants $A_m$ and $A_n$ in equation (22) for two-dimensional and axisymmetric cases**

| Two-dimensional case | | Axisymmetric case | |
|---|---|---|---|
| m | $A_m$ | n | $A_n$ |
| 0 | 0.683 | 0 | 0.761 |
| 1 | 1.156 | 2 | 1.082 |
| 2 | 1.268 | 3 | 1.196 |
| 3 | 1.500 | 4 | 1.297 |

$$\mathrm{Nu}_m = (h_m L/k) = -\phi_m'(0) \tag{21}$$

which is tabulated in Table 2 for Pr = 0.7 and 1 over a range of the Reynolds numbers 0 to 2000. Other Prandtl numbers were also computed [6] but not tabulated in the present paper. The variation of the Nusselt number and the pressure gradient $K$ versus the Reynolds number is shown in Fig. 5. It is noteworthy that for Re > 10 the heat-transfer coefficient already obeys the square-root relation, i.e., $h_m \sim \mathrm{Re}^{1/2}$.

For Re > 10, the range of engineering interest, it is possible to express the nondimensional parameters in the following relations:

$$\mathrm{Nu}_m = A_m \, \mathrm{Pr}^{0.38}\sqrt{\mathrm{Re}} \tag{22}$$

From a fairly extensive tabulation of the computer output, the constants $A_m$ are listed in Table 3 together with the axisymmetric case to be discussed later.

## Axisymmetric Case

Parallel to the two-dimensional analysis, the analogous problems of cooling a circular disk by injecting cooling air from a perforated parallel disk was also investigated. Not only is this problem closely related to the two-dimensional case from a theoretical viewpoint, but also its application to turbine cooling technology is akin to the blade cooling.

From an analysis standpoint, only minor modifications are necessary. Fig. 2 can be interpreted as a two-disk configuration with the upper one perforated and admitting cooling flow first downward and then radially outward ($x$). The stream function $\psi$ is now ($u = \psi_y/x, \quad v = -\psi_x/x$)

$$\psi = (x^2 V/2L) f(y/L) \tag{23}$$

which gives the radial ($x$) and transverse ($y$) velocities, $u$ and $v$. The resulting equation corresponding to (10) is

$$f'^2 - 2ff'' = K + 2f'''/\mathrm{Re} \tag{24}$$

where the pressure parameter $K$ and the four boundary conditions are

$$K = -4P_x L^2/(\rho V^2 x) \tag{25}$$

$$f(0) = f'(0) = f'(1) = 1 - f(1) = 0 \tag{26}$$

From here on the procedure for solving equation (24) completely parallels that for equation (10). Using again the transformation (13), the transformed equation and boundary conditions are

$$F'^2 - 2FF'' = 1 + F'''$$
$$F(0) = F'(0) = F'(b) = F(b) - 1/a = 0 \tag{27}$$

The relations between $a$, $b$, $K$, and Re are as follows: $a^2 b^2 = K$, $2b = a\,\mathrm{Re}$. Equation (27) is associated [5] with the boundary-layer flow at the stagnation point of a body of revolution. The solution was obtained in a manner similar to that for (10) by letting $F(0) = F'(0) = 0$ and $F''(0) < 1.3120$. The latter value corresponds to an infinite Reynolds number. An interesting point to be noted is that for asymptotically large Reynolds numbers, the radial velocity profile exhibits a straight-line relation except on the lower disk, where a sharp drop of the boundary-layer type develops.

By analyzing equation (24) for the asymptotic cases of Re → 0 and Re → ∞ in a similar manner as for equation (10$a$), the following relations result:

$$\mathrm{Re} \to 0 \qquad K\,\mathrm{Re} \to 24$$
$$\mathrm{Re} \to \infty \qquad K \to 4 \quad \text{and} \quad f''(0)/\sqrt{\mathrm{Re}} \to 2.6240$$

These asymptotic results were well confirmed by direct numerica integration, Table 1.

For the heat-transfer part, however, a slight difference exists in the prescribed surface-temperature variation of the solid disk. For the axisymmetric case the permissible temperature variation is of the form

$$T_w = T_0 + \sum_{n=0} C_n (x/L)^n \tag{28}$$

which excludes the first-power term for the reason of avoiding a singularity in the energy equation at $x = 0$.

These corresponding results are shown in conjunction with the figures and tables for the two-dimensional case. The Nusselt number is also expressed by equation (22), wherein the correlation constant $A_n$ is listed in Table 3 for various values of $n$.

## Summary and Conclusion

Within the limitations of the physical assumptions made on the flow configurations considered, solutions for the temperature and velocity distributions in the channel were obtained for both the two-dimensional and axisymmetric cases. To illustrate the utilization of the information contained in the present paper, consider a turbine blade in a high-temperature stream with a constant stagnation temperature $T_e$ and an external heat-transfer coefficient $h_e$ which may be variable. The heat flux from the external stream to the blade surface is then $q_x = h_e[T_e - T_w]$, where $T_w$ is the blade-surface-temperature variation given by equation (16) containing undetermined coefficients $C_m$.

Equating the external heat flux with internal heat-removal rate results in the following equation:

$$h_e \left\{ T_e - \left[ T_0 + \sum_{m=0} C_m (x/L)^m \right] \right\} = -(k/L) \sum_{m=0} C_m (x/L)^m \phi_m'(0)$$

For a uniform external heat-transfer coefficient $h_e$, all $C_m$'s except $C_0$ are zero. From the above relation the value of $C_0$ can be determined, which in turn fixes the wall temperature $T_w$ as

$$T_w = \frac{T_e h_e + T_0 h_0}{h_e + h_0}$$

For variable $h_e$ the above equation may be solved by applying a collocation procedure, i.e., at discrete points of $x$ the number of which equals the number of $\phi_m'(0)$ available. In this way the $C_m$'s can be solved.

The evaluation of the surface-temperature variation is now in progress and will be made in comparison with other methods of internal cooling, and their relative performance will be reported later.

## Acknowledgments

The authors wish to acknowledge the helpful discourse provided by Dr. Kervin Mach in the solution of this problem, and the continuing interest of and encouragements from Messrs. C. Bentz and J. Richens of the Air Force Propulsion Laboratory, U.S.A.F. Their review of the paper and release for publication is appreciated. A reviewer's help in clarifying some obscure paragraphs and enhancing the readability of the paper is appreciated.

## References

1 Metzger, D. E., Yamashita, T., and Jenkins, C. W., "Impingement Cooling of Concave Surfaces With Lines of Circular Air Jets," *Journal of Engineering for Power*, TRANS. ASME, Series A, Vol. 91, No. 3, July 1969, p. 149–158.

2 Yuan, S. W., and Finkelstein, A. B., "Laminar Pipe Flow With Injection and Suction Through a Porous Wall," TRANS. ASME, Vol. 78, May 1956, pp. 719–724.

3 White, F. M., Jr., Barfield, B. F., and Goglia, M. J., "Laminar Flow in a Uniformly Porous Channel," *Journal of Applied Mechanics*, TRANS. ASME, Vol. 80, Dec. 1958, pp. 613–617.

4 Terrill, R. M., "Laminar Flow in Uniformly Porous Channel with Large Injection," *Aeronautical Quarterly*, Vol. 16, 1965, pp. 323–332.

5 Schlichting, H., *Boundary Layer Theory*, McGraw-Hill, New York, N. Y., 1960, p. 82.

6 Debruge, L., "Heat Transfer and Velocity Analysis in Channels with a Porous Wall," MSc thesis, Ohio State University, Columbus, Ohio, 1971; or A.F.A.P.L.T.R.

R. A. SEBAN
Professor.
Fellow ASME

T. C. HSIEH
Research Assistant.

R. GREIF
Associate Professor.
Mem. ASME

Department of Mechanical Engineering,
University of California,
Berkeley, Calif.

# Laminar Counterflow Exchangers: An Approximate Account of Wall Resistance and Variable Transfer Coefficients

*There is considered the calculation of the average value of the overall heat-transfer coefficient for counterflow between parallel plates or in concentric tubes when the flows are laminar and the thermal entry lengths for one or both streams extend over a significant part of the exchanger length. It is shown that if this length is at least less than the total length for one of the fluids, the average value of the overall coefficient can be calculated with adequate accuracy from the average values of the individual coefficients by means of the usual definition of the overall coefficient. When both thermal entry lengths exceed the exchanger length, then a special calculation is needed to obtain suitable average overall values. This result is given in graphical form and supported by more exact results from the literature and as obtained here.*

## Introduction

Nunge and Gill [1][1] studied analytically the counterflow heat exchange between parallel plates and concentric tubes in which the flow is laminar and fully developed by obtaining the eigenfunctions necessary for the solution for the relatively long exchanger and by using numerical methods for short exchangers for which the number of eigenfunctions as obtained was insufficient for a solution. Tien and Srinivasan [2] presented an approximate solution by integral methods; this, still involving substantial computation, was shown to give results in general accord with those calculated in reference [1].

Nunge and Gill noted that adequate results were obtainable for long exchangers by using for the average overall heat-transfer coefficient the value determined from the asymptotic values of the coefficients for each of the streams. For short exchangers adequate results were obtainable by using for the overall coefficient the mean coefficients given by the Leveque solution which approximates this quantity in the thermal entrance region. This paper gives a more comprehensive application of this view, with the Leveque solution for constant heat flux taken to approximate the local heat-transfer coefficient in the thermal entrance region. Its use is continued until the analytically exact asymptotic value of the coefficient is attained at a distance $x_A$ from the point where heating began. This combination of the Leveque and asymptotic coefficients produces too low a value of the coefficient in the region of the join, but the procedure simplifies the specification of the average overall heat-transfer coefficient and is shown to give good agreement with the more exact calculations of references [1, 2], with the thesis of Nunge [3], and with the additional solution for the short exchanger contained in the Appendix.

## Local Heat-Transfer Coefficients

The local heat-transfer coefficients for constant heat flux, used for the thermal entry region and continued to the position at which the asymptotic coefficients for constant flux are obtained, are given by the Leveque–Lighthill solution [4]

$$h = 0.645\ \rho c \left(\frac{\tau_0}{\rho}\right)^{1/3} \nu^{1/3} \Big/ \left(\frac{\nu}{\alpha}\right)^{2/3} x^{1/3} \qquad (1)$$

This coefficient is specified in Table 1 for parallel plates, pipes, and annuli with an insulated exterior surface. It applies up to distance $x_A$; downstream of this point the coefficient has the constant (asymptotic) value $h_A$, also specified in the table for $x > x_A$. The asymptotic values in the table for parallel plates and the pipe are well known or may easily be derived; those for the annulus are taken from Kays [5] and are shown in Fig. 1. The friction needed for the annulus was calculated and the results are shown in Fig. 1 in terms of the quantity $F^{1/3}$.

It is to be remembered that the use of these coefficients is an approximation for the calculation of the overall heat-transfer coefficient, which this work shows to be a satisfactory one. Actually the local coefficient depends as well upon the spatial variation of the difference between the wall and the fluid tem-

[1] Numbers in brackets designate References at end of paper.

Contributed by the Heat Transfer Division of The American Society of Mechanical Engineers and presented at the AIChE-ASME Heat Transfer Conference, Denver, Colo., August 6–9, 1972. Manuscript received by the Heat Transfer Division April 7, 1972. Paper No. 72-HT-40.

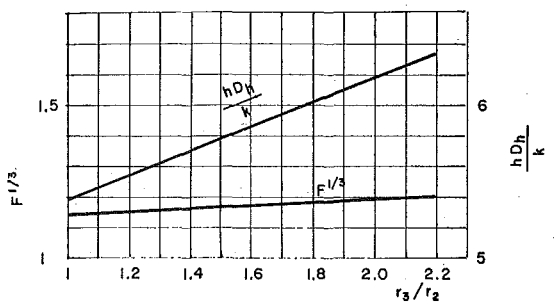


**Fig. 1 Nusselt number and Leveque functions for laminar flow in an annulus; outside insulated**

peratures. Analyses such as those of reference [1] or those indicated in the Appendix are required for the specification of the true local coefficients.

## Average Overall Heat-Transfer Coefficients

Introducing $h_w$ as the conductance of the wall itself, referred to the pipe side in the case of the concentric-tube system, the local value of the overall heat-transfer coefficient is given as

$$\frac{1}{U_x} = \frac{1}{h_1} + \frac{1}{h_w} + \frac{r_1}{r_2}\frac{1}{h_2} \tag{2}$$

Here $r_1$ and $r_2$ are the inner and outer radii of the inner pipe and $h_1$ and $h_2$ are the corresponding heat-transfer coefficients. The ratio $r_1/r_2$ is of course absent in the parallel-plate case.

The average value of the overall coefficient for the exchanger length $l$ is then

$$U = \frac{1}{l}\int_0^l \frac{dx}{\frac{1}{h_1} + \frac{1}{h_w} + \frac{r_1}{r_2}\frac{1}{h_2}} \tag{3}$$

With the local coefficients defined in Table 1, this average value of the overall coefficient can be determined, and much of this paper is devoted to special forms of equation (3) suitable for various exchanger lengths. Before proceeding thereto, it is useful to note an alternative prescription that can be made for the average overall coefficient, to the effect that its value may be obtained accurately enough in terms of the average coefficients for each of the exchanger surfaces.

$$\frac{1}{U} = \frac{1}{h_{m1}} + \frac{1}{h_w} + \frac{r_1}{r_2}\frac{1}{h_{m2}} \qquad h_m = \frac{1}{l}\int_0^l h\,dx \tag{4}$$

In very long exchangers, in which $l^+_1 \gg x^+_{A1}$ and $l^+_2 \gg x^+_{A2}$, the individual coefficients will be almost constant over much of the exchanger length at nearly their asymptotic values, and equations (3) and (4) then yield essentially the same results. As the exchanger becomes shorter the two equations yield different results because of the predominance of the regions in which the coefficients are variable.

**Table 1**

| | $\frac{\tau_0}{\rho}$ | $x^+$ | $x_A{}^+$ | $x^+ < x_A{}^+$ | $x^+ > x_A{}^+$ |
|---|---|---|---|---|---|
| Plates<br>$b$ = half-width* | $\frac{3u_m\nu}{b}$ | $\frac{x\alpha}{8b^2u_m}$ | 0.04 | $\frac{0.93}{(x^+)^{1/3}} = \frac{2hb}{k} = 2.70$ | |
| Pipe<br>$D_h = 2r_1$ | $\frac{8\nu u_m}{2r_1}$ | $\frac{x\alpha}{2u_m r_1{}^2}$ | 0.056 | $\frac{1.64}{(x^+)^{1/3}} = \frac{hD_h}{k} = 4.38$ | |
| Annulus<br>$D_h = 2(r_3 - r_2)$ | $\frac{8\nu u_m F}{2(r_3 - r_2)}$ | $\frac{x\alpha}{u_m D_h{}^2}$ | | $\frac{1.29F^{1/3}}{(x^+)^{1/3}} = \frac{hD_h}{k} =$ Fig. 1 | |
| $r_3 = 2r_2$ | | | 0.0156 | $\frac{1.55}{(x^+)^{1/3}} = \frac{hD_h}{k} = 6.18$ | |

* The Nusselt number for parallel plates is usually given in terms of the hydraulic radius $D_h = 4b$, so that $(4hb/x)_0 = 5.40$. The Nusselt number is here taken as $2bh/k$ to be consistent with references [1–3].

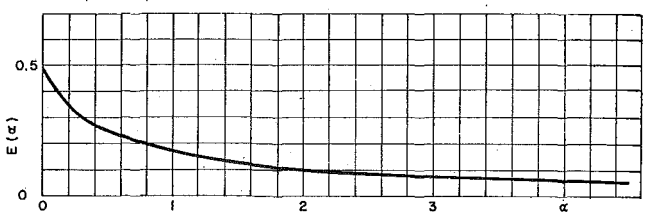


**Fig. 2 The function $E(\alpha)$ of equation (6)**

## Long Exchanger

If $l^+_1 > x^+_{A1}$ and $l^+_2 > x^+_{A2}$ and $(x_{A1}/l^+_1) + (x_{A2}/l^+_2) < 1$, there exists a large central region in which both coefficients are constant at the asymptotic values that are specified in Table 1. Each continues to its end of the exchanger, but there the other coefficient varies. For this long-exchanger case, it is convenient to restate equation (3) with the local coefficients (in $x < x_A$) specified as $h = Ax^{1/3}$ and the asymptotic values as $h_A$.

$$dU = \int_0^{x_{A1}} \frac{dx_1}{\frac{x_1{}^{1/3}}{A_1} + \frac{1}{k_w} + \frac{r_1}{r_2}\frac{1}{h_{A2}}} + \int_{x_{A1}}^{l-x_{A2}} \frac{dx_1}{\frac{1}{h_{A1}} + \frac{1}{h_w} + \frac{r_1}{r_2}\frac{1}{h_{A2}}} + \int_{l-x_{A2}}^{l} \frac{dx_1}{\frac{1}{h_{A1}} + \frac{1}{h_w} + \frac{r_1}{r_2}\frac{(l-x_1)^{1/3}}{A_2}} \tag{5}$$

If terms are redefined as

| Integral | $L$ | $\xi$ | $r$ | $s$ |
|---|---|---|---|---|
| $a$ | $x_{A1}$ | $\left(\frac{x}{L}\right)^{1/3}$ | $\frac{1}{h_w} + \frac{r_1}{r_2}\frac{1}{h_{A2}}$ | $\frac{L^{1/3}}{A_1}\left(= \frac{1}{h_{A1}}\right)$ |
| $b$ | $x_{A2}$ | $\left(\frac{l-x}{L}\right)^{1/3}$ | $\frac{1}{h_w} + \frac{L}{h_{A1}}$ | $\frac{r_1}{r_2}\frac{L^{1/3}}{A_2}\left(= \frac{r_1}{r_2}\frac{1}{h_{A2}}\right)$ |

and $U_0 = \left[\frac{1}{h_{A1}} + \frac{1}{h_w} + \frac{r_1}{r_2}\frac{1}{h_{A2}}\right]^{-1}$, then equation (5) becomes

$$lU = U_0[l - x_{A2} - x_{A1}] + \frac{3L_a}{s_a{}^3}\left[\frac{s^2 - 2rs}{2} + r^2\log\left(1 + \frac{s}{r}\right)\right]_a + \frac{3L_b}{s_b{}^3}\left[\frac{s^2 - 2rs}{2} + r^2\log\left(1 + \frac{s}{r}\right)\right]_b$$

The further definition

$$\frac{1}{\alpha_1} = \frac{s_a}{r_a} \qquad \frac{1}{\alpha_2} = \frac{s_b}{r_b} \qquad \frac{h_{A1}}{U_0} = 1 + \alpha_1 \qquad \frac{h_{A2}}{U_0} = 1 + \alpha_2$$

yields

$$\frac{U}{U_0} = \left[1 - \frac{x^+_{A1}}{l^+_1} - \frac{x^+_{A2}}{l^+_2}\right] + \frac{3x^+_{A1}}{l^+_1} \times (1 + \alpha_1)\left[\frac{1}{2} - \alpha_1 + \alpha_1{}^2\log\left(1 + \frac{1}{\alpha_1}\right)\right] + \frac{3x^+_{A2}}{l^+_2}(1 + \alpha_2)\left[\frac{1}{2} - \alpha_2 + \alpha_2{}^2\log\left(1 + \frac{1}{\alpha_1}\right)\right]$$

or

$$\frac{U}{U_0} = 1 + \frac{x_{A1}}{l^+_1}E(\alpha_1) + \frac{x_{A2}}{l^+_2}E(\alpha_2) \tag{6}$$

Figure 2 shows the function $E(\alpha)$. Table 2 gives the correspondence between the present nomenclature and that used in references [1–3]. There the symbols $N_A$, $N_B$ are the asymptotic Nusselt numbers, $r_3$ the outer radius of the annulus, and $C_1$ and $C_2$ the capacity rates of the two streams.

Also, in these terms the average overall heat-transfer coefficient defined by equation (4) becomes, with $h_{m1} = \frac{1}{l}\left[\int_0^{x_{A1}} h dx + h_{A1}(l - x_{A1})\right] = h_{A1}\left[\frac{3}{2}\frac{x_{A1}}{l} + \left(1 - \frac{x_{A1}}{l}\right)\right]$ and similarly for $h_{m2}$:

$$U_0/U = 1 - \frac{\left[1 - \frac{1}{1 + \frac{1}{2}\frac{x_{A1}}{l}}\right] + \left[1 - \frac{1}{1 + \frac{1}{2}\frac{x_{A2}}{l}}\right]\frac{N_{A1}}{N_{A2}} K\left(\frac{\Delta}{1 - \Delta}\right)}{1 + \alpha_1} \tag{7}$$

For the parallel-plate situation, $\frac{N_{A1}}{N_{A2}}\frac{\Delta}{1 - \Delta} = 1$ in this equation.

Predictions made from equations (6) and (7) have been compared to all of the results presented by Nunge [3, p. 140] for the long-concentric-tube exchanger with an annulus radius ratio $r_3/r_2$ of 2 ($\Delta = 0.5$). The predictions from equation (6) are lower but are within 5 percent of the values of Nunge; those from equation (7) are higher and are also within the 5 percent limit. Table 3 exemplifies some of the results in terms of the overall coefficient in the form $2r_1U/k_1$; the entries in this table being for the "shorter" of the long exchangers, for which the differences between equations (6) and (7) and the results of Nunge are the greatest. This comparison, seen to be favorable, is contained in the last three columns of the table. These results establish the acceptability of either equation (6) or equation (7), and the latter is recommended for design because of its simplicity.

Similar results, with like conclusions, are derived from a comparison with the results of Nunge [3, p. 152] for the parallel-plate exchanger. Table 4 contains these results and the prediction from equation (7) for the more critical cases, and the acceptability of equation (7) is again demonstrated.

## Intermediate Exchanger

This is the exchanger that is short enough so that there is within it a region in which both heat-transfer coefficients vary simultaneously, though long enough so that at least one of the coefficients attains its asymptotic value. This occurs for $x_{A1}/l < 1$, $x_{A2}/l > 1$; $x_{A1}/l > 1$, $x_{A2}/l < 1$; or $x_{A1}/l < 1$, $x_{A2}/l < 1$, with $(x_{A1}/l) + (x_{A2}/l) > 1$. Equation (3) then includes one or two intervals in which one of the coefficients is constant, giving integrals like "a" or "b" of equation (5), which can, as there, be integrated formally. But the remaining integral is like equation (3) with both coefficients variable, and formal integration is impossible. Acceptable results are obtained by numerical integration, but the success of equation (7) for the long exchanger suggests its use for the intermediate case. When $x_{A1}/l > 1$ its form changes slightly, since then $h_{m1} = \frac{1}{l}\int_0^l h dx = \frac{3}{2} h_{A1}\left(\frac{x_{A1}}{l}\right)^{1/3}$ and the term $1 + {}^1/_2(x_{A2}/l)$ in equation (7) is replaced by ${}^3/_2(x_{A1}/l)^{1/3}$, or similarly for the term $x_{A2}/l$ when it exceeds unity.

Essentially all of Nunge's results for this intermediate case are for the concentric-tube exchanger ($r_3/r_2 = 2$), with $x_{A1}/l > 1$. They are all contained in Table 5 in which the last two columns indicate excellent correspondence with predictions made from equation (7) and indicate this equation to be suitable for design.

**Table 2**

| | | | | | | | | |
|---|---|---|---|---|---|---|---|---|
| Concentric, here | $\frac{C_2}{C_1}$ | $\frac{k_1}{k_2}$ | $\frac{h_1}{r_1 h_w}$ | $\frac{r_3 - r_2}{r_3}$ | $\alpha_1$ | $\alpha_2$ | $\frac{l_1^+}{l_2^+}$ | $\frac{hDh}{k}$ |
| References [1–3] | $H$ | $K$ | $K_w$ | $\Delta$ | $\frac{N_{A1}K_w}{2} + K\frac{N_{A2}}{N_{A1}}\left(\frac{\Delta}{1-\Delta}\right)$ | $\frac{N_{A2}K_w}{2K} + \frac{N_{A2}}{N_{A1}}K\left(\frac{1-\Delta}{\Delta}\right)$ | $2HK\left(\frac{\Delta}{2-\Delta}\right)$ | $N$ |
| Parallel, here | $\frac{C_2}{C_1}$ | $\frac{k_1 b_2}{k_2 b_1}$ | $\frac{k_1}{2b_1 h_w}$ | | $\alpha_1$ | $\alpha_2$ | $\frac{l_1^+}{l_2^+}$ | $\frac{2hb}{k}$ |
| References [2, 3] | $H$ | $K_N$ | $K_w$ | | $N_{A1}K_w + K_N$ | $N_{A1}\frac{K_w}{K_N} + \frac{1}{K_N}$ | $HK$ | $N$ |

**Table 3 Long concentric exchangers**

| | $H$ | $K$ | $K_w$ | $\alpha_1$ | $\alpha_2$ | $\frac{N_{A1}}{\alpha_1 + 1}$ | $E_1$ | $E_2$ | $l_1^+$ | $l_2^+$ | $\frac{.056E_1}{l_1^+}$ | $\frac{.0156E_1}{l_2^+}$ | $\frac{U}{U_0}$ eq. (6) | $\frac{2r_1U}{k_1}$ eq. (6) | $\frac{2r_1U}{k_1}$ ref. [3] | $\frac{2r_1U}{k_1}$ eq. (7) |
|---|---|---|---|---|---|---|---|---|---|---|---|---|---|---|---|---|
| 2(b) | 0.2 | 4 | 0.2 | 2.38 | .50 | 1.02 | .07 | .25 | .10 | .187 | .039 | .020 | 1.059 | 1.09 | 1.11 | 1.10 |
| 3(b) | 0.5 | 2 | 0 | 1.42 | .70 | 1.81 | .13 | .21 | .50 | .75 | .014 | .004 | 1.02 | 1.85 | 1.90 | 1.87 |
| 4(b) | 0.5 | 2 | 0.2 | 1.86 | 1.01 | 1.53 | .10 | .17 | .50 | .75 | .011 | .003 | 1.01 | 1.54 | 1.59 | |
| 5(b) | 0.5 | 4 | 0 | 2.84 | .352 | 1.14 | .08 | .27 | .10 | .075 | .04 | .056 | 1.096 | 1.24 | 1.30 | 1.31 |
| (c) | | | | | | | | | .50 | .375 | .011 | .011 | 1.02 | 1.16 | 1.18 | 1.17 |
| 6(b) | 0.5 | 4 | 1 | 5.03 | 1.12 | 0.73 | .04 | .16 | .10 | .075 | .022 | .033 | 1.055 | .77 | .80 | .79 |
| 7(b) | 2.25 | .6 | 0 | .425 | 2.35 | 3.08 | .26 | .08 | .10 | .11 | .146 | .016 | 1.16 | 3.56 | 3.59 | 3.66 |
| 8(b) | 2.25 | 2 | 0 | 1.42 | .702 | 1.81 | .13 | .21 | .10 | .033 | .067 | .043 | 1.11 | 2.00 | 2.40 | 2.26 |
| 9 | 2.25 | 2 | 0.2 | 1.86 | 1.01 | 1.53 | .10 | .17 | .10 | .033 | .056 | .035 | 1.09 | 1.67 | 1.91 | 1.84 |
| 10 | 2.25 | 2 | 1 | 3.61 | .06 | 0.95 | .06 | .18 | .10 | .033 | .033 | .037 | 1.07 | 1.01 | 1.08 | 1.05 |
| 11 | 2.75 | .6 | 0 | 0.425 | 2.35 | 3.08 | .26 | .08 | .10 | .091 | .146 | .016 | 1.16 | 3.58 | 3.60 | 3.70 |
| 12 | 2.75 | .6 | .2 | 0.86 | 3.41 | 2.36 | .18 | .07 | .10 | .091 | .10 | .014 | 1.11 | 2.62 | 2.65 | 2.72 |
| 13 | 2.75 | .6 | 1.0 | 2.61 | 7.49 | 1.22 | .07 | .03 | .10 | .091 | .04 | .0062 | 1.046 | 1.27 | 1.29 | 1.31 |
| 15 | 7.5 | .6 | 0.2 | 0.86 | 3.47 | 2.36 | .21 | .09 | .10 | .033 | .12 | .014 | 1.134 | 2.68 | 2.74 | 2.85 |
| 16 | 7.5 | .6 | 1.0 | 2.61 | 7.49 | 1.22 | .07 | .03 | .10 | .033 | .04 | .006 | 1.046 | 1.27 | 1.31 | 1.32 |

**Table 4 Long parallel-wall exchangers**

| | $H$ | $K$ | $K_w$ | $\alpha_1$ | $\alpha_2$ | $\frac{N_{A2}}{\alpha_1 + 1}$ | $E_1$ | $E_2$ | $l_1^+$ | $l_2^+$ | $\frac{.04E_1}{l_1^+}$ | $\frac{.04E_2}{l_2^+}$ | $\frac{U}{U_0}$ eq. (6) | $\frac{2Ub_1}{k_1}$ eq. (6) | $\frac{2Ub_1}{k_1}$ ref. [3] |
|---|---|---|---|---|---|---|---|---|---|---|---|---|---|---|---|
| 1(a) | 0.125 | 4 | 0 | 4 | 0.25 | 1.08 | .06 | .32 | .15 | .30 | .0021 | .043 | 1.045 | 1.13 | 1.12 |
| 2(c) | 0.375 | 1.33 | 0 | 1.33 | 0.75 | 2.32 | .13 | .20 | .15 | .30 | .0316 | .0266 | 1.06 | 2.46 | 2.56 |
| 3(b) | 0.5 | 4 | 0 | 4 | 0.25 | 1.08 | .06 | .32 | .15 | .075 | .016 | .170 | 1.186 | 1.28 | 1.26 |
| 4(b) | 0.5 | 10 | 0 | 10 | 0.10 | 0.49 | .023 | .40 | .30 | .06 | .004 | .267 | 1.27 | 0.62 | 0.634 |
| 5(a) | 0.5 | 10 | 0.5 | 11.35 | 0.235 | 0.44 | .02 | .33 | .30 | .06 | .003 | .22 | 1.25 | 0.55 | 0.548 |
| 6(a) | 0.5 | 10 | 2.0 | 15.4 | 0.64 | 0.33 | .016 | .021 | .30 | .06 | .002 | .14 | 1.14 | 0.38 | 0.390 |
| 7(b) | 0.75 | 2 | 0 | 2 | 0.75 | 1.80 | .10 | .20 | .15 | .10 | .026 | .080 | 1.11 | 2.00 | 2.18 |
| 8(b) | 1.125 | 1.33 | 0 | 1.33 | 0.75 | 2.32 | .13 | .20 | .15 | .10 | .034 | .080 | 1.11 | 2.58 | 2.72 |
| 9(a) | 1.125 | 1.33 | 0.10 | 1.60 | 0.96 | 2.08 | .12 | .17 | .15 | .10 | .048 | .068 | 1.12 | 2.33 | 2.40 |
| 10(a) | 1.125 | 1.33 | 2.0 | 6.73 | 4.80 | 0.70 | .03 | .04 | .15 | .10 | .008 | .016 | 1.02 | 0.71 | 0.73 |
| 11(b) | 2.5 | 2.0 | 0 | 2.0 | 0.50 | 1.80 | .10 | .24 | .30 | .06 | .013 | .16 | 1.17 | 2.10 | 2.30 |
| 12(b) | 3.0 | 0.5 | 0 | 0.5 | 2.0 | 3.60 | .24 | .10 | .15 | .10 | .064 | .040 | 1.10 | 4.00 | 4.12 |
| 13(a) | 3.0 | 0.5 | 0.10 | 0.77 | .254 | 3.05 | .20 | .08 | .15 | .10 | .054 | .032 | 1.09 | 3.32 | 3.42 |
| 14(a) | 3.0 | 0.5 | 1.0 | 3.2 | 7.4 | 1.29 | .07 | .03 | .15 | .10 | .019 | .012 | 1.03 | 1.33 | 1.36 |

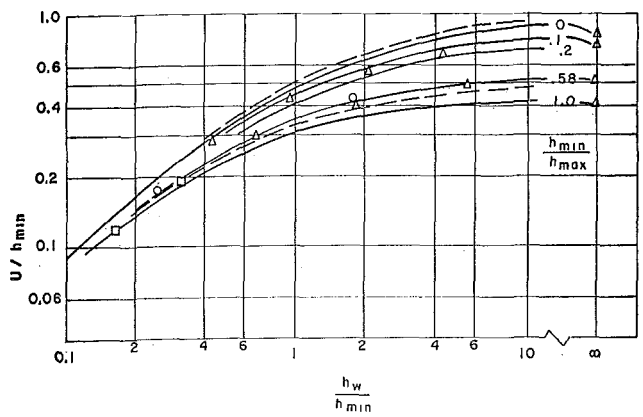


Fig. 3 Average overall coefficients for short exchangers; coefficients $h_{min}$, $h_{max}$ are average values for constant heat flux for the two fluids, that for an annulus being referred to the tube-side area; triangles correspond to parameter values of 0, 0.1, 0.58, circles correspond to 0.58, and the square points are from reference [2] and correspond to 0.86

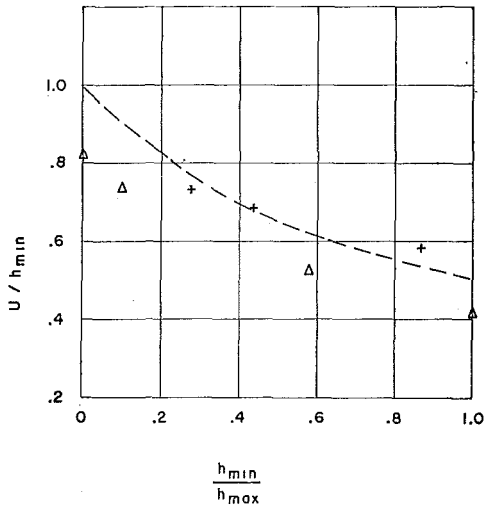


Fig. 4 Short exchangers with no wall resistance; triangles from equation (17), crosses from reference [1], the curve is equation (10)

## Short Exchanger

In the short exchanger $x_{A1}/l > 1$ and $x_{A2}/l > 1$, so that both coefficients are variable over the whole length of the exchanger. In this situation the specification of the Leveque–Lighthill solution is the best and to some extent the only available specification of the local coefficient. Moreover, the exchanger effectiveness becomes so low that the mean fluid temperature varies only slightly from its initial value and the effective temperature difference is essentially that between the wall and the inlet value, the situation for which equation (1) is analytically derived. For this short exchanger equation (3) can be written

$$U = h_w \int_0^1 \frac{d\left(\frac{x_1}{l}\right)}{1 + \frac{r_1}{r_2}\frac{h_w l^{1/3}}{A_2}\left[\frac{r_2}{r_1}\frac{A_2}{A_1}\left(\frac{x}{l}\right)^{1/3} + \left(1 - \frac{x}{l}\right)^{1/3}\right]} \tag{8}$$

This equation can be altered to take advantage of the symmetry of the problem. Reference of the annulus-side coefficient to the tube-side area removes the ratio $r_2/r_1$, and reference is then made to the minimum average coefficient in the length $l$, so that the equation is then expressed in terms of the "maximum" and "minimum" average heat-transfer coefficients (for the constant-flux case). Equation (8) then becomes

$$\frac{U}{h_{min}} = \frac{h_w}{h_{min}} \int_0^1 \frac{d\left(\frac{x}{l}\right)}{1 + 1.5\,\frac{h_w}{h_{min}}\left[\frac{h_{min}}{h_{max}}\left(\frac{x}{l}\right)^{1/3} + \left(1 - \frac{x}{l}\right)^{1/3}\right]} \tag{9}$$

In like manner equation (7) becomes

$$\frac{U}{h_{min}} = \left[\frac{h_{min}}{h_{max}} + \frac{h_{min}}{h_w} + 1\right]^{-1} \tag{10}$$

Table 5 Intermediate concentric-tube exchanger

| | $\alpha_1$ | $l_1^+$ | $l_2^+$ | $\frac{.056}{l_1^+}$ | $\frac{.0156}{l_2^+}$ | $\frac{2r_1U}{k_1}$ eq. (7) | $\frac{2r_1U}{k_1}$ ref. [3] |
|---|---|---|---|---|---|---|---|
| 1 | 2.84 | .05 | .093 | 1.1 | .17 | 1.35 | 1.34 |
| 2 | 2.38 | .05 | .093 | 1.1 | .17 | 1.19 | 1.18 |
| 3 | 1.42 | .05 | .075 | 1.1 | .21 | 2.26 | 2.28 |
| 4 | 1.86 | .05 | .075 | 1.1 | .21 | 1.83 | 1.86 |
| 5 | 2.84 | .05 | .0375 | 1.1 | .41 | 1.45 | 1.50 |
| 6 | 5.03 | .05 | .0375 | 1.1 | .41 | 0.85 | 0.86 |
| 7 | 0.425 | .05 | .055 | 1.1 | .28 | 4.29 | 4.14 |
| 8 | 1.42 | .05 | .0165 | 1.1 | .94 | 2.70 | 2.74 |
| 9 | 1.86 | .05 | .0165 | 1.1 | .94 | 2.13 | 2.16 |
| 10 | 3.61 | .05 | .0165 | 1.1 | .94 | 1.14 | 1.08 |
| 11 | .425 | .05 | .045 | 1.1 | .35 | 4.34 | 4.19 |
| 12 | .86 | .05 | .045 | 1.1 | .35 | 3.02 | 2.99 |
| 13 | 2.61 | .05 | .045 | 1.1 | .35 | 1.37 | 1.36 |

Figure 3 shows by solid curves the value of $U/h_{min}$ calculated numerically from equation (9) for four indicated values of $h_{min}/h_{max}$. Clearly, these are increasingly in error as $h_w/h_{min}$ increases and $h_{min}/h_{max}$ decreases, for, in the limit where $h_w/h_{min} = \infty$ and $h_{min}/h_{max} = 0$ the exchanger surface becomes isothermal and $U/h_{min}$ is then 1/1.21, where 1.21 is the ratio of the average coefficient for constant heat flux to that for an isothermal surface. In contrast, equation (9) gives a value of $U/h_{min} = 1$ for this situation, and on the figure the curves terminate for $h_w/h_{min} = 10$, where the error should be substantially less.

Dashed curves in Fig. 3 indicate predictions from equation (10) for $h_{min}/h_{max}$ of 0 and 1. They exceed the values from equation (9) and are indeed less applicable in this situation.

The only points available for comparison are two from reference [2], for $h_{min}/h_{max} = 0.86$; these are shown as squares in Fig. 3. They are in reasonable position with respect to the appropriate curve for equation (9). Some additional points have been calculated by methods indicated in the Appendix. The circles, for $h_{min}/h_{max} = 0.58$, result from an analytically exact application of the Leveque–Lighthill solution; these points agree well with equation (9). Triangles, for $h_{min}/h_{max} = 0.10$ and 0.58, result from an integral solution and for $h_w/h_{min} < 10$ are also in good agreement with equation (9), but there is an increased departure at the higher values of $h_w/h_{min}$.

Some ambiguity remains in the situation for infinite wall conductance, $h_w/h_{min} = \infty$, for which it has already been noted that both equations (9) and (10) give results that become 20 percent too high as $h_{min}/h_{max} \to 0$. Figure 4 shows results from equation (10) as a dashed curve and contains triangles for results obtained from the integral method of the Appendix. These triangles are lower than the curve and are a more realistic assessment of operation in this case of no wall resistance. There are, however, some results from reference [3] which apply to this situation, and these, obtained by numerical analysis, are shown as crosses in Fig. 4. They are in the region of equation (10). There are grounds for an estimate that these may be somewhat inaccurate, and the best present appraisal seems to be that of the triangles, guided in form by the curve from equation (10).

## Further Comments

The apparent success in the use of equation (4) for long and intermediate counterflow exchangers and of equation (9) for short exchangers when the individual heat-transfer coefficients are evaluated from Table 1 implies that the method will be applicable to other systems as well, and note is taken here of these prospects.

**Mass Transfer.** While this presentation has been in terms of heat transfer, the solutions are applicable to all those cases of mass transfer in which the transfer rate is small enough not to affect the hydrodynamics and consequently the shear as it is expressed in Table 1. Such an analogy tends to apply when the Schmidt number is large and the potential differences are not too great. Also, with wall resistance, the wall conductance must be realistically specified in terms of the potential differences across the wall, as it would be for gas transport through a membrane.

**Non-Newtonian Flow.** McKillop [6] has shown the applicability of the Leveque solution for non-Newtonian flow, and consequently the present analysis should apply to an exchanger containing such fluids. A new Table 1 would, however, need to be constructed for them.

**Turbulent Flow.** By using the Leveque–Lighthill solution for turbulent flow as in reference [4], it is in principle possible to arrange a Table 1 at least for Prandtl numbers near unity. Because of the short thermal entry length for turbulent flow, however, most heat exchangers will be very long and the mean values of the individual coefficients will be very near the asymptotic values, so that the overall coefficient will be very close to the value as usually obtained directly from the asymptotic values.

## Conclusions

It has been shown that a good approximation to the average value of the overall heat-transfer coefficient for counterflow heat exchangers with laminar flow in concentric tubes or parallel plates can be obtained from an approximate specification of the local heat-transfer coefficients based on the Leveque and on the asymptotic values for constant heat flux. For long and intermediate exchangers the average overall coefficient can be specified from the average coefficients for each of the fluids by the conventional definition of the overall coefficient, while for short exchangers a special formulation is required; this is shown in Fig. 3.

## References


1 Nunge, R. J., and Gill, W. N., "An Analytical Study of Laminar Counterflow Double Pipe Heat Exchangers," *AIChE Journal*, Vol. 12, No. 2, pp. 279–289.

2 Tien, C., and Srinivasan, S., "An Approximate Solution for Countercurrent Heat Exchangers," *AIChE Journal*, Vol. 15, No. 1, pp. 39–46.

3 Nunge, R. J., "On the Theory of Multiphase Indirect Contact Forced Convection Laminar Heat Transfer," PhD dissertation, Syracuse University, Syracuse, N. Y., 1965.

4 Back, L. H., and Seban, R. A., "On Constant Property Turbulent Boundary Layers With Variable Temperature or Heat Flow at the Wall," JOURNAL OF HEAT TRANSFER, TRANS. ASME, Series C, Vol. 87, No. 1, Feb. 1965, pp. 151–156.

5 Kays, W. M., *Convective Heat and Mass Transfer*, McGraw-Hill, New York, N. Y., 1966.

6 McKillop, A. A., "Heat Transfer for Laminar Flow on Non-Newtonian Fluids in the Entrance Region of a Tube," *International Journal of Heat and Mass Transfer*, Vol. 7, No. 8, 1964, pp. 853–862.

7 Viskanta, R., and Abrams, M., "Thermal Interaction of Two Streams in Boundary-Layer Flow Separated by a Plane," *International Journal of Heat and Mass Transfer*, Vol. 14, No. 9, 1971, pp. 1311–1322.


# APPENDIX

## Solutions for the Short Exchanger

To provide more accurate solutions for the short heat exchanger, both the superposition of the Leveque–Lighthill solutions and integral methods were used, these being quite simply applied since in the short heat exchanger the mixed mean fluid temperatures differ little from the inlet values, so that the heat-transfer coefficients can be expressed in terms of the difference between local wall and inlet fluid temperatures. Viskanta and Abrams [7] use similar methods for the cocurrent problem and also discuss the countercurrent exchanger.

The inlet temperature of the fluid of stream 2 is taken as the datum; $T_{01}$ is the inlet temperature of stream 1. Then if $\phi$ is the reciprocal of the heat-transfer coefficient that is given in Table 1, the usual superposition typified by the Duhamel integral gives the temperatures $T_1$ and $T_2$ of the two fluids at the exchanger wall as[2]

$$T_0 - T_{01} = \int_0^{x_1} q(\lambda_1) \frac{\partial \phi}{\partial x_1} (x_1 - \lambda_1) dx_1 \tag{11}$$

$$T_2 = \int_0^{x_2} q(\lambda_2) \frac{\partial \phi}{\partial x_2} (x_2 - \lambda_2) dx_2 \tag{12}$$

Introducing $q = h_w(T_1 - T_2)$, defining $\Delta\theta = (T_1 - T_2)/T_{01}$, and combining equations (11) and (12), there is obtained an integral equation for $\Delta\theta$

$$\Delta\theta = 1 - \frac{(h_w l^+_1)^{1/3}}{3A_1} \int_0^{x_1/l} \Delta\theta(\alpha) \left(\frac{x_1}{l} - \alpha\right)^{-2/3} d\alpha + \frac{(h_w l^+_2)^{2/3}}{3A_2} \int_{x_1/l}^1 \Delta\theta(\alpha) \left(\alpha - \frac{x_1}{l}\right)^{-2/3} d\alpha \tag{13}$$

It is evident that equation (13) can be further transformed to incorporate the quantities $h_w/h_{\min}$ and $h_{\min}/h_{\max}$ as defined before.

Equation (13) must be solved by iteration, and the slow convergence of this process makes the procedure unattractive. When $\Delta\theta$ is obtained, the average value of the overall heat-transfer coefficient is then obtained from $U = h_w \int_0^1 \Delta\theta d(x/l)$. The two points shown as circles in Fig. 3 were calculated in this way.

A more rapid but less exact solution is obtained by integral methods in which the linear velocity distribution $u = (\tau_0/\mu)y$ of the Leveque solution is retained, with $\tau_0$ as specified in Table 1, and the temperature distribution is taken as $(T - T_{01})/(T_1 - T_{01}) = 1 - {}^3/_2(y/\delta) + {}^1/_2(y/\delta)^3$ (for fluid one, and similarly for fluid two), where $\delta$ is the thermal layer thickness. With $\theta_1 = T_1/T_{01}$ and $\theta_2 = T_2/T_{02}$ the energy equations for the two fluids are

$$\rho_1 c_1 \frac{d}{dx_1} \left(\frac{\tau_1}{\mu_1} \delta_1^2 \frac{1 - \theta_1}{10}\right) = \frac{q}{T_{01}} \tag{14}$$

$$\rho_2 c_2 \frac{d}{dx_1} \left(\frac{\tau_2}{\mu_2} \delta_2^2 \frac{\theta_2}{10}\right) = -\frac{q}{T_{01}} \tag{15}$$

At the exchanger surface

$$\frac{q}{T_{01}} = \frac{3}{2} \frac{k_2}{\delta_2} \theta_2 = \frac{3}{2} \frac{k_1}{\delta_1} (1 - \theta_1) = h_w(\theta_1 - \theta_2) \tag{16}$$

Combination of equations (14), (15), and (16), and integration, yields

$$\left(\frac{h_{m1}}{h_{m2}}\right)^3 \frac{(1 - \theta_1)^3}{(\theta_1 - \theta_2)^2} + \frac{\theta_2^3}{(\theta_1 - \theta_2)^2} = \frac{40}{9} \left(0.915 \frac{h_w}{h_{m2}}\right)^3 \frac{1}{l} \int_0^l (\theta_1 - \theta_2) dx \tag{17}$$

Here the term on the right is the constant of integration and $h_{m1}$ and $h_{m2}$ are the mean values of the individual coefficients for constant heat flux as specified by solutions of equations (14). The translation to $h_{\min}/h_{\max}$ can be made as before.

Equation (17) can be solved directly by choosing $h_{\min}/h_{\max}$, $(h_w/h_{\min})^3(1/l)$, and a value of the integral which is $Q/T_{01}h_w$ where $Q$ is the total heat transfer. Then $\theta_1$ is determined as a function of $\theta_2$ to enable a numerical integration of equation (14)

[2] In this Appendix the application is formally to the parallel-wall case. The concentric-tube case requires the introduction of the ratio $r_2/r_1$ as a factor in the right side of equation (12) and the definition of the flux contained there on the inner tube area.

with $q$ specified from equation (16). This determines $x$ and consequently the length $l$. The average overall coefficient is then found as $U/h_w = Q/T_{01}h_w l$. When $h_w \to \infty$ the flux $q = h_w(\theta_1 - \theta_2)T_{01}$ is retained in the equations. Then $\int_0^1 \frac{q}{T_{01}} d\frac{x}{l}$ is assumed, together with $h_{\min}/h_{\max}$ and $h_{\min}{}^2 l$, to give the wall temperature, now the same for both fluids, as a function of the flux. Equation (14) can then be integrated to find the length, and the average overall coefficient is then determined.

The triangles shown in Figs. 3 and 4 were determined in this way.

Of course, equations (14) and (15) can be solved formally by introducing $q = h_w(T_1 - T_2)$, using equation (16) to specify $\delta_1$ and $\delta_2$ in terms of $h_w$, $\theta_1$, and $\theta_2$, and then integrating and combining to obtain

$$\Delta\theta = 1 - \left(\frac{40}{9}\right)^{1/3} (\Delta\theta)^{2/3} \left(0.915 \frac{h_w}{h_{m2}}\right) \times \left\{\frac{h_{m2}}{h_{m1}} \left[\int_0^{x/l} \Delta\theta d\frac{x}{l}\right]^{1/3} + \left[\int_{x/l}^1 \Delta\theta d\frac{x}{l}\right]^{1/3}\right\} \quad (18)$$

The determination of $\Delta\theta$ from this integral equation involves the iteration avoided by the use of equation (17). If the first iteration assumes that $\Delta\theta$ is a constant, then the first iterate of equation (18) gives a $\Delta\theta$ which, if used to specify the total heat transfer and so the average overall coefficient, gives for that coefficient

$$\frac{U}{h_{m2}} = \frac{h_w}{h_{m2}} \int_0^1 \frac{d\left(\frac{x}{l}\right)}{1 + 1.5 \frac{h_w}{h_{m2}} \left[\frac{h_{m2}}{h_{m1}} \left(\frac{x}{l}\right)^{1/3} + \left(1 - \frac{x}{l}\right)^{1/3}\right]} \quad (19)$$

This gives an indication of the type of approximation involved in equation (3), from which was derived equation (9), identical to equation (19).

Finally, another solution is derivable for the case in which $h_{\min}/h_{\max} = 0$, so that the temperature on one side of the exchanger surface becomes essentially constant. If the number 1 stream has this high coefficient, then equation (12) becomes

$$T_2 = \int_0^{x_2} h_w(T_{01} - T_2) \frac{l^{1/3}}{3A_2} \left(\frac{x_2}{l} - \frac{\lambda_2}{l}\right)^{-2/3} d\lambda_2 = \int_0^{x_2/l} h_w(T_{01} - T_2) \frac{1.5}{3} \frac{1}{h_{m2}} \left(\frac{x_2}{l} - \frac{\lambda_2}{l}\right)^{-2/3} d\left(\frac{\lambda_2}{l}\right) = \frac{1}{\Gamma\left(\frac{1}{3}\right)} \int_0^{\xi} (T_{01} - T_2)(\xi - \alpha)^{-2/3} d\alpha \quad (20)$$

where

$$\xi = \left[\frac{1.5}{3} \frac{h_w}{h_{m2}} \Gamma\left(\frac{1}{3}\right)\right]^3 \frac{x_2}{l} \quad \text{or} \quad \xi = \xi_1 \frac{x_2}{l}$$

The Laplace transform of equation (20) is $\bar{T}_2 = T_{01}/[S(1 + S^{1/3})]$ and a convergent solution is obtained for large values of $S$ as

$$\bar{T}_2 = T_{01}\left(\frac{1}{S^{4/3}} - \frac{1}{S^{6/3}} + \frac{1}{S^{6/3}} - \frac{1}{S^{7/3}} \cdots\right)$$

The inverse transform gives the variation of wall temperature

$$T_2 = T_\infty \left(\frac{\xi^{1/3}}{\Gamma\left(\frac{4}{3}\right)} - \frac{\xi^{2/3}}{\Gamma\left(\frac{5}{3}\right)} + \frac{\xi}{\Gamma(2)} - \frac{\xi^{4/3}}{\Gamma\left(\frac{7}{3}\right)} \cdots\right)$$

The average overall coefficient can then be determined; it is

$$\frac{U}{h_{\min}} = \frac{h_w}{h_{\min}} \left(1 - \frac{\xi_1^{1/3}}{1.19} + \frac{\xi_1^{2/3}}{1.51} - \frac{\xi_1}{2} - \frac{\xi_1^{4/3}}{2.78} \cdots\right)$$

This corresponds to the curve for $h_{\min}/h_{\max} = 0$ in Fig. 3 up to an abscissa of about 0.5 and verifies the approximation of equation (9) in this region.

J. F. HUMPHREYS
J. LAWTON
The Electricity Council Research Centre, Capenhurst, Chester, England

# Heat Transfer in Plasma Systems using Magnetically Rotated Arcs

*A study has been made of heat transfer from an argon-arc plasma to a constraining tubular enclosure down which the plasma was discharged. An applied axial magnetic field caused the arc to rotate rapidly. Large increases in the heat-transfer rates to the tube were observed with rotation and it was shown that these increases were due to the swirling flow and turbulence caused by the arc's motion.*

## Introduction

THE TRANSFER of energy from an arc-heated gas, at or about its plasma state, is of interest in such widely differing fields as cutting and welding [1],[1] particle treatment [2], chemical synthesis [3], and space reentry simulation [4]. It clearly is desirable in these applications to arrange for the radial distribution of temperature of the plasma stream to be uniform, and Chen and Lawton [5] have shown that magnetic rotation of the arc is helpful in this respect. Moreover, Mayo and Davis [6] report that anode erosion and hence contamination is reduced by magnetic rotation. Chen and Lawton [5] have shown that the arc rotation produced by the interaction of the arc current with the applied magnetic field has a significant effect on the transport rates of the plasma. For example, even with low magnetic fields (ca. 0.1 tesla) large increases in heat-transfer rates (ca. 100 percent) to an enclosing tube with a stepped diameter were reported. In fact, very high magnetic fields in the plasma can slightly reduce heat-transfer rates [7, 8] by suppression of eddy and electron thermal conductivities, e.g., 2 tesla produced a reduction of 20 percent in a non-current-bearing air plasma [7]. Other effects of magnetic fields on non-current-bearing plasma flows have been reported which result from induced currents, see, for example, [9]; however, these effects require much larger magnetic fields than are needed for control of heat transfer from plasmas by the interaction of a magnetic field with an arc current, and consequently they are not relevant to the present investigation.

In the present work a study has been made of heat transfer from an arc plasma stream to a tube down which the stream was discharged; a schematic diagram of the geometry is shown in Fig. 1. The axial distribution of heat transfer to the tube was studied both with and without magnetic rotation of the arc. The arc rotates within the gas stream at a rate which is dependent on the electromagnetic force and the aerodynamic drag of the arc. In so doing, the arc acts mechanically on the gas producing swirl and turbulence, swirl arising from viscous drag and turbulence from form drag. If these two phenomena can be generated to a high degree and are sufficiently long-lived, then it can be expected that they would have a pronounced effect on heat transfer to the tube. In practical terms, the tube can be thought of, for example, as a deep cut or chemical reactor.

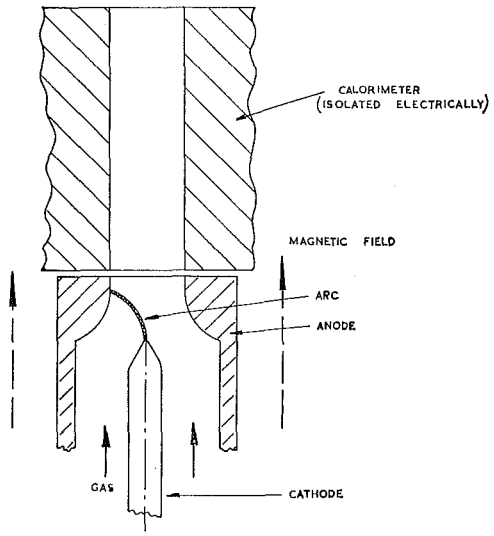


**Fig. 1 Basic geometry**

In the present study, temperatures up to about 10,000 deg K exist with consequent high heat fluxes and large changes in fluid properties with position. For example, the local Reynolds number may double over the length of the tube. Studies of this nature are still few, stemming from problems concerning rocket nozzles, nose cones, and plasma chemistry. Skrivan and Jaskowsky [10] studied heat transfer from nitrogen, hydrogen, and argon plasmas to a segmented tube situated downstream from a diffuser, and obtained a correlation of the experimental data.

[1] Numbers in brackets designate References at end of paper.

Contributed by the Heat Transfer Division of THE AMERICAN SOCIETY OF MECHANICAL ENGINEERS and presented at the AIChE-ASME Heat Transfer Conference, Denver, Colo., August 6–9, 1972. Manuscript received by the Heat Transfer Division May 6, 1971. Paper No. 72-HT-41.

The object was to predict the axial distribution of bulk enthalpy of the fluid. In the work of Johnson, Choksi, and Eubank [11] with the same three gases, the diameter of the heat exchanger was large compared to the nozzle diameter of the plasma torch, causing a flow pattern much different from that considered in the present study. Wethern and Brodkey [12], using a helium plasma, showed that the type of constant-property solution obtained by Graetz, reported by Knudsen and Katz [13], for example, can be applied with reasonable accuracy even under conditions of extreme temperature differences and with velocity distributions which are not parabolic. Again, Schmidt and Leppert [14], using an argon plasma, showed that a model based on the assumption of constant properties applies quite well to plasma flow, the agreement being best at distances greater than five diameters downstream from the nozzle.

The above works provide useful guidelines for the present study but are different from it in an important respect. No account was taken of the fact that the plasma was produced by an arc discharge with its attendant fluctuations, the flow being characterized solely by a Reynolds number. However, it is not difficult to envisage that such parameters as arc shape and stability could have an important influence on the character of the plasma, on, for example, its intensity of turbulence and velocity distribution. It is significant in this respect that Schmidt and Leppert [14] deliberately discarded a series of test data because of strong instability in the arc. Whereas such "arc effects" have tended to be ignored in the past, they form an important part of the present investigation, both in the presence and absence of applied magnetic fields.

The purpose of the present study is to investigate some of the major factors that can influence heat transfer from an arc-heated plasma. Emphasis is placed on the particular case of a magnetically rotated arc, and an attempt is made to evaluate the significance of the turbulence and swirl so produced.

## Theoretical Considerations

It is possible to make estimates of the levels of turbulence and swirl likely to be encountered in systems in which the arc is rotated by a magnetic field. Such estimates are useful both for providing physical insight and as a basis of comparison between the present work and previous work in which the effects of swirl and turbulence on heat transfer were investigated. The detailed distribution of the parameters of flow is very complex indeed; therefore the analysis presented here is based upon a consideration of average values.

The nozzle is considered as the boundary of a control volume into which cold gas enters normally. Within the control volume the gas receives heat from the arc and is also acted upon mechanically by the rotating arc. It is assumed that the influence of the arc extends over the full length of the nozzle and that conditions within the nozzle can be typified by the arithmetic mean of inlet and outlet conditions.

It is first required to estimate the mean angular velocity $\omega$ of the gas at outlet from the nozzle. This is distinct from the angular velocity of the arc relative to the laboratory frame of reference, $\Omega$, which can be measured quite easily. The exact nature of the drag law between the arc and the gas is unknown, but fortunately a mean swirl velocity can be deduced in a manner that is independent of the drag law by resort to consideration of angular momentum. The axial component of magnetic torque, $T_m$, exerted by the arc on the gas is equal to the sum of the circumferential wall-friction torque, $T_c$, and the rate of change of the angular momentum, $M$, of the gas, both these vectors having only axial components.

The equation is

$$T_m - T_c = \frac{dM}{dt} \tag{1}$$

Now

$$\frac{dM}{dt} = \dot{m}Z\omega \tag{2}$$

where $\dot{m}$ is the mass flow rate of gas, $Z$ is the moment of area of the emergent gas stream, and $\omega$ is the mean angular velocity of the gas.

From Chen and Lawton [5]

$$T_m = \frac{IBR^2}{2} \tag{3}$$

where $I$ is the arc current, $B$ is the magnetic-field strength, and $R$ is the projected length of the arc perpendicular to the gas flow, i.e., ignoring the radius of the cathode, $R$ is equal to the radius of the nozzle. Equation (1) becomes, after substitution from (2) and (3)

$$\frac{IBR^2}{2} - T_c = \dot{m}Z\omega \tag{4}$$

Assuming an isotropic eddy viscosity, the circumferential wall shear stress $S_c$ and the axial shear stress $S_A$ can be related to the mean circumferential and mean axial gas velocities as follows:

$$\frac{S_c}{S_A} = R\frac{\omega}{2}\Big/\frac{W}{2} = \frac{R\omega}{W} \tag{5}$$

where $W$ is the average gas velocity at exit from the nozzle and can be readily calculated.

Hence, from a knowledge of the pressure drop across the nozzle (allowing for gas acceleration on heating) and the nozzle geometry, the angular velocity $\omega$ of the gas at exit from the nozzle can be found from equations (4) and (5).

Having calculated the gas angular velocity, the intensity of turbulent velocity fluctuations at the nozzle outlet can be derived from energy considerations. The electromagnetic power expended by the arc on the gas, $T_m\Omega$, is equated to the sum of the mean wall-friction work rate, $T_c(\omega/2)$, the rate of change of rotational energy of the gas, $\dot{m}Z\omega^2/2$, and the power of turbulent velocity fluctuations, $3\dot{m}u^2/2$. Thus

$$T_m\Omega = T_c\frac{\omega}{2} + \frac{\dot{m}Z\omega^2}{2} + \frac{3\dot{m}u^2}{2} \tag{6}$$

where $u$ is the root-mean-square value of turbulent velocity fluctuations at the nozzle exit, generated by virtue of the arc's rotation. In formulating equation (6) it has been assumed that the work of the viscous shear at the wall is dissipated entirely as heat. Using the previously calculated value of $\omega$, a value of $u$ can be obtained from equation (6).

The above analysis provides rough estimates of the turbulence and swirl present in the gas flow as it enters the calorimeter and provides a guide as to their possible significance. In order to find out more about the relative importance of turbulence and swirl in the actual system, an experimental technique was employed, the theoretical basis of which will be presented here. The motion of the arc relative to the gas, and hence the turbulence generated, is governed by the electromagnetic force and the aerodynamic drag acting on the arc, and should remain unchanged if the current and magnetic field are constant. Therefore, if the incoming cold gas is given a swirling component of velocity by tangential injection to the nozzle, the observed rate of arc rotation $\Omega$ should increase or decrease depending on the sense of the tangential injection, whereas the turbulence level should be unchanged. For positive and negative injection

$$\Omega^+ = \Omega + \alpha \tag{7}$$

$$\Omega^- = \Omega - \alpha \tag{8}$$

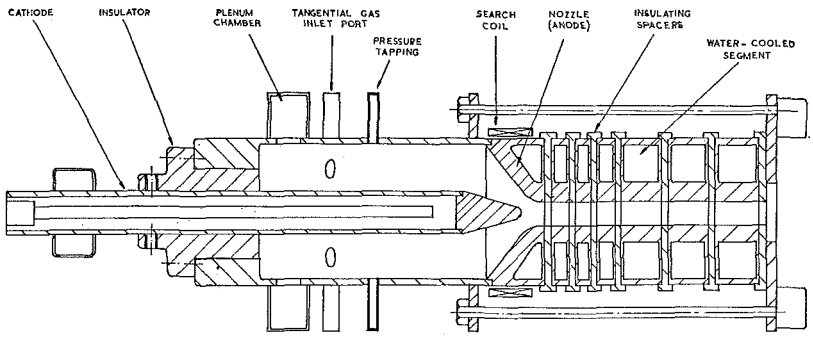


**Fig. 2 Diagram of the plasma torch and calorimeter**

where $\alpha$ is the superimposed rotation of the gas. By this means the swirl in the plasma stream can be increased or decreased while keeping the turbulence constant. Hence if the heat-transfer rate is strongly influenced by swirl the results with positive and negative gas injection should show significant changes. Subtraction of equations (7) and (8) gives

$$\alpha = \frac{\Omega^+ + \Omega^-}{2} \tag{9}$$

and this can be compared with the electromagnetic swirl $\omega$ as calculated earlier.

In the presentation of results, as is conventional in dissociated flows, use is made of a local heat-transfer coefficient $h$ defined as

$$h = \frac{q}{H_b - H_w}$$

where $q$ is the heat flux to the wall and $H_b$ and $H_w$ are the gas enthalpies at bulk gas temperature and wall temperature respectively. The variation of this and other parameters with axial distance from the nozzle outlet will be presented.

## Apparatus

The plasma torch and calorimeter used in the study are shown in Fig. 2. The nozzle of the torch was arranged to be the anode and was made of copper with a bore of 0.8-cm diameter. The cathode was concentric with the nozzle and insulated from it by a Tufnol bush in which it could slide. The tip of the cathode was made of thoriated tungsten. The gas supply could be fed to the torch either through an annular plenum chamber which produced no swirl or through small tangential ports which produced a high degree of swirl. A pressure tapping was situated in the torch body such that, with the calorimeter removed, the pressure drop across the nozzle could be measured. A U-tube manometer filled with carbon tetrachloride was used for this purpose.

The calorimeter consisted of six segments each of 0.8-cm bore and made of copper. The first three segments were 0.6 cm long and the last three were 1.4 cm long with thermally and electrically insulating Sindanyo spacers each 0.2 cm thick. Thus the effective lengths of the two sizes of segments when arranged in the calorimeter were one and two flow diameters respectively. This arrangement of segment sizes was used in order to measure more accurately the large axial changes in heat-transfer rates which usually occur in the entrance regions of a tube flow.

The power to the arc was supplied from a 30-kva welding rectifier with an open-circuit voltage of 70 v, and was measured using moving-coil meters. The arc was initially struck by touching the two electrodes together.

The arc rotation was measured by two search coils situated diametrically opposite one another on the nozzle. The output from each coil was taken to an oscilloscope where the signals were subtracted before being displayed. By this means the effects of extraneous magnetic fields could be reduced, leaving only the pulses from the arc rotation. The traces thus obtained were recorded on a storage oscilloscope and photographed.

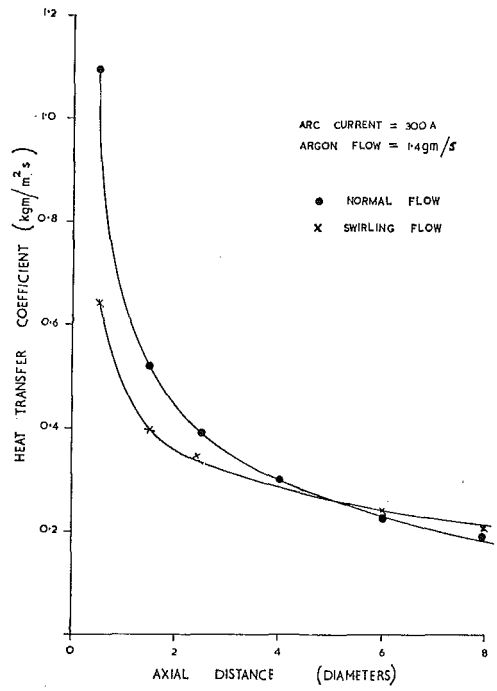


**Fig. 3 Influence of gas inlet mode on heat transfer; arc current 300 amp; argon flow 1.4 gram/sec**

The magnetic field was provided by a multi-turn coil which was calibrated with a Bell gaussmeter. The maximum available field strength was 0.16 tesla.

## Results and Discussion

In presenting the results of this investigation, attention will first be given to the case of zero magnetic field, then to the effects of a magnetic field, and finally to discussion of mechanisms that might account for these effects. In any particular series of tests, the total power of the arc was kept constant by varying the current. By this means the Reynolds number (as calculated in the conventional manner) at exit from the nozzle was approximately constant. Due to the high temperature and hence viscosity of the plasma, the Reynolds number was always below 2000, although the flow was not always laminar. The gas used was argon in all cases.

A typical example of the axial variation of heat-transfer coefficient in the calorimeter, for both normal (non-swirling) and tangential (swirling) inlet gas flow, is shown in Fig. 3, in which there is no applied magnetic field. The curves exhibit a rapid decrease in the heat-transfer coefficient as the flow develops, a familiar characteristic of heat transfer in entry regions. Moreover, the data compare quite well with constant-property solutions such as Graetz flow and slug flow, in agreement with the findings of previous workers.

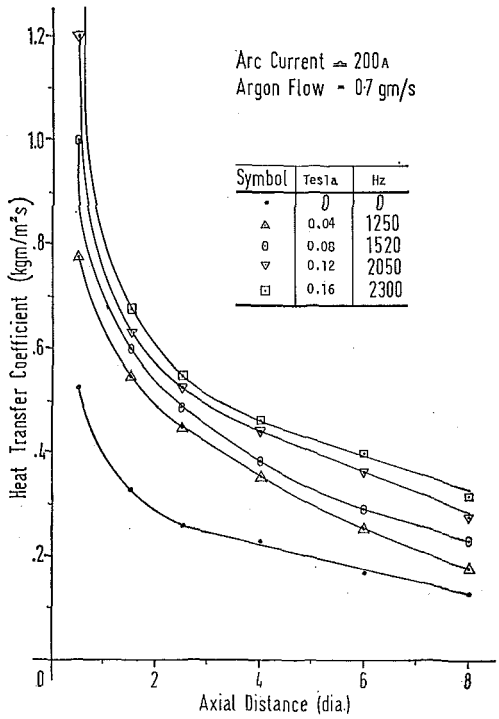


**Fig. 4 Influence of magnetic field on heat transfer; arc current 200 amp; argon flow 0.7 gram/sec**

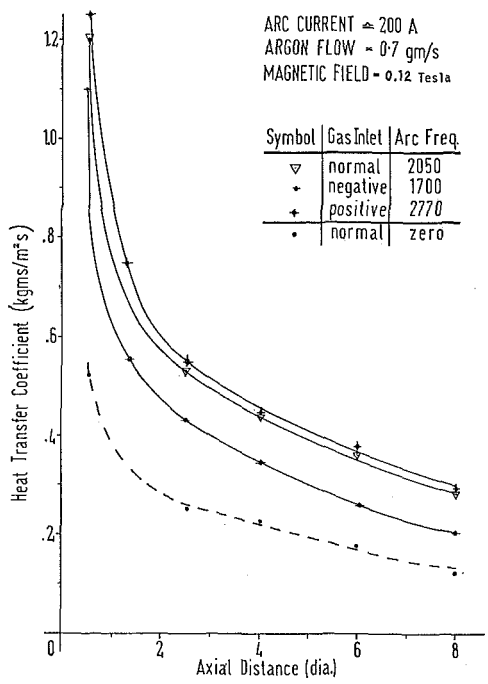


**Fig. 5(a) Effect of swirling inlet gas flow on heat transfer from magnetically rotated arcs; arc current 200 amp; argon flow 0.7 gram/sec; magnetic field 0.12 tesla**

It is apparent that the use of tangential flow caused a reduction in the heat-transfer coefficients in the first few diameters of the tube. Since the Reynolds number at inlet to the calorimeter was constant, the reasons for the differences in heat transfer must concern such matters as a change in the inlet velocity profile, the occurrence of swirl-induced laminarization, or reduction in turbulence level. It has been shown by Smithberg and Landis [15] that the effect of superimposing swirl onto an axial flow is to cause the axial velocity profile to become more square, i.e., the velocity gradients and transport coefficients at the wall are increased. Since this would result in an increase in heat transfer rather than a decrease, it seems unlikely that a flattening of the velocity profile is an important agency here. Laminarization is very difficult to assess, but it was shown by Kreith and Margolis [16], using water, that even when some laminarization did occur, heat transfer was still greater than without swirl. They also pointed out that in the case of swirling gases the Ranque–Hilsch phenomenon [17] may be in evidence, which would lead to improved heat transfer in the present circumstances. Bearing in mind some general observations concerning the varying stability of the arc, it seems most likely that the principal reason for the effects recorded was change in turbulence level. Thus it was noted that for the case of Fig. 3 the noise made by the arc in swirling inlet flow was considerably reduced and of a different nature than that with normal flow; the significance of this observation is that noise level has been related to turbulence by Incropera and Leppert [18]. Moreover, the signals from the search coils clearly indicated that in general the arc fluctuations were of greater amplitude and more random with normal flow than with tangential flow.

At stations farther downstream the heat-transfer coefficients became larger with tangential flow than with normal flow. This could indicate, for example, that although an initial reduction was caused by a reduction in turbulence, the reduction was counteracted downstream by a residual swirl which has a longer lifetime than turbulence [5].

A survey of many results showed that the degree of the overall suppression in heat-transfer coefficient could not readily be correlated with arc current and gas flow rate. However, these initial results provide two important pointers for the main study involving magnetic rotation of the arc. Firstly, turbulence generated by the arc appears to be significant in the present system, i.e., it is not damped out so quickly as to have no appreciable effect. Secondly, swirling gas flow in the calorimeter can be helpful to radially outward heat transfer as witnessed by the downstream portion of Fig. 3.

The effect of magnetic rotation on heat-transfer coefficients in the calorimeter is shown in Fig. 4, the results being typical of those over a wide range of currents and gas flows. The rotational rates of the arc were of the order of kilocycles per second. In each instance the increases in heat-transfer coefficient were large, being of the order of 100 percent at four diameters downstream for the largest magnetic field (0.16 tesla). It is seen that the increases in the heat-transfer coefficient are manifest over the full length of the calorimeter, the already high values at inlet to the calorimeter are further increased, and there is no tendency for effects to tail off at downstream stations. It does appear, however, that there are diminishing returns at larger magnetic fields. In order to quantify the experimental conditions, the arc rotational speed was considered in relation to the hot gas velocity at outlet from the nozzle. Multiplying the measured arc angular velocity by the nozzle radius to obtain the speed of the anode spot over the anode surface and dividing this by the outlet gas velocity gives a dimensionless number which, for the present tests, was of the order of 0.25 at maximum field strength. It appears that increasing this parameter beyond 0.25 does not produce very significant increases in heat-transfer coefficients. Although it does seem likely a priori that a parameter of this kind will be important in determining events, the figure itself is quoted just as a guide to the conditions prevailing in the present tests, and no significance can be attached to this particular value at the present time.

In order to distinguish the roles of swirl and turbulence in causing the increases in heat-transfer coefficient in the calorimeter, an aerodynamic swirl was superimposed on the magnetically produced swirl, following the reasoning presented in the section "Theoretical Considerations." Typical results are shown in Figs. 5(*a*) and 5(*b*). The results with zero magnetic field and normal flow are also shown for comparison.

Before considering the heat-transfer results in detail it is useful

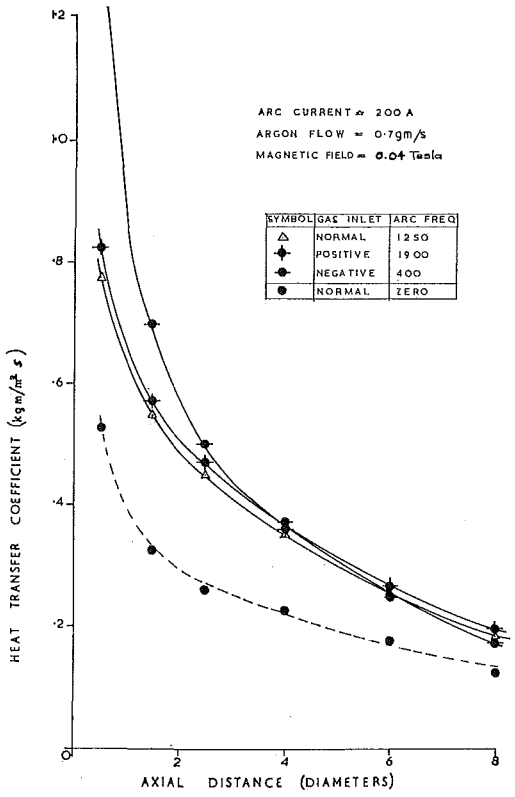


**Fig. 5(b) Effect of swirling inlet gas flow on heat transfer from magnetically rotated arcs; arc current 200 amp; argon flow 0.7 gram/sec; magnetic field 0.04 tesla**

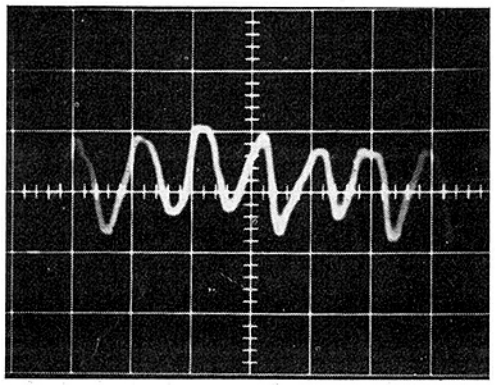

**(a) Positive inlet gas swirl; arc rotation 1900 Hz; stable arc**

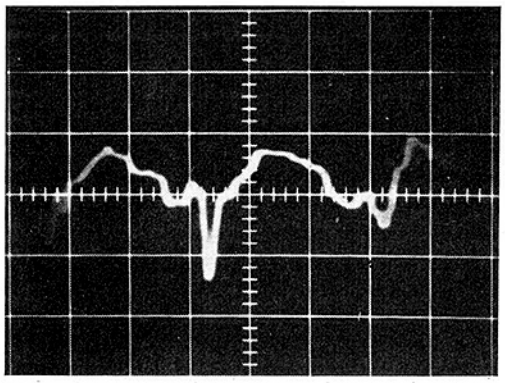

**(b) Negative inlet gas swirl; arc rotation 400 Hz; unstable arc**

**Fig. 6 Arc rotation data obtained from the search coils; arc current 200 amp; argon flow 0.7 gram/sec; magnetic field 0.04 tesla**

to make certain general observations concerning the magnitude of the aerodynamic parameters. From the recorded values of arc rotation rates, inset in Fig. 5, the swirls superimposed by tangential injection can be deduced using equation (9); they are 535 and 750 Hz for (*a*) and (*b*) respectively. These values are to be compared with those resulting from the electromagnetically induced swirl which were estimated from equations (4) and (5) as 1100 and 600 Hz respectively. For case (*a*), although the superimposed negative swirl caused a net reduction in rotational rate, the emergent stream was still rotating rapidly. For case (*b*) the superimposed negative swirl caused a small net negative swirl at outlet.

It was noted in case (*b*) that when a negative swirl was applied the arc became unstable, as recorded by the probe coils used for measurements of arc rotation rates. Examples of "stable" and "unstable" oscilloscope traces are shown in Fig. 6. The onset of instability as recorded by the probe coils was accompanied by erratic changes in the noise made by the discharge.

In addition, estimates were made of the intensity of turbulence created by the arc's motion, using equation (6). The values were found to be very high, a value of 15 percent, referred to the velocity of the emergent plasma, being typical.

We turn now to the heat-transfer results of Fig. 5 and to possible explanations for their character.

In every case, the heat-transfer coefficients are larger in the presence of a magnetic field, irrespective of the presence of a positive or negative superimposed swirl. A positive superimposed swirl consistently gives larger heat-transfer coefficients than the case of normal flow. However, the behavior of a negative swirl is erratic, sometimes giving decreases and sometimes increases, by comparison with the other two flow regimes.

A tentative explanation of the results can be found using the following set of hypotheses:

(*a*) Turbulence, created either by the rotation of the arc or by arc instabilities, will, while it persists, increase heat transfer. Its effect will be felt only at stations immediately downstream because of its rapid rate of decay. It should be noted that the Reynolds number was always such that the developed flow would be in the laminar regime.

(*b*) Rotation of the gas, either by tangential injection or arc rotation, will tend to increase heat transfer, e.g., by squaring the velocity and/or temperature profiles. The effect of rotation is long-lived owing to its low rate of decay as compared to turbulence.

(*c*) Irregular and noisy rotation of the arc implies enhanced levels of turbulence.

Consider the entry regions of the calorimeter first in terms of the hypotheses. As already noted, the heat-transfer coefficients were always enhanced in the case of an applied magnetic field. In the case of Fig. 5(*a*), arc stability, as indicated by noise level and the oscilloscope trace from the search coils, was unaffected by the presence of swirl in either direction, i.e., turbulence levels would be expected to be similar in all three cases of Fig. 5(*a*) with an applied field. In this case it was found, as would be anticipated from the hypotheses, that the heat-transfer coefficient increased with the amount of swirl, an increase that was maintained along the complete length of the calorimeter. In Fig. 5(*b*) the presence of a positive swirl produced no instabilities and therefore presumably no significant changes in turbulence, and caused an increase in heat transfer over the case of normal flow. However, in this case negative swirl caused the arc to become unstable, see, e.g., Fig. 6(*b*), thereby increasing the turbulence level and producing the largest heat-transfer coefficients measured.

Consider now the downstream portions. The case of Fig. 5(*a*) has already been discussed, the increases in heat transfer being maintained far downstream because of the long-lived character of swirl. For the case of Fig. 5(*b*) it is seen that the very high levels of heat transfer for the case of negative swirl are short-lived, disappearing just a few diameters downstream in accord

with the assumption that these were associated with high levels of turbulence that are short-lived. Well downstream where turbulence would be expected to have decayed very greatly, the heat-transfer coefficients increase in the order of increasing rates of swirl.

To summarize the findings of the experiments with tangential gas injection, it appears that both swirl and turbulence contribute to the increases in heat transfer caused by arc rotation, shown in Fig. 4, the effect of swirl being longer-lived than that of turbulence. In addition, because of the nature of the discharge, in the presence of a negative swirl which is sufficiently strong to bring about large reductions in the arc rotational speed, arc instabilities can be set up that result in very high turbulence levels which cause large increases in heat transfer.

## Conclusions

It has been demonstrated that the heat transfer from an arc plasma to a constraining tubular enclosure can be significantly increased by the application of an axial magnetic field used to rotate the arc. These findings have been explained in terms of the turbulence and swirl of the plasma. Turbulence, generated by arc rotation and arc instability, persists a few tube diameters downstream, during which time it produces large increases in heat transfer. Swirl, generated by arc rotation or tangential injection, persists throughout the length of the calorimeter, producing increases in heat transfer everywhere, these being especially notable far downstream after the turbulence has decayed.

## References


1 Rieppel, P. J., "Plasma-Jet Cutting, Machining, and Welding," *Metals Engineering Quarterly*, Vol. 3, No. 4, Nov. 1963, pp. 33–38.

2 Wahll, M. J., Van Orsdel, J. R., and Fischer, R. B., "Spheroidization of Irregularly Shaped Metal Powders," *Powder Metallurgy*, No. 8, 1961, pp. 48–64.

3 Leutner, H. W., and Stokes, C. S., "Producing Acetylene in a Plasma Jet," *Ind. and Eng. Chem.*, Vol. 53, No. 5, May 1961.

4 Allen, H. J., and Eggers, A. J., "A Study of the Motion and Aerodynamic Heating of Missiles entering the Earth's Atmosphere at High Supersonic Speeds," NACA TN 4047, 1957.

5 Chen, D. C. C., and Lawton, J., "Discharge Heaters Based on Magnetically Rotated Arcs," *Trans. Inst. Chem. Engrs.*, Vol. 46, 1968.

6 Mayo, R. F., and Davis, D. D., "Magnetically Diffused Radial Electric-Arc Air Heater Employing Water-Cooled Copper Electrodes," A.R.S. Electric Propulsion Conference, Berkeley, Calif., Mar. 1962.

7 Raelson, V. J., and Dickerman, P. J., "Heat Transfer From Partially Ionized Gases in the Presence of an Axial Magnetic Field," JOURNAL OF HEAT TRANSFER, TRANS. ASME, Series C, Vol. 84, No. 2, May 1962, pp. 169–176.

8 Cann, G. L., "Energy Transfer Processes in a Partially Ionized Gas," California Institute of Technology, GALCIT Memo No. 61, 1961.

9 Yuen, M. C., "Stability of the Poiseuille Plasma Arc in an Axial Magnetic Field," *Physics of Fluids*, Vol. 9, 1966, pp. 1140–1150.

10 Scrivan, J. F., and von Jaskowsky, W., "Heat Transfer from Plasmas to Water-cooled Tubes," *I.&E.C. Process Design and Development*, Vol. 4, No. 4, Oct. 1965.

11 Johnson, J. R., Choksi, N. M., and Eubank, P. T., "Entrance Heat Transfer from a Plasma Stream in a Circular Tube," *I.&E.C. Process Design and Development*, Vol. 7, No. 1, Jan. 1968.

12 Wethern, R. J., and Brodkey, R. S., "Heat and Momentum Transfer in Laminar Flow: Helium Initially at Plasma Temperatures," *AIChE Journal*, Vol. 9, No. 1, Jan. 1963.

13 Knudsen and Katz, *Fluid Dynamics and Heat Transfer*, McGraw-Hill, New York, N. Y., 1958.

14 Schmidt, P. S., and Leppert, G., "Heat Transfer From Plasma in Tube Flow," JOURNAL OF HEAT TRANSFER, TRANS. ASME, Series C, Vol. 92, No. 3, Aug. 1970, pp. 483–489.

15 Smithberg, E., and Landis, F., "Friction and Forced Convection Heat-Transfer Characteristics in Tubes With Twisted Tape Swirl Generators," JOURNAL OF HEAT TRANSFER, TRANS. ASME, Series C, Vol. 86, No. 1, Feb. 1964, pp. 39–49.

16 Kreith, F., and Margolis, D., "Heat Transfer and Friction in Turbulent Vortex Flow," *Appl. Sci. Res.*, Section A, Vol. 8, 1959.

17 Hartnett, J. P., and Eckert, E. R. G., "Experimental Study of the Velocity and Temperature Distribution in a High-Velocity Vortex-Type Flow," TRANS. ASME, Vol. 79, 1957, pp. 751–758.

18 Incropera, F., and Leppert, G., "Flow Transition Phenomena in a Subsonic Plasma Jet," *AIAA Journal*, Vol. 4, No. 6, 1966.

**V. HUPLIK**
Engineer,
N.H.K.G. Research Institute,
Ostrava, Czechoslovakia

**G. D. RAITHBY**
Assistant Professor,
University of Waterloo,
Waterloo, Canada.
Mem. ASME

# Surface-Tension Effects in Boiling from a Downward-facing Surface

*An experimental investigation of the effect of surface-tension variation around air and vapor bubbles on a downward-facing heated surface is reported. For air bubbles, and vapor bubbles at moderate heat fluxes, regimes of flow where surface-tension forces and buoyancy forces respectively dominate are defined. For boiling at heat fluxes near the burnout limit, flow driven by surface-tension forces appears to play a large role in cooling the heated surface. It is shown that small amounts of surfactant added to the liquid result in dramatic changes in the boiling mechanism, and at high heat fluxes a substantial improvement in the heat transfer. Most of the experiments were conducted with the liquid at temperatures less than the saturation temperature.*

## Introduction

In many situations of practical importance, interfaces between two phases, such as liquid and gas or vapor, are encountered. The fact that the interface can play an important role in the fluid flow near this boundary and in heat and mass transfer across the boundary has been recognized for more than a century. For example, variations in the tangential stress, or surface tension, along an interface result in a motion of the interface which in turn induces motion, by viscous shear, in the fluids near the interface. Variations in surface tension are usually produced by concentration or temperature gradients along the interface. Phenomena arising from interfacial surface-tension gradients are usually termed Marangoni effects. An excellent film [1][1] and two comprehensive reviews [2, 3] on surface-tension effects are available.

Although a large volume of literature on Marangoni effects exists, there appears to be little known of the role of surface-tension variations in the related problems of nucleate boiling and dropwise condensation. Concerning dropwise condensation, Trefethen [4] has suggested that internal circulation due to surface-tension variations could result in a significant increase in the heat-transfer contribution of the large drops. Lorenz and Mikic [5] have carried out a numerical analysis which fails to confirm this, but no quantitative experimental data are available.

In nucleate boiling a similar situation exists. A complex numerical analysis was carried out by Gaddis [6] to determine the effect of surface-tension variations along the interface of a stationary hemispherical vapor bubble. The agreement between measured and computed heat-transfer results was inconclusive. A later approximate analysis by Raithby and Huplik [7] indicated that the "infinity" boundary conditions in Gaddis' analysis were probably applied much too close to the interface in the numerical scheme.

It appeared, from preliminary experiments at Professor Grigull's laboratory at the Technical University in Munich, Germany, that Marangoni effects were perhaps important in boiling from a downward-facing plate. In earlier experiments with this geometry by Ishigai et al. [8] this was not reported. Some related qualitative observations were reported by McGrew et al. [9] for vapor and air bubbles in a horizontal channel with a heated upper plate and a cooled lower plate.

The purpose of this investigation was to establish the role of Marangoni flow around single air bubbles and in natural nucleate boiling at moderate and high heat fluxes. Streak photographs and shadowgraphs were used to establish fluid flow patterns, the effect of single air bubbles on the heat transfer from the heater surface was measured, the values of Marangoni number and Rayleigh number for transition from Marangoni flow to free-convection flow are presented in a correlation, and the effect of surfactant on the flow pattern and heat transfer is reported. A downward-facing heater was chosen for these experiments because the effect to be observed is often dominant for this geometry; the results reported herein are probably the first quantitative, or perhaps semi-quantitative, measurements of the effect of surface-tension gradients in boiling heat transfer. In addition, this geometry is of practical importance, having been the subject of intense investigation for cooling by free convection [10]. It is hoped that the results of this investigation will lead to an increased understanding of the role of surface-tension gradients in boiling heat transfer from other geometries.

## Experimental Apparatus

A schematic of the apparatus is shown in Fig. 1. De-ionized water was used as the working fluid in a cubic glass tank, 300 mm per side. A large heating coil was located at the bottom of the

[1] Numbers in brackets designate References at end of paper.

Contributed by the Heat Transfer Division of The American Society of Mechanical Engineers and presented at the AIChE-ASME Heat Transfer Conference, Denver, Colo., August 6-9, 1972. Manuscript received by the Heat Transfer Division April 21, 1971. Paper No. 72-HT-42.

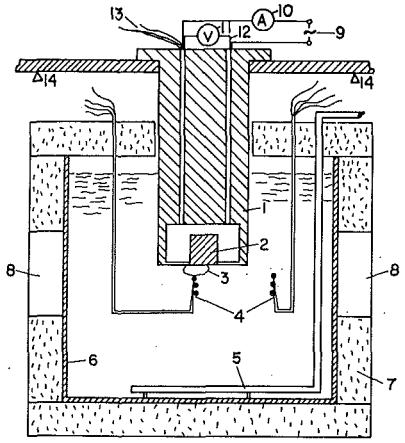


1 Heater Body (Insulator)
2 Copper Heater
3 Vapor Bubble
4 Thermocouple Rakes (Adjustable)
5 1500 W Heater
6 Glass Test Section
7 1·5in. Styrofoam Insulation
8 View Ports
9 A.C. Power Supply
10 Ammeter (±1%)
11 Voltmeter (±1%)
12 Voltage Taps
13 Leads For 8 Thermocouples
14 Leveling Device

**Fig. 1 Schematic of apparatus**

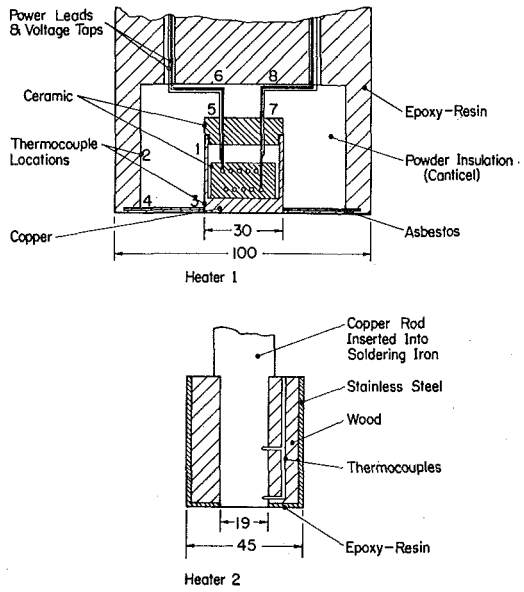


**Fig. 2 Schematic showing lower portion of heater 1 and heater 2; units in mm**

tank to bring the bulk temperature of the fluid to the required level. All sides of the tank were insulated with 40-mm sheets of styrofoam so that once the required temperature was achieved the fluid could be held at essentially a constant temperature for a long period of time without further heating; this virtually eliminated bulk convective motion in the tank during experiments.

The two heaters shown in Fig. 2 were used. Heater 1 was used for more precise measurements. A mechanism was provided for levelling the heater surfaces. Heat fluxes and surface temperatures for heater 1 were obtained respectively from power-input determinations (i.e., current and voltage readings, Fig. 1) and thermocouple measurements. Heat losses other than to the heated surface were estimated using the output of eight thermocouples embedded in the heater; appropriate corrections were made. The thermal inertia of this heater and the thermocouple characteristics were such that essentially a full response to a typical surface temperature change was achieved in about 1 sec. Approximate heat fluxes and surface temperatures were obtained from heater 2 using two thermocouples.

Liquid temperatures were measured using two thermocouple rakes, each consisting of three thermocouples spaced in the vertical direction. A mechanism allowed these to be adjusted to any location quickly and precisely. Usually one of the probes was located under the heating surface with the uppermost thermocouple just below the crown of the bubble under consideration; the other was located at the same elevation, but removed from the heating surface. All thermocouple outputs, and important potential differences, were measured using strip recorders (accuracy $\simeq \pm 0.1$ deg C). Each thermocouple was also calibrated to this accuracy.

Flow-pattern observations were made using two techniques. In the "particle method" plastic particles (Goodyear "Pliolite VT") of density $1.026 \times 10^3$ kg/m$^3$ and an average diameter of about 50 micron were used at a concentration of approximately 100 parts per million. An intense beam of parallel light, about 3 mm wide, was passed through the fluid below the central portion of the heater and photographs were made perpendicular to the beam direction utilizing the scattered light. Another method, termed the "shadowgraph method," was employed to make observations without the necessity of introducing foreign particles. This was accomplished by projecting an image of the heater and surrounding fluid on a ground glass screen using a mercury-arc lamp.

A Hycam camera was used for film documentation of the flow. The film record and the thermocouple recordings were synchronized to enable data to be obtained from the records.

## Results

**Flow around Air Bubbles.** The interpretation of the flow pattern observed under nucleate boiling conditions was, at first, not evident. Therefore a simpler case, utilizing air bubbles, was considered. At low heat fluxes, the fluid motion around the heater was typical of that for free convection. First, this flow

## Nomenclature

$g$ = gravitational constant
$L$ = length of interface along which motion is observed
Ma = $(T_0 - T_c)L(\partial\sigma/\partial T)/\mu^*\alpha_B$, local Marangoni number
Nu = Nusselt number, free convection $= (qR_H)/[k(T_0 - T_B)]$
$\mathrm{Nu_{Ma}}$ = Nusselt number with air bubble on surface
$q$ = net heat flux from surface
$R_0$ = radius of bubble base
Ra = $g\beta(T_c - T_B)R_0^3/\nu_c\alpha_B$, local Rayleigh number
$t$ = time (sec)
$t_T$ = transition time (sec)
$T_c$ = temperature at crown of bubble
$T_0$ = surface temperature of heater
$T_{\mathrm{sat}}$ = saturation temperature
$T_B$ = bulk liquid temperature
$v$ = velocity
$v^*$ = $vR_0/\alpha_B$, dimensionless velocity
$\alpha_B$ = thermal diffusivity of liquid at $T_B$
$\beta$ = expansion coefficient
$\mu^*$ = viscosity of liquid at $T = (T_0 + T_c)/2$
$\nu_c$ = kinematic viscosity of liquid at $T = T_c$
$\sigma$ = surface tension
$\psi$ = dimensionless stream function in liquid
$\psi'$ = dimensionless stream function in gas
$\theta$ = spherical coordinate (angle from the axis of symmetry)
$R_H$ = radius of the heated surface

**Subscripts**

0 = heater surface
$c$ = bubble crown
$B$ = bulk liquid

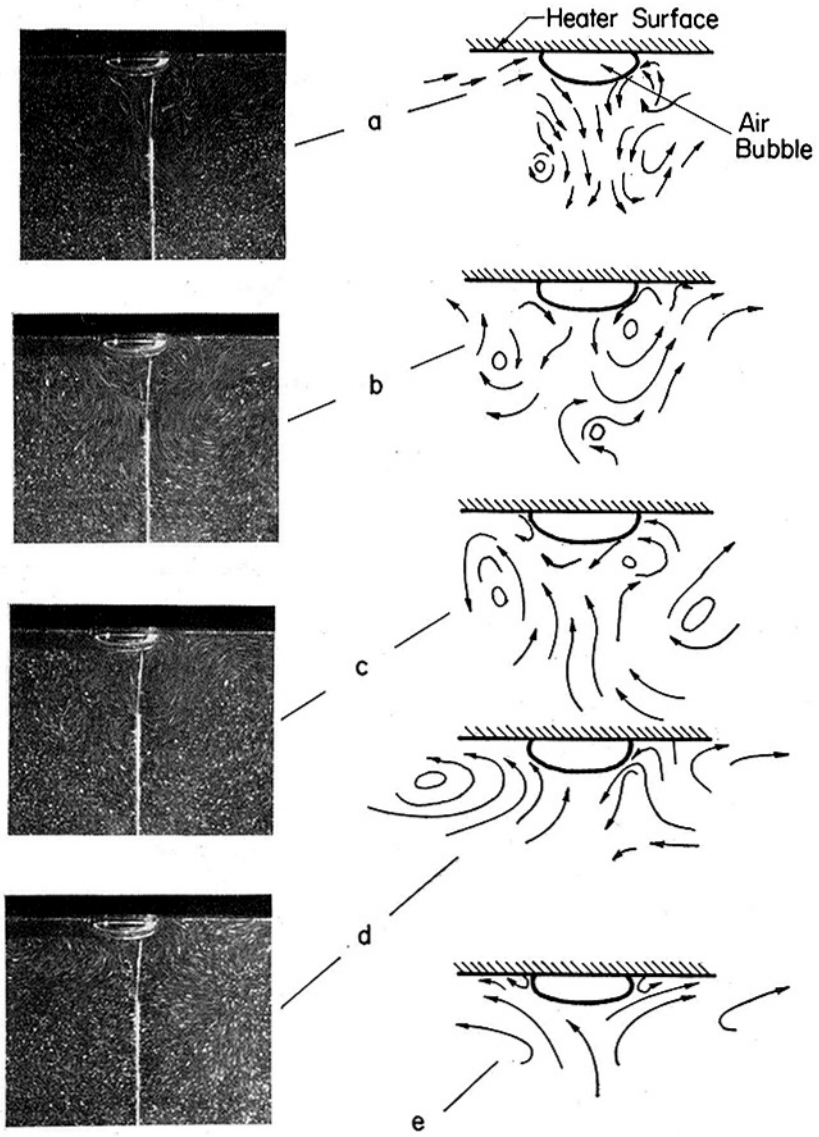


**Fig. 3 Flow around an air bubble on heated surface showing surface-tension-dominated flow (*a*), increasingly important effect of buoyancy (*b*, *c*), transition (*d*), free-convection flow regime (*e*); $T_B$ = 23 deg C, $q = 2.2 \times 10^4$ W/m$^2$, $R_0$ = 10 mm; interval between photos about 0.5 sec**

was disrupted by introducing the end of a hypodermic tube close to the center of the heater and forcing several air bubbles over the surface.[2] When carefully done, this destroyed the free convective motion and left the fluid in a relatively quiescent state. Immediately after, the experimental bubble was introduced to the center of the heated surface through the same tube and the tube removed. The flow pattern and the temperatures were then recorded simultaneously until a steady state was reached.

The flow pattern observed using the neutral-density particles is shown in the photographs and drawings in Fig. 3. Fig. 3(*a*) was taken immediately after placing the bubble on the surface. There is a very strong jet of fluid projected downward from the center of the bubble with cooler liquid being drawn inward toward the heater surface and the upper portion of the bubble (Stage A). After a short time secondary vortices appear, Fig. 3(*b*, *c*), the jet becomes weaker, and the tangential velocity near the crown of the bubble decreases (Stage B). The vortices are gradually convected upward and outward along the heater surface and at some instant the tangential velocity of the bubble surface near the crown is zero (transition). The transition point is shown in Fig. 3(*d*). Following this, the large-scale motion resembles that for free convection with flow moving upward toward the bubble crown and outward along the heater surface. However, small vortices persist near the base of the bubble as shown in Fig. 3(*e*). This is called Stage C.

The flow pattern can be explained simply by considering the surface-tension vs. temperature curve for pure water in Fig. 4. When the bubble is placed on the surface, its base is at a higher temperature than its crown and therefore the surface tension increases from crown to base. This results in a vigorous interface movement which drags along the liquid external to the bubble and the air inside and projects the liquid vertically downward at the crown where the interface is destroyed. Because the thermal boundary layer was removed earlier, there are no strong buoyancy forces retarding the liquid motion. As the motion described above becomes established, the heater surface is cooled by the liquid which is drawn in by the moving interface. In addition, the warm jet of water moving downward is subjected to buoyancy forces which return the warm water, through the secondary vortices, to the bubble crown, thus further decreasing the temperature gradient along the interface. Finally the interface near the crown becomes essentially isothermal and the motion stops. This is referred to as transition because before this time the

[2] This was intended to simulate the disturbance created by the growth and collapse of individual bubbles in nucleate boiling.

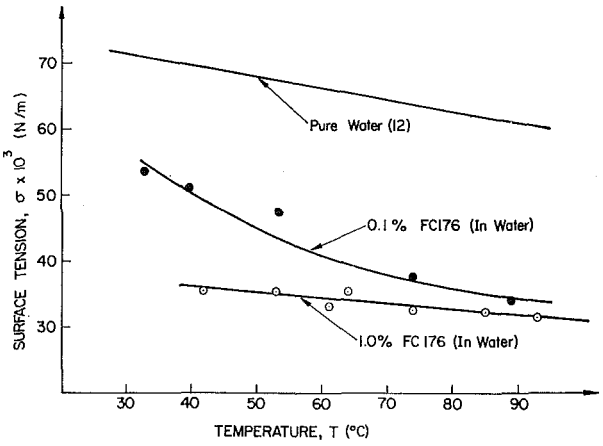


**Fig. 4 Dependence of surface tension on temperature for pure water and solutions of water and the surfactant FC-176**

Marangoni-type flow has dominated and after this the pattern is similar to one for pure free convection. However, there is always a strong temperature gradient near the heater which causes the small rotating vortices near the bubble base to persist.

The unknown parameter in the above description is the influence of small traces of contamination on the interface motion. It has been clearly demonstrated that contamination may lead to large effects for small bubbles [3, 6]; the influence here is not known. However, the effect of relatively large, artificially introduced surfactant concentrations will be described below. In addition, it will be shown that, at transition, there is a strong correlation between dimensionless groups representing respectively buoyancy and surface-tension forces. This would not be expected if the contamination played a dominating role.

**Analysis of Steady Flow around a Hemispherical Bubble.** In order to predict the fluid flow pattern produced by surface-tension forces around a single bubble, a simple analysis was carried out [7]. In this investigation, a closed-form solution for the flow around a hemispherical stable bubble resting on a downward-facing surface was obtained. Buoyancy forces were neglected in this analysis and the no-slip boundary condition at the solid surface was not met. The latter assumption did not appear to substantially affect the results. If, in addition, it is assumed that there is a cosine variation of the interface temperature (this assumption is not required to carry out the analysis) a particularly simple solution is obtained. The dimensionless stream functions external to and inside the bubble were respectively

$$\psi = [1 - (r/R_0)^{-2}] \sin\theta \sin 2\theta$$

$$\psi' = [(r/R_0)^5 - (r/R_0)^3] \sin\theta \sin 2\theta$$

where $r$ is the radius for spherical coordinates with origin at the center of the bubble base, $R_0$ is the bubble radius, and $\theta$ is the angle from the axis of symmetry. These streamlines are shown in Fig. 5. It will be noted that the flow pattern is similar to that shown in Fig. 3($a$). However, it appears that buoyancy forces never allow a steady flow pattern, like that in Fig. 5, to develop.

**Transition.** If one performs a dimensional analysis on the complete equations describing flow around an air bubble resting on a heated surface, assuming constant properties, the dimensionless groupings which arise involve the geometry and the ratio of the properties inside and outside the bubble. In addition, the Marangoni number Ma, the Rayleigh number Ra, and the Prandtl number Pr, appear; but if the inertial terms are neglected in the equations of motion, as would be reasonable in this case, the explicit dependence on Pr disappears. Ma characterizes the surface-tension forces and Ra the buoyancy forces.

The method of introducing the bubble leads to small buoyancy forces initially, and therefore Marangoni or surface-tension-driven flow dominates. As time passes, buoyancy appears to play an important role in destroying this flow, and, after transition, finally dominates. To study this transition Ma and Ra were defined as follows

$$\mathrm{Ma} = L(T_0 - T_c)(\partial\sigma/\partial T)/\mu^*\alpha_B$$

$$\mathrm{Ra} = \beta g(T_c - T_B)R_0^3/\nu_c\alpha_B$$

where $L$ is the length of bubble interface along which motion was observed; this was obtained from film records. $T_c$ was measured using the top thermocouple in the rake below the bubble shown in Fig. 1. The subscripts 0, $c$, and $B$ refer respectively to heater surface, bubble crown, and the bulk fluid.

For various surface and bulk temperatures and various bubble sizes, the required measurements were taken, along with synchronized films, to establish the values of Ma and Ra at the time transition occurred. The flow was made visible initially using particles and the results are shown in Fig. 6. It is clear that with increasing values of Ma, also increasingly large Ra is required for transition. For observations of Ma and Ra which yield data points above the curves shown, a Marangoni flow would be expected, and, similarly, for points falling below the curves a free-convection or buoyancy-dominated flow would occur. However, the scatter in the data is quite large.

The results of similar experiments conducted using the shadowgraph method are shown in Fig. 7. Here the trends are the same but the scatter in the data is greatly reduced. A comparison of Figs. 6 and 7 reveals the rather important fact that the small particles have a substantial influence on the surface-tension-induced flow. In many cases the particles adhered to the interface, accumulating near the crown, thus stopping the motion prematurely.

**Effect of Marangoni Flow in Heat Transfer.** The effect on heat transfer of the Marangoni flow produced by a single air bubble on the heater surface was determined as follows. First the thermal

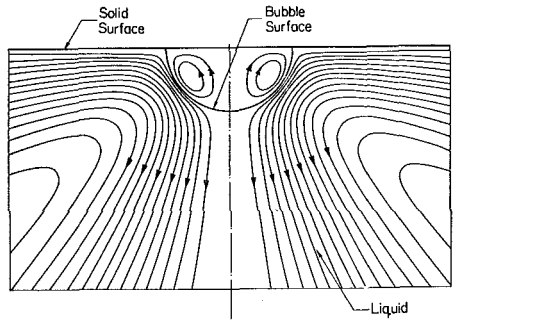


**Fig. 5 Analytical solution to flow induced by a cosine temperature variation along bubble interface; buoyancy forces ignored**

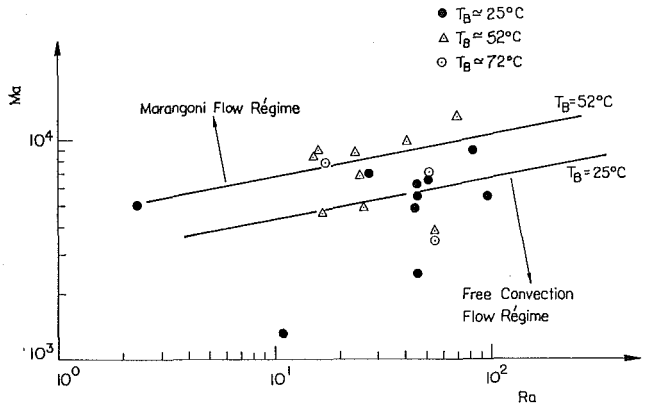


**Fig. 6 Plot of Marangoni number vs. Rayleigh number at transition, obtained using particle technique**

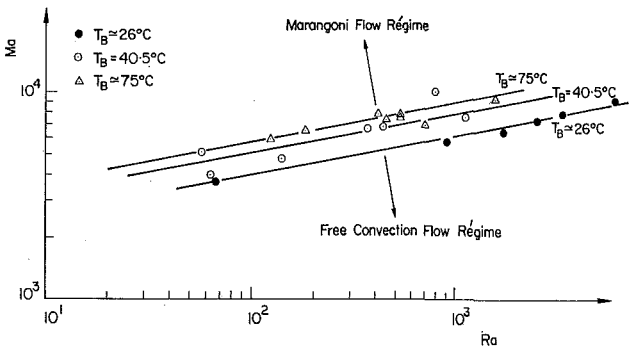


**Fig. 7 Plot of Marangoni number vs. Rayleigh number at transition, obtained using shadowgraph technique**

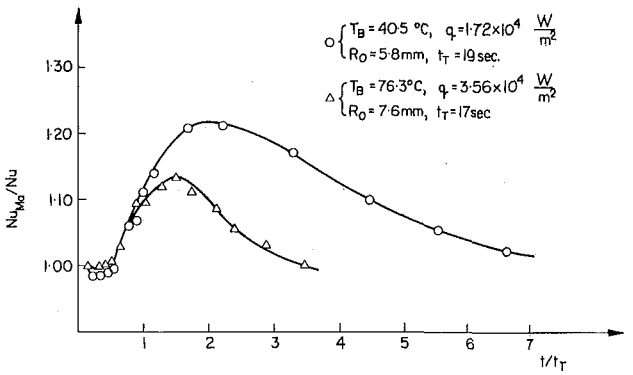


**Fig. 8 Plot of ratio of Nusselt number with air bubble on surface to that without bubble, after removal of thermal boundary layer**

boundary layer was disturbed by the method described above and the transient Nusselt number Nu was measured during the boundary-layer re-formation. Precisely the same procedure was followed again except a small air bubble was placed at the center of the heater as a source of Marangoni flow. The ratio of the two Nusselt numbers $Nu_{Ma}/Nu$ was then plotted against dimensionless time $t/t_T$, where $t_T$ is the time interval between the introduction of the bubble and transition. The results are shown in Fig. 8. The bubbles occupied 15 percent of the surface area of the heater for $T_B = 40.5$ deg C and 25 percent for $T_B = 76.3$ deg C. It will be noted that, particularly for low bulk temperatures, the cooling effect of the flow driven by surface tension is considerable.

**Marangoni Flow in Nucleate Boiling: Low Heat Flux.** At heat fluxes large enough to produce a large number of vapor bubbles, some bubbles grew quickly beyond the depth of the thermal boundary layer and collapsed, while others grew slowly and still others reached quite stable equilibrium sizes. Also, as the heat flux increased, the tendency of bubbles to coalesce increased. Although the possible effect of particles on the flow pattern was fully realized, only the particle technique was suitable for flow visualization. Cine photographs were taken to study the growth of the bubbles and simultaneously the liquid flow pattern around the bubbles. Typical results of bubble growth, coalescence, and collapse for a heat flux of $3.48 \times 10^4$ W/m² and a bulk temperature of 79.5 deg C are shown in Fig. 9. The real time between any two adjacent sketches was about 0.5 sec. The sketches were made by tracing projections of frames of the cine film on drawing paper. Fig. 9(*a–c*) depicts the growth of several small bubbles, many of which suddenly coalesce, Fig. 9(*d*), and subsequently collapse. Over the total 2.5-sec period, the bubble shown on the left has remained quite stable.

Not shown in the drawings but visible on the film are the flow patterns around the bubbles. Immediately after the appearance of a bubble on the surface, a strong jet-type flow was created similar to Stage A for the air bubble. It was obvious that surface-tension forces dominated buoyancy forces in the

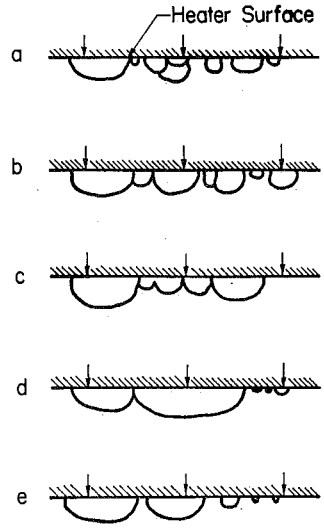


**Fig. 9 Nucleate boiling pattern at moderate heat flux; $T_B = 79.5$ deg C, $q = 3.48 \times 10^4$ W/m²**

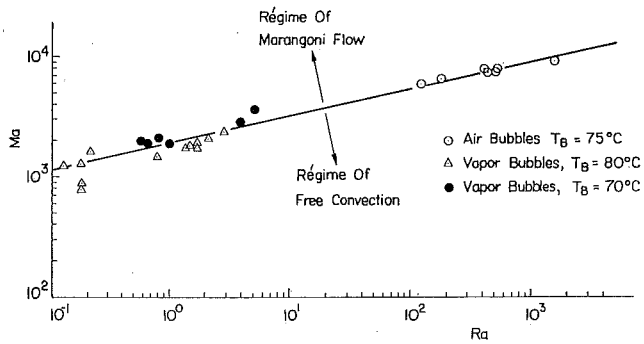


**Fig. 10 Marangoni and Rayleigh numbers at transition for vapor bubbles (left-hand side) and air bubbles**

bubble vicinity. The interface motion was observed to decrease near the bubble crown as the vapor volume increased. The bubbles which reached a stable shape, or more often oscillated slightly about an equilibrium shape, may be considered to be at the transitional stage where the fluid near the interface at the crown does not move. For smaller bubbles Marangoni forces appear to dominate.

A plot of the Marangoni number vs. Rayleigh number for the stable bubbles is shown on the left portion of Fig. 10. Ma and Ra are defined by the same equations as for air bubbles. Here the small values of Ma and Ra result from the small bubble diameters. Exactly the same trend is seen as for the air bubbles earlier. In fact, the transition values of Ma vs. Ra for the air bubbles for $T_B \simeq 75$ deg C, drawn at the right-hand side in the same figure, are seen to lie on an extension of the curve for the vapor bubbles. This curve delineates the free-convection regime from the Marangoni-flow regime.

**High-Heat-Flux Boiling.** As the heat flux is increased, the activity of the bubbles on the surface becomes more vigorous and the tendency for smaller vapor bubbles to coalesce becomes very strong. The reason given for the coalescence by Trefethen [1] and McGrew et al. [9] appears to be correct. Between two closely adjacent bubbles there is a region where the liquid circulates vigorously and becomes warmer than the liquid on other sides of the bubbles. The interface responds to the lateral temperature gradient and accelerates fluid from the hotter toward the cooler regions. The reaction forces on the bubbles then drive them together.

The coalescing bubbles form a blanket of vapor which covers a large portion of the heater surface and overlaps on the insulator surrounding the heated surface. Along the portion of the

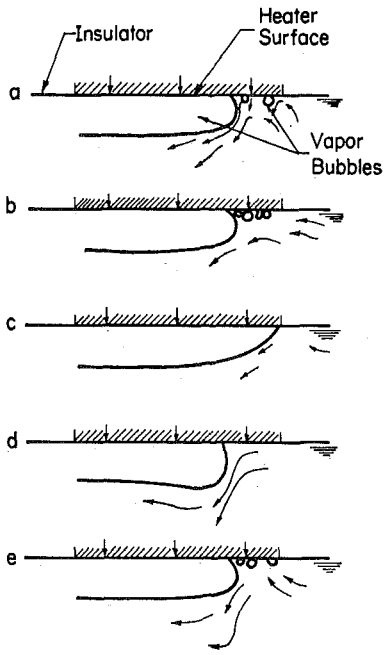


Fig. 11 High-heat-flux boiling; $q = 9.94 \times 10^4$ W/m$^2$, $T_B = 89$ deg C

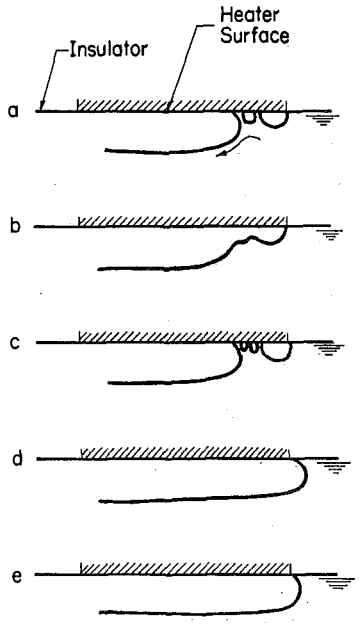


Fig. 12 Saturated boiling near the burnout point; $q = 12.56 \times 10^4$ W/m$^2$, $T = T_{sat}$

blanket near the heated surface there is a strong temperature gradient which results in a vigorous Marangoni flow. This draws the cool liquid over the heater surface and propels it along the interface. This is shown in Fig. 11($a$, $b$, $e$). At sufficiently high heat fluxes, bubbles also grow on the exposed surface and the vapor blanket periodically extends itself, Fig. 11($c$, $d$), to absorb these.

Upon further increasing the heat flux and/or increasing $T_B$, the volume of the vapor blanket increases and a larger portion of the heater surface is covered. In addition, the vapor bubbles on the exposed portion of the heater grow to larger sizes before being swept into the vapor blanket, Fig. 12($a$, $b$, $c$). A slight increase in heat flux at this point causes the steam blanket to envelop the heater surface, Fig. 12($d$, $e$), and the power must be shut off immediately to avoid destruction of the heater. When the steam blanket covers the entire surface and does not retreat, the liquid motion around the bubble immediately ceases.

From the particle streak lengths and the film speed of the camera, the maximum velocities along the blanket interface were calculated for several cases. The dimensionless velocity $v^*$ as a function of Ma is plotted in Fig. 13. As would be expected, the maximum velocity increases with Ma. The maximum observed velocity was about 0.05 m/sec.

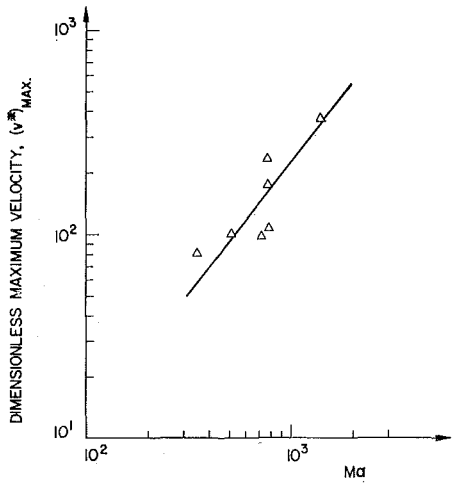


Fig. 13 Maximum velocities of liquid along vapor film for high-heat-flux boiling; maximum observed velocity was 0.05 m/sec

**The Effect of Surfactants on Boiling.** Surfactants can be used to decrease the value of $\partial\sigma/\partial T$ and thus decrease the importance of surface-tension forces. The surfactant FC-176, produced by 3M, was used in four volume concentrations. The results of surface-tension measurements for concentrations of 0.1 and 1.0 percent are shown in Fig. 4. The measurements are quite crude for several reasons, but it is seen that $\partial\sigma/\partial T$ for a 1 percent concentration is substantially smaller than that for pure water.

The flow patterns around air and vapor bubbles were observed with added surfactant using both the particle and shadowgraph techniques. Using air bubbles, even at a concentration of 0.1 percent, the interface motion was found to be very weak and was observed only a very short time after the introduction of the bubble.

For natural boiling at moderate to burnout heat fluxes, the boiling pattern with surfactant is entirely different than for pure water. Instead of forming a steam blanket, the surface is completely covered by small bubbles which slowly grow in unison and suddenly collapse, leaving the entire surface free of bubbles. This process of growth and collapse repeats itself at a frequency which increases with the heat flux. This pattern is essentially the same as that observed by Frost and Kippenhan [11] in forced-convection boiling. The large number of nucleation sites results apparently from the decreased surface tension which enables essentially all sites to become active simultaneously at a very low superheat. Since $\partial\sigma/\partial T$ is also smaller, there is almost no driving force for bubble coalescence. According to Frost and Kippenhan the collapse of the bubbles occurs when the supply of trapped liquid between the bubbles is completely exhausted through evaporation.

To determine the effect of the surfactant on heat transfer, several experiments were conducted, with and without surfactant, at the same surface heat fluxes and bulk temperatures. It was found that at low heat fluxes the resistance to heat transfer was higher with the surfactant. For example, $T_0 - T_{sat}$ was found to be 15 deg C and 9 deg C with and without surfactant respectively for $q = 3.54 \times 10^4$ W/m$^2$ and $T_B = 71.5$ deg C. On the other hand, the surfactant substantially decreased the resistance near the burnout limit. For $q = 12.56 \times 10^4$ W/m$^2$ and $T_B \simeq 88$ deg C, $T_0 - T_{sat}$ was found to be only 19 deg C with the 0.6 percent FC-176 solution compared to 27 deg C for pure

water. At high heat fluxes with pure water, the steam blanket covers most of the heater surface while the remainder is intensively cooled by Marangoni flow and the periodic sweeping of the surface by the steam blanket. Apparently this is a less efficient cooling mechanism than the periodic collapse of a large population of small bubbles on the surface for water with surfactant. As the heat flux decreases, the latter mechanism becomes less effective because the frequency of collapse of the bubble population decreases, and the former mechanism becomes relatively more effective.

## Acknowledgments

This investigation was supported by the National Research Council of Canada. The initial work was conducted at Professor Grigull's laboratory in Munich, Germany; the greater portion was the subject of a Master of Applied Science thesis by the first author. Our thanks to Professors W. Rohsenow and I. Glassman for helpful discussions and to Mr. R. Kaptein for his assistance with the experiments.

## References

1 Trefethen, L., "Surface Tension in Fluid Mechanics," Educ. Services Inc. for Nat. Comm. Fluid Mech. Films, 1964.

2 Scriven, L. E., and Sternling, C. V., "The Marangoni Effects," *Nature*, Vol. 187, 1960, pp. 186–188.

3 Kenning, D. B. R., "Two-Phase Flow with Nonuniform Surface Tension," *Applied Mechanics Reviews*, Vol. 21, No. 11, 1968, pp. 1101–1111.

4 Tefethen, L., "Dropwise Condensation and the Possible Importance of Circulation within Drops Caused by Surface Tension Variation," General Electric Co. Report 58GL47, 1958.

5 Lorenz, J. J., and Mikic, B. B., "The Effect of Thermocapillary Flow on Heat Transfer in Dropwise Condensation," JOURNAL OF HEAT TRANSFER, TRANS. ASME, Series C, Vol. 92, No. 1, Feb. 1970, pp. 46–52.

6 Gaddis, E. S., "The Thermal Equilibrium of a Vapor Bubble on a Heated Solid Surface," PhD thesis, Manchester University, Manchester, England, 1968.

7 Raithby, G. D., and Huplik, V., "Analysis of Thermocapillary Flow Around a Hemispherical Bubble," Department of Mechanical Engineering Technical Note 14, University of Waterloo, Waterloo, Canada, Oct. 1970.

8 Ishigai, S., Inoue, K., Kiwaki, Z., and Inai, T., "Boiling Heat Transfer from a Flat Surface Facing Downward," *Proceedings of the 1961–1962 International Heat Transfer Conference*, Boulder, Colo., pp. 224–229.

9 McGrew, J. L., Bamford, F. L., and Rehm, T. R., "Marangoni Flow: An Additional Mechanism in Boiling Heat Transfer," *Science*, Vol. 153, 1966, pp. 1106–1107.

10 Birkebak, R. C., and Abdul Kabir, A., "Heat Transfer by Natural Convection from the Lower Side of Finite Horizontal, Heated Surface," *Proceedings of 4th International Heat Transfer Conference*, 1970, Paper NC 2.2.

11 Frost, W., and Kippenhan, C. J., "Bubble Growth and Heat-Transfer Mechanisms in the Forced Convection Boiling of Water Containing a Surface Active Agent," *International Journal of Heat and Mass Transfer*, Vol. 11, 1967, pp. 931–949.

12 *CRC Handbook of Chemistry and Physics*, 51st ed., The Chemical Rubber Co., 1970–1971, p. F.30.

A. ALKIDAS
Graduate Research Assistant.

P. DURBETAKI
Associate Professor.
Mem. ASME

School of Mechanical Engineering,
Georgia Institute of Technology,
Atlanta, Ga.

# Stagnation-Point Heat Transfer: The Effect of the First Damköhler Similarity Parameter

*The present study considers the heat interaction between a combustible mixture and a constant-temperature surface near the stagnation region of a blunt body. The steady-state governing equations have been solved numerically for the case of* Le = *1. A second-order Arrhenius law is assumed to describe the chemical kinetics of the mixture. The first Damköhler similarity parameter is shown to critically influence the surface heat transfer. The parameter represents a measure of the convective time to the chemical time.*

## Introduction

Similarity considerations in the field of aerothermochemistry [1, 2][1] reveal the existence of two dimensionless groups in addition to the well-known dimensionless parameters obtained for nonreactive mixtures. These two parameters, the first Damköhler number, $D_I$, and the second Damköhler number, $D_{II}$, are characteristic of the chemical processes in the flow field. The parameter $D_I$ represents the ratio of the convective time to the chemical time, while the parameter $D_{II}$ represents the ratio of the heat addition by chemical reaction to the heat addition associated with the convection of enthalpy.

In chemically reacting flows the transition between the two limiting states of "frozen" flow and equilibrium flow can be described by the first Damköhler number. For $D_I \gg 1$ the chemical reaction time is much faster than the residence time of the gas particles, and the system is considered to exist in thermodynamic equilibrium. On the other hand, for $D_I \ll 1$ the convection time is much faster than the chemical time and the state of the system is "frozen." The degree of reactivity of chemically reacting flows past solid boundaries is directly related to the surface heat-transfer rates to and from the boundaries, and consequently it is important to study the effect of the first Damköhler number on the surface heat-transfer rate.

Stagnation flows in practical applications are important due to the fact that the stagnation region encounters the maximum local heat-transfer rate. A considerable amount of research has been carried out during the last two decades on stagnation flows dealing with heat transfer of reactive mixtures. Most of the work has been associated with the dissociation or recombination processes. Lees [3] studied the laminar heat-transfer problem in dissociated air where he considered the two limiting cases of "frozen" and equilibrium flow. Fay and Riddell [4] analyzed the nonequilibrium stagnation-point heat transfer in dissociated air for both catalytic and noncatalytic surfaces. The work reported in the present paper represents an analysis concerning the surface heat-transfer rate of a combustible mixture near the stagnation point of a noncatalytic blunt body. An important aspect of this work contrasting with the above work is that the surface heat transfer in the current study shows a multiple transition from "frozen" to equilibrium state compared to the single transition curve obtained by Fay and Riddell. The multivalued nature of the problem was first demonstrated by Fendell [5, 6] who considered the problem of ignition and extinction of initially unmixed reactants. Chung et al. [7], using physical intuition, derived criteria by which the single and multiple transitions between "frozen" and equilibrium states are distinguished from each other. The recent works of Fay and Kemp [8], Blottner [9], and Fay and Kaye [10] represent further contributions in the field. The last two studies deal with the application of finite-difference numerical methods on the nonequilibrium boundary layers.

## Formulation of the Problem

**Flow Configuration.** A reacting mixture approaches the noncatalytic surface of an axisymmetric blunt body situated with its axis parallel to the oncoming flow. The temperature of the wall of the blunt body is maintained constant at $T_w$ and at a higher value than the temperature of the incoming gaseous stream, $T_e$. The schematic diagram in Fig. 1 illustrates the coordinate system employed in this study.

**Governing Equations.** The boundary-layer equations governing the flow of a reacting mixture near the stagnation region of a blunt body are [11]

[1] Numbers in brackets designate References at end of paper.

Contributed by the Heat Transfer Division of The American Society of Mechanical Engineers and presented at the AIChE-ASME Heat Transfer Conference, Denver, Colo., August 6–9, 1972. Manuscript received by the Heat Transfer Division June 23, 1971. Paper No. 72-HT-44.

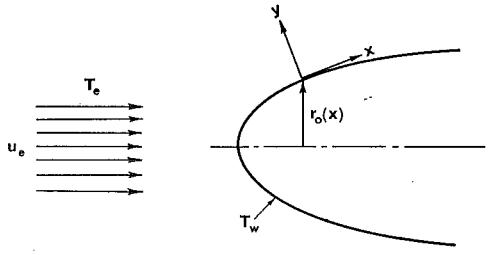


**Fig. 1 Coordinate system**

Momentum

$$(Cf'')' + ff'' = (1/2)[(f')^2 - (\rho_e/\rho)] \quad (1)$$

"Oxidizer" species conservation

$$\left(\frac{C}{\mathrm{Sc}}\alpha_O'\right)' + f\alpha_O' = (1/2)Y_{F,e}\mathrm{D_I}\nu_O W_O(1/\theta)\alpha_O\alpha_F e^{-E^*/\theta} \quad (2)$$

"Fuel" species conservation

$$\left(\frac{C}{\mathrm{Sc}}\alpha_F'\right)' + f\alpha_F' = (1/2)Y_{O,e}\mathrm{D_I}\nu_F W_F(1/\theta)\alpha_O\alpha_F e^{-E^*/\theta} \quad (3)$$

"Inert gas" species conservation

$$\left(\frac{C}{\mathrm{Sc}}\alpha_N'\right)' + f\alpha_N' = 0 \quad (4)$$

Energy

$$\left(\frac{C}{\mathrm{Pr}}\theta'\right)' + f\theta' = -(1/2)Y_{O,e}Y_{F,e}\mathrm{D_I}\mathrm{D_{II}}(1/\theta)\alpha_O\alpha_F e^{-E^*/\theta} \quad (5)$$

The primes denote differentiation with respect to the similarity variable $\eta$ which was used to transform the partial differential equations in the $x$, $y$ plane to the ordinary differential equations in the $s$, $\eta$ plane. These particular transformation coordinates were first introduced by Lees [3]. The overall continuity equation was satisfied by the introduction of a stream function defined as

$$\psi(s, \eta) = (2s)^{1/2}f(\eta) \quad (6)$$

The assumptions used in the formulation of the governing equations are:

(*a*) Laminar steady-state flow.
(*b*) Boundary-layer approximations valid.
(*c*) Diffusion velocity given by Fick's law

$$\mathbf{V}_i = -D\nabla \ln Y_i \quad (7)$$

(*d*) Specific-heat coefficient of all species is the same and equal to a constant, i.e., $c_{p,i} = c_p = c_{p,e}$.
(*e*) Eckert number much smaller than unity, i.e., low-speed flow.
(*f*) Radiation is negligible.
(*g*) Four species exist in the boundary layer: fuel, oxidizer, inert gases, and products.
(*h*) The kinetics of the mixture is represented by one-step chemical reaction and the reaction rate is given by a second-order Arrhenius kinetic expression of the form

$$\omega = B\rho^2 Y_O Y_F \exp(-E/RT) \quad (8)$$

where

$$\omega = -\frac{\omega_O}{\nu_O W_O} = -\frac{\omega_F}{\nu_F W_F} = \frac{\omega_P}{\nu_P W_P} \quad (9)$$

In a multicomponent reacting mixture, neglecting radiant heat transfer, the heat-transfer vector is given by

$$\mathbf{q} = -k\nabla T + \rho\sum_i h_i Y_i \mathbf{V}_i + RT \times \sum_{i=1}^{N}\sum_{j=1}^{N}\left(\frac{X_j D_{T,i}}{W_i D_{ij}}\right)(\mathbf{V}_i - \mathbf{V}_j) \quad (10)$$

Using assumptions *b* and *c*, and neglecting thermal diffusion, equation (10) becomes

$$q = -k\left(\frac{\partial T}{\partial y}\right) - \rho D\sum_i h_i\left(\frac{\partial Y_i}{\partial y}\right) \quad (11)$$

Next, employing the relation

$$d\eta = \left(\frac{2a}{\rho_e\mu_e}\right)^{1/2}\rho dy \quad (12)$$

we obtain

$$q = -(2a\rho_e\mu_e)^{1/2}\frac{c_p T_e C}{\mathrm{Pr}}\left(\theta' + \frac{\mathrm{Le}}{c_p T_e}\sum_i h_i Y_{i,e}\alpha_i'\right) \quad (13)$$

## Nomenclature

$a$ = coefficient of the potential flow velocity
$B$ = overall frequency factor
$C$ = $\rho\mu/\rho_e\mu_e$
$c_p$ = specific heat at constant pressure
$D$ = mass diffusivity
$D_{ij}$ = binary mass diffusivity for species pair $i - j$
$D_{T,i}$ = thermal diffusivity for species $i$
$\mathrm{D_I}$ = Damköhler's first dimensionless group, $B\rho_e/a$
$\mathrm{D_{II}}$ = Damköhler's second dimensionless group, $q^\circ/c_{p,e}T_e\nu_F W_F$
$\overline{\mathrm{D}}_\mathrm{I}$ = $(1/2)\nu_0 W_0 Y_{F,e}\mathrm{D_I}$
$\overline{\mathrm{D}}_{\mathrm{I},e}$ = critical first Damköhler number for extinction
$\overline{\mathrm{D}}_{\mathrm{I},i}$ = critical first Damköhler number for ignition
$\overline{\mathrm{D}}_\mathrm{II}$ = $\mathrm{D_{II}}Y_{F,e}/\nu_F W_F$
$E$ = activation energy
$E^*$ = $E/RT_e$, dimensionless activation energy
$f'(\eta)$ = dimensionless velocity, $u/u_e$
$h$ = specific enthalpy
$k$ = thermal conductivity
Le = Lewis number, $\rho_e D c_{p,e}/k_e$
$n_e$ = dimensionless "stoichiometry" measure, equation (31)
Nu = Nusselt number, $q_w x/k_w(T_e - T_w)$
Pr = Prandtl number, $c_{p,e}\mu_e/k_e$
$\mathbf{q}$ = heat-flux vector
$q^\circ$ = standard heat of reaction
$r_0$ = cylindrical radius of surface
$R$ = universal gas constant
Re = Reynolds number, $u_e x\rho_w/\mu_w$
$s$ = $\int_0^x \rho_e u_e \mu_e r_0^2 dx$
Sc = Schmidt number, $\mu_e/\rho_e D$
$T$ = temperature
$u, v$ = velocity coordinates
$W$ = molecular weight
$X$ = mole fraction
$x$ = distance along surface
$y$ = distance normal to surface
$Y$ = mass fraction
$\alpha$ = $Y_i/Y_{i,e}$
$\beta$ = defined by equation (22)
$\eta$ = $(\rho_e u_e r_0)/(2s)^{1/2}\int_0^y (\rho/\rho_e)dy$
$\theta$ = $T/T_e$
$\mu$ = viscosity
$\nu$ = stoichiometric coefficient
$\xi$ = transition criterion, equation (32)
$\rho$ = density
$\psi$ = stream function, equation (6)
$\omega$ = reaction rate of combustible component, equation (8)

### Subscripts

$e$ = free stream
$F$ = fuel
$i$ = $i$th species
$N$ = inert gas
$O$ = oxidant
$P$ = products
$w$ = at the wall surface

For low-speed flow the Nusselt number can be defined as

$$\mathrm{Nu} = q_w x / k_w (T_e - T_w) \tag{14}$$

Then from equation (13)

$$\frac{\mathrm{Nu}}{(\mathrm{Re})^{1/2}} = -(2C_w)^{1/2}\left(\frac{1}{1-\theta_w}\right)\left[\theta' + \frac{\mathrm{Le}}{c_{p,w}T_e}\sum_i h_i Y_{i,e}\alpha_i'\right] \tag{15}$$

where

$$\mathrm{Re} = \frac{u_e x}{\mu_w/\rho_w} \tag{16}$$

The boundary conditions for this problem are

$$\text{at } \eta = 0: \quad f = 0 \quad f' = 0 \quad \theta = \theta_w$$
$$\alpha_i' = 0 \qquad \text{for } i = O, F, N, P \tag{17a}$$

$$\text{at } \eta \to \infty: \quad f' \to 1 \quad \theta \to 1$$
$$\alpha_i \to 1 \qquad \text{for } i = O, F, N, P \tag{17b}$$

## Method of Solution

With the aid of equation (9), the conservation-of-species equations (2) and (3) can be combined and readily integrated to give

$$\alpha_O = 1 - \frac{\nu_O W_O Y_{F,e}}{\nu_F W_F Y_{O,e}}(1 - \alpha_F) \tag{18}$$

The solution of equation (4) with the prescribed conditions yields

$$\alpha_N = 1 \tag{19}$$

A further reduction of the nonlinear equations to be solved is achieved through the use of the following additional assumptions:

($i$) Lewis number is equal to unity.
($j$) $C = 1$, i.e., $\rho\mu = \rho_e\mu_e$.
($k$) The velocity profile $f(\eta)$ is given by the incompressible form of the momentum equation.

Assumptions $i$ and $j$ are a usual practice in combustion theory. Assumption $k$ is used to make it possible to decouple the momentum from the energy and conservation-of-species equations. With the wall temperature $\theta_w$ selected to be 2.0 and 2.5 in the present study, only in the region near equilibrium does this last assumption introduce an appreciable error. Use of this assumption is therefore justified by the fact that the multivalued nature of the nonlinear differential equations can be indicated without resorting to an excessive numerical effort. Excessive numerical effort is not justified because of the inaccuracies introduced by other modeling assumptions such as the single-step reaction.

Equations (3) and (5) can now be combined with the use of assumption $i$ to yield the following linear differential equation:

$$\left(\alpha_F + \frac{\theta}{\bar{\mathrm{D}}_{\mathrm{II}}}\right)'' + \mathrm{Pr}\, f\left(\alpha_F + \frac{\theta}{\bar{\mathrm{D}}_{\mathrm{II}}}\right)' = 0 \tag{20}$$

where

$$\bar{\mathrm{D}}_{\mathrm{II}} = \mathrm{D}_{\mathrm{II}}\frac{Y_{F,e}}{\nu_F W_F} \tag{21}$$

Let

$$\beta \equiv [(\alpha_F + \theta/\bar{\mathrm{D}}_{\mathrm{II}}) - (\alpha_F + \theta/\bar{\mathrm{D}}_{\mathrm{II}})_w]/[(\alpha_F + \theta/\bar{\mathrm{D}}_{\mathrm{II}})_e - (\alpha_F + \theta/\bar{\mathrm{D}}_{\mathrm{II}})_w] \tag{22}$$

and equation (20) reduces to

$$\beta'' + \mathrm{Pr}\, f\beta' = 0 \tag{23}$$

with boundary conditions

$$\beta(0) = 0 \quad \text{and} \quad \beta(\infty) = 1 \tag{24}$$

For a noncatalytic surface, $(dY_i/d\eta)_w = 0$, the gradient of $\beta$ at the wall is related to the surface heat transfer by the relation

$$q_w = -(2a\rho_e\mu_e)^{1/2}\frac{c_p T_e}{\mathrm{Pr}}\left[1 - \theta_w + \bar{\mathrm{D}}_{\mathrm{II}}(1 - \alpha_{F,w})\right]\left(\frac{d\beta}{d\eta}\right)_w \tag{25a}$$

or

$$\frac{\mathrm{Nu}}{(\mathrm{Re})^{1/2}} = -\frac{(2)^{1/2}}{(1-\theta_w)}[1 - \theta_w + \bar{\mathrm{D}}_{\mathrm{II}}(1 - \alpha_{F,w})]\left(\frac{d\beta}{d\eta}\right)_w \tag{25b}$$

It was discussed in the Introduction that the surface heat transfer varies with the degree of reactivity of the system. The two extreme cases, then, are given for equilibrium flow as $\mathrm{D_I} \to \infty$ by

$$\frac{\mathrm{Nu}}{(\mathrm{Re})^{1/2}} = -\frac{(2)^{1/2}}{(1-\theta_w)}(1 - \theta_w + \bar{\mathrm{D}}_{\mathrm{II}})\left(\frac{d\beta}{d\eta}\right)_w \tag{26}$$

and for "frozen" flow as $\mathrm{D_I} \to 0$ by

$$\frac{\mathrm{Nu}}{(\mathrm{Re})^{1/2}} = -(2)^{1/2}\left(\frac{d\beta}{d\eta}\right)_w \tag{27}$$

Of greatest interest for this analysis are the values of surface heat transfer at the intermediate values of $\mathrm{D_I}$. These results can be achieved for each given value of $\mathrm{D_I}$ by simultaneously solving equations (1), (5), and (23). We define

$$\bar{\mathrm{D}}_{\mathrm{I}} = \tfrac{1}{2}\nu_O W_O Y_{F,e}\mathrm{D_I} \tag{28}$$

and with assumptions $i$, $j$, and $k$ the differential equations that remain to be solved are

$$f''' + ff'' = \tfrac{1}{2}[(f')^2 - 1] \tag{29}$$

$$\beta'' + \mathrm{Pr}\, f\beta' = 0 \tag{23}$$

and

$$\theta'' + \mathrm{Pr}\, f\theta' = -\mathrm{Pr}\,\bar{\mathrm{D}}_{\mathrm{I}}\bar{\mathrm{D}}_{\mathrm{II}}\left(\frac{1}{\theta}\right)(n_e + \alpha_F)\alpha_F e^{-E^*/\theta} \tag{30}$$

where

$$n_e = \frac{Y_{O,e}\nu_F W_F}{Y_{F,e}\nu_O W_O} - 1 \tag{31}$$

The dimensionless number $n_e$ represents a measure of the "stoichiometry" of the reactants. For $n_e = 0$ the mixture is in stoichiometric composition, while for $n_e > 0$ the mixture is lean and for $n_e < 0$ the mixture is rich.

Subject to assumption $k$, the momentum equation and the $\beta$ equation are independent of the energy equation. Consequently equations (29) and (23) can be solved independently of equation (30) and their solution is then used to obtain a numerical solution of equation (30) for different values of $\bar{\mathrm{D}}_{\mathrm{I}}$.

## Numerical Procedure

To carry out the numerical calculations, the momentum equation (29), the $\beta$ equation (23), and the energy equation (30) were integrated by Gill's modified Runge–Kutta fourth-order method. The solution of equation (29) can be found elsewhere [12]. The $\beta$ equation, being linear and independent of the energy equation, was solved simultaneously with equation (29) using the method of "particular solution" [13, 14]. The computed value of $\beta'(0) = 0.4806$ is in excellent agreement with the result obtained using Sibulkin's [15] interpolation formula, $\beta'(0) = 0.4783$. For the

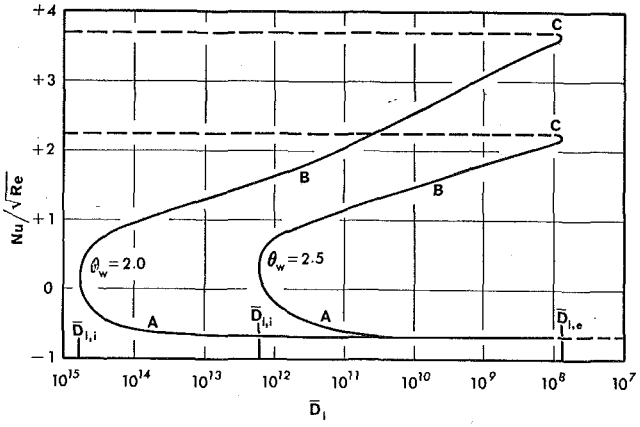


**Fig. 2 Dependence of the surface heat transfer on the first Damköhler number**

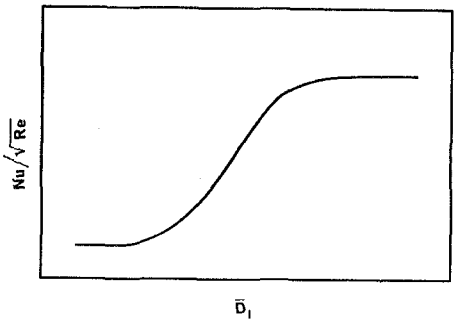


**Fig. 3 Schematic representation of a single-transition curve**

final integration of the governing equations, only the energy equation remained as a boundary-value problem.

At a given value of $\bar{D}_I$ the energy equation was integrated for $\theta(0) = \theta_w$ and an assumed value of $\theta'(0)$. The resulting value of $\theta(\eta = 7.0)$ was then compared to the true boundary condition of $\theta(\infty) = 1$. The temperature gradient at the wall was subsequently adjusted and the integration was repeated until the desired accuracy was achieved in the temperature gradient at $\eta = 7.0$.

## Results and Discussion

The numerical computations of the surface heat transfer were carried out using the following values of dimensionless parameters and boundary conditions for the governing equations:

$$\text{Pr} = 0.74 \quad E^* = 67.1366 \quad \bar{D}_{II} = 6.44518$$

$$n_e = 0.0 \quad \theta_w = 2.0 \text{ and } 2.5$$

These values correspond to the case of an incoming stoichiometric mixture of methane and air at a temperature $T_e = 300$ deg K and an activation energy of 40 kcal/g-mole.

The established results of $\text{Nu}/(\text{Re})^{1/2}$ for the range of $\bar{D}_I$ values encompassing the transition from "frozen" to equilibrium flow are displayed in Fig. 2 for the two $\theta_w$ values of 2.0 and 2.5. Both curves can be divided into three regions based on the value of the surface heat transfer: (*a*) region of no reaction where the value of $\text{Nu}/(\text{Re})^{1/2}$ is minimum, (*b*) region of intense reaction where the value of $\text{Nu}/(\text{Re})^{1/2}$ is maximum, and (*c*) central region where the surface heat transfer is multivalued. In the central region, $\text{Nu}/(\text{Re})^{1/2}$ can have one of three values depending upon whether the state of the mixture at the wall lies on the "frozen" flow branch A, the equilibrium flow branch C, or the intermediate branch B (see also Fig. 4).

Two critical values of the Damköhler number specified as $\bar{D}_{I,e}$ and $\bar{D}_{I,i}$ are used to separate the three regions discussed above. The critical Damköhler number $\bar{D}_{I,e}$ establishes the boundary between the no-reaction zone and the multivalued region, while the critical Damköhler number $\bar{D}_{I,i}$ establishes the boundary between the intense-reaction zone and the multivalued region. In combustion theory the terms $\bar{D}_{I,e}$ and $\bar{D}_{I,i}$ can be referred to as the critical ignition and extinction first Damköhler numbers, respectively.

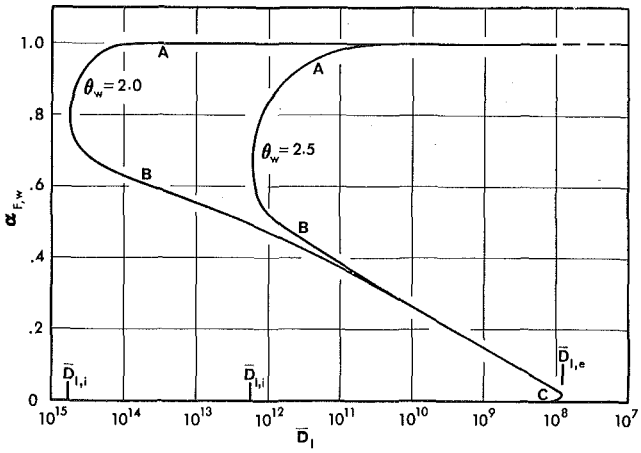


**Fig. 4 Effect of the first Damköhler number on the fuel mass fraction at the wall**

**Table 1 Critical Damköhler numbers at two wall temperatures**

| $\theta_w$ | $\bar{D}_{I,i}$ | $\bar{D}_{I,e}$ |
|---|---|---|
| 2.0 | $5.6 \times 10^{14}$ | $7.35 \times 10^{7}$ |
| 2.5 | $1.55 \times 10^{12}$ | $7.35 \times 10^{7}$ |

Although a stability analysis was not attempted for this work, it can be postulated that the solution of the governing equations corresponding to branch B on the curves is unstable [5]. Therefore, if the mixture is initially identified by a value of $\bar{D}_I < \bar{D}_{I,e}$ and this Damköhler number, $\bar{D}_I$, is increased (by decreasing the free-stream velocity of the mixture) to bring the mixture to the region $\bar{D}_{I,e} < \bar{D}_I < \bar{D}_{I,i}$, then the surface heat transfer will be given by its value on branch A. On the other hand, if the mixture is initially identified by a value of $\bar{D}_I > \bar{D}_{I,i}$ and the Damköhler number is now decreased to move the mixture in the region $\bar{D}_{I,i} > \bar{D}_I > \bar{D}_{I,e}$, the surface heat transfer in this instance will be given by its value on branch C.

The values of the critical Damköhler numbers for the two wall temperatures considered are given in Table 1. This comparison indicates that $\bar{D}_{I,i}$ is a strong function of the wall temperature $\theta_w$, and that $\bar{D}_{I,e}$ is practically independent of $\theta_w$.

On branch A of the curves, for a range of values of $\bar{D}_I$ up to $10^{10}$, the quantity $\text{Nu}/(\text{Re})^{1/2}$ is independent of the first Damköhler number and the wall temperature. This complies with the familiar Nusselt–Reynolds type equation for nonreactive heat transfer where $\text{Nu}/(\text{Re})^{1/2} = \phi(\text{Pr})$. On the other hand, for branch C, although the parameter $\text{Nu}/(\text{Re})^{1/2}$ is independent of $\bar{D}_I$, it is very much dependent on the wall temperature $\theta_w$.

The effect of the wall temperature on $\bar{D}_{I,i}$ is of practical importance. For a given fuel mixture, since $\bar{D}_{I,i} \propto 1/u_e$, in the case of $\theta_w = 2.5$ the free-stream velocity of the mixture may be increased by about three orders of magnitude beyond the case of $\theta_w = 2.0$, while the state of the mixture remains in equilibrium. In other words, combustion may take place at free-stream velocities three orders of magnitude higher for $\theta_w = 2.5$ than it will for $\theta_w = 2.0$.

An important aspect of the work presented here is establishment of the existence of a multiple transition from the "frozen" to the equilibrium state, compared to the single transition obtained by Fay and Riddell [4]. A sketch of the single transition curve is shown in Fig. 3. The difference between the shape of the curves in Fig. 2 and in Fig. 3 is due to the chemical source term in the governing equations. In describing the recombina-

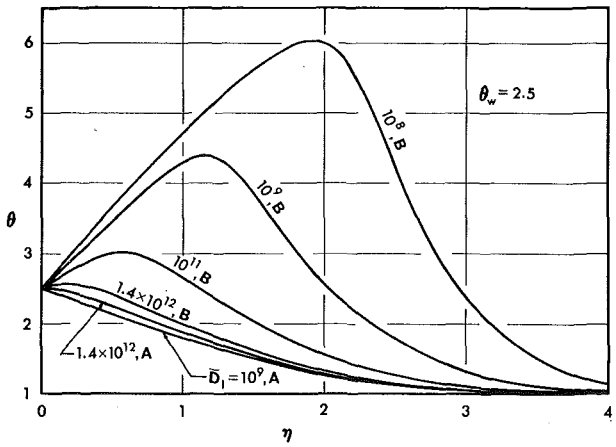


Fig. 5 Temperature profiles

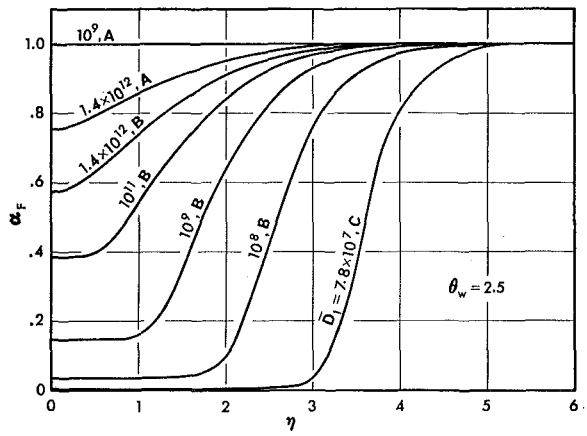


Fig. 6 Concentration profiles

tion rate of dissociated air Fay and Riddell assume a source term which is a function of $\theta^{-3.5}$, while in the present work the temperature dependence of the source term is of the form $(1/\theta)\exp(-E^*/\theta)$. The latter expression in the governing equations can yield a transition region which is either single-valued or multi-valued. The type of transition that can result depends on the chemical and thermal parameters of the flow. Chung et al. [7], in their study on ignition and extinction characteristics of diffusion flames, presented a criterion by which the two types of transition can be differentiated. In our notation their criterion becomes

$$\xi = \left(\frac{1+\bar{D}_{II}}{\theta_w}\right)^{\nu_F+\nu_O-1} \exp\left[-E^*\left(\frac{1}{\theta_w} - \frac{1}{\bar{D}_{II}+1}\right)\right] \times 10^4 \tag{32}$$

When $\xi \ll 1$ a multi-valued transition is expected to occur, and with $\xi \gg 1$ the transition is expected to be single-valued. The two cases considered in the present work with $\theta_w = 2.0$ and 2.5 each have a value of $\xi \simeq 0$ $(10^{-6})$.

The normalized fuel mass fractions at the wall, as a function of the first Damköhler similarity parameter, are displayed in Fig. 4 for the two wall temperatures considered. In a similar manner to the curves in Fig. 2, these plots are also divided into the three regions discussed earlier. At the same time both of the critical Damköhler numbers are specified. In the "frozen" region, the wall mass fraction of the fuel is unity, signifying no fuel consumption. In the equilibrium region, the fuel wall mass fraction is zero, signifying consumption of all the fuel at the wall, and consequently verifying that the mixture has reacted to complete combustion.

The temperature distributions adjacent to the wall and extending toward the free stream are shown in Fig. 5 for different magnitudes of the first Damköhler number. For branch A of the curves in Figs. 2 and 4, the maximum temperature is at the wall, signifying the absence of reaction until the critical ignition first Damköhler number is reached. On branch B, on the other hand, a maximum temperature greater than the wall temperature exists at a location away from the wall, illustrating the establishment of a reaction region. With decreasing first Damköhler numbers the reaction region moves farther away from the solid wall.

Finally, Fig. 6 represents the normalized fuel-concentration profiles. The important fact illustrated by these curves is that the concentration remains constant between the wall and the reaction zone. It is only through the reaction zone where the concentration changes occur, and they reach the free-stream concentrations on the upstream side of the reaction zone.

## Summary

1 For a combustible mixture at the stagnation region the surface heat-transfer rate represented by the parameter $\mathrm{Nu}/(\mathrm{Re})^{1/2}$ is multi-valued for a range of the first Damköhler similarity parameter.

2 Two critical first Damköhler numbers $\bar{D}_{I,e}$ and $\bar{D}_{I,i}$ were defined and these were used as criteria to classify the reactive state of the mixture.

3 The extinction Damköhler number $\bar{D}_{I,e}$ was found to be independent of the wall temperature $\theta_w$.

4 For the range of values of $\bar{D}_I$ up to $10^{10}$ the parameter $\mathrm{Nu}/(\mathrm{Re})^{1/2}$ is independent of the first Damköhler number $\bar{D}_I$ and the wall temperature $\theta_w$.

## References


1 Damköhler, G., "Einflüsse der Strömung, Diffusion und der Wärmeübertragung auf die Leisturng von Reactionsöfen," *Zeitsch. Elektrochem.*, Vol. 42, 1936, pp. 846–862.

2 Penner, S. S., "Similarity Analysis for Chemical Reactors and the Scaling of Liquid Fuel Rocket Engines," *Combustion Research Reviews*, Butterworth's, London, England, 1955, pp. 140–162.

3 Lees, L., "Laminar Heat Transfer over Blunt-Nosed Bodies at Hypersonic Flight Speed," *Jet Propulsion*, Vol. 26, 1956, pp. 259–268.

4 Fay, J. A., and Riddell, F. R., "Theory of Stagnation Point Heat Transfer in Dissociated Air," *Journal of the Aeronautical Sciences*, Vol. 25, 1958, pp. 73–85.

5 Fendell, F. E., "Ignition and Extinction in Combustion of Initially Unmixed Gaxes," PhD thesis, Harvard University, Cambridge, Mass., 1964.

6 Fendell, F. E., "Ignition and Extinction in Combustion of Initially Unmixed Reactants," *Journal of Fluid Mechanics*, Vol. 21, 1965, pp. 281–303.

7 Chung, P. M., Fendell, F. E., and Holt, J. F., "Nonequilibrium Anomalies in the Development of Diffusion Flames," *AIAA Journal*, Vol. 4, 1966, pp. 1020–1026.

8 Fay, J. A., and Kemp, J. H., "Theory of Stagnation Point Heat Transfer in Partially Ionized Diatomic Gas," *AIAA Journal*, Vol. 1, 1963, pp. 2741–2751.

9 Blottner, F. G., "Chemical Nonequilibrium Boundary Layer," *AIAA Journal*, Vol. 2, 1964, pp. 232–240.

10 Fay, J. A., and Kaye, H., "A Finite Difference Solution of Similar Nonequilibrium Boundary Layers," *AIAA Journal*, Vol. 5, 1967, pp. 1949–1953.

11 Alkidas, A., and Durbetaki, P., "Ignition Characteristics of a Stagnation Point Combustible Mixture," *Combustion Science and Technology*, Vol. 3, 1971, pp. 187–194.

12 Goldstein, S., ed., *Modern Developments in Fluid Mechanics*, Vol. 1, Dover Publications, New York, N. Y., 1965.

13 Heideman, J. C., "Use of the Method of Particular Solutions in Nonlinear, Two-Point Boundary-Value Problems; Part I—Uncontrolled Systems; Part II—Controlled Systems," Aero-Astronautics Reports No. 50 and 51, Rice University, Houston, Texas, 1968.

14 Lee, E. S., Chen, S. S., Fan, L. T., and Hwang, C. L., "Application of Quasilinearization to the Solution of Non-linear Differential Equations," *Kansas State University Bulletin*, Special Report No. 78, Vol. 51, 1967.

15 Sibulkin, M., "Heat Transfer near the Forward Stagnation Point of a Body of Revolution," *Journal of the Aeronautical Sciences*, Vol. 19, 1952, pp. 570–571.

C. LIMPIYAKORN
Graduate Student.

L. BURMEISTER
Associate Professor.
Mem. ASME

Department of Mechanical Engineering,
University of Kansas,
Lawrence, Kan.

# The Effect of Thermal Radiation on Transient Vaporization of a Saturated Liquid at a Constant-Temperature Plate

*An analysis of the effect of thermal radiation on transient vaporization of a saturated liquid at a constant-temperature plate is presented. The realistic assumption of a constant-vapor-density–thermal-conductivity product gives results identical to the case in which all properties are constant. If radiation is neglected, identical coincidence with classical analytical results is found. With radiation considered, numerical solutions are obtained which are satisfactorily compared with data from the literature.*

## Introduction

Problems involving heat transfer with a change of phase have attracted the attention of experimental and analytical investigators for some time. An important and interesting part of these problems is determination of the instantaneous position of the interface between the two phases. The treatise of Carslaw and Jaeger [1][1] presents solutions for slab, cylinder, and sphere geometries which show that the interfacial position varies as the square root of time for cases in which each phase is of constant, though not necessarily equal, density.

More recently Hamill and Bankoff [2] numerically solved a change-of-phase problem in which one phase's density was not constant. A downward-facing plate immersed in a large pool of stagnant and saturated liquid suddenly attains and thereafter maintains a temperature much higher than its initial liquid temperature. As a result, a vapor film forms between the plate and the saturated liquid. The vapor density was variable, related to temperature by the perfect-gas relation, while the vapor thermal conductivity and pressure were assumed constant. They found that the thickness of the vapor film in this variable-density case is also proportional to the square root of the elapsed time, but their constant of proportionality is given by a relation different from that reported by Carslaw and Jaeger.

Hamill and Bankoff did not account for the temperature-dependence of vapor thermal conductivity. Neither did they account for thermal radiation from the hot surface to the liquid-vapor interface. Although the first assumption would not be expected to introduce large error, the second one could at large times. Then, the thick vapor film could decrease conductive heat flow into the interface to the point that radiative heat transfer would play an important part in the vaporization of liquid. The influence of thermal radiation on steady film boiling was treated early by Bromley [3] and later by Sparrow [4], who demonstrated that water vapor was transparent at the temperatures of interest. Although they both showed that radiation was significant in some cases, it seems that no detailed analysis directly applicable to Hamill and Bankoff's problem has been published.

The purpose of the present work is twofold. First, it will be shown that, if thermal radiation is neglected, the more realistic assumption of a constant-vapor-density–thermal-conductivity product yields results identical to those of Carslaw and Jaeger. Second, the effect of thermal radiation will be assessed. Only a saturated liquid pool will be considered.

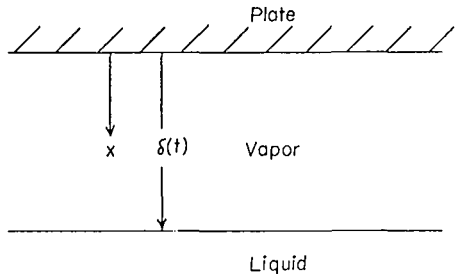


**Fig. 1 Physical configuration and coordinate system**

## Problem Formulation

As shown in Fig. 1, a very large downward-facing plate is immersed in a very large pool of saturated and stagnant liquid. The plate, initially at the liquid temperature, is suddenly raised to a much higher temperature which is thereafter maintained constant. The plate's new temperature being substantially greater than the liquid's boiling point, a film of vapor is formed

[1] Numbers in brackets designate References at end of paper.

Contributed by the Heat Transfer Division of The American Society of Mechanical Engineers and presented at the AIChE-ASME Heat Transfer Conference, Denver, Colo., August 6–9, 1972. Manuscript received by the Heat Transfer Division July 20, 1971. Paper No. 72-HT-43.

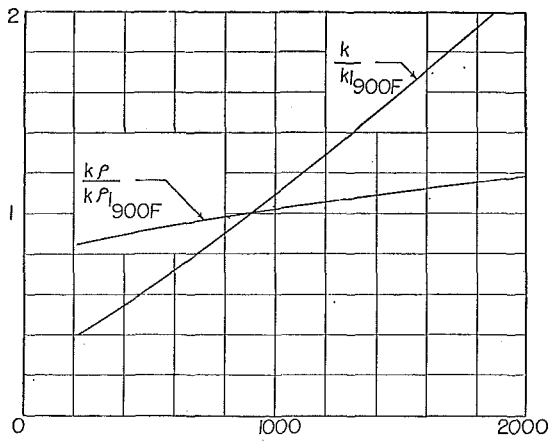


**Fig. 2 Dependence of $k$ and $k\rho$ upon temperature for water vapor at 1 atm**

between the plate and the liquid. Heat flows into the liquid–vapor interface by conduction through the vapor and by thermal radiation from the plate. Laminar flow is presumed. The temperature distribution in the vapor film and the instantaneous position of the liquid–vapor interface are to be determined.

The one-dimensional forms of the describing equations are the continuity equation

$$\partial\rho/\partial t + \partial(\rho u)/\partial x = 0 \tag{1}$$

and the energy equation

$$\rho C_p(\partial T/\partial t + u\partial T/\partial x) = \partial(k\partial T/\partial x)/\partial x \tag{2}$$

for $0 \leq x \geq \delta$, assuming that pressure is constant and that viscous dissipation is negligible, where $\delta$ is the vapor-film thickness.

Boundary conditions imposed on the vapor are that at the constant temperature and impermeable plate

$$T(0, t) = T_w \tag{3}$$

$$u(0, t) = 0 \tag{4}$$

while at the liquid–vapor interface

$$T(\delta, t) = T_s \tag{5}$$

and

$$q_r - k\partial T(\delta, t)/\partial x = \Omega d\left(\int_0^\delta \rho dx\right)/dt \tag{6}$$

A Lagrangian transformation is effected by setting $m = \int_0^x \rho dx$ which, in conjunction with the continuity equation (1) and the impermeable-plate condition of equation (4), removes the convective terms from the energy equation. Additionally letting $y = m/\bar{M}$, where $\bar{M} = \int_0^\delta \rho dx$ represents the total vapor mass per unit area and $y$ represents a dimensionless position in the film, gives the energy equation (2) in the form

$$\bar{M}^2\partial T/\partial t = C_p^{-1}\partial(k\rho\partial T/\partial y)/\partial y + (y/2)(d\bar{M}^2/dt)\partial T/\partial y \tag{7}$$

Representation of the vapor as a perfect gas, $p = \rho RT$, points out the importance of the product $k\rho$ which appears in the transformed energy equation (7). Hamill and Bankoff assumed that $k$ was a constant, so that equation (7) was nonlinear in its second-order term and resulted in their solutions differing from those given by Carslaw and Jaeger. Fig. 2 shows that $k\rho$ is more accurately assumed to be a constant, as was done by Chapman and Rubesin [5] in their treatment of a variable-property laminar-boundary-layer problem.

With $k\rho$ and $C_p$ constant, equations (2)–(6) are found in their final dimensionless form as

$$M^2\partial\theta/\partial\tau = (\partial^2\theta/\partial y^2) + (y/2)(dM^2/d\tau)(\partial\theta/\partial y) \tag{8}$$

for $0 \leq y \leq 1$ with boundary conditions of

$$\theta(0, \tau) = 1 \tag{9}$$

$$\theta(1, \tau) = 0 \tag{10}$$

$$dM^2/d\tau = 2C[M - \partial\theta(1, \tau)/\partial y] \tag{11}$$

$$M(0) = 0 \tag{12}$$

Here $C = C_p(T_w - T_s)/\Omega$, $\theta = (T - T_s)/(T_w - T_s)$, $M = q_r\bar{M}/[k\rho(T_w - T_s)]$, and $\tau = q_r^2 t/[k\rho C_p(T_w - T_s)^2]$. The dimensionless time variable $\tau$ is recognizable as a Fourier number inasmuch as it is equivalent to $\alpha t/l^2$ where $l = k\Delta T/q_r$. The first term in parentheses on the right-hand side of equation (11) represents heat flow into the interface by thermal radiation, while the second term there represents conduction. If $M$ is small (a thin vapor film), radiation is negligible compared to conduction in the vaporization process at the interface. If $M$ is large on the other hand (a thick vapor film), radiation predominates over conduction.

The thickness of the vapor film $\delta$ is determined from the previously used transformation $m = \int_0^x \rho dx$. From this relation $dx = dm/\rho$, or, $dx = \bar{M}dy/\rho$. Introducing the perfect-gas equa-

## Nomenclature

$C$ = dimensionless parameter, $C = C_p(T_w - T_s)/\Omega$
$C_p$ = specific heat at constant pressure
erf $(t)$ = error function, erf $(t) = (2/\pi^{1/2})\int_0^t \exp(-z^2)dz$
$I$ = integral, $I = \int_0^1 \theta dy$
$k$ = thermal conductivity
$K$ = constant
$l$ = characteristic length, $l = k\Delta T/q_r$
$m$ = transformed distance from plate, $m = \int_0^x \rho dx$
$\bar{M}$ = mass per unit area in film, $\bar{M} = \int_0^\delta \rho dx$
$M$ = dimensionless mass per unit area in film, $M = q_r\bar{M}/[k\rho(T_w - T_s)]$
$p$ = pressure
$q$ = heat flux
$R$ = gas constant
$T$ = temperature
$t$ = time
$u$ = velocity
$x$ = distance from plate
$y$ = dimensionless transformed distance from plate, $y = m/\bar{M}$
$\alpha$ = thermal diffusivity, $\alpha = k/\rho C_p$
$\beta$ = parameter
$\Omega$ = latent heat of vaporization
$\delta$ = film thickness
$\Delta$ = finite difference of a quantity
$\epsilon$ = emissivity
$\eta$ = similarity variable, $\eta = Cyt^{1/2}/2$
$\theta$ = dimensionless temperature, $\theta = (T - T_s)/(T_w - T_s)$
$\rho$ = mass density
$\sigma$ = Stefan–Boltzmann constant, $\sigma = 0.1714 \times 10^{-8}$ Btu/hr-ft$^2$-deg R$^4$
$\tau$ = dimensioness time, $\tau = q_r^2 t/[k\rho C_p(T_w - T_s)^2]$

**Subscripts**

0 = initial value
$n$ = index
$N$ = largest value of index
$r$ = radiative quantity
$s$ = saturation value
$w$ = wall value

tion of state and integrating this last relation over the film thickness yields

$$\delta/\bar{M} = (R/p)\int_0^1 T dy \tag{13}$$

Manipulation of equation (13) gives

$$\delta/\bar{M} = (1/\rho_w - 1/\rho_s)I + 1/\rho_s \tag{14}$$

where $I = \int_0^1 \theta dy$. Equation (14) also enables computation of average vapor density $\bar{M}/\delta$.

## Solutions

**Radiation Neglected.** The case in which radiation can be neglected, $M \ll \partial\theta/\partial y$ in equation (11), is easily solved and is pertinent to a thin film. It is anticipated in such a circumstance that an equilibrium conduction-limited temperature profile exists so that $\partial\theta/\partial\tau = 0$ in equation (8). In other words, a similarity solution is then possible if $dM^2/d\tau = 4\beta^2$ as shown by Hamill and Bankoff. Equations (8)–(12) are then satisfied by

$$\theta = 1 - \text{erf}\,(\beta y)/\text{erf}\,(\beta) \tag{15}$$

with, from equation (11), $\beta$ related to $C$ by

$$\Pi^{1/2}\beta \exp(\beta^2)\,\text{erf}\,(\beta) = C \tag{16}$$

which are results identical to those of Carslaw and Jaeger. If $C$ is known, $\beta$ is determined from equation (16) to allow computation of $M^2 = 4\beta^2\tau$ (if $C$ is small, $C \approx 2\beta^2$). From equation (16), $I$ is obtained as

$$I = [1 - \exp(-\beta^2)]/[\Pi^{1/2}\beta\,\text{erf}\,(\beta)] \tag{17}$$

Conductive heat flux at the hot plate is found via

$$q = -k\frac{\partial T(0,t)}{\partial x}$$

to be

$$q/q_r = -\frac{\partial\theta(0,\tau)/\partial y}{M}$$

Introducing equation (15) into this result yields

$$q/q_r = 1/[2\,\text{erf}\,(\beta)\tau^{1/2}]$$

**Conduction Neglected at Interface.** If conduction is neglected, $M \gg \partial\theta/\partial y$ in equation (11), the effect of cold vapor blowing from the liquid–vapor interface toward the hot plate can be discerned. In particular, the results are applicable to a thick film.

With conduction at the interface neglected and a transparent vapor, the constant radiative heat flux absorbed at the interface should cause liquid to be vaporized at a constant rate. Equation (11) does indeed exhibit such a limiting behavior, giving

$$dM^2/d\tau = 2CM$$

from which it is found that

$$M = C\tau \tag{18}$$

Introducing the linear result of equation (18) into the energy equation (8) gives

$$C^2\tau^2\partial\theta/\partial\tau = (\partial^2\theta/\partial y^2) + C^2 y\tau(\partial\theta/\partial y) \tag{19}$$

Of course, equations (18) and (19) are accurate only for large times when the vapor film is of a thickness sufficient to render conductive heat flow into the interface negligible compared to radiation.

On physical grounds it is expected that the cold vapor blowing from the interface will progressively collapse the initial temperature profile closer and closer against the hot plate, leading to a very small temperature gradient at the interface. The region of substantial temperature variation then occupies but a small portion of the film; the film is reasonably approximated as being of infinite thickness. This understanding, together with the expected exponential decay of initial conditions, indicates that conditions at zero time and at the interface need not be rigorously satisfied to obtain an acceptable large-time solution.

Indeed, subject to the conditions that $\theta(y, 0) = 1 = \theta(0, \tau)$ and $\theta(\infty, \tau) = 0$, a similarity solution to equation (19) is

$$\theta = 1 - \text{erf}\,(\eta) \tag{20}$$

with $\eta = Cy\tau^{1/2}/[2(1 + K/\tau)^{1/2}]$. Note that $K$ is an arbitrary constant whose effect disappears when $\tau$ is large so that $\eta = Cy\tau^{1/2}/2$ in practical terms. Equation (20) also gives

$$I = \int_0^\infty \theta dy = 2/[C(\Pi\tau)^{1/2}] \tag{21}$$

and

$$q/q_r = 1/2\tau^{1/2}$$

The above last result agrees with that found when radiation is negligible and $\beta$ is large (rapid vaporization and large blowing).

**Numerical Method.** When radiation and conduction are both important, equations (8)–(12) must be solved as they stand. Unfortunately, no exact analytical solution was found, so a numerical solution was necessary. All calculations were executed on a GE 635 digital computer, using the MIMIC program [6].

Dimensionless temperature $\theta$ was evaluated at $N = 21$ equally spaced positions throughout the vapor film. Thus $\Delta y = 0.05$. The first and second spatial derivatives of equation (8) were approximated by upwind and central differences as

$$\partial\theta_n/\partial y \approx (\theta_{n+1} - \theta_n)/\Delta y$$

and

$$\partial^2\theta_n/\partial y^2 \approx (\theta_{n+1} - 2\theta_n + \theta_{n-1})/(\Delta y)^2$$

A backward difference was used to approximate the first spatial derivative of equation (11) as

$$\partial\theta_N/\partial y \approx (\theta_{N-2} - 4\theta_{N-1} + 3\theta_N)/2\Delta y$$

The resulting finite-difference approximation of equations (8)–(12) was then

$$d\theta_n/d\tau \approx [(\theta_{n+1} - 2\theta_n + \theta_{n-1})/(\Delta y)^2 + (dM^2/d\tau)(y_n/2\Delta y)(\theta_{n+1} - \theta_n)]/M^2$$
$$n = 1, 2, \ldots, 21 \tag{22}$$

$$\theta_1 = 1 \tag{23}$$

$$\theta_{21} = 0 \tag{24}$$

$$dM^2/d\tau = 2C[M - (\theta_{19} - 4\theta_{20})/2\Delta y] \tag{25}$$

$$M(0) = M_0 \tag{26}$$

Difficulties at zero time caused by the condition of equation (12) were circumvented by setting all $d\theta_n/d\tau = 0$ in equation (22) and specifying a numerical value of $\beta$. Then, with $dM^2(0)/d\tau = 4\beta^2$, the unknown $\theta_n(0)$ were determined from the ensuing algebraic equation (22). With this accomplished, a value of $C$ was determined from equation (25)—$M_0$ was selected to have only a 1 percent influence on $C$ and ranged from $10^{-4}$ to $10^{-2}$ as $\beta^2$ ranged from 2 to 0.1—and used in all later stages of the numerical solution.

## Comparison and Discussion

Numerical calculation of transient temperature profiles gave results illustrated in Fig. 3 for the particular case of $\beta^2 = 0.28$.

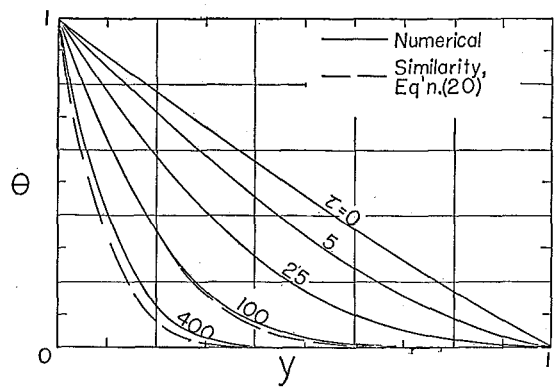


Fig. 3 Transient temperature profiles in vapor film, $\beta^2 = 0.28$

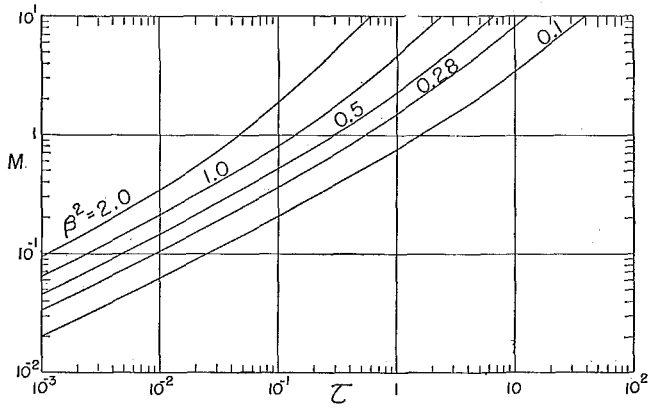


Fig. 4 Dimensionless mass per unit area versus dimensionless time

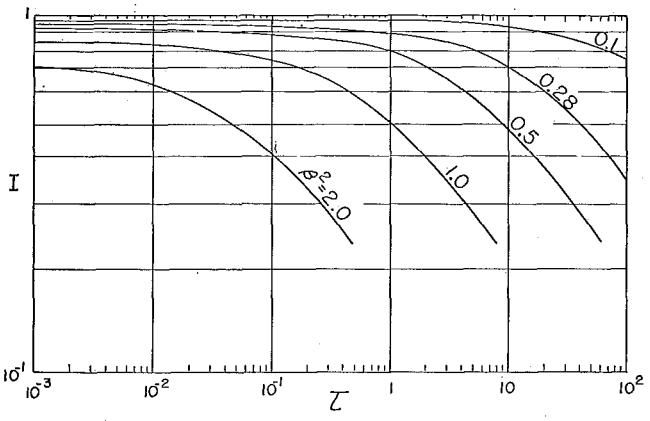


Fig. 5 Dimensionless temperature integrated over vapor film versus dimensionless time

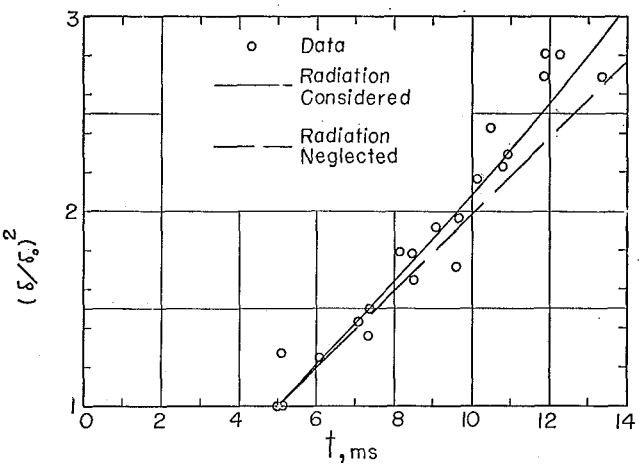


Fig. 6 Comparison with data of Pitts, Yen, and Jackson

It is seen there that the profile of equation (20) is confirmed by close agreement with the numerical results. The initial profile is nearly linear (so long as $\beta$ is not too large) and is blown toward the plate by the cold vapor issuing from the interface.

The vaporized mass per unit area is shown by the numerical results displayed in Fig. 4 to be proportional to the square root of time for thin films and to time for thick films. As $\beta$ (and $C$) increases, the transition from a conduction-limited to a radiation-limited process occurs at an earlier time. The film thickness can be evaluated at any time from $M$ and the $I$ behavior of Fig. 5 as set forth by equation (14).

Pitts, Yen, and Jackson [7] performed a relevant experiment which consisted of a horizontal wire immersed in a stagnant and saturated water pool. The wire was suddenly heated by a capacitor discharge and a cylindrical film of vapor formed between the wire and the liquid. It is pertinent to note that the vapor was free to rise and escape from the vicinity of the wire, so that a steady-state vapor-film thickness was ultimately achieved. In their experiment the wire's temperature gradually decreased from its maximum value as the vaporization process progressed and may be more closely represented as a constant-heat-flux surface than as one of constant temperature. The difference between their cylindrical geometry and the present flat-plate geometry prevents accurate prediction of their $\delta$, a difficulty somewhat circumvented by considering only $\delta/\delta_0$.

Both geometries show a square-root-of-time film-thickness behavior if thermal radiation is neglected. The departure of $\delta/\delta_0$ from this behavior demonstrates the effect of thermal radiation. Thus, despite points of difference it is believed that the data of Pitts et al. serve usefully in a comparison. In their experiment $T_w = 1548$ deg F, $T_s = 211$ deg F, $C_p = 0.5$ Btu/lb$_m$-deg F, $\Omega = 971$ Btu/lb$_m$, and $k = 0.035$ Btu/hr-ft-deg F. From this information the radiative heat flux is computed by $q_r = \epsilon\sigma(T_w^4 - T_s^4)$ so that, with $\epsilon = 0.13$ according to Singham [8], $q_r = 3520$ Btu/hr-ft$^2$. If a heat flux tenfold greater were transmitted across the vapor by conduction, a corresponding vapor thickness given by $\delta = k(T_w - T_s)/10q_r = 0.016$ in. would be required and was exceeded at large times in Pitts' experiment. It seems, therefore, that radiation is of some importance. The experimental conditions indicate that $C = 0.688$ with, from equation (16), a corresponding value $\beta^2 = 0.28$. Fig. 6 compares Pitts' data with the predicted variation of $(\delta/\delta_0)$. It is observed there that inclusion of radiation better fits the trend of the data than if radiation were neglected. Lack of radiation in the analytical model predicts a vapor-thickness ratio which is too small at large times, although it agrees well with data at small times.

## References


1 Carslaw, H. S., and Jaeger, J. C., *Conduction of Heat in Solids*, 2nd ed., Oxford University Press, 1959, pp. 282–296.

2 Hamill, T. D., and Bankoff, S. G., "Growth of Vapor Film at a Rapidly Heated Plane Surface," *Chemical Engineering Science*, Vol. 18, June 1963, p. 355.

3 Bromley, L. A., "Heat Transfer in Stable Film Boiling," *Chem. Engr. Prog.*, Vol. 46, 1950, pp. 221–227.

4 Sparrow, E. M., "The Effect of Radiation on Film-Boiling Heat Transfer," *International Journal of Heat and Mass Transfer*, Vol. 7, Feb. 1964, pp. 229–238.

5 Chapman, D. R., and Rubesin, M. W., "Temperature and Velocity Profiles in the Compressible Laminar Boundary Layer with Arbitrary Distribution of Surface Temperature," *Journal of the Aeronautical Sciences*, Vol. 16, No. 9, 1949, p. 547.

6 Sansom, F. J., and Petersen, H. E., *Mimic Programming Manual*, Technical Report SEG-TR-67-31, Systems Engineering Group, Aeronautical Systems Division, Air Force Systems Command, Wright–Patterson Air Force Base, Ohio, July 1967.

7 Pitts, D. R., Yen, H. H., and Jackson, T. W., "Transient Film Boiling of Water on a Horizontal Wire," JOURNAL OF HEAT TRANSFER, TRANS. ASME, Series C, Vol. 90, No. 4, Nov. 1968, pp. 476–481.

8 Singham, J. R., "Tables of Emissivity of Surfaces," *International Journal of Heat and Mass Transfer*, Vol. 5, Jan.-Feb. 1962, pp. 67–76.

G. S. H. LOCK
Professor.
Mem. ASME

R. S. KO

Department of Mechanical Engineering,
University of Alberta,
Edmonton, Alberta, Canada

# Laminar Free Convection from a Rotating Radial Plate

*The paper presents a theoretical analysis of conduction through, and free convection from, a radial plate rotating in a synchronous environment of air. The plate resembles a tapered, radially protruding fin heated at the root. Ordering of the governing equations reveals three controlling parameters, under the condition of steady high-speed rotation. Numerical solutions to the combined conduction–convection problem reveal the effect of the parameters on the velocity and temperature profiles, the overall heat-transfer relation, and the fin effectiveness.*

## Introduction

Despite numerous and extensive studies of free convection in the uniform gravitational field at the earth's surface, comparatively little attention has been devoted to systems in which the body force field is not uniform. Among the latter are rotating systems, examples of which are to be found in both the geosciences (e.g., meteorology and oceanography) and in engineering. Specific engineering examples include: electric motors and generators, rotating boilers and condensers, steam and gas turbines, and spacecraft.

A recent paper by Kreith [1][1] provides a comprehensive survey of convective heat transfer in rotating systems. The survey covers both forced and free convection in a wide range of circumstances and gives an especially detailed review of the rotating-disk and rotating-cylinder problems. The discussion of free convection adjacent to radially located surfaces is, however, rather limited.

The first study of free convection from a rotating radial plate appears to be that of Lemlich [2]. This early work, along with several subsequent studies [3–5] by the same author and his coworkers, is concerned with boundary-layer flow along a cold plane which contains the axis about which it rotates. Under these circumstances the cooled fluid flows radially outward in what was recognized as a similarity situation. Only the latest of these papers [5] makes any reference to the effect of Coriolis forces. No attempt was made to formally delineate the range of conditions under which they might be neglected.

A similar type of study was carried out by Catton [6] who treated an isothermal plate with its leading edge parallel to, but not coincident with, the axis of rotation. Although restricted to large-Prandtl-number fluids, Catton's work is the only work known to the authors which discusses both heated and cooled plates.

One of the most serious limitations imposed on the applicability of published work in free convection is the assumption that the thermal boundary conditions can be completely prescribed. Normally, this is untrue because the flow field exists adjacent to a solid body which, by virtue of gaining or losing heat, is the source of the motion. For completeness, the solution of the associated conduction problem is also necessary [7, 8]. It is, of course, generally quite difficult to solve such a combined conduction–convection problem, and the particular set of circumstances to be found in rotating systems reveals no obvious exceptions to this fact.

In this paper the problem of conduction through, and free convection from, a rotating radial plate will be considered. As a logical extension of previous work [7], the specific example chosen is a slender triangular plate heated uniformly along its inner edge. In effect the plate behaves like a radially protruding fin rotating in a synchronous, and otherwise quiescent, isothermal fluid.

Under the conditions of interest the general equations governing heat transfer in the individual conduction and convection problems reduce to simplified forms, the range of validity of which is revealed by an ordering procedure. Formulation and solution of the reduced set of equations are discussed separately for each of the conductive and convective systems. The separate solutions are then combined to give the solution of the overall problem. In addition to generating such data as velocity and temperature profiles, the solutions are used to determine the overall heat-transfer relation for the system and the fin effectiveness.

## Governing Equations

**Convection System.** Consider the steady rotating system shown diagrammatically in Fig. 1. Heat supplied at the root of the fin

[1] Numbers in brackets designate References at end of paper.

Contributed by the Heat Transfer Division of The American Society of Mechanical Engineers and presented at the AIChE-ASME Heat Transfer Conference, Denver, Colo., August 6–9, 1972. Manuscript received by the Heat Transfer Division January 11, 1971; revised manuscript received June 28, 1971. Paper No. 72-HT-46.

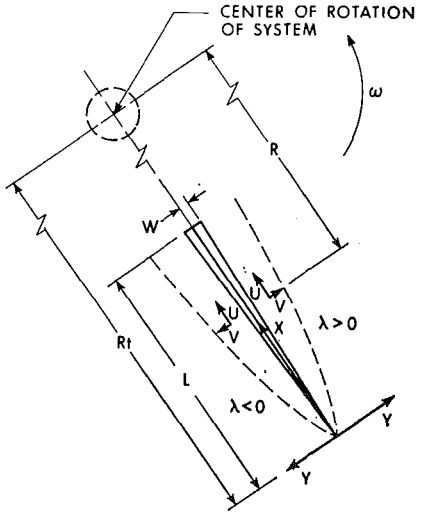


**Fig. 1 Description of system**

is conducted into the surrounding fluid, thus leading to a free-convection system.

Using the following variables (see Appendix 1)

$$\left.\begin{aligned} x &= X/L & y &= Y\,\mathrm{Ra}^{1/4}/L \\ u &= UL/\kappa\,\mathrm{Ra}^{1/2} & v &= VL/\kappa\,\mathrm{Ra}^{1/4} \\ p &= P/\rho\kappa\omega\,\mathrm{Ra}^{1/4} & \phi &= \theta/\theta_r = (T - T_\infty)/(T_r - T_\infty) \end{aligned}\right\} \quad (1)$$

the continuity, momentum, and energy equations reduce to the boundary-layer forms

$$\left.\begin{aligned} u_x + v_y &= 0 \\ \frac{1}{\mathrm{Pr}}(uu_x + vu_y) &= (1 - \gamma x)\phi + u_{yy} \\ u\phi_x + v\phi_y &= \phi_{yy} \end{aligned}\right\} \quad (2)$$

provided that the rotational speed is high, Ek, $\mathrm{Ra}^{1/4}$, and Fr are much greater than unity, and both $\beta\theta_r$ and Os are much less than unity.

The above system of equations is very similar to those studied previously by others [2–6]. The principal difference is due to the surface temperature considered here being above the fluid temperature. This apparently minor difference leads to a much more complicated mathematical problem by virtue of the fact that similarity does not exist, as it does for a cold surface, if the leading edge marks the origin of the coordinate system. With this difference, the boundary conditions may be taken as

$$\left.\begin{aligned} y = 0: &\quad u = v = 0, \quad \phi = \phi_0(x) \\ y = \infty: &\quad u = \phi = 0. \\ x = 0: &\quad u = \phi = 0 \end{aligned}\right\} \quad (3)$$

Despite the absence of similarity it is convenient at this point to rewrite the boundary-layer equations (2) incorporating a similarity variable $\eta$. Introducing a stream function $\psi(x, y)$ satisfying continuity, and following in the spirit of the Blasius-Howarth transformation [9], we define

$$\left.\begin{aligned} \xi &= \gamma x, \quad \eta = \frac{F_1(\xi)}{[F_2(\xi)/\gamma]^{1/4}}\,y \\ f(\xi, \eta) &= \left[\frac{\gamma}{F_2(\xi)}\right]^{3/4}\psi(x, y) \\ \Phi(\xi, \eta) &= \phi(x, y)/\phi_0(\xi) \end{aligned}\right\} \quad (4)$$

where

$$\phi_0(x) = \phi_0(\xi)$$

$$F_1(\xi) = \phi_0^{1/3}(\xi) \quad \text{and} \quad F_2(\xi) = \frac{4}{3}\int_0^\xi \phi_0^{1/3}(s)ds$$

Substituting in equations (2) we obtain

$$\left.\begin{aligned} \mathrm{Pr}(f_{\eta\eta\eta} + \Phi) + ff_{\eta\eta} - \frac{2}{3}f_\eta^2 &= \frac{F_2(\xi)}{3F_1^4(\xi)}\frac{dF_1^3(\xi)}{d\xi}f_\eta^2 \\ &\quad + \frac{F_2(\xi)}{F_1(\xi)}[f_\eta f_{\eta\xi} - f_{\eta\eta}f_\xi] + \mathrm{Pr}\,\xi\Phi \end{aligned}\right\} \quad (5)$$

and

$$\Phi_{\eta\eta} + f\Phi_\eta = \frac{F_2(\xi)}{F_1^4(\xi)}\frac{dF_1^3(\xi)}{d\xi}f_\eta\Phi + \frac{F_2(\xi)}{F_1(\xi)}[f_\eta\Phi_\xi + \Phi_\eta f_\xi]$$

Inspection of these equations reveals that their right-hand sides, which contain an explicit dependence on $\xi$, become independent of it (by vanishing) as $\xi \to 0$, providing that the surface temperature distribution $\Phi_0(\xi)$ increases monotonically from a non-zero value at the fin tip. If $\phi_0(0) = 0$ the coefficients of $f_\eta^2$ and $f_\eta\Phi$ no longer vanish[2] of necessity as $\xi \to 0$, but the equations are still rendered independent of $\xi$. For the limiting (static) situation of $\gamma \to 0$, these latter coefficients may tend to a bounded constant which is zero if the surface is isothermal (see Appendix 2). This behavior of the coefficients on the right-hand side of equations (5) is completely consistent with the requirements as $\gamma \to 0$ [7]. The boundary conditions given by equations (3) transform to

$$\left.\begin{aligned} f(\xi, 0) = f_\eta(\xi, 0) = \Phi(\xi, 0) - 1 = 0 \\ \text{and} \\ f_\eta(\xi, \infty) = \Phi(\xi, \infty) = 0 \end{aligned}\right\} \quad (6)$$

**Conduction System.** Heat conduction in the plate would in general be governed by Laplace's equation if the plate properties

[2] The vanishing of the $\xi$-dependent coefficient is obviously not a sufficient condition for suppression of every term. Assuming boundedness in the derivatives of $f$ and $\Phi$ is justified a posteriori.

## Nomenclature

$\xi, x, X$ = radial displacement from fin tip
$R$ = radial displacement from axis of rotation
$y, Y$ = lateral displacement from fin surface
$\eta$ = similarity variable
$u, U$ = radial velocity
$v, V$ = circumferential velocity
$f, \psi$ = stream function
$\Phi, \phi, \theta, T$ = temperature
$\omega$ = angular velocity
$A$ = cross-sectional area of fin
$L$ = fin length (radially)
$W$ = root half-width
$g$ = gravitational acceleration
$k$ = thermal conductivity
$\beta$ = thermal-expansion coefficient
$\nu$ = momentum diffusivity
$\kappa$ = thermal diffusivity
$c_p$ = constant-pressure specific heat
$h$ = heat-transfer coefficient
Nu = Nusselt number ($hL/k_f$)
Ra = Rayleigh number ($\beta\omega^2R_t\theta_rL^3/\nu\kappa$)
Pr = Prandtl number ($\nu/\kappa$)
Bi = Biot number ($hW/k_s$)
Ek = Ekman number ($\nu/\omega L^2$)
Fr = Froude number ($R_t\omega^2/g$)
Os = Ostrach number ($\beta R_t\omega^2L/c_p$)
$\gamma$ = length-radius ratio ($L/R_t$)
$C$ = dimensionless group ($\mathrm{Ra}^{1/4}Lk_f/Wk_s$)

**Subscripts**

0 = fin
$r, t$ = fin root, tip
$\infty$ = outside boundary layer
$f, s$ = fluid, solid
$\eta, \xi, y, x$ = differentiation with respect to $\eta, \xi, y, x$

were constant. For a slender plate, such as the fin considered, a simpler description of the system is available provided that the Biot number is small [10]. Thus, if Bi $\ll 1$, the symmetric fin equation

$$\frac{d}{dx}\left(A\frac{d\theta_0}{dx}\right) - \frac{2h}{k}L\theta_0 = 0 \tag{7}$$

where $\theta_0(x) = T_0(x) - T_\infty$, adequately describes the heat flow.

Using previously defined variables this may be rewritten for the triangular fin in question as

$$\frac{d}{d\xi}\left(\xi\frac{d\phi_0}{d\xi}\right) + \left[\frac{CF_1}{\gamma^{3/4}F_2^{1/4}}\Phi_\eta(\xi, 0)\right]\phi_0 = 0 \tag{8}$$

where $C = LK_f\mathrm{Ra}^{1/4}/Wk_s$ is a nondimensional group which is essentially the same as that discussed in an earlier study [7]. This equation is seen to be nonlinear through the appearance of the functions $F_1$ and $F_2$ which were defined as functions of $\phi_0(\xi)$; their explicit dependency on $\xi$ is unknown a priori.

The solution of equation (8), which is second-order in $\phi_0$, would normally require the prescription of two boundary conditions. At the root, it is clear that we must take $\phi_0(\gamma) = 1$, whereas at the tip the singular behavior of the equation complicates matters. This difficulty is readily resolved in simpler situations, such as if a constant heat-transfer coefficient exists, when inspection of the general solution of the corresponding *linear* equation immediately reveals the necessary condition for the tip temperature to be bounded [11].

An alternative approach is to regard equation (8) as a first-order nonlinear equation in $\xi(d\phi_0/d\xi)$, in which case a single boundary condition on this variable would suffice. Integrating the equation (8) once gives

$$\xi\frac{d\phi_0}{d\xi} = -\int\left[\frac{CF_1}{\gamma^{3/4}F_2^{1/4}}\Phi_\eta(\xi, 0)\right]\phi_0(\xi)d\xi + B_1$$

Now the required monotonic behavior of $\phi_0(\xi)$ mentioned in the earlier discussion of the convective system implies that the integral in the equation immediately above vanishes as $\xi \to 0$; hence

$$B_1 = \left(\xi\frac{d\phi_0}{d\xi}\right)_{\xi=0}$$

Integrating once more we obtain

$$\phi_0(\xi) = -\int\frac{1}{\xi}\int\left[\frac{CF_1}{\gamma^{3/4}F_2^{1/4}}\Phi_\eta(\xi, 0)\right]\phi_0(\xi)d\xi d\xi + B_1\ln\xi + B_2$$

from which it is immediately evident that $B_1 = 0$ if $\phi_0$ is to be bounded. Thus $(\xi d\phi_0/d\xi)_{\xi=0} = 0$, which may be interpreted as follows. The monotonicity of $\phi_0(\xi)$ implies that the total amount of heat conduction through the fin cross section vanishes as $\xi \to 0$. But equation (8) is a first-order equation in the total heat flux, represented by $\xi d\phi_0/d\xi$, for which $(\xi d\phi_0/d\xi)_{\xi=0} = 0$ provides the single required boundary condition. It thus appears that a zero tip heat flux and a bounded tip temperature are equivalent boundary conditions for a pointed fin.

## Solution of Equations

**Boundary-Layer Solutions.** The boundary-layer equations (5) may be solved numerically using either of two principal schemes. One possibility is to expand $f(\xi, \eta)$ and $\Phi(\xi, \eta)$ in Görtler series [8, 12] and thus convert a single set of partial differential equations to an infinite set of ordinary differential equations, truncated short of the limit of patience. The scheme favored in this paper was to solve the original set of equations using the concept of local similarity [13] in which the search for a solution consists in determining the variation of $f$ and $\Phi$ with $\eta$ for several values of $\xi$, at each of which any $\xi$-dependence is incorporated explicitly. That is, in integrating with respect to $\eta$ at any of a progressively increasing set of $\xi$-values, the $\xi$-derivatives on the right-hand sides of equations (5) are replaced by explicit finite-difference approximations. The starting solution is generated by simply suppressing the right-hand sides.

Numerical integration was accomplished following Hayday et al. [13] with satisfaction of the asymptotic boundary conditions incorporating a least-squares technique and a refined convergence algorithm. Several $(\eta, \xi)$ grid spacings were used in the early stages of the study but eventually it was found that with a fourth-order Runge–Kutta integration scheme (with respect to $\eta$) and three-point difference formulae for the $\xi$-derivatives, an accuracy of the order of 1 percent in the eigenvalues was attainable with $\Delta\eta = 0.04$, $\Delta\xi = 0.02$, and $0 \le \eta \le 10.0$, $0 \le \xi \le \gamma$.

**Fin Solutions.** Integration of the fin equation was formally carried out in the previous section, thus converting the problem to the solution of an integral equation. Such a solution could have been accomplished by a numerical iterative technique but in fact it was found to be more convenient to integrate the original equation (8) using a modified Runge–Kutta technique. With $\Phi_\eta(\xi, 0)$ fixed, as prescribed from the solution of the boundary-layer problem, the equation was integrated as a *linear* equation by substituting into $F_1$ and $F_2$ the temperature distribution $\phi_0^{(1)}$ assumed in the convection solution. The fin solution thus generated, $\phi_0^{(2)}$, was then used to determine improved forms for $F_1$ and $F_2$ which were substituted for the initial functions and the equation integrated once more. Such an iterative scheme was found to behave in accordance with the proximity of the initial distribution $\phi_0^{(1)}$ to its final form $\phi_0^{(n)}$.

To maintain an accuracy of better than 1 percent in the root heat flux at any given stage of the above iterative process, a step size of 0.02 was used for $\Delta\xi$. Solutions were sought using a shooting method, starting at the root of the fin where the temperature was prescribed. The solution was finally accepted when $(\xi d\phi_0/d\xi)_{\xi=0}$ was close enough to zero to give the required accuracy in root heat flux.

**Matching.** A priori it is not at all certain that the iterative processes employed in the solution of the individual convection and conduction problems will converge rapidly to sufficiently accurate solutions. Therefore it is obvious that if these individual solutions are to be adjusted until, in combination, they give the solution of the overall problem, the convergence behavior of the adjustment process is even less certain.

In the boundary-layer problem the use of refinements in the satisfaction of the asymptotic boundary conditions kept computing time down to the minimum possible for the accuracy demanded, but, as anticipated, this time was found to be an order of magnitude greater than that required in the conduction solution. The latter thus exhibited none of the convergence difficulties associated with an asymptotic boundary condition and consumed relatively small amounts of time. For this reason, as much as possible of the overall iteration was executed in the conduction loop. As mentioned earlier, although the fin equation was solved for $\phi_0(\xi)$ with the heat-transfer coefficient prescribed, because the latter is dependent on temperature the equation was re-solved several times with additional iterations on $h$ through successive modifications of the functions $F_1$ and $F_2$.

The requirements of continuity of temperature and heat flux across the solid–fluid interface were met as follows. First, the boundary-layer problem was solved using any of a wide variety of monotonic fin temperature distributions as a prescribed boundary condition. The surface heat-flux distribution generated from this solution was then used in the iterative solution of the fin equation as outlined earlier. The resulting temperature distribution in the fin was then used as a new boundary condition in the boundary-layer problem which was re-solved. The overall solution was accepted when continuity along the interface was realized to within $10^{-16}$ with an accuracy of about $10^{-4}$.

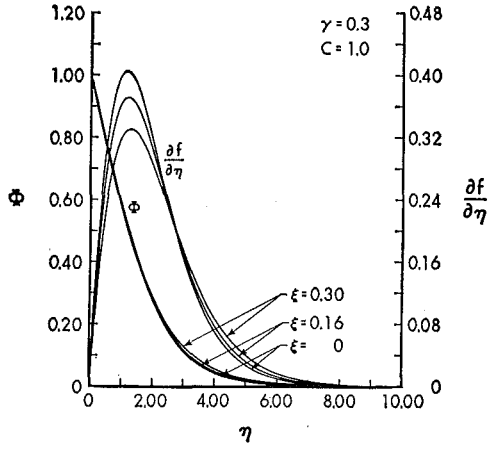


Fig. 2 Departure from similarity

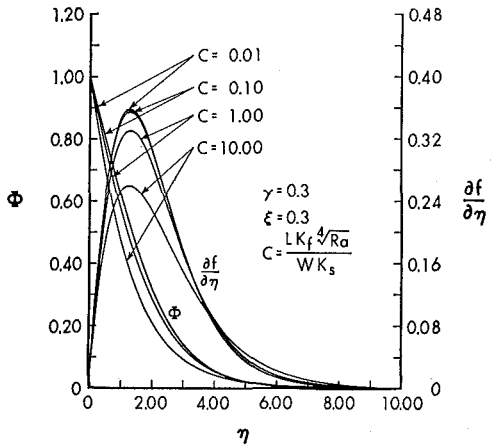


Fig. 4 Effect of C

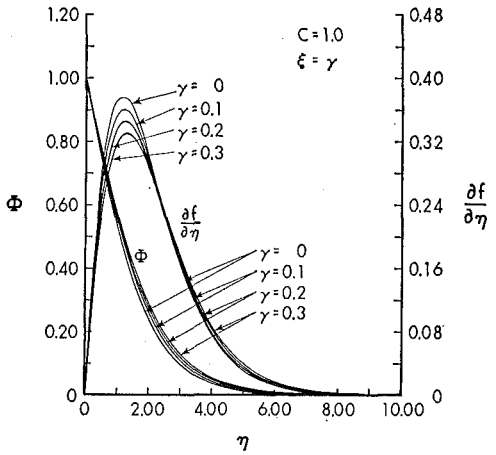


Fig. 3 Effect of $\gamma$

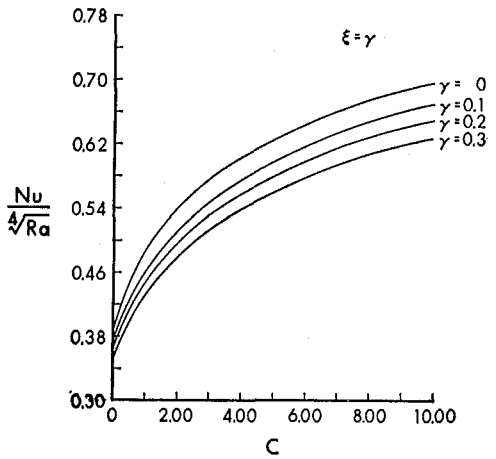


Fig. 5 Heat-transfer relation: parameter $\gamma$

As an additional check, comparisons of prescribed root flux and calculated fin surface flux were made; these revealed errors again of the order of 1 percent.

## Discussion and Conclusions

As mentioned above, the solutions presented in this paper refer to a triangular fin immersed in air (Pr = 0.72). The numerical results plotted in Figs. 2–7 are believed to be accurate to 1 percent or better. The time required to generate a set of solutions up to $\xi = \gamma = 0.3$ was about 40 min on an IBM 360/67 machine. Typically, a solution required five iterations of the overall loop to achieve the desired accuracy.

Since the functions $f$ and $\Phi$ are not simply described through variations in the similarity variable $\eta$, it is of interest to determine their additional dependence on the variable $\xi$, that is, to determine the departure of the solutions from similarity. Figure 2 shows velocity and temperature profiles for several values of $\xi$ with $C = 1.0$ and $\gamma = 0.3$. It is immediately apparent from these profiles that departures from the basic similarity solution ($\xi = 0$) are not large, particularly in the temperature field. However, it is quite likely that a significant departure would occur in the velocity field as $\gamma$ and $\xi$ approached unity.

Figure 3 is an attempt to illustrate the effect of $\gamma$, with $C$ again held at unity. In this figure $\xi$ is not held constant but taken equal to $\gamma$ so that the profiles accentuate the effect of $\gamma$ by referring to the root of the fin. Again it is apparent that the temperature field is not much different from the similarity situation. The limiting profile with $\gamma = 0$ is not generally a similarity situation (see Appendix 2) because it does not always suppress the effect of $\xi$ in equations (5). However, a comparison of Figs. 2 and 3 clearly shows that for practical purposes the profiles generated with $\gamma = 0$ are virtually coincident with the basic similarity profiles. Complete agreement between these sets of profiles would be obtained if the fin were isothermal, and therefore the close agreement evident when the fin is not isothermal strongly suggests that variations in temperature along the fin surface must be quite large before departures from the similarity solutions become significant.

The effect of the parameter $C$ is shown in Fig. 4 with $\gamma = \xi = 0.3$. The three-decade range chosen reveals that the parameter $C$ produces significant changes in both the temperature and velocity profiles. Because $C$ is a composite parameter, an increase in its magnitude may represent any of a wide variety of possibilities. In particular, it could imply an increasing rotational speed which, as the profiles indicate, evidently leads to a flattening of the velocity profile and a thickening of the velocity boundary layer. Another interesting feature of these profiles is their behavior as $C \to 0$. Although the curves for $C = 0$ are not shown, it appears that they would represent asymptotic forms not very different from those shown for $C = 0.01$. Again, the condition $C \to 0$ admits of a variety of interpretations.

It is obvious that the Nusselt number calculated at the root of a rotating fin will generally be a function of more than the Prandtl number and the Rayleigh number. In fact it is readily shown that function takes the form

$$\mathrm{Nu}/\mathrm{Ra}^{1/4} = F(C, \gamma)$$

for a particular fluid, in this case air. This relation is shown plotted in Fig. 5 with $\gamma$ as a parameter. As expected, the function is of unit order of magnitude and reveals a monotonic in-

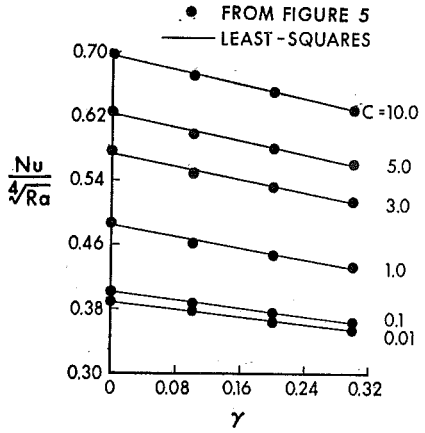


Fig. 6 Heat-transfer relation: parameter C

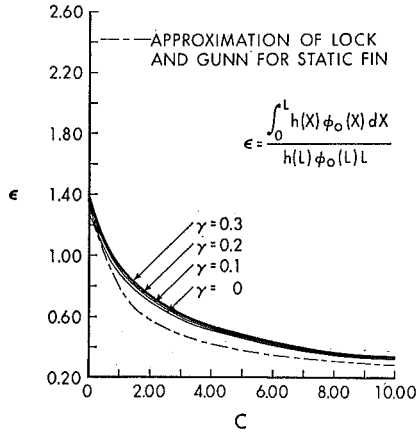


Fig. 7 Fin effectiveness

crease with increasing values of $C$, e.g., with increasing speed. The effect of $\gamma$ on the heat-transfer relation is seen to be moderate for the range investigated. $C$ was chosen to include and extend the range of values considered theoretically and experimentally in previous work [7]. An alternative heat-transfer plot is shown in Fig. 6 with $C$ as a parameter. Within the estimated numerical error, it appears that $\mathrm{Nu/Ra}^{1/4}$ is a linear function of $\gamma$, though the theoretical basis of such a relationship has yet to be demonstrated.

An alternative measure of the efficacy of the system is the fin effectiveness. Using a previous definition [7] this may be calculated as a function of $C$; the results are shown in Fig. 6 with $\gamma$ as a parameter. Also shown is the curve developed in [7]. The improvement in fin effectiveness is seen to be significant, even for small values of $\gamma$.

The solutions presented in this paper are subject to the restrictions outlined in the ordering procedure. First, they were obtained with $\mathrm{Pr} = 0.72$ and therefore apply only to gases, although it might be added that no special difficulty would likely arise if the results were extended to nonmetallic liquids. Second, they are subject to the Boussinesq approximation which evidently does not impose a serious restriction on the root temperature.

Conflict arises in the requirement that $\mathrm{Fr} \gg 1$ together with $\mathrm{Os} \ll 1$. However, these conditions are met if $c_p/\beta L \gg \omega^2 R_t \gg g$, which, typically, is realized without difficulty. Similarly, the pair of conditions $\mathrm{Ra}^{1/4} \gg 1$ with $\mathrm{Bi} \ll 1$ appear to contradict each other because Bi is a monotonically increasing function of Ra. But Fig. 5 shows that $\mathrm{Nu/Ra}^{1/4} = \mathrm{O}[1]$, and hence Bi, which is equal to $(Wk_f/Lk_s)\mathrm{Nu}$, is much less than unity for laminar flow. In a typical example (Appendix 1), $c_p/\beta L \simeq 10^7$ ft/sec$^2$, $\omega^2 R_t \simeq 10^3$ ft/sec$^2$, $\mathrm{Ra}^{1/4} \simeq 10^2$, and $\mathrm{Bi} \simeq 10^{-3}$.

As a general concluding remark it might be stated that combined conduction–convection problems of this type appear amenable to numerical treatment. Despite the absence of similarity, the convergence exhibited in the overall loop was quite acceptable. Computing time required was not much greater than that for the boundary-layer solutions alone.

## Acknowledgment

This work is part of a free-convection research program sponsored by the National Research Council of Canada, to whom the authors are indebted.

## References

1 Kreith, F., "Convection Heat Transfer in Rotating Systems," in: *Advances in Heat Transfer*, Vol. 5, Academic Press, New York, N. Y., 1968, pp. 129–251.

2 Lemlich, R., "Natural Convection to Isothermal Flat Plate with a Spatially Non-Uniform Acceleration," *Ind. Eng. Chem. Fund.*, Vol. 2, No. 2, 1963, pp. 157–159.

3 Lemlich, R., and Vardi, J., "Steady Free Convection to a Flat Plate With Uniform Surface Heat Flux and Nonuniform Acceleration," JOURNAL OF HEAT TRANSFER, TRANS. ASME, Series C, Vol. 86, No. 4, Nov. 1964, pp. 562–563.

4 Lemlich, R., and Steinkamp, J. S., "Laminar Natural Convection to an Isothermal Flat Plate with a Spatially Varying Acceleration," *AIChE Journal*, Vol. 10, No. 4, 1964, pp. 445–447.

5 Manoff, M., and Lemlich, R., "Free Convection to a Rotating Central Plate in Synchronously Rotating Surroundings with and without Consideration of Coriolis Forces," *Chem. Eng. Prog. Symp. Series* (in press).

6 Catton, I., "Effect of a Gravity Gradient on Free Convection from a Vertical Plate," *Chem. Eng. Prog. Symp. Series*, Vol. 64, No. 82, 1968, pp. 146–149.

7 Lock, G. S. H., and Gunn, J. C., "Laminar Free Convection From a Downward-Projecting Fin," JOURNAL OF HEAT TRANSFER, TRANS. ASME, Series C, Vol. 90, No. 1, Feb. 1968, pp. 63–70.

8 Kelleher, M. D., and Yang, K.-T., "A Steady Conjugate Heat Transfer Problem with Conduction and Free Convection," *Appl. Sci. Res.*, Vol. 17, 1967, pp. 249–269.

9 Howarth, L., "On Calculation of the Steady Flow in the Boundary Layer near the Surface of a Cylinder in a Stream," *Rep. Memor. Res. Coun.*, London, No. 1632, 1934–5.

10 Irey, R. K., "Errors in the One-Dimensional Fin Solution," JOURNAL OF HEAT TRANSFER, TRANS. ASME, Series C, Vol. 90, No. 1, Feb. 1968, pp. 175–176.

11 Arpaci, V., *Conduction Heat Transfer*, Addison-Wesley, Reading, Mass., 1966, p. 151.

12 Kuiken, H. K., "Axisymmetric Free Convection Boundary-Layer Flow past Slender Bodies," *International Journal of Heat and Mass Transfer*, Vol. 11, 1968, pp. 1141–1153.

13 Hayday, A. A., Bowlus, D. A., and McGraw, R. A., "Free Convection From a Vertical Flat Plate With Step Discontinuities in Surface Temperature," JOURNAL OF HEAT TRANSFER, TRANS. ASME, Series C, Vol. 89, No. 3, Aug. 1967, pp. 244–250.

# APPENDIX 1

## Orders of Magnitude

The equations governing two-dimensional free convection in cartesian coordinates are well known. For an incompressible fluid for which the density is a linear function of temperature, the normalized continuity equation may be written

$$u_x + \left[\frac{V_c X_c}{U_c Y_c}\right] v_y = -\beta\theta_c \left(u\phi_x + \left[\frac{V_c X_c}{U_c Y_c}\right] v\phi_y + \left[\frac{X_c}{U_c t_c}\right] \phi_\tau\right)$$

where the subscript $c$ refers to a reference value. At high (quasi-steady) speed, $X_c/U_c t_c \ll 1$, and therefore when $\beta\theta_c$ is also much less than unity it follows that for the remaining terms to be of equal order of magnitude

$$\frac{V_c X_c}{U_c Y_c} = \mathrm{O}[1]$$

or, arbitrarily,

$$\frac{V_c X_c}{U_c Y_c} = 1 \tag{9}$$

With the above approximations and definition, the energy and momentum equations are written in normalized form as

$$uu_x + vu_y = -\left[\frac{P_c}{\rho U_c^2}\right] P_x + \left[\frac{\beta\omega^2 R_t X_c \theta_c}{U_c^2}\right] \phi - \left[\frac{\beta\omega^2 X_c^2 \theta_c}{U_c^2}\right] x\phi + \left[\frac{\nu}{U_c X_c}\right] u_{xx} + \left[\frac{\nu X_c}{U_c Y_c^2}\right] u_{yy} + 2\lambda \left[\frac{\beta\omega V_c X_c \theta_c}{U_c^2}\right] v\phi$$

$$uv_x + vv_y = -\left[\frac{P_c}{\rho V_c^2}\right] P_y - \left[\frac{\beta\omega^2 Y_c^2 \theta_c}{V_c^2}\right] y\phi + \left[\frac{\nu Y_c}{V_c X_c^2}\right] v_{xx} + \left[\frac{\nu}{V_c Y_c}\right] v_{yy} - 2\lambda \left[\frac{\beta\omega U_c Y_c \theta_c}{V_c^2}\right] u\phi$$

$$u\phi_x + v\phi_y = \left[\frac{\kappa}{U_c X_c}\right] \phi_{xx} + \left[\frac{\kappa X_c}{U_c Y_c^2}\right] \phi_{yy} + 2\left[\frac{\nu U_c}{c_p X_c \theta_c}\right] u_x^2 + 2\left[\frac{\nu V_c^2 X_c}{c_p U_c Y_c^2 \theta_c}\right] v_y^2 + \left[\frac{\nu U_c X_c}{c_p Y_c^2 \theta_c}\right] u_y^2 + 2\left[\frac{\nu V_c}{c_p Y_c \theta_c}\right] u_y v_x + \left[\frac{\nu V_c^2}{c_p U_c X_c \theta_c}\right] v_x^2$$

where $\lambda = -1$ or $+1$ for the trailing and leading faces, respectively. The velocity and lateral length scales may now be set by appealing to the physics of the problem. A priori, the lateral conduction and advection terms in the energy equation are not likely to be much different in magnitude. Likewise, the centrifugal acceleration and lateral viscous terms in the longitudinal momentum equation will not differ greatly for gases. Thus by taking

$$\frac{\kappa X_c}{U_c Y_c^2} = 1$$

and

$$\frac{\beta\omega^2 R_t X_c \theta_c}{U_c^2} = \frac{\nu X_c}{U_c Y_c^2}$$

along with equation (9), we find that

$$Y_c = L/\mathrm{Ra}^{1/4} \qquad U_c = \kappa \mathrm{Ra}^{1/2}/L \qquad V_c = \kappa \mathrm{Ra}^{1/4}/L$$

where $X_c$ and $\theta_c$ have been set at $L$ and $T_r - T_\infty$ respectively. Finally, by equating the pressure and Coriolis terms in the lateral momentum equation we obtain

$$P_c = \rho\kappa\omega\beta(T_r - T_\infty)\mathrm{Ra}^{1/4}$$

Using the above reference quantities the governing equations reduce to the following boundary-layer forms:[3]

$$u_x + v_y = \mathrm{O}[\beta\theta_r]$$

$$\frac{1}{\mathrm{Pr}}(uu_x + vu_y) = (1 - \gamma x)\phi + u_{yy} + \mathrm{O}[\beta\theta_r \mathrm{Ek}^{-1}\mathrm{Ra}^{-3/4}] + \mathrm{O}[\mathrm{Fr}^{-1}] + \mathrm{O}[\mathrm{Ra}^{-1/2}]$$

$$\beta\theta_r \mathrm{Ek}^{-1}\mathrm{Ra}^{-1/2}(P_y + 2\lambda u) + \mathrm{O}[\mathrm{Ra}^{-1/4}] + \mathrm{O}[\mathrm{Fr}^{-1}] = \mathrm{O}[\mathrm{Pr}^{-1}\mathrm{Ra}^{-1/4}]$$

$$u\phi_x + v\phi_y = \phi_{yy} + \mathrm{O}[\mathrm{Ra}^{-1/2}] + \mathrm{O}[\mathrm{Os}]$$

neglecting terms of higher order in the coefficients. Hence, when Ek, $\mathrm{Ra}^{1/4}$, and Fr are all much greater than unity while $\beta\theta_r$ and Os are both much less than unity, the above equations simplify to

$$u_x + v_y = 0$$
$$uu_x + vu_y = (1 - \gamma x)\phi + u_{yy}$$
$$u\phi_x + v\phi_y = \phi_{yy}$$

for fluids of unit Prandtl number.

As a typical example, consider the rotation of a 6-in-long aluminum fin positioned 12 in. from its axis of rotation. For synchronous rotation at 300 rpm, with a root temperature 10 deg F in excess of the bulk (air) temperature, then

$$\mathrm{Fr}^{-1} \simeq 0.02$$
$$\mathrm{Ra}^{-1/4} \simeq 0.011$$
$$\beta\theta_r \simeq 0.019$$
$$\beta\theta_r \mathrm{Ek}^{-1}\mathrm{Ra}^{-1/2} \simeq 0.1$$
$$\mathrm{Os} \simeq 10^{-4}$$

revealing that the largest neglected coefficient corresponds to the effect of Coriolis forces but has no effect on the velocity and temperature fields.

## APPENDIX 2

### Form of the Static Solutions

With the coefficients written as functions of $x$, equations (5) become

$$\mathrm{Pr}(f_{\eta\eta\eta} + \Phi) + ff_{\eta\eta} - \frac{2}{3} f_\eta^2 = H_1(\phi_0) f_\eta^2 + H_2(\phi_0)[f_\eta f_{\eta\xi} + f_{\eta\eta} f_\xi] + \mathrm{Pr}\,\gamma\xi\Phi$$

and

$$\Phi_{\eta\eta} + f\Phi_\eta = 3H_1(\phi_0) f_\eta \Phi + H_2(\phi_0)[f_\eta \Phi_\xi + \Phi_\eta f_\xi]$$

where $\xi = x$,

$$H_1(\phi_0) = -\frac{4}{3}\frac{d}{dx}[\phi_0^{-1/3}(x)] \int_0^x \phi_0^{1/3}(s)ds$$

and

$$H_2(\phi_0) = \frac{4\int_0^x \phi_0^{1/3}(s)ds}{3\phi_0^{1/3}(x)}$$

Clearly, as $\gamma \to 0$, if $H_2(\phi_0)$ is bounded, $f_\xi$ and $\Phi_\xi$ may be zero when $H_1(\phi_0)$ is constant. For the special case of a power-law surface-temperature distribution, e.g., $\phi_0(x) = x^m$,

$$H_1(\phi_0) = \frac{4m}{3(m+3)}$$

from which it follows that $H_1 = 0$ for an isothermal surface. Generally, $\phi_0(x)$ will not be a power law, in which case the $\xi$-dependency in equations (5) will not be suppressed when $\gamma = 0$.

[3] At high speed, i.e., $t_c \gg L^2/\kappa \mathrm{Ra}^{1/2}$.

R. SIEGEL
Mem. ASME

M. E. GOLDSTEIN
National Aeronautics and Space Administration, Lewis Research Center, Cleveland, Ohio

# Theory of Heat Transfer in a Two-dimensional Porous Cooled Medium and Application to an Eccentric Annular Region

*A class of incompressible solutions has been obtained for the heat-transfer characteristics of a two-dimensional porous cooled medium. The particular type of geometry considered herein is a doubly connected region. To illustrate the application of this class of solutions, it is applied to an eccentric annular region. The two boundaries of the porous medium are each at a different constant pressure, and hence can each be regarded as having a constant velocity potential. As a result, the porous region occupies a rectangle in a potential plane. The energy equation is transformed into a separable equation in potential-plane coordinates, and general solutions are obtained for an arbitrary surface temperature or heat flux. Conformal mapping can then be used to transform the solution into the physical plane.*

## Introduction

A MEANS for extending the usefulness of a metallic structural material to higher temperature applications is to provide transpiration cooling. This is accomplished by making the metal porous and forcing a coolant through it from a reservoir toward the boundary exposed to the high temperature. Possible applications are for cooling rocket nozzles, arc electrodes, reentry bodies, and turbine blades.

In many instances the thermal communication is so good that the local fluid temperature can be assumed to be the same as the local temperature of the solid matrix material. A single energy equation can then be written. The difficulty in solving this energy equation is that for anything other than a very simple geometry the velocity in the convective term is usually a complicated function of position within the porous material. The analytical solutions in the literature have consequently been limited to one-dimensional situations [1–3].[1] Two recent numerical solutions in two dimensions are given in [4, 5].

Since the geometries in practical applications would generally not be one-dimensional, the present authors devised in [6] an analytical method for obtaining the heat-transfer behavior in a two-dimensional porous medium and applied the method to a wall of varying thickness. In this paper the method will be extended and general solutions obtained for a multiply connected region. To illustrate the use of these solutions, heat-transfer results will be obtained for an eccentric annular region with arbitrary imposed surface heat flux or surface temperature.

The analytical method utilizes the fact that for the slow, viscous incompressible flow often encountered in porous media, the local fluid velocity is proportional to the local pressure gradient as expressed by Darcy's law. The pressure can, therefore, be regarded as a velocity potential. When the real and imaginary parts of the corresponding complex potential are taken as the new independent variables, the energy equation transforms into a separable equation.

The porous boundary exposed to the coolant reservoir and the boundary from which the coolant exits are each at constant pressure, and thus are each at constant velocity potential. In the potential plane these boundaries are parallel lines and this provides a simple geometry in which to solve the transformed energy equation. Because of these facts a general solution to the energy equation can be obtained in the potential plane. The particular solution for any given physical geometry can then be found simply by transforming the general solution into the specific geometry by conformal mapping. This can be done analytically for simple two-dimensional geometries or numerically for more complicated shapes.

## General Heat-Transfer Analysis for Two-Dimensional Porous Region

**Governing Equations.** The porous configuration treated here is a doubly connected region of arbitrary shape and is shown schematically in Fig. 1(*a*). This is a two-dimensional region and hence the figure is the cross section of a long hollow shape having an irregular wall thickness. Although the flow could be in either

[1] Numbers in brackets designate References at end of paper.

Contributed by the Heat Transfer Division of THE AMERICAN SOCIETY OF MECHANICAL ENGINEERS and presented at the AIChE-ASME Heat Transfer Conference, Denver, Colo., August 6–9, 1972. Manuscript received by the Heat Transfer Division October 12, 1970; revised manuscript received August 16, 1971. Paper No. 72-HT-47.

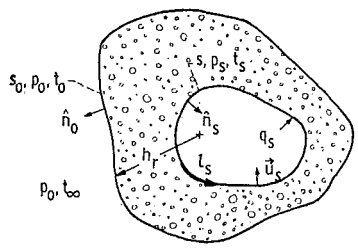


(a) Physical plane.

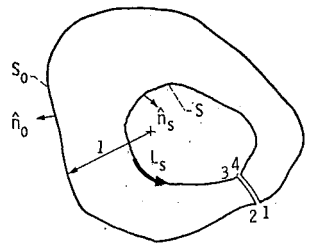


(b) Dimensionless physical plane.

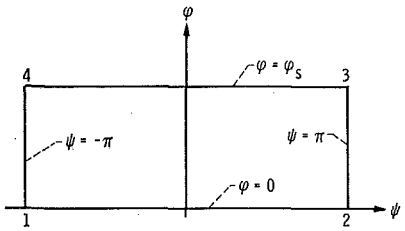


(c) Complex potential plane.

**Fig. 1 Doubly connected porous region**

direction, the present analysis will be for flow from the outside into the internal space. Surrounding the region is a reservoir at constant pressure $p_0$, and the interior surface $s$ is at uniform pressure $p_s$ such that $p_s < p_0$. Since in applications the flow resistance of the porous region is usually very high, any pressure drops that occur due to fluid motion in the reservoir are negligible compared with the pressure drop across the porous region.

The porous medium has a uniform permeability $\kappa$, and the fluid flowing through the region has constant properties $\rho$, $C_p$, and $\mu$. Since the pressure is uniform at both surfaces $s$ and $s_0$, the flow velocity entering and leaving the porous medium will be locally normal to each surface. The symbol $\mathbf{u}$ denotes the Darcy velocity of the fluid; this is the local volume flow divided by the entire cross-sectional area rather than by the pore cross-sectional area.

The porous region has an "effective" thermal conductivity $k_m$; the term effective means that the entire cross-sectional area of the porous region (rather than just the solid matrix area) is used with this conductivity to compute heat flows. It is assumed that the thermal communication between the fluid and the matrix is sufficiently good that the local fluid temperature is essentially equal to the local solid matrix temperature; this common temperature is denoted by $t$. It is also assumed that $k_m$ is large compared with the thermal conductivity of the fluid.

With the foregoing assumptions, the heat and mass flow within the porous material are governed by the following equations [6]:

continuity

$$\nabla \cdot \mathbf{u} = 0 \tag{1}$$

Darcy's law

$$\mathbf{u} = -\frac{\kappa}{\mu} \nabla p \tag{2}$$

## Nomenclature

$a$ = mapping quantity defined in equation (22$b$)

$A_n, a_n, b_n$ = Fourier coefficients defined, respectively, by equations (34), (17), and (18)

$C_p$ = specific heat of fluid

$F, G$ = functions in specified temperature and heat-flux distributions

$h_r$ = reference length in porous material

$\mathbf{i}, \mathbf{j}$ = unit vectors in $x$ and $y$ directions, respectively

$k_m$ = effective thermal conductivity of porous region

$L_s$ = dimensionless coordinate along boundary $S$, $l_s/h_r$

$l_s$ = coordinate measured along boundary $s$

$M$ = heat-flux parameter, $(q_2 - q_1)/q_1$

$N$ = temperature parameter, $(t_2 - t_1)/(t_1 - t_\infty)$

$n$ = integer

$\mathbf{n}$ = outward normal vector

$p$ = pressure

$Q_f$ = volume flow rate of fluid per unit depth

$q$ = heat flux

$R_0$ = outer radius of region in $\omega$ plane, equation (22$c$)

$S, s$ = inner bounding surface of doubly connected porous region in dimensionless and physical coordinate systems, respectively

$S_0, s_0$ = outer boundary surface of doubly connected porous region in dimensionless and physical coordinate systems, respectively

$T$ = dimensionless temperature, $(t - t_\infty)/\Delta$

$t$ = temperature

$t_\infty$ = reservoir temperature

$\mathbf{U}, \mathbf{u}$ = dimensionless and physical Darcy velocities, respectively,

$$\mathbf{U} = \frac{\mu}{\kappa} \frac{\phi_s h_r}{(p_0 - p_s)} \mathbf{u}$$

$W$ = complex potential, $W = \psi + i\phi$

$X_a, X_b$ = dimensionless coordinates locating inner circle of eccentric porous region

$X, Y$ / $x, y$ = rectangular coordinates in dimensionless and physical planes, respectively,

$$X = \frac{x}{h_r}, \quad Y = \frac{y}{h_r}$$

$Z$ = dimensionless physical plane, $Z = X + iY$

$\alpha$ = integer in sinusoidal surface temperature equation (32)

$\gamma_n$ = quantity defined as $\sqrt{\Lambda^2 + n^2}$

$\Delta$ = $(t_1 - t_\infty)$ or $q_1 h_r/k_m$ when boundary conditions (5$a$) or (5$b$) apply

$\theta$ = dependent variable related to $T$ defined by equation (12)

$\kappa$ = permeability of porous material

$\Lambda$ = parameter, $\lambda/\phi_s$

$\lambda$ = parameter, $\frac{\rho C_p}{2k_m} \frac{\kappa(p_0 - p_s)}{\mu}$

$\mu$ = fluid viscosity

$\rho$ = fluid density

$\sigma$ = $aR_0$ defined in equation (26$b$)

$\phi, \phi_s$ = velocity potential, respectively, in porous region and along surface $S$, imaginary part of $W$, $\phi = (p_0 - p) \frac{\kappa}{\mu} \frac{2\pi}{Q_f}$, $\phi_s = (p_0 - p_s) \frac{\kappa}{\mu} \frac{2\pi}{Q_f}$

$\psi$ = real part of $W$

$\omega$ = intermediate mapping plane, see equation (22$a$)

$\tilde{\nabla}$ = $\mathbf{i}\partial/\partial X + \mathbf{j}\partial/\partial Y$

### Subscripts

1, 2 = values defining range of $t_s$ and $q_s$, equations (5$a$) and (5$b$)

0 = outer boundary

$s$ = inner boundary

energy equation

$$k_m \nabla^2 t - \rho C_p \mathbf{u} \cdot \nabla t = 0 \tag{3}$$

**Boundary Conditions.** As the fluid in the reservoir at $t_\infty$ approaches the boundary $s_0$ of the porous region, the temperature rises to $t_0$ which varies in an a priori unknown fashion along $s_0$. In most instances of practical interest the fluid velocity is sufficiently high and the fluid thermal conductivity sufficiently low relative to the thermal conductivity of the solid that the temperature change from $t_\infty$ to $t_0$ occurs in a thin fluid region near $s_0$. This region is therefore assumed to be locally one-dimensional, and since the velocity is perpendicular to $s_0$, there is no flow along this thin thermal layer. By applying an energy balance across this thermal layer the boundary conditions at $s_0$ are found to be

$$\left.\begin{aligned} k_m \mathbf{n}_0 \cdot \nabla t &= \rho C_p (t - t_\infty) \mathbf{n}_0 \cdot \mathbf{u} \\ p &= p_0 = \text{constant} \end{aligned}\right\} \quad \text{for } (x, y) \text{ on } s_0 \tag{4}$$

On the inner surface $s$ of the porous region two types of boundary conditions will be considered. The first corresponds to an arbitrary temperature variation on $s$ and can be written as

$$\left.\begin{aligned} t &= t_s = t_1 + (t_2 - t_1) F(l_s) \\ p &= p_s = \text{constant} \end{aligned}\right\} \quad \text{for } (x, y) \text{ on } s \tag{5a}$$

while the second corresponds to an arbitrary heat-flux variation and can be written as

$$\left.\begin{aligned} k_m \mathbf{n}_s \cdot \nabla t &= q_s = q_1 + (q_2 - q_1) G(l_s) \\ p &= p_s = \text{constant} \end{aligned}\right\} \quad \text{for } (x, y) \text{ on } s \tag{5b}$$

The functions $F(l_s)$ and $G(l_s)$ can be any functions which are equal to zero at $l_s = 0$ and have a maximum absolute value of unity.

**Dimensionless Equations.** Upon making equations (1) to (5) dimensionless, and using equation (2) to eliminate $\mathbf{u}$ in equations (1) and (3), we obtain

$$\tilde{\nabla}^2 \phi = 0 \tag{6a}$$

$$\mathbf{U} = \tilde{\nabla} \phi \tag{6b}$$

$$\tilde{\nabla}^2 T - 2\Lambda \tilde{\nabla} \phi \cdot \tilde{\nabla} T = 0 \tag{6c}$$

$$\mathbf{n}_0 \cdot \tilde{\nabla} T = 2\Lambda \mathbf{n}_0 \cdot \mathbf{U} T, \qquad \phi = 0 \quad \text{for } (X, Y) \text{ on } S_0 \tag{7}$$

$$T = 1 + NF(L_s), \qquad \phi = \phi_s \quad \text{for } (X, Y) \text{ on } S \tag{8a}$$

or

$$\mathbf{n}_s \cdot \tilde{\nabla} T = 1 + MG(L_s), \qquad \phi = \phi_s \quad \text{for } (X, Y) \text{ on } S \tag{8b}$$

The porous region in the dimensionless physical plane is shown in Fig. 1(*b*). The cut through the region is introduced for mathematical convenience and will be explained subsequently. Since the two surfaces of the porous region are each at constant pressure, the function $\phi$ is constant on both $S_0$ and $S$. Hence the unit normal vectors can be written as

$$\mathbf{n}_0 = -\frac{\tilde{\nabla} \phi}{|\tilde{\nabla} \phi|} \qquad \text{for } (X, Y) \text{ on } S_0 \tag{9a}$$

$$\mathbf{n}_s = \frac{\tilde{\nabla} \phi}{|\tilde{\nabla} \phi|} \qquad \text{for } (X, Y) \text{ on } S \tag{9b}$$

Equations (9) along with equation (6*b*) are used in the boundary conditions (7) and (8*b*) to yield

$$\tilde{\nabla} \phi \cdot \tilde{\nabla} T = 2\Lambda T |\tilde{\nabla} \phi|^2, \qquad \phi = 0 \quad \text{for } (X, Y) \text{ on } S_0 \tag{10}$$

$$\tilde{\nabla} \phi \cdot \tilde{\nabla} T = |\tilde{\nabla} \phi| [1 + MG(L_s)], \qquad \phi = \phi_s \quad \text{for } (X, Y) \text{ on } S \tag{11}$$

Equations (6*a*) and (6*c*), which are related to the flow and energy equations, are to be solved subject to the boundary conditions (10) on $S_0$ and either (8*a*) or (11) on $S$. Note that since the flow is independent of temperature, the dimensionless pressure $\phi$ can be found independently of the temperature by solving $\tilde{\nabla}^2 \phi = 0$ subject to $\phi = 0$ and $\phi = \phi_s$ on $S_0$ and $S$, respectively.

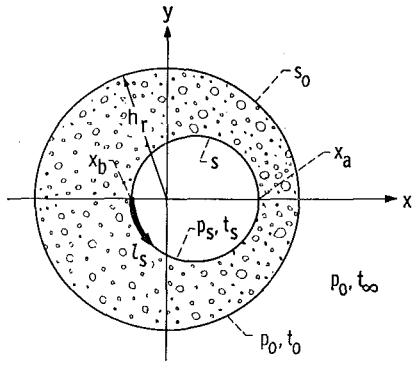


(a) Physical plane.

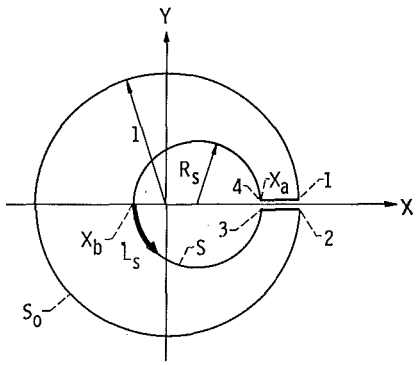


(b) Dimensionless physical plane Z = X + iY.

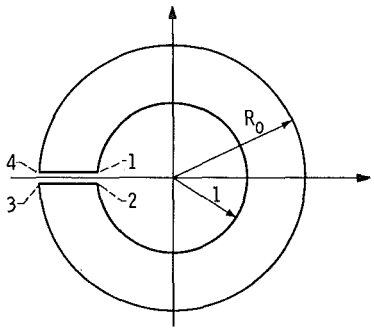


(c) Intermediate $\omega$-plane.

**Fig. 2 Porous eccentric annulus**

**Porous Region in Potential Plane.** Equation (6*a*) shows that $\phi$ satisfies Laplace's equation, and hence there must exist a harmonic function $\psi$ and an analytic function $W$ of the complex variable $Z = X + iY$ such that $W = \psi + i\phi$. Physically, the change in $\psi$ between any two points in the $W$ plane is equal to the dimensionless volume flow of liquid crossing any curve joining these two points. A consideration of the change in $\psi$ corresponding to the entire flow through the porous region and the fact that the manner of nondimensionalization implies that the total nondimensional flow through the porous material is $2\pi$ shows that $\Delta\psi = -2\pi$ where $\Delta\psi$ denotes the increment in $\psi$ in traversing the contour $S$ in a positive (clockwise) direction. The transformation $Z \rightarrow W$ therefore maps the porous region into the rectangular region shown in Fig. 1(*c*) where corresponding points in Figs. 1(*b*) and (*c*) have the same numbers.

**Transformation of Boundary-Value Problem into Potential Plane.** The solution for the temperature distribution can be obtained by transforming the boundary-value problem from the $Z$ plane into the rectangular region in the $W$ plane. The independent variables

$X$ and $Y$ will be changed to $\psi$ and $\phi$ and the resulting differential equation solved in the rectangular region of Fig. 1($c$). It will also be convenient to introduce a new dependent variable by

$$\theta \equiv e^{\Lambda(\phi_s - \phi)}T \tag{12}$$

Once the solution for $\theta$ and therefore for $T$ as a function of $\psi$ and $\phi$ is found, the mapping $W \rightarrow Z$ is used to obtain the solution for the temperature in the physical plane.

The algebraic details of the transformation will not be given here, but a number of relations which simplify the manipulations are given in [6]. The results of transforming equation (6$c$) and the boundary conditions (10), (8$a$), and (11) are

$$\frac{\partial^2\theta}{\partial\psi^2} + \frac{\partial^2\theta}{\partial\phi^2} - \Lambda^2\theta = 0 \qquad \text{for} \quad 0 \le \phi \le \phi_s, \quad -\pi \le \psi \le \pi \tag{13}$$

$$\frac{\partial\theta}{\partial\phi} - \Lambda\theta = 0 \qquad \text{for} \quad \phi = 0, \quad -\pi \le \psi \le \pi \tag{14}$$

$$\left.\begin{aligned} &\theta = 1 + NF[L_s(\psi)] \qquad (15a)\\ &\text{or}\\ &\frac{\partial\theta}{\partial\phi} + \Lambda\theta = \left|\frac{dZ}{dW}\right|\{1 + MG[L_s(\psi)]\} \qquad (15b) \end{aligned}\right\} \quad \text{for} \quad \phi = \phi_s, \quad -\pi \le \psi \le \pi$$

The remaining boundary conditions needed to complete the formulation in the potential plane are obtained from the continuity requirements at the cut in Fig. 1($b$)

$$\theta(-\pi, \phi) = \theta(\pi, \phi) \tag{16a}$$

$$\frac{\partial\theta}{\partial\psi}(-\pi, \phi) = \frac{\partial\theta}{\partial\psi}(\pi, \phi) \tag{16b}$$

**General Solution of Boundary-Value Problem in Potential Plane.** The differential equation (13) can be solved by separation of variables. After applying the boundary conditions (14), (16$a$), (16$b$), and either condition (15$a$) or (15$b$) corresponding respectively to either a specified surface temperature or a specified surface heat flux, we obtain the solutions for specified surface temperature

$$\theta = e^{\Lambda(\phi - \phi_s)} + N\sum_{n=-\infty}^{\infty} a_n\left(\frac{\Lambda\sinh\gamma_n\phi + \gamma_n\cosh\gamma_n\phi}{\Lambda\sinh\gamma_n\phi_s + \gamma_n\cosh\gamma_n\phi_s}\right) \times e^{in\psi} \tag{17}$$

where

$$a_n = \frac{1}{2\pi}\int_{-\pi}^{\pi} F[L_s(\psi)]e^{-in\psi}\,d\psi \qquad n = 0, \pm1, \pm2, \ldots$$

and for specified surface heat flux

$$\theta = \sum_{n=-\infty}^{\infty} b_n\left[\frac{\Lambda\sinh\gamma_n\phi + \gamma_n\cosh\gamma_n\phi}{(\gamma_n^2 + \Lambda^2)\sinh\gamma_n\phi_s + 2\Lambda\gamma_n\cosh\gamma_n\phi_s}\right] \times e^{in\psi} \tag{18}$$

where

$$b_n = \frac{1}{2\pi}\int_{-\pi}^{\pi}\left|\frac{dZ}{dW}\right|_{\phi_s}\{1 + MG[L_s(\psi)]\}e^{-in\psi}d\psi \qquad n = 0, \pm1, \pm2, \ldots$$

For a specified surface temperature it is of practical interest to determine the heat flux entering the surface. This can be obtained from

$$q_s = k_m\mathbf{n}_s\cdot\nabla t \qquad \text{for } (x, y) \text{ on } s \tag{19}$$

Upon using equation (9$b$), introducing the change of variables described previously, and inserting equations (15$a$) and (17) into the result, we obtain the following expression for the surface heat flux:

$$\frac{q_s h_r}{k_m(t_1 - t_\infty)} = \left|\frac{dW}{dZ}\right|_{\phi_s}\left[\Lambda\{2 + NF[L_s(\psi)]\} + N\sum_{n=-\infty}^{\infty} a_n\gamma_n\left(\frac{\Lambda\cosh\gamma_n\phi_s + \gamma_n\sinh\gamma_n\phi_s}{\Lambda\sinh\gamma_n\phi_s + \gamma_n\cosh\gamma_n\phi_s}\right)e^{in\psi}\right] \tag{20}$$

When the surface heat flux is specified it is the surface temperature distribution that is of practical interest. From equation (12) the dimensionless surface temperature is equal to $\theta$ evaluated at $\phi = \phi_s$, which gives

$$T_s = \frac{t_s - t_\infty}{\frac{q_1 h_r}{k_m}} = \sum_{n=-\infty}^{\infty} b_n \times\left[\frac{\Lambda\sinh\gamma_n\phi_s + \gamma_n\cosh\gamma_n\phi_s}{(\gamma_n^2 + \Lambda^2)\sinh\gamma_n\phi_s + 2\Lambda\gamma_n\cosh\gamma_n\phi_s}\right]e^{in\psi} \tag{21}$$

The general solutions for $q_s$ and $t_s$ given by equations (20) and (21) can be applied to any doubly connected geometry by finding the conformal transformation of the coordinates in the potential plane into the physical coordinates for that geometry. A convenient method for doing this is by conformal mapping. A specific illustration will now be given.

## Application of Theory to Porous Eccentric Annulus

To illustrate the use of the general solution, heat-transfer results will be obtained for a porous eccentric annular region, shown in the physical plane in Fig. 2($a$). The radius of the outer circle is used as the characteristic dimension $h_r$, and the porous region is shown in the dimensionless physical plane in Fig. 2($b$) where a particular choice for the location of the cut (along the positive real axis) is also shown.

**Mapping Relations for $|dW/dZ|_{\phi_s}$ and $L_s(\psi)$.** The general solution was obtained in the $W$ plane and hence the heat-transfer quantities given by equations (20) and (21) are in terms of the variable $\psi$ along the boundary $\phi = \phi_s$ in Fig. 1($c$). The relation between $\psi$ and $L_s$ along the inner boundary must be found to relate the solution to the physical plane. It is also necessary to determine the quantity $|dW/dZ|_{\phi_s}$ as a function of $\psi$ for use in equation (20) and in the coefficients $b_n$ of equation (21). These relations can be obtained from the conformal mapping $Z \rightarrow W$ which transforms the region in Fig. 2($b$) into the region in Fig. 1($c$).

To this end an intermediate mapping is performed. This mapping from the eccentric region in the $Z$ plane of Fig. 2($b$) to the concentric region in the $\omega$ plane of Fig. 2($c$) is given in [7, p. 287] as

$$\omega = \frac{Z - a}{aZ - 1} \tag{22a}$$

where $a$ is related to the coordinates $X_a$ and $X_b$ of the inner circle in Fig. 2($b$) by

$$a = \frac{1 + X_aX_b + [(1 - X_a^2)(1 - X_b^2)]^{1/2}}{X_a + X_b} \tag{22b}$$

and the outer radius $R_0$ in Fig. 2($c$) is given by

$$R_0 = \frac{1 - X_aX_b + [(1 - X_a^2)(1 - X_b^2)]^{1/2}}{X_a - X_b} \tag{22c}$$

A logarithmic transformation can then be used to map the slit annular region in Fig. 4 into the rectangle in Fig. 2. This gives

$$W = i \ln \omega = i \ln \left( \frac{Z - a}{aZ - 1} \right) \tag{23}$$

Along the boundary $\overline{34}$ the imaginary part of $W$ in Fig. 1($c$) is $\phi_s$ while the imaginary part of $i \ln \omega$ is $\ln R_0$. Hence by use of equation (22$c$)

$$\phi_s = \ln R_0 = \ln \left[ \frac{1 - X_a X_b + [(1 - X_a^2)(1 - X_b^2)]^{1/2}}{X_a - X_b} \right] \tag{24}$$

In order to obtain an expression for $dW/dZ$, notice that when equation (23) is solved for $Z$ we obtain

$$Z = \frac{a - e^{-iW}}{1 - ae^{-iW}} \tag{25}$$

Equation (25) is differentiated with respect to $W$ and the absolute value of the reciprocal of the result is taken to express $|dW/dZ|$ as a function of $W$. Then, on the boundary $S$ (i.e., $W = \psi + i\phi_s$), we find upon using equations (24), (22$b$), and (22$c$) that

$$\left| \frac{dW}{dZ} \right|_{\phi_s} = \frac{1 - 2\sigma \cos \psi + \sigma^2}{[(X_a - X_b)/2](\sigma^2 - 1)} \tag{26a}$$

where we have set

$$\sigma \equiv aR_0 = \frac{(1 - X_b^2)^{1/2} + (1 - X_a^2)^{1/2}}{(1 - X_b^2)^{1/2} - (1 - X_a^2)^{1/2}} \tag{26b}$$

To obtain the relation between the length coordinate $L_s$ along the inner circle in Fig. 2($b$) and the coordinate $\psi$ along the boundary $\overline{34}$ in Fig. 1($c$), notice that the origin $L_s = 0$ in the physical plane corresponds to the position where $\psi = 0$ in the potential plane. Integrating the differential arc length along the inner contour and then transforming to an integral along the line $\overline{34}$ in Fig. 1($c$) gives

$$L_s(\psi) = \int_{Z=X_b}^{Z(\psi+i\phi_s)} |dZ| = \int_{W=i\phi_s}^{\psi+i\phi_s} \left| \frac{dZ}{dW} \right| |dW|$$

However, along the line $\phi = \phi_s$, $dW = d\psi$, so that upon inserting equation (26$a$) into the integral we obtain

$$L_s(\psi) = \frac{(X_a - X_b)}{2} (\sigma^2 - 1) \int_0^{\psi} \frac{d\psi}{1 - 2\sigma \cos \psi + \sigma^2}$$

$$= (X_a - X_b) \left\{ \tan^{-1} \left[ \left( \frac{1 - X_b^2}{1 - X_a^2} \right)^{1/2} \tan \frac{\psi}{2} \right] \right\}$$

$$(-\pi \leq \psi \leq \pi) \tag{27}$$

**Magnitude of Fluid Exit Velocity and Volume Flow Rate from Porous Medium.** From equation (6$b$) the local dimensionless velocity in the porous material is $\mathbf{U} = \tilde{\nabla}\phi$. Since the inner boundary is at constant potential the exit velocity will everywhere be normal to this boundary. Since (see, e.g., [7, p. 182]) $|\tilde{\nabla}\phi| = |dW/dZ|$, it follows from (26$a$) that the magnitude of the exit velocity of the fluid is

$$\frac{|\mathbf{u}_s|}{\dfrac{\kappa(p_0 - p_s)}{\mu h_r}} = \frac{|\mathbf{U}|_{\phi_s}}{\phi_s} = \frac{1}{\phi_s} \left| \frac{dW}{dZ} \right|_{\phi_s}$$

$$= \frac{1}{\phi_s} \left[ \frac{1 - 2\sigma \cos \psi + \sigma^2}{[(X_a - X_b)/2](\sigma^2 - 1)} \right] \tag{28a}$$

The volume flow rate is found from the definition of $\phi_s$ and equation (24) as

$$Q_f = \frac{2\pi}{\ln R_0} \frac{\kappa}{\mu} (p_0 - p_s) \tag{28b}$$

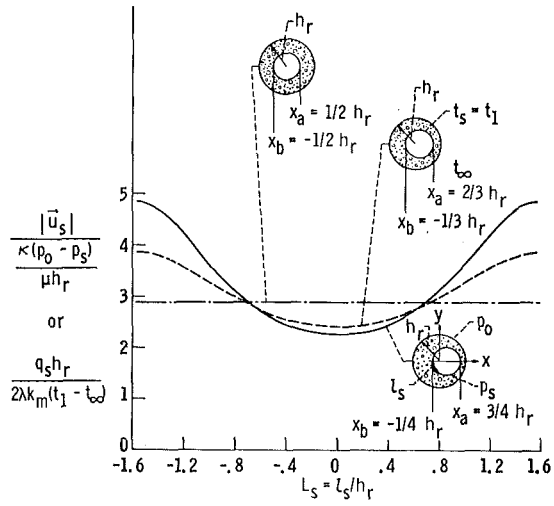


**Fig. 3 Variation with eccentricity of dimensionless exit-velocity distribution at inner surface, or dimensionless heat flux corresponding to a uniform inner surface temperature**

**Surface Temperature for Imposed Uniform Heat Flux.** We shall now apply the general expression for the surface temperature distribution, equation (21), to the special case of a uniform heat flux along the interior surface of the porous region. The parameter $M$ is zero in this case, and the surface heat flux has the constant value $q_1$. Then the coefficients $b_n$ in equation (18) become

$$b_n = \frac{1}{2\pi} \int_{-\pi}^{\pi} \left| \frac{dZ}{dW} \right|_{\phi_s} e^{-in\psi} d\psi \qquad n = 0, \pm 1, \pm 2, \ldots$$

Upon inserting equation (26$a$) in this equation and using the method of residues to evaluate the integral we obtain

$$b_n = \frac{X_a - X_b}{2\sigma^n} \qquad n = 0, \pm 1, \pm 2, \ldots \tag{29}$$

Insert this into equation (18) and note that the coefficients of the exponentials are real. Then

$$\frac{t_s - t_\infty}{\dfrac{q_1 h_r}{k_m}} = (X_a - X_b) \left\{ \frac{1}{4\Lambda} + \sum_{n=1}^{\infty} \frac{1}{\sigma^n} \right.$$

$$\left. \times \left[ \frac{\Lambda \sinh \gamma_n \phi_s + \gamma_n \cosh \gamma_n \phi_s}{(\gamma_n^2 + \Lambda^2) \sinh \gamma_n \phi_s + 2\Lambda \gamma_n \cosh \gamma_n \phi_s} \right] \cos n\psi \right\} \tag{30}$$

**Surface Heat Flux Corresponding to Imposed Uniform Surface Temperature.** When the inner surface temperature is uniform at $t_1$, i.e., $t_2 = t_1$ in equation (5$a$), equation (20) for the surface heat flux simplifies to

$$\frac{q_s h_r}{k_m(t_1 - t_\infty)} = 2\Lambda \left| \frac{dW}{dZ} \right|_{\phi_s} = \frac{2\Lambda}{\phi_s} \left[ \frac{1 - 2\sigma \cos \psi + \sigma^2}{[(X_a - X_b)/2](\sigma^2 - 1)} \right] \tag{31}$$

Thus by comparing equation (31) with equation (28$a$) the surface heat flux is found to be proportional to the magnitude of the fluid exit velocity from the porous region.

**Surface Heat Flux Corresponding to Imposed Sinusoidal Surface Temperature.** As a last example the surface heat flux will be derived for an imposed sinusoidal surface temperature. The dimensionless temperature is given by an expression of the form

$$T = 1 + NF[L_s(\psi)] = 1 + N \sin \left[ \alpha \frac{L_s(\psi)}{(X_a - X_b)/2} \right],$$

$$\frac{-\pi(X_a - X_b)}{2} \leq L_s \leq \frac{\pi(X_a - X_b)}{2} \tag{32}$$

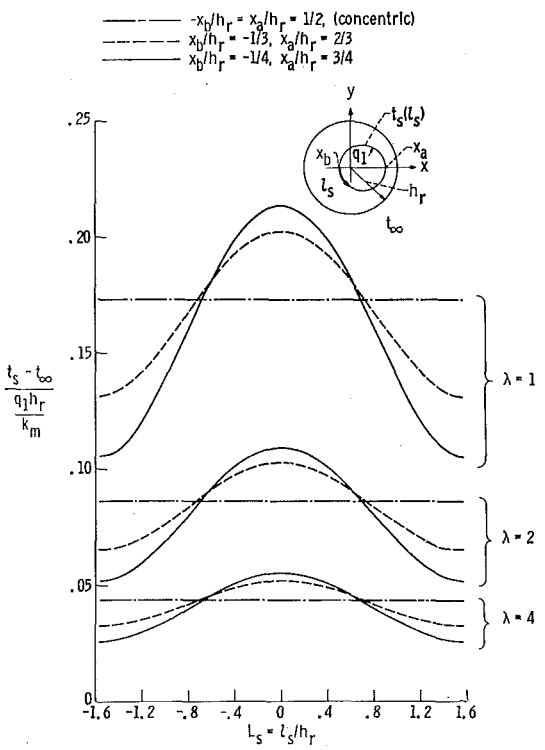


**Fig. 4 Effect of λ and eccentricity on inner surface temperature when the heat flux at the inner surface is uniform**

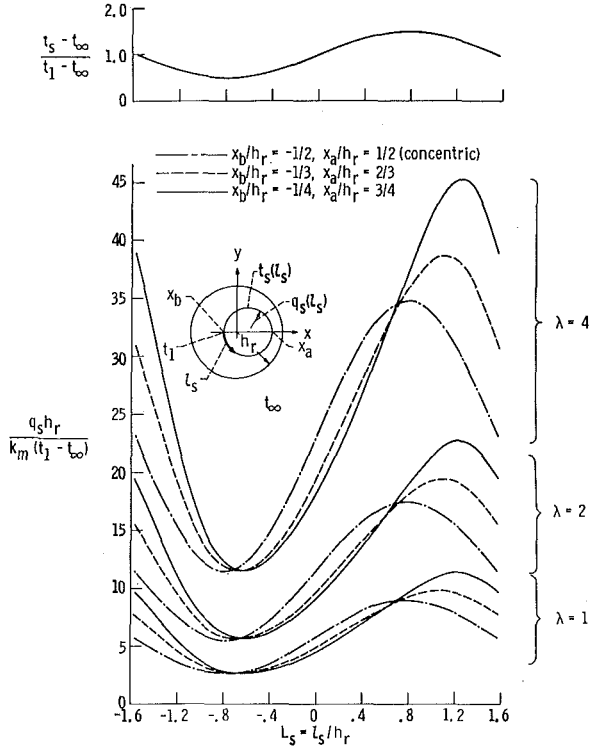


**Fig. 5 Effect of λ and eccentricity on inner surface heat flux corresponding to a sinusoidal surface temperature**

where $\alpha = 1, 2, 3, \ldots$. Since in this case $F[L_s(-\psi)] = -F[L_s(\psi)]$, the coefficients $a_n$ of equation (17) become

$$a_n = -\frac{2i}{2\pi}\int_0^\pi F[L_s(\psi)] \sin(n\psi)d\psi \tag{33}$$

When the expression for $F[L_s(\psi)]$ given by equations (32) and (27) and the expression for the coefficients $a_n$ given by equations (33) and (27) are substituted into equation (20), the surface heat-flux distribution is obtained as

$$\frac{q_s h_r}{k_m(t_1 - t_\infty)} = \left|\frac{dW}{dZ}\right|_{\phi_s}\left[\Lambda\left(2 + N\sin\left\{2\alpha\tan^{-1}\left[\left(\frac{1 - X_b^2}{1 - X_a^2}\right)^{1/2}\tan\frac{\psi}{2}\right]\right\}\right)\right.$$
$$\left. + N\sum_{n=1}^{\infty} A_n\gamma_n\left(\frac{\Lambda\cosh\gamma_n\phi_s + \gamma_n\sinh\gamma_n\phi_s}{\Lambda\sinh\gamma_n\phi_s + \gamma_n\cosh\gamma_n\phi_s}\right)\sin(n\psi)\right] \tag{34}$$

where

$$A_n = \frac{2}{\pi}\int_0^\pi \sin\left\{2\alpha\tan^{-1}\left[\left(\frac{1 - X_b^2}{1 - X_a^2}\right)^{1/2}\tan\frac{\psi}{2}\right]\right\}\sin(n\psi)d\psi$$

The special case of a concentric annulus with constant surface temperature has been considered in [8] and can be obtained by taking the proper limits in the above formulas.

## Discussion

To illustrate the characteristics of a porous region in the shape of an eccentric annulus, thereby showing how the two-dimensional shape influences the heat-transfer behavior, some typical numerical results will now be considered.

Fig. 3 shows the magnitude of the fluid velocity as it exits from the porous region along the interior surface. This was obtained from equation (28*a*) along with equation (27) to relate $\psi$ to $L_s$. Velocities are given for two eccentricities and for the concentric case. The two eccentricities are such that the ratios of the maximum to minimum wall thicknesses are 2:1 and 3:1, and the ratio of the inner to outer wall diameter is 1:2. As would be expected the highest exit velocities correspond to the thin portion of the porous region. As indicated in relation to equation (31), these curves also give the dimensionless heat flux $q_s h_r/(2\lambda k_m)(t_1 - t_\infty)$ corresponding to a uniform temperature along the inner boundary.

Fig. 4 gives the surface temperature variation for the case where a uniform heat flux is imposed along the inner boundary. These results were found using equation (30) along with equation (27) to relate $\psi$ to $L_s$. The porous-region geometries are the same as in Fig. 3. High surface temperatures are associated with low fluid exit velocities, and the results demonstrate the nature of this inverse relation for the velocity distributions shown in Fig. 3. The effect of the parameter $\lambda = \rho C_p \kappa(p_0 - p_s)/2k_m\mu$ is also demonstrated. A large value of λ is associated with a large pressure difference $p_0 - p_s$ across the porous region, which produces a large flow. Hence for a specified surface heat flux, the inner surface temperature decreases as λ is increased.

The heat flux corresponding to an imposed sinusoidal surface temperature is plotted in Fig. 5. A large value of λ (large flow) provides an increased surface heat flux for a given surface temperature. As the eccentricity is increased there is an increased deviation from an antisymmetric shape as a result of two-dimensional effects.

## Conclusions

A general analytical solution was obtained for the heat-transfer characteristics of a two-dimensional porous cooled medium of

arbitrary shape; the particular situation considered here is for a doubly connected porous region. General solutions for either arbitrary surface temperature or heat flux were obtained by transforming the equations into a potential plane in which the porous region maps into a rectangle regardless of its actual physical shape. When the independent variables of the energy equation are changed into potential-plane coordinates, the equation becomes separable and a general solution for the temperature distribution is obtained in the potential plane. The general solution can be applied to any specific physical geometry by mapping the rectangle in the potential plane into the physical region. This can be done numerically or by analytical means such as conformal mapping.

To illustrate the application of the solution, some specific results were obtained for an eccentric annular region. These results include the surface temperature corresponding to an imposed uniform surface heat flux, the heat flux entering the porous region corresponding to a specified uniform surface temperature, and the heat flux corresponding to an imposed sinusoidal surface temperature.

## References


1 Schneider, P. J., *Conduction Heat Transfer*, Addison-Wesley Publishing Co., Reading, Mass., 1955.

2 Grootenhius, P., "The Mechanism and Application of Effusion Cooling," *The Journal of the Royal Aeronautical Society*, Vol. 63, No. 578, Feb. 1959, pp. 73–89.

3 Koh, J. C. Y., and del Casal, E., "Heat and Mass Flow Through Porous Matrices for Transpiration Cooling," *Proceedings of the 1965 Heat Transfer and Fluid Mechanics Institute*, Charwat, A. F., ed., Stanford University Press, Stanford, Calif., 1965, pp. 263–281.

4 Schneider, P. J., Mauer, R. E., and Strap, M. G., "Two-Dimensional Transpiration Cooling," AIAA Paper No. 69-96, Jan. 1969.

5 del Casal, E. P., "The Effects of Multidimensional Flow through Porous Matrices in Mass Transfer Cooling," AIAA Paper No. 69-149, Jan. 1969.

6 Siegel, R., and Goldstein, M. E., "Analytical Method for Heat Transfer in Two-Dimensional Porous Media," NASA TN D-5878, Cleveland, Ohio, July 1970.

7 Churchill, R. V., *Complex Variables and Applications*, 2nd ed., McGraw-Hill, New York, N. Y., 1960.

8 Mayer, E., and Bartas, J. G., "Transpiration Cooling in Porous Metal Walls," *Jet Propulsion*, Vol. 24, No. 6, Nov.-Dec. 1954, pp. 366–368, 378.

**K. R. CHUN**
Member,
Senior Technical Staff,
Northrop Corporate Laboratories,
Hawthorne, Calif.
Assoc. Mem. ASME

**R. A. SEBAN**
Professor,
Department of Mechanical Engineering,
University of California,
Berkeley, Calif.
Fellow ASME

# Performance Prediction of Falling-Film Evaporators

*Three experimental results in the literature involving the evaporation of water and of brine in falling-film evaporators have been compared to predictions in which were used the local heat-transfer coefficients experimentally correlated as* $h = A(\Gamma/\mu)^n$, *where the constants* A *and* n *take on different values depending on the flow regime of the falling film, and* $(4\Gamma/\mu)$ *is the film Reynolds number. The relatively good accord between theory and experiment supports the use of those coefficients for design.*

## Introduction

THE PREDICTION of the performance of a falling-film evaporator in which the heat is provided by condensation involves the integration (with respect to length) of the product of the local value of the overall heat-transfer coefficient and the difference in the temperatures of the liquid–vapor interfaces, $T_C$ and $T_E$ as shown in Fig. 1. The overall coefficient depends upon the magnitude of the local coefficients for the evaporant and condensate films, and the temperature difference may be affected by the boiling-point rise if the solute concentration in the evaporant becomes large. In most of the data from test evaporators as given by Dukler and Elliot [1],[1] Sephton [2], and Webb et al. [3], the latter effect is not significant, and the key to a successful prediction is the appropriate specification of the local heat-transfer coefficient for the condensate and evaporant films. In fact, lack of success of such predictions as originally tried led to the experiments which produced the values of the local heat-transfer coefficient for the evaporating film in turbulent flow as reported by Chun and Seban [4].

Table 1 summarizes the values $A$ and $n$ that appear in the specification of the local heat-transfer coefficient as $h = A(\Gamma/\mu)^n$ for three regimes of flow; these are deemed to apply both for condensation and evaporation, presuming the system geometry is such that the effects of pressure gradient and vapor drag on the liquid layer remain small. For the evaporators considered, where the feed was essentially at the saturation temperature, there is a length required for the temperature profile to develop fully, and there was a simultaneous hydraulic development. This length, presumably small in relation to the total height of the evaporator, was neglected here, and the coefficients of Table 1 were used for the entire tube length.

The local value of the overall coefficient was then taken as

$$\frac{1}{U} = \frac{r_E}{r_C h_C} + \frac{1}{h_E} + \frac{1}{h_W} \tag{1}$$

where $h_W$ is the conductance of the tube wall referred to the radius $r_E$ of the evaporating surface $h_W = k_W/[r_E \log (r_C/r_E)]$ and the coefficient $U$ pertains to the tube area on the evaporant side. Subscripts $C$ and $E$ refer to the condensate side and the evaporant side, respectively.

Neglecting the changes in the energy stored in the liquid layers themselves, the rates of condensation and evaporation are given by

$$-\lambda_E \frac{d\Gamma_E}{dx} = \lambda_C \frac{d\Gamma_C}{dx} = U(T_C - T_E) \tag{2}$$

The overall energy balance gives

$$\Gamma_C = \frac{r_E}{r_C} \frac{\lambda_E}{\lambda_C} (\Gamma_{E0} - \Gamma_E) \tag{3}$$

where $\Gamma_{E0}$ is the feed rate per unit periphery.

Equations (1) and (2), together with the heat-transfer coefficients as given in Table 1, combine to give the specification for the variation in the evaporant flow as

$$-\lambda_E \frac{d\Gamma_E}{dx} = \frac{T_C - T_E}{\frac{r_E}{r_C} \frac{1}{A_C \left(\frac{\Gamma_C}{\mu_C}\right)^{nc}} + \frac{1}{A_E \left(\frac{\Gamma_E}{\mu_E}\right)^{nE}} + \frac{1}{h_W}} \tag{4}$$

## Evaporation of a Pure Liquid

With pure components on both the condensing and evaporating sides the interface temperatures $T_C$ and $T_E$ depend only on the pressures, and if these pressures can be assumed to be constant, equation (4) can be integrated between an initial point $x_A$ and $x$ using equation (3) to give

[1] Numbers in brackets designate References at end of paper.

Contributed by the Heat Transfer Division of THE AMERICAN SOCIETY OF MECHANICAL ENGINEERS and presented at the AIChE-ASME Heat Transfer Conference, Denver, Colo., August 6–9, 1972. Manuscript received by the Heat Transfer Division November 9, 1970. Paper No. 72-HT-48.

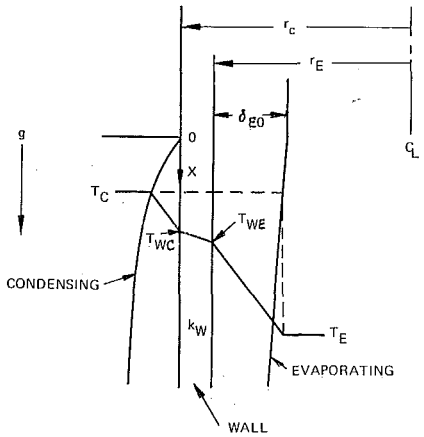


**Fig. 1 Sketch of a falling-film evaporator (laminar films assumed as shown)**

$$\frac{1}{A_C(1-n_C)}\left(\frac{r_E}{r_C}\right)^{1-nc}\left(\frac{\mu_E\lambda_E}{\mu_C\lambda_C}\right)^{-nc}\times\left[-\left(\frac{\Gamma_{E0}}{\mu_E}-\frac{\Gamma_E}{\mu_E}\right)^{1-nc}+\left(\frac{\Gamma_{E0}}{\mu_E}-\frac{\Gamma_{EA}}{\mu_E}\right)^{1-nc}\right]+\frac{1}{A_E(1-n_E)}\left[\left(\frac{\Gamma_E}{\mu_E}\right)^{1-n_E}-\left(\frac{\Gamma_{EA}}{\mu_E}\right)^{1-n_E}\right]+\left(\frac{\Gamma_E-\Gamma_{EA}}{\mu_E}\right)\frac{1}{h_W}=\frac{-(T_C-T_E)(x-x_A)}{\lambda_E\mu_E}\quad(5)$$

At $x_A = 0$, $\Gamma_{EA} = \Gamma_{E0}$, the condensate film is laminar, and the evaporant film is specified by its Reynolds number. Equation (5), with the values of $n$ and $A$ so specified, can be used until the first transition point, which will ordinarily be the transition of the laminar condensate layer to wavy-laminar flow. This is the initial point for another application of equation (5) with the new values of $n$ and $A$ for the condensate layer. With water the Reynolds number for the occurrence of wavy-laminar flow is so low that the laminar region can usually be ignored and the wavy-laminar flow can reasonably be assumed to begin at the top of the evaporator. The first important transition is then to turbulence on the condensate side, or, if the initial Reynolds number of the evaporant is in the low turbulent range, perhaps from turbulent to wavy-laminar flow in the evaporant stream.

## Comparison to Experimental Results

The majority of results to which comparisons are to be made involve either the evaporation of pure water or water containing such a small amount of salt that the boiling-point rise is not important. Table 2 summarizes the operating conditions for the results for which the comparisons are made. Heating is by condensation of water in all cases. Webb et al. [3] used a promoter to obtain dropwise condensation and thus referred their results to the nearly constant measured wall temperature.

Inspection of Table 2 shows that for Dukler's results the evaporant flow was wholly in the turbulent regime, except perhaps for the lowest feed rates, and the condensate almost entirely in the wavy-laminar regime, with so small a part of the condensate layer in the laminar regime as to make that negligible. Fig. 2 shows by curves the prediction[2] from equation (5), all for turbulent–wavy-laminar except for the lowest Reynolds numbers, for

[2] The small tube-side pressure variation was considered by using the average pressure in evaluating the saturation temperature for the evaporant side.

**Table 1 Constants $A$ and $n$ for the local heat-transfer coefficients**

| | Laminar [6] $\left(\frac{\Gamma}{\mu}\right) \le \left(\frac{\Gamma}{\mu}\right)_i^*$ | Wavy-laminar [6] $\left(\frac{\Gamma}{\mu}\right)_i < \left(\frac{\Gamma}{\mu}\right) \le \left(\frac{\Gamma}{\mu}\right)_{tr}^{**}$ | Turbulent [4] $\left(\frac{\Gamma}{\mu}\right) > \left(\frac{\Gamma}{\mu}\right)_{tr}^{***}$ |
|---|---|---|---|
| $A$ | $\left(\frac{k^3g}{3\nu^2}\right)^{1/3}$ | $0.606\left(\frac{k^3g}{\nu^2}\right)^{1/3}$ | $6.61\times10^{-3}\left(\frac{k^3g}{\nu^2}\right)^{1/3}\left(\frac{\nu}{\alpha}\right)^{0.65}$ |
| $n$ | $-1/3$ | $-0.22$ | $+0.4$ |

* $\left(\frac{\Gamma}{\mu}\right)_i = 0.61\left(\frac{\mu^4 g}{\rho\sigma^3}\right)^{-1/11}$

** $\left(\frac{\Gamma}{\mu}\right)_{tr} = 1450\ \mathrm{Pr}^{-1.06}$.

*** Upper limits of data [4] on which this specification established:

| Pr | 5.7 | 2.91 | 1.77 |
|---|---|---|---|
| $\frac{4\Gamma}{\mu}$ | 9000 | 15000 | 22000 |

## Nomenclature

$A$ = dimensional constant (Btu/hr-deg F-ft²)
$B$ = dimensional constant (deg F)
$c_p$ = specific heat of liquid (Btu/lb-deg F)
$D$ = diffusion coefficient of a solute in a solvent (ft²/hr)
$g$ = gravitational acceleration (ft/hr²)
$h$ = local heat-transfer coefficient (Btu/hr-deg F-ft²)
$k$ = thermal conductivity (Btu/hr-deg F-ft)
$m$ = thickness as defined in Fig. 5 in relation to the concentration boundary layer (ft)
$n$ = numerical constant
Pr = Prandtl number, $c_p\mu/k$
$p$ = vapor pressure ($lb_f/ft^2$)
Re = film Reynolds number, $4\Gamma/\mu$
$r$ = radius of evaporator tube (ft)
$T$ = temperature (deg F)
$U$ = heat-transfer conductance (Btu/hr-deg F-ft²)
$w$ = solute concentration (lb/ft³)
$\bar{w}$ = average concentration over thickness $\delta$ (lb/ft³)
$x$ = coordinate down the wall (ft)
$y$ = coordinate normal to the wall (ft)
$\alpha$ = thermal diffusivity (ft²/hr)
$\Gamma$ = mass flow rate per unit width of the wall (lb/hr-ft)
$\delta$ = film thickness (ft)
$\mu$ = absolute viscosity (lb/ft-hr)
$\varkappa$ = dimensional constant (deg F-ft³/lb)
$\nu$ = kinematic viscosity (ft²/hr)
$\rho$ = density (lb/ft³)
$\sigma$ = surface tension ($lb_f$/ft)
$\lambda$ = latent heat of vaporization (Btu/lb)

**Subscripts**

$C$ = condensing side
$E$ = evaporating side
$F$ = condition at the bottom of the tube
$i$ = wave inception
0 = condition at $x = 0$
sat = saturation condition corresponding to the vapor pressure
tr = transition to turbulent flow
$W$ = at the wall or of the wall

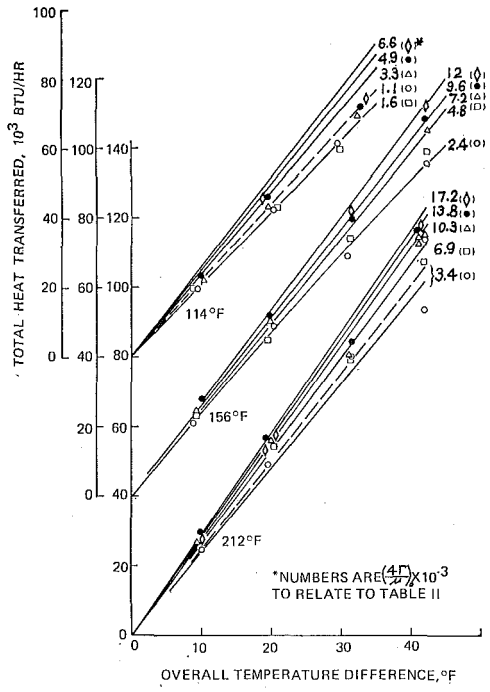


Fig. 2 Comparison with data of Dukler and Elliot [1]

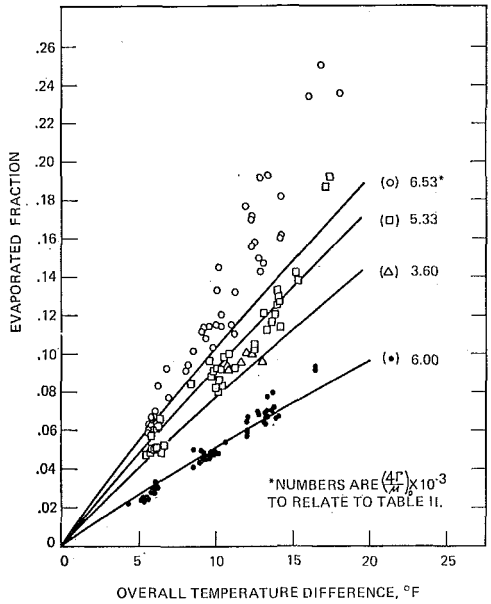


Fig. 3 Comparison with data of Sephton [2]

which both films were taken as wavy-laminar and a dashed curve is used. The data are shown by points. For the lowest temperature the correspondence with the prediction is less satisfactory, though the largest discrepancies are about 7 percent in the ordinate. At the 156 and 212 deg F temperatures the agreement is good. Because of the thick stainless tube used for heat metering, with the attendant low wall conductance as indicated in Table 2, the solid-wall thermal resistance is of approximately the same magnitude as the resistance attributable to the liquid films. Hence, the percent deviation observed in Fig. 2 would be about doubled if the wall resistance were negligible.

The results for the 212 deg F case, showing correspondence to the highest temperature difference, imply that no significant amount of nucleate boiling occurred. At the highest Reynolds number the evaporant heat-transfer coefficient at the top of the tube was 1500, so that of the 43 deg F temperature difference, 11 deg F occurred across the evaporating film, while at the lowest Reynolds number, 3440, the evaporant heat-transfer coefficient was 830 and the temperature difference was 16 deg F. At the lower pressures the superheat required for nucleation increases, and nucleation would not be anticipated if it did not occur at the highest pressure.

Fig. 3 shows the data of Sephton [2] and the prediction as curves, all being for the turbulent–wavy-laminar combination. Here the agreement is not as good as revealed in Fig. 2. An average line drawn through the data for 210 deg F for $(T_C - T_E) < 15$ deg F indicates the prediction to be about 8 percent low, but this is not so much a variance with Fig. 2 considering the small thermal resistance of the copper tube used in these experiments. The data for the higher feed rate at 125 deg F begin to show discrepancy at $(T_C - T_E) > 12.5$. While nucleation might have occurred at atmospheric pressure at such temperature differences, it would not be expected at lower pressures, so that the possibility of nucleation does not explain the discrepancies that exist.

**Table 2 Summary of experimental conditions**

| Reference | $l$ ft | $r_E$ in. | $r_C$ in. | $T_E$* deg F | $\left(\frac{4\Gamma}{\mu}\right)_{E0}$ | $\left(\frac{\nu}{\alpha}\right)_E$ | $\left(\frac{4\Gamma}{\mu}\right)_{trE}$ | $\left(\frac{4\Gamma}{\mu}\right)_{iC}$ | Maximum fraction evaporated | $\left(\frac{4\Gamma}{\mu}\right)_{CF}$ | Feed lb/hr | Feed % salt |
|---|---|---|---|---|---|---|---|---|---|---|---|---|
| Dukler [1] (stainless steel tube) | 20 | 0.95 | 1.18 | 114 | 6,600 to 1,100 | 3.9 | 1370 | 26 | 0.065 to 0.310 | 350 to 277 | 1200 to 200 | 0 |
| | $h_W = 525 \frac{\text{Btu}}{\text{hr-ft}^2\text{-deg F}}$ | | | 156 | 12,000 to 2,400 | 2.6 | 2100 | 30 | 0.084 to 0.350 | 810 to 680 | 1500 to 300 | 0 |
| | | | | 212 | 17,200 to 3,440 | 1.8 | 3200 | 33 | 0.086 to 0.350 | 1200 to 960 | 1500 to 300 | 0 |
| Sephton [2] (Cu tube) | 20 | 0.935 | 1.00 | 125 | 6,000 | 3.7 | 1460 | 27 | 0.09 | 510 | 1000 | 3.5 |
| | | | | 125 | 3,600 | 3.7 | 1460 | 27 | 0.10 | 340 | 600 | |
| | $h_W = 37{,}700 \frac{\text{Btu}}{\text{hr-ft}^2\text{-deg F}}$ | | | 175 | 5,330 | 2.4 | 2360 | 31 | 0.19 | 950 | 600 | |
| | | | | 210 | 6,530 | 1.8 | 3260 | 33 | 0.24 | 1470 | 600 | |
| Webb et al. [3] (Cu tube) | 1.33 | 1.987 | 1.750 | 216 | 528 | 1.8 | 3200 | 33 | 0.19 | dropwise | 95 | 0 |
| | | | | | 405 | | | | 0.35 | | 70 | |
| | | | | | 264 | | | | 0.48 | | 45 | |
| | | | | 216 | 492 | 1.9 | 2960 | | 0.28 | dropwise | 95 | 7 |
| | | | | | 246 | | | | 0.64 | | 45 | |
| | | | | 216 | 410 | 2.31 | 2380 | | 0.27 | dropwise | 95 | 14 |
| | | | | | 328 | | | | 0.36 | | 70 | |
| | | | | | 205 | | | | 0.46 | | 45 | |

* Steam saturation temperature corresponding to evaporant pressure.

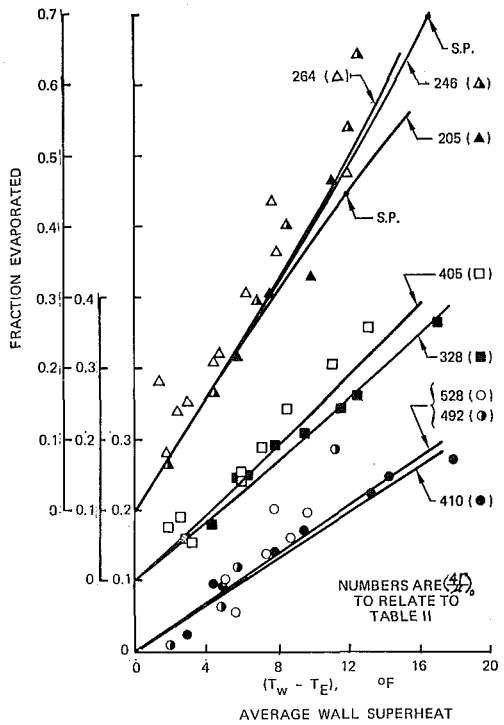


**Fig. 4 Comparison with data of Webb et al. [3]**

Fig. 4, which shows the results of Webb et al. for which the evaporating layer was always in the wavy-laminar regime, contains open points for which pure water was evaporated. The associated predictions, made now for no condensate layer and $h_W \to \infty$, are at the most 15 percent below an average line drawn through the data. There is no explanation for the discrepancy, though Webb et al. noted with pure water a tendency toward rivulets and sometimes partially dry surfaces; both effects would elevate the experimental data. The surface was observed visually and only minimal nucleation was noted at temperature differences greater than 14 deg F.

## Evaporation of Brine

If the evaporant contains a solute then its interface temperature exceeds the saturation temperature corresponding to the adjacent vapor pressure because of the boiling-point rise produced by the solute. To determine this rise the interface concentration of the solute is needed, and even an approximate calculation thereof is complicated. Chun [5] has done this for laminar flow, and a few elements of that calculation are included here to indicate that for salt in water it is sufficiently accurate to consider the interface concentration to be the same as the average concentration.

The approximate calculation is based on an integral method in which is assumed a parabolic concentration distribution as shown in Fig. 5.

$$w = a + b(\delta - y) + c(\delta - y)^2 \tag{6}$$

In the initial region the increased concentration of salt in the outer region, due to the evaporation of liquid from the interface, has not yet reached the wall. There the terms $a$, $b$, and $c$ in equation (6) are determined by

$$w = w_0 \quad \text{and} \quad \frac{\partial w}{\partial y} = 0 \qquad \text{at} \quad y = m$$

and

$$-D\frac{\partial w}{\partial y} = \frac{w}{\rho}\frac{d\Gamma}{dx} \qquad \text{at} \quad y = \delta \tag{7}$$

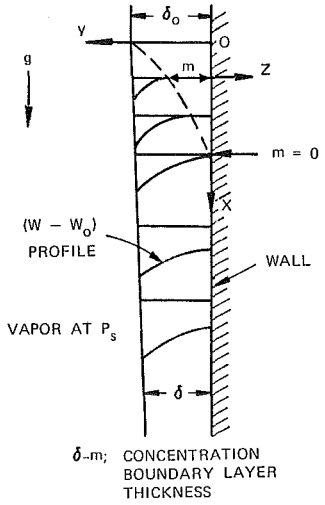


**Fig. 5 Evaporation from a falling film with a solute**

With the constants determined in this way, equation (6) gives, at $y = \delta$,

$$\frac{w_\delta}{w_0} = \left[1 + \frac{\delta - m}{2\rho D}\frac{d\Gamma}{dx}\right]^{-1} \tag{8}$$

But $d\Gamma/dx = -(k/\delta\lambda)\Delta T$ where $\Delta T$ is the local temperature difference across the layer, which actually varies due to the boiling-point rise. Using this, equation (8) becomes

$$\frac{w_\delta}{w_0} = \left[1 - \frac{\delta - m}{2\delta}\frac{\alpha}{D}\frac{c_p\Delta T}{\lambda}\right]^{-1}$$

The variation of distance $m$ with $x$ is specified by the condition for conservation of the solute, $\int_0^\delta u\,w\,dy = \frac{\Gamma_0}{\rho}w_0$, and the resulting expression is complicated. It indicates that $m = 0$ at the position where

$$\left(1 - \frac{\Gamma_0}{\Gamma}\right) = \frac{10}{20 + 40\{\rho D/[\delta(d\Gamma/dx)]\}}$$

For salt in water $\alpha/D \simeq 20$, so that for a 10 deg F temperature difference $-(\delta/\rho D)(d\Gamma/dx) \simeq (\alpha/D)(c_p\Delta T/\lambda)$ is about 0.20 and the value of $m$ is zero at about 5 percent evaporation. Equation (8) indicates that at this point $w_\delta/w_0 \simeq 1.10$, and the local average concentration ratio $\bar{w}/w_0 = \Gamma_0/\Gamma \simeq 1.05$.

Downstream of this point the wall concentration increases from its initial value $w_0$ and equation (6) is evaluated with $\partial w/\partial y = 0$ at $y = 0$, and the conservation condition specifies how the wall concentration varies with length. The interface concentration is then obtained as

$$\frac{w_\delta}{w_0} = \frac{\Gamma_0}{\Gamma}\left(1 + \frac{\delta}{5\rho D}\frac{d\Gamma}{dx}\right)^{-1} \tag{9}$$

For the example of $(\alpha/D)(c_p\Delta T/\lambda) = 0.20$ this is $w_\delta/w_0 = (\Gamma_0/\Gamma)(1 - 0.04)^{-1}$, or $\bar{w}/w_\delta = (1 - 0.04)$. Thus for typical conditions, the interface concentration for the evaporation of brine is only slightly above the local average concentration.

With the local brine concentration specified, here in terms of $\Gamma$, the problem proceeds to the integration of equation (4) with $T_E$ now specified by the saturation temperature corresponding to the vapor pressure and a specified relation for the boiling-point rise. This can of course be accomplished numerically but it is appropriate here to visualize a linear approximation $BPE = B + \varkappa w$ where the line is drawn to give a reasonable approximation in the operating range and $B$ is the vertical intercept on the $BPE$ vs. $w$ representation. Then equation (4) becomes, for an isothermal wall,

$$-\frac{d\Gamma}{dx} = \frac{A(\Gamma/\mu)^n}{\lambda}[T_W - T_{sat} - B - \kappa w_\delta] \qquad (10)$$

If we consider the problem in the neglect of the short initial region and use equation (9) to specify $w_\delta$, equation (10) still needs to be integrated numerically. An approximation of fair accuracy, however, consists in first evaluating $w_\delta(x)$ from a value of $\Gamma(x)$ obtained by neglecting the boiling-point elevation and then inserting this value into equation (10).

Brine was evaporated in those experiments of Webb et al. which are indicated by shaded and partially shaded points of Fig. 4. For the experimental data the interface temperature $T_E$ was evaluated as that corresponding to a salinity which was the average of the salinities of the feed and product streams. The associated predictions were made by determining $w_\delta$ on the basis of laminar flow, though in the experiments the flow was wavy-laminar and the ratios $\bar{w}/w_\delta$ would be even closer to unity than they are predicted to be for laminar flow. Also, the temperature $T_E$, used in the abscissa of Fig. 4 for the prediction, is the average of the interface temperatures at 10 equally spaced points along the height of the evaporator; this is a minor difference in comparison to the way in which this quantity was evaluated for the representation of the data. The comparison of experiment and prediction is generally favorable, and the curves for the prediction show also the points, designated S.P., for the temperature differences at which salt will precipitate at the bottom of the evaporator. At larger temperature differences salt will precipitate above the bottom, and for the 7 percent solution at a Reynolds number of 246 and 18 deg F temperature difference, Webb et al. observed salt precipitation at about one-third the height measured from the bottom of the tube.

## Conclusions

The results of three experiments involving the evaporation of water and of brine have been compared to predictions in which were used the local heat-transfer coefficients specified in Table 1. The relatively good accord between theory and experiment supports the use of those coefficients for design.

The only results in which the boiling-point elevation was significant involved wavy-laminar flow of brine. For these results the boiling-point elevation could be appraised satisfactorily from theoretical considerations based on laminar flow, which indicated that the interface concentration differed little from the average value.

## Acknowledgment

This research was supported by the Sea Water Conversion Laboratory of the University of California.

## References

1 Dukler, A. E., and Elliot, L. C., "Experimental and Analytical Studies of Heat Transfer in a Falling Film System," Final Report, Part II, Houston Research Institute, Mar. 1968.

2 Sephton, H. M., "An Investigation of Vertical Tube Evaporation Utilizing the Sephton Flash Tube," U.S. Department of the Interior OSW R&D Progress Report No. 361, 1969.

3 Webb, R. W., Unterberg, W., and Gregson, W., Jr., "Evaporation Experiments with Wiped and Falling Saline Water Films," UCLA Report No. 64-23, May 1964.

4 Chun, K. R., and Seban, R. A., "Heat Transfer to Evaporating Liquid Films," JOURNAL OF HEAT TRANSFER, TRANS. ASME, Series C, Vol. 93, No. 4, Nov. 1971, pp. 391–396.

5 Chun, K. R., "Evaporation from Thin Liquid Films," PhD dissertation, University of California, Berkeley, Calif., 1969.

6 Kutadeladze, S. S., *Fundamentals of Heat Transfer*, Edward Arnold, London, England, 1963, p. 307.

LLOYD H. BACK
Technical Staff.
Mem. ASME

PAUL F. MASSIER
Group Supervisor.

Jet Propulsion Laboratory,
California Institute of Technology,
Pasadena, Calif.

# Viscous Non-adiabatic Laminar Flow through a Supersonic Nozzle: Experimental Results and Numerical Calculations[1]

*Flow and thermal regimes found in relatively low Reynolds-number flows of high-temperature gases in cooled convergent divergent nozzles used in propulsion systems and in research facilities are investigated by a combined experimental and numerical approach. The experiments were conducted with argon at temperatures up to 14,200 deg R, and the throat Reynolds number ranged from 2200 to 2800. The numerical calculations involved the laminar-flow equations in differential form. Taken together, the experiments and the numerical calculations provide information on the pressure, heat-flux, and shear-stress distributions along internal flows with heat transfer, and on the velocity and enthalpy distributions across the flow as well as along the flow. The influence of heat conduction and of the viscous shear extended to the centerline all along the nozzle.*

## Introduction

An experimental investigation has been conducted in conjunction with numerical calculations to evaluate the flow field and the thermal environment in a convergent divergent nozzle when the flow is laminar and the core flow is non-adiabatic and viscous. These flow and thermal regimes are found in relatively low Reynolds-number flows of high-temperature gases in cooled nozzles which can be used in propulsion systems and in research facilities to accelerate gases to supersonic speeds. Such conditions exist, for example, in arc-heated flows of negligible ionization at pressures on the order of 1 atm or below. The non-adiabatic core flow situation differs significantly from that found in higher Reynolds-number flows through nozzles, such as those found in rocket engines used for primary propulsion where the boundary layer is usually relatively thin and the core flow can be regarded as adiabatic and inviscid. An important aspect of these flows is the calculation of heat transfer to the nozzle wall which requires external cooling in many applications in order to retain its structural integrity.

In this investigation a direct approach was used to learn as much about the actual flow as possible. To accomplish this, numerical calculations were carried out in conjunction with the experimental measurements.

The experiments were conducted with argon at temperatures up to 14,200 deg R which flowed through the axisymmetric nozzle shown in Fig. 1. The nozzle wall was maintained at a much lower temperature of 560 deg R. Even though the gas temperature is very high, ionization effects and thermal radiation to the wall are comparatively small for the experimental conditions that are indicated in Table 1. For example, the analysis of [1][2] indicates a negligible influence of ionization on heat transfer when the ionization energy fraction is as small as it is in this investigation (Table 1). The contribution of the radiative heat flux to the wall is expected to be less than 2 percent of the convective heat flux as indicated by measurements with argon by Roschke [2] with a window-covered cavity over a range of operating conditions which span the experimental conditions herein. Hence, ionization and radiation effects were not believed to be important and were not considered in the numerical calculations.

The Reynolds number at the throat based on throat diameter $Re_{D_{th}}$ ranged from 2200 to 2800.

The conservation equations describing the viscous heat-conducting laminar flow of a monatomic gas through a variable-area axisymmetric channel were solved numerically on a digital computer. Experimental values of the wall pressure distribution and of the mass flow rate were introduced into the analysis. The calculated distribution of the heat flux was then compared with the experimental heat flux to assess the validity of the

[1] This paper presents the results of one phase of research carried out in the Propulsion Research and Advanced Concepts Section at the Jet Propulsion Laboratory, California Institute of Technology, under Contract No. NAS7-100, sponsored by the National Aeronautics and Space Administration.

Contributed by the Heat Transfer Division of The American Society of Mechanical Engineers and presented at the AIChE-ASME Heat Transfer Conference, Denver, Colo., August 6-9, 1972. Manuscript received by the Heat Transfer Division January 21, 1971; revised manuscript received June 12, 1971. Paper No. 72-HT-49.

[2] Numbers in brackets designate References at end of paper.

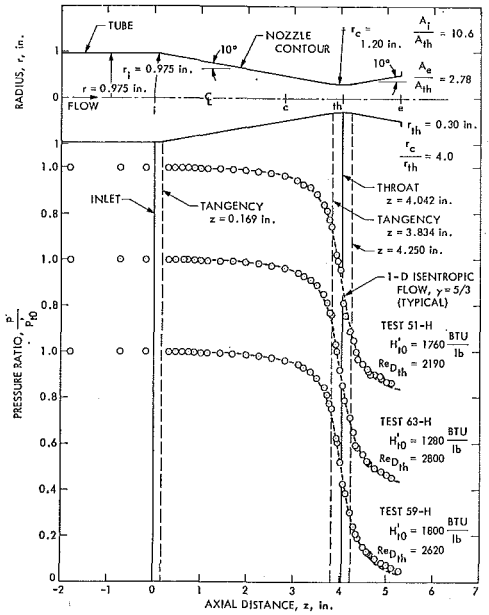


**Fig. 1 Wall-static-pressure distributions along the nozzle**

numerical calculations and to establish confidence in the evaluation of the flow field, which was not obtainable from the direct measurements.

The calculations span the subsonic, transonic, and supersonic flow regimes found in a choked convergent–divergent nozzle. The important viscous-stress and heat-flux components considered are the viscous shear stress in the axial flow direction and the radial heat flux. These considerations, for which the equations are parabolic in type, imply that changes in cross-sectional area of the nozzle are gradual and that the Reynolds numbers are not so low that the full Navier–Stokes equations need be included, nor that slip effects become important. The analysis takes into account variable properties across the flow, radial convection, and viscous dissipation. The pressure was allowed to vary across the flow in the initial part of the investigation, but the numerical calculations were found to be unstable. Consequently the pressure was taken to be uniform across the flow, which is believed to be a reasonable assumption since for a nozzle with gradual changes in cross-sectional area, curvature of the streamlines is small.

**Table 1 Conditions for argon flow**

| Location | | Test No. 51-H | 59-H | 63-H |
|---|---|---|---|---|
| Upstream tube inlet 0 | $H_{t_0}'$, Btu/lb | 1760 | 1800 | 1280 |
| | $H_w'/H_{t_0}'$ | 0.040 | 0.039 | 0.055 |
| | $Re_{D_0} = \frac{\rho_0' w_0' D}{\mu_0'}$ | 450 | 560 | 590 |
| | $M_0$ | 0.076 | 0.073 | 0.072 |
| | $\left(\frac{\alpha I}{H_t'}\right)_0$ Ionization energy fraction | 0.017 | 0.019 | 0.0003 |
| | $p_{t_0}'$, psia | 4.20 | 5.93 | 4.09 |
| | $\dot{m}$, lb/sec | 0.00944 | 0.0126 | 0.0104 |
| | $T_{t_0}'$, °R | 13,900 | 14,200 | 10,300 |
| Nozzle inlet $i$ | $\frac{H_{t_{\mathfrak{C}i}}'}{H_{t_0}'}$ | 0.93 | 0.96 | 0.97 |
| | $\frac{\bar{H}_{t_i}}{H_{t_0}'}$ | 0.60 | 0.64 | 0.65 |
| | $\frac{w_{\mathfrak{C}i}'}{w_0'}$ | 0.90 | 0.91 | 0.93 |
| | $M_{\mathfrak{C}i}$ | 0.071 | 0.068 | 0.068 |
| Nozzle throat $th$ | $\frac{H_{t_{\mathfrak{C}th}}'}{H_{t_0}'}$ | 0.82 | 0.86 | 0.84 |
| | $\frac{\bar{H}_{t_{th}}'}{H_{t_0}'}$ | 0.565 | 0.605 | 0.588 |
| | $M_{\mathfrak{C}th}$ | 1.11 | 1.10 | 1.10 |
| | $Re_{D_{th}} = \frac{\dot{m}}{A_{th}} \frac{D_{th}}{\mu_{\mathfrak{C}th}'}$ | 2190 | 2620 | 2800 |

It is realized at the outset that a more satisfactory numerical calculation of such flows should involve the specification of less information, i.e., given the nozzle contour and the wall enthalpy distribution and inlet flow conditions (stagnation pressure, stagnation enthalpy, and profile shapes), one should be able to carry out the calculations. Such a method would involve using a form of the integral momentum equation in conjunction with the mass-flow constraint to also calculate the pressure distribution, e.g., see Rae's method [3] which just involves the mass-flow constraint. However, such calculations must not only cope

## Nomenclature

$c_p'$ = specific heat at constant pressure
$D$ = channel diameter
$H'$ = static enthalpy
$H_w$ = wall to total enthalpy ratio, $H_w = \frac{H_w'}{H_{t_i}'}$
$H_t'$ = stagnation enthalpy, $H_t' = H' + \frac{(w')^2 + (u')^2}{2}$
$I$ = first ionization potential
$I_m, I_M, I_H$ = mass, momentum, and enthalpy integrals, equations (16) and (20)
$k'$ = thermal conductivity
$\dot{m}$ = mass flow rate
$\mathbf{M}$ = Mach number
$p'$ = static pressure
Pr = Prandtl number
$P$ = pressure parameter, $p_0'/\rho_0'(w_0')^2$
$q'$ = heat flux, $q' = -k' \frac{\partial T'}{\partial r}$
$r$ = radial distance
$r_w$ = nozzle radius
$R$ = gas constant
$\mathrm{Re}_0$ = Reynolds number based on radius, $\mathrm{Re}_0 = \frac{\rho_0' w_0' r_w}{\mu_0'}$
$\mathrm{Re}_D$ = Reynolds number based on diameter, $\mathrm{Re}_D = \frac{\rho' w' D}{\mu'}$
$T'$ = static temperature
$T_t'$ = stagnation temperature
$u'$ = radial velocity component
$w'$ = axial velocity component
$z$ = axial distance
$\alpha$ = degree of ionization
$\gamma$ = specific-heat ratio
$\epsilon$ = tolerance
$\zeta$ = dimensionless radial distance, $\zeta = \frac{r}{r_w}$
$\Delta\zeta_w$ = radial increment at wall
$K$ = flow-speed parameter, $K = \frac{(w_0')^2}{H_{t_0}'}$
$\mu'$ = viscosity
$\xi$ = dimensionless axial distance, $\xi = \int_0^z \frac{dz}{r_w}$
$\rho'$ = density
$\tau$ = shear stress, $\tau = \mu' \frac{\partial w'}{\partial r}$
$\Upsilon$ = temperature parameter, $\Upsilon = \frac{c_p' T_0'}{H_{t_0}'}$
$\omega$ = exponent of viscosity–temperature relation

### Subscripts

$\mathfrak{C}$ = condition at channel centerline
$i$ = nozzle inlet
0 = inlet condition at centerline, upstream of tube
$th$ = nozzle throat
$w$ = condition at channel wall

### Superscripts

$(\ )'$ = dimensional quantity
$(\ )^j$ = $j$th iterate
$(\bar{\ })$ = average value across flow

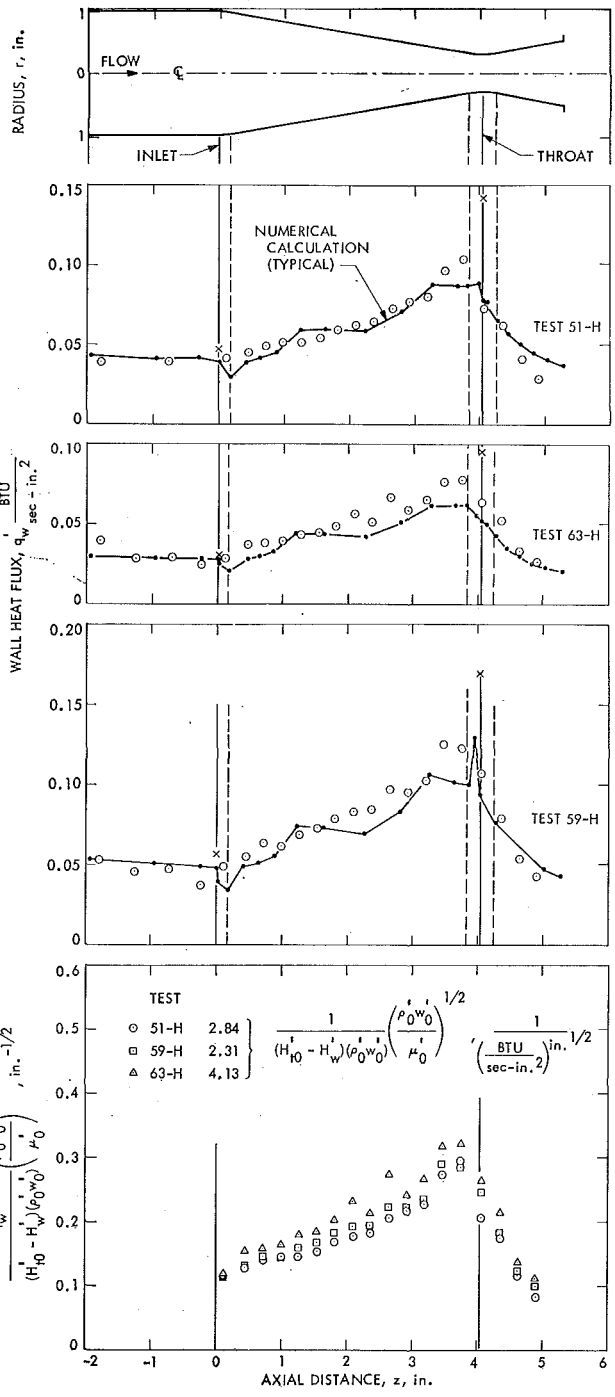


**Fig. 2 Wall-heat-flux distributions along the nozzle and attempt to correlate heat-transfer results based on laminar-boundary-layer theory**

with the saddle point in the throat region, but also must take into account flow separation that is believed to occur in the nozzle inlet where the flow is turned to follow along the nozzle wall. Consideration of the saddle point corresponds to accommodating only the appropriate mass flow rate which is not known a priori and which must be calculated. This behavior exhibited by the viscous-flow equations for two-dimensional flow is analogous (as one would expect) to that for isentropic one-dimensional flow through a nozzle when the nozzle shape is given and the flow is to be calculated. If separation occurs in the nozzle inlet region the appropriate conservation equations that apply are no longer parabolic, but instead are elliptic since the parabolic form of the equations does not allow for the propagation of conditions in the upstream direction. Clearly, the general calculation of viscous heat-conducting gas flows through supersonic nozzles is a formidable task.

Before discussing the results there is merit in indicating for completeness the scope of prior theoretical investigations of viscous laminar flow through variable-area channels. These analyses have been mostly for rather ideal flow and thermal conditions and for specific nozzle shapes. For nozzles of particular shapes Williams [4] obtained similarity solutions for either incompressible or compressible flow for the insulated-wall condition, i.e., no heat transfer, and more recently Adams and Williams [5] have found other similar solutions in the divergent region provided that the cross-sectional area increases exponentially with axial distance and the wall is adiabatic. Sichel [6, 7] has also obtained similarity solutions in the throat region, but these solutions are restricted to a region where the shear stress and heat flux are small. Other solutions have been obtained for incompressible isothermal flow through converging or diverging channels with straight walls, e.g., [8], and a converging flow through a conical tube [9]. Calculations of heat transfer have been made for constant-property incompressible flows through converging or diverging passages with straight walls [10] or conical tubes [11, 12]; however, these analytic solutions were obtained for assumed fully developed flow conditions. More recently Williams [13] obtained a class of exact solutions of the Navier–Stokes equations for compressible flow through a conical nozzle, including heat transfer and internal heat generation, but for special types of velocity, temperature, pressure, and density distributions that were assumed.

Only the numerical calculations by Myers [14] and Rae [3] cope with calculating the viscous heat-conducting flow in the subsonic, transonic, and supersonic regions of nozzles of more general shape. Myers' calculations were made for compressible flow through a nozzle with a rectangular cross section, but with an insulated wall along which the pressure was taken to be specified by the requirements of the similarity solution of Williams [4]. Rae's calculations do involve the consideration of the saddle point in the throat region and the prediction of the pressure distribution along the nozzle. His calculations, however, do not treat the turning of the flow in the nozzle inlet region and thus do not take into account separation which may occur there. Since Rae was interested in predicting the operation of microthrust rocket nozzles, the throat Reynolds numbers $Re_{D_{th}}$ were rather small, ranging from 60 to 700, and consequently viscous effects were more significant than in this investigation. An interesting aspect of these rather low Reynolds-number flows considered by Rae is that viscous shear forces which retard the flow apparently can become large enough in the supersonic region to decelerate the flow to subsonic speeds at the exit. Recent measurements by Rothe [15] support this predicted trend [3] and indicate such behavior at throat Reynolds numbers $Re_{D_{th}}$ less than about 80 for a nearly adiabatic flow.

The description of the analysis and finite-difference formulation used herein appears in the Appendixes.

## Experimental Results and Numerical Calculations

**Test Apparatus and Instrumentation.** The nozzle that was used in the experiments had convergent and divergent half-angles of 10 deg, a throat diameter of 0.6 in., and an inlet diameter of 1.95 in. (Fig. 1). Pressures were measured along the nozzle wall with manometers that contained silicone oil and the heat flux was obtained by calorimetry in separate circumferential coolant passages. Each coolant passage was instrumented with a rotameter and three pairs of series-connected thermocouple junctions. The longitudinal distribution of heat flux was then determined from the coolant-water flow rates, water-temperature rises, and surface areas of the coolant passages. The gas-side wall temperatures, which are essentially negligible compared to the very high gas temperatures, were calculated from the average

coolant-water temperatures, a calculated water-side heat-transfer coefficient, and the measured heat flux used in conjunction with the heat-conduction equation for the wall. The gas flow rate was obtained from a rotameter located in the gas feed line. The test apparatus consisted of an arc heater, a plenum chamber, a tube, a nozzle, and a vacuum system. The ratio of the total heat load, which consisted of the sum of the heat loads to 73 individual coolant passages along the test apparatus, to the applied power, computed from voltage and current measurements at the arc heater, was near 1.0 for all the tests. The test apparatus is described in more detail in [16] where measurements were presented along the tube upstream of the nozzle. Measurements along the nozzle are presented herein.

**Test-Condition Range.** The test conditions indicated in Table 1 span a range of total enthalpies from about 1300 to 1800 Btu/lb and mass flow rates from about 0.009 to 0.013 lb/sec. For this range of conditions the level of the heat fluxes (Fig. 2) did not vary greatly from test to test.

**Pressure Distributions.** Distributions of pressure in terms of the pressure ratio $p'/p_{t_0}'$ are shown along the nozzle in Fig. 1 for the various tests. The measured pressure distributions are similar to those which have been observed in higher Reynolds-number flows where the core flow is essentially isentropic, e.g., [17]. Along the convergent section, the measured pressures exceed the values for one-dimensional isentropic flow, through the throat region they generally become less, and then they become greater again in the divergent section. This overall trend is consistent with deviations from one-dimensional flow caused by the taper and curvature of the nozzle. The trend indicates that viscous shear forces do not have a predominant effect on the global flow field compared to pressure forces for the Reynolds numbers of this investigation. Subsequently, the ratio of shear forces that retard the flow to pressure forces that accelerate the flow will be shown along the nozzle.

**Experimental Heat-Flux Distributions.** The wall heat flux (Fig. 2) increases along the convergent section of the nozzle, reaches a peak value upstream of the throat, and then decreases through the rest of the throat section and in the divergent section. This trend is similar to that found for turbulent-boundary-layer flows (e.g., [18] and subsequent investigations [19, 20]) and laminar-boundary-layer flows through nozzles but at higher Reynolds numbers ([21], $\mathrm{Re}_{D_{th}}$ from 500,000 to 1,000,000). It is also similar to that observed in [22] for laminar flow through a nozzle ($\mathrm{Re}_{D_{th}}$ from 2100 to 3400) from an upstream jet that discharged into a chamber preceding the nozzle. The relative increase in heat flux along the convergent section is less in a laminar than in a turbulent flow however, as is vividly indicated in [19, 20] where laminarization of a turbulent boundary layer occurred along the convergent section of nozzles because of flow acceleration. This different behavior primarily results from a weaker dependence of heat flux on mass flux for laminar flows, e.g., $q_w \propto (\rho w)^m$, where $m = 0.5$ for a laminar boundary layer and $m = 0.75$ or 0.80 for a turbulent boundary layer. Therefore, a smaller increase in heat flux is found for laminar-boundary-layer flow along a nozzle with a given contraction-area ratio or for a given mass-flux increase. In the inlet region of the nozzle the local "hump" in the heat flux is believed to be associated with reattachment of the flow that apparently separated in the wall vicinity in flowing into the nozzle because of turning to follow along the conical wall. This variation of the heat flux in the inlet region is similar to that observed in the higher Reynolds-number investigation in [23]. Because of the relatively low dynamic pressures in the present investigation, however, the adverse pressure gradient along the wall that caused the flow to separate was not detectable, i.e., no rise in wall pressure was observed within the 0.001-psi pressure-difference accuracy of the measurements.

**Numerical Calculations.** The numerical calculations were initiated at the inlet of the externally cooled tube that was 7 diameters long and which preceded the nozzle. A contraction section

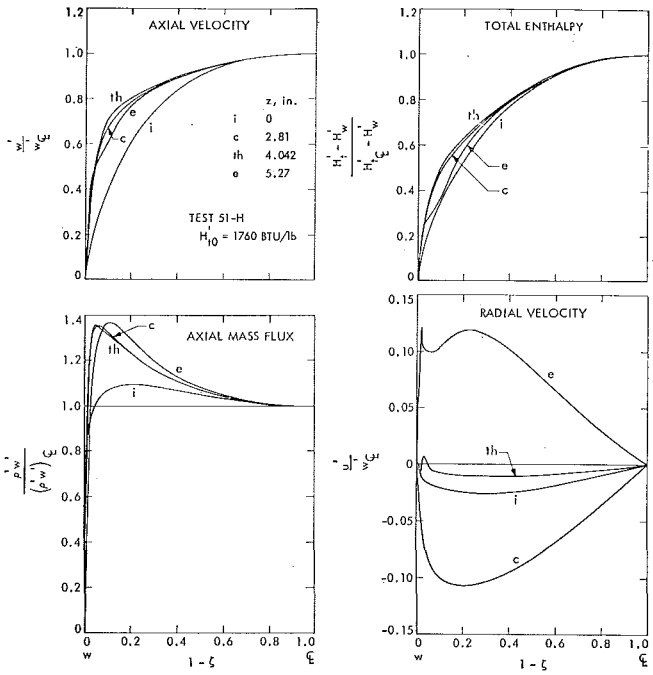


**Fig. 3 Axial-velocity, total-enthalpy, mass-flux, and radial-velocity profiles across the flow**

located upstream of the tube produced a nearly uniform flow at the tube inlet. The velocity and thermal boundary layers then grew to the centerline a few diameters downstream of the tube inlet and the core flow became viscous and non-adiabatic. Predicted profiles across the flow at the nozzle inlet are shown in Fig. 3, in particular for test 51-H. Confidence in these profiles at the nozzle inlet was established by the good agreement between both the predicted and the measured heat flux along the tube and the predicted and measured profiles obtained from calorimetric-probe and spectroscopic measurements across the flow at a location 1.6 diameters downstream of the tube inlet [24]. The flow through the nozzle was then calculated by using the measured pressure distributions shown in Fig. 1 and the measured mass flow rates. Appendix C contains a discussion of the numerical parameters used in the calculations. The results which were obtained by using the following properties for argon with negligible ionization are discussed in this section: Pr = 2/3, $\omega = 3/4$, $\gamma = 5/3$.

**Predicted Heat-Flux Distributions and Global Conservation Equations.** The predicted wall-heat-flux distributions along the nozzle are seen to be generally in good agreement with the measured values (Fig. 2). The dip in the predicted values in the inlet region reflects the difficulty in calculating the flow field in the vicinity of the wall where pressure measurements were not available and a uniform pressure was assumed. Consequently, local separation was not predicted in the inlet region. The predicted heat flux, however, recovered quickly and agrees well with the measurements along the convergent section. Upstream of the throat the prediction is a little low, and through the circular-arc throat section the predicted decrease in the heat flux is generally less than observed experimentally. This latter behavior is believed to be associated with the curvature of the throat which apparently causes a reduction in the heat flux [25]. However, there is agreement in magnitude with the measurements on an average basis through the circular throat section. The prediction is also in general agreement with the measurements along the divergent section. In this connection it should be noted that heat-flux measurements are not shown in the last coolant passage in the nozzle since these values were higher than just upstream and were influenced by the corner at the nozzle exit and the coolant-passage surface area around the corner.

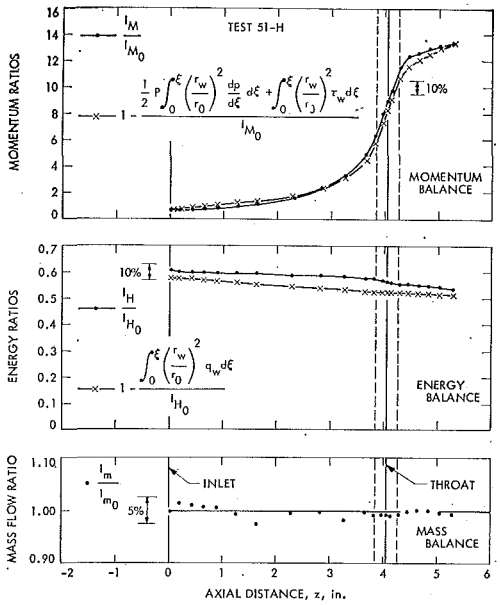


**Fig. 4 Mass, momentum, and energy balances along the nozzle**

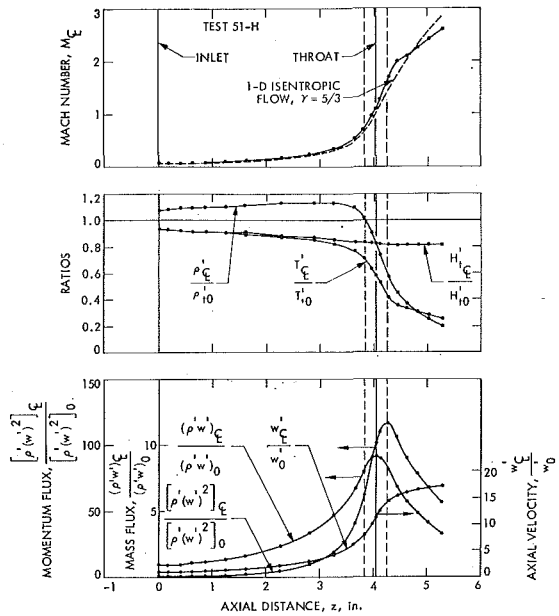


**Fig. 5 Mach-number, density, temperature, total-enthalpy, axial-velocity, mass-flux, and momentum-flux distributions along the nozzle centerline**

The extent to which the global mass, momentum, and energy balances, equations (16), (18), and (19), are satisfied along the nozzle is shown in Fig. 4 for test 51-H. The results are similar for the other tests. Although the check is not precise, the agreement is considered to be satisfactory for the very high temperature flow considered, where as much as about 50 percent of the energy in the inlet flow upstream of the tube was lost by heat transfer to the tube and nozzle walls. In particular, about 10 percent of the energy in the flow at the nozzle inlet was lost by heat transfer to the nozzle wall. Correspondingly, the total enthalpy decreases along the nozzle centerline (middle part of Fig. 5).

The "jagged" appearance of some of the curves shown is probably also associated to some extent with the accuracy with which the pressure gradient $dp/dz$ could be determined from the wall pressure measurements.

**Predicted Velocity, Enthalpy, and Flux Profiles.** Because of the general agreement in the wall-heat-flux distributions and satisfaction of the global conservation equations, confidence is gained in the calculations, and in particular in the detailed profiles across the flow. Profiles are shown in Fig. 3 for one test, 51-H, at locations $i$, $c$, $th$, and $e$ identified in the nozzle sketch in Fig. 1. The various flow and thermal quantities are normalized by the local centerline values (shown in Fig. 5) so that they vary from 0 to 1, as also does the relative distance across the flow $1 - \zeta$.

Along the convergent section of the nozzle $c$, the axial-velocity profile (Fig. 3) becomes steeper near the wall and somewhat flatter in the outer part of the flow compared to the nozzle inlet profile $i$ as a result of flow acceleration. The velocity profile is similar in shape at the throat $th$, but deviates again away from the wall at the nozzle exit $e$, presumably because of viscous dissipation. The centerline Mach-number distribution is shown in the upper part of Fig. 5. The "kink" in the exit profile near the wall has also been observed experimentally in a much higher Reynolds-number flow where the shear layer was turbulent [26]. The influence of viscous shear extends to the centerline all along the nozzle.

Because of the combined effects of flow acceleration and the relatively large amount of wall cooling ($H_w'/H_{t_0}' = 0.04$) which increases the density in the wall region, the mass flux near the wall considerably exceeds the centerline value along the nozzle (Fig. 3). The profiles in the convergent section and throat are nearly the same, but then the profile is less steep near the wall at the nozzle exit as a result of viscous dissipation which decreases the density near the wall.

The total-enthalpy profiles vary along the nozzle (Fig. 3) similar to the axial-velocity profiles. They, however, lie below the axial-velocity profiles which can be observed by superposition, and this indeed should be the case in an accelerating flow, e.g., [27], and also because the Prandtl number is less than unity, e.g., see the profiles at the nozzle inlet. The influence of heat conduction extends to the centerline all along the nozzle, hence the flow has been designated as non-adiabatic core flow.

Profiles of the radial velocity are shown in Fig. 3. At the nozzle inlet the radial velocity is toward the centerline, i.e., $u'/w_\zeta'$ is negative, presumably because of the effect of wall cooling. Along the convergent section the radial velocities become more negative, as might be expected because of the inward contraction of the flow. At the throat the radial velocity is slightly negative still, and then it becomes positive along the divergent section as indicated by the exit profile. Of note is that the radial velocity at the wall of an inviscid flow $u_w'/w_\zeta' \simeq \pm \tan 10$ deg would be about 0.18. The actual flow tends toward a value of this magnitude along the convergent and divergent section before being reduced to zero at the wall. The calculated radial velocities appear to oscillate somewhat in the wall vicinity, probably because of the difficulty in making the numerical calculations mentioned in Appendix B. Of note is that the contribution of the radial velocity component to the kinetic energy in the total-enthalpy expression is negligible, i.e., $(u')^2/2 \ll (w')^2/2$, and could have been deleted.

**Predicted Density Distribution.** As a result of cooling, the gas density increases not only toward the wall but also along the centerline in most of the convergent section of the nozzle (middle part of Fig. 5). The density then decreases rapidly through the throat section as the gas expands and cools, primarily by conversion of thermal to kinetic energy, although the total enthalpy along the centerline still decreases because of heat transfer to the wall. Along the centerline in the divergent section the density eventually becomes less than the static temperature, as would be the case for an inviscid adiabatic (isentropic) expansion.

**Predicted Shear Stress.** The wall shear stress, nondimensionalized with respect to the upstream momentum flux, is seen in the upper part of Fig. 6 to increase along the convergent section of the nozzle, like the wall heat flux (Fig. 2). The peak shear stress, however, occurs downstream of the throat in the vicinity of the tangency between the circular-arc throat section and the

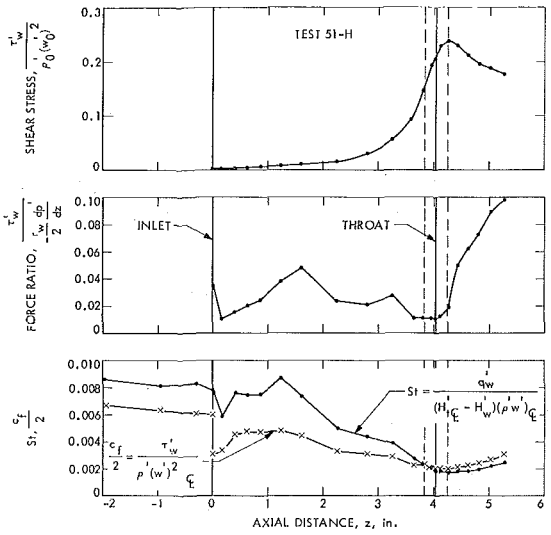


**Fig. 6 Wall-shear-stress, force-ratio, and friction coefficients and Stanton numbers along the nozzle**

conical divergent section. In this connection it should be noted that the momentum flux along the centerline (lower part of Fig. 5) is also largest where the peak shear stress is found. The mass flux, however (lower part of Fig. 5), is largest at the throat, whereas the peak heat flux occurs upstream of the throat. Along the divergent section the shear stress remains relatively high and in this region the ratio of the shear force which retards the flow to the pressure force which accelerates the flow becomes increasingly larger (middle part of Fig. 6).

**Friction and Heat-Transfer Relationship.** The relationship between wall friction and heat transfer is shown in the lower part of Fig. 6. The friction coefficient $c_f$ is based on the local shear stress and the momentum flux along the centerline: The Stanton number St is based on the local heat flux, centerline mass flux, and total-enthalpy driving potential between the centerline and the wall. Upstream in the tube St exceeds $c_f/2$ by about 30 percent, which is consistent with that for a laminar boundary layer for argon, Pr = 2/3 [28]. Along the convergent section the difference between St and $c_f/2$ is greater before they become nearly the same in the throat region. In the divergent section $c_f/2$ exceeds St, a trend indicated by laminar-boundary-layer calculations [27] because of the effect of acceleration on the relationship between wall friction and heat transfer.

Similar results as shown in Figs. 3–6 for test 51-H were found for the other tests and therefore are not included.

**Heat-Transfer Correlation.** Some idea of the magnitude of the wall heat flux predicted from laminar-boundary-layer theory is shown in Fig. 2 by the crosses at the nozzle inlet and throat. These predictions which were initiated at the tube inlet were based on using similarity solutions on a local basis [29] for a presumed one-dimensional inviscid adiabatic core flow. Of course there is no adiabatic and inviscid region in the flow under consideration, and consequently the predicted heat flux is too high, partly because the driving potential for heat transfer is less than the difference $H_{t_0}' - H_w'$ just downstream of the tube inlet. An attempt to correlate the heat-transfer data for the different tests based on laminar-boundary-layer theory was not very successful (lower part of Fig. 2), although the spread of the results is not too great.

Clearly the flow under consideration is not boundary-layer in character, i.e., relatively thin velocity and thermal boundary layers compared to the channel radius and with an inviscid adiabatic core flow. The allusion to laminar-boundary-layer theory was made only with regard to some of the qualitative trends which one might expect to find because of flow acceleration, wall cooling, and compressibility effects present in a nozzle flow.

## Summary and Conclusions

A procedure for the numerical solution of the differential form of the laminar-flow equations on a finite-difference basis was carried out in conjunction with experimental measurements. This involved using the experimental values of the wall pressure distribution and of the mass flow rate of a gas flow at temperatures as high as 14,200 deg R through an externally cooled supersonic nozzle. The validity of the numerical calculations was established by the good agreement between the experimental distribution of the wall heat flux (the important result which governs the cooling requirements and energy loss from the flow) and the corresponding distribution calculated by means of the analysis.

From the combined experimental and analytical approach it was found that:

1 Along the convergent section of the nozzle the measured pressures exceeded the values for one-dimensional isentropic flow, through the throat region they generally became less, and then they became greater again in the divergent section. This overall trend is consistent with deviations from one-dimensional flow caused by the taper and curvature of the nozzle, rather than by much departure from the condition for isentropic flow.

2 The wall heat flux increased along the convergent section of the nozzle, reached a peak value upstream of the throat, and then decreased through the rest of the throat section and in the divergent section. This trend is similar to that found for turbulent-boundary-layer flows and laminar-boundary-layer flows through nozzles at higher Reynolds numbers. In the inlet region of the nozzle a local "hump" in the experimental heat flux was observed which is believed to be associated with reattachment of the flow that apparently separated in the wall vicinity as the flow proceeded into the nozzle. This occurred because of the turning of the flow as it progressed along the wall; however, the adverse pressure gradient along the wall that caused the flow to separate was not detectable within the accuracy of the pressure measurements. About 10 percent of the energy in the flow at the nozzle inlet was lost by heat transfer to the nozzle wall. Correspondingly, the total enthalpy decreased along the nozzle centerline.

3 The influence of heat conduction and of the viscous shear extended to the centerline all along the nozzle; hence the flow was designated as non-adiabatic core flow as opposed to boundary-layer flow.

4 Because of the combined effects of flow acceleration and the relatively large amount of wall cooling $H_w'/H_{t_0}' = 0.04$ which increased the density in the wall region, the mass flux near the wall exceeded the centerline value along the nozzle by as much as 35 percent.

5 Along the convergent section of the nozzle and at the throat, the profile of the axial velocity became steeper near the wall and somewhat flatter in the outer part of the flow, as compared to the profile at the nozzle inlet.

6 The wall shear stress, like the wall heat flux, increased along the convergent section of the nozzle. The peak shear stress, however, occurred slightly downstream of the throat at the same axial location that the momentum flux along the centerline was a maximum. The mass flux, however, was largest in the throat, whereas the peak heat flux occurred upstream of the throat. Along the divergent section the shear stress remained relatively high, and in this region the ratio of the shear force which retarded the flow to the pressure force that accelerated the flow became increasingly larger and amounted to about 10 percent at the nozzle exit.

7 Upstream in the tube the Stanton number St, which is based on the total-enthalpy driving potential between the centerline and the wall, exceeded the skin friction coefficient $c_f/2$ by about 30 percent. Along the convergent section the maximum difference between St and $c_f/2$ was greater than 30 percent but the values became nearly the same in the throat region. In the

divergent section, however, $c_f/2$ exceeded St by as much as 20 percent.

In conclusion it should be noted that the numerical-calculation procedure, although useful in revealing the flow field and thermal environment in the nozzle investigated, is inappropriate for the more general calculation of internal viscous flows through ducts of variable area and for various thermal boundary conditions. Further discussion of this point appears in the Introduction along with a brief description of a more general approach, which, however, must cope with the saddle point in the throat region and the apparent flow separation in the inlet region.

## Acknowledgment

The authors express their gratitude to Mr. M. Diethelm of JPL for programming and carrying out the numerical calculations on a digital computer, and to Mr. M. Noel and Mr. S. Kikkert for acquisition and reduction of the experimental data.

## References

1 Back, L. H., "Laminar Boundary Layer Heat Transfer from a Partially Ionized Monatomic Gas," *Physics of Fluids*, Vol. 10, No. 4, Apr. 1967, pp. 807–819.

2 Roschke, E. J., "Thermal Radiation from Ionized Argon: Results Obtained with an Annular Hohlraum," SPS 37-43, Vol. IV, pp. 206–216 and 222–223, Jet Propulsion Laboratory, Pasadena, Calif., Feb. 1967.

3 Rae, W. J., "Some Numerical Results on Viscous Low-Density Nozzle Flows in the Slender-Channel Approximation," *AIAA Journal*, Vol. 9, No. 5, May 1971, pp. 811–820.

4 Williams, J. C., III, "Viscous Compressible and Incompressible Flow in Slender Channels," *AIAA Journal*, Vol. 1, No. 1, Jan. 1963, pp. 186–195.

5 Adams, J. C., Jr., and Williams, J. C., III, "Viscous Compressible Laminar Flow in Slender Axisymmetric Channels with Adiabatic Walls," *Appl. Sci. Res.*, Vol. 21, No. 2, Sept. 1969, pp. 113–137.

6 Sichel, M., "The Effect of Longitudinal Viscosity on the Flow at a Nozzle Throat," *Journal of Fluid Mechanics*, Vol. 25, Part 4, Aug. 1966, pp. 769–786.

7 Sichel, M., and Yin, Y. K., "An Axisymmetric Similarity Solution for Viscous Transonic Nozzle Flow," University of Michigan ORA Rep. No. 07146-1-T, July 1966.

8 Schlichting, H., *Boundary Layer Theory*, 6th ed., McGraw-Hill, New York, N. Y., 1968, p. 99.

9 Sutterby, J. L., "Finite Difference Analysis of Viscous Laminar Converging Flow in Conical Tubes," *Appl. Sci. Res.*, Sec. A, Vol. 15, No. 4–5, 1965, pp. 241–252.

10 Sparrow, E. M., and Starr, J. B., "Heat Transfer to Laminar Flow in Tapered Passages," *Journal of Applied Mechanics*, Vol. 32, Trans. ASME, Series E, Vol. 87, No. 3, Sept. 1965, pp. 684–689.

11 Cobble, M. H., "Nusselt Number for Flow in a Cone," Journal of Heat Transfer, Trans. ASME, Series C, Vol. 84, No. 3, Aug. 1962, pp. 264–265.

12 Lumsdaine, E., "Heat Transfer for Flow in a Cone," Journal of Heat Transfer, Trans. ASME, Series C, Vol. 91, No. 1, Feb. 1969, pp. 173–175.

13 Williams, J. C., III, "Conical Nozzle Flow of a Viscous Compressible Gas with Energy Extraction," *Appl. Sci. Res.*, Vol. 19, July 1968, pp. 285–301.

14 Myers, W. A., "A Numerical Solution of Viscous Compressible Flow in Slender Channels," MS thesis, University of Tennessee, June 1964, N65-14576, AD-605441.

15 Rothe, D. E., "Electron-Beam Studies of Viscous Flow in Supersonic Nozzles," *AIAA Journal*, Vol. 9, No. 5, May 1971, pp. 804–811.

16 Massier, P. F., Back, L. H., and Roschke, E. J., "Heat Transfer and Laminar Boundary-Layer Distributions in an Internal Subsonic Gas Stream at Temperatures Up to 13,900 Deg R," Journal of Heat Transfer, Trans. ASME, Series C, Vol. 91, No. 1, Feb. 1969, pp. 83–90.

17 Back, L. H., Massier, P. F., and Gier, H. L., "Comparison of Measured and Predicted Flows through Conical Supersonic Nozzles, with Emphasis on the Transonic Region," *AIAA Journal*, Vol. 3, 1965, pp. 1606–1614.

18 Bartz, D. R., "Turbulent Boundary-Layer Heat Transfer from Rapidly Accelerating Flow of Rocket Combustion Gases and of Heated Air," in: *Advances in Heat Transfer*, Vol. 2, T. F. Irvine and J. P. Hartnett, eds., Academic Press, New York, N. Y., 1965.

19 Back, L. H., Massier, P. F., and Cuffel, R. F., "Flow Phenomena and Convective Heat Transfer in a Conical Supersonic Nozzle," *Journal of Spacecraft and Rockets*, Vol. 4, No. 8, Aug. 1967, pp. 1040–1047.

20 Back, L. H., Cuffel, R. F., and Massier, P. F., "Laminarization of a Turbulent Boundary Layer in Nozzle Flow—Boundary Layer and Heat Transfer Measurements With Wall Cooling," Journal of Heat Transfer, Trans. ASME, Series C, Vol. 92, No. 3, Aug. 1970, pp. 333–344.

21 Back, L. H., Massier, P. F., and Cuffel, R. F., "Effect of Inlet Boundary Layer Thickness and Structure on Heat Transfer in a Supersonic Nozzle," *Journal of Spacecraft and Rockets*, Vol. 5, No. 1, Jan. 1968, pp. 121–123.

22 Carden, W. H., "Local Heat-Transfer Coefficients in a Nozzle with High-Speed Laminar Flow," *AIAA Journal*, Vol. 3, No. 12, Dec. 1965, pp. 2183–2188.

23 Back, L. H., Massier, P. F., and Cuffel, R. F., "Flow and Heat Transfer Measurements in Subsonic Air Flow through a Contraction Section," *International Journal of Heat and Mass Transfer*, Vol. 12, No. 1, Jan. 1969, pp. 1–13.

24 Back, L. H., "Very High Temperature Laminar Flow of a Gas through the Entrance Region of a Cooled Tube—Numerical Calculations and Experimental Results," *International Journal of Heat and Mass Transfer*, Vol. 15, No. 5, May 1972, pp. 1001–1021.

25 Back, L. H., "Transonic Laminar Boundary Layers with Surface Curvature," to be published in *International Journal of Heat and Mass Transfer*.

26 Back, L. H., and Cuffel, R. F., "Turbulent Boundary Layer and Heat Transfer Measurements Along a Convergent–Divergent Nozzle," Journal of Heat Transfer, Trans. ASME, Series C, Vol. 93, No. 4, Nov. 1971, pp. 397–407.

27 Back, L. H., "Acceleration and Cooling Effects in Laminar Boundary Layers—Subsonic, Transonic, and Supersonic Speeds," *AIAA Journal*, Vol. 8, No. 4, Apr. 1970, pp. 794–802.

28 Back, L. H., "Effects of Severe Surface Cooling and Heating on the Structure of Low-Speed, Laminar Boundary-Layer Gas Flows with Constant Free-Stream Velocity," TR No. 32-1301, Jet Propulsion Laboratory, Pasadena, Calif., 1968.

29 Back, L. H., and Witte, A. B., "Prediction of Heat Transfer From Laminar Boundary Layers, With Emphasis on Large Free-Stream Velocity Gradients and Highly Cooled Walls," Journal of Heat Transfer, Trans. ASME, Series C, Vol. 88, No. 3, Aug. 1966, pp. 249–256.

# APPENDIX A

## Analysis

For steady axisymmetric laminar flow, the conservation equations that are taken to describe the flow through a nozzle with gradual changes in cross-sectional area are as follows:

continuity

$$\frac{\partial}{\partial z}(\rho' w') + \frac{1}{r}\frac{\partial}{\partial r}(r\rho' u') = 0 \tag{1}$$

axial momentum

$$\rho' w'\frac{\partial w'}{\partial z} + \rho' u'\frac{\partial w'}{\partial r} = -\frac{dp'}{dz} + \frac{1}{r}\frac{\partial}{\partial r}\left(r\mu'\frac{\partial w'}{\partial r}\right) \tag{2}$$

total energy

$$\rho' w'\frac{\partial H_t'}{\partial z} + \rho' u'\frac{\partial H_t'}{\partial r} = \frac{1}{r}\frac{\partial}{\partial r}\left(rk'\frac{\partial T'}{\partial r}\right) + \frac{1}{r}\frac{\partial}{\partial r}\left(rw'\mu'\frac{\partial w'}{\partial r}\right) \tag{3}$$

In these equations where the primes refer to dimensional quantities, $w'$ and $u'$ are the axial and radial velocity components in the $z$ and $r$ directions, respectively, and the total enthalpy is

$$H_t' = H' + \frac{(w')^2 + (u')^2}{2}$$

Independent variables are introduced as follows:

$$\zeta = \frac{r}{r_w}, \qquad \xi = \int_0^z \frac{dz}{r_w}$$

so that the radial coordinate $\zeta$ is 0 at the centerline and 1 at the wall, and the axial distance is expressed by $\xi$. The conservation

equations are then made dimensionless with respect to a reference condition upstream of the nozzle along the centerline denoted by the subscript 0

$$w = \frac{w'}{w_0'}, \quad u = \frac{u'}{w_0'}, \quad H_t = \frac{H_t'}{H_{t_0}'}, \quad T = \frac{T'}{T_0'},$$

$$\rho = \frac{\rho'}{\rho_0'}, \quad p = \frac{p'}{p_0'}, \quad \mu = \frac{\mu'}{\mu_0'}$$

to give

$$\frac{\partial}{\partial \xi}(\rho w) - \frac{\zeta}{r_w}\frac{dr_w}{d\xi}\frac{\partial}{\partial \zeta}(\rho w) + \frac{1}{\zeta}\frac{\partial}{\partial \zeta}(\zeta \rho u) = 0 \tag{4}$$

$$\frac{\partial w}{\partial \xi} = \left(\frac{\zeta}{r_w}\frac{dr_w}{d\xi} - \frac{u}{w}\right)\frac{\partial w}{\partial \zeta} - \frac{P}{\rho w}\frac{dp}{d\xi} + \frac{1}{\rho w \mathrm{Re}_0}\left\{\mu\frac{\partial^2 w}{\partial \zeta^2} + \left[\frac{\partial \mu}{\partial \zeta} + \frac{\mu}{\zeta}\right]\frac{\partial w}{\partial \zeta}\right\} \tag{5}$$

$$\frac{\partial H_t}{\partial \xi} = \left(\frac{\zeta}{r_w}\frac{dr_w}{d\xi} - \frac{u}{w}\right)\frac{\partial H_t}{\partial \zeta} + \frac{\Upsilon}{\rho w \mathrm{Re}_0 \mathrm{Pr}}\left\{\mu\frac{\partial^2 T}{\partial \zeta^2} + \left[\frac{\partial \mu}{\partial \zeta} + \frac{\mu}{\zeta}\right]\frac{\partial T}{\partial \zeta}\right\} + \frac{K}{\rho w \mathrm{Re}_0}\left\{\mu\left[w\frac{\partial^2 w}{\partial \zeta^2} + \left(\frac{\partial w}{\partial \zeta}\right)^2\right] + \left[\frac{\partial \mu}{\partial \zeta} + \frac{\mu}{\zeta}\right] w\frac{\partial w}{\partial \zeta}\right\} \tag{6}$$

The parameters in these equations, in addition to the Prandtl number $\mathrm{Pr} = \mu' c_p'/k'$ which is $^2/_3$ for non-ionized argon, refer to the reference condition and are given by

$$\left.\begin{aligned} P &= \frac{p_0'}{\rho_0'(w_0')^2} = \frac{1}{\gamma M_0^2}, \qquad K = \frac{(w_0')^2}{H_{t_0}'} = \frac{(\gamma - 1)M_0^2}{1 + \dfrac{\gamma - 1}{2}M_0^2} \\ \Upsilon &= \frac{c_p' T_0'}{H_{t_0}'} = \frac{1}{1 + \dfrac{\gamma - 1}{2}M_0^2}, \qquad \mathrm{Re}_0 = \frac{\rho_0' w_0' r_w}{\mu_0'} \end{aligned}\right\} \tag{7}$$

Note that the Reynolds number $\mathrm{Re}_0$ contains the local nozzle radius and thus varies along the nozzle.

Other relations that describe the flow are the perfect-gas relation $p' = \rho' R T'$, which in dimensionless form is

$$p = \rho T \tag{8}$$

the viscosity–temperature relation $\mu'(T')$, which can be described empirically by the power-law relation

$$\mu = T^{\omega} \tag{9}$$

and the total enthalpy, which in dimensionless form is

$$H_t = \Upsilon T + K\left(\frac{w^2 + u^2}{2}\right) \tag{10}$$

The parameters $\Upsilon$ and $K$, which are a measure of the thermal and kinetic energies in the inlet flow, are interrelated: $1 = \Upsilon + K/2$, since $u_0 = 0$ because of symmetry.

The following inlet and boundary conditions are considered. Upstream of the nozzle the axial-velocity and enthalpy distributions are prescribed and the radial velocity is taken to be zero, i.e.,

$$\text{at} \quad \xi = 0: \qquad \frac{w'}{w_0'} = w(\zeta), \quad \frac{H_t'}{H_{t_0}'} = H_t(\zeta), \quad u = 0 \tag{11}$$

The nozzle wall is taken to be impermeable and at a specified temperature dictated by external cooling, so that the enthalpy at the wall is known, i.e.,

$$\text{at} \quad \zeta = 1: \qquad w = 0, \quad u = 0, \quad H = H_w(\xi) \tag{12}$$

Other boundary conditions along the wall could be treated as well, e.g., mass-transfer cooling by including the diffusion equation too, or radiation cooling. Along the centerline the radial velocity must vanish, and symmetry conditions give

$$\text{at} \quad \zeta = 0: \qquad u = 0, \quad \frac{\partial w}{\partial \zeta} = 0, \quad \frac{\partial H_t}{\partial \zeta} = 0 \tag{13}$$

# APPENDIX B

## Method of Numerical Solution

The finite-difference formulation is described briefly for calculating flow through a variable-cross-section channel. The treatment differs in some respects from the description given in [24], where calculations were made for a very high temperature gas flow through the entrance region of an externally cooled tube, i.e., $r_w = \text{const}$.

By expressing equations (5) and (6) in finite-difference form the numerical solution can be carried out in the axial direction $\xi$ because of the parabolic nature of the equations. The calculation scheme consists of using equations (5) and (6) to directly solve for the axial velocities and total enthalpies across the flow at the $\xi + \Delta\xi$ location from the known values at the prior $\xi - \Delta\xi$ and $\xi$ locations when the pressure is prescribed by a method of successive iterations. The other relations given by equations (8), (9), and (10) are used to express $\rho$, $\mu$, and $T$ in terms of $w$ and $H_t$. Radial velocities are obtained by integration of the continuity equation (4).

$$u = \frac{1}{\rho\zeta}\left\{\frac{1}{r_w}\frac{dr_w}{d\xi}\int_0^{\zeta}\frac{\partial}{\partial \zeta}(\rho w)\zeta^2 d\zeta - \int_0^{\zeta}\frac{\partial}{\partial \xi}(\rho w)\zeta d\zeta\right\} \tag{14}$$

In this expression, the first integral is evaluated at the $\xi + \Delta\xi$ location from the prior iteration and the $\xi$-derivative in the second integral is evaluated from a backward difference.

The numerical formulation allows for variable axial and radial increments $\Delta\xi$ and $\Delta\zeta$. The axial derivatives were approximated by a three-point Lagrangian formula that can be obtained by writing Taylor-series expansions in the $-\xi$ direction. The radial increment can be chosen to become progressively smaller as the wall is approached, where gradients are larger. The radial derivatives were obtained from Taylor-series expansions in the $+$ and $-\zeta$ directions and then weighed between the $\xi$ and $\xi + \Delta\xi$ axial locations by a factor $\sigma$ in order to reduce the calculation time. A value of $\sigma = 1$ was used, i.e., the radial derivatives were evaluated at $\xi + \Delta\xi$.

The heat flux to the wall and the shear stress at the wall were obtained from the following expressions:

$$q_w' = -k_w'\left(\frac{\partial T'}{\partial r}\right)_w = -\frac{k_w' H_{t_0}'}{r_w c_{p_w}'}\left(\frac{\partial H_t}{\partial \zeta}\right)_w$$

$$\tau_w' = \mu_w'\left(\frac{\partial w'}{\partial r}\right)_w = \frac{\mu_w' w_0'}{r_w}\left(\frac{\partial w}{\partial \zeta}\right)_w$$

The slopes of the enthalpy and velocity profiles at the wall were established by extrapolating a parabola from the three points nearest the wall to a point halfway between the wall and the first point away from the wall. A cubic was then fit through the first two points away from the wall, the extrapolated point, and the point on the wall. From this curve fit, the slope of the profiles at the wall was determined. Even with the small radial mesh size near the wall (a value of $\Delta\zeta_w = 0.0033$ was used), it was necessary to use this extrapolation procedure to obtain accurate heat fluxes and shear stresses that check the global energy and momentum balances. Smaller radial increments yet near the wall resulted in smaller axial increments and thus longer computation time.

In the iteration scheme, terms on the right side of equations (5) and (6) are evaluated from the $j$th iteration to obtain the

$j + 1$ iterate directly from the left side of the equations. This scheme avoids matrix inversion of the algebraic equations. The iteration scheme is continued until all variables converge to within some specified tolerance $\epsilon$ ($10^{-2}$ was used). The calculation then proceeds to the next axial location. In the calculations, values of $w$, $H_t$, and $u$ in the iteration scheme were weighed between the $j + 1$ and $j$ iterations to avoid overcorrections, i.e.,

$$f^{j+1} = (1 - \Delta) f_{\text{computed}}{}^{j+1} + \Delta f^{j} \tag{15}$$

Experience indicated that the weighing factor $\Delta$ ($\Delta = 0$, new value; $\Delta = 1$, prior value) should be about 0.5 at the nozzle inlet, increase to about 0.9 at the throat, and then decrease to about 0.5 again at the exit for the radial velocity $u$: A value of $\Delta$ of 0.5 was used for $w$ and $H_t$. The weighed iterates for $w$ and $H_t$ were then smoothed near the wall by fitting a cubic through 15 points away from the wall and then using the smoothed 4 points nearest the wall. The values near the wall would tend to oscillate unless they were smoothed.

For the calculations to be consistent, a method needs to be employed to insure that calculated values from the iteration scheme converge to the true values. This was accomplished by satisfying the continuity equation (1) on a global basis, as indeed must be the case

$$I_{m_0} - I_m = 0 \qquad \text{where} \quad I_m = \left(\frac{r_w}{r_0}\right)^2 \int_0^1 \rho w \zeta \, d\zeta \tag{16}$$

New values of the axial velocity $w$ across the flow, which more closely satisfied the mass-flow constraint, were calculated after each iteration from the following expression:

$$w_{\text{corrected}} = w_{\text{computed}} \left\{\frac{I_{m_0}}{I_{m_{\text{computed}}}}\right\}^n \tag{17}$$

Various values of the exponent $n$, which is a measure of how much $w$ is corrected after each iteration ($n = 1$, full correction; $n = 0$, no correction), were tried. A value of $n = 0.25$ was used in the nozzle inlet region to $z = 0.85$ in. and then a value of 0.025 was used along the rest of the nozzle. Of note is that this scheme is self-corrective, i.e., too-small velocities are made larger and vice versa, since the velocity is contained in the computed integral $I_m$. These corrected velocities along with the other variables were then used as the $j$th iterate to obtain the $j + 1$ iterate. The calculation then continues until convergence within the tolerance $\epsilon$ is achieved. By using the values of $n$ indicated, the calculations could not be continued through the entire nozzle unless the iterates were also weighed, as in equation (15), and then smoothed near the wall.

The integral form of the momentum and energy equations (2) and (3) also should be satisfied. In nondimensional form these relations obtained by integration of equations (2) and (3), both across and along the flow, are as follows:

$$I_{M_0} - I_M = {}^1/_2 P \int_0^\xi \left(\frac{r_w}{r_0}\right)^2 \frac{dp}{d\xi} \, d\xi + \int_0^\xi \left(\frac{r_w}{r_0}\right)^2 \tau_w d\xi \tag{18}$$

$$I_{H_0} - I_H = \int_0^\xi \left(\frac{r_w}{r_0}\right)^2 q_w d\xi \tag{19}$$

where the momentum and enthalpy integrals are

$$I_M = \left(\frac{r_w}{r_0}\right)^2 \int_0^1 \rho w^2 \zeta \, d\zeta, \qquad I_H = \left(\frac{r_w}{r_0}\right)^2 \int_0^1 \rho w H_t \zeta \, d\zeta \tag{20}$$

and the nondimensional wall shear stress and heat flux to the wall are

$$\tau_w = \frac{\tau_w'}{\rho_0'(w_0')^2}, \qquad q_w = \frac{q_w'}{\rho_0' w_0' H_{t_0}'} \tag{21}$$

These relations are referred to in the section Predicted Heat-Flux Distributions and Global Conversion Equations, also in connection with momentum changes and energy losses in the flow.

## APPENDIX C

## Numerical-Calculation Parameters for Nozzle Flow

The calculations were made by using 40 radial increments between the centerline and the wall. The radial increment at the wall $\Delta\zeta_w$ was as small as 0.0033. The radial increment then became successively larger in going from the wall to the centerline. The axial increment $\Delta\xi$ was 0.0125 and there were 840 axial steps for the entire nozzle. The more coarse spacing where the predictions are shown in the figures corresponds to computer-printout locations. One iteration per axial step was usually found to be sufficient. Other numerical parameters used in the calculations were mentioned in Appendix B. The values of the numerical parameters quoted reflect much trial-and-error experience for which the actual computation time was considerably greater than the 3 to 4 min per test required for the final calculations which were carried out on a UNIVAC 1108 computer. A description of the numerical-calculation parameters in the tube upstream appears in [24].

**IVAN CATTON**
Assistant Professor,
School of Engineering and Applied Science,
University of California,
Los Angeles, Calif.
Mem. ASME

# Effect of Wall Conduction on the Stability of a Fluid in a Rectangular Region Heated from Below

*The initiation of natural convection in a fluid confined above and below by rigid, perfectly conducting surfaces and laterally by vertical walls of arbitrary thermal conductivity which form a rectangle is examined. The linearized perturbation equations are obtained in the usual manner and reduced to an eigenvalue problem. The Rayleigh number is the eigenvalue and is a function of the lateral-wall conductance and horizontal plan form (aspect ratios). The problem associated with satisfying the no-slip boundary conditions on all surfaces is surmounted by using the Galerkin method. Results are compared with experiments and shown to be in good agreement.*

## Introduction

THE PROBLEM of initiation of natural convection in a completely confined fluid has been of interest for a number of years. Possible applications range from interest in heat transfer across honeycomb sandwich material to micrometerology and solar-energy collectors. This author's interest arose through trying to avoid thermal instabilities while investigating the onset of electroconvection.

Many investigators have studied the classical Rayleigh thermal-stability problem of an infinite horizontal fluid layer heated from below, and an excellent summary can be found in Chandrasekhar [1].[1] Their analyses indicate that a critical temperature gradient exists, below which small perturbations of the initial quiescent state would be damped out. Addition of lateral walls, which confine the fluid, requires that the fluid do more work in overcoming the additional viscous shear. If these lateral walls conduct heat, there is a damping of perturbations due to the cooling or heating of the fluid adjacent to the walls. The net result is that a conducting wall requires increasing the critical temperature gradient over that of a nonconducting wall.

Two approaches have been used to solve problems of this type. The first approach is to simplify the problem in such a way as to be able to obtain an analytic solution through separation of variables. The impossibility of using separation of variables when all surfaces are rigid leads one to allow one (or more) of the coordinate surfaces to be shear-free. Some examples of this approach include Ostrach and Pnueli [2], Catton and Edwards [3], Yih [4], and Edwards [5]. These works have been successful to varying degrees. Ostrach and Pnueli's work is restricted to perfectly conducting walls, whereas Catton and Edwards' work is restricted to aspect ratios (height/diameter) greater than 1.5. Yih concerned himself with either perfectly conducting or perfectly insulating lateral boundaries and infinite height. Edwards considered the case of arbitrarily conducting side walls but was restricted to narrow width of the closed region relative to its height and depth.

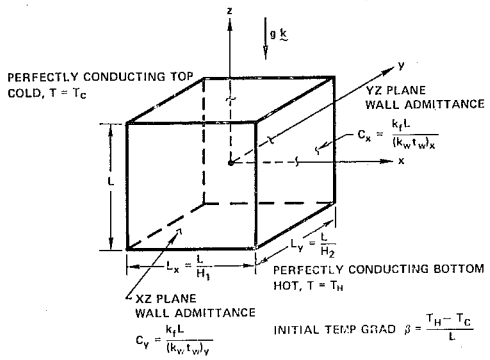


**Fig. 1 Geometry and coordinate system of the rectangular region**

The second approach to this type of thermal-stability problem is to satisfy all the boundary conditions (rigid walls) and approximate the solution to the differential equations. Davis [6], Charlson and Sani [7], and Catton [8] have used this approach. Davis considered a rectangular region heated from below with perfectly conducting surfaces and Catton considered a similar region with perfectly insulating surfaces. Charlson and Sani determined the critical temperature gradient at which axisymmetric convection would occur in a cylinder with various aspect ratios and either perfectly conducting or perfectly insulating surfaces.

[1] Numbers in brackets designate References at end of paper.

Contributed by the Heat Transfer Division for publication (without presentation) in the JOURNAL OF HEAT TRANSFER. Manuscript received by the Heat Transfer Division February 10, 1971; revised manuscript received September 29, 1971. Paper No. 72-HT-G.

The approximating technique used in these investigations has been the Rayleigh–Ritz procedure or its equivalent.

In this paper, the much more general case of vertical walls with arbitrary thermal conductivity will be considered. The problem will be solved using the Galerkin method, which was shown by Davis to be equivalent to a Rayleigh–Ritz procedure using a maximum principle due to Sani [9]. The trial functions are made up of orthogonal functions which satisfy four boundary conditions. These functions are called beam functions and were tabulated with the required integrals by Harris and Reid [10]. Results are presented for depth-to-width ratios from $^1/_3$ to 8 and wall conductances from perfectly conducting (wall thermal conductivity is infinite) to perfectly insulating (wall thermal conductivity is zero).

## Governing Equations

Initially a quasi-incompressible (Boussinesq) fluid fills a rectangular region as shown in Fig. 1. The base of the rectangular region is fixed at a temperature higher than the top and an adverse temperature gradient is established in the fluid in the direction of the body force (the negative $z$ axis). The initial velocity, temperature, and pressure distributions are given by

$$\mathbf{v}_0 = 0, \quad \nabla T_0 = \beta\mathbf{k}, \quad \nabla P_0 = \rho g(1 - \alpha\beta z)\mathbf{k} \tag{1}$$

where $\rho$ is the mean fluid density, $\mathbf{k}$ a unit vector along the $z$ axis, $\beta$ the negative mean temperature gradient, $\alpha$ the volumetric thermal-expansion coefficient, and $g$ the acceleration due to gravity.

Small disturbances from the initial state are assumed and products of small terms neglected. The resulting equations are time-independent as shown by Sherman and Ostrach [11] (for a simple extension of their work to the present situation, see the Appendix). In dimensionless form, the disturbance equations are

$$\text{div } \mathbf{v} = 0 \tag{2}$$

$$\nabla^2\mathbf{v} + R\theta\mathbf{k} - \text{grad } p = 0 \tag{3}$$

$$\nabla^2\theta + w = 0 \tag{4}$$

where $\mathbf{v}$, $\theta$, and $p$ are the velocity, temperature, and pressure disturbances measured in units of $\kappa/L$, $\beta L$, and $\rho\nu\kappa/L^2$ respectively. The characteristic length $L$ is the height of the rectangular region and $\nu$ and $\kappa$ are the kinematic viscosity and thermal diffusivity. The horizontal coordinates $x$ and $y$ are measured in units of the height. The Rayleigh number is defined

$$\mathrm{R} = \frac{\alpha g\beta L^4}{\nu\kappa} \tag{5}$$

The boundary conditions on the velocity are

$$\mathbf{v} = 0 \quad \text{on} \quad z = \pm\frac{1}{2}, \quad x = \pm\frac{1}{2H_1}, \quad y = \pm\frac{1}{2H_2} \tag{6}$$

where $H_1$ is the height-to-width ratio and $H_2$ is the height-to-depth ratio. The boundary conditions on the temperature are obtained by assuming that they are thin enough to use the fin approximation. The result is

$$\frac{\partial^2\theta_w}{\partial x^2} + \frac{\partial^2\theta_w}{\partial z^2} = \left(\frac{k_f L}{k_w t_w}\right)\frac{\partial\theta}{\partial y} \quad \text{at} \quad y = \pm\frac{1}{2H_2} \tag{7}$$

and

$$\frac{\partial^2\theta_w}{\partial y^2} + \frac{\partial^2\theta_w}{\partial z^2} = \frac{k_f L}{k_w t_w}\frac{\partial\theta}{\partial x} \quad \text{at} \quad x = \pm\frac{1}{2H_1} \tag{8}$$

where the subscript $w$ denotes the wall and $f$ the fluid, and $t$ is the wall thickness. Defining two wall conductances and setting $\theta_w = \theta_f$ allows the boundary condition to be written

$$\frac{\partial^2\theta}{\partial x^2} + \frac{\partial^2\theta}{\partial z^2} = C_y\frac{\partial\theta}{\partial y} \tag{9}$$

$$\frac{\partial^2\theta}{\partial y^2} + \frac{\partial^2\theta}{\partial z^2} = C_x\frac{\partial\theta}{\partial x} \tag{10}$$

where

$$C_y = \frac{k_f L}{(k_w t_w)_y}, \qquad C_x = \frac{k_f L}{(k_w t_w)_x} \tag{11}$$

are the dimensionless wall admittances. Equations (2) to (4) with the boundary conditions given by equations (6), (9), and (10) constitute an eigenvalue problem for the Rayleigh number. The smallest eigenvalue is the desired critical Rayleigh number.

## Method of Solution

The Galerkin method will be used to solve the eigenvalue problem stated in the previous section. The Galerkin method applies to the solution of

$$L(U) = 0 \tag{12}$$

where $L$ is a differential operator in three variables and $U$ is one of the dependent variables. The independent variable $U$ is approximated by

$$\tilde{U} = \sum_{i=1}^{N} C_i\phi_i(x, y, z) \tag{13}$$

where the $\phi_i$ satisfy the boundary conditions, and if possible some of the differential equations. Then the method requires the solution of the $N$ equations

$$\int_V L(\tilde{U})\phi_j dV = \int_V L\left\{\sum_{i=1}^{N} C_i\phi_i(x, y, z)\right\}\phi_j(x, y, z)dV = 0 \qquad j = 1, 2, \ldots, N \tag{14}$$

for the $C_i$, which will give the best approximation. The superiority of the Galerkin method is twofold. First, the formalism of the variational principle is not required and one can go directly to the form above. Second, it can be applied to diverse equations without the necessity of forming a variational problem. The trial functions $\phi_i$ should meet the boundary conditions and have sufficient freedom to resemble the function being approximated.

Following the formalism associated with the Galerkin method, equations (3) and (4) become $2N$ equations

$$\sum_j^N \int_V (\nabla^2\mathbf{v}_j + \mathrm{R}\theta_j\mathbf{k} - \text{grad } p_j)\cdot\mathbf{v}_k dV = 0 \qquad k = 1, 2, \ldots, N \tag{15}$$

$$\sum_j^N \int_V (\nabla^2\theta_j + \mathbf{v}_j\cdot\mathbf{k})\theta_k dV = 0 \qquad k = 1, 2, \ldots, N \tag{16}$$

where $\mathbf{v}_j$, $\theta_j$, and $p_j$ are represented by

$$\mathbf{v}_j = a_j\mathbf{F}_j(x, y, z), \quad \theta_j = b_j G_j(x, y, z), \quad p_j = c_j H_j(x, y, z) \tag{17}$$

with the $\mathbf{v}_j$ being selected such that

$$\nabla\cdot\mathbf{v}_j = 0$$

as well as meeting the boundary conditions given by equation (6). The $\theta_j$ is selected to meet the boundary conditions given by equations (9) and (10).

When the expressions given by equation (17) are substituted into equations (15) and (16) and the indicated integration carried out, the pressure will vanish due to the solenoidal characteristic of $\mathbf{v}_j$ and there results

$$\sum_j^N \left\{ a_j \int_V \mathbf{F}_k \cdot \nabla^2 \mathbf{F}_j dV + \mathrm{R} b_j \int_V G_j \mathbf{k} \cdot \mathbf{F}_k dV \right\} = 0$$

$$k = 1, 2, \ldots, N \quad (18)$$

$$\sum_j^N \left\{ a_j \int_V G_k \mathbf{k} \cdot \mathbf{F}_j dV + b_j \int_V G_k \nabla^2 G_j dV \right\} = 0$$

$$k = 1, 2, \ldots, N \quad (19)$$

The requirement that the $2N$ equations resulting from substitution, weighting, and integrating have non-trivial solutions ($a_j$ and $b_j$ non-zero) is that the secular determinant be zero

$$\det \begin{vmatrix} M_{11} & \mathrm{R}M_{12} \\ M_{21} & M_{22} \end{vmatrix} = 0 \quad (20)$$

where $M_{11}$, $M_{12}$, $M_{21}$, and $M_{22}$ are $N \times N$ matrices defined as

$$M_{11} = \int_V \mathbf{F}_k \cdot \nabla^2 \mathbf{F}_j dV \qquad M_{12} = \int_V \mathbf{k} \cdot \mathbf{F}_k G_j dV$$
$$M_{21} = \int_V \mathbf{k} \cdot \mathbf{F}_j G_k dV \qquad M_{22} = \int_V G_k \nabla^2 G_j dV \quad (21)$$

The symmetry of the determinant given by equation (20) allows it to be reduced from a $2N \times 2N$ problem to

$$\left| M_{22}^{-1} M_{21} M_{11}^{-1} M_{12} - \frac{I}{\mathrm{R}} \right| = 0 \quad (22)$$

which is an $N \times N$ eigenvalue problem rather than a $2N \times 2N$ determinant whose zeros must be found. Solutions may be obtained quite quickly using an iterative procedure developed for investigations of mechanical vibrations.

The trial-velocity sequence $\mathbf{v}$ is constructed from a linear combination of a complete set of orthogonal basis vectors $\mathbf{v}_j^{(1)}$ and $\mathbf{v}_j^{(2)}$ given by

$$\mathbf{v}_j^{(1)} = \mathrm{curl}\,\{\psi_j(x, y, z)\mathbf{j}\} \quad (23)$$

where $\mathbf{j}$ denotes the unit vector in the $y$ direction and $\psi$ is an arbitrary defining scalar and

$$\mathbf{v}_j^{(2)} = \mathrm{curl}\,\{\phi_j(x, y, z)\mathbf{i}\} \quad (24)$$

where $\phi_j$ is also an arbitrary defining scalar. In a system of cartesian coordinates $(x, y, z)$, the components of $\mathbf{v}_j^{(1)}$ and $\mathbf{v}_j^{(2)}$ are

$$u_j^{(1)} = -\frac{\partial \psi_j}{\partial z}, \quad v_j^{(1)} = 0, \quad w_j^{(1)} = \frac{\partial \psi_j}{\partial x} \quad (25)$$

$$u_j^{(2)} = 0, \quad v_j^{(2)} = -\frac{\partial \phi_j}{\partial z}, \quad w_j^{(2)} = \frac{\partial \phi_j}{\partial y} \quad (26)$$

where $u$, $v$, and $w$ denote $x$, $y$, and $z$ components of the velocity field. Hence the trial velocity is assumed to be given by (going back to the functional notation $\mathbf{F}$)

$$\mathbf{v} = \sum_{j=1}^N a_j^{(1)} \mathbf{F}_j^{(1)} + \sum_{j=1}^N a_j^{(2)} \mathbf{F}_j^{(2)} \quad (27)$$

In the above expression for the trial velocity, the $a_j^{(1)}$ and $a_j^{(2)}$ represent the variational parameters associated with the two arbitrary defining scalars. Now with

$$\mathbf{F}_j^{(1)} = \mathrm{curl}\,(\psi_j \mathbf{j}) \quad (28)$$

odd and even scalars that satisfy the boundary conditions are

$$\psi_j^{(e)} = C_{p_j}(xH_1) \cos\{(2q_j - 1)\pi y H_2\} C_{r_j}(z) \quad (29)$$

$$\psi_j^{(o)} = S_{p_j}(xH_1) \cos\{(2q_j - 1)\pi y H_2\} C_{r_j}(z) \quad (30)$$

and with

$$\mathbf{F}_j^{(2)} = \mathrm{curl}\,(\phi_j \mathbf{i}) \quad (31)$$

the defining scalars are

$$\phi_j^{(e)} = \cos\{(2p_j - 1)\pi x H_1\} C_{q_j}(yH_2) C_{r_j}(z) \quad (32)$$

$$\phi_j^{(o)} = \cos\{(2p_j - 1)\pi x H_1\} S_{q_j}(yH_2) C_{r_j}(z) \quad (33)$$

where

$$C_{q_j}(x) = \frac{\cosh(\lambda_{q_j} x)}{\cosh(\lambda_{q_j}/2)} - \frac{\cos(\lambda_{q_j} x)}{\cos(\lambda_{q_j}/2)} \quad (34)$$

$$S_{q_j}(x) = \frac{\sinh(\mu_{q_j} x)}{\sinh(\mu_{q_j}/2)} - \frac{\sin(\mu_{q_j} x)}{\sin(\mu_{q_j}/2)} \quad (35)$$

are the beam functions and the superscripts $e$ and $o$ indicate even and odd. The roots $\lambda$ and $\mu$ are selected to make the derivative zero at $x = \pm 1/2$ and are tabulated along with all the required integrals in Harris and Reid [10].

The trial functions selected for the temperature disturbances are selected to have the same symmetry as the vertical velocity component. This selection is made based on the symmetry implied by the energy equation. Therefore a set of trial functions for temperature is chosen for each defining scalar. The resulting choices are

$$G_j^{(1,e)} = \sin\{[(2p_j - 1) + \alpha_{p_j}^{(1,e)}]\pi x H_1\} \cos\{[(2q_j - 2) + \beta_{q_j}^{(1,e)}]\pi y H_2\} \cos\{(2r_j - 1)\pi z\} \quad (36)$$

$$G_j^{(1,o)} = \cos\{(2p_j - \alpha_{p_j}^{(1,o)})\pi x H_1\} \times \sin\{[(2q_j - 1) + \beta_{q_j}^{(1,o)}]\pi y H_2\} \cos\{(2r_j - 1)\pi z\} \quad (37)$$

$$G_j^{(2,e)} = \cos\{[(2p_j - 2) + \alpha_{p_j}^{(2,e)}]\pi x H_1\} \times \sin\{[(2q_j - 1) + \beta_{q_j}^{(2,e)}]\pi y H_2\} \cos\{(2r_j - 1)\pi z\} \quad (38)$$

$$G_j^{(2,o)} = \cos\{[(2p_j - 2) + \alpha_{p_j}^{(2,o)}]\pi x H_1\} \times \cos\{(2q_j - \beta_{q_j}^{(2,o)})\pi y H_2\} \cos\{(2r_j - 1)\pi z\} \quad (39)$$

where $p_j$, $q_j$, and $r_j$ are integers. The roots $\alpha$ and $\beta$ are found by solving the set of transcendental equations resulting by substitution into equations (9) and (10). Only the smallest root was used. The limiting case of perfectly insulating walls is recovered by setting $\alpha$ and $\beta$ to zero and that of the perfectly conducting walls by setting $\alpha$ and $\beta$ to unity.

An example of the transcendental equations is obtained by substituting the expression for $G_j^{(1,e)}$ into equations (9) and (10). The resulting expressions are

$$\{[(2q_j - 2) + \beta_{q_j}^{(1,e)}]\pi\} \tan\left\{[(2q_j - 2) + \beta_{q_j}^{(1,e)}]\frac{\pi}{2}\right\} = \left(\frac{H_1^2}{C_y H_2}\right)\left\{[(2p_j - 1) + \alpha_{p_j}^{(1,e)}]^2\pi^2 + \frac{(2r_j - 1)^2\pi^2}{H_1^2}\right\} \quad (40)$$

$$\{[(2p_j - 1) + \alpha_{p_j}^{(1,e)}]\pi\} \cot\{[(2p_j - 1) + \alpha_{p_j}^{(1,e)}]\pi/2\} = -\left(\frac{H_2^2}{C_x H_1}\right)\left\{[(2q_j - 2) + \beta_{q_j}^{(1,e)}]^2\pi^2 + \frac{(2r_j - 1)^2\pi^2}{H_2^2}\right\} \quad (41)$$

For a given $j$ (prescribes numerical value of $p_j$, $q_j$, and $r_j$), aspect ratio $H_1$ and $H_2$, and wall admittances, values of $\alpha_{p_j}^{(1,e)}$ and $\beta_{q_j}^{(1,e)}$ between 0 and 1 are found using a modified Newton–Raphson technique. Note that the relationship between the roots and parameters of the problem ($H_1$, $H_2$, $C_x$, $C_y$) is not a simple one.

## Numerical Results

Calculations were carried out for many combinations of the two types of basis vectors. These combinations of basis vectors fell into four non-combining subsets. The subsets were composed of only one type of basis vector, either odd or even. This reduced the complexity of the problem because a combination of all types was unnecessary. With a small amount of experience, one could guess the correct subset to use and reduce the number

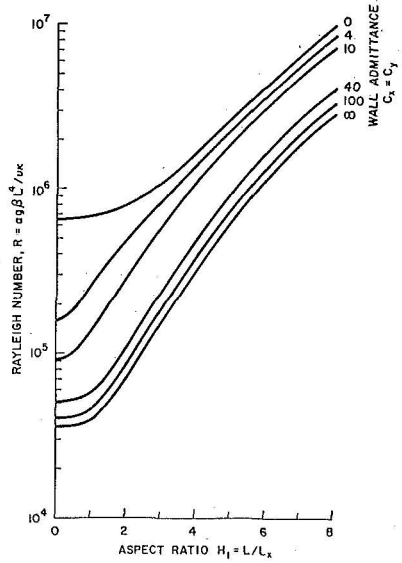


Fig. 2 Critical Rayleigh number for $H_2 = 8$ and equal wall admittances

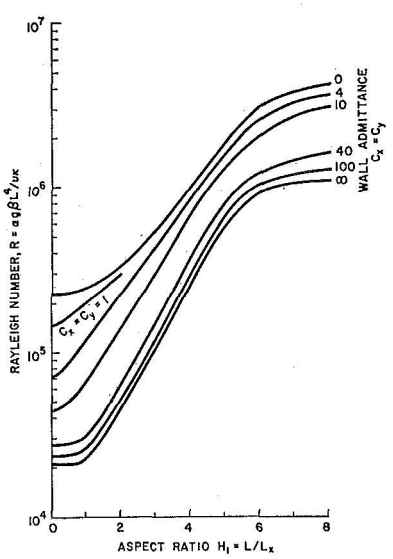


Fig. 4 Critical Rayleigh number for $H_2 = 6$ and equal wall admittances

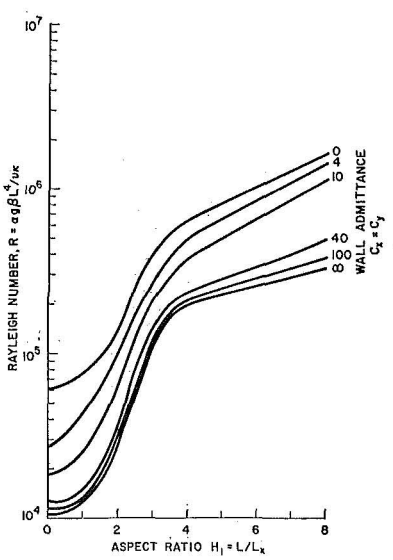


Fig. 6 Critical Rayleigh number for $H_2 = 4$ and equal wall admittances

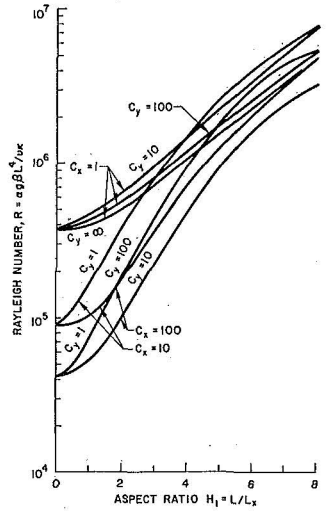


Fig. 3 Critical Rayleigh number for $H_2 = 8$ and unequal wall admittances

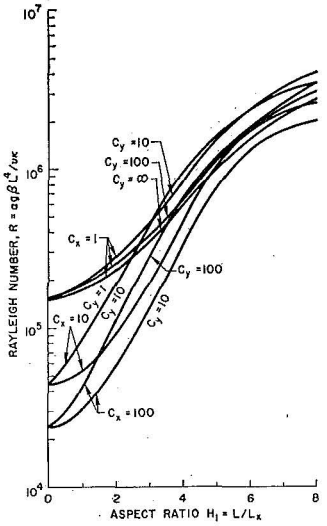


Fig. 5 Critical Rayleigh number for $H_2 = 6$ and unequal wall admittances

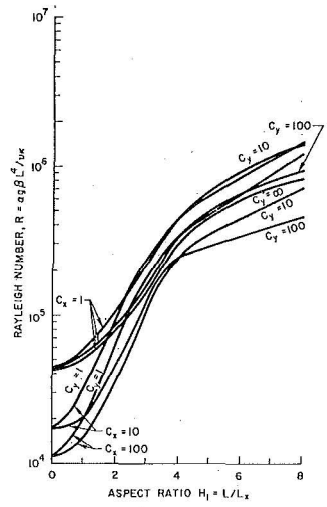


Fig. 7 Critical Rayleigh number for $H_2 = 4$ and unequal wall admittances

of required computations. Even though each subset is basically a two-dimensional motion, the dependence of the velocity and temperature on the three coordinate directions was found to be extremely important.

The numerical results are presented in graphical form in Figs. 2 to 13 for convenience of use. In each figure one of the aspect ratios is held fixed and the other aspect ratio is the ordinate. Several wall admittances are shown in each figure. One set of figures (2, 4, 6, 8, 10, 12) presents the results for equal wall admittances, and another (3, 5, 7, 9, 11, 13), the results for unequal wall conductances. The aspect ratios were varied from large values, where limiting solutions such as Edwards' [5] are valid, to very small where the lateral walls play no role. Wall admittances were varied from the case corresponding to infinite wall conductances ($k_w = \infty$) to the case corresponding to perfectly insulating walls ($k_w = 0$).

## Discussion

The effect of confining walls of varying thermal conductivity and thickness has been determined for rectangular plan forms of various aspect ratios. The minimum Rayleigh numbers were obtained for trial functions representing rolls whose axes were perpendicular to the longer dimension. If the plan form is square, the axis of the roll is perpendicular to the wall with the highest thermal conductivity. A surprising result of this work was the degree to which the wall admittances, defined by equation (11), could affect the critical Rayleigh number. When the configuration approaches a slot (long and narrow), up to a twentyfold increase in critical Rayleigh number can occur as the walls become perfect conductors. When the plan form is square or cylindrical, the increase is only threefold. The wall effect can be explained by referring to Fig. 15 and noting the fullness of the temperature-disturbance profile for nonconducting walls. The temperature profile yields a buoyant force on the fluid which will in turn net the flow profiles shown in Fig. 16. The fuller profile will more easily cause motion, hence a lower critical Rayleigh number for low-conductance walls than for high. Several investigators have noted kinks in the Rayleigh-number–aspect-ratio curve and they occur in this problem as well. This author defined the aspect ratios inversely to Davis [6] or Catton [8] and the kinks get hidden at small aspect ratios.

Heitz and Westwater [12] recently made some measurements in rectangular regions with square cross section. Fig. 14 was prepared to compare with their data. Unfortunately, not enough information was available to calculate the wall admittance. Nevertheless the comparison is quite good and indicates a wall

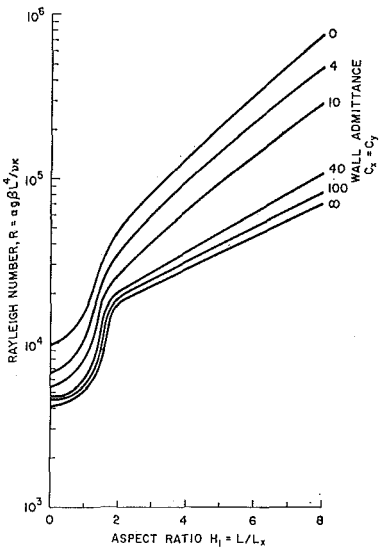


Fig. 8 Critical Rayleigh number for $H_2 = 3$ and equal wall admittances

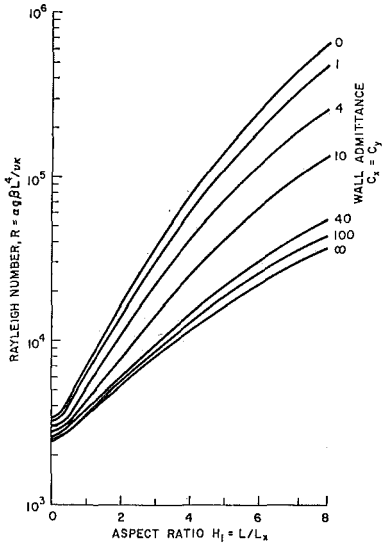


Fig. 10 Critical Rayleigh number for $H_2 = 2$ and equal wall admittances

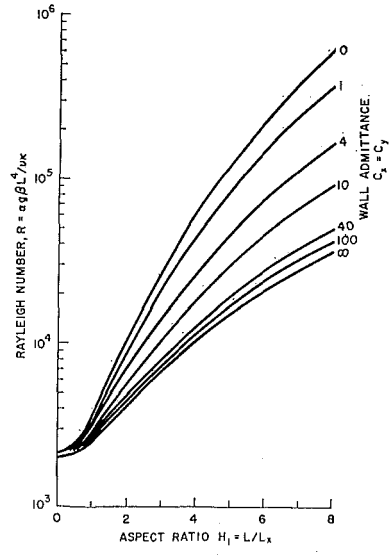


Fig. 12 Critical Rayleigh number for $H_2 = 1$ and equal wall admittances

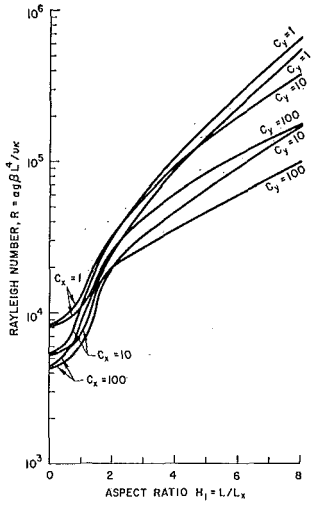


Fig. 9 Critical Rayleigh number for $H_2 = 3$ and unequal wall admittances

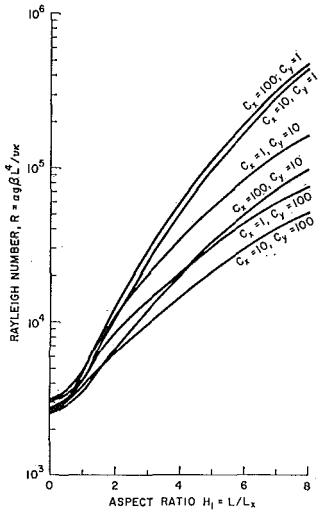


Fig. 11 Critical Rayleigh number for $H_2 = 2$ and unequal wall admittances

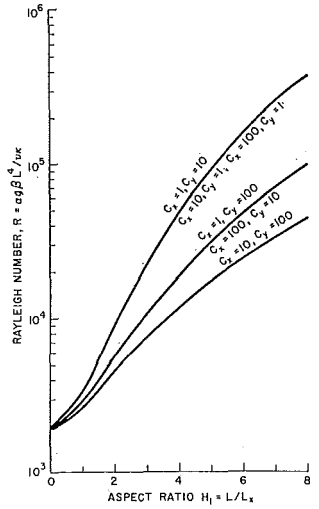


Fig. 13 Critical Rayleigh number for $H_2 = 1$ and unequal wall admittances

admittance of approximately 40. This is not unreasonable for water against glass. Some measurements made in hexagonal cells by Catton and Edwards [13] are also shown. For the hexagons, the aspect ratio becomes height-to-diameter. The upper set of points was for aluminum side walls and lies above the curve for zero wall admittance. The lower set of points was for fiberglass walls and lies slightly above the curve for infinite wall admittance. It appears as if the onset in a hexagon takes place at a critical Rayleigh number slightly above that of a square plan form. The predictions, even for the hexagons, are quite satisfactory.

Measurements were made by Edwards and Sun [14] for some large-aspect-ratio configurations to test their theory. The measurements and their predictions of the critical Rayleigh number are shown in Table 1 along with predictions based on this work. The measurements and predictions compare very well with one another at low values of the wall-admittance parameter. At the high values of the wall admittances, this work's predictions are about 15 percent low. There are several explanations for this. The critical Rayleigh number is extremely sensitive to the aspect ratio, and for $H_1 = 4$ and $H_2 = 2$, a 2 percent change in $H_1$ can cause up to a 15 percent increase in the critical Rayleigh number. The honeycomb material used in the experiments was pliable and could shift during experimental setup. This would yield a rather slow onset of motion as the cells with wide gaps would start to convect long before those with narrower gaps.

**Table 1 Comparison of predictions with experiment and other theoretical predictions**

| Aspect ratios $H_1 = L/L_x$ | Aspect ratios $H_2 = L/L_y$ | Admittance parameter | Measured result [14] | Predicted result [14] | Predicted result, this work |
|---|---|---|---|---|---|
| 3.96 | 2.0 | 130 | 35,000 | 35,300 | 30,000 |
| 3.96 | 1.0 | 130 | 15,200 | 16,100 | 13,000 |
| 4.0 | 0.47 | 130 | 13,000 | 15,500 | 11,800 |
| 3.88 | 0.255 | 100 | 13,000 | 14,500 | 11,600 |
| 3.96 | 2.0 | 12 | ... | 43,200 | 50,000 |
| 3.96 | 1.0 | 10* | 27,800 | 24,100 | 25,000 |
| 4.0 | 0.47 | 9.2* | 26,000 | 24,900 | 24,000 |
| 4.0 | 0.255 | 8* | 21,400 | 20,500 | 21,000 |

* Contains thermal radiation, see reference [14].

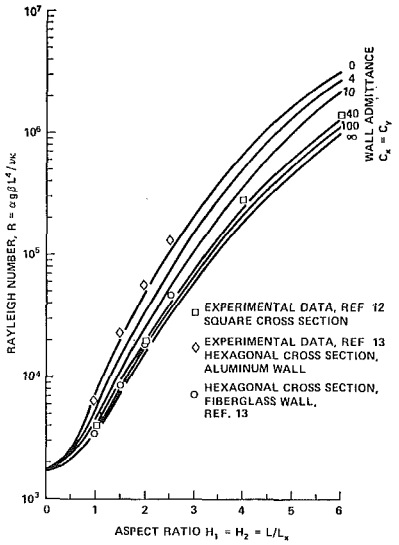


**Fig. 14 Critical Rayleigh number for square cross section and walls of equal admittance**

This makes the critical point hard to determine from the data. The predictions made by Edwards and Sun required adjustments to their theoretical solution, of the type made by Catton and Edwards [13], and the boundary conditions on the wall spanning the shortest distance are uncertain. To better point this out, one can see from Fig. 6 that an increase in the short-wall admittance can raise the critical Rayleigh number to well above the predictions of Edwards and Sun. With these considerations in mind, the predictions are quite good.

## Summary and Conclusions

The Galerkin method was applied to the problem of onset of motion in a confined region with conducting walls. Critical Rayleigh numbers were determined for a wide range of aspect ratios and wall admittances. Up to a twentyfold increase in critical Rayleigh number can occur at some aspect ratios as the wall admittance is decreased from infinity to zero. Even though the motion has only two components (a roll), it depends strongly all three coordinate directions. Comparison was made with experiment and other theory and found to be good.

## Acknowledgments

This work was supported by a National Science Foundation grant and was motivated by a need to eliminate natural convection under two different circumstances. One of the situations involved reduction of natural-convection losses in solar collectors and the other was to design an apparatus that would measure the onset of electroconvection without thermal convection.

## References

1 Chandrasekhar, S., *Hydrodynamic and Hydromagnetic Stability*, Clarendon Press, Oxford University, London, England, 1961, pp. 9–73.

2 Ostrach, S., and Pnueli, D., "The Thermal Instability of Completely Confined Fluids Inside Some Particular Configurations," JOURNAL OF HEAT TRANSFER, TRANS. ASME, Series C, Vol. 85, No. 4, Nov. 1963, pp. 346–354.

3 Catton, I., and Edwards, D. K., "Initiation of Thermal Convection in Finite Right Circular Cylinders," *AIChE Journal*, Vol. 16, 1970, pp. 594–601.

4 Yih, C. S., "Thermal Stability of Viscous Flows," *Quarterly of Applied Mathematics*, Vol. 17, 1959, pp. 25–42.

5 Edwards, D. K., "Suppression of Cellular Convection by Lateral Walls," JOURNAL OF HEAT TRANSFER, TRANS. ASME, Series C, Vol. 91, No. 1, Feb. 1969, pp. 145–150.

6 Davis, S. H., "Convection in a Box," *Journal of Fluid Mechanics*, Vol. 30, Part 3, 1967, pp. 465–478.

7 Charlson, G. S., and Sani, R. L., "Thermoconvective Instability in a Bounded Cylindrical Fluid Layer," *International Journal of Heat and Mass Transfer*, Vol. 13, 1970, pp. 1479–1496.

8 Catton, I., "The Effect of Insulating Vertical Walls on the Onset of Motion in a Fluid Heated from Below," submitted to the *International Journal of Heat and Mass Transfer*.

9 Sani, R. L., "Convective Instability," PhD thesis, University of Minnesota, Minneapolis, Minn., 1963.

10 Harris, R. L., and Reid, W. H., "On Orthogonal Functions which Satisfy Four Boundary Conditions. I. Tables for Use in Fourier-Type Expansions," *Astrophys. J. Supp. Ser.*, Vol. 13, 1958, pp. 429–447.

11 Sherman, M., and Ostrach, S., "On the Principle of Exchange of Stabilities for the MHD Stability in Completely Confined Fluids," *Journal of Fluid Mechanics*, Vol. 24, Part 4, 1966, pp. 661–671.

12 Heitz, W. L., and Westwater, J. W., "Critical Rayleigh Numbers for Natural Convection of Water Confined in Square Cells With $L/D$ From 0.5 to 8," JOURNAL OF HEAT TRANSFER, TRANS. ASME, Series C, Vol. 93, No. 2, May 1971, pp. 188–196.

13 Catton, I., and Edwards, D. K., "Effect of Side Walls on Natural Convection Between Horizontal Plates Heated From Below," JOURNAL OF HEAT TRANSFER, TRANS. ASME, Series C, Vol. 89, No. 4, Nov. 1967, pp. 295–299.

14 Edwards, D. K., and Sun, W. M., "Prediction of the Onset of Natural Convection in Rectangular Honeycomb Structures," Paper No. 7/62, International Solar Energy Society Conference, Melbourne, Australia, Mar. 1970.

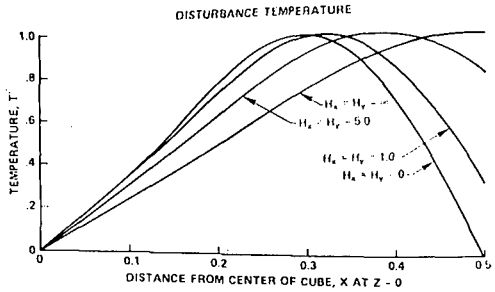


**Fig. 15 Disturbance temperature**

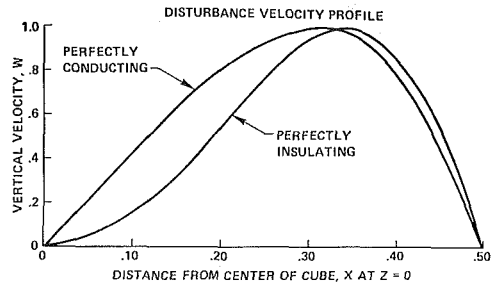


**Fig. 16 Disturbance velocity profile**

# APPENDIX

## The Principle of Exchange of Stabilities

Sherman and Ostrach [11] derive the relationship (see their equation (18))

$$\frac{n}{\mathrm{Pr}} I_1 - R(I_1 + I_3) - Rn^* I_4 + I_5 = 0 \tag{42}$$

where

$$I_1 = \int_\tau \mathbf{V}\cdot\mathbf{V}^* d\tau \quad I_2 = \int_\tau \nabla\theta\cdot\nabla\theta^* d\tau \quad I_3 = \int_s B_i^n \theta\theta^* ds$$
$$I_4 = \int_\tau \theta\theta^* d\tau \quad I_5 = \int_\tau \mathrm{curl}\,\mathbf{V}\cdot\mathrm{curl}\,\mathbf{V}^* d\tau \tag{43}$$

for the lateral-wall boundary condition

$$\nabla\theta\cdot\mathbf{n} = -B_i\theta \tag{44}$$

where $B_i$ is the Biot number. They show that if all of the inte-

grals are positive definite, the principle of exchange of stabilities holds.

For this problem, the thermal boundary condition on the lateral walls is

$$\nabla\theta\cdot\mathbf{n} = -\frac{1}{c}\nabla_{2D}{}^2\theta + \frac{\kappa_f}{\kappa_w}n\theta \tag{45}$$

and the third and fourth integrals become

$$I_3 = -\frac{1}{c}\int_s \theta\nabla_{2D}{}^2\theta^* ds \tag{46}$$

$$I_4 = \frac{1}{c}\frac{\kappa_f}{\kappa_w}\int_s \theta\theta^* ds + \int_\tau \theta\theta^* d\tau \tag{46}$$

Applying Green's theorem to $I_3$ and noting that the line integral is zero yields

$$I_3 = \frac{1}{c}\int_s \nabla_{2D}\theta\cdot\nabla_{2D}\theta^* ds \tag{47}$$

All of the integrals in equation (42) are positive. Therefore, the principle of exchange of stabilities holds for the completely confined region with walls of arbitrary thermal conductivity when the fin approximation is used.

T. E. HORTON
Professor.
Assoc. Mem. ASME

J. H. McDERMIT
NDEA Fellow.

Department of Mechanical Engineering,
University of Mississippi,
University, Miss.

# Design of a Specular Aspheric Surface to Uniformly Radiate a Flat Surface using a Nonuniform Collimated Radiation Source

*When uniform radiative heating is desired on a surface the radiative heating system normally suffers from either (1) low efficiency or (2) the heating not being as uniform as desired. Using an axisymmetric collimated but nonuniform source of radiation and a properly designed specular surface, uniform heating can be obtained at 100 percent efficiency. The differential equation which describes such a surface is derived. The derivation is facilitated by the use of a vectorial ray-trace formulation. The differential equation has been solved and results are presented for the case of an axisymmetric nonuniform collimated source uniformly heating a flat surface.*

## Introduction

THE DESIRABILITY of surface heating from radiative sources for industrial and experimental work is well known. The usual procedure is to place the surface to be heated and the source in a reflecting enclosure, thus relying on the specular reflections from the enclosure to transfer a large fraction of the radiation from the source to the heated surface. In more sophisticated designs conventional optical ray-trace techniques lead to the use of spherical, parabolic, or elliptical surfaces to insure a maximum transfer to the surface to be heated. When uniform heating is required such designs are ineffective since the distribution of the radiative flux over the receiver surface is dependent on the extent of and the directional characteristics of the source. Uniform heating in most cases is achieved by using only a fraction of the emission from the source. Thus a prescribed spatial heating rate could be achieved by using multiple sources and using only a small fraction of their emitted radiation.

The advent of the field of space and reentry environmental simulation has revealed a variety of heat-transfer problems which could be investigated only by radiative heating. This is due to the dominant role of radiative transfer as an external source of heating, both in deep space and very high speed reentry. Moreover, the demands of this field have emphasized the need for high-efficiency radiative-transfer systems which can achieve a carefully prescribed spatial heating rate [1 4].[1]

As an example, consider the problem of simulating shock-layer radiative heating for reentry missions to the larger planets. These conditions cannot be simulated for a meaningful period of time aerodynamically. Thus, to investigate the behavior of materials subjected to the very large radiative heating loads which are anticipated, an external source must be used. The laser has been proposed as such a source because of the high power levels which are available together with the large but collimated beam.

Recently, Brewer [5] reported on ablative material performance in high-radiative-flux environment using a carbon dioxide laser. Because of the excitation mechanism in the gas laser, the beam intensity is not uniform. Since a uniform heating flux was desired on the test material, only a fraction of the energy output of the laser was used.

The objective of this investigation is to determine the shape of a specular surface which will enable one to use a nonuniform axisymmetric source of radiation to achieve uniform heating of a flat surface. Although the results given in this paper are for a uniform distribution on a flat surface, the development presented below can be used to design specular surfaces which will give any desired axisymmetric radiative distribution on an arbitrary surface using an axisymmetric collimated source. With this specular-surface design procedure one can (1) utilize all the energy output by the source and (2) specify the intensity distribution on the receiver surface.

In an earlier paper [6] a general procedure was outlined for treating systems of specular surfaces. The paper considered only "problems of analysis" (i.e., given the receiver surfaces, a system of specular surfaces, and a fully described source, the problem is to determine the radiative distribution on the receiver surfaces). The use of a vector representation of the rays between surfaces and the use of the concept that the gradient of a function representing a surface is a vector normal to that surface facilitate the formulation of the ray-trace equations. The analysis problem consists of (1) solving the system of algebraic ray-trace equations to determine the relation between source and receiver ray coordinates and (2) relating differential changes in source coordinates to differential changes in receiver coordinates

[1] Numbers in brackets designate References at end of paper.

Contributed by the Heat Transfer Division for publication (without presentation) in the JOURNAL OF HEAT TRANSFER. Manuscript received by the Heat Transfer Division April 12, 1971. Paper No. 72-HT-J.

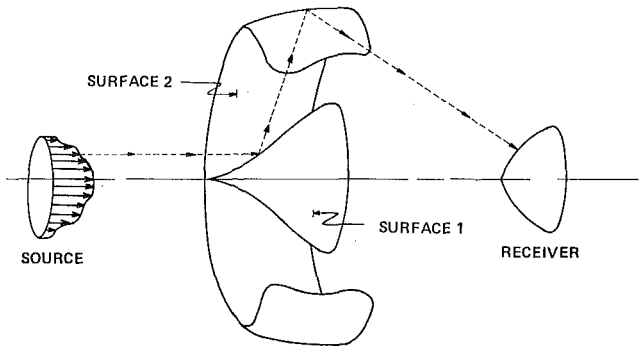


**Fig. 1 Schematic of arrangement of source, specular surfaces, and receiver**

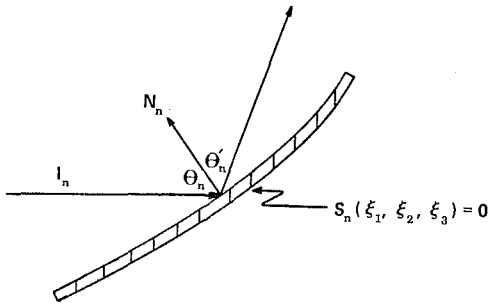


**Fig. 2 Specular reflection**

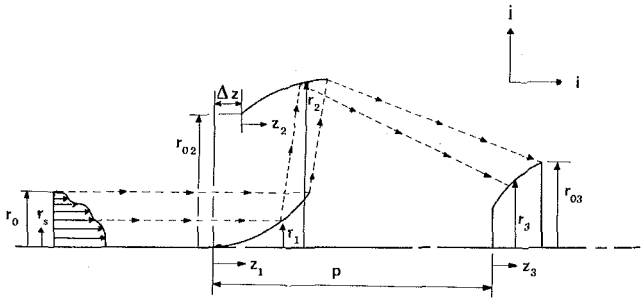


**Fig. 3 Nomenclature**

so that the view function or an equivalent radiative transfer function is obtained.

By contrast, the situation treated here is a "problem of design" (i.e., given a fully described source and receiver surface, the problem is to determine the form of the specular surfaces which will result in a specified relationship between source and receiver intensity distributions). With this specified relationship and the vectorial ray-trace formulation of [6], one obtains a system of differential equations which describes the specular surface. Appropriate differentiation and rearrangement of the system of ray-trace differential equations will yield a relation between differential changes in source and receiver coordinates. These differential expressions used with an energy balance between receiver and source points yield differential equations for the specular surfaces in terms of the source and receiver intensity distributions. The solution of these differential equations for the form of the specular surfaces is the solution to the design problem.

The problem treated here is related to the problem of optical design in that the problem of optical design also relies upon ray tracing. However, the optical designer must be concerned with achieving minimum image distortion and aberration with maximum resolution in addition to achieving a specified intensity distribution. As a result the general approach to the optical design problem is to select a tentative geometric configuration and to solve the ray-trace or "analysis" problem repetitiously, systematically changing the parameters describing the lenses or specular surfaces, until the ultimate performance of the system is within allowable limits. For this purpose general ray-trace methods treating aspheric surfaces as polynominals have been developed and incorporated into automatic design procedures [7, 8].

## Formulation of the Design Problem

Consider a circular collimated source of radiation with an arbitrary axisymmetric intensity distribution, a typical ray of which is shown in Fig. 1, reflecting off two specular surfaces and onto an arbitrary receiver surface. The overall objective is to obtain expressions for surfaces 1 and 2 such that with a specified source intensity distribution and a given receiver shape, uniform heating of the receiver will be achieved.

The first aspect of the formulation is to obtain the ray-trace expressions which satisfy the "law of reflection" on each surface. The law of reflection for the perfectly specular case requires that the angle between an incident ray and the surface normal be equal to the angle between the reflected ray and the surface normal, and that the intensity of the radiation not be diminished by the reflection. The additional requirement of the law of reflection that the incident ray, reflected ray, and the surface normal all be coplanar is automatically satisfied here because of the symmetry of the problem. Consider the general reflection depicted in Fig. 2. For the $n$th surface in a system, the law of reflection requires $\cos\theta_n = \cos\theta_n'$, which is satisfied provided that

$$\left[\frac{\mathbf{I}_n}{|\mathbf{I}_n|} + \frac{\mathbf{I}_{n+1}}{|\mathbf{I}_{n+1}|}\right]\cdot\mathbf{N}_n = 0 \tag{1}$$

The formulation is aided by recalling that the gradient of a surface function is a vector normal to the surface so that

$$\text{grad } S_n = \nabla S_n = \mathbf{N}_n \tag{2}$$

Thus the general reflection expression

$$\left[\frac{\mathbf{I}_n}{|\mathbf{I}_n|} + \frac{\mathbf{I}_{n+1}}{|\mathbf{I}_{n+1}|}\right]\cdot\nabla S_n = 0 \tag{3}$$

## Nomenclature

$S$ = general surface function
$f$ = specific surface function
$\mathbf{I}$ = ray vector
$\mathbf{N}$ = surface-normal vector
$\mathbf{i}$ = unit vector in axial direction
$\mathbf{j}$ = unit vector in radial direction
$\theta$ = angle between ray and surface normal
$Q$ = radiation intensity
$\xi_1, \xi_2, \xi_3$ = generalized coordinates
$r$ = radial coordinate
$z$ = axial coordinate
$\Delta z$ = see Fig. 3
$p$ = axial distance from first reflecting surface to receiver
$\sigma = f_2/r_{02}$, nondimensional surface function
$\zeta = z_2/r_0$, normalized axial coordinate
$\rho = r_3/r_0$, nondimensional receiver radial coordinate
$P = p/r_0$, nondimensional axial distance from reflecting surface to receiver
$R = r_{03}/r_0$, nondimensional outer radius of receiver
$A = r_{01}/r_0$, nondimensional inner radius of 2nd reflecting surface
$M$ = defined by equation (28)
$\Delta\sigma$ = defined by equation (29)

**Subscripts**

$n$ = denotes $n$th surface
0 = outer radius of source
1 = denotes 1st reflecting surface
2 = denotes 2nd reflecting surface
3 = denotes receiver surface
02 = inner radius of 2nd reflecting surface
03 = outer radius of receiver surface
$s$ = denotes source
$c$ = centerline source intensity

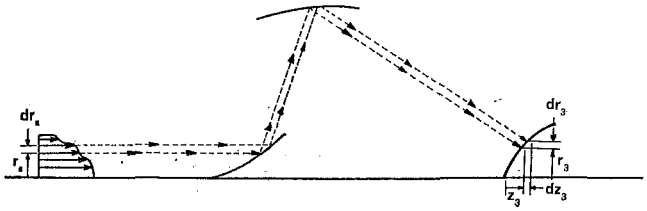


**Fig. 4 Energy balance**

is seen to be a partial differential equation in terms of the surface function. A set of equations of this type for $n = 1, 2, 3, \ldots, q$ for a system composed of $q$ specular surfaces constitutes the ray-trace equations for the system.

In order to translate these expressions into forms which describe the specific problem of two surfaces, consider the coordinates and notation depicted in Fig. 3.

The expressions for the ray vectors can be written

$$\frac{\mathbf{l}_1}{|\mathbf{l}_1|} = \mathbf{j} \tag{4}$$

$$\frac{\mathbf{l}_2}{|\mathbf{l}_2|} = \frac{\mathbf{i}z_{12} + \mathbf{j}r_{12}}{\sqrt{z_{12}^2 + r_{12}^2}} \tag{5}$$

$$\frac{\mathbf{l}_3}{|\mathbf{l}_3|} = \frac{\mathbf{i}z_{23} + \mathbf{j}r_{23}}{\sqrt{z_{23}^2 + r_{23}^2}} \tag{6}$$

where

$$z_{12} = z_2 + \Delta z - z_1$$
$$r_{12} = r_2 - r_1$$
$$z_{23} = p + z_3 - \Delta z - z_2$$
$$r_{23} = r_3 - r_2$$

considering the two axisymmetric specular surfaces to be denoted by

$$r_1 = f_1(z_1) \quad \text{and} \quad r_2 = f_2(z_2)$$

so the surface function can be written as

$$S_1(r_1, z_1) = r_1 - f_1(z_1) = 0$$
$$S_2(r_2, z_2) = r_2 - f_2(z_2) = 0$$

Using the operator $\nabla$ for two-dimensional rectangular coordinates

$$\nabla = \mathbf{i}\frac{\partial}{\partial z} + \mathbf{j}\frac{\partial}{\partial r}$$

one obtains the normals to the two surfaces

$$\nabla S_1 = -\mathbf{i}f_1' + \mathbf{j} = \mathbf{N}_1 \tag{7}$$

$$-\nabla S_2 = +\mathbf{i}f_2' - \mathbf{j} = \mathbf{N}_2 \tag{8}$$

where

$$f_1' = \frac{df_1}{dz_1} \quad \text{and} \quad f_2' = \frac{df_2}{dz_2}$$

Combining the ray-vector equations (4) and (5) with the surface normal of equation (7), as prescribed by equation (3) applied to surface 1, one has

$$\left[\mathbf{i} + \frac{\mathbf{i}z_{12} + \mathbf{j}r_{12}}{\sqrt{z_{12}^2 + r_{12}^2}}\right] \cdot [-\mathbf{i}f_1' + \mathbf{j}] = 0 \tag{9}$$

which can be simplified to

$$f_1' = \frac{r_{12}}{z_{12} + \sqrt{z_{12}^2 + r_{12}^2}} \tag{10}$$

Similarly, combining the ray-vector equations (5) and (6) with the surface normal of equation (8), as prescribed by equation (3) applied to surface 2, one has

$$\left[\frac{\mathbf{i}z_{12} + \mathbf{j}r_{12}}{\sqrt{z_{12}^2 + r_{12}^2}} + \frac{\mathbf{i}z_{23} + \mathbf{j}r_{23}}{\sqrt{z_{23}^2 + r_{23}^2}}\right] \cdot [+\mathbf{i}f_2' - \mathbf{j}] = 0 \tag{11}$$

which can be simplified to

$$f_2' = \frac{r_{12}\sqrt{z_{23}^2 + r_{23}^2} + r_{23}\sqrt{z_{12}^2 + r_{12}^2}}{z_{12}\sqrt{z_{23}^2 + r_{23}^2} + z_{23}\sqrt{z_{12}^2 + r_{12}^2}} \tag{12}$$

Equations (10) and (12) are the ray-trace equations for this system. Equation (10) relates the source, first-reflection, and second-reflection coordinates. This is made clearer by a rearrangement of this expression

$$r_{12}\left[\frac{1 - (f_1')^2}{2f_1'}\right] = z_{12} \tag{13}$$

Likewise using equation (13) to eliminate $r_{12}$ and $z_{12}$ from equation (12), an expression relating the terminal coordinates is obtained

$$4f_1'\{f_2'[1 - (f_1')^2] - f_1'[1 - (f_2')^2]\}z_{23}^2 + [1 - (f_1')^2]\{[1 - (f_1')^2][1 - (f_2')^2] + 4f_1'f_2'\}r_{23}^2 - 2f_2'[1 + (f_1')^2]2z_{23}r_{23} = 0 \tag{14}$$

The above forms of the ray-trace equations, in addition to clearly showing the relationship between ray coordinates, indicate an obvious condition for which the coupled differential equations are separable, i.e., $(f_1')^2 = 1$. This condition also requires $z_{12} = 0$ for equation (13) to be satisfied, which implies $\Delta z = 0$ and $z_2 = z_1 = r_1 = r_2$. Therefore only designs in which surface 1 is a right circular cone with a half-angle of 45 deg are considered. This assumption reduces equation (14) to the form

$$(p + z_3 - z_2)\left[\frac{(f_2')^2 - 1}{2f_2'}\right] = r_3 - f_2 \tag{15}$$

To see that there is still an infinite set of functions which satisfies the ray-trace equation, consider the specification of a point $r_s$ on the source (this specifies $z_1$ and $z_2$). There is still a range of values for $z_3$ (this with a particular receiver specifies $r_3$) and $f_2$ which satisfies equation (15). Thus, further constraint on the coordinates is required before a unique solution can be found. This additional constraint is a relationship between source and receiver surface coordinates which comes from considering the intensity distributed over the receiver and source surfaces and is termed the energy-balance relation.

## Energy-Balance Relation

Considering the energy emitted from a differential ring on the source surface, transported by the beam depicted in Fig. 4, and "illuminating" a differential ring on the receiver surface. If the specular reflectors are assumed to be perfect and if the directional properties of the receiver are neglected so all radiation striking the receiver is absorbed, then the energy emitted into the beam must equal the energy received at the terminal surface. Thus, balancing the energy between the radial increment on the source and receiver requires

$$2\pi r_s dr_s Q_s = 2\pi r_3\sqrt{(dr_3)^2 + (dz_3)^2}\,Q_3$$

or

$$\frac{dz_3}{dr_s} = \frac{Q_s}{Q_3}\frac{r_s}{r_3}\frac{1}{\sqrt{(dr_3/dz_3)^2 + 1}} \tag{16}$$

For the specific case here of $f_1' = 1$ and $r_s = r_1 = z_2$, the above can be written

$$\frac{dz_3}{dz_2} = \frac{Q_s}{Q_3}\frac{z_2}{r_3}\frac{1}{\sqrt{(r_3')^2+1}} \tag{17}$$

## Design Differential Equations

A differential relationship between these same coordinates can be obtained from a suitable differentiation of the ray-trace equation (15)

$$\frac{dz_3}{dz_2}\{2f_2'r_3' - [(f_2')^2 - 1]\} - [(f_2')^2 + 1] + 2f_2''[(r_3 - f_2) - f_2'(p + z_3 - z_2)] = 0 \tag{18}$$

Substituting from equation (15) for $r_3 - f_2$ the above can be rearranged to yield the differential equation

$$\frac{f_2''}{f_2'} = \frac{1}{p + z_3 - z_2}\left\{\frac{dz_3}{dz_2}\left[\frac{2f_2'r_3'}{1+(f_2')^2} + \frac{1-(f_2')^2}{1+(f_2')^2}\right] - 1\right\} \tag{19}$$

Now using equation (17) to eliminate the differential relation between source and receiver, the above becomes

$$\frac{f_2''}{f_2'} = \frac{1}{p + z_3 - z_2}\left\{\frac{Q_s}{Q_3}\frac{z_2}{r_3}\frac{1}{\sqrt{(r_3')^2+1}} \times \left[\frac{2f_2'r_3'}{1+(f_2')^2} + \frac{1-(f_2')^2}{1+(f_2')^2}\right] - 1\right\} \tag{20}$$

Solutions to this differential equation satisfy both the energy-balance and ray-trace conditions and thus represent general solutions to the design problem.

## Flat Receiver Surface

To realize a solution to this differential equation, consider the case of a flat circular receiver, i.e., $z_3 = 0$ and $r_3' \to \infty$, so that equation (20) becomes

$$\frac{f_2''}{f_2'} = \frac{1}{p - z_2}\left[\frac{Q_s}{Q_3}\frac{z_2}{r_3}\frac{2f_2'}{1+(f_2')^2} - 1\right] \tag{21}$$

For an upright image (i.e., no ray crossing) the two boundary conditions on the specular surface require

$$f_2 = r_{02} \quad \text{at} \quad z_2 = 0 \quad \text{and} \quad r_3 = 0 \quad \text{at} \quad z_2 = 0$$

Introducing the dimensionless variables

$$\zeta = z_2/r_0 \quad \sigma = f_2/r_{02} \quad \rho = r_3/r_0$$

and letting

$$P = p/r_0 \quad R = r_{03}/r_0 \quad A = r_{02}/r_0$$

equation (21) can be transformed into

$$\frac{\sigma''}{\sigma'} = \frac{1}{P - \zeta}\left[\frac{Q_s}{Q_3}\frac{2A\zeta\sigma'}{\rho[1+(A\sigma')^2]} - 1\right] \tag{22}$$

and the ray-trace equation (15) can be transformed into

$$\rho = A\sigma + (P - \zeta)\left[\frac{(A\sigma')^2 - 1}{2A\sigma'}\right] \tag{23}$$

Finally, writing the source intensity distribution as $Q_s = Q_cF(\zeta)$ and considering the gross energy balance between the source and receiver, assuming the receiver heating to be uniform,

$$2\pi Q_c\int_0^1 \zeta F(\zeta)d\zeta = Q_3\pi R^2$$

so

$$\frac{Q_c}{Q_3} = \frac{R^2}{2\int_0^1 \zeta F(\zeta)d\zeta} \quad \text{or} \quad \frac{Q_s}{Q_3} = \frac{R^2F(\zeta)}{2\int_0^1 \zeta F(\zeta)d\zeta} \tag{24}$$

Substituting equations (23) and (24) into equation (22) the differential equation becomes

$$\frac{\sigma''}{\sigma'} = \frac{1}{P - \zeta}\left[\frac{2(RA\sigma')^2F(\zeta)\zeta}{\left[\int_0^1 \zeta F(\zeta)d\zeta\right][1+(A\sigma')^2]\{2A^2\sigma\sigma' + (P-\zeta)[(A\sigma')^2 - 1]\}} - 1\right] \tag{25}$$

subject to the boundary conditions

$$\text{at} \quad \zeta = 0: \quad \sigma = 1 \quad \text{and} \quad \rho = 0$$

## Solution Procedure

Integrating equation (25) twice and applying the boundary conditions one obtains

$$\sigma' = \frac{\sigma_{02}'}{P}(P - \zeta)e^M \tag{26}$$

$$\sigma = 1 + \int_0^\zeta \sigma' d\zeta \tag{27}$$

where $\sigma_{02}'$ is the derivative of $\sigma$ at $\zeta = 0$ and $M$ is the integral

$$M = \int_0^\zeta \left\{\left[\frac{1}{P - \zeta}\right]\left[\frac{2(RA\sigma')^2F(\zeta)\zeta}{\left[\int_0^1 \zeta F(\zeta)d\zeta\right][1+(A\sigma')^2]\{2A^2\sigma\sigma' + (P-\zeta)[(A\sigma')^2 - 1]\}}\right]\right\}d\zeta \tag{28}$$

for a specified intensity distribution and an assumed initial specular-surface shape equation (28) can be evaluated. Then these values of $M$ are substituted into equations (26) and (27) to yield new values of $\sigma$ and $\sigma'$ which are used to repeat the process until equation (25) is satisfied within the desired precision.

Looking at equation (22) one can see the ratio $\zeta/\rho$ is indeterminate at the origin, i.e., when $\zeta \to 0$ and $\rho \to 0$. However, this difficulty can be easily overcome by using the ray-trace equation (23) to solve for $\sigma'$ at $\zeta = 0$. With the slope the function can be approximated near the origin.

## Results

For the case of uniform intensity on a flat receiver surface from an axisymmetric parabolic source intensity distribution of the form $F(\zeta) = 1 - \zeta^2$, equation (25) has been solved for a range of receiver to source concentration ratios ($r_{03}/r_0$) and nondimensional focal lengths ($p/r_0$) considering different nondimensional inner radii ($r_{02}/r_0$) of the second reflecting surface. The solution specular surfaces are found to be very nearly frustums of cones. For this reason the solutions will be presented in two parts. The first part represents the variation of each surface from a frustum which passes through the end points of the surface. This variation $\Delta\sigma$ expressed as

$$\Delta\sigma(\zeta) = \sigma(\zeta) - \sigma(0) - \zeta[\sigma(1) - \sigma(0)] \tag{29}$$

is plotted as a function of the normalized axial coordinate $\zeta$ for various values of $r_{02}/r_0$, $p/r_0$, and $r_{03}/r_0$ in Figs. 5–9 (note that $\sigma(0) = 1$). The second part of the solution is the tangent of the

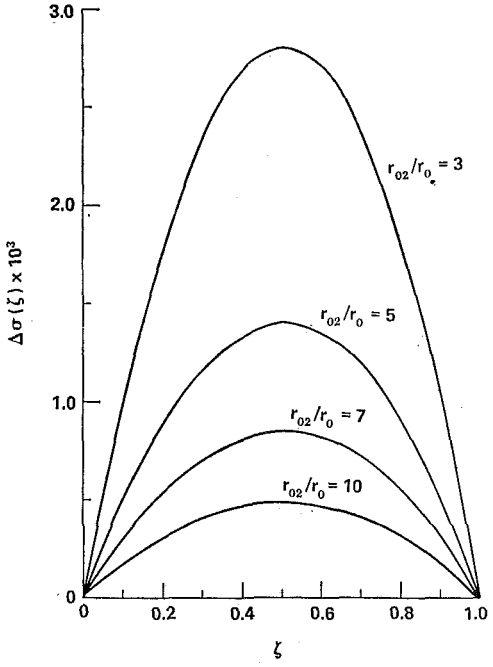


**Fig. 5 Surface variations for $r_{03}/r_0 = 0.1$, $p/r_0 = 10$, and $r_{02}/r_0 = 3$, 5, 7, and 10**

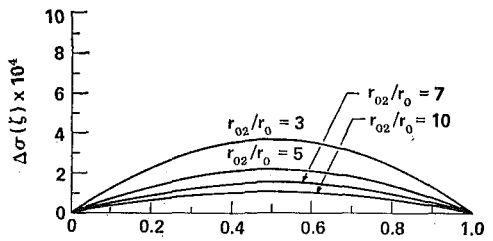


**Fig. 6 Surface variations for $r_{03}/r_0 = 0.1$, $p/r_0 = 100$, and $r_{02}/r_0 = 3$, 5, 7, and 10**

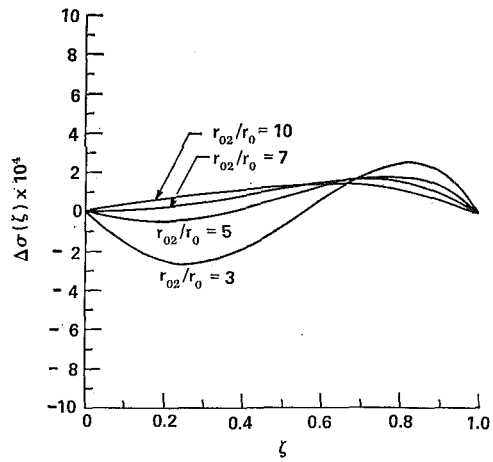


**Fig. 7 Surface variations for $r_{03}/r_0 = 1$, $p/r_0 = 10$, and $r_{02}/r_0 = 3$, 5, 7, and 10**

half-angle of the cone associated with the frustum passing through the end points of the design specular surface.

For the case of the concentration $r_{03}/r_0 = 0.1$, the intensity on the receiver is greater than that at any point on the source and the entire specular surface acts as a concentrator. Thus, as is clear from the variations from the cone frustum in Figs. 5 and 6, the surface is concave and the curvature of the surface decreases with increases in focal length. The surface curvature is proportional to the second derivative of the surface variation and to the nondimensional inner radius of the specular surface, $r_{02}/r_0$. As

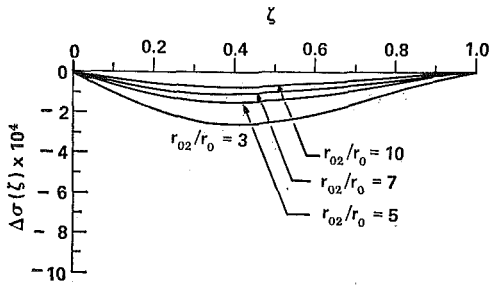


**Fig. 8 Surface variations for $r_{03}/r_0 = 1.5$, $p/r_0 = 10$, and $r_{02}/r_0 = 3$, 5, and 7**

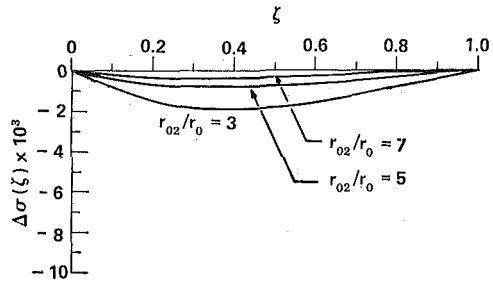


**Fig. 9 Surface variations for $r_{03}/r_0 = 1.5$, $p/r_0 = 100$, and $r_{02}/r_0 = 3$, 5, 7, and 10**

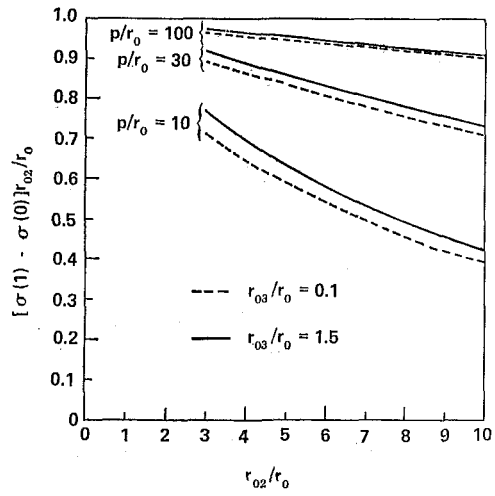


**Fig. 10 Specular-surface frustum slope $[\sigma(1) - \sigma(0)]r_{02}/r_0$ as a function of geometric parameters**

the concentration ratio $r_{03}/r_0$ is increased, one would expect the curvature to decrease and the surface to eventually become convex. This is verified by comparing Figs. 5, 7, and 8. In the case where $r_{03}/r_0 = 1.0$, the source and receiver have the same area, so the intensity on the receiver is the average intensity of the source. The ray from the source with this average intensity strikes the second surface at $\zeta = 0.707$. However, the inflection point for the specular surface (the point of change from convex to concave surface) does not occur at this point. This is due to the fact that the heating on the receiver depends not only on the beam intensity but also on the angle the beam makes with the receiver. Thus as the inner radius of the specular surface increases, the inflection point will change locations. The variation of the inflection point is quite apparent in Fig. 7 and less obvious in the predominantly convex array of designs with concentration ratio greater than one in Figs. 8 and 9. Just as in the fully concave cases the absolute value of the maximum surface curvature decreases with increases in focal length.

The cone-frustum tangent of the specular surfaces is plotted for various values of the ratios $r_{02}/r_0$, $p/r_0$, and $r_{03}/r_0$ in Fig. 10. As one might suspect the cone-frustum tangent decreases as the

surface is moved away from the centerline and increases with increases in axial position of the receiver surface. The cone-frustum tangent varies only slightly for an order-of-magnitude change in the concentration ratio $r_{03}/r_0$.

## Conclusions

The design problem for a nonuniform axisymmetric collimated source has been fully developed for arbitrary source and receiver intensity distributions considering a general receiver surface. As an illustrative example, a design involving two specular surfaces has been developed where the first surface is a 45 deg cone. Equation (20) is the differential equation which describes the general design surface. For the specific case of uniformly heating a flat circular receiver, the differential equation (25) describes the specular design surface.

The results presented here have been restricted to designs using a parabolic collimated source distribution to produce uniform distributions on flat receiver surfaces which are normal to the optical axis. By following the general outline used here of combining the differential form of the ray-trace equation with a differential energy balance, a procedure can be developed for design problems considering the angular variation of intensity of point sources.

## Acknowledgments

Acknowledgment is made to the Engineering Experiment Station, University of Mississippi, for support of a portion of this work through state funds HR1133 and HR1337 and to the Jet Propulsion Laboratory, California Institute of Technology, for support of a portion of this work under Contract No. NAS7-100 sponsored by the National Aeronautics and Space Administration.

## References

1 Bartera, R. E., Riise, H. N., and Miller, C. G., "Solar Simulators at the Jet Propulsion Laboratory," *Applied Optics*, Vol. 9, No. 5, May 1970, pp. 1068–1074.

2 Harris, T. I., and Wilson, M. N., "Application of Variable Optics to Solar Simulation Systems for Generation of High Intensity Light Beams," AIAA Paper 69-997 presented at the AIAA/ASTM/IES 4th Space Simulation Conference, Los Angeles, Calif., Sept. 8–10, 1969.

3 Bobco, R. P., "Radiation From a Directional Source: Beam Divergence in Solar Simulators," *Journal of Engineering for Power*, TRANS. ASME, Series A, Vol. 87, No. 3, July 1965, pp. 259–269.

4 Malliaris, A. C., "The Formation of Uniform Beams from Long and Thin Radiators," *Applied Optics*, Vol. 9, No. 3, Mar. 1970, pp. 553–560.

5 Brewer, W. D., "Ablative Material Performance in High Radiative Flux Environment Produced by a Carbon Dioxide Laser," AIAA Paper No. 70-864, AIAA 5th Thermophysics Conference, Los Angeles, Calif., June 29–July 1, 1970.

6 Plamondon, J. A., and Horton, T. E., "On the Determination of the View Function to the Images of a Surface in a Nonplanar Specular Reflector," *International Journal of Heat and Mass Transfer*, Vol. 10, 1966, pp. 665–679.

7 Shannon, R. R., "Closing the Loop in Optical System Design," *IEEE Transactions on Aerospace and Electronic Systems*, Vol. AES-5, No. 2, Mar. 1969, pp. 273–278.

8 Feder, D. P., "Differentiation of Ray-Trace Equations with Respect to Construction Parameters of Rotationally Symmetric Optics," *Journal of the Optical Society of America*, Vol. 58, No. 11, Nov. 1968, pp. 1494–1505.

J. S. TOOR[1]
David Ross Fellow.
Student Mem. ASME

R. VISKANTA
Professor.
Mem. ASME

School of Mechanical Engineering,
Purdue University,
Lafayette, Ind.

# Experiment and Analysis of Directional Effects on Radiant Heat Transfer

*Validity of the commonly used simplified models for predicting local and overall radiant heat interchange among real surfaces is critically examined. The spectral local irradiation was measured at wavelengths of 3.08 and 4.51 μ in a configuration consisting of three plane parallel surfaces of finite extent. The test surfaces were gold with mechanical roughness and temperature varying from 0.02 to 7.1 μ and 77 to 760 deg K respectively. Comparisons between experimental data and predictions for six different models ranging from the simple diffuse to the most detailed diffuse-plus-specular-directional-property model with specular component calculated according to Beckmann are presented. It is shown that the calculation of the overall irradiation using appropriate constant-property models agrees well with the experimental data to within combined experimental and analytical uncertainty. In general it is concluded that for accurate prediction of local irradiation the directional characteristics of the surfaces must be considered.*

## Introduction

THE KNOWLEDGE of radiant heat transfer is essential in the design of furnaces, high-temperature chemical equipment, high-temperature energy-conversion devices, long-life storage cryogenic systems, and space vehicles. In some of these applications radiation heat transfer is the major or the only mode of energy transfer. The inability to accurately predict radiant heat transfer in real enclosures has been illustrated by, among other things, overheating of the Mariner II spacecraft [1].[2] Temperatures not only exceeded the upper design tolerances but even the upper measuring range. Future-generation spaceships with tighter thermal tolerances and much longer active lives will demand improved thermal design and control.

In spite of the importance of radiant heat transfer, only a modest amount of combined analytical and experimental work has been reported. Analysis has been limited only to simple surface-property models and enclosures because of the complexity of the problem and the lack of accurate knowledge of radiation properties of surfaces. However, the validity of these simple models has not been substantiated by more realistic analyses or experiments. Experimental studies have been few. The existing data are not conclusive and are in some cases contradictory [2–4], but the findings are based on comparison of measured total heat transfer with gray or semigray analysis. This illustrates how incomplete our understanding is at the present time and indicates a need for additional research effort.

Specifically, this study is undertaken with the purpose of critically examining the validity of the commonly used simplified models for predicting local as well as overall radiation interchange among real surfaces. The directional and spectral effects are examined separately by comparing the experimental data with the predictions based on simple and more detailed models for the radiation characteristics of surfaces. These comparisons are made on a spectral basis. Emphasis is placed on the experiment. The analysis is only summarized and the details can be found elsewhere [5].

## Analysis

The radiation heat exchange in an enclosure (accounting for the spectral, directional, and surface-roughness effects) can be formulated with as few idealizing assumptions as possible using the integral or the Monte Carlo methods. The integral method was found to be impractical even on a fast digital computer (CDC 6500) and was abandoned in favor of the Monte Carlo method, which was found to be superior [5]. Hence the problem is formulated and the calculations are performed using the Monte Carlo method. It is assumed in the analysis that the geometric optics theory is valid for radiant heat transfer and that the surfaces are separated by a nonparticipating medium having an index of refraction of unity. In addition the polarization effects are ignored.

All the radiant-heat-transfer quantities of interest such as the spectral heat flux, spectral-radiation interchange, or spectral irradiation can be readily calculated once the spectral-absorption factors $B_{\lambda di-j}$ are calculated [5]. The factor $B_{\lambda di-j}$ is defined as the fraction of spectral energy emitted from an elementary area $dA_i$ which is absorbed at surface $A_j$ (directly and indirectly after all the possible interreflections in the enclosure). The

[1] Currently with Systems, Science and Software, La Jolla, Calif.
[2] Numbers in brackets designate References at end of paper.

Contributed by the Heat Transfer Division for publication (without presentation) in the JOURNAL OF HEAT TRANSFER. Manuscript received by the Heat Transfer Division August 4, 1971. Paper No. 72-HT-K.

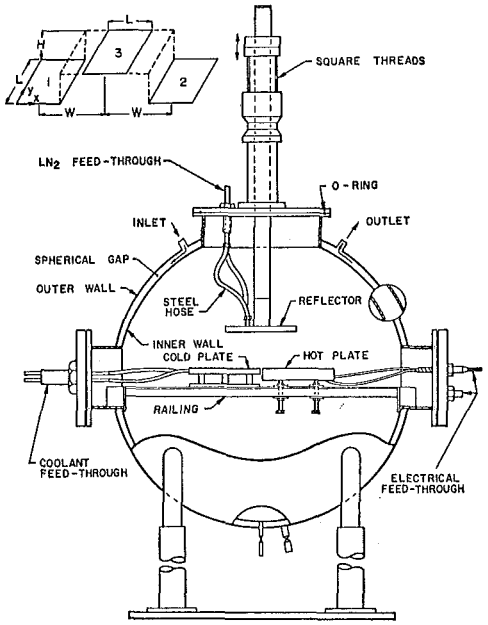


**Fig. 1 Configuration and schematic diagram of test assembly**

spectral energy absorbed at the elementary area $dA_i$ due to emission from all the $N$ isothermal surfaces in the enclosure can be expressed as

$$E_{ai\lambda} = \sum_{j=1}^{N} A_j \epsilon_{j\lambda} B_{\lambda j-di} E_{bj\lambda} \tag{1}$$

and the spectral local radiant heat flux is given by

$$q_{i\lambda} = dQ_{i\lambda}/dA_i = \epsilon_{i\lambda} E_{bi\lambda} - \left[\sum_{j=1}^{N} A_j \epsilon_{j\lambda} E_{bj\lambda} B_{\lambda j-di}\right] \Big/ dA_i \tag{2}$$

It follows from equation (1) that the spectral irradiation at $dA_i$ is

$$G_{i\lambda} = \sum_{j=1}^{N} A_j \epsilon_{j\lambda} E_{bj\lambda} B_{\lambda j-di}/\alpha_{i\lambda} dA_i \tag{3}$$

where $\epsilon_{j\lambda}$ and $\alpha_{i\lambda}$ are the spectral hemispherical emissivity and absorptivity respectively. Using the reciprocity relation $A_j \epsilon_{j\lambda} B_{\lambda j-di} = dA_i \epsilon_{i\lambda} B_{\lambda di-j}$ one can express equation (3) as

$$G_{i\lambda} = \sum_{j=1}^{N} \epsilon_{i\lambda} E_{bj\lambda} B_{\lambda di-j}/\alpha_{i\lambda} \tag{4}$$

Note that equation (4) is not in a convenient form because in general, for surfaces with direction-dependent properties, $\alpha_\lambda \neq \epsilon_\lambda$ and its evaluation demands the knowledge of the incident radiation field. However, this difficulty can be bypassed if the absorption factors $B'_{\lambda di-j}$ are calculated by considering emission from $dA_i$ as diffuse [5]. This amounts to introducing a fictitious surface $dA_i$ having constant properties. With this equation (4) reduces to

$$G_{i\lambda} = \sum_{j=1}^{N} E_{bj\lambda} B'_{\lambda di-j} \tag{5}$$

Note that the introduction of this fictitious surface $dA_i$ does not alter the character of the enclosure because in all the interreflections it is the real surface which participates in the radiation interchange. Equation (3) has been purposely cast in the form of equation (5) because all $B'_{\lambda di-j}$ can be calculated simultaneously, which results in considerable saving in computer time. Also $B_{\lambda di-j} \gg B_{\lambda j-di}$, and it is on this fact that the accuracy of the Monte Carlo method depends. Also, some of the shortcuts can be used more fruitfully for a single point than for an entire area [6]. The details of the simulation of radiant heat transfer by the Monte Carlo method are well known [7, 8] and are omitted for the sake of brevity.

## Experimental Apparatus and Procedure

**General Design.** Previous studies [8, 9] have shown that it is not the overall but the local heat transfer which is more sensitive to the choice of the model for the radiation characteristics. It is therefore desirable that the local heat flux be measured. There are, however, extreme difficulties associated with a measurement of the net local spectral heat flux. Instead, local spectral incident flux was measured.

The configuration chosen for the study consisted of three square plates arranged as shown in the inset of Fig. 1. The choice of the configuration was dictated by previous studies which showed that with finite-extent surfaces it yields a very critical comparison between the predictions of the various models. Some of the other reasons are: (*a*) this configuration has a simple geometrical character and is suitable for experiment and analysis, (*b*) it can be made to represent both open and closed systems by easy change of parameters, (*c*) by a proper choice of the hot and cold surfaces the energy emitted from the hot surface is not directly incident on the radiation detectors located in the cold surface (this is necessary to avoid large energy incident directly from masking the small energy carrying the history of interreflections), and (*d*) this configuration was recommended by Bobco [10] also for experimental study.

For the measurement of the local irradiation due to emission from surfaces only, the extraneous influences had to be eliminated. This was achieved by mounting the test assembly inside a black $LN_2$-cooled spherical chamber shown schematically in Fig. 1. The chamber was evacuated to $1.333 \times 10^{-2}$ N/m$^2$ or lower during the testing. Evacuation of the chamber decreased the

## Nomenclature

$A$ = surface area
$a_m$ = mechanical correlation distance
B = bidirectional
$B_{di-j}$ = absorption factor
$B'_{di-j}$ = absorption factor with diffuse emission from $dA_i$
D = diffuse
CP = constant-property (direction-independent) model
DP = directional-property (emission and absorption according to Fresnel's equations) model
EXP = experimental
$E_b$ = blackbody-emitted flux
$E_a$ = rate of energy absorption
$G$ = irradiation
$L, W, H$ = see Fig. 1
$N$ = number of surfaces in the enclosure
$Q$ = overall (average) heat-transfer rate
$q$ = local heat flux
S = specular
S-1 = specular surface 1
S-B-S = surfaces in positions 1, 2, and 3 respectively
$T$ = temperature
UR = uniform-radiosity diffuse model
$x, y, z$ = coordinates
$\alpha$ = absorptance, absorptivity
$\gamma, \delta$ = $H/L$ and $W/L$ respectively
$\epsilon$ = emittance, emissivity
$\lambda$ = wavelength
$\mu$ = micron
$\xi, \eta$ = dimensionless coordinates $x/L$ and $y/L$ respectively
$\rho$ = reflectance, reflectivity
$\sigma_m$ = mechanical rms roughness

**Subscripts**

$b$ = refers to blackbody
$i, j$ = dummy indices
$\lambda$ = refers to spectral values

**Superscripts**

$s$ = specular component of reflectance
$*$ = dimensionless, i.e., $G^* = G/\epsilon E_b$

convective heat transfer to an insignificant fraction of the total heat transfer. This also helped to obtain uniform temperatures of the surfaces and to eliminate condensation on surface 3, which was cooled by $LN_2$. The entire chamber was insulated on the outside with an aluminum-backed thick blanket of glass wool to reduce heat gain from the environment. Surface 3 could be raised or lowered by a graduated moving mechanism projecting out through the top port.

**Test Assembly.** The cold test surface was attached to a cold copper block which had eight holes for the thermopiles. Eight nuts welded on the back of the test surface were sufficient to hold it against the cold copper block to obtain a good thermal contact so that uniform temperature could be obtained. Surface 1 was cooled by running coolant through the cold block from a Kryomat. The reflector block was also made of copper, with holes drilled parallel to the surface for circulating $LN_2$.

Considerable difficulty was encountered in obtaining a uniform temperature over the 15.24-cm-square hot surface. Finally, bonding of graphite cloth (HITCO-G-1550, Materials Division of HITCO) to the back of the test plate with Sauereisen cement and heating it electrically gave very satisfactory results. Temperatures measured at five locations on the hot surface showed variation of only 1.2 percent. To stiffen this assembly a transite plate was bolted so that the graphite cloth became sandwiched in between the test plate and the transite plate. The ends of the carbon cloth were sandwiched between two copper strips to insure good electrical contact between copper and graphite.

**Instrumentation.** The local spectral-irradiation measurements were made at eight locations on the cold surface 1. Thermopiles with interference filters installed in front of them were the radiation detectors. The emf's produced by the thermopiles were measured with a Vidar digital voltmeter. The thermopiles were installed flush with the cold test surfaces. These were 6 mm in diameter, evacuated, uncompensated, of the end-on-pencil type with KBr windows. It is recognized that the transmittance of KBr is dependent on wavelength, direction, and polarization, but these effects are eliminated to a large extent because of the relative calibration procedure employed for thermopile calibration.

The filters used were of the narrow-band-pass interference type manufactured by the Optical Coating Laboratory of Santa Rosa, Calif. The transmission scans showed that the bandwidths of the 3.08-$\mu$ and 4.51-$\mu$ filters at normal incidence were 0.069 $\mu$ and 0.194 $\mu$ respectively. The two filters were selected because the maxima of the blackbody-radiation curve at the expected operating temperatures were near these wavelengths.

**Test Surfaces and Preparation.** Gold was used as the test-surface material because the previous studies [2, 8, 11] had shown that it was for highly reflecting materials that choice of the model is most critical. It also meets the other requirements, namely: (*a*) easily available, solid and stable at high temperature over extended period of time, (*b*) low vapor pressure at operating temperatures, (*c*) radiation properties are easily predictable [12], and (*d*) unlike silver, gold does not tarnish in air.

Test surfaces were prepared by goldplating the polished or sandblasted stainless-steel sheets. Sandblasting was in a normal direction to get isotropic surfaces. The blasting grit used was 80-mesh angular-shaped hard steel for "diffuse" surfaces and 120-mesh round-shaped glass beads for "bidirectional" surfaces. The surfaces to be prepared as "specular" were polished to a smooth finish and again buffed slightly after goldplating. Thickness of goldplating is estimated to be 5 $\mu$, which is sufficient to insure complete masking of the substrate.

The rms mechanical surface roughness was measured with a Bendix profilometer, Model QB, which included a Model LK tracer. Measurements were made with 2.5-$\mu$- as well as with 12.5-$\mu$-radius stylii but with different profilometers, and the calibration of the instruments was checked before use. The results are reported in Table 1. The roughnesses given are the average of five measurements made over each test surface of 12.7 cm square; the maximum variation from the mean was less than 6 percent. Measurements at the same location from different directions resulted in essentially the same roughness values, indicating that surfaces are isotropic.

The autocorrelation coefficient and roughness height density of test surfaces were calculated from the surface-profile measurements [5]. Over large distances the autocorrelation function is close to the normal [5], the one assumed by Beckmann [13] in deriving the reflection distribution function. However, for very large distances it oscillates in a random fashion with a decreasing amplitude about zero while the assumed coefficient approaches zero monotonically. The measured roughness height density also showed departure from the Gaussian distribution [5].

After the test surfaces were used in the experiment they were checked for any impurities or defects on the surface. X-ray microprobe analysis with a scanning electron microscope (Model JSM-2) showed that various pieces cut from the test surfaces contained only the gold. To visualize the structure of the surface topography, micrographs of surfaces with different magnifications (up to 10,000 $\times$) were taken with a scanning electron microscope. The surface profile was also traced on these very micrographs which are shown in Fig. 2. For comparison purposes a 1-$\mu$-dia particle (approximately) is illustrated in Fig. 2-A and shows the smoothness of the specular surface. The grain structure is absent. This is due to slight buffing of the surface after electroplating. Comparison of surface profile by scanning electron microscope and that traced by profilometer has revealed small details in the former which are absent in the latter [5]. Hence, the values of $\sigma_m$ and $a_m$ calculated from the two profiles are not expected to be the same. Also, the grain structure in the figure clearly shows that the surface is not smooth locally but has a secondary roughness.

**Experimental Procedure.** The first step in the experimental procedure was to calibrate the thermopiles. Either the relative or the absolute method was possible, but the former was preferred. In this method the effects of thermopile mounting, KBr window, extraneous radiation, and other sources of error are reduced but not completely eliminated. Also, the calibration of the thermopiles on an absolute basis would not have been meaningful since it was impossible to simulate the conditions under which they were to be used.

The thermopiles were calibrated in position by using surfaces of known properties so that irradiation could be accurately calculated. The surfaces chosen were 3M Black Velvet paint for the cold surface and Pyromark paint for the hot surface. Surface 3 was a very smooth goldplated surface cooled by $LN_2$ so that it could be considered a nonemitting specular reflector. The Pyromark paint was chosen since it is known to be a gray diffuse emitter [14], a good absorber, and can withstand high tempera-

**Table 1 Description of surfaces and the measured roughness**

| Designation of surfaces | Roughness $\sigma_m$ in $\mu$ stylus radius 2.5 $\mu$ | 12.5 $\mu$ | Correlation distance $a_m$ in $\mu$ | Method of preparation Goldplated after being: |
|---|---|---|---|---|
| *S*-1 | 0.02 | — | — | polished |
| *S*-2 | 0.03 | — | — | polished |
| *S*-3 | 0.02 | — | — | polished |
| *B*-2 | 1.50 | 0.90 | 40.0 | blasted with glass beads |
| *B*-3 | 0.75 | 0.50 | 14.0 | blasted with glass beads |
| *D*-3 | 7.10 | 5.50 | 25.0 | blasted with steel grit |

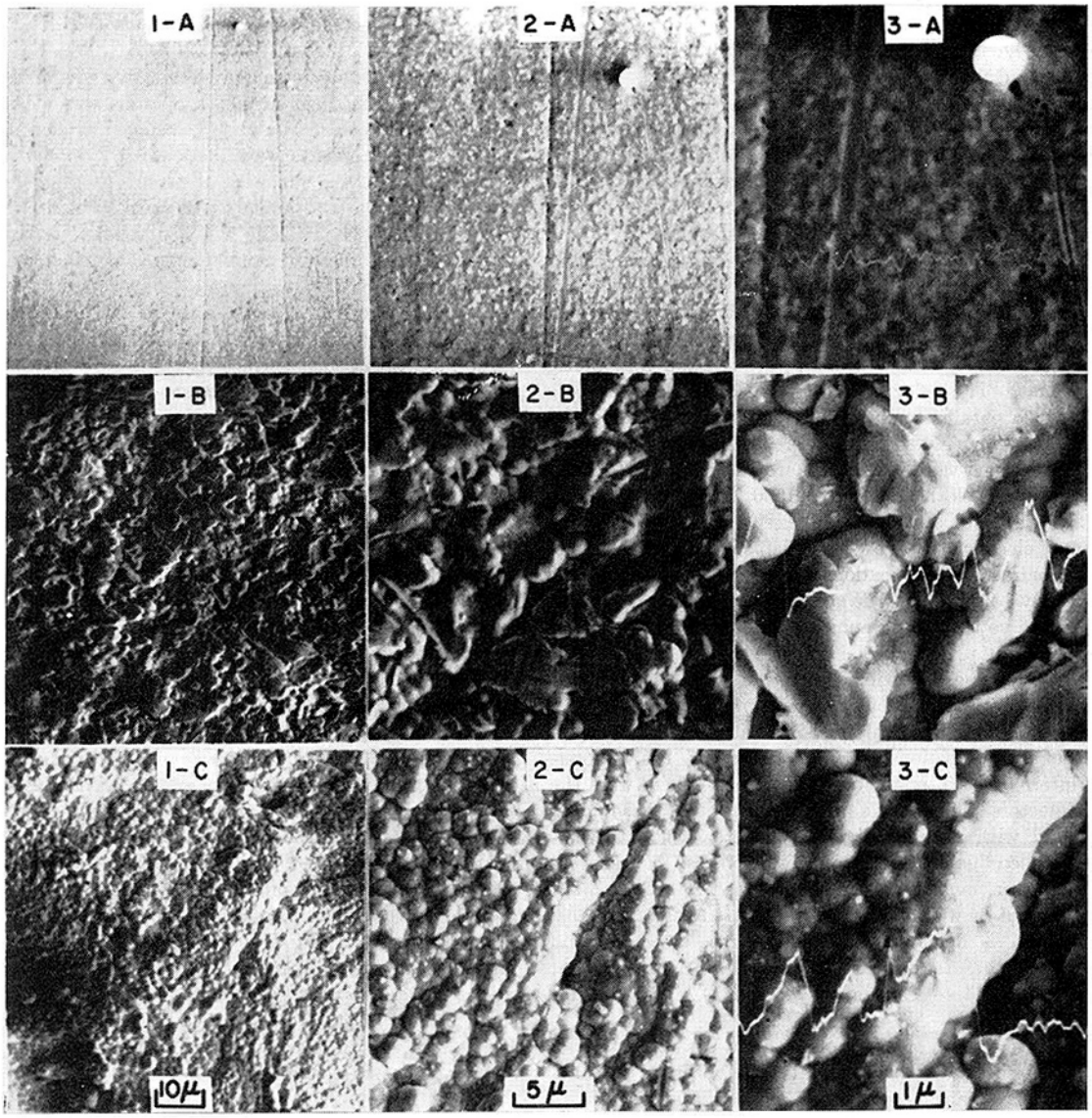


**Fig. 2 Micrographs and roughness profiles of test surfaces S-2, B-3, and D-3 by scanning electron microscope**

tures, while 3M Black Velvet paint is diffuse, gray, and a very good absorber [15, 16]. Even if the painted surfaces were not perfectly diffuse reflectors, the error introduced was small since little energy was reflected because of the high absorptivities of the paints.

A step-by-step procedure for calibration and for taking the experimental data is described elsewhere [5]. It suffices to note that all the electrical connections inside and outside the chamber were properly shielded to avoid the influence of stray electromagnetic waves on the measurements. Also, care was taken to use the same filters and thermopiles in the same locations and orientations as during calibration.

## Radiation Characteristics of Surfaces

An analysis of radiation interchange among surfaces requires an acceptable description of the emittance, absorptance, and bidirectional reflectance of the participating surfaces. In the present application, where an attempt is made to evaluate the importance of real surface effects, considerable detail is required in specifying the radiation properties. Hence, for a meaningful comparison of the experimental data and the predictions, the dependence of radiation characteristics on direction, wavelength, temperature, and surface roughness should be accounted for accurately in the analysis. However, the intent here is to adopt simple models that predict the radiant heat exchange realistically, rather than to calculate the radiant exchange from more complicated models. It has been mentioned that use of the incoherent part of the reflection distribution function is too complicated for engineering calculations [8, 17], and such a detailed analysis is not justified in view of the fact that radiation characteristics of surfaces in general are not known accurately. In the calculations the following models are considered:

**Constant-Property (Direction-independent) Models:**

1 Diffuse emission and reflection, D.
2 Diffuse emission and specular reflection, S.
3 Diffuse emission and diffuse + specular reflection, D + S.

**Directional-Property (Direction-dependent) Models:**

4 Directional emission and specular reflection, DP(S).
5 Directional emission and absorption, and direction-independent diffuse + specular reflection, DP(D + S).
6 Directional emission and absorption, and direction-dependent diffuse + specular reflection, B(D + S).

The diffuse, specular and diffuse + specular constant-property models are the ones commonly used in engineering calculations [18]. The specular component of the D + S model is calculated in [5] and accounts for the wavelength, surface roughness, and geometry. The direction-independent specular component of

reflectance for model DP(D + S) is again calculated in a similar way. For the B(D + S) model the specular component of reflectance corresponds to the coherent component of the Beckmann reflection distribution function and is dependent on the wavelength, surface roughness, and direction of incidence [13]. According to this model the specular part of reflectance is given by

$$\rho^s(\theta', \sigma/\lambda) \simeq \rho(\theta', \lambda) \exp\{-[4\pi(\sigma/\lambda)\cos\theta']^2\} \quad (6)$$

where $\rho(\theta', \lambda)$ is the directional reflectivity of the smooth material with finite conductivity. This is necessary because the Beckmann reflection distribution function was derived for perfectly reflecting material. Correcting for finite conductivity this way does not introduce any appreciable error and is justified on the basis of experimental evidence [19]. However, this approximation violates Helmholtz's reciprocity condition in the incoherent component. Use of equation (6) is partly justified by the difficulty in accounting for the finite conductivity rigorously in the theory [19].

The directional and spectral dependences of radiation surface properties are predicted for an ideal engineering surface from Fresnel's equations. The optical constants are calculated from Drude's relation, corresponding to the electrical resistivity at that temperature and frequency. Recently Bennett et al. [12] have demonstrated that the simple Drude's theory is in excellent agreement with measurements and predicts the optical constants in the infrared for ultra-high-vacuum-deposited gold. Since the emittance of pure metals is smaller [20, 21] than that deposited commercially, due to contamination and surface damage, the values calculated from Fresnel's equations using optical indices predicted by Drude's theory were proportioned to yield the selected experimental total hemispherical emittance. The available experimental data, including that compiled by the Thermophysical Property Research Center at Purdue University [22], were carefully examined and those values were selected which corresponded to samples prepared in a manner similar to that used in this study.

## Results and Discussion

Radiation heat exchange among surfaces depends on the geometry of the system, on the radiation characteristics of the surfaces, i.e., material used and its surface topography, and on the boundary conditions prescribed. There is, of course, an infinite number of combinations of the various independent parameters, and so it is necessary to be selective. The choice of geometry and surface materials has been discussed before. The separation distances between the surfaces were mainly governed by the space in the chamber and the energy requirement of the thermopiles. The lower temperature level of hot surface was also governed by the latter while the high temperature level was dictated by the materials and the cooling-capacity limitation of the chamber. Surface 1 was maintained at about room temperature. This was necessary for good performance of the thermopiles. Surface 3 was cooled by $LN_2$ (77 deg K). Since the absorption of gold at this temperature is very low in the infrared, it served as an adiabatic surface. It has been shown [11] that in the presence of an adiabatic surface in an enclosure a large discrepancy occurs between experiment and analysis.

All the data presented are in terms of spectral irradiation at the cold surface. They have been nondimensionalized with respect to the spectral emissive power of the cold surface, i.e., $G^*_{1\lambda} = G_{1\lambda}/\epsilon_{1\lambda}E_{1b\lambda}$. In the presentation of the data the subscript 1 has been dropped for convenience. The overall (average) irradiation results presented in Table 2 were obtained from the local values.

Before presenting the results it is appropriate to reexamine equation (5) by rewriting it in dimensionless form

$$G^*_{1\lambda} = [B'_{\lambda d1-1} + B'_{\lambda d1-2}(E_{2b\lambda}/E_{1b\lambda}) + B'_{\lambda d1-3}(E_{3b\lambda}/E_{1b\lambda})]/\epsilon_{1\lambda} \quad (7)$$

It is clear from equation (7) that the spectral irradiation depends on the absorption factors and the spectral blackbody-emitted flux. When $B'_{\lambda di-j}$ are of the same order of magnitude, the main contribution to $G^*_{1\lambda}$ is from $B'_{\lambda d1-2}$ when $E_{2b\lambda}/E_{1b\lambda}$ is large. In the present study $E_{3b\lambda}/E_{1b\lambda}$ is very small as compared to $E_{2b\lambda}/E_{1b\lambda}$ both for $\lambda = 3.08$ and 4.51 $\mu$. In such a case $B'_{\lambda d1-3}$ makes little contribution to $G^*_{1\lambda}$ and hence can be ignored. Consequently, in the calculations surface 3 was assumed nonemitting.

**Measured and Predicted Spectral Local Irradiation.** In Figs. 3 and 4 the analytical predictions for the constant-property diffuse, specular, and directional-property specular DP(S) models of spectral irradiation at $\lambda = 3.08$ $\mu$ are compared with the experimental data (circles) when all the surfaces are "specular" ($\sigma_m/\lambda < 0.01$). Examination of the figures reveals that the experimental data are in best agreement with the predictions of the DP(S) analysis; however, at some points (Fig. 3) these predictions are about 40 percent lower than the data. The results based on diffuse analysis (Fig. 3) are about 80 percent lower than the experimental data. At both temperature levels, for Figs. 3 and 4 the predictions of the D analysis are always lower than those of the constant-property S analysis. Since the local heat flux at the cold surface is given by

$$q^*_{1\lambda} = 1 - \epsilon_{1\lambda}G^*_{1\lambda} \quad (8)$$

this means that the diffuse analysis would predict too high a heat flux. The lower irradiation shows that more of the energy

**Table 2 Overall measured irradiation and fractional departure from experiment for various analyses on spectral basis, $\lambda = 3.08$ $\mu$**

| Surfaces 1-2-3 | $\gamma$ | $T_1$, deg K | $T_2$, deg K | $G^*_{EXP}$ | (Analysis–Experiment)/Experiment UR | S | D | DP(S) | B(D + S) |
|---|---|---|---|---|---|---|---|---|---|
| S-S-S | 1/6 | 284.8 | 594.1 | 2309 | −0.21 | −0.03 | −0.21 | 0.09 | |
| | | 284.3 | 752.9 | 9152 | 0.20 | 0.45 | 0.18 | 0.04 | |
| | 1/2 | 284.1 | 586.5 | 1003 | −0.38 | −0.07 | 0.73 | −0.01 | |
| | | 283.6 | 758.5 | 4323 | 0.00 | 0.51 | −0.14 | 0.01 | |
| S-S-D | 1/6 | 283.4 | 588.0 | 1573 | 0.16 | 0.05 | 0.15 | 0.20 | |
| | | 283.8 | 750.2 | 7002 | 0.58 | 0.42 | 0.56 | 0.03 | |
| | 1/2 | 283.5 | 590.1 | 586 | 0.15 | −0.02 | −0.01 | 0.03 | |
| | | 283.1 | 754.9 | 2258 | 0.92 | 0.63 | 0.65 | 0.06 | |
| S-S-B | 1/6 | 283.7 | 593.4 | 1792 | 0.08 | 0.33 | 0.12 | | −0.02 |
| | | 283.7 | 760.9 | 8662 | 0.40 | 0.71 | 0.45 | | −0.14 |
| | 1/2 | 283.7 | 759.5 | 3403 | 0.15 | 0.97 | 0.07 | | −0.04 |
| S-B-S | 1/6 | 284.0 | 596.6 | 1892 | 0.04 | 0.29 | 0.09 | | 0.15 |
| | | 284.8 | 758.6 | 6753 | 0.66 | 1.03 | 0.71 | | 0.13 |
| | 1/2 | 283.9 | 594.1 | 997 | −0.30 | 0.08 | −0.41 | | −0.07 |
| | | 284.7 | 755.5 | 3881 | 0.02 | 0.58 | −0.14 | | −0.16 |
| S-B-B | 1/6 | 283.6 | 596.0 | 1952 | 0.03 | 0.27 | 0.07 | | 0.10 |
| | | 284.4 | 768.5 | 10087 | 0.22 | 0.50 | 0.27 | | −0.17 |
| | 1/2 | 283.9 | 592.8 | 583 | 0.17 | 0.82 | −0.01 | | 0.25 |
| | | 284.4 | 758.5 | 2804 | 0.47 | 1.28 | 0.24 | | −0.16 |

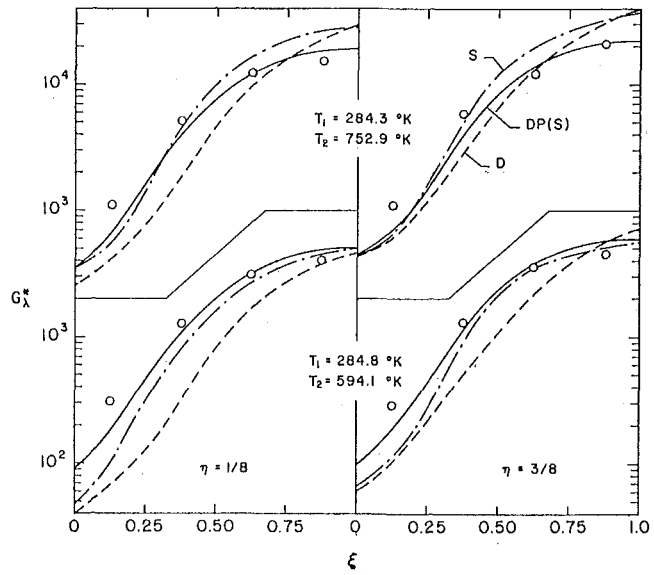


**Fig. 3 Comparison between measured and predicted irradiation for different models; surface arrangement S-S-S, $\lambda = 3.08\ \mu$, $\delta = 1$, $\gamma = 1/6$**

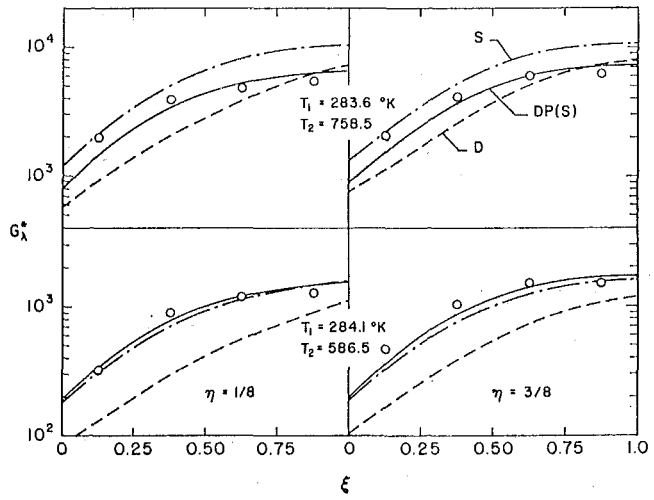


**Fig. 4 Comparison between measured and predicted irradiation for different models; surface arrangement S-S-S, $\lambda = 3.08\ \mu$, $\delta = 1$, $\gamma = 1/2$**

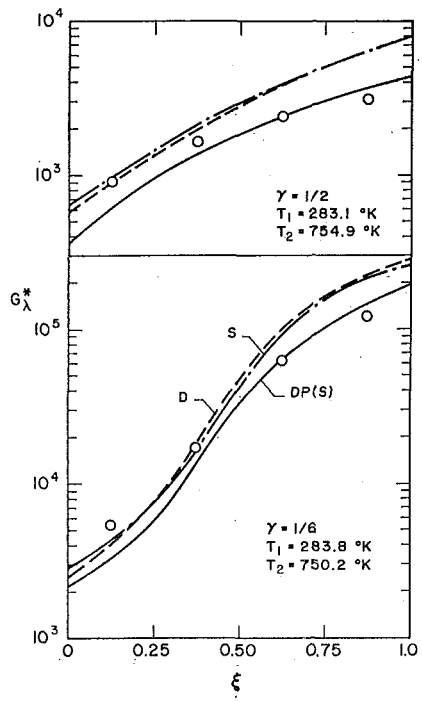


**Fig. 5 Comparison between measured and predicted irradiation for different models; surface arrangement S-S-D, $\lambda = 3.08\ \mu$, $\delta = 1$, $\eta = 1/8$**

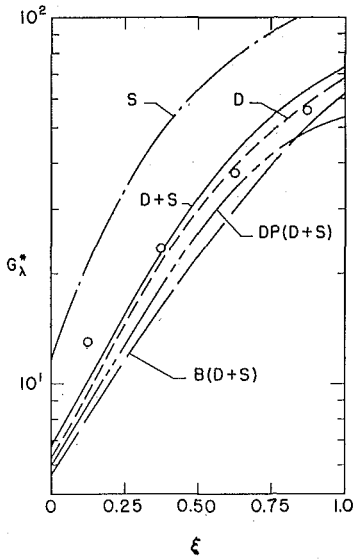


**Fig. 6 Comparison between measured and predicted irradiation for different models; surface arrangement S-S-B, $\lambda = 4.51\ \mu$, $T_1 = 283.7$ deg K, $T_2 = 588.6$ deg K, $\delta = 1$, $\gamma = 1/2$, $\eta = 1/8$**

leaves the enclosure for the diffuse than for the specular reflection model. This is typical of enclosures which exchange a large portion of their energy in near-normal directions. As an example, for two parallel plates with a large separation distance, the irradiation based on the specular model is always higher [2, 8, 17] than that based on the diffuse model. This seems plausible due to the fact that at each reflection from a diffuse surface the energy is uniformly distributed. On the contrary, when more of the energy exchange occurs in directions other than the normal (adjoint-plate system) the diffuse analysis would predict higher irradiation [2, 6].

The largest discrepancy between the various analyses and the experiments in Fig. 3 occurs on the open end of the closed configuration ($\gamma = 1/6$). The temperature level appears to have little effect on the trends of the CP results. This is due to the fact that for both cases $T_2/T_1$ is sufficiently high so that $G^*_\lambda$ is controlled by $B_{\lambda d1-2}$. With the rise in temperature, the DP(S) analysis tends to fall in between the S and D analyses. The trends in Fig. 4 ($\gamma = 1/2$) are the same as in Fig. 3. The DP analysis is in closest agreement with experimental data. For a more open configuration the irradiation is more uniform. The change in temperature level does not seem to have an appreciable effect on the trends of the results except to increase the irradiation and reduce $G^*_\lambda$ based on the DP(S) model below that of the S model. This is due to the fact that most of the energy emitted at oblique angles leaves the system without being absorbed. Mostly, the energy emitted in the near-normal directions contributes to irradiation, and the emission in the normal direction for metals is always higher for the CP model than for the DP model

When surface 3 is replaced by a "diffuse" surface ($\sigma_m = 7.1\ \mu$), Fig. 5, the differences between the predictions (in all calculations surface 3 is assumed diffuse) of the three models in general decrease, and the experimental results agree best (within 40 percent) with the DP(S) analysis. Over a large part of the surface the predictions of the S and D models are almost identical. However, at some locations the CP analyses yield values which are twice the measured results. The largest difference occurs at high temperatures and for the more open system ($\gamma = 1/2$). It is recognized, however, that the diffuse limit does not

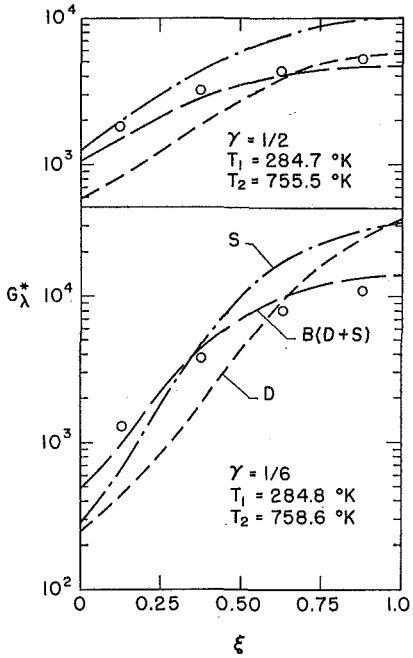


**Fig. 7 Comparison between measured and predicted irradiation for different models; surface arrangement S-B-S, $\lambda = 3.08\ \mu$, $\delta = 1$, $\eta = 1/8$**

exist. A part of the disagreement between analysis and experiments can be attributed to this reason.

With surfaces 1 and 2 (specular) and surface 3 (bidirectional) ($\sigma_m/\lambda \simeq 0.17$), the results for $\lambda = 4.51\ \mu$ are presented in Fig. 6. While the trends for the S and D models are the same as already discussed, the B(D + S) model predicts a lower irradiation than is indicated by the experimental data. The experimental results are in closer agreement with predictions based on the diffuse rather than the specular constant-property models. This seems to be due to the small specular component of reflectance ($\simeq 0.1$). The agreement of the DP(D + S) analysis with the experiment, equally good as or better than that of the B(D + S) analysis, can also be due to the small specular component of reflectance.

In agreement with the conclusions of the previous studies [2, 11], the constant-property specular model usually predicts higher irradiation, at some locations more than 3 times the values from the DP predictions. For $\gamma = 1/2$ (Fig. 6), predictions of the S analysis more than 100 percent higher than in the experiments is quite common. Consistently, the experimental data are much higher than the B(D + S) analysis on the open end of the system. This may be due to the limitation in the model itself. Actually, the incoherently reflected energy is peaked in the specular direction, but this energy has been assumed to be reflected diffusely in the B(D + S) model. The direction of energy flow is from surface 2 to surface 1 via surface 3. Thus the B(D + S) model would predict that less energy is reflected toward the open end of surface 1 than is actually reflected. Hence the irradiation predicted from this model will be lower than the experimental data.

The results when surfaces 1 and 3 are specular and surface 2 is bidirectional ($\sigma_m/\lambda \simeq 0.5$) are presented in Fig. 7. The agreement between the predictions based on the B(D + S) model and the experimental data is much better than in the previous cases already discussed. In the worst example the DP analysis is about 30 percent lower and the S analysis is 150 percent higher than the data. Note that for $\gamma = 1/6$ the experimental data are more than four times the predictions based on diffuse analysis.

The experimental results for a system consisting of specular surface 1 and bidirectional surfaces 2 and 3 are not presented here, since they do not add anything new, but are available elsewhere [5].

**Measured and Predicted Overall (Average) Irradiation.** For the sake of brevity, the results presented are only for $\lambda = 3.08\ \mu$ (Table 2), but the conclusions are supported also by the results for $\lambda = 4.5\ \mu$ [5]. All constant-property analyses (UR, D, S, D + S) are in better agreement with the measurements on overall than on local basis. The S analysis always overpredicts the irradiation, but for a specular enclosure it is within 50 percent of the data. However, with bidirectional surfaces in the enclosure, the S analysis for some arrangements predicts $G^*_\lambda$ too high by as much as 130 percent. In general, agreement of the D analysis with the measurements is better than that for the S analysis. In the worst, the D analysis is only 70 percent higher than the experiments. Surprisingly, the UR analysis yields equally as good agreement with the experiments as the D analysis.

In contrast to the S analysis, the DP(S) analysis with bidirectional surfaces usually underpredicts the irradiation. Although the overall agreement of the DP analysis with the experiments is significantly better than that of the CP analysis, the appropriate constant-property models predict the irradiation reasonably well in view of the fact that radiation characteristics of surfaces are not known to a great accuracy. The calculations given elsewhere [5] show that the more detailed B(D + S) model does not have any advantage over the DP(D + S) model.

## Conclusions

As a result of this study on radiant heat exchange between surfaces, the following conclusions may be drawn for predicting the spectral local irradiation:

1 In general the best agreement between predictions and data is for DP analysis with direction-dependent specular component of reflectance; however, the agreement is also good with direction-independent specular component.

2 The constant-property diffuse and specular models do not yield the upper and lower bounds, and both can fail badly. The constant-property specular analysis, in general, predicts higher irradiation than the diffuse analysis.

3 The greatest discrepancy between the data and the analysis occurs at locations which are irradiated at oblique angles.

4 A diffuse surface in the enclosure appears to destroy the effect of specularity of the other surfaces.

For the evaluation of the overall (average) irradiation on a spectral basis the following conclusions may be drawn:

1 The directional-property models, in general, show better agreement with the experiments than the constant-property models. However, the appropriate constant-property models as well as the zonal-uniform-radiosity-type (UR) analyses also predict the irradiation reasonably well.

2 Use of the more detailed B(D + S) model with direction-dependent specular component of the reflectance does not provide any advantage over the DP(D + S) model which considers direction-independent specular component of reflectance.

The above conclusions were based on the results obtained for a particular system, material, and temperature levels. The configuration considered may not be representative of other types of enclosures. Therefore, care should be exercised in extending the results and conclusions to situations very much different from those studied here.

## Acknowledgments

This research was sponsored, in part, by the Manned Spacecraft Center, National Aeronautics and Space Administration, under Contract No. NAS 9-8118, and was technically monitored by Mr. R. E. Durkee. Purdue Research Foundation provided financial support to J. S. Toor in the form of a David Ross Fellowship and made available additional computer funds. The authors wish to acknowledge many helpful discussions with Prof. E. R. F. Winter during the initial phases of the work. Special appreciation is expressed to Prof. R. J. Schoenhals for his valuable comments.

## References


1 Heller, G. B., "Preface," in: *Progress in Aeronautics and Astronautics*, Vol. 18, Academic Press, New York, N. Y., 1966, pp. xi–xv.

2 Schornhorst, J. R., and Viskanta, R., "An Experimental Examination of the Validity of the Commonly Used Methods of Radiant Heat Transfer Analysis," JOURNAL OF HEAT TRANSFER, TRANS. ASME, Series C, Vol. 90, No. 4, Nov. 1968, pp. 429–436.

3 Howell, J. R., and Durkee, R. E., "Radiative Transfer Between Surfaces in a Cavity With Collimated Incident Radiation: A Comparison of Analysis and Experiment," JOURNAL OF HEAT TRANSFER, TRANS. ASME, Series C, Vol. 93, No. 2, May 1971, pp. 129–135.

4 Toor, J. S., Viskanta, R., and Winter, E. R. F., "Radiant Heat Transfer between Simply Arranged Surfaces with Direction Dependent Properties," AIAA Paper No. 69-624.

5 Toor, J. S., "An Experimental and Analytical Study of Spectral and Directional Effects on Radiant Heat Transfer," PhD thesis, Purdue University, Lafayette, Ind., 1971.

6 Toor, J. S., "Radiant Heat Transfer Analysis among Surfaces Having Direction Dependent Properties by the Monte Carlo Method," MSME thesis, Purdue University, Lafayette, Ind., 1967.

7 Howell, J. R., "Application of Monte Carlo to Heat Transfer Problems," in: *Advances in Heat Transfer*, T. J. Irvine and J. P. Hartnett, eds., Vol. 5, Academic Press, New York, N. Y., 1968, pp. 1–54.

8 Toor, J. S., and Viskanta, R., "A Numerical Experiment on Radiant Heat Interchange by the Monte Carlo Method," *International Journal of Heat and Mass Transfer*, Vol. 11, 1968, pp. 883–897.

9 Toor, J. S., and Viskanta, R., "Effect of Direction Dependent Properties on Radiation Interchange," *Journal of Spacecraft and Rockets*, Vol. 5, 1968, pp. 742–743.

10 Bobco, R. P., "Analytical Determination of Radiation Interchange Factors," Hughes Aircraft Co., Space Systems Div., SSD 90190R, 1968.

11 Engstrom, P. M., Viskanta, R., and Toor, J. S., "Study of Radiation Interchange in an Enclosure Consisting of Plane Isothermal and Adiabatic Surfaces," *Wärme- und Stoffübertragung*, Vol. 3, 1970, pp. 63–69.

12 Bennett, H. E., and Bennett, J. M., "Validity of the Drude Theory," in: *Optical Properties and Electronic Structure of Metals and Alloys*, F. Abeles, ed., John Wiley & Sons, New York, N. Y., 1966, pp. 173–188.

13 Beckmann, P., and Spizzichino, A., *The Scattering of Electromagnetic Waves from Rough Surfaces*, Macmillan, New York, N. Y., 1963.

14 Wade, W. R., and Slemp, W. S., "Measurements of Total Emittance of Several Refractory Oxides, Cements, and Ceramics for Temperatures from 600°F to 2000°F," NASA TN D-998, 1961.

15 Stierwalt, D. L., "Infrared Spectral Emittance Measurements of Optical Materials," *Applied Optics*, Vol. 5, 1966, pp. 1911.

16 Optical Product Bulletin 28-2, Reflective Products Div., 3M Co., Litho, 1968.

17 Schornhorst, J. R., and Viskanta, R., "Effect of Direction and Wavelength Dependent Surface Properties on Radiant Heat Transfer," *AIAA Journal*, Vol. 6, 1968, pp. 1450–1455.

18 Sparrow, E. M., and Cess, R. D., *Radiation Heat Transfer*, Brooks/Cole Publishing Co., Belmont, Calif., 1969.

19 Houchens, A. F., and Hering, R. G., "Bidirectional Reflectance of Rough Metal Surfaces," in: *Progress in Aeronautics and Astronautics*, Vol. 20, Academic Press, New York, N. Y., 1967, pp. 65–90.

20 Khrustalev, B. A., "Radiative Properties of Solids," *Heat Transfer—Soviet Research*, Vol. 2, No. 5, 1970, pp. 149–170.

21 Bennett, H. E., discussion of "Theoretical and Experimental Studies of the Total Emittance of Metals," by Parker, W. J., and Abbott, G. L., in: *Symposium on Thermal Radiation of Solids*, S. Katzoff, ed., NASA SP-55, 1965, pp. 11–28.

22 Touloukian, Y. S., and DeWitt, D. P., "Thermal Radiation Properties—Metallic Elements and Alloys," *Thermophysical Properties of Matter*, Vol. 7, Plenum, New York, N. Y. 1970.

C. H. FORSBERG
Graduate Student.

G. A. DOMOTO
Assistant Professor.
Assoc. Mem. ASME

Department of Mechanical Engineering,
Columbia University,
New York, N. Y.

# Thermal-Radiation Properties of Thin Metallic Films on Dielectrics[1]

*The spectral radiation properties of thin metallic films are obtained through the numerical solution of the governing integrodifferential equation for the anomalous skin effect with size effects included. The theory predicts that at low temperatures there will be a film thickness for which the emittance is a minimum. This minimum, which is lower than the emittance for a bulk specimen, is apparently due to interference effects arising from the finite film thickness. It is also found that for certain cases transmission through a film is not negligible compared with the emission from the film. The analysis is extended to include metal-coated dielectric films, and the theoretical results are compared with existing experimental data.*

## Introduction

Accurate knowledge of the thermal-radiation properties of metal surfaces at cryogenic temperatures has become increasingly important in the design of thermal-isolation systems and spacecraft thermal-control surfaces. Of particular interest are the radiation properties of thin metallic films and metal-coated dielectric films which have found extensive use in multilayer insulations [1].[2]

Thermal-radiation properties of thin metallic films were first calculated by means of the Drude single-electron (DSE) theory of optical properties [2, 3]. This theory strictly applies to unbounded media. However, if it is assumed that the introduction of finite boundaries does not alter the Drude-theory results, then radiation properties of a thin film may be calculated from the following formulae [4]:

$$R = \left| \frac{(1 - \tilde{n})(\tilde{n} + 1)e^{i\Delta} + (1 + \tilde{n})(\tilde{n} - 1)e^{-i\Delta}}{(1 + \tilde{n})^2 e^{i\Delta} - (1 - \tilde{n})^2 e^{-i\Delta}} \right|^2 \quad (1)$$

$$T = \left| \frac{4\tilde{n}}{(1 + \tilde{n})^2 e^{i\Delta} - (1 - \tilde{n})^2 e^{-i\Delta}} \right|^2 \quad (2)$$

$$A = 1 - R - T \quad (3)$$

The above expressions were derived for the case of a single thin film, bounded by vacua, with radiation impinging normally.

DSE theory implicitly assumes that the current density at a point within the metal depends only upon the electric field at that point and not upon the spatial variation of the field. At sufficiently high temperatures Drude theory is valid. For metals at cryogenic temperatures and moderate frequencies, however, the spatial variation of the electric field must be taken into account. This is known as the anomalous skin effect (ASE). A comprehensive comparison of the Drude and anomalous-skin-effect theories—including a discussion of their respective temperature and frequency ranges of applicability—is given by Domoto et al. [5].

A second effect, the size effect, must be considered when the electron mean free path is comparable to or greater than the film thickness.

The theory of the anomalous skin effect for a semi-infinite medium was first formulated by Reuter and Sondheimer [6]. Dingle [7, 8] generalized the ASE theory to include internal photoelectric current, atomic polarization, and magnetic permeability. He also obtained series solutions for the surface impedance of the metal and extended the theory to include films of finite thickness.

The interaction of electrons with the film boundaries is described by a parameter $p$ which was introduced in Fuchs' treatment of d-c conductivity [9]. A fraction $p$ of the electrons arriving at a surface are scattered specularly, while the rest are scattered diffusely.

Equations (1), (2), and (3) were derived for the classical case in which the electric field decays exponentially with depth. ASE theory predicts an electric field which is not, in general, of exponential form, and the classical concept of the complex refractive index has no physical meaning. However, the radiation properties are expressible in terms of the surface impedance $Z$. If the complex index of refraction is redefined as

$$\tilde{n} = n - ik = \frac{4\pi}{cZ} \quad (4)$$

[1] This work was supported in part by the Heat and Mass Flow Analyzer Laboratory of Columbia University and NSF grant GK-4900.

[2] Numbers in brackets designate References at end of paper.

Contributed by the Heat Transfer Division for presentation at the Winter Annual Meeting, New York, N. Y., November 26–30, 1972, of The American Society of Mechanical Engineers. Manuscript received by the Heat Transfer Division May 25, 1971. Paper No. 72-WA/HT-7.

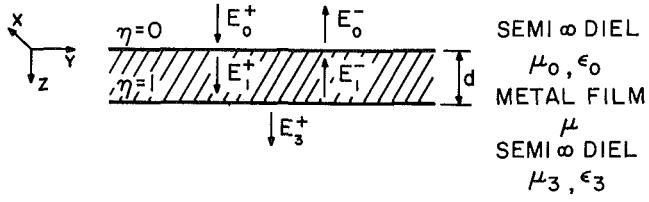


**Fig. 1 Configuration of the single metallic film system**

then the radiation properties for a general electric field satisfying continuity requirements at the boundaries are given by

$$R = 1 - \frac{4n}{(n+1)^2 + k^2} \tag{5}$$

$$T = \frac{4}{(n+1)^2 + k^2} \left|\frac{E(d)}{E(0)}\right|^2 \tag{6}$$

$$A = 1 - R - T \tag{7}$$

where $E(d)$ is the complex electric field at the back surface of the film and $E(0)$ is that at the front surface.

The above discussion has been kept necessarily brief. A recent survey by Tien and Cravalho [10] should be consulted for further details and additional literature references.

## Analysis

**Finite-Difference Numerical Technique: Single Metallic Film.** For the case of normal incidence and diffuse electron scattering at the surfaces, the electric field in a metal, as given by ASE theory including size effect, obeys the following integrodifferential equation:

$$\frac{d^2E(\eta)}{d\eta^2} + \frac{P\mu\omega^2 d^2}{c^2} E(\eta) = i\alpha \left(\frac{d}{l}\right)^3 \int_0^1 E(\xi) \left[E_1\left(w\,\frac{d}{l}\,|\eta - \xi|\right) - E_3\left(w\,\frac{d}{l}\,|\eta - \xi|\right)\right] d\xi \tag{8}$$

$$\alpha = 8\left(\frac{\pi e m v}{c}\right)^2 \frac{\mu\omega l^3}{h^3} = \frac{3}{2}\,\frac{l^2}{\delta^2} \tag{9}$$

$$w = 1 + i\omega\tau \tag{10}$$

$$P = 1 + \frac{4\pi P_{ph}}{E} + \frac{4\pi P_c}{E} \tag{11}$$

Gaussian units are used throughout. Factor $P$ contains the core polarization and the internal photoelectric current. The former may be estimated from the tables in Mott and Jones [3] and Van Vleck [11]. Since the frequencies of interest are below the threshold frequency for photoelectric phenomena in metals, $P_{ph} = 0$.

Equation (8) was obtained from equation (3.1) of [8] by changing the independent variable and using the definition of the exponential integral.

Consider Fig. 1. The boundary conditions for the single thin film were derived by means of the resultant-wave method [4] and are as follows:

$$E_0^+ + E_0^- = E_1^+(0) + E_1^-(0) \tag{12}$$

$$\sqrt{\frac{\epsilon_0}{\mu_0}}\,(E_0^+ - E_0^-) = \frac{ic}{\mu\omega d}\left[\frac{dE_1^+}{d\eta}(0) + \frac{dE_1^-}{d\eta}(0)\right] \tag{13}$$

$$E_1^+(1) + E_1^-(1) = E_3^+ \tag{14}$$

$$\sqrt{\frac{\epsilon_3}{\mu_3}}\,E_3^+ = \frac{ic}{\mu\omega d}\left[\frac{dE_1^+}{d\eta}(1) + \frac{dE_1^-}{d\eta}(1)\right] \tag{15}$$

Elimination of $E_0^-$ and $E_3^+$ leads to the final form of the boundary conditions

$$1 - F(0) = \frac{ic}{\mu\omega d}\sqrt{\frac{\mu_0}{\epsilon_0}}\,\frac{dF}{d\eta}(0) \tag{16}$$

$$F(1) = \frac{ic}{\mu\omega d}\sqrt{\frac{\mu_3}{\epsilon_3}}\,\frac{dF}{d\eta}(1) \tag{17}$$

where

$$F(\eta) = \frac{E_1^+(\eta) + E_1^-(\eta)}{2E_0^+} \tag{18}$$

It is seen that through its definition $F(\eta)$ obeys equation (8).

In terms of the normalized field $F(\eta)$ the normal reflectance and transmittance of the film are

## Nomenclature

$A$ = spectral normal absorptance
$A_d$ = spectral normal absorptance in metal–dielectric case with incidence on dielectric
$A_m$ = spectral normal absorptance in metal–dielectric case with incidence on metal
$c$ = speed of light in vacuum
$d$ = thickness of metallic film or dielectric layer
$e$ = electronic charge
$E$ = electric field in metallic film
$E_1$, $E_3$ = exponential integrals of first and third orders, respectively
$E_i^+$ = amplitude of electric wave propagating in positive direction in the $i$th medium
$E_i^-$ = amplitude of electric wave propagating in negative direction in the $i$th medium
$F$ = normalized electric field defined in equation (18)
$h$ = Planck's constant
$i$ = imaginary unit, $\sqrt{-1}$
$I_i$ = functions involving exponential integrals used in equations (21), (23), and (24)
$k$ = absolute value of the complex part of the complex index of refraction $\tilde{n}$
$l$ = electron mean free path
$m$ = effective electron mass
$n$ = real part of the complex index of refraction $\tilde{n}$
$\tilde{n}$ = $n - ik$ = complex index of refraction
$N$ = number of nodal points for finite-difference analysis
$N_e$ = number density of conduction electrons
$p$ = fraction of electrons arriving at film surface that are scattered specularly, in this work $p = 0$
$P$ = factor defined in equation (11) that contains core polarization and internal photoelectric current
$R$ = spectral normal reflectance
$T$ = temperature or spectral normal transmittance
$v$ = velocity at surface of the Fermi distribution
$w$ = $1 + i\omega\tau$
$Z$ = surface impedance of metallic film
$\alpha$ = parameter defined in equation (9)
$\epsilon$ = permittivity
$\Delta$ = $\omega\tilde{n}d/c$
$\eta$ = depth normal to the film thickness measured in units of film thickness $d$
$\delta$ = classical skin depth
$\sigma$ = d-c electrical conductivity
$\lambda$ = wavelength
$\lambda_{max}$ = wavelength as calculated from Wien's formula
$\mu$ = permeability
$\tau$ = electron relaxation time defined in equation (39)
$\Phi_i$ = functions defined in equations (28), (31), (34), (35), and (38)
$\omega$ = circular frequency of incident radiation

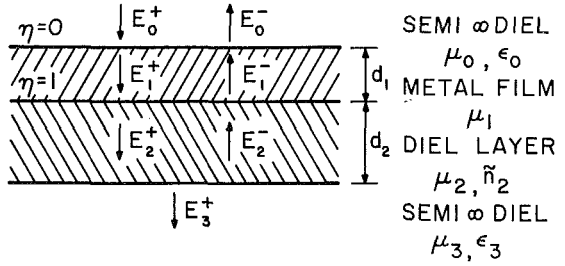


**Fig. 2(a) Configuration of the metal–dielectric system; incidence on metal**

$$R = \left|\frac{E_0^-}{E_0^+}\right|^2 = |2F(0) - 1|^2 \tag{19}$$

$$T = \frac{\sqrt{\frac{\epsilon_3}{\mu_3}}}{\sqrt{\frac{\epsilon_0}{\mu_0}}}\left|\frac{E_3^+}{E_0^+}\right|^2 = \frac{\sqrt{\frac{\epsilon_3}{\mu_3}}}{\sqrt{\frac{\epsilon_0}{\mu_0}}}|2F(1)|^2 \tag{20}$$

The problem of equation (8) together with boundary conditions (16) and (17) may be reduced to the problem of $N$ simultaneous linear algebraic equations in $N$ unknowns by the following procedure:

Equation (8), with $F$ as the dependent variable, is integrated with respect to $\eta$, thus obtaining

$$\frac{dF}{d\eta}(\eta) - \frac{dF}{d\eta}(0) + \frac{P\mu\omega^2 d^2}{c^2}\int_0^\eta F(\xi)d\xi = i\alpha\left(\frac{d}{l}\right)^3\int_0^1 F(\xi)I_1(\xi, \eta)d\xi \tag{21}$$

where $I_1$ and the following $I_i$, $i = 2, \ldots, 5$ are known functions involving exponential integrals.

In order to use finite-difference techniques the interval $\eta = 0$ to $\eta = 1$ is divided into $N - 1$ equal segments. Then

$$F(\eta) = F\left(\frac{j-1}{N-1}\right) = F_j \qquad j = 1, \ldots, N \tag{22}$$

It is assumed that for a given segment $F$ is constant and equal to the mean of its values at the end points of the segment. Then equation (21) may be written as

$$\frac{dF}{d\eta}\left(\frac{j-1}{N-1}\right) - \frac{dF}{d\eta}(0) + \frac{P\mu\omega^2 d^2}{2c^2(N-1)}\sum_{k=1}^{j-1}(F_k + F_{k+1}) = \frac{i\alpha}{2}\left(\frac{d}{l}\right)^3\sum_{k=1}^{j-1}(F_k + F_{k+1})I_2(j, k) + \frac{i\alpha}{2}\left(\frac{d}{l}\right)^3\sum_{k=j}^{N-1}(F_k + F_{k+1})I_3(j, k) \qquad j = 2, \ldots, N \tag{23}$$

Equation (21) is then integrated with respect to $\eta$, obtaining

$$F_j - F_1 - \left(\frac{j-1}{N-1}\right)\frac{dF}{d\eta}(0) + \frac{P\mu\omega^2 d^2}{c^2}\int_0^{\frac{j-1}{N-1}}\int_0^t F(s)dsdt = \frac{i\alpha}{2}\left(\frac{d}{l}\right)^3\sum_{k=1}^{j-1}(F_k + F_{k+1})I_4(j, k) + \frac{i\alpha}{2}\left(\frac{d}{l}\right)^3\sum_{k=j}^{N-1}(F_k + F_{k+1})I_5(j, k) \qquad j = 2, \ldots, N \tag{24}$$

The double integration may be approximated in finite-difference form as

$$\int_0^{\frac{j-1}{N-1}}\int_0^t F(s)dsdt \cong \frac{1}{4(N-1)^2}(F_1 + F_2) \qquad j = 2 \tag{25}$$

$$\cong \frac{1}{2(N-1)^2}\left[\sum_{i=2}^{j-1}\sum_{k=1}^{i-1}(F_k + F_{k+1}) + \sum_{i=2}^{j-1}F_i\right] + \frac{1}{4(N-1)^2}(F_1 + F_j) \qquad j = 3, \ldots, N \tag{25}$$

Finally equations (16), (17), (23), (24), and (25) may be combined to yield $N$ linear algebraic equations for the $N$ unknowns $F_i$. Once the electric field within the film is known the radiation properties may be calculated from equations (19) and (20).

**Metal–Dielectric System.** The reflectance and absorptance of a two-layer metal–dielectric system are dependent upon which side of the system faces the incident radiation. The two possible configurations are shown in Fig. 2. The thin metallic film obeys ASE theory while the dielectric layer is assumed to exhibit classical behavior characterized by a complex index of refraction.

Consider Fig. 2(a). This is the case where radiation is incident upon the metal side of the system. The boundary conditions for the thin metallic film are found to be

$$1 - F(0) = \frac{ic}{\mu_1\omega d_1}\sqrt{\frac{\mu_0}{\epsilon_0}}\frac{dF}{d\eta}(0) \tag{26}$$

$$F(1) = \left(\frac{1 + \Phi_1}{1 - \Phi_1}\right)\frac{ic}{\mu_1\omega d_1}\frac{\mu_2}{\tilde{n}_2}\frac{dF}{d\eta}(1) \tag{27}$$

where

$$\Phi_1 = \frac{\left(\frac{\tilde{n}_2}{\mu_2} - \sqrt{\frac{\epsilon_3}{\mu_3}}\right)}{\left(\frac{\tilde{n}_2}{\mu_2} + \sqrt{\frac{\epsilon_3}{\mu_3}}\right)}\exp\left(-2i\frac{\omega}{c}\tilde{n}_2 d_2\right) \tag{28}$$

$\eta$ and $F(\eta)$ are defined as in the single-film case.

The reflectance and transmittance of the system may then be expressed in terms of the normalized electric fields at the metallic film boundaries

$$R = \left|\frac{E_0^-}{E_0^+}\right|^2 = |2F(0) - 1|^2 \tag{29}$$

$$T = \frac{\sqrt{\frac{\epsilon_3}{\mu_3}}}{\sqrt{\frac{\epsilon_0}{\mu_0}}}\left|\frac{E_3^+}{E_0^+}\right|^2 = \frac{\sqrt{\frac{\epsilon_3}{\mu_3}}}{\sqrt{\frac{\epsilon_0}{\mu_0}}}|2F(1)|^2\Phi_2 \tag{30}$$

where

$$\Phi_2 = \left|\frac{\left[1 + \frac{\left(\frac{\tilde{n}_2}{\mu_2} - \sqrt{\frac{\epsilon_3}{\mu_3}}\right)}{\left(\frac{\tilde{n}_2}{\mu_2} + \sqrt{\frac{\epsilon_3}{\mu_3}}\right)}\right]\exp\left(-i\frac{\omega}{c}\tilde{n}_2 d_2\right)}{1 + \frac{\left(\frac{\tilde{n}_2}{\mu_2} - \sqrt{\frac{\epsilon_3}{\mu_3}}\right)}{\left(\frac{\tilde{n}_2}{\mu_2} + \sqrt{\frac{\epsilon_3}{\mu_3}}\right)}\exp\left(-2i\frac{\omega}{c}\tilde{n}_2 d_2\right)}\right|^2 \tag{31}$$

A similar procedure may be used for the case of radiation incident upon the dielectric surface as depicted in Fig. 2(b). For this situation the boundary conditions for the metallic film and the radiation properties of the system are found to be

$$1 - \Phi_3 F(0) = \frac{ic}{\mu_1\omega d_1}\sqrt{\frac{\mu_0}{\epsilon_0}}\Phi_4\frac{dF}{d\eta}(0) \tag{32}$$

$$F(1) = \frac{ic}{\mu_1\omega d_1}\sqrt{\frac{\mu_3}{\epsilon_3}}\frac{dF}{d\eta}(1) \tag{33}$$

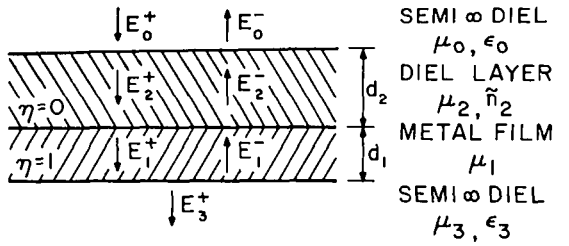


**Fig. 2(b) Configuration of the metal–dielectric system; incidence on dielectric**

where

$$\Phi_3 = \frac{1}{2}\sqrt{\frac{\mu_0}{\epsilon_0}}\left[\left(\frac{\tilde{n}_2}{\mu_2}+\sqrt{\frac{\epsilon_0}{\mu_0}}\right)\exp\left(i\frac{\omega}{c}\tilde{n}_2 d_2\right) - \left(\frac{\tilde{n}_2}{\mu_2}-\sqrt{\frac{\epsilon_0}{\mu_0}}\right)\exp\left(-i\frac{\omega}{c}\tilde{n}_2 d_2\right)\right] \quad (34)$$

$$\Phi_4 = \frac{1}{2}\frac{\mu_2}{\tilde{n}_2}\left[\left(\frac{\tilde{n}_2}{\mu_2}+\sqrt{\frac{\epsilon_0}{\mu_0}}\right)\exp\left(i\frac{\omega}{c}\tilde{n}_2 d_2\right) + \left(\frac{\tilde{n}_2}{\mu_2}-\sqrt{\frac{\epsilon_0}{\mu_0}}\right)\exp\left(-i\frac{\omega}{c}\tilde{n}_2 d_2\right)\right] \quad (35)$$

and

$$R = \left|\left[2F(0)\exp\left(-i\frac{\omega}{c}\tilde{n}_2 d_2\right)-1\right] + \left[1-\exp\left(-2i\frac{\omega}{c}\tilde{n}_2 d_2\right)\right]\Phi_5\right|^2 \quad (36)$$

$$T = \frac{\sqrt{\frac{\epsilon_3}{\mu_3}}}{\sqrt{\frac{\epsilon_0}{\mu_0}}}|2F(1)|^2 \quad (37)$$

where

$$\Phi_5 = \frac{2\sqrt{\frac{\epsilon_0}{\mu_0}}+2\left(\frac{\tilde{n}_2}{\mu_2}-\sqrt{\frac{\epsilon_0}{\mu_0}}\right)F(0)\exp\left(-i\frac{\omega}{c}\tilde{n}_2 d_2\right)}{\left(\frac{\tilde{n}_2}{\mu_2}+\sqrt{\frac{\epsilon_0}{\mu_0}}\right)+\left(\frac{\tilde{n}_2}{\mu_2}-\sqrt{\frac{\epsilon_0}{\mu_0}}\right)\exp\left(-2i\frac{\omega}{c}\tilde{n}_2 d_2\right)} \quad (38)$$

Simultaneous equations for the electric field within the metal may be obtained by combining either equations (23), (24), (25), (26), and (27) or (23), (24), (25), (32), and (33), depending upon whether incidence is on the metal or dielectric surface, respectively. Once the field within the metal is known the radiation properties of the two-layer system may be calculated from equations (29) and (30) or (36) and (37).

**Existing Approximate Methods.** The numerical results for a single metallic film obtained through the above procedure may be compared with results from existing approximate analyses. As mentioned previously, Dingle obtained series solutions for the surface impedance of a semi-infinite metal [7]. The complex index of refraction is then given by equation (4) and the radiation properties of the bulk metal may be obtained from equations (1), (2), and (3) by letting the film thickness approach infinity. This will be called the "ASE bulk" approximation. One way of taking into account the finite film thickness is to use a corrected value for the electrical conductivity. This value is usually obtained through Fuchs' theory [9]. The resulting combination of the ASE bulk method and the finite film electrical conductivity will be called the "ASE bulk–size effect" approximation. Two other approximate methods may be obtained by using the above procedures but leaving the classical equations (1), (2), and (3)

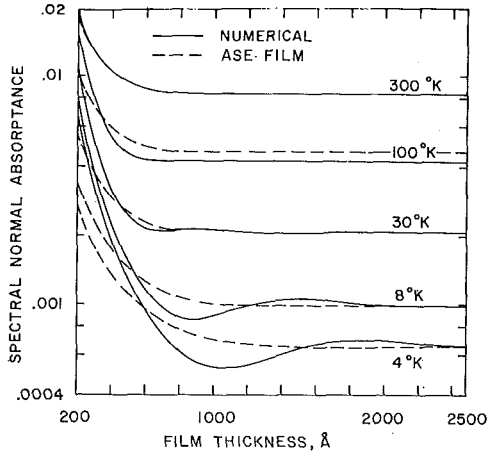


**Fig. 3 Spectral normal absorptance vs. film thickness for pure gold films at different temperatures, $\lambda = \lambda_{max}$**

in their finite form. These will be called "ASE film" and "ASE film–size effect", respectively.

The foregoing techniques are approximate in that they attempt in various ways to apply the semi-infinite ASE theory to finite-thickness films. Dingle [8], on the other hand, obtained an approximate analytical solution for equation (8) which was derived for a finite film. Unfortunately, for most good conductors Dingle's solution is only valid when the wavelength of the incident radiation is less than about 30 $\mu$. Armaly and Tien [12] recently obtained a numerical solution for equation (8). However, their results do not agree with the results of the present study. The details of Armaly and Tien's numerical technique are given in [13].

## Results and Discussion

The $N$ simultaneous linear algebraic equations for the normalized electric field at the nodal points of the thin metallic film were solved by the Gauss elimination technique. The value of $N$ had little effect for $N \geq 21$, and $N = 41$ was chosen as the standard.

The permittivities and permeabilities of the surrounding semi-infinite dielectric layers and the permeability of the metallic layer were taken as unity. The d-c electrical conductivity $\sigma$ was calculated from the Bloch–Grüneisen formula, Matthiessen's rule being invoked for specimens containing impurities. The relaxation time $\tau$ was obtained from the classical relation

$$\tau = \frac{m\sigma}{N_e e^2} \quad (39)$$

Electric-field results were checked and confirmed by means of Poynting's theorem.

The single-film results were for a pure gold film with one conduction electron per atom and with an effective electron mass equal to the free electron rest mass [14]. Introduction of a residual resistivity of $9 \times 10^{-9}$ ohm-cm raises the low-temperature absorptance by less than 2 percent, and using an effective mass of 0.9 times the free electron mass [15] would lower the absorptance by less than 5 percent.

Figure 3 shows the spectral normal absorptance versus film thickness for single films at various temperatures. For temperatures below about 30 deg K the numerical analysis predicts a minimum in the absorptance. The ASE film approximation gives excellent results for thick films and approaches the correct bulk-specimen limit. An exception to this statement is shown by the 100 deg K curve. This exception will be discussed later.

Figure 4 shows the spectral normal absorptance versus wavelength for single films of various thicknesses. Dingle's thin-film solution [8] is shown for thicknesses of 200 and 400 Å. The

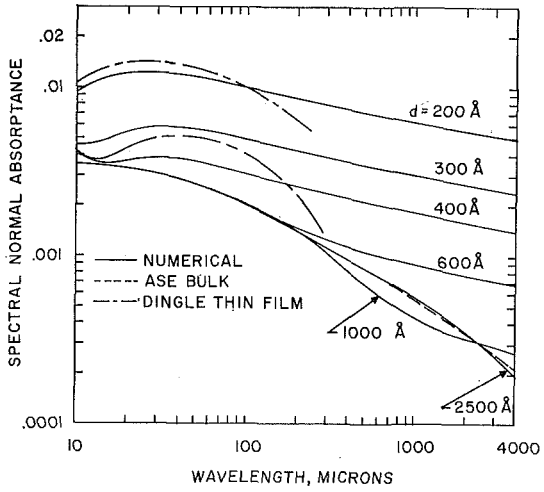


**Fig. 4 Spectral normal absorptance vs. wavelength for pure gold films of different thicknesses, $T = 4$ deg K**

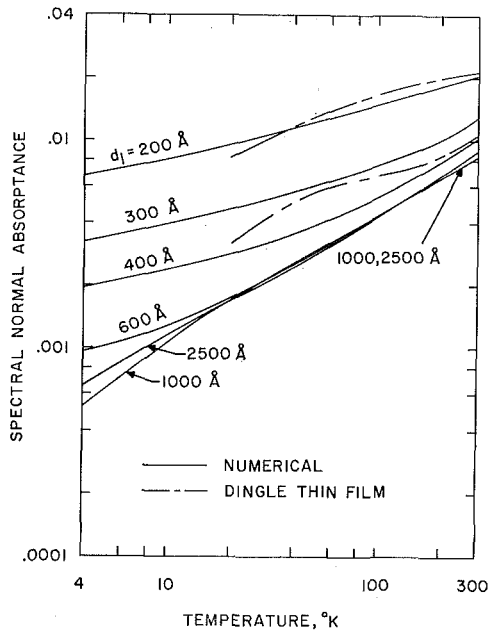


**Fig. 5 Spectral normal absorptance vs. temperature for pure gold films of different thicknesses, $\lambda = \lambda_{max}$**

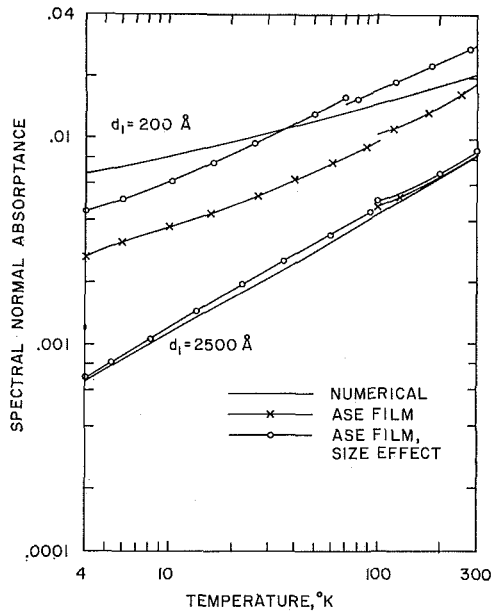


**Fig. 6 Comparison of numerical and other approximate results: spectral normal absorptance vs. temperature for pure gold films of different thicknesses, $\lambda = \lambda_{max}$**

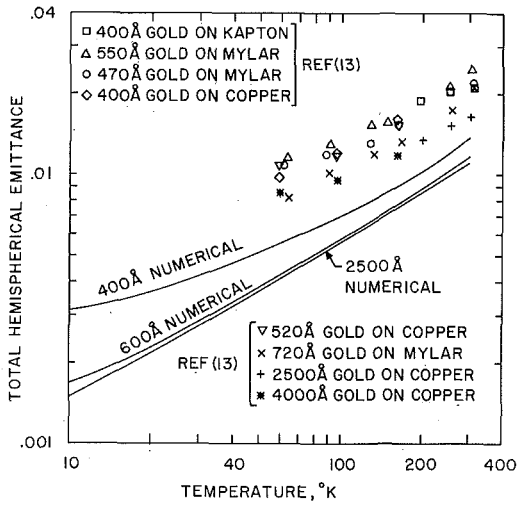


**Fig. 7 Comparison of numerical results and experimental data; theoretical results are for pure gold films with $\lambda = \lambda_{max}$**

ASE bulk solution coincides with the 2500-Å numerical solution for all but extremely long wavelengths.

Figure 5 shows the spectral normal absorptance versus temperature for single films of various thicknesses. As before, Dingle's solution is presented for 200- and 400-Å films.

Figure 6 compares the numerical results with the results from two approximate analyses. For the thick 2500-Å film, the numerical, ASE film, and ASE bulk solutions coincide for temperatures below 100 deg K. The ASE film–size effect approximation is shown to be valid only for very thin films at low temperatures. The discontinuities in the approximate-method curves are due to the existence of two series expansions for the surface impedance of the film. One expansion is valid above a certain value of a specific parameter and the other is valid below this value. The expansions are not well joined and the transition point occurs near 100 deg K for the cases investigated. This explains the discrepancy mentioned in regard to the 100 deg K curve in Fig. 3.

Table 1 shows the ratio of the spectral normal transmittance to the spectral normal absorptance for 200-Å films at different temperatures and with various wavelengths of incident radiation. It is seen that at low temperatures and fairly short wavelengths the transmittance may be of the same order of magnitude as the absorptance. This means, for example, that transmission through shields may not always be neglected in multilayer insulation analyses.

Figure 7 compares the numerical results with the experimental data obtained by Cunnington et al. [16]. For reasons of clarity the room-temperature results of Ruccia and Hinckley [17] are not shown. They are consistent with the presented data. Caren

**Table 1 Transmittance–absorptance ratio vs. wavelength for 200-Å pure gold films at different temperatures**

| Wavelength, $\mu$ | Temp., deg K | $T/A$ | Wavelength, $\mu$ | Temp., deg K | $T/A$ |
|---|---|---|---|---|---|
| 2 | 4 | 1.639 | 20 | 4 | .01457 |
| | 20 | 1.632 | | 20 | .01454 |
| | 50 | 1.497 | | 50 | .01409 |
| | 100 | 1.250 | | 100 | .01325 |
| 4 | 4 | .391 | 40 | 4 | .00678 |
| | 20 | .389 | | 20 | .00677 |
| | 50 | .360 | | 50 | .00662 |
| | 100 | .306 | | 100 | .00662 |
| 10 | 4 | .0646 | 100 | 4 | .00386 |
| | 20 | .0643 | | 20 | .00386 |
| | 50 | .0591 | | 50 | .00387 |
| | 100 | .0499 | | 100 | .00407 |

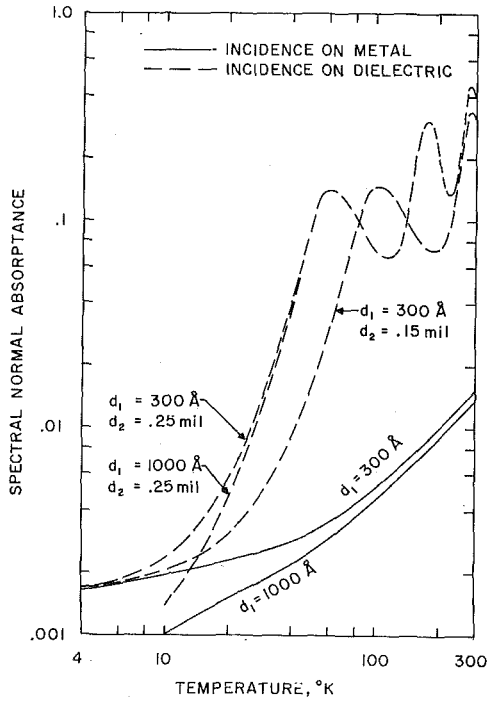


**Fig. 8 Spectral normal absorptance vs. temperature for metal–dielectric system; impure aluminum; $\tilde{n}_2 = (2, -0.02)$; $\lambda = \lambda_{max}$**

[18] also measured the emittance of gold films. His results lie above the data points shown. This probably may be explained by the fact that his films were chemically deposited and were of unspecified thickness. Since the experimental values are for total hemispherical emittance, the theoretical curves are obtained by multiplying the normal spectral emittance (with $\lambda = \lambda_{max}$) by 1.33 [19]. Cunnington et al. [16] say that the measured effect of film thickness is not as pronounced as that predicted by their theory. The results of the present study show substantially less film-thickness-dependence and are in better agreement with the experimental data.

Figure 8 shows the normal spectral absorptance versus temperature for a metal–dielectric system. The aluminum is assumed to have a residual resistivity of $9 \times 10^{-9}$ ohm-cm. Little experimental information is available concerning the complex refractive indices of dielectric materials. Tien et al. [20] obtained some room-temperature results; however, they mentioned that preliminary investigations indicate that the refractive index is quite temperature-dependent. For lack of additional information the complex index of refraction of the dielectric layer was taken as a constant, $\tilde{n}_2 = (2, -0.02)$. It was assumed that aluminum has 2.6 free electrons per atom [21].

Table 2 shows some typical transmittance and absorptance values for a 300-Å aluminum film on a 0.25-mil dielectric base. The transmittances are the same regardless of whether the radiation is incident upon the metal or the dielectric surface.

**Table 2 Spectral normal absorptance and transmittance for metal–dielectric system consisting of a 300-Å aluminum film on a 0.25-mil dielectric base, $\tilde{n}_2 = (2, -0.02)$**

| Wavelength, $\mu$ | Temp., deg K | $T$ | $A_m$ | $A_d$ |
|---|---|---|---|---|
| 2 | 4 | $.271 \times 10^{-3}$ | $.547 \times 10^{-2}$ | .730 |
| | 30 | .271 | .549 | .730 |
| | 60 | .271 | .592 | .730 |
| | 100 | .272 | .748 | .731 |
| 4 | 4 | .133 | .530 | .643 |
| | 30 | .133 | .532 | .643 |
| | 60 | .134 | .573 | .643 |
| | 100 | .137 | .725 | .643 |
| 10 | 4 | $.422 \times 10^{-4}$ | .436 | .469 |
| | 30 | .422 | .438 | .469 |
| | 60 | .419 | .479 | .470 |
| | 100 | .421 | .622 | .473 |
| 20 | 4 | $.398 \times 10^{-5}$ | .418 | .122 |
| | 30 | .400 | .420 | .122 |
| | 60 | .432 | .451 | .122 |
| | 100 | .621 | .565 | .124 |

## References


1 "Thermal Insulation Systems—A Survey," NASA SP-5027, 1967, pp. 5–12, 39–61.

2 Barnes, R. B., and Czerny, M., "Concerning the Reflection Power of Metals in Thin Layers for the Infrared," *Physical Review*, Vol. 38, 1931, pp. 338–345.

3 Mott, N. F., and Jones, H., *The Theory of the Properties of Metals and Alloys*, Clarendon, Dover, 1936.

4 Heavens, O. S., *Optical Properties of Thin Solid Films*, Butterworths, Dover, 1955.

5 Domoto, G. A., Boehm, R. F., Tien, C. L., "Predictions of the Total Emissivity of Metals at Cryogenic Temperatures," *Advances in Cryogenic Engineering*, Vol. 14, 1969, pp. 230–239.

6 Reuter, G. E. H., and Sondheimer, E. H., "The Theory of the Anomalous Skin Effect in Metals," *Proc. Roy. Soc.*, London, Series A, Vol. 195, 1948, pp. 336–364.

7 Dingle, R. B., "The Anomalous Skin Effect and the Reflectivity of Metals, I," *Physica*, Vol. 19, 1953, pp. 311–347.

8 Dingle, R. B., "The Anomalous Skin Effect and the Reflectivity of Metals, IV," *Physica*, Vol. 19, 1953, pp. 1187–1199.

9 Fuchs, K., "The Conductivity of Thin Metallic Films According to the Electron Theory of Metals," *Camb. Phil. Soc.*, Vol. 34, pp. 100–108.

10 Tien, C. L., and Cravalho, E. G., "Thermal Radiation of Solids at Cryogenic Temperatures," *Chem. Eng. Prog. Symp. Series*, Vol. 64, No. 87, 1968, pp. 56–66.

11 Van Vleck, J. H., *Theory of Electrical and Magnetic Susceptibilities*, Oxford University Press, 1932, p. 225.

12 Armaly, B. F., and Tien, C. L., "Emissivities of Thin Metallic Films at Cryogenic Temperatures," in: *Heat Transfer 1970*, Vol. III, Elsevier, Amsterdam, 1970.

13 Armaly, B. F., "Emissivities of Metals at Cryogenic Temperatures," PhD thesis, University of California, Berkeley, Calif., 1969.

14 Dingle, R. B., "The Anomalous Skin Effect and the Reflectivity of Metals, II," *Physica*, Vol. 19, 1953, pp. 348–364.

15 *American Institute of Physics Handbook*, 2nd ed., McGraw-Hill, New York, N. Y., 1963, pp. 9–45.

16 Cunnington, G. R., Bell, G. A., Armaly, B. F., and Tien, C. L., "Total Emittance Measurements of Thin Metallic Films at Cryogenic Temperatures," AIAA Paper 70–63.

17 Ruccia, F. E., and Hinckley, R. B., "The Surface Emittance of Vacuum-Metallized Polyester Film," *Advances in Cryogenic Engineering*, Vol. 12, 1967, pp. 300–307.

18 Caren, R. P., "Low-Temperature Emittance Determinations," *Prog. in Astro. and Aero.*, Vol. 18, 1966, pp. 61–73.

19 Dunkle, R. V., "Emissivity and Inter-reflection Relationships for Infinite Parallel Specular Surfaces," in: *Symposium on Thermal Radiation of Solids*, NASA SP-55, 1965, p. 39.

20 Tien, C. L., Chan, C. K., and Cunnington, G. R., "Infrared Radiation of Thin Plastic Films," JOURNAL OF HEAT TRANSFER, TRANS. ASME, Series C, Vol. 94, No. 1, Feb. 1972, pp. 41–45.

21 Bennett, H. E., Silver, M., Ashley, E. J., "Infrared Reflectance of Aluminum Evaporated in Ultra-High Vacuum," *J. Opt. Soc. Am.*, Vol. 53, 1963, pp. 1089–1095.

D. G. DOORNINK[1]
Assistant Professor,
Department of Mechanical Engineering,
South Dakota School of
Mines and Technology,
Rapid City, S. D.
Assoc. Mem. ASME

R. G. HERING[2]
Professor and Chairman,
Department of Mechanical Engineering,
University of Iowa,
Iowa City, Iowa.
Mem. ASME

# Transient Combined Conductive and Radiative Heat Transfer

*Transient simultaneous conductive and radiative transfer in a plane gray layer bounded by black walls is studied. The analytical development yields a nonlinear integro-differential equation which is numerically solved for a layer initially at a uniform temperature when the temperature of one wall is suddenly decreased. Instantaneous temperature and flux distributions illustrate the conduction–radiation interaction during cooling for a wide range of values for the influencing parameters which include layer optical thickness $\tau_0$ and the conduction–radiation interaction parameter N. Results are compared to those for an optically thin and optically thick medium, as well as to those for purely conductive and purely radiative transfer.*

## Introduction

Simultaneous conductive and radiative transfer under transient conditions is a complex phenomenon important in a number of engineering applications. Reported studies of this energy transport process are characterized either by simplifications and approximations which limit the utility and accuracy of the results or by limiting of consideration to specific materials. Nemchinov [1][3] used a two-flux approximation for radiative flux and linearization while Lick [2] employed an exponential kernel approximation in conjunction with linearization to develop short- and long-time solutions for the semi-infinite gray medium. Heinisch and Viskanta [3] found similarity solutions for the same system utilizing the optically thick approximation. Results of limited scope have also been reported for a plane gray layer [4, 5], as well as for a gray medium confined between concentric cylinders [6], utilizing a differential approximation for radiative flux. A more general situation for a plane nongray layer including scattering as well as convective and radiative transfer at a boundary was considered by Perez and Baldo [7], but the nonlinear local radiative emission term in the energy equation was ignored. Emission was also neglected in a recent general study by Heinisch, Singer, and Viskanta [8] as well as by Cobble [9] in a study of the thermal-trap effect in glass. Interest in glass manufacturing processes, as well as in aircraft window design, has fostered a number of studies [10, 11] devoted to the heating and cooling of glass. Although the excellent pioneering formulation of Gardon [10] is particularly noteworthy, quantitative results were limited to a specific material, namely glass, and therefore this and similar studies on glass do not generally provide insight into the transient energy transfer process for materials whose physical properties are significantly different.

The purpose of this study is threefold: first, to examine the fundamental problem of interaction of conductive and radiative transfer under transient conditions without the limitations of previous efforts; second, to delineate the situations in which interaction between the two energy transport mechanisms must be considered; finally, to examine the usefulness and accuracy of some common approximations for radiative flux which greatly simplify the analysis of the transient energy transfer system. To accomplish our objectives without introducing unnecessary geometrical complexity or parameters of only secondary interest, a stationary plane layer of homogeneous nonscattering material confined between black planes is considered. Thermophysical and radiative properties are considered temperature-independent. For the purposes of this study, the layer is assumed gray. It is recognized that the gray assumption does not adequately describe the radiative characteristics of many engineering materials. Nevertheless, gray results may be considered a first step toward meaningful results for engineering materials which provide insight into the energy transport process and predict the correct trends while significantly reducing the complexity of an already difficult problem.

## Analysis

Consider a plane layer of stationary nonscattering gray medium of unit refractive index confined between uniform-temperature black planes separated by distance $L$ (see Fig. 1). The temperature of each wall is specified, while the enclosed medium is isotropic, homogeneous, and isobaric. Ionization and dissociation phenomena are not considered and it is assumed that radiation energy density level can be neglected in comparison to the material's molecular energy density. Under these conditions the

[1] Formerly Teaching Assistant and NSF Trainee, Department of Mechanical Engineering, University of Illinois, Urbana, Ill.

[2] Formerly Professor, Department of Mechanical Engineering, University of Illinois, Urbana, Ill.

[3] Numbers in brackets designate References at end of paper.

Based on a paper contributed by the Heat Transfer Division and presented at the ASME-AIChE Heat Transfer Conference, Tulsa, Okla., August 15–18, 1971, as Paper No. 71-HT-22. Manuscript received by the Heat Transfer Division April 20, 1971; revised manuscript received February 14, 1972.

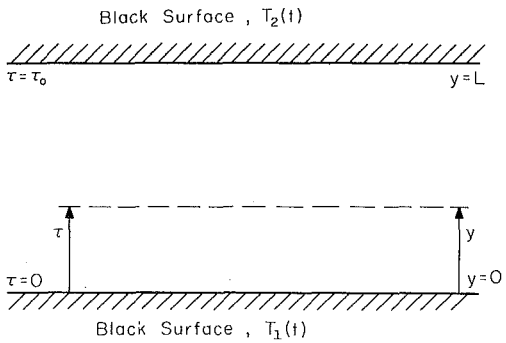


**Fig. 1 Schematic diagram of system**

energy equation for the medium, presented in dimensionless form [12], is

$$\frac{\partial\theta}{\partial t^*} = \frac{\partial^2\theta}{\partial\xi^2} + \frac{\tau_0^2}{2N}\left[\theta_1{}^4 E_2(\tau_0\xi) + E_2[\tau_0(1-\xi)] - 2\theta^4(\xi,t^*) + \tau_0\int_0^1 \theta^4(\xi',t^*)E_1[\tau_0(|\xi-\xi'|)]d\xi'\right] \quad (1)$$

Transient temperature distributions are evaluated for a medium initially at uniform temperature $T_2$ when the temperature of the lower black wall is suddenly reduced to and thereafter maintained at temperature $T_1$. The upper wall is maintained at the initial temperature $T_2$. These conditions were chosen to correspond to the extensive results available for steady radiative and conductive transfer [13] and for transient conductive transfer [14]. For this situation the initial condition is given by

$$\theta(\xi, 0) = 1 \quad (2)$$

while the boundary conditions are

$$\theta(0, t^*) = \theta_1 \qquad \theta(1, t^*) = 1 \quad (3)$$

The dimensionless expressions for the conductive and radiative fluxes are

$$F_c{}^*(\xi, t^*) = -\frac{4N}{\tau_0}\frac{\partial\theta}{\partial\xi} \quad (4)$$

$$F_r{}^*(\xi, t^*) = 2\left[\theta_1{}^4 E_3(\tau_0\xi) - E_3[\tau_0(1-\xi)] + \tau_0\int_0^1 \theta^4(\xi',t^*)E_2[\tau_0(|\xi-\xi'|)]\,\text{sign}\,(\xi-\xi')d\xi'\right] \quad (5)$$

It is observed that the dimensionless temperature distribution depends on three dimensionless parameters: optical thickness $\tau_0$, wall temperature ratio $\theta_1$, and the parameter $N$ which measures the relative importance of conductive to radiative transfer.

Considerable simplification of equation (1) occurs when the medium may be considered optically thin ($\tau_0 \ll 1$) or optically thick ($\tau_0 \gg 1$). In the optically thin approximation, the radiative flux expression, equation (5), correct to terms of the order of $\tau_0$, becomes [15]

$$F_r{}^*(\xi, t^*) = 2\left\{\theta_1{}^4\left(\frac{1}{2} - \tau_0\xi\right) - \left[\frac{1}{2} - \tau_0(1-\xi)\right] + \tau_0\int_0^1 \theta^4(\xi', t^*)\,\text{sign}\,(\xi-\xi')d\xi'\right\} \quad (6)$$

The corresponding energy equation simplifies to the differential equation

$$\frac{\partial\theta}{\partial t^*} = \frac{\partial^2\theta}{\partial\xi^2} + \frac{\tau_0^2}{2N}[\theta_1{}^4 + 1 - 2\theta^4(\xi, t^*)] \quad (7)$$

Note that, in the optically thin limit, the two dimensionless parameters $\tau_0$ and $N$ influence temperature only through the ratio $\tau_0{}^2/N$.

In optically thick materials, emitted radiant energy is absorbed within the emitting element's immediate neighborhood and the dimensionless radiative flux [15] is

$$F_r{}^*(\xi, t^*) = -(16\theta^3/3\tau_0)(\partial\theta/\partial\xi) \quad (8)$$

The energy equation reduces to the differential equation

$$\frac{\partial\theta}{\partial t^*} = \frac{\partial}{\partial\xi}\left[\left(1 + \frac{4\theta^3}{3N}\right)\frac{\partial\theta}{\partial\xi}\right] \quad (9)$$

In the optically thick limit, radiative transfer ceases to retain its global-interaction mechanism since it is determined solely by the local temperature distribution. Also note that the temperature distribution is independent of optical thickness.

## Method of Solution

The energy equation, equation (1), is a nonlinear, integro-partial differential equation for which analytical closed-form solutions do not appear possible, and therefore numerical methods were employed. Numerical solution is complicated by the fact that $E_1(\tau_0|\xi - \xi'|)$ is singular when $\xi = \xi'$, even though the integral exists and is finite. A functional approximation technique recently reported [16] was used to evaluate the integral and the Saul'ev numerical integration method [17] was utilized to integrate the resulting set of equations to steady state for selected values of the influencing parameters. The accuracy of the solution method was investigated by comparing results to those available for transient conduction in a nonradiating medium [14], radiative heating in a nonconducting material [18], and steady conditions in radiating and conducting materials [13]. These comparisons showed agreement to better than 1 percent in most cases investigated. As a consequence of these numerical studies, the results of this study are estimated to be at least of this accuracy.

## Results and Discussion

The dimensionless temperature distribution at each instant of dimensionless time $t^*$ depends on optical thickness $\tau_0$, wall temperature ratio $\theta_1$, and the parameter $N$. All results presented are

## Nomenclature

$E_n$ = exponential integral function of order $n$
$F$ = heat flux, Btu/hr-ft$^2$
$F^*$ = dimensionless heat flux, $F/\sigma T_2{}^4$
$k$ = thermal conductivity, Btu/hr-ft-deg F
$L$ = normal distance between plates, ft
$N$ = dimensionless conduction–radiation parameter, $k\kappa/4\sigma T_2{}^3$
$t$ = time, hr
$t^*$ = dimensionless time, $\alpha t/L^2$
$t^{**}$ = dimensionless time, $4k\kappa\sigma T_2{}^3 t/\alpha$
$T$ = absolute temperature, deg R
$y$ = position coordinate, ft
$\alpha$ = thermal diffusivity, ft$^2$/hr
$\theta$ = dimensionless temperature, $T/T_2$
$\theta_1$ = dimensionless wall temperature ratio, $T_1/T_2$
$\Theta$ = dimensionless normalized temperature, $(\theta - \theta_1)/(1 - \theta_1)$
$\kappa$ = absorption coefficient, 1/ft
$\xi$ = dimensionless position coordinate, $y/L$
$\sigma$ = Stefan–Boltzmann constant, Btu/hr-ft$^2$-deg R$^4$
$\tau, \tau_0$ = optical depth and optical thickness

**Subscripts**

$c$ = conductive heat flux
$r$ = radiative heat flux
1 = lower wall
2 = upper wall

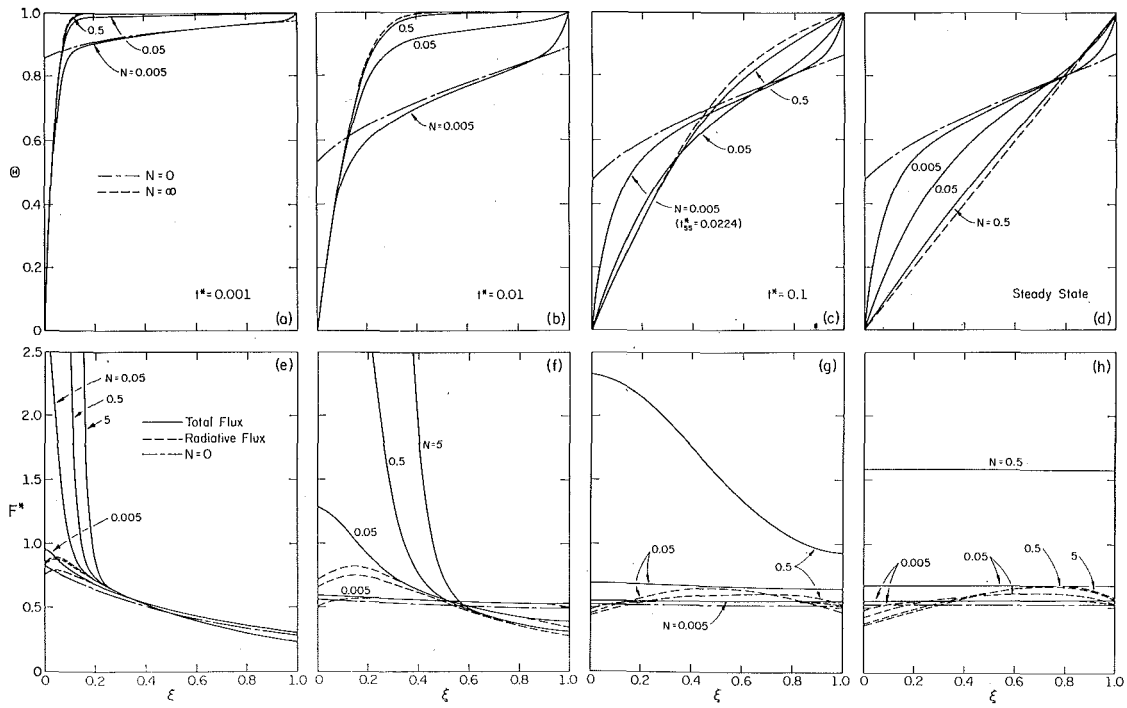


**Fig. 2 Influence of conduction–radiation parameter $N$ on temperature and flux distributions ($\tau_0 = 1$, $\theta_1 = 0.5$)**

for $\theta_1 = 0.5$, since only limited additional insight into the transient energy transfer process was obtained for other $\theta_1$ values. Results were evaluated for optical-thickness values of 0.1, 1.0, and 10 with the conduction–radiation parameter $N$ taking on values in a range which includes both conduction-dominant and radiation-dominant situations. For purposes of comparison, results are also presented for transient conduction in the absence of radiation ($N = \infty$) and for transient radiation in nonconducting materials ($N = 0$). Since the dimensionless time $t^*$ introduced for the combined conduction and radiation situation is undefined in a nonconducting material, the temperature and flux distributions presented in purely radiating materials were evaluated at a dimensionless time $t^{**}[= 4k\kappa\sigma T_2^3 t/\alpha]$ corresponding to the $t^*$ value of the radiation-dominant case. The two dimensionless times are related by $t^{**} = \tau_0^2 t^*/N$. Transient temperature results are normalized in the form

$$\Theta(\xi, t^*) = \frac{\theta(\xi, t^*) - \theta_1}{1 - \theta_1} \tag{10}$$

which is commonly used for steady-state results.

The influence of the conduction–radiation parameter $N$ on temperature and flux distributions during cooling is illustrated in Fig. 2 for a material of unit optical thickness at dimensionless times of 0.001, 0.01, 0.1, and steady state. These results indicate that for $N > 0.5$ the temperature distributions correspond closely to those of pure conduction. The temperature and flux distributions in a material with $N = 0.005$ are similar to pure radiation results except near the walls. This discrepancy in wall regions occurs because the presence of conductive transfer eliminates temperature slip at the walls, which is characteristic of pure radiation results. Therefore, insofar as the temperature distribution is concerned, radiative transfer effects are negligible when $N$ exceeds unity, and conduction effects may be ignored in the interior for values of $N$ less than 0.005 when $\tau_0 = 1.0$.

At early times, conduction is the dominant transfer mode near the cold wall because of the large temperature gradients present. Consequently, the temperature distributions for $\xi < 0.1$ and $t^* = 0.001$ are independent of $N$ and are essentially identical to pure conduction results. The principal influence of radiation is to provide, through its global-interaction mechanism, a means to cool material far removed from the cold wall. This results in lower interior temperatures than in a purely conducting material. As $N$ decreases, radiative transfer becomes more important, the amount of cooling increases, and the deviation from pure conduction results becomes larger.

The flux distributions illustrated in Fig. 2($e$) confirm the relative importance of radiative and conductive transfer at early times for $\tau_0 = 1.0$. In this figure, a positive slope corresponds to heating and a negative slope to cooling. Thus, near the cold wall, the energy transfer process is dominated by conductive cooling, while simultaneously radiative heating occurs. The radiant heating phenomenon is explained by the fact that low-temperature material in the neighborhood of the cold wall emits considerably less energy than it absorbs from the large region of high-temperature material confined between the cool element and the hot wall. In regions removed from the cold wall, the energy transfer process is one of radiative cooling, and conduction effects are negligible.

As time increases, the importance of radiant heating in the cold-wall region becomes greater and radiative heating effects extend further into the layer, yielding temperatures which exceed those in a purely conducting material. Near the hot wall, conductive heating begins to be observed, but radiant cooling dominates and the result is temperatures which are lower than those for pure conduction, but higher than those for pure radiation. Thus, as time increases, the similarity between temperature profiles for simultaneous conductive and radiative transfer and purely conductive transfer diminishes. The difference in profiles is particularly noticeable at small $N$ values.

Steady-state results are illustrated in Figs. 2($d$) and 2($h$). At steady state, the total flux is uniform across the layer. For the total flux to be uniform, it is necessary for variations in conductive flux to be compensated for by opposite variations in radiative flux. Thus temperature gradients in the wall regions are always greater than those for pure conduction and increase with decreasing value of the parameter $N$. Hence conductive heat transfer to the walls increases if the material is radiating.

Of considerable practical importance is the dimensionless time at which steady-state conditions are attained. Table 1 contains the values $t_{ss}^*$ for the range of parameters investigated. Steady state is characterized by a uniform total flux throughout the material. The quantity $t_{ss}^*$ is the time at which the difference between the wall fluxes is within 1 percent of the steady-state value.

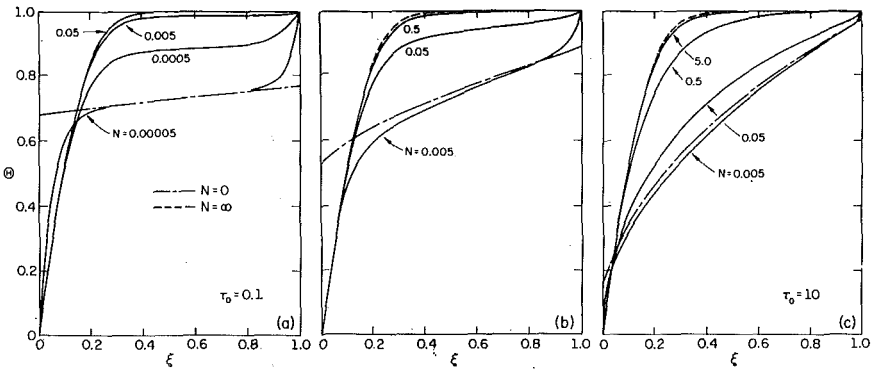


**Fig. 3 Influence of optical thickness $\tau_0$ on temperature distribution ($t^* = 0.01$, $\theta_1 = 0.5$)**

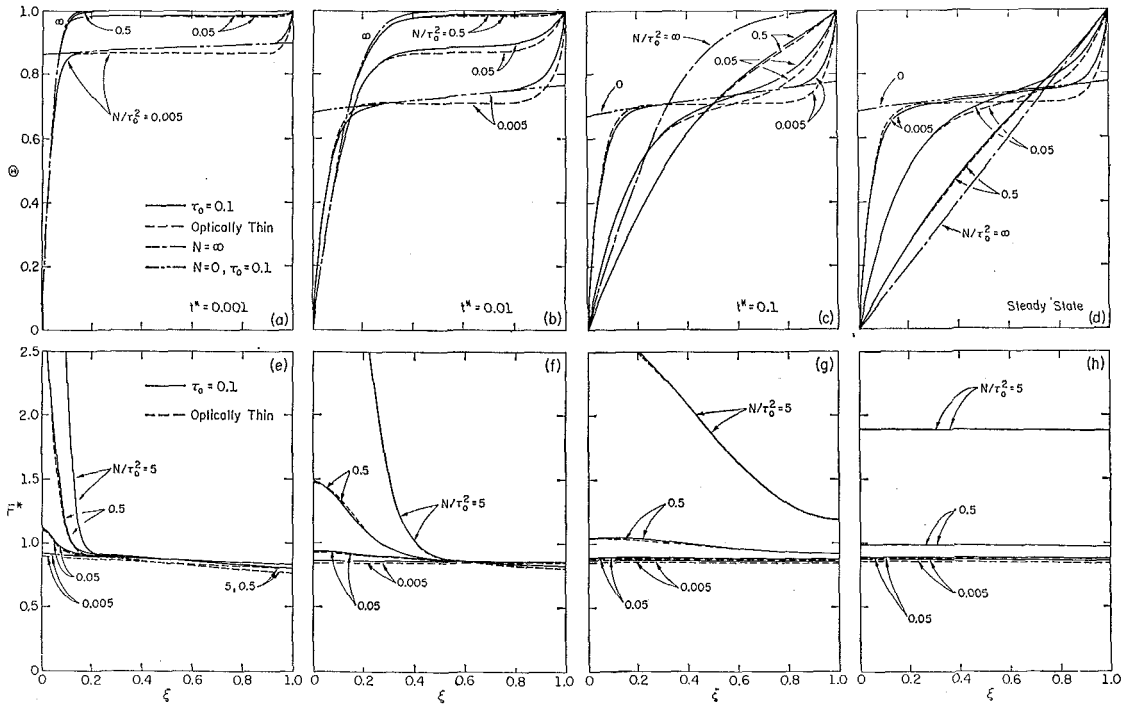


**Fig. 4 Comparison of optically thin approximate results to exact temperature and flux distributions ($\tau_0 = 0.1$, $\theta_1 = 0.5$)**

The dimensionless time to steady state is shortened as $N$ is decreased. Such results should be expected since conductive transfer is augmented by increasingly greater radiative transfer. Also, the mean steady-state temperature of the layer increases as $N$ decreases, so less energy is removed from the material to attain steady-state conditions.

Fig. 3($a$–$c$) illustrates, for a range of $N$ values, the normalized temperature distributions at dimensionless time 0.01 in materials of optical thickness 0.1, 1.0, and 10.0, respectively. Examination of these figures reveals that optical thickness has a marked influence on the temperature distribution in materials when radiation is a significant transfer mode. In materials with $\tau_0 = 0.1$ the temperature distributions are nearly uniform in interior regions, which is characteristic of results determined using the optically thin approximation. In optically thin materials, only the wall temperature and the local temperature influence the local radiant-flux gradient, so an initially constant-temperature material is uniformly radiatively cooled. Conversely, the nearly complete absorption of emitted radiant energy by material in the immediate neighborhood causes materials of optical thickness 10.0 to exhibit temperature profiles similar to optically thick materials in which radiative transfer is determined by local temperature gradient.

Fig. 4($a$–$d$) shows temperature profiles at dimensionless times 0.001, 0.01, 0.1, and steady state, respectively, in materials with $\tau_0 = 0.1$ when the parameter $N/\tau_0^2$ takes on the values shown. Exact results are compared to results obtained by using the optically thin expressions, equations (6) and (7). These figures indicate that the temperature and flux distributions during cooling for $\tau_0 < 0.1$ can be determined quite accurately by utilizing the optically thin approximate expressions. However, the optically thin approximation does suffer from loss of accuracy as $N/\tau_0^2$ becomes small. Since the energy equation is less complex than the general energy-conservation equation, considerable computing effort and time are saved.

Fig. 5($a$–$d$) illustrates the temperature profiles at dimensionless times 0.001, 0.01, 0.1, and steady state, respectively, in a material with $\tau_0 = 10$ when the parameter $N$ takes on the values shown. Exact results are compared with those obtained by using the optically thick approximations, equations (8) and (9). These figures indicate the steady-state temperature distribution in materials for which $\tau_0 > 10$ can be accurately calculated by utilizing the optically thick approximation. The correspondence between results is particularly good at large $N$ values and late times. However, at early times, the temperatures evaluated using the optically thick approximation are considerably lower in the cold-wall region. Although the low temperatures predicted at early time could be attributed at least partially to the failure of the Rosseland approximation at the walls, it is more likely attributable to the fact that the initial radiant-flux gradient at the cold wall is infinite in optically thick materials, but is finite in materials of finite optical thickness.

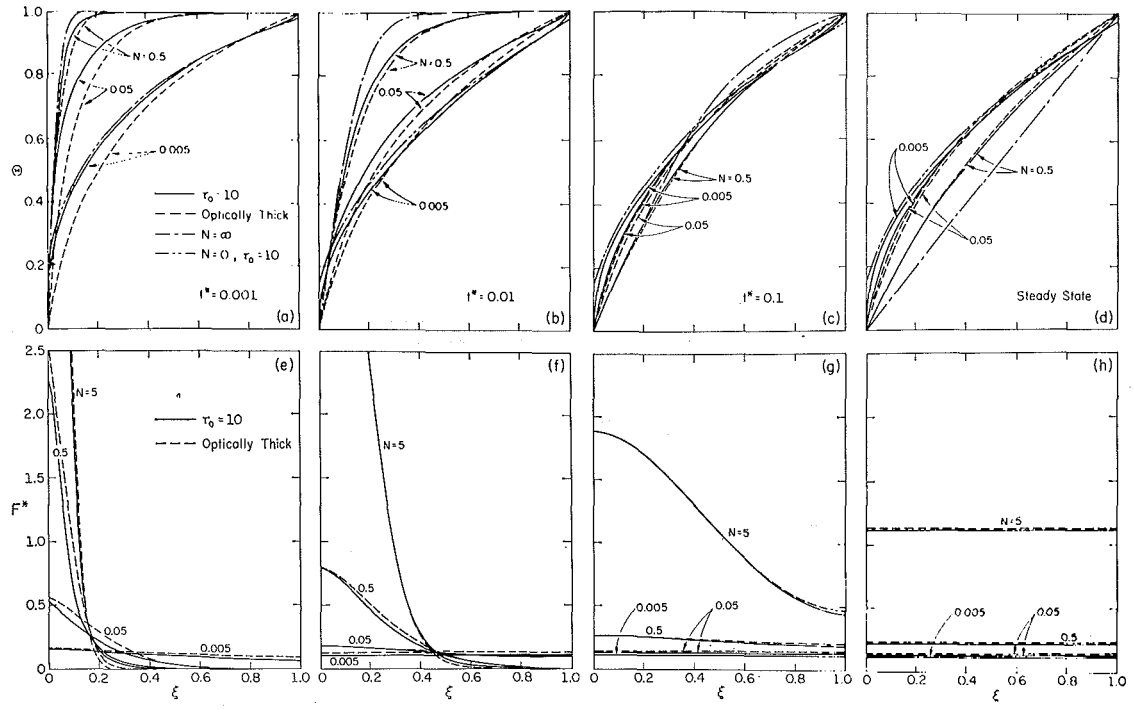


**Fig. 5 Comparison of optically thick approximate results to exact temperature and flux distributions ($\tau_0 = 10$, $\theta_1 = 0.5$)**

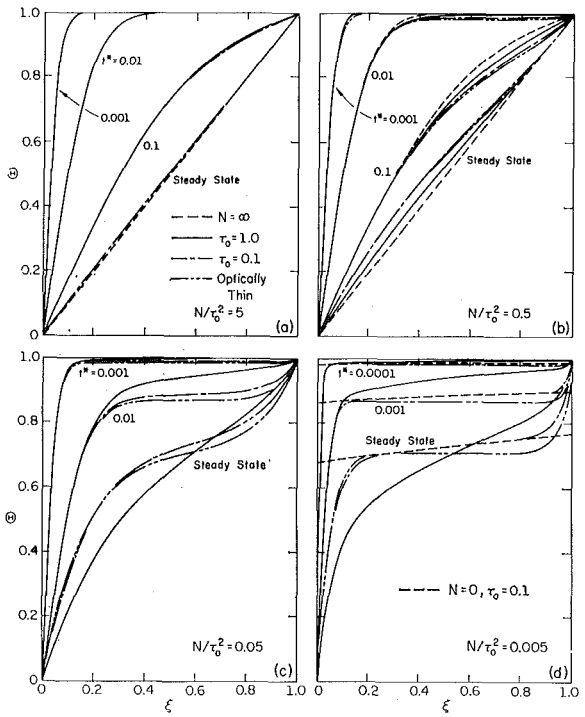


**Fig. 6 Correlation of temperature distributions with $N/\tau_0^2$ ($\theta_1 = 0.5$, $\tau_0 \leq 1$)**

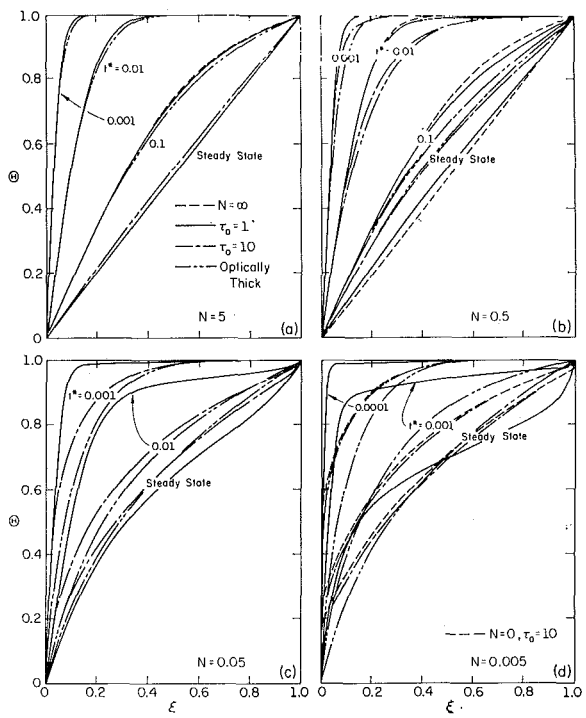


**Fig. 7 Correlation of temperature distributions with $N$ ($\theta_1 = 0.5$, $\tau_0 \geq 1$)**

Optical thickness also influences the magnitude of $N$ at which radiation or conduction is the dominant transfer mode. Fig. 3 indicates radiative transfer influences the temperature distribution when $N < 5$ in materials with $\tau_0 = 10$, but its effects in materials of optical thickness 0.1 need be considered only when $N < 0.05$. Furthermore, for $N = 0.005$, conduction is dominant when $\tau_0 = 0.1$, but when $\tau_0 = 10$, radiation is the dominant transfer mode. A correlation of the transient temperature profiles for different $N$ and $\tau_0$ values is suggested by the optically thin and thick limits. In Fig. 6, the parameter $N/\tau_0^2$ is used to correlate the transient temperature results in materials with $\tau_0 = 1.0$, 0.1, and $\tau_0 \ll 1$, while Fig. 7 shows the temperature results for materials with $\tau_0 = 1$, 10, and $\tau_0 \gg 1$ as a function of the parameter $N$. The dimensionless time and optical thickness of each temperature distribution are indicated. For comparative purposes, the temperature profile in purely conducting materials ($N = \infty$) is shown in the figures for the conduction-dominant situations, and the temperature distributions in purely radiating materials ($N = 0$) of optical thickness 0.1 and 10 are shown in the figures for which radiation is the dominant transfer mode.

These figures indicate that radiative transfer does not significantly affect the temperature when $N/\tau_0^2 > 5.0$ in materials for which $\tau_0 < 1.0$, or when $N > 5.0$ in materials for which $\tau_0 > 1.0$. The deviation from pure conduction results increases as $N/\tau_0^2$ or $N$ decreases and greater interaction of radiative and

**Table 1 Dimensionless time to steady state, $t_{ss}^*$ ($\theta_1 = 0.5$)**

| $N$ | thin | 0.1 | $\tau_0$ 1.0 | 10.0 | thick |
|---|---|---|---|---|---|
| $\infty$ | 0.624 | 0.624 | 0.624 | 0.624 | 0.624 |
| 5.0 | ... | ... | 0.621 | 0.531 | 0.596 |
| 0.5 | ... | ... | 0.303 | 0.247 | 0.250 |
| 0.05 | 0.510 | 0.531 | 0.163 | 0.0393 | 0.0358 |
| 0.005 | 0.275 | 0.291 | 0.0224 | 0.0052 | 0.0039 |
| 0.0005 | 0.0465 | 0.0528 | ... | ... | ... |
| 0.00005 | 0.0052 | 0.0058 | ... | ... | ... |

conductive transfer occurs. For radiation-dominant situations, i.e., when $N/\tau_0^2 < 0.005$ in materials for which $\tau_0 < 1.0$, and when $N < 0.005$ in materials for which $\tau_0 > 1.0$, the temperature distributions are similar to pure radiation results, except near the walls where conduction eliminates temperature slip.

Table 1 summarizes the influence of optical thickness and of the conduction–radiation parameter on the dimensionless time required to attain steady state. As should be expected, the time required to attain steady state is shortened at each optical thickness as the interaction parameter value decreases, since conductive transfer is augmented by larger amounts of radiative transfer. Using the parameters $N/\tau_0^2$ and $N$ to compare $t_{ss}^*$ for materials of different optical thickness indicates that materials of unit optical thickness take the longest time to attain steady state. For materials with $\tau_0 < 1$ and similar $N/\tau_0^2$ values, as well as for materials with $\tau_0 < 1$ and similar $N$ values, $t_{ss}^*$ generally decreases as optical thickness departs from unity.

## Conclusions

Transient combined conductive and radiative transfer in a plane gray layer confined between black walls has been presented for a layer initially at a uniform temperature when one wall is suddenly decreased in temperature. The interaction of conduction and radiation during cooling has been examined for a wide range of values for the influencing parameters, which include optical thickness $\tau_0$ and the conduction–radiation parameter $N$. The following conclusions may be drawn from the study. First, insofar as its effects on temperature distribution are concerned, radiative transfer is important when $N/\tau_0^2 < 1$ and is dominant when $N/\tau_0^2 < 0.005$ in materials with optical thickness less than unity. For larger values of optical thickness, radiative transfer effects are significant when $N < 1$ and are dominant for $N < 0.005$. Second, transient temperature and flux distributions in materials of small optical thickness ($\tau_0 < 0.1$) may be accurately evaluated at all times using the less complex optically thin approximation. On the other hand, although steady-state temperature and flux distributions are adequately predicted with the simpler optically thick approximation, temperature results in the cold-wall region at early times are significantly in error for materials of large optical thickness ($\tau_0 > 10$). Third, the general influence of radiative transfer is to provide, through its global-interaction mechanism, a means to cool material far removed from the cold wall, to increase the cooling rate of the layer, and to increase the mean temperature of the layer at steady state.

## References


1 Nemchinov, I. V., "Some Non-Stationary Problems of Radiative Heat Transfer," *Zh. Prinkl. Mekh. Tekh. Fiz.*, 1960, pp. 36–57.

2 Lick, W., "Transient Energy Transfer by Radiation and Conduction," *International Journal of Heat and Mass Transfer*, Vol. 8, 1965, pp. 119–127.

3 Heinisch, R. P., and Viskanta, R., "Transient Combined Conduction–Radiation in an Optically Thick Semi-Infinite Medium," *AIAA Journal*, Vol. 6, No. 7, 1968, pp. 1409–1411.

4 Chang, Y. P., and Kang, C. S., "Transient and Steady Heat Transfer in a Conducting and Radiating Medium," *AIAA Journal*, Vol. 8, No. 4, 1970, pp. 609–614.

5 Hazzah, A. S., and Beck, J. V., "Unsteady Combined Conduction–Radiation Energy Transfer Using a Rigorous Differential Method," *International Journal of Heat and Mass Transfer*, Vol. 13, 1970, pp. 517–522.

6 Chang, Y. P., and Smith, R. S., "Steady and Transient Heat Transfer by Radiation and Conduction in a Medium Bounded by Two Coaxial Cylindrical Surfaces," *International Journal of Heat and Mass Transfer*, Vol. 13, 1970, pp. 69–80.

7 Perez, M., and Baldo, A. F., "Radiant Heating of an Absorbing and Scattering Slab," *Journal of the Franklin Institute*, Vol. 285, No. 6, 1968, pp. 424–435.

8 Heinisch, R. P., Singer, R., and Viskanta, R., "Transient Combined Conduction and Radiation in an Absorbing Non-Emitting Medium," Argonne National Laboratory, Report No. ANL-7407, 1968.

9 Cobble, M. H., "Irradiation into Transparent Solids and the Thermal Trap Effect," *Journal of the Franklin Institute*, Vol. 278, No. 6, 1964, pp. 383–393.

10 Gardon, R., "Calculation of Temperature Distribution in Glass Plates Undergoing Heat Treatment," *Journal of the American Ceramic Society*, Vol. 41, No. 6, 1958, pp. 200–209.

11 Fowle, A. A., Strong, P. F., Comstock, D. F., and Sax, C., "Computer Program to Predict Heat Transfer through Glass," *AIAA Journal*, Vol. 7, No. 3, 1969, pp. 478–483.

12 Doornink, D., and Hering, R. G., "Transient Combined Conductive and Radiative Heat Transfer," ASME Paper No. 71-HT-22.

13 Viskanta, R., and Grosh, R. J., "Heat Transfer by Simultaneous Conduction and Radiation in an Absorbing Medium," JOURNAL OF HEAT TRANSFER, TRANS. ASME, Series C, Vol. 84, No. 1, Feb. 1962, pp. 63–72.

14 Schneider, P. J., *Temperature Response Charts*, John Wiley & Sons, New York, N. Y., 1963.

15 Sparrow, E. M., and Cess, R. D., *Radiation Heat Transfer*, Brooks/Cole Publishing Co., Belmont, Calif., 1966.

16 Prasad, K. K., and Hering, R. G., "Numerical Integration of a Nonlinear, Singular Integro–Partial Differential Equation," *Journal of Computational Physics*, Vol. 6, 1970, pp. 406–416.

17 Saul'ev, V. K., "Methods of Increased Accuracy and Two-Dimensional Approximations to Solutions of Parabolic Equations," *Dokl. Akad. Nauk SSSR(NS)*, Vol. 118, 1958, pp. 1088–1090, *RZh*, 1959.

18 Prasad, K. K., and Hering, R. G., "Transient Radiative Heat Transfer in a Plane Layer," *International Journal of Heat and Mass Transfer*, Vol. 12, 1969, pp. 1331–1337.

C. L. TIEN
Professor.
Mem. ASME

A. R. ROHANI

Department of Mechanical Engineering,
University of California,
Berkeley, Calif.

# Theory of Two-component Heat Pipes[1]

*A theoretical framework for predicting the steady-state operational characteristics of two-component heat pipes is established. The laws of conservation of mass and energy as well as thermodynamic phase equilibrium relations are applied to the system, and the governing relations between the various system parameters are specified. Measurements of the operational characteristics of a water–ethanol heat pipe indicate that complete separation into two pure components did not occur in any of the experiments. The observed degrees of separation and other operational characteristics agree well with the predictions.*

## Introduction

THE OPERATION of a heat pipe in which a mixture of fluids rather than a single component is used as the working medium has received considerable attention in several recent investigations [1–5].[2] In particular, the simplest case of steady-state two-component heat pipes has been studied from both analytical and experimental viewpoints. Before any experimental information on two-component heat pipes [3–5] became available, it was predicted on the basis of a simple analytical consideration [1, 2] that complete separation into two pure components should occur in two-component heat pipes. It was further suggested that the two pure-component zones would be separated by a narrow transition zone.

A different qualitative description was subsequently offered by Tien [3] of the operational characteristics of two-component heat pipes. Based on a more detailed consideration of the thermodynamic phase equilibrium for binary mixtures, he indicated that the degree of separation depends on the type of mixture used, its initial composition, and the heat-pipe geometry, as well as the thermal input and output conditions. Complete separation occurs only in restrictive operating conditions. While all existing experimental results [3–5] agree qualitatively with this description, no quantitative analysis is available for calculation and comparison.

It is the purpose of the present paper to establish a theoretical framework for predicting the operational characteristics of two-component heat pipes. Simplified mass- and energy-conservation relations combined with a binary phase equilibrium relation show how the temperature variation along the heat pipe and the pressure inside are related to the type of the binary working medium, initial mixture composition, heat-pipe geometry, and the rate of heat transmitted through the heat pipe. A measure of the degree of separation is then defined in accordance with that commonly used in the distillation-column analysis [6]. It is shown that good quantitative agreement exists between predicted and observed values of the degree of separation and other operational characteristics in each of the experimental runs performed on a water–ethanol heat pipe.

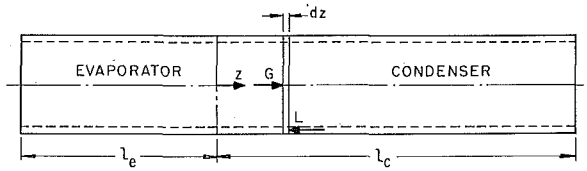


**Fig. 1 Schematic diagram of heat pipe**

## Analysis

The operation of two-component heat pipes resembles in certain aspects that of a distillation column with total reflux [6]. There exists, however, a fundamental difference between the two systems resulting from the different roles played by the operating pressures of the two systems. In the case of distillation columns, the system pressure is pre-set, usually at the atmospheric pressure, and does not interact directly with other system parameters. The pressure inside the heat pipe, however, is a major characteristic of the heat-pipe operation and is influenced by many system parameters in a rather complicated manner. Even in the special case of an externally regulated constant-pressure heat pipe, the operating pressure is maintained constant at the expense of adjusting other system parameters. For instance, in a gas-controlled heat pipe [7], the displacement of the vapor–gas interface alters the condenser area.

**Basic Consideration.** The physical system under consideration in the present study is the simple cylindrical heat pipe (Fig. 1) with a two-component working medium. The theoretical framework for describing the analytical behavior of the system rests on the general conservation laws for momentum, energy, and mass, as well as on the thermodynamic equation of state (i.e., binary phase equilibrium diagram in the present case). In order to provide a clear physical picture of the analytical description, without being drawn into unnecessarily complex formulation and solu-

[1] This research was supported by the National Science Foundation through grant NSF GK-11548.

[2] Numbers in brackets designate References at end of paper.

Contributed by the Heat Transfer Division and presented at the Winter Annual Meeting, Washington, D. C., November 28–December 2, 1971, of THE AMERICAN SOCIETY OF MECHANICAL ENGINEERS. Manuscript received by the Heat Transfer Division August 9, 1971; revised manuscript received December 15, 1971. Paper No. 71-WA/HT-30.

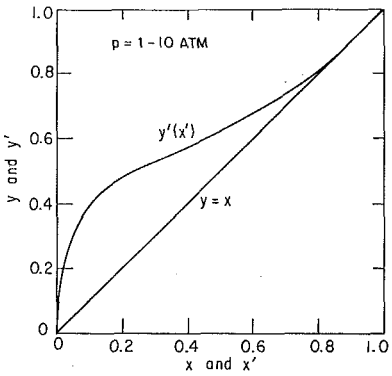


**Fig. 2 Binary phase diagram for water–ethanol mixtures**

tions, it is intended here, as a first analytical attempt, to seek a simple approximate analytical basis. The present analysis is one-dimensional along the axial direction in the vapor region. Proper consideration is given to the heat and mass transfer across the vapor–liquid interface and the binary phase equilibrium.

The complex momentum-conservation equation is further eliminated through the following simplifying assumptions:

1 Since the bulk velocity and molar flow rates in both the liquid and vapor phases are maximum near the evaporator–condenser interface and zero at the two ends, it should be a good approximation that they both vary linearly along the heat pipe from zero at the evaporator end to maximum at the evaporator–condenser interface and again to zero at the condenser end. This assumption implies also that the liquid and vapor molar densities are uniform along the heat pipe. This of course is an approximation because the molar-composition variation along the heat pipe results in changes in molar density.

2 The pressure variations inside the heat pipe are small, such that the binary phase equilibrium relation at a given pressure is applicable everywhere in the heat pipe.

**Mass-Balance Relations.** As first pointed out by Cotter [1], the gross mass balance for any section of the heat pipe results in the following relations:

$$G + L = 0 \tag{1}$$

and for one component

$$Gy + Lx = 0 \tag{2}$$

where the symbols are defined in the Nomenclature. Thus at any cross section along the heat pipe there exists, on the bulk basis,

$$x = y \tag{3}$$

In a phase diagram, the line $x = y$ is called the operation line, which will be different from the equilibrium curve $y'(x')$ characterizing the equilibrium condition at the vapor–liquid interface (Fig. 2).

For a differential section $dz$ of the heat pipe as shown in Fig. 1, the change in the molar flow rate of the more volatile component can be expressed as

$$Gdy = \pi DK(y^* - y)dz \tag{4}$$

where the overall mass-transfer coefficient $K$ depends on the particular flow conditions. Integration over the length $z$ results in

$$\int_{y_i}^{y} \frac{dy}{y^* - y} = \int_0^z \frac{\pi DK}{G}\, dz \tag{5}$$

which defines the relation beween $y$ and $z$ along the heat pipe.

An overall mass-balance relation can also be written. The relation specifies that the composition variation along the heat pipe must be in such a way that its average value over the entire heat pipe equals the initial mixture mole composition. Neglecting the amount of mixture in the vapor phase as compared to that in the liquid phase, there follows the overall mass balance

$$x_0 = \frac{1}{\rho_{f0}{}^l V_w} \int_l \rho_f{}^l A_w x dz \tag{6}$$

**Energy-Balance Relations.** In order to describe the axial temperature distribution in a two-component heat pipe, it was assumed, in an earlier analysis [2], that the heat is transferred axially only by conduction through the wall and the liquid–wick matrix. Subsequent qualitative analysis [3] as well as experimental observations [3–5] indicate, however, that the axial heat transfer is primarily due to the changes in latent heat as a result of evaporation and condensation along the heat pipe. For instance, it can be shown that on the basis of the observed temperature gradients in the experiments reported in the present paper, the heat that is transferred by axial conduction in the vapor, wick, and wall accounts for less than 3 percent of the total heat transferred through the heat pipe.

By neglecting axial heat conduction, the energy balance for the

## Nomenclature

$A_c$ = exterior surface area of the heat-pipe condenser
$A_w$ = open cross-sectional area of the wick
$c$ = molar density of mixture at $x_0$
$D$ = diameter of the vapor–liquid cylindrical interface
$\mathfrak{D}$ = binary mass diffusivity
$G$ = molar flow rate of vapor
$h_{fg}$ = heat of vaporization
$H$ = overall heat-transfer coefficient
$k$ = mass-transfer coefficient
$K$ = overall mass-transfer coefficient
$L$ = molar flow rate of liquid
$l$ = length of the heat pipe
$M$ = molecular weight
$m$ = slope of the phase equilibrium curve (Fig. 2)
$N$ = degree of separation defined in equation (13)
$p$ = absolute total pressure inside the heat pipe
$Q$ = rate of heat transferred across the liquid–vapor interface
$t$ = time
$T$ = temperature
$T_a$ = ambient temperature
$T_s$ = temperature at the heater surface
$u$ = bulk velocity of fluid
$v$ = specific volume
$V_w$ = void volume of the wick
$W$ = rate of heat produced in the heater
$x_v$ = initial mixture volume composition of the more volatile component
$x$ = liquid-mixture bulk mole composition of the more volatile component
$y$ = vapor-mixture bulk mole composition of the more volatile component
$y^*$ = vapor mole composition of the more volatile component in equilibrium with $x$
$z$ = axial distance as designated by Fig. 1
$\mu$ = liquid-mixture viscosity with $x_0$ mole composition
$\chi$ = dimensionless parameter in equation (24), a function of the mixture type
$\rho$ = molar density

**Superscripts**

$l$ = values for less volatile component
$m$ = values for more volatile component
$'$ = values at the vapor–liquid interface

**Subscripts**

$c$ = values for condenser
$e$ = values for evaporator
$f$ = liquid-phase values
$g$ = vapor-phase values
$i$ = values at the evaporator–condenser interface
0 = initial values

differential section $dz$ can be written on the basis of the changes in latent heat in the vapor phase alone:

$$dQ = h_{fg}{}^m d(Gy) + h_{fg}{}^l d[G(1 - y)] \tag{7}$$

where $dQ$ is the differential heat rate across the vapor–liquid interface. In setting up equation (7), equation (1) has been used. The differential heat rate $dQ$ can be expressed in terms of an overall heat-transfer coefficient $H$:

$$dQ = -\pi DH[T(z) - T_a] \tag{8}$$

where $H$ takes into account all thermal resistances between the vapor inside and the ambient outside. It should be noted that the ambient temperatures (or equivalent ones) of the condenser and evaporator sections are different.

Integration of equation (7) over the condenser length gives

$$Q_{\text{out}} = h_{fg}{}^m G_i y_i + h_{fg}{}^l G_i(1 - y_i) \equiv Q_i \tag{9}$$

where $Q_i$ is the total heat rate across the interface between evaporator and condenser. Equation (8) after integration leads to

$$Q_{\text{out}} = \int_{l_c} \pi DH[T(z) - T_{ac}]dz \tag{10}$$

Similar integrations can be made for the evaporator section and and it can easily be established that

$$Q_i = Q_{\text{out}} = Q_{\text{in}} \tag{11}$$

**Binary Phase Equilibrium Relations.** Despite the bulk composition relation $x = y$, which resulted from the overall mass-balance relations, local compositions at the liquid–vapor interface should satisfy the binary phase equilibrium relation

$$f(x', y', p, T) = 0 \tag{12}$$

which is often presented in the form of a phase diagram for a specific binary mixture [8]. The operational characteristics of two-component heat pipes differ greatly for different types of phase diagrams [3].

The mass- and energy-balance relations combined with the equilibrium relation complete the present analytical framework. The primary system parameters which are usually known a priori are the heat input or output ($Q_{\text{in}}$ or $Q_{\text{out}}$), the initial liquid-mixture composition ($x_0$), and the condenser ambient temperature ($T_{ac}$). Once these three parameters are given, the above analytical framework can be employed to obtain all the information regarding the two-component-heat-pipe operation, including the operating pressure as well as temperature or composition (which are related to each other) distributions. Actual numerical calculations, however, are rather involved, because the governing relations are closely related and the binary phase equilibrium relation is of the implicit form (i.e., presented in diagrams) and highly complicated. The calculations presented below are based on the trial-and-error method.

**Degree of Separation.** A measure of the degree of separation commonly used in distillation-column studies [6] is the theoretical number of trays defined as

$$N = \int_{y_i}^{y} \frac{dy}{y^* - y} \tag{13}$$

The parameter has a precise physical meaning in differential distillation columns composed of distillation trays. When a tray is 100 percent efficient, the bulk composition of the vapor in contact with the tray changes from $y$ to $y^*$ and the value of $N$ which is defined as

$$N = \Sigma \frac{\Delta y}{y^* - y} \tag{14}$$

changes by one. Thus $N$ designates the number of trays in the system. The same parameter has been adopted for use in continuous columns but defined in the integral form, equation (13).

**Solution Procedure.** It is intended here to demonstrate through implicit relationships the way that the solution can be obtained from given system parameters, i.e., $Q$ ($Q_{\text{in}}$ or $Q_{\text{out}}$), $x_0$, and $T_{ac}$. In general $y^* = y^*(y, p)$, and according to equation (13), $N = N(y_i, y, p)$. Based on equation (5), however, $N$ can also be written as

$$N = \int_0^z \frac{\pi DK}{G} dz \tag{15}$$

where $K$ and $G$ depend on the flow conditions. With the assumption of linear variations of $G$ and average velocity in both the evaporator and condenser sections, the flow conditions are completely prescribed when $G_i$ is given. From equation (9) which shows $G_i(Q, p, y_i)$, there follows $N = N(Q, p, y_i, z)$. The two implicit relations of $N$ imply that

$$y = y(y_i, p, Q, z) \tag{16}$$

Combining equations (3), (6), and (16) results in

$$x_0 = x_0(Q, p, y_i) \tag{17}$$

The above relation can be presented in graphical form as will be seen later.

A trial-and-error method of calculation is then instituted with an assumption of pressure. Based on the given values of $Q$ and $x_0$ and the assumed $p$, equation (17) yields the value of $y_i$ that in turn determines $y(z)$ from equation (16). With $p$ and $y(z)$ known, $T(z)$ can be calculated through the use of the binary phase equilibrium diagram, equation (12). Equation (10) is then employed to determine $T_{ac}$. If this value of $T_{ac}$ does not agree with the value given initially, a new pressure is assumed and the calculations are repeated until the calculated $T_{ac}$ equals the given value. The predicted $T(z)$ and $p$ can be compared with measurements.

For the specific case of water–ethanol mixtures used in the present experimental study, the calculation is considerably simplified due to the very weak dependence of $y^*$ and $h_{fg}$ on pressure in the experimental pressure range from 1 to 10 atm. As a result, the pressure-dependence in the relations for $N$ and in equations (16) and (17) can all be neglected from a practical point of view. Indeed, the trial-and-error solution can be achieved with relative ease.

## Experimental Setup and Measurements

In order to substantiate the validity of the theoretical framework, a series of experiments was carried out for the purpose of a detailed comparison between predictions and measurements. These experiments are quite similar to those reported before [3] and involve essentially the same apparatus and working fluid (water–ethanol mixtures), but as a result of previous experience, more refined experimental preparation and measurements as well as data reduction have been instituted in the present sequence of experiments. In particular, the present experiments were performed with the heat pipe in the horizontal position. This would reduce the possibility of having any undesirable wick-wetting phenomena that might occur in a condenser-up vertical position. It should be pointed out, however, that no appreciable difference in the experimental performance has been noticed between the corresponding vertical and horizontal cases.

One major system parameter that cannot be easily determined by direct measurements is the heat input to the heat pipe. It must be calculated by subtracting the heat loss from the heater to the ambient from the heat input to the heater. An accurate method of estimating the heater heat loss is essential to this calculation, especially when this heat loss accounts for a substantial portion of the total heat input to the heater as in the present setup. To eliminate the uncertainty in determining the heat input to the heat pipe, a new method (i.e., different from

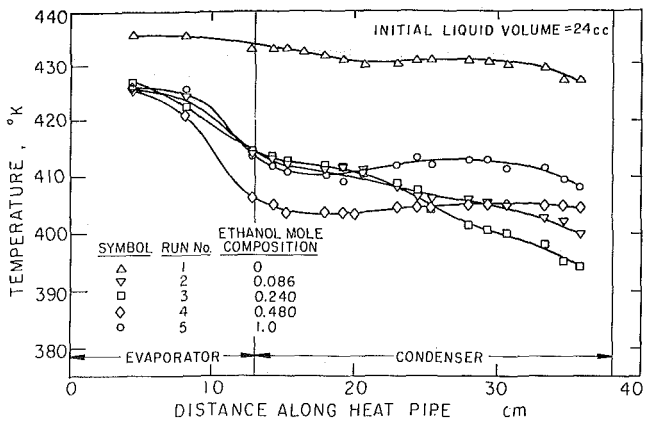


Fig. 3 Measured exterior wall temperature distribution

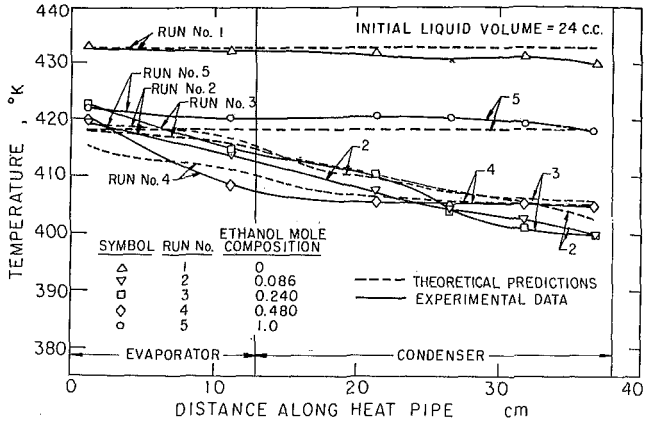


Fig. 4 Measured and predicted vapor temperature distributions

Table 1 Primary and deduced experimental data of system parameters

| Run No. | $x_v$ | $p$(atm) | $T_a$(°K) | $T_s$(°K) | $W$(watt) | $x_0$ | $Q_{in}$(watt) |
|---|---|---|---|---|---|---|---|
| 1 | 0 | 5.61 | 299.9 | 348.6 | 155.0 | 0 | 51.5 |
| 2 | 0.23 | 4.27 | 295.3 | 345.8 | 151.5 | 0.086 | 40.5 |
| 3 | 0.50 | 4.67 | 296.6 | 347.2 | 150.0 | 0.240 | 39.0 |
| 4 | 0.75 | 5.49 | 299.4 | 350.1 | 150.5 | 0.480 | 39.5 |
| 5 | 1 | 8.89 | 291.4 | 341.2 | 153.5 | 1 | 45.1 |

Table 2 The operating pressure (in atm) inside the heat pipe

| Run No. | 1 | 2 | 3 | 4 | 5 |
|---|---|---|---|---|---|
| Predicted | 5.66 | 4.10 | 4.60 | 5.66 | 8.75 |
| Measured | 5.61 | 4.27 | 4.67 | 5.60 | 8.89 |

the previous one [3]) for calculating the heat loss from the heater was used. The heater was turned on with the dry heat pipe in the experimental position. In steady state the temperature at a specific point on the heater surface was measured and its difference from the ambient temperature $\Delta T$ was calculated. A curve was plotted showing the variation of power input to the heater with $\Delta T$. In actual experiments, this curve was then taken as a basis for calculation of heat loss from the heater as a function of its surface temperature difference from the ambient. The results were within 2 percent deviation of those based on the previous calculation method [3].

Before each experiment, in order to dry out the heat pipe, it was left for 3 hr in the oven at a low power input. Then it was washed with the same mixture that was to be used in the experiment. The heat pipe was then placed in the horizontal position and inserted into the opening of the heater that has a depth of 12 cm. Heat was applied to the heat pipe until a steady volume of vapor was seen to be blowing out of the hole on the flange. The hole was then sealed. Since some amounts of the two components were boiled off when displacing the noncondensible gases from the pipe, the exact quantities of the two components left inside the heat pipe would be slightly less than the initial values. Next, the power input to the heat pipe was adjusted at the desired level and the whole system was covered by a shield. The metallic shield was used for stabilizing the free-convection mode of heat transfer, between the heat-pipe condenser and the ambient, which is very sensitive to the ambient air currents. The steady-state condition (e.g., pressure remained constant) for each test was reached in approximately 3 hr. Each of the reported readings was made 5 hr after starting the heat pipe. Three measurements were made in 15-min time intervals to insure the existence of the steady state, and the average readings were recorded.

Experimental measurements and reduced data are presented in Table 1 and Figs. 3 and 4. The temperature readings inside the heat pipe were made along the centerline in the vapor phase and were used to determine the vapor or the liquid bulk mole composition of ethanol at the heat-pipe pressure at any section along the heat pipe.

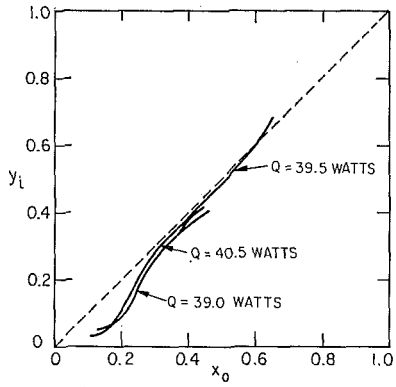


Fig. 5 Functional dependence among $y_i$, $Q$, and $x_0$

## Results and Discussion

In each of the experiments, the known system parameters are the heat load of the heat pipe ($Q_{in}$ or $Q_{out}$), the initial mixture mole composition ($x_0$), and the condenser ambient temperature ($T_{ac}$). These given values are used to predict, in accordance with the theoretical framework described above, the pressure inside the heat pipe and the axial temperature distribution in the vapor region. The predicted values are then compared with those measured in each experiment.

The detailed calculation of predicted behaviors follows closely what was indicated in the Solution Procedure. First a set of curves designating $N(y_i, y)$ was obtained by using equation (13) and Fig. 2. Another set of curves for $N(y_i, z)$ for given values of $Q$ was also calculated (see Appendix A). Combination of these two sets of curves gave the relation $y(y_i, z)$ which was then integrated according to equation (6) to yield $x_0(y_i, Q)$ as shown in Fig. 5. Thus the given values of $x_0$ and $Q$ in each experiment were sufficient to determine the value of $y_i$ and also $y(z)$. The trial-and-error method was then used to determine $p$ corresponding to the given value of $T_{ac}$ by way of the phase equilibrium diagram and the energy-conservation relation, equation (10). The overall heat-transfer coefficient $H$ was calculated on the basis of free convection and radiation from a horizontal cylinder of uniform temperature. The calculated $H$ agrees well with that determined from measurements (see Appendix B).

Table 2 shows the predicted values of pressure for each run, and the prediction is in good agreement with the measurement in

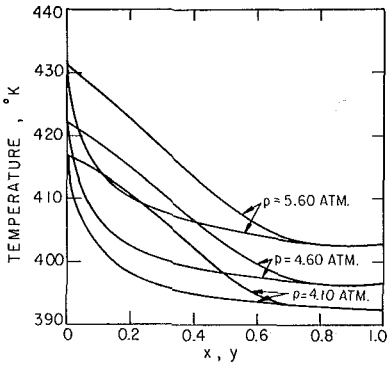


**Fig. 6 Binary phase equilibrium diagram of water–ethanol mixtures at different pressures**

all cases. Fig. 6 shows the binary phase equilibrium diagrams for the water–ethanol mixture corresponding to these calculated pressures [8]. Predicted temperature distributions are shown in Fig. 4 in comparison with measured values. Again, the general agreement is quite remarkable in view of the many simplifications made in the analysis.

It should also be noted that the $y_i(x_0)$ curves as shown in Fig. 5 are close to the relation $y_i\ (=x_i) = x_0$. This result is indeed expected by simple physical reasoning, but by assuming $y_i = x_0$ in the beginning of the calculation process, a much more rapid calculation can be achieved.

Table 3 presents the experimental and the predicted values of the degree of separation for both the evaporator and the condenser sections as defined by the relations

$$N_e = \int_{y_i}^{y_e} \frac{dy}{y^* - y} \tag{18}$$

$$N_c = \int_{y_i}^{y_c} \frac{dy}{y^* - y} \tag{19}$$

Good agreement exists between the experimental and predicted values of $N_c$. The predicted results for the evaporator section, however, are only in fair agreement with those obtained by measurement. This difference is probably due to the relatively complicated heat- and mass-transfer mechanisms in the evaporator section of the heat pipe which were not considered in the present analysis.

The analysis was also applied to the experimental results reported by Feldman [4]. In that paper, a possible error of 3 percent in the temperature measurement has been indicated. The possible range of $N$ in his experiments was therefore determined and compared with the predicted results. The calculation was performed only for the condenser section in view of the fact that only in this section can the vapor temperature distribution be reliably inferred from the reported exterior wall temperatures. The bulk mole composition of the mixture at the evaporator–condenser interface was taken equal to the initial mixture mole composition. The experimental and predicted values of $N_c$ are given in Table 4 for different initial mixture compositions.

Recently, Hessel and Jankowski [11] reported experiments on a two-component gas-controlled heat pipe in which they obtain complete separation of the two components. They used a lithium–sodium mixture as the working fluid and argon as the controlling gas. In order to apply the present analysis to their experiments, effort was made to obtain information on the vapor–liquid phase equilibrium diagram of lithium–sodium mixtures. Use of this diagram would result in the determination of the theoretical number of trays $N$ necessary for complete separation. There exists, however, no information on the vapor–liquid phase equilibrium diagram for lithium–sodium mixtures, nor any information on the liquid or vapor mass diffusivity. Consequently, only a qualitative indication of the lithium–sodium separation characteristics can be made. Based on the physical properties of pure lithium and sodium [12] and by using equation (27), it was estimated that the theoretical number of trays in the lithium–sodium heat pipe is about twice larger than that in a water–ethanol heat pipe. This is mainly due to the high heats of vaporization of lithium and sodium. Thus, the 10-cm length of the transition zone as reported in their experiments is quite plausible in accordance with the present analysis.

**Table 3 Comparison of the values of $N$**

| Run No. | 2 | 3 | 4 |
|---|---|---|---|
| Experiment of $N_c$ | 1.60 | 2.13 | 1.65 |
| Theoretical $N_c$ | 1.57 | 1.68 | 1.93 |
| Experiment of $N_e$ | 0.85 | 0.9 | 0.5 |
| Theoretical $N_e$ | 0.29 | 0.30 | 0.58 |

## References


1 Cotter, C. P., "Theory of Heat Pipes," LA-3246-MS, Los Alamos Scientific Laboratory, Los Alamos, N. M., Mar. 1965.

2 Katzoff, S., "Heat Pipes and Vapor Chambers for Thermal Control of Spacecraft," in: *Thermophysics of Spacecraft and Planetary Bodies*, Academic Press, New York, N. Y., 1967, pp. 761–818.

3 Tien, C. L., "Two-component Heat Pipes," in: *Thermophysics: Application to Thermal Design of Spacecraft*, Academic Press, New York, N. Y., 1970, pp. 423–436.

4 Feldman, K. T., Jr., and Whitlow, G. L., "Experiments with a Two-Fluid Heat Pipe," *Proceedings of the 4th Intersociety Energy Conversion Engineering Conference*, Sept. 1969.

5 Barsch, W. O., Winter, E. R. F., Schoenhals, R. J., and Viskanta, R., "The Study and Classification of Two and Multi-Component, High Thermal Conductance Devices," NASA Interim Report, School of Mechanical Engineering, Purdue University, Lafayette, Ind., Aug. 20, 1970.

6 Treybal, R. E., *Mass Transfer Operations*, McGraw-Hill, New York, N. Y., 1952, p. 229.

7 Marcus, B. D., and Fleischman, G. L., "Steady State and Transient Performance of Hot Reservoir, Gas-Controlled Heat Pipes," ASME Paper No. 70-HT/SpT-11.

8 Chu, T. C., et al., *Vapor Liquid Equilibrium Data*, T. W. Edwards, Ann Arbor, Mich., 1954, pp. 260–271.

9 Bird, R. B., Stewart, W. E., and Lightfoot, E. N., *Transport Phenomena*, John Wiley & Sons, New York, N. Y., 1960, pp. 655, 537, and 515.

10 Kreith, F., *Principles of Heat Transfer*, International Textbook Co., Scranton, Pa., 1967, pp. 238, 342.

11 Hessel, M. M., and Jankowski, P., "Two-metal Heat Pipe Oven: Operation, Dynamics, and Use in Spectroscopic Investigations," *J. Appl. Phys.*, Vol. 43, 1972, pp. 209–211.

12 Miller, R. R., "Physical Properties of Liquid Metals," in: *Liquid Metals Handbook*, R. N. Lyon, ed., 2nd ed., U. S. Office of Naval Research, Washington, D. C., 1952.


## APPENDIX A

This Appendix presents the detailed calculation of $N(Q, p, y_i, z)$ on the basis of equation (15).

Consider first the overall mass-transfer coefficient $K$. Based on the gas-phase resistance, $K$ is defined as [9]

$$\frac{1}{K} = \frac{1}{k_g} + \frac{m}{k_f} \tag{20}$$

The relatively high velocity and large mass-transfer coefficient in the gas phase makes $k_g$ much larger as compared with $k_f$ and thus $(1/k_g)$ can be neglected in equation (20). This was also confirmed by a few preliminary calculations. Equation (15) can then be expressed as

**Table 4 Comparison of the experimental and theoretical values of $N_c$ for Feldman's experiments**

| Input power (watt) | 47.5 | 37.5 | 47.5 | 37.5 | 47.5 | 37.5 |
|---|---|---|---|---|---|---|
| $x_v$ | 0.25 | 0.25 | 0.50 | 0.50 | 0.75 | 0.75 |
| Experimental $N_c$ | 0 | 0–0.7 | 5.55–12 | 1.45–7.90 | 4.95–11.40 | 4.55–11 |
| Theoretical $N_c$ | 0.88 | 1.70 | 5.25 | 5.30 | 5.35 | 5.60 |

Table 5 Theoretical and experimental values of the overall heat-transfer coefficient (watt/cm²-deg K)

| Run No. | 1 | 2 | 3 | 4 | 5 |
|---|---|---|---|---|---|
| Theoretical | $1.97 \times 10^{-3}$ | $1.82 \times 10^{-3}$ | $1.83 \times 10^{-3}$ | $1.83 \times 10^{-3}$ | $1.87 \times 10^{-3}$ |
| Experimental | $2.01 \times 10^{-3}$ | $1.87 \times 10^{-3}$ | $1.86 \times 10^{-3}$ | $1.85 \times 10^{-3}$ | $1.90 \times 10^{-3}$ |

$$N = \int_0^z \frac{\pi D k_f}{mG}\, dz \tag{21}$$

In calculating $k_f$, the falling-film model of mass transfer [9] was used

$$k_f = \frac{1}{v_f{}^{ml}} \left(\frac{\mathfrak{D}_f}{\pi t}\right)^{1/2} \tag{22}$$

where

$$t = \int_0^z \frac{dz}{u(z)} \tag{23}$$

and $\mathfrak{D}_f$ is the average of the diffusivities of dilute water–ethanol mixtures and ethanol–water mixtures evaluated at $T = 400$ deg K [9]

$$\mathfrak{D}_f = 7.4 \times 10^{-8} \frac{(\chi^m M^m)^{1/2} T}{\mu (v_f{}^l)^{0.6}} \tag{24}$$

With the assumption of linear variation of $u$, there result

$$\begin{aligned} u_f &= u_{fi}(1 + z/l_e) \qquad z \leq 0 \\ u_f &= u_{fi}(1 - z/l_c) \qquad z \geq 0 \end{aligned} \tag{25}$$

and from equation (23)

$$\begin{aligned} t &= \frac{l_e}{u_{fi}} \ln\left(1 + \frac{z}{l_e}\right) \qquad z \leq 0 \\ t &= -\frac{l_c}{u_{fi}} \ln\left(1 - \frac{z}{l_c}\right) \qquad z \geq 0 \end{aligned} \tag{26}$$

Substitution of equations (22) and (26) into equation (21) yields

$$\begin{aligned} N &= \frac{2cDl_e{}^{1/2}}{G_i m_e} \left[-\pi \mathfrak{D}_f u_{fi} \ln\left(1 + \frac{z}{\rho_e}\right)\right]^{1/2} \qquad z \leq 0 \\ N &= \frac{2cDl_c{}^{1/2}}{G_i m_c} \left[-\pi \mathfrak{D}_f u_{fi} \ln\left(1 - \frac{z}{\rho_c}\right)\right]^{1/2} \qquad z \geq 0 \end{aligned} \tag{27}$$

Since $G_i$ can be obtained from given values of $Q$, $p$, and $y_i$ through equation (9), and $u_{fi}$ from $G_i$ and $x_i$ ($x_i = y_i$), the relation $N(Q, p, y_i, z)$ is established.

## APPENDIX B

This Appendix is concerned with the calculation of the overall heat-transfer coefficient $H$. It can easily be shown that the thermal resistance due to the liquid–wick matrix and pipe wall was negligible as compared to that from the pipe wall to the ambient. Thus $H$ was calculated on the basis of free convection and radiation from a horizontal cylinder of uniform temperature $T_{av}$ [10]

$$H = h_c + \frac{\sigma \epsilon (T_{av}{}^4 - T_{ac}{}^4)}{(T_{av} - T_{ac})} \tag{28}$$

where $h_c$ is the free-convection contribution, $\sigma = 5.668 \times 10^{-12}$ watt/cm²-deg K⁴, and $\epsilon \approx 0.7$.

In order to show the validity of this theoretical estimate of $H$, experimental values of $H$ were also calculated from the following relation:

$$H = \frac{Q}{A_c(T_{av} - T_{ac}) + A_f(T_f - T_{ac})} \tag{29}$$

where $T_{av}$ is the average condenser wall temperature, $T_f$ the average end-flange temperature, $A_c$ the condenser area, and $A_f$ the end-flange area. The comparison is presented in Table 5.

**H. Y. PAK**
Head,
Department of Ordnance Engineering,
Korean Military Academy,
Seoul, Korea

**E. R. F. WINTER**
Professor.

**R. J. SCHOENHALS**
Professor.
Assoc. Mem. ASME

School of Mechanical Engineering,
Purdue University,
Lafayette, Ind.

# Convection Heat Transfer in a Contained Fluid Subjected to Vibration[1]

*An experimental investigation of the effect of vibration on convection heat transfer from a horizontal cylinder has been performed for the case in which the entire system, both the heated surface and the fluid, are simultaneously subjected to vibration. A 0.032-in-dia horizontal wire served as the heated surface. The ranges of the experimental variables were: temperature difference, 10 to 100 deg F; vibration frequency, 30 to 240 Hz; acceleration amplitude, 1 to 5 g's. Improvements in heat transfer due to vibration were observed, with the maximum increase being 200 percent. According to dimensional analysis, the Nusselt number depends on five independent parameters. A dimensionless correlation describing the measured heat-transfer data is given.*

## Introduction

During recent years there has been considerable interest in the effect of oscillatory phenomena on convection heat transfer. Most previous studies in this area can be classified according to two different categories. The first category is characterized by the external oscillatory motion being imposed on the surface itself which is immersed in an otherwise undisturbed fluid as shown in Fig. 1(*a*) [1–6].[2] In the second category the oscillatory motion is imposed on the fluid medium surrounding the surface which is held stationary as shown in Fig. 1(*b*) [7–9]. Both techniques have the same objective of creating an oscillating relative velocity between the heated surface and the adjacent fluid medium. However, in a number of practical applications the heated surface and the fluid itself are both subjected to the vibration simultaneously, Fig. 1(*c*). A special case of simultaneous vibration of both the heated surface and fluid arises when the enclosing surface for the fluid is heated and vibrated, Fig. 1(*d*). This situation appears to have considerable importance since it is encountered frequently in practical applications. An example is the cryogenic oxidizer supply tank in a liquid-fuel rocket which is subjected to severe vibrations from its engines [10]. Few investigators [11–13] have been concerned with simultaneous vibration of both the heated surface and the fluid adjacent to it.

In the present experimental study a 0.032-in-dia platinum wire was mounted inside a container which was filled with water. This arrangement enhanced the convenience and precision

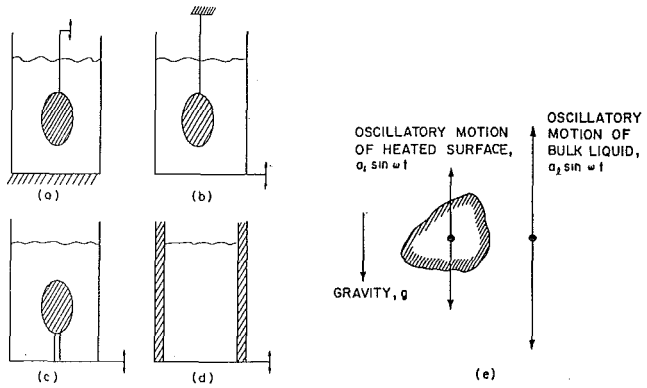


**Fig. 1 Heat-transfer systems exposed to vibration**

associated with the heat-transfer measurements. Vibration was applied at the base of the container, thus imposing vibratory motions on the heated surface and the fluid simultaneously and in phase. This gave rise to relative motions between the heated surface and the fluid which were considerably smaller than those associated with most of the previous investigations mentioned above [1–9], although the acceleration levels used were comparable. Penney and Jefferson [3] have investigated small relative motions of the order of magnitude of those encountered in the present study, however. Sizable improvements in heat transfer due to vibration were observed in the present work with the maximum increase being 200 percent. In evaluating the experimental results consideration is given to factors which influence the magnitude of the relative motion, the mechanism which was found to provide the most important contribution to the increase in the heat-transfer rate. However, when the relative motion becomes negligible, which occurs under some conditions of simultaneous vibration, the vibrational acceleration level of the system can still produce an effect on the heat-transfer

[1] Results presented in this paper are based on a PhD thesis submitted to the faculty of Purdue University, Lafayette, Ind., reference [21].

[2] Numbers in brackets designate References at end of paper.

Based on a paper contributed by the Heat Transfer Division and presented at the Winter Annual Meeting, New York, N. Y., November 29–December 3, 1970, of The American Society of Mechanical Engineers. Revised manuscript received by the Heat Transfer Division April 5, 1971.

rate. This mechanism has not been studied in previous investigations, apparently because it has been outweighed by the influence of large relative motions. From results of the present study it was found that this effect can be significant. Further details and results of this investigation can be found in reference [14], which forms the basis for this paper.

## Discussion of the Problem

Consider the situation illustrated in Fig. 1(*c*) when the heated surface and the surrounding fluid in the vicinity of that surface are vibrated vertically and in phase due to vibratory motion of the container base, $a_0 \sin \omega t$. In general there is some relative motion between the two for the following reasons:

1 The fluid column is not rigid, so that the bulk liquid in the vicinity of the heated surface does not have the same motion as the container base. The compressibility of the fluid column is a result of the compressibility of the liquid itself and the lateral flexing of the container wall.

2 The support for the heated surface is not rigid so that the surface does not have the same motion as the container base.

The situation in the vicinity of the heated surface is illustrated in Fig. 1(*e*). Note that in general the vibrational amplitudes for the surface and for the bulk liquid are not the same, and incidentally the vibrational amplitude of the container base is different from both of these amplitudes. A study of the dimensionless parameters associated with the heat-transfer problem for this situation revealed that

$$\overline{\mathrm{Nu}} = F(\mathrm{Gr}, \mathrm{Pr}, \mathrm{Re}, \Omega, \mathrm{Ac}) \tag{1}$$

where the Reynolds number, Re, is based on the vibratory relative velocity between the heated surface and the bulk liquid. $\Omega$ and Ac represent the dimensionless frequency and acceleration, respectively. Equation (1) contains the usual parameters associated with free-convection heat transfer, namely $\overline{\mathrm{Nu}}$, Gr, and Pr. In addition, it shows that when vibration is present both the motion of the liquid relative to the surface (Re parameter) and the vibratory acceleration (Ac parameter) may play important roles in affecting the heat-transfer rate. $\Omega$ indicates the frequency of the imposed vibration and is associated with the extent of retardation due to the inertia of the system.

In the absence of vibration all three of the vibratory parameters are zero, and ordinary free convection occurs. In this case equation (1) is reduced to

$$\overline{\mathrm{Nu}}_0 = F_0(\mathrm{Gr}, \mathrm{Pr}) \tag{2}$$

For the special case in which the heated surface is stationary, but with vibratory motion imparted to the fluid, two additional parameters (Re and $\Omega$) are required to define the features of the imposed vibration (frequency and amplitude). The third vibratory parameter, Ac, is zero since the heated surface does not move. Thus for this situation equation (1) becomes

$$\overline{\mathrm{Nu}} = F_1(\mathrm{Gr}, \mathrm{Pr}, \mathrm{Re}, \Omega) \tag{3}$$

Heat-transfer measurements for stationary heated cylinders in the presence of acoustically generated fluid oscillations have been reported by many investigators including those associated with references [7–9].

For the special case in which the bulk fluid is stationary, but the heated surface is oscillated, specification of any two of the dimensionless vibratory parameters allows calculation of the third. This is easily verified by the fact that $\sqrt{2}\ \mathrm{Re}\ \Omega = \mathrm{Ac}$ for this situation. Thus a correlation with four independent dimensionless groups is again obtained.

Dougall, Chang, and Fand [15] have also shown that there are four independent dimensionless groups, in agreement with equation (3). There is some choice involved, of course, in specifying which of the parameters are to be used when either the heated surface or the bulk fluid is stationary. For example, $\mathrm{Re}/\Omega = a_l/\sqrt{2}\ d$ or $a_s/\sqrt{2}\ d$ depending on whether the fluid or the heated surface is oscillated. Hence for either of these situations equation (3) can be replaced by

$$\overline{\mathrm{Nu}} = F_2(\mathrm{Gr}, \mathrm{Pr}, \mathrm{Re}, a/d) \tag{4}$$

where $a$ refers either to $a_l$ or to $a_s$. Penney and Jefferson [3] have presented measurements obtained with an oscillating wire immersed in a stationary container filled with liquid and have discussed the possibility of applying the correlation indicated by equation (4). In correlating their data, however, only Gr, Pr, and Re were considered, but it was concluded that future research should include attempts to investigate the effect of $a/d$ as an independent dimensionless group for that situation.

In the present study three vibratory parameters, rather than two, were necessary to completely specify the vibratory conditions (frequency, heated-surface amplitude, and amplitude of the bulk fluid in the vicinity of the heated surface). This, of course, resulted in the use of three dimensionless vibratory parameters and led to the implicit relation described by equation (1).

A study of the literature revealed that there is no universal

## Nomenclature

Ac = dimensionless vibratory acceleration, $a_s\omega^2 d^3/\nu^2$
$a$ = amplitude of vibration
$a_l$ = amplitude of displacement of liquid
$a_{l0}$ = amplitude of displacement of liquid with respect to container base
$a_0$ = amplitude of vibration of container base
$a_s$ = amplitude of vibration of heated surface
$a_{s0}$ = amplitude displacement of heated surface with respect to container base
$\hat{a}$ = amplitude of displacement of liquid with respect to heated surface, $|a_l - a_s|$
$c$ = wave velocity of the system
$d$ = diameter of wire
$F, F_0, F_1, F_2$ = functions
$f$ = frequency
$g$ = acceleration due to gravity
$G$ = dimensionless acceleration amplitude of container base, $a_0\omega^2/g$
Gr = Grashof number, $g\beta\Delta T d^3/\nu^2$
$\bar{h}$ = average heat-transfer coefficient
$\bar{h}_0$ = average heat-transfer coefficient in free convection
$k$ = thermal conductivity
$L$ = height of liquid in container
$\overline{\mathrm{Nu}}$ = average Nusselt number in the presence of vibration, $\bar{h}d/k$
$\overline{\mathrm{Nu}}_0$ = average Nusselt number for free convection, $\bar{h}_0 d/k$
$P$ = pressure
$P_u$ = ullage pressure
$\Delta P$ = amplitude of fluctuating pressure
Pr = Prandtl number
Ra = Rayleigh number, GrPr
Re = Reynolds number, $\hat{a}\omega d/\sqrt{2}\nu$
$\Delta T$ = temperature difference between heated surface and bulk fluid
$t$ = time
$V$ = relative velocity of water with respect to test wire
$\beta$ = thermal expansion coefficient
$\nu$ = kinematic viscosity
$\xi$ = distance measured downward from liquid surface
$\rho$ = density
$\Psi$ = Ac parameter in equation (8), $\dfrac{\mathrm{Ac}^{0.46}}{\mathrm{Ra}^{0.21}\Omega^{0.1}}$
$\omega$ = angular frequency
$\Omega$ = dimensionless frequency, $\omega d^2/\nu$

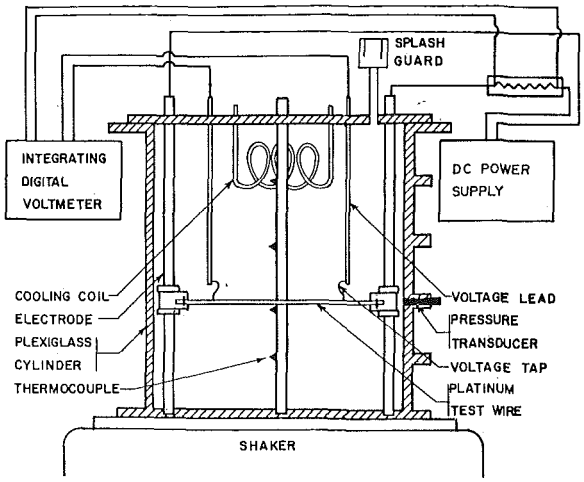


**Fig. 2 Schematic diagram of experimental apparatus**

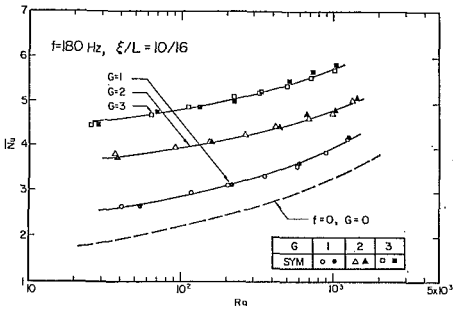


**Fig. 3 Effect of vibration on heat transfer at 180 Hz and at various acceleration levels**

agreement among various investigators concerning the specific relationship between $\overline{Nu}$ and the four independent dimensionless groups, corresponding to equation (3) or equation (4); for the two cases in which either the heated surface or the bulk fluid is stationary. In attempting to correlate vibratory heat-transfer data it has been common in the past to combine some of the parameters and even to completely disregard one of the four, as was done by Penney and Jefferson [3], for example, in the case of the $a/d$ parameter mentioned above. These limitations have caused considerable scatter of the data with respect to any individual correlation. In the current study experimentally determined values of $\overline{Nu}$ were correlated in terms of the five independent parameters appearing in equation (1) for the general case in which both the fluid and the heated surface are vibrated. Comparisons are made with the measurements and with correlations given by previous investigators [1–6, 16–18, 22].

## Experiments

The experimental facility consisted of the convection apparatus, an electrodynamic vibrator, and a data-acquisition system. The test section itself was a horizontal 0.032-in-dia platinum wire which was used simultaneously as a resistance thermometer and as a heated surface. The wire was installed in the convection apparatus which was mounted on the horizontal shaker table. A schematic diagram of the apparatus is given in Fig. 2. The cylindrical container of the liquid was made of Plexiglas tubing, 18 in. in length with $5^1/_2$ in. inside diameter and $^1/_2$ in. wall thickness. Four Plexiglas blocks were glued to the outside of the Plexiglas cylinder and served for the installation of pressure transducers. The test apparatus was securely mounted on the electrodynamic vibrator which possessed a frequency range from 10 to 3000 Hz and was capable of delivering forces up to a maximum of 5000 lb.

Distilled and deionized water of a high degree of purity was used as the test fluid. The height of the water column was always maintained at 16 in. Since the inner vertical clearance of the cylindrical container was 18 in., the surface of the water remained free during all experiments. After obtaining the desired vibratory conditions (frequency $f$ and acceleration level $G$), the oscillating pressure in the water in the plane of the test wire was measured with a fast-response pressure transducer. The transducer signal was conditioned with a charge amplifier and was displayed on an oscilloscope.

The test wire was heated with a continuously adjustable d-c power supply. At a desired constant electrical current, the voltage drops across the test wire and a shunt resistor connected in series with the heating wire were measured and printed with a digital voltmeter. The voltage drop across the shunt resistance provided a measure of the current applied to the heated wire. The heat flux from the test wire to the water was determined from the voltage and current measurements. Axial-conduction losses from the test wire were neglected since it was determined that these losses were less than 1 percent of the energy transferred directly to the fluid.

The test wire was calibrated as a resistance thermometer by immersing it in a constant-temperature bath, passing a direct current of approximately 50 milliamp through it, and measuring the current and the voltage drop across the wire. It was established that with currents of this small magnitude the temperature of the wire was not appreciably different from the measured temperature of the bath.

Among four thermocouples mounted on a vertical Plexiglas rod, Fig. 2, a pair of thermocouples was used for measurement of the bulk water temperature at the vertical location of the heated wire. The horizontal distance between the hot junction of the thermocouple and the test wire was $1^1/_2$ in. After each series of experiments for given frequency and acceleration levels, the bulk water was cooled down to the original temperature with the cooling coil, Fig. 2. A waiting period of approximately 20 min followed each series of experiments in order to allow subsidence of any free-convective flow due to still-existing temperature differences between the cooling coil and the water.

## Results

In order to assure that the experimental techniques were appropriate for the present investigation, a series of free-convection studies was performed prior to the measurements in the presence of vibration. Results of these free-convection experiments and comparison with an accepted correlation are given in reference [14].

Vibratory experiments were performed with the horizontal test wire at various depths beneath the surface of the water. However, most of the data were obtained with the test wire located 10 in. beneath the surface of the water, while a few experiments were performed with the wire located at 1 and 13 in. below the water surface, respectively. In order to minimize the sloshing effect, the acceleration level $G$ was restricted to values below 2 when the wire was located only 1 in. beneath the free surface. For the other wire locations $G$ was restricted to values no greater than 5 in order to obtain reproducible data under single-phase conditions. Large acceleration levels lead to the formation of bubbles in the liquid [20]. These two-phase conditions were avoided for purposes of this investigation.

Four physical variables could be controlled experimentally; they were $\xi/L$, $G$, $f$, and $\Delta T$. Typical results obtained under vibratory conditions for a frequency of 180 Hz are presented in Fig. 3 as plots of $\overline{Nu}$ versus Ra on semi-log coordinates with $G$ as a parameter. In order to check the reproducibility of the data, two sets of experiments were performed on different days for each vibratory condition. These two sets of results are distinguished by the open and closed symbols. The data for each set of conditions were fitted to a single solid line with the free-convection curve for nonvibratory conditions shown as a dashed line for purposes of comparison. The deviation between each solid

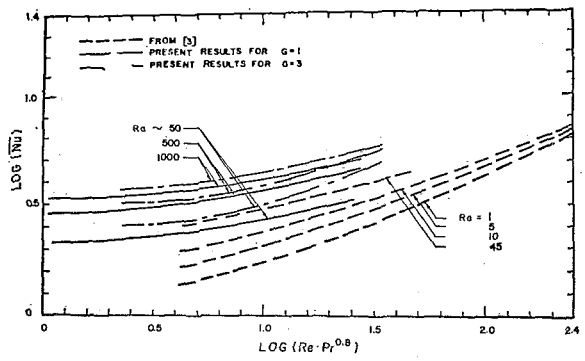


Fig. 4 Comparison of present results with results of Penney and Jefferson [3]

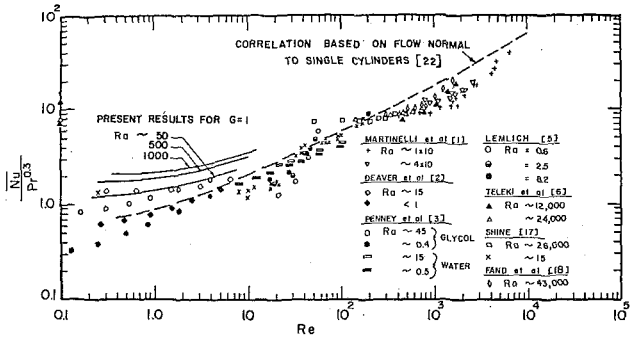


Fig. 5 Comparison of present results with those of other investigations [1–3, 5, 6, 17, 18] using correlating method suggested by Bergles and Morton [22]

line and the dashed line represents the improvement in heat transfer due to vibration.

In every case it was found that $\overline{Nu}$ increases with $G$ when Ra, frequency, and the test-wire location are maintained constant, as illustrated in Fig. 3. The increase of $\overline{Nu}$ with increasing $G$ was observed to be larger at the higher frequencies. Also, $\overline{Nu}$ increased with frequency when all other variables were held constant. Further, the Nusselt number was found to decrease as the test wire was lowered toward the bottom of the container. Detailed data plots illustrating these effects are reported in reference [14].

## Analysis

In order to determine a numerical value of the Reynolds number for given vibratory conditions, it is necessary to determine the relative velocity of the water with respect to the test wire. Direct measurements of these relative velocities were not attempted in this investigation, however. Instead, a simplified theory presented by Schoenhals and Overcamp [20] was employed. Assuming a one-dimensional dissipation-free physical model, solution of the resulting wave equation gives

$$P(\xi, t) = P_u + \rho g \xi + \rho a_0 \omega c \left[ \frac{\sin \dfrac{\omega \xi}{c}}{\cos \dfrac{\omega L}{c}} \right] \sin \omega t \qquad (5)$$

where the amplitude of the fluctuating pressure component, $\Delta P$, is obtained from the last term. Favorable comparison of pressure-amplitude measurements of this study with the prediction from equation (5) supported the validity of this simplified theory. The operating frequencies employed (30–240 Hz) were lower than the first natural frequency of the system (300 Hz), and for this condition the liquid motion is everywhere in phase with the container bottom. The predicted amplitude of the relative displacement of the water with respect to the container bottom can be obtained as

$$a_{l0} = \frac{g}{\omega^2} G \left[ \frac{\cos \dfrac{\omega \xi}{c}}{\cos \dfrac{\omega L}{c}} - 1 \right] \qquad (6)$$

The relative velocity of the water with respect to the test wire is written as

$$V = \bar{a}\omega \cos \omega t \qquad (7)$$

where $\bar{a} = |a_l - a_s|$ which is also equal to $|a_{l0} - a_{s0}|$; $a_{s0}$ is the displacement of the heated surface with respect to the container base, or the dynamic deflection of the test wire when subjected to vibration. This was predicted and approximated as a third-order polynomial in order to represent its variation along the test wire. For each experimental test a suitable value of $\bar{a}$ was obtained by averaging $|a_{l0} - a_{s0}|$ over the length of the test section. This procedure was appropriate in view of the fact that $a_{s0}$ varied somewhat along the test wire, although $a_{l0}$, as given by equation (6), was constant along the wire.

For correlation of the experimental data, the Reynolds number was based on the root-mean-square values of velocity, that is, $\bar{a}\omega/\sqrt{2}$. A study [21] of the magnitude of the relative velocity of the water with respect to the test wire revealed that it increased with $f$ and $G$ and decreased with $\xi$ in the frequency range below the first resonant frequency of the system. This largely explains the corresponding effects on $\overline{Nu}$, as described in the preceding section, which are apparently dominated by the relative motion phenomenon. For example, the decrease in $\overline{Nu}$ as the test wire was lowered was primarily due to a decrease in the relative motion between the test wire and the water. An order-of-magnitude analysis is also given in reference [21] which indicates that there were no appreciable heat-transfer effects due to secondary motions generated in the bulk fluid by the vibrations.

## Comparison with Previous Studies

The vibratory system employed in this study, Fig. 1(*c*), is different from those used in other studies as shown in Figs. 1(*a*) and 1(*b*). As discussed, three vibratory parameters, rather than two, were necessary to completely specify each vibratory condition for the present study. Apparently there are no experimental data in the previous literature for the particular kind of system under discussion. Accordingly, no other experimental results are available for direct comparison with the present measurements. However, an effort was made to compare the present results with those obtained from systems for which the mechanical vibrations were imposed on a heated horizontal cylinder in a stationary fluid.

Penney and Jefferson [3] have studied the effect of vibration on heat transfer from a vibrating wire in stationary water and ethylene glycol, have plotted the measured results in terms of $\overline{Nu}$ versus $Re \cdot Pr^{0.8}$ with Ra as a parameter, and have indicated that this method was valid only for the range of variables investigated in that particular experimental study. Using the present results, an attempt was made to plot $\overline{Nu}$ versus $Re \cdot Pr^{0.8}$, but it was difficult to distinguish the constant Ra lines because of considerable scattering of the data. However, by grouping the results for distinct values of the acceleration level, a meaningful display of the present results and those of Penney and Jefferson was obtained. The comparison is shown in Fig. 4. In spite of the different systems employed, comparison between the present results and those of Penney and Jefferson appears quite reasonable. A more complete explanation of the basis for this kind of plot now follows.

Bergles and Morton [22], in a survey of techniques employed to augment convective heat transfer, have shown that vibrational effects can often be reasonably well correlated by considering quasi-steady oscillating flow and utilizing the standard correlation for forced flow normal to a cylinder [19]. However,

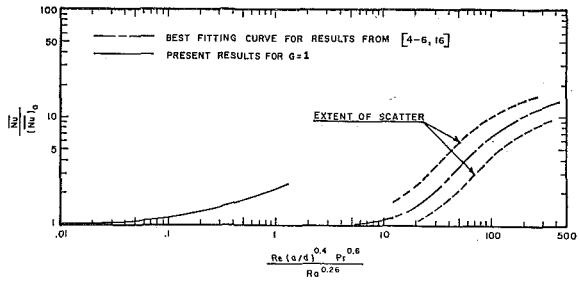


**Fig. 6 Comparison of present results with those of other investigations [4–6, 16] using correlating method suggested by Lemlich and Rao [4]**

when Ra is large enough and when Re is small, free-convection effects are also important, causing the actual heat transfer to be larger than the prediction based on quasi-steady forced convection alone. This effect is shown by the comparison of the present data with this prediction given in Fig. 5. The present results lie above the proposed correlation curve, the deviation increasing with increasing values of Ra, as expected. These results compare favorably with some of the plotted data of other investigators in the low Re range which correspond to Ra values of approximately the same order of magnitude. Clearly, the present results lie in the mixed flow regime, where both free-convection and vibratory forced-convection effects are significant. Accordingly, there is no single correlation line in this range valid for various Ra values using the representation given in Fig. 5.

Bergles [23] has surveyed the data of many investigators and has stated that the method of plotting given in Fig. 5 can be expected to apply only when the flow is approximately quasi-steady, a condition expected to be valid only if $a/d \gg 1$. When this condition is not met, thermo-acoustic streaming becomes a dominant effect, and the coordinates given in Fig. 5 fail to yield a satisfactory comparison of data. Bergles [23] has illustrated this quite vividly by plotting the dimensionless heat-transfer coefficient as a function of Re based on data from a number of different studies which were conducted with $a/d \lesssim 1$. The resulting curves show considerable scatter. It is of interest to note that in the present study the amplitude-to-diameter ratio was in this same range. This implies that the coordinates of Fig. 5 are inappropriate for this study and also suggests that any modest data-correlation attempt can be expected to yield sizable deviations.

Lemlich and Rao [4] have attempted to alleviate the situation by correlating $\overline{Nu}/\overline{Nu}_0$ in terms of $Re(a/d)^{0.4}\ Pr^{0.6}/Ra^{0.26}$, and have presented their own measurements along with those of three other investigations [5, 6, 16] as shown in Fig. 6. The scatter of the previous data on this plot is as much as 100 percent from the best-fitting curve. The present data for $G = 1$ are also compared with these results in Fig. 6. The disagreement is quite evident. In evaluating these discrepancies, it is well to keep in mind the fact that the vibratory conditions for the present study were different from those imposed in the previous investigations. Also, the method of correlating the data among the several dimensionless parameters is fairly arbitrary, and is not unique. There is little evidence to suggest that it should correlate all the data in general.

## Correlation

Despite the difficulty in comparing and correlating data, as described in the previous section, an attempt was made to correlate the present data in terms of all the parameters associated with simultaneous vibration of the heated surface and the fluid. As shown by equation (1), the parameters which affect the Nusselt number are Gr, Pr, Re, Ac, and Ω. However, without solving the governing partial differential equations, the quantitative relation among these parameters can be obtained only by correlating experimental measurements. In correlating the data,

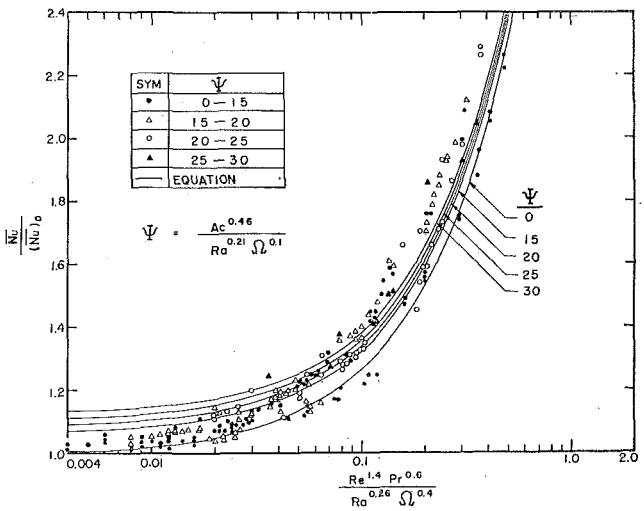


**Fig. 7 Comparison of data with the correlation given in equation (8) with the acceleration term as a parameter**

$\overline{Nu}/\overline{Nu}_0$ was used instead of $\overline{Nu}$ itself. The advantage of having the correlation in terms of the ratio of the Nusselt numbers is that any small error in the measurement technique affects both the numerator and denominator by approximately the same amount. The effect of such possible errors on this ratio is therefore minimized since they tend to cancel out. The highest value of $\overline{Nu}/\overline{Nu}_0$ obtained in this investigation was approximately three.

Based on the data obtained from the present study, the following correlation was developed:

$$\frac{\overline{Nu}}{\overline{Nu}_0} = 1 + 2.64\frac{Re^{1.4}Pr^{0.6}}{Ra^{0.26}\Omega^{0.4}} + 4 \times 10^{-3}\frac{Ac^{0.46}}{Ra^{0.21}\Omega^{0.1}} \qquad (8)$$

The details of the development of correlation (8) are described elsewhere [21]. The last two terms on the right-hand side of equation (8) were expected to account for the relative motion and acceleration effects, respectively, with allowance being made for the attenuation of these effects by Ra and by Ω. This correlation was found to possess an average deviation of about 10 percent among all the data obtained in this study. The maximum deviation among all of the individual data points was 20 percent. In Fig. 7 the results are plotted as $\overline{Nu}/\overline{Nu}_0$ versus $Re^{1.4}Pr^{0.6}/Ra^{0.26}\Omega^{0.4}$ with $Ac^{0.46}/Ra^{0.21}\Omega^{0.1}$ (denoted as Ψ) as a parameter. The relative motion effect was found to be generally much more significant than the acceleration effect, described by the Ψ parameter, for the range covered by these experiments. In fact, a study of the relative magnitudes of the terms on the right-hand side of equation (8) revealed that the last term, $4 \times 10^{-3}\Psi$, did not contribute more than 12 percent to the total value of $\overline{Nu}/\overline{Nu}_0$ for any of the measured data points [21].

Another important fact which can be deduced from equation (8) is that the average Nusselt number decreases as Ω increases. This observation may appear somewhat confusing in view of the result that $\overline{Nu}$ increases with frequency. However, examination of the velocity term involved in the Reynolds number indicates that the frequency plays a role in determining Re as well as Ω. This explains how it is possible for $\overline{Nu}$ to decrease with Ω when Ra, Re, and Ac are held constant even though it increases with frequency when Ra, $G$, and $\xi/L$ are kept constant.

Another interesting feature can be derived from Fig. 8 which contains a plot of $\overline{Nu}/\overline{Nu}_0$ versus Ra for fixed values of $G$, $\xi/L$, and frequency. In this particular plot, Re varies from three to five due to changes of the property values of water, although the velocity remains constant. However, this change of Re is very small compared with the variation of Ra, which ranged from 30 to 1400. In view of this large range of Ra, Re can be considered to be essentially constant by comparison. Thus, as Ra

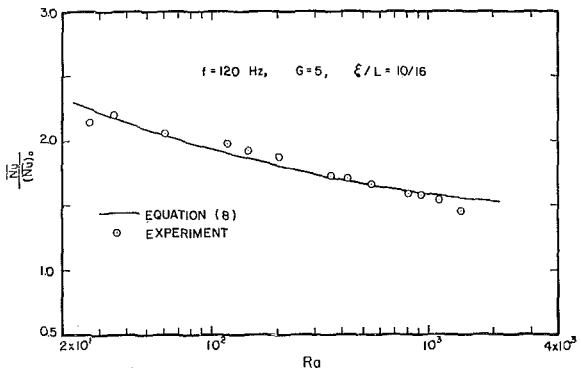


**Fig. 8 Attenuation of the effect of vibration on heat transfer with increasing Rayleigh number**

increases, $\overline{Nu}/\overline{Nu}_0$ decreases when Re does not vary appreciably. This conclusion can also be obtained by inspecting equation (8). A graphical comparison of the correlation curve of equation (8) with the test data is also displayed in Fig. 8.

## Conclusions

1 When the external oscillating motion is imposed either on the heated surface or fluid medium surrounding the surface, the heat transfer is then correlated in terms of four independent dimensionless parameters by

$$\overline{Nu} = F_1(\mathrm{Gr}, \mathrm{Pr}, \mathrm{Re}, \Omega)$$

or

$$\overline{Nu} = F_2(\mathrm{Gr}, \mathrm{Pr}, \mathrm{Re}, a/d)$$

2 When the fluid and heated surface are enclosed in a container subjected to vibration, thus imposing the vibratory motion on both the fluid and the heated surface simultaneously, there exists a relative motion of the fluid with respect to the heated surface due to the compressibility of the fluid and the flexibilities of the container walls, the support structure for the heated surface and the heated surface itself. The heat transfer in this case is correlated in terms of five independent dimensionless parameters by

$$\overline{Nu} = F(\mathrm{Gr}, \mathrm{Pr}, \mathrm{Re}, \Omega, \mathrm{Ac})$$

3 Based on the experimental data, the following correlation was developed:

$$\frac{\overline{Nu}}{\overline{Nu}_0} = 1 + 2.64\frac{\mathrm{Re}^{1.4}\mathrm{Pr}^{0.6}}{\mathrm{Ra}^{0.26}\Omega^{0.4}} + 4 \times 10^{-3}\frac{\mathrm{Ac}^{0.46}}{\mathrm{Ra}^{0.21}\Omega^{0.1}}$$

4 Under experimental conditions used in the present study the maximum increase in the heat-transfer rate due to vibration was about 200 percent, and the acceleration parameter was found to be significant. Nevertheless, the effect of the acceleration parameter in determining the heat-transfer rate appeared to be very moderate, providing contributions less than 12 percent within the range of imposed test conditions.

## References


1 Martinelli, R. C., and Boelter, L. M. K., "The Effect of Vibration on Heat Transfer by Free Convection from a Horizontal Cylinder," *Proceedings of the 5th International Congress for Applied Mechanics*, 1938, pp. 578–584.

2 Deaver, F. K., Penney, W. R., and Jefferson, T. B., "Heat Transfer From an Oscillating Horizontal Wire to Water," JOURNAL OF HEAT TRANSFER, TRANS. ASME, Series C, Vol. 84, No. 3, Aug. 1962, pp. 251–256.

3 Penney, W. R., and Jefferson, T. B., "Heat Transfer From an Oscillating Horizontal Wire to Water and Ethylene Glycol," JOURNAL OF HEAT TRANSFER, TRANS. ASME, Series C, Vol. 88, No. 4, Nov. 1966, pp. 359–366.

4 Lemlich, R., and Rao, M. A., "The Effect of Transverse Vibration on Free Convection from a Horizontal Cylinder," *International Journal of Heat and Mass Transfer*, Vol. 8, 1965, pp. 27–33.

5 Lemlich, R., "Effect of Vibration on Natural Convective Heat Transfer," *Industrial and Engineering Chemistry*, Vol. 47, 1955, pp. 1175–1180.

6 Teleki, C., Fand, R. M., and Kaye, J., "Influence of Vertical Vibration on the Rate of Heat Transfer from a Horizontal Cylinder in Air," WADC TN 59-357, Oct. 1960.

7 Fand, R. M., and Kaye, J., "The Influence of Sound on Free Convection From a Horizontal Cylinder," JOURNAL OF HEAT TRANSFER, TRANS. ASME, Series C, Vol. 83, No. 2, May 1961, pp. 133–148.

8 Holman, J. P., and Mott-Smith, T. P., "The Effect of High Constant Pressure Sound Fields on Free Convection Heat Transfer from a Horizontal Cylinder," WADC TN 58-352, Dec. 1958.

9 Richardson, P. D., "Heat Transfer from a Circular Cylinder by Acoustic Streaming," *Journal of Fluid Mechanics*, Vol. 30, Part 2, 1967, pp. 337–355.

10 Fashbaugh, R. H., and Streeter, V. L., "Resonance in Liquid Rocket Engine Systems," *Journal of Basic Engineering*, TRANS. ASME, Series D, Vol. 87, No. 4, Dec. 1965, pp. 1011–1017.

11 Schoenhals, R. J., and Clark, J. A., "Laminar Free Convection Boundary-Layer Perturbations Due to Transverse Wall Vibration," JOURNAL OF HEAT TRANSFER, TRANS. ASME, Series C, Vol. 84, No. 3, Aug. 1962, pp. 225–234.

12 Forbes, R. E., Carley, C. T., and Bell, C. J., "Vibration Effects on Convective Heat Transfer in Enclosures," JOURNAL OF HEAT TRANSFER, TRANS. ASME, Series C, Vol. 92, No. 3, Aug. 1970, pp. 429–438.

13 Smith, G. V., and Forbes, R. E., "Effect of Random Vibration on Natural Convective Heat Transfer in Rectangular Enclosures," in: *Augmentation of Convective Heat and Mass Transfer*, A. E. Bergles and R. L. Webb, eds., ASME, New York, N. Y., 1970, pp. 158–162.

14 Pak, H. Y., Winter, E. R. F., and Schoenhals, R. J., "Convection Heat Transfer in a Contained Fluid Subjected to Vibration," in: *Augmentation of Convective Heat and Mass Transfer*, A. E. Bergles and R. L. Webb, eds., ASME, New York, N. Y., 1970, pp. 148–157.

15 Dougall, R. S., Chang, T., and Fand, R. M., "A Study of the Differential Equation of Coupled Vibrations and Free Convection from a Heated Horizontal Cylinder," ARL-148, Part 1, 1961.

16 Lemlich, R., and Levy, M. R., "The Effect of Vibration on Natural Convective Mass Transfer," *AIChE Journal*, Vol. 7, No. 2, June 1961, pp. 240–242.

17 Shine, A. J., discussion on paper by Deaver, et al., JOURNAL OF HEAT TRANSFER, TRANS. ASME, Series C, Vol. 84, No. 3, Aug. 1962, p. 255.

18 Fand, R. M., and Peebles, E. M., "A Comparison of the Influence of Mechanical and Acoustical Vibrations on Free Convection From a Horizontal Cylinder," JOURNAL OF HEAT TRANSFER, TRANS. ASME, Series C, Vol. 84, No. 3, Aug. 1962, p. 268.

19 McAdams, W. H., *Heat Transmission*, 3rd ed., McGraw-Hill, New York, N. Y., 1954, pp. 175–178, 266–268.

20 Schoenhals, R. J., and Overcamp, T. J., "Pressure Distribution and Bubble Formation Induced by Longitudinal Vibration of a Flexible Liquid-Filled Cylinder," *Journal of Basic Engineering*, TRANS. ASME, Series D, Vol. 89, No. 4, Dec. 1967, pp. 737–747.

21 Pak, H. Y., "Free Convection Heat Transfer in a Contained Fluid Subjected to Vibration," PhD thesis, Purdue University, Lafayette, Ind., Jan. 1970.

22 Bergles, A. E., and Morton, H. L., "Survey and Evaluation of Techniques to Augment Convective Heat Transfer," M.I.T. Engineering Projects Laboratory Report No. 5382-34, 1965; also, see discussion following reference [3].

23 Bergles, A. E., "Survey and Evaluation of Techniques to Augment Convective Heat and Mass Transfer," in: *Progress in Heat and Mass Transfer*, Vol. 1, U. Grigull and E. Hahne, eds., Pergamon Press, 1969, pp. 331–424.

journal of heat transfer

# technical briefs

This section consists of contributions of 1500 words or less (about 5 double-spaced typewritten pages, including figures). Technical briefs will be reviewed and approved by the specific division's reviewing committee prior to publication. After approval such contributions will be published as soon as possible, normally in the next issue of the journal.

## Oscillation Effects upon Film Boiling from a Sphere

**WILLIAM E. SCHMIDT**[1] **and L. C. WITTE**[2]

### Nomenclature

$a$ = acceleration of liquid system, ft/sec$^2$
$A$ = area of sphere, ft$^2$
$C_p$ = specific heat, Btu/lb$_m$-deg F
$d$ = sphere diameter, ft
$f$ = oscillation frequency, Hz
Fr = Froude number, $v^2/gL$
$g$ = acceleration of gravity, 32.17 ft/sec$^2$
$h_{fg}$ = latent heat of vaporization, Btu/lb$_m$
$L$ = characteristic length of oscillating body
Nu = Nusselt number, $hd/k$
Pr = Prandtl number
$q$ = heat-transfer rate, Btu/hr-ft$^2$
$T$ = temperature, deg F
$v$ = characteristic velocity of sphere, ft/sec
$V$ = volume of sphere, ft$^3$
$x$ = amplitude, ft
$\Delta T$ = temperature difference, $T_{\text{sphere}} - T_{\text{sat}}$, deg F
$\rho$ = density, lb$_m$/ft$^3$
$\mu$ = viscosity, lb$_m$/ft-sec
$\theta$ = time

### Subscripts

$v$ = vapor
$l$ = liquid
exp = experimental

### Introduction

Considerable enhancement of film-boiling heat-transfer rates by oscillation has been noted by several investigators. For example, Rhea and Nevins [1][3] examined this effect for spheres oscillating in liquid nitrogen and found that they could account for the oscillation effect by modifying the equation proposed by Frederking and Clark [2] to correlate data for a nonoscillating sphere. The modification took the form of a vibrational Froude number.

Heat-transfer rates from a 3/4-in-dia silver-plated copper sphere were obtained as the sphere was oscillated in saturated liquid nitrogen and Freon-11. The frequency range was from zero up to 13 Hz and the amplitude-to-diameter ratio varied from zero to 2.67. The experimental apparatus used to obtain harmonic oscillation is discussed in detail in [3].

The sphere was plated with a flash of silver to prevent oxidation and had a thermocouple located near the lower stagnation point. The sphere was attached to a 1/4-in-dia thin-walled stainless-steel tube that served as a support rod. Photographs were obtained with a Fastax WF-3 16mm movie camera at about 2000 frames/sec.

### Heat-Transfer Data

Where the internal resistance may be taken as negligible, the temperature–time history of a body is governed by the surface resistance. Such a case arises when the body has a high thermal conductivity compared with the surface-film coefficient, so that the interior temperature of the body may be taken as uniform at any instant.

Merte and Clark [4] showed experimentally that the center-to-surface temperature difference in a 1-in-dia copper sphere cooling in $LN_2$ is approximately 2 deg F at the peak heat flux for nucleate boiling. Heat fluxes for film boiling in this study were considerably less than for nucleate boiling, and hence the maximum temperature difference in the sphere was proportionally less. A heat balance on the sphere yields

$$q = \frac{\rho V}{A} C_p \frac{dT}{d\theta} \tag{1}$$

Temperature slopes were computed at convenient time intervals via a digital computer and the heat fluxes were obtained in the same computation. Instantaneous heat-transfer coefficients were then computed and put into the Nusselt-number form $hd/k$.

### Data Correlation

The Froude number is $v^2/gL$, where $v$ is a characteristic velocity and $L$ is a characteristic length. Letting $v$ be the rms average of the harmonic motion and letting $L$ be the sphere diameter, one obtains

$$\text{Fr} = \frac{x^2 f^2}{1.5gd} \tag{2}$$

The correlating equation involving Froude number evaluated in this manner gives

$$\text{Nu} = 0.14 \left[ \frac{gd^3 \rho_v (\rho_l - \rho_v)}{\mu_v^2} \text{Pr}_v \left( \frac{h_{fg}}{C_p \Delta T} + 0.5 \right) \times \left( \frac{a}{g} + \frac{x^2 f^2}{1.5gd} \right) \right]^{1/3} \tag{3}$$

Equation (3) is similar to an equation proposed by Merte to correlate film boiling from spheres at low gravities. The modification is the addition of $x^2f^2/1.5gd$, which represents the effects of a vibrational Froude number.

Fig. 1 shows a comparison of the data to equation (3). All data obtained in this study are not included in Fig. 1. Much data fall upon each other, indicating excellent reproducibility. Other

---

[1] Department of Mechanical Engineering, University of Houston, Houston, Texas; currently with NASA Ames Research Center.
[2] Associate Professor and Chairman, Department of Mechanical Engineering, University of Houston, Houston, Texas.
[3] Numbers in brackets designate References at end of technical brief.

Contributed by the Heat Transfer Division of The American Society of Mechanical Engineers. Manuscript received by the Heat Transfer Division February 23, 1972.

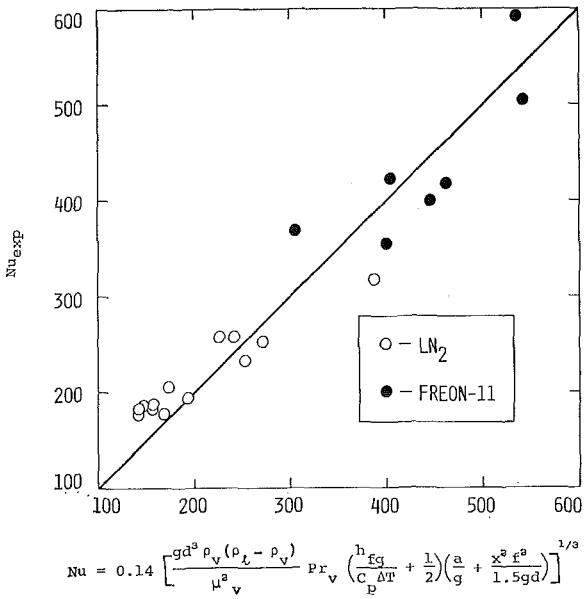


**Fig. 1 Correlation of experimental data**

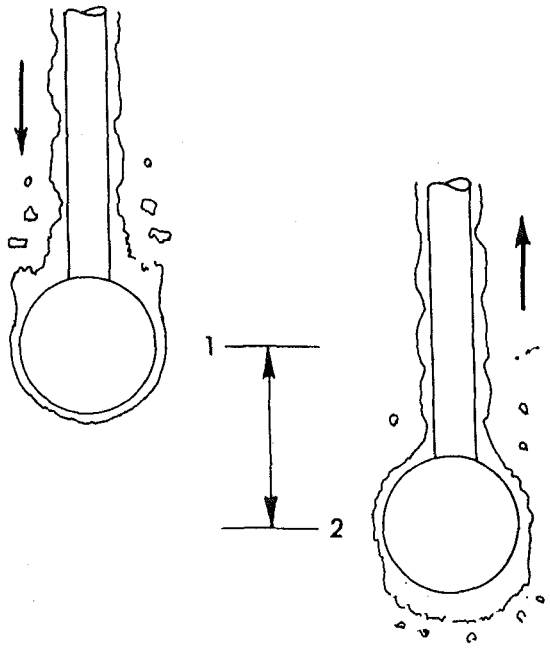


(b) $x/d = 1.33, f = 6$ Hz

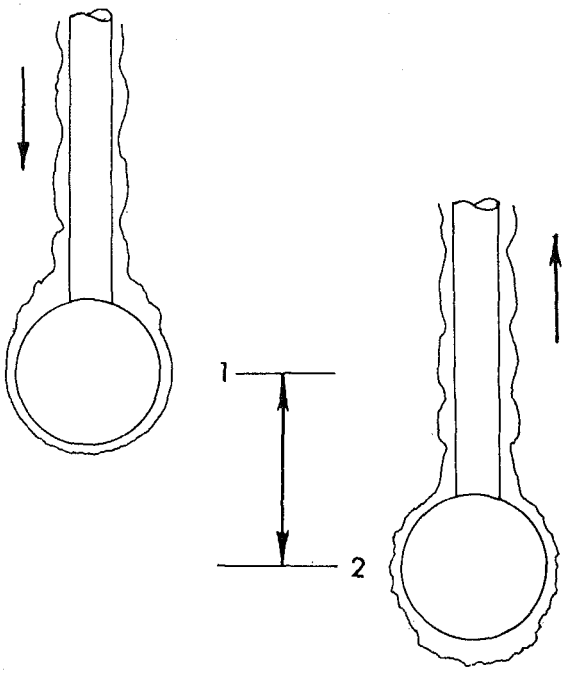


(a) $x/d = 1.33, f = 3$ Hz

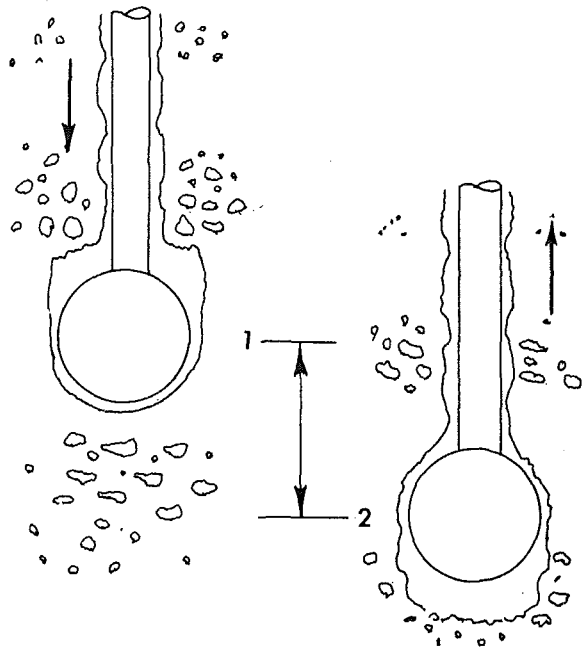


(c) $x/d = 1.33, f = 11$ Hz

**Fig. 2 Sketches made from high-speed photographs showing the effect of oscillation on boiling behavior of Freon-11**

data were omitted for the following reason. As the sphere–support tube assembly cools, transition to nucleate boiling occurs first on the tube because of its smaller thermal capacity. At this point, a significant change in the cooling rate is evident. Apparently the tube acts as a very effective fin to conduct energy away from the sphere. Rhea and Nevins noted similar behavior in their work. Consequently, the data include only those points where the effect of conduction up the support tube is not significant (i.e., at times prior to the onset of nucleate boiling around the support tube). The points also represent an average, usually of three data points calculated from each temperature–time history.

The $LN_2$ and Fr-11 data are correlated well by equation (3), with the Fr-11 data lying at significantly higher Nusselt numbers than the $LN_2$ data.

## Photographic Studies

High-speed photographs were obtained with Fr-11 to characterize the behavior of the vapor cavity around the sphere and to investigate the mode of vapor removal from the cavity. The photographs clearly show a basic difference between vapor removal for higher frequency oscillation in contrast to lower frequency oscillations. Fig. 2 shows the effect of frequency from 3 to 11 Hz for an $x/d$ of 1.33 in Fr-11. Fig. 2 shows sketches of the vapor-film shape at (1) the beginning of the downstroke and (2) the beginning of the upstroke.

At low frequency, the cavity is relatively stable with vapor removed at the top much the same as Daniels and Frederking [5] and Hendricks and Baumeister [6] observed for free-convection boiling, Fig. 2(*a*). However, no multiple domes were observed as in [6]. Apparently, the support tube significantly influences

the vapor motion. That is, since boiling is also occurring from the tube, a "chimney" is formed and offers a path of low resistance for vapor flow and multiple domes are not formed. A support tube smaller than that used would be desirable, but strength considerations dictated otherwise.

At higher frequencies, Fig. 2(*b*, *c*), vapor is shed directly into the bulk liquid and this occurs primarily at the ends of the downstroke and upstroke. As the sphere is decelerated, the liquid inertia apparently forces the shedding which occurs as a toroidal ring separating from the sphere near the 90-deg point. There is apparently not a threshold for this behavior, rather, more vapor is shed as the frequency rises.

The same effect was noted as the amplitude is increased for a given oscillation frequency.

The increased shedding of vapor undoubtedly accounts for the enhancement of heat transfer during oscillation. The effect is twofold. First, the vapor forced into the liquid carries with it the latent heat of vaporization, and second, the vapor film is "thinned" by the vapor removal and more heat may be conducted across the film. Although no measurements of the amount of vapor removed in the toroidal manner were possible, it appeared to be a significant fraction of the vapor being generated in each oscillation cycle.

### References


1 Rhea, L. G., and Nevins, R. G., "Film Boiling Heat Transfer From an Oscillating Sphere," JOURNAL OF HEAT TRANSFER, TRANS. ASME, Series C, Vol. 91, No. 2, May 1969, pp. 267–272.

2 Frederking, T. H. K., and Clark, J. A., "Natural Convection Film Boiling on a Sphere," *Advances in Cryogenic Engineering*, Vol. 8, 1963, p. 501.

3 Schmidt, W. E., "An Investigation of Film Boiling Heat Transfer from an Oscillating Sphere," unpublished MS thesis, University of Houston, Houston, Texas, 1970.

4 Merte, H., Jr., and Clark, J. A., "Boiling Heat Transfer With Cryogenic Fluids at Standard, Fractional, and Near-Zero Gravity," JOURNAL OF HEAT TRANSFER, TRANS. ASME, Series C, Vol. 86, No. 3, Aug. 1964, pp. 351–359.

5 Frederking, T. H. K., and Daniels, D. J., "The Relation Between Bubble Diameter and Frequency of Removal From a Sphere During Film Boiling," JOURNAL OF HEAT TRANSFER, TRANS. ASME, Series C, Vol. 88, No. 1, Feb. 1966, pp. 87–93.

6 Hendricks, R. L., and Baumeister, K. J., "Film Boiling from Submerged Spheres," NASA TND-5124, June 1969.


## Nonviscous Nonconducting Flow of a Radiating Plasma over a Flat Boundary[1]


**R. PURI[2] and D. A. MANDELL[3]**


THIS NOTE discusses the flow of a radiating nonviscous nonconducting hydrogen plasma over a black isothermal flat boundary. Even though this analysis greatly oversimplifies the problem of laminar boundary-layer flow of a plasma, it serves to illustrate the mechanism of nongray radiative heat transfer of a plasma over an external boundary. The problem being considered is the optically thin solution of the laminar boundary-layer problem and is the outer solution of that problem [1].[4] Linearized radiation and local thermodynamic equilibrium are assumed.


[1] This research was supported by the National Science Foundation through grant number GK 5276.



[2] University of Minnesota.

[3] Assistant Professor, Department of Mechanical Engineering, Washington State University, Pullman, Wash. Assoc. Mem. ASME.


[4] Numbers in brackets designate References at end of technical brief.


Contributed by the Heat Transfer Division of THE AMERICAN SOCIETY OF MECHANICAL ENGINEERS. Manuscript received by the Heat Transfer Division April 5, 1972.


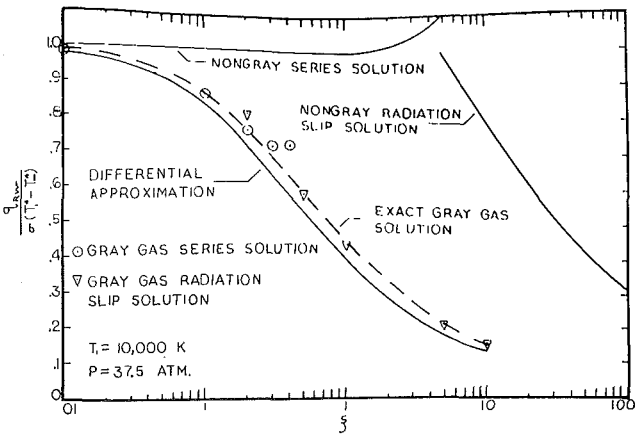


**Fig. 1 Comparison of dimensionless heat-flux solutions**

The energy equation is [2]

$$\frac{\partial\theta}{\partial\xi} = \frac{4P_H}{\kappa_{Lp}}\int_0^\infty \theta(\xi, u')F_1|(u-u')|du' - 8\theta(\xi, u) \qquad (1)$$

where $\theta = T - T_1/T_\infty - T_1$ is the dimensionless temperature, $\xi = 2\sigma\kappa_{Lp}T_1^3x/\rho c_p u_\infty$ is the dimensionless axial coordinate, $u = P_H y$, $\kappa_{Lp}$ is the linear Planck mean coefficient, $P_H$ is the atomic hydrogen partial pressure, $T_1$ is the boundary temperature, and $F_1$ is the first transmission function [3]. Three methods of solution are considered: (*a*) a series solution for small $\xi$, (*b*) a radiation-slip solution for moderately large optical thicknesses, and (*c*) a differential-approximation solution valid for all optical thicknesses.

For small $\xi$ a series solution is assumed [1]

$$\theta(\xi, u) = 1 + g_1(u)\xi + g_2(u)\xi^2 \qquad (2)$$

Substitution of equation (2) into equation (1) results in equations for $g_1$ and $g_2$ [2]. Tables of $g_1$ and $g_2$ are given in [2].

The radiation-slip formulation is similar to the formulation in [1] and the resulting equation is easily solved

$$\theta(\xi, u) = \exp\left(\frac{3\kappa_R u}{2P_H} + \frac{6\kappa_R}{\kappa_{Lp}}\xi\right)\operatorname{erfc}\left[\left(\frac{6\xi\kappa_R}{\kappa_{Lp}}\right)^{1/2} + \frac{u}{4P_H}\left(\frac{3\kappa_R\kappa_{Lp}}{2\xi}\right)^{1/2}\right] + \operatorname{erf}\left[\frac{u}{4P_H}\left(\frac{3}{2}\frac{\kappa_R\kappa_{Lp}}{\xi}\right)^{1/2}\right] \qquad (3)$$

For a gray gas $\kappa_{Lp} = \kappa_R$ and equation (3) reduces to the solution obtained by Cess [1].

The differential approximation is obtained in a manner similar to that of [1]. In order to satisfy the boundary conditions, the nongray- and gray-gas solutions must be identical.

### Results

The dimensionless wall heat flux is given by

$$\frac{q_{Rw}}{\sigma(T_1^4 - T_\infty^4)} = 2\int_0^\infty \theta(\xi, u')F_2(u')du' \qquad (4)$$

where $F_2$ is the second transmission function [4].

Typical results are shown in Fig. 1 for $T_1 = 10{,}000$ deg K and $P = 37.5$ atm. In addition to the results discussed above, exact gray-gas results obtained by Williams [5] are shown. Williams shows that the series solution is a good approximation to the exact gray-gas solution up to $\xi = 0.2$. At this value of $\xi$ the nongray series solution and the exact gray-gas solution differ by 24 percent. For a gray gas the radiation-slip and exact solutions differ by 0.25 percent at $\xi = 10$ [5]. The nongray radiation-slip and the exact gray-gas solutions differ by about 84 percent at $\xi = 10$. Similar results have been obtained for infrared gaseous radiation [6].

In summary, for flow of a high-temperature radiating gas over

the vapor motion. That is, since boiling is also occurring from the tube, a "chimney" is formed and offers a path of low resistance for vapor flow and multiple domes are not formed. A support tube smaller than that used would be desirable, but strength considerations dictated otherwise.

At higher frequencies, Fig. 2(*b*, *c*), vapor is shed directly into the bulk liquid and this occurs primarily at the ends of the downstroke and upstroke. As the sphere is decelerated, the liquid inertia apparently forces the shedding which occurs as a toroidal ring separating from the sphere near the 90-deg point. There is apparently not a threshold for this behavior, rather, more vapor is shed as the frequency rises.

The same effect was noted as the amplitude is increased for a given oscillation frequency.

The increased shedding of vapor undoubtedly accounts for the enhancement of heat transfer during oscillation. The effect is twofold. First, the vapor forced into the liquid carries with it the latent heat of vaporization, and second, the vapor film is "thinned" by the vapor removal and more heat may be conducted across the film. Although no measurements of the amount of vapor removed in the toroidal manner were possible, it appeared to be a significant fraction of the vapor being generated in each oscillation cycle.

### References


1 Rhea, L. G., and Nevins, R. G., "Film Boiling Heat Transfer From an Oscillating Sphere," JOURNAL OF HEAT TRANSFER, TRANS. ASME, Series C, Vol. 91, No. 2, May 1969, pp. 267–272.

2 Frederking, T. H. K., and Clark, J. A., "Natural Convection Film Boiling on a Sphere," *Advances in Cryogenic Engineering*, Vol. 8, 1963, p. 501.

3 Schmidt, W. E., "An Investigation of Film Boiling Heat Transfer from an Oscillating Sphere," unpublished MS thesis, University of Houston, Houston, Texas, 1970.

4 Merte, H., Jr., and Clark, J. A., "Boiling Heat Transfer With Cryogenic Fluids at Standard, Fractional, and Near-Zero Gravity," JOURNAL OF HEAT TRANSFER, TRANS. ASME, Series C, Vol. 86, No. 3, Aug. 1964, pp. 351–359.

5 Frederking, T. H. K., and Daniels, D. J., "The Relation Between Bubble Diameter and Frequency of Removal From a Sphere During Film Boiling," JOURNAL OF HEAT TRANSFER, TRANS. ASME, Series C, Vol. 88, No. 1, Feb. 1966, pp. 87–93.

6 Hendricks, R. L., and Baumeister, K. J., "Film Boiling from Submerged Spheres," NASA TND-5124, June 1969.


# Nonviscous Nonconducting Flow of a Radiating Plasma over a Flat Boundary[1]


**R. PURI[2] and D. A. MANDELL[3]**


THIS NOTE discusses the flow of a radiating nonviscous nonconducting hydrogen plasma over a black isothermal flat boundary. Even though this analysis greatly oversimplifies the problem of laminar boundary-layer flow of a plasma, it serves to illustrate the mechanism of nongray radiative heat transfer of a plasma over an external boundary. The problem being considered is the optically thin solution of the laminar boundary-layer problem and is the outer solution of that problem [1].[4] Linearized radiation and local thermodynamic equilibrium are assumed.


[1] This research was supported by the National Science Foundation through grant number GK 5276.



[2] University of Minnesota.

[3] Assistant Professor, Department of Mechanical Engineering, Washington State University, Pullman, Wash. Assoc. Mem. ASME.


[4] Numbers in brackets designate References at end of technical brief.


Contributed by the Heat Transfer Division of THE AMERICAN SOCIETY OF MECHANICAL ENGINEERS. Manuscript received by the Heat Transfer Division April 5, 1972.


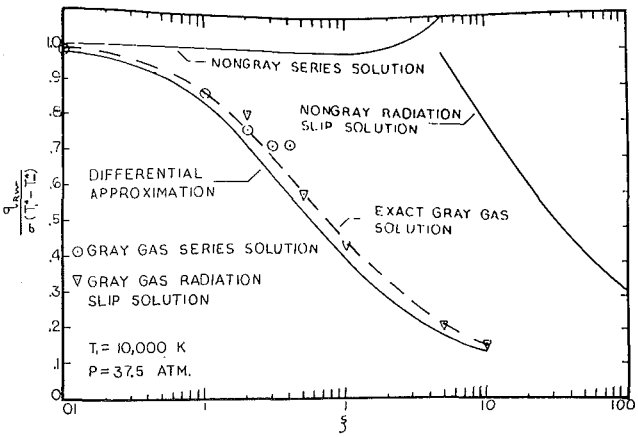


**Fig. 1 Comparison of dimensionless heat-flux solutions**

The energy equation is [2]

$$\frac{\partial\theta}{\partial\xi} = \frac{4P_H}{\kappa_{Lp}}\int_0^\infty \theta(\xi, u')F_1|(u-u')|du' - 8\theta(\xi, u) \qquad (1)$$

where $\theta = T - T_1/T_\infty - T_1$ is the dimensionless temperature, $\xi = 2\sigma\kappa_{Lp}T_1^3x/\rho c_p u_\infty$ is the dimensionless axial coordinate, $u = P_H y$, $\kappa_{Lp}$ is the linear Planck mean coefficient, $P_H$ is the atomic hydrogen partial pressure, $T_1$ is the boundary temperature, and $F_1$ is the first transmission function [3]. Three methods of solution are considered: (*a*) a series solution for small $\xi$, (*b*) a radiation-slip solution for moderately large optical thicknesses, and (*c*) a differential-approximation solution valid for all optical thicknesses.

For small $\xi$ a series solution is assumed [1]

$$\theta(\xi, u) = 1 + g_1(u)\xi + g_2(u)\xi^2 \qquad (2)$$

Substitution of equation (2) into equation (1) results in equations for $g_1$ and $g_2$ [2]. Tables of $g_1$ and $g_2$ are given in [2].

The radiation-slip formulation is similar to the formulation in [1] and the resulting equation is easily solved

$$\theta(\xi, u) = \exp\left(\frac{3\kappa_R u}{2P_H} + \frac{6\kappa_R}{\kappa_{Lp}}\xi\right)\operatorname{erfc}\left[\left(\frac{6\xi\kappa_R}{\kappa_{Lp}}\right)^{1/2} + \frac{u}{4P_H}\left(\frac{3\kappa_R\kappa_{Lp}}{2\xi}\right)^{1/2}\right] + \operatorname{erf}\left[\frac{u}{4P_H}\left(\frac{3}{2}\frac{\kappa_R\kappa_{Lp}}{\xi}\right)^{1/2}\right] \qquad (3)$$

For a gray gas $\kappa_{Lp} = \kappa_R$ and equation (3) reduces to the solution obtained by Cess [1].

The differential approximation is obtained in a manner similar to that of [1]. In order to satisfy the boundary conditions, the nongray- and gray-gas solutions must be identical.

### Results

The dimensionless wall heat flux is given by

$$\frac{q_{Rw}}{\sigma(T_1^4 - T_\infty^4)} = 2\int_0^\infty \theta(\xi, u')F_2(u')du' \qquad (4)$$

where $F_2$ is the second transmission function [4].

Typical results are shown in Fig. 1 for $T_1 = 10{,}000$ deg K and $P = 37.5$ atm. In addition to the results discussed above, exact gray-gas results obtained by Williams [5] are shown. Williams shows that the series solution is a good approximation to the exact gray-gas solution up to $\xi = 0.2$. At this value of $\xi$ the nongray series solution and the exact gray-gas solution differ by 24 percent. For a gray gas the radiation-slip and exact solutions differ by 0.25 percent at $\xi = 10$ [5]. The nongray radiation-slip and the exact gray-gas solutions differ by about 84 percent at $\xi = 10$. Similar results have been obtained for infrared gaseous radiation [6].

In summary, for flow of a high-temperature radiating gas over

a flat boundary the nongray solutions differ significantly from the gray results and the differential approximation does not join the two limiting solutions in the nongray case as it does in the gray case.

### References


1 Sparrow, E. M., and Cess, R. D., *Radiation Heat Transfer*, Brooks/Cole, Belmont, Calif., 1966.

2 Puri, R., "Nonviscous, Nonconducting Flow of a Radiating Hydrogen Plasma over a Flat Plate," MS thesis, Washington State University, Pullman, Wash., 1971.

3 Mandell, D. A., "Transmission Functions in the Numerical Solution of Radiative Heat Transfer Problems," *J. Quant. Spectrosc. Radiat. Trans.*, Vol. 11, 1971, pp. 1741–1748.

4 Mandell, D. A., "Exponential Kernel Approximation in Radiative Energy Transfer within a Hydrogen Plasma," *AIAA Journal*, Vol. 8, 1970, pp. 1510–1512.

5 Williams, M. M. R., "The Temperature Distribution in a Radiating Fluid Flowing over a Flat Plate," *Quart. J. Mech. Appl. Math.*, Vol. 22, 1969, pp. 487–500.

6 Pergament, S. P., "The Application of Perturbation Methods to Boundary Layer Flow of Radiating Gases," PhD thesis, State University of New York at Stony Brook, 1970.


## Significance of the Pressure Gradient on Fully Developed Turbulent Flow in a Pipe


**R. J. GROSS[1] and L. C. THOMAS[1]**


### Introduction

Surface-renewal-and-penetration-type models have been adapted to a variety of turbulent transport processes associated with solid–fluid interfaces [5, 6, 11].[2] The basic surface-renewal-and-penetration model was first set forth by Danckwerts [3]. This class of turbulent transport model is based on the notion that eddies intermittently move from the core to the wall region, thus "renewing" the surface. In addition, simple one-dimensional molecular transport has been presumed to occur within individual elements of fluid within the wall region. For applications involving turbulent momentum transfer, the contribution of the axial pressure gradient has been assumed to be negligible, such that the momentum equation for a Newtonian fluid has been written for individual elements of fluid as [5, 6]

$$\frac{\partial u}{\partial \theta} = \nu \frac{\partial^2 u}{\partial y^2} \tag{1}$$

with initial and boundary conditions

$$\begin{aligned} u &= U_i \quad \text{at} \quad \theta = 0 \\ u &= 0 \quad \text{at} \quad y = 0 \\ u &= U_i \quad \text{at} \quad y = \infty \end{aligned} \tag{2}$$

$U_i$ represents the eddy velocity at the first instant of renewal, $u$ is the instantaneous velocity profile, and $\theta$ is the instantaneous contact time.

The assumption of negligible pressure-gradient effects on the momentum transfer for flow conditions such as hydrodynamically fully developed tube flow has generally been justified by dimensional-analysis–order-of-magnitude arguments [9]. Because of the pertinence of this formulation in obtaining an analogical relationship for the mean frequency of surface renewal, a more rigorous analysis of the effect of the pressure gradient will now be presented for incompressible flow.

### Analysis

The inclusion of the pressure-gradient term $dP/dx$ in the formulation of the basic surface-renewal-and-penetration model for momentum transfer requires an expression of the form

$$\frac{\partial u}{\partial \theta} = \nu \frac{\partial^2 u}{\partial y^2} - \frac{1}{\rho}\frac{dP}{dx} \tag{3}$$

The solution of this equation for constant pressure gradient coupled with the initial and boundary conditions given previously leads to an expression for the local instantaneous velocity profile of the form [2]

$$\frac{u}{U_i} = \operatorname{erf}\left(\frac{y}{2\sqrt{\nu\theta}}\right) + \frac{1}{\rho}\frac{dP}{U_i dx}\left[\left(\theta + \frac{y^2}{2\nu}\right)\operatorname{erfc}\left(\frac{y}{2\sqrt{\nu\theta}}\right) - y\left(\frac{\theta}{\pi\nu}\right)^{1/2}\exp\left(\frac{-y^2}{4\nu\theta}\right) - \theta\right] \tag{4}$$

As $dP/dx \to 0$ this expression reduces to the solution of equations (1) and (2), or

$$u/U_i = \operatorname{erf}\left[y/\left(2\sqrt{\nu\theta}\right)\right] \tag{5}$$

The time-averaging of the expression for $u$ given by equation (4) in terms of the random contact time distribution proposed by Danckwerts [3] leads to a relationship for the local mean velocity profile $\bar{u}$ of the form

$$\frac{\bar{u}}{U_i} = \left[1 - \frac{\tau}{\rho U_i}\frac{dP}{dx}\right]\left[1 - \exp\left(\frac{-y}{\sqrt{\nu\tau}}\right)\right] \tag{6}$$

where $\tau$ is the mean residence time of all eddies arriving at the surface. The differentiation of this expression yields a relationship for $\tau$ in terms of the local mean friction velocity $U^*$ of the form

$$U^*\sqrt{\frac{\tau}{\nu}} = \frac{2U_i/U^*}{1 + \sqrt{1 + \dfrac{4\nu}{\rho U^{*4}}U_i\dfrac{dP}{dx}}} \tag{7}$$

For hydrodynamically fully developed flow in a circular tube

$$\frac{dP}{dx} = -\frac{4\rho U_b^2}{D}\frac{f}{2}$$

such that equation (7) becomes

$$U^*\sqrt{\frac{\tau}{\nu}} = \frac{2U_i/U^*}{1 + \sqrt{1 - \dfrac{16U_i}{U^*\mathrm{Re}}\sqrt{\dfrac{2}{f}}}} \tag{8}$$

$f$ is the Fanning friction factor such that $U^* = \sqrt{f/2}\,U_b$. For $dP/dx = 0$, equation (7) reduces to an expression of the form

$$U^*\sqrt{\frac{\tau}{\nu}} = \frac{U_i}{U^*} \tag{9}$$

This expression and a similar relationship obtained by the use of Higbie's [7] uniform contact time distribution has been previously utilized in turbulent momentum-, heat-, and mass-transfer analyses [5, 6, 11].

### Discussion and Conclusion

Equations (8) and (9) can be compared in terms of the dimensionless parameters $Y$ $[\equiv(U^*\sqrt{\tau/\nu})(U^*/U_i)]$ and $X$ $[\equiv(\mathrm{Re}\sqrt{f/2})(U^*/U_i)]$. Equation (9) indicates that $Y$ is identically equal to unity, while equation (8), which reflects the effect of the pressure drop, indicates that $Y$ increases from a value of unity at large $X$ to a value of two at $X$ equal to 16.


[1] Associate Professor, Mechanical Engineering Department, University of Akron, Akron, Ohio. Assoc. Mem. ASME.


[2] Numbers in brackets designate References at end of technical brief.


Contributed by the Heat Transfer Division of THE AMERICAN SOCIETY OF MECHANICAL ENGINEERS. Manuscript received by the Heat Transfer Division April 26, 1972.

a flat boundary the nongray solutions differ significantly from the gray results and the differential approximation does not join the two limiting solutions in the nongray case as it does in the gray case.

### References


1 Sparrow, E. M., and Cess, R. D., *Radiation Heat Transfer*, Brooks/Cole, Belmont, Calif., 1966.

2 Puri, R., "Nonviscous, Nonconducting Flow of a Radiating Hydrogen Plasma over a Flat Plate," MS thesis, Washington State University, Pullman, Wash., 1971.

3 Mandell, D. A., "Transmission Functions in the Numerical Solution of Radiative Heat Transfer Problems," *J. Quant. Spectrosc. Radiat. Trans.*, Vol. 11, 1971, pp. 1741–1748.

4 Mandell, D. A., "Exponential Kernel Approximation in Radiative Energy Transfer within a Hydrogen Plasma," *AIAA Journal*, Vol. 8, 1970, pp. 1510–1512.

5 Williams, M. M. R., "The Temperature Distribution in a Radiating Fluid Flowing over a Flat Plate," *Quart. J. Mech. Appl. Math.*, Vol. 22, 1969, pp. 487–500.

6 Pergament, S. P., "The Application of Perturbation Methods to Boundary Layer Flow of Radiating Gases," PhD thesis, State University of New York at Stony Brook, 1970.


## Significance of the Pressure Gradient on Fully Developed Turbulent Flow in a Pipe


**R. J. GROSS[1] and L. C. THOMAS[1]**


### Introduction

Surface-renewal-and-penetration-type models have been adapted to a variety of turbulent transport processes associated with solid–fluid interfaces [5, 6, 11].[2] The basic surface-renewal-and-penetration model was first set forth by Danckwerts [3]. This class of turbulent transport model is based on the notion that eddies intermittently move from the core to the wall region, thus "renewing" the surface. In addition, simple one-dimensional molecular transport has been presumed to occur within individual elements of fluid within the wall region. For applications involving turbulent momentum transfer, the contribution of the axial pressure gradient has been assumed to be negligible, such that the momentum equation for a Newtonian fluid has been written for individual elements of fluid as [5, 6]

$$\frac{\partial u}{\partial \theta} = \nu \frac{\partial^2 u}{\partial y^2} \tag{1}$$

with initial and boundary conditions

$$\begin{aligned} u &= U_i \quad \text{at} \quad \theta = 0 \\ u &= 0 \quad \text{at} \quad y = 0 \\ u &= U_i \quad \text{at} \quad y = \infty \end{aligned} \tag{2}$$

$U_i$ represents the eddy velocity at the first instant of renewal, $u$ is the instantaneous velocity profile, and $\theta$ is the instantaneous contact time.

The assumption of negligible pressure-gradient effects on the momentum transfer for flow conditions such as hydrodynamically fully developed tube flow has generally been justified by dimensional-analysis–order-of-magnitude arguments [9]. Because of the pertinence of this formulation in obtaining an analogical relationship for the mean frequency of surface renewal, a more rigorous analysis of the effect of the pressure gradient will now be presented for incompressible flow.

### Analysis

The inclusion of the pressure-gradient term $dP/dx$ in the formulation of the basic surface-renewal-and-penetration model for momentum transfer requires an expression of the form

$$\frac{\partial u}{\partial \theta} = \nu \frac{\partial^2 u}{\partial y^2} - \frac{1}{\rho}\frac{dP}{dx} \tag{3}$$

The solution of this equation for constant pressure gradient coupled with the initial and boundary conditions given previously leads to an expression for the local instantaneous velocity profile of the form [2]

$$\frac{u}{U_i} = \operatorname{erf}\left(\frac{y}{2\sqrt{\nu\theta}}\right) + \frac{1}{\rho}\frac{dP}{U_i dx}\left[\left(\theta + \frac{y^2}{2\nu}\right)\operatorname{erfc}\left(\frac{y}{2\sqrt{\nu\theta}}\right) - y\left(\frac{\theta}{\pi\nu}\right)^{1/2}\exp\left(\frac{-y^2}{4\nu\theta}\right) - \theta\right] \tag{4}$$

As $dP/dx \to 0$ this expression reduces to the solution of equations (1) and (2), or

$$u/U_i = \operatorname{erf}\left[y/\left(2\sqrt{\nu\theta}\right)\right] \tag{5}$$

The time-averaging of the expression for $u$ given by equation (4) in terms of the random contact time distribution proposed by Danckwerts [3] leads to a relationship for the local mean velocity profile $\bar{u}$ of the form

$$\frac{\bar{u}}{U_i} = \left[1 - \frac{\tau}{\rho U_i}\frac{dP}{dx}\right]\left[1 - \exp\left(\frac{-y}{\sqrt{\nu\tau}}\right)\right] \tag{6}$$

where $\tau$ is the mean residence time of all eddies arriving at the surface. The differentiation of this expression yields a relationship for $\tau$ in terms of the local mean friction velocity $U^*$ of the form

$$U^*\sqrt{\frac{\tau}{\nu}} = \frac{2U_i/U^*}{1 + \sqrt{1 + \dfrac{4\nu}{\rho U^{*4}} U_i \dfrac{dP}{dx}}} \tag{7}$$

For hydrodynamically fully developed flow in a circular tube

$$\frac{dP}{dx} = -\frac{4\rho U_b^2}{D}\frac{f}{2}$$

such that equation (7) becomes

$$U^*\sqrt{\frac{\tau}{\nu}} = \frac{2U_i/U^*}{1 + \sqrt{1 - \dfrac{16U_i}{U^*\mathrm{Re}}\sqrt{\dfrac{2}{f}}}} \tag{8}$$

$f$ is the Fanning friction factor such that $U^* = \sqrt{f/2}\, U_b$. For $dP/dx = 0$, equation (7) reduces to an expression of the form

$$U^*\sqrt{\frac{\tau}{\nu}} = \frac{U_i}{U^*} \tag{9}$$

This expression and a similar relationship obtained by the use of Higbie's [7] uniform contact time distribution has been previously utilized in turbulent momentum-, heat-, and mass-transfer analyses [5, 6, 11].

### Discussion and Conclusion

Equations (8) and (9) can be compared in terms of the dimensionless parameters $Y$ $[\equiv (U^*\sqrt{\tau/\nu})(U^*/U_i)]$ and $X$ $[\equiv (\mathrm{Re}\sqrt{f/2})(U^*/U_i)]$. Equation (9) indicates that $Y$ is identically equal to unity, while equation (8), which reflects the effect of the pressure drop, indicates that $Y$ increases from a value of unity at large $X$ to a value of two at $X$ equal to 16.

---

[1] Associate Professor, Mechanical Engineering Department, University of Akron, Akron, Ohio. Assoc. Mem. ASME.

[2] Numbers in brackets designate References at end of technical brief.


Contributed by the Heat Transfer Division of THE AMERICAN SOCIETY OF MECHANICAL ENGINEERS. Manuscript received by the Heat Transfer Division April 26, 1972.

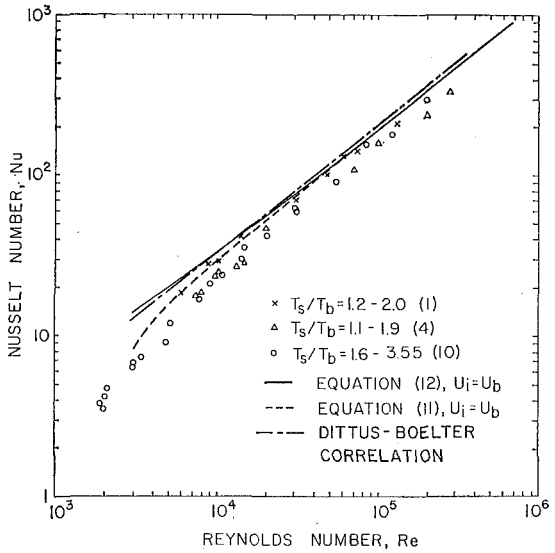


**Fig. 1 Comparison of predictions for Nusselt number with experimental data, after Lawn [8]**

The implementation of equations (8) and (9) in this study requires a reasonable approximation for the parameter $U_i$. Various assumptions for this parameter have been set forth by Einstein and Li [5], Hanratty [6], Meek and Baer [9], and Thomas [11]. Hanratty set $U_i/U^*$ equal to 13.5 and Thomas set $U_i$ equal to the bulk stream velocity $U_b$, whereas Meek and Baer obtained a value for $U_i$ by equating the predicted bulk stream velocity, derived from the use of their wall-region model and a mixing-length model for the turbulent core, to the Prandtl formula for the friction factor.

An indication of the possible importance of the pressure gradient in formulations of the surface-renewal-and-penetration model can be seen by a consideration of turbulent heat transfer for fully developed tube flow. The solution of the appropriate energy equation and initial-boundary conditions and the use of the random contact time distribution lead to a relationship for the mean coefficient of heat transfer of the form [11]

$$h = \frac{T_0 - T_i}{T_0 - T_b}\sqrt{\frac{\rho c k}{\tau}} \tag{10}$$

$T_i$ is the eddy temperature at the first instant of renewal. The substitution of the expression for $\tau$ given by equation (8) into equation (10) gives

$$\mathrm{Nu} = \frac{hD}{k} = \frac{T_0 - T_i}{T_0 - T_b}\frac{U_b}{U_i}\frac{f}{2}\,\mathrm{Re}\sqrt{\mathrm{Pr}}\left[\frac{1 + \sqrt{1 - (16/X)}}{2}\right] \tag{11}$$

As $dP/dx \to 0$ this expression reduces to

$$\mathrm{Nu} = \frac{T_0 - T_i}{T_0 - T_b}\frac{U_b}{U_i}\frac{f}{2}\,\mathrm{Re}\sqrt{\mathrm{Pr}} \tag{12}$$

presented previously [11]. Equation (11) lies below equation (12) by the factor $[1 + \sqrt{1 - (16/X)}]/2$ which equals $1/2$ at $X = 16$ and zero for large values of $X$.

Equations (11) and (12) along with the Dittus-Boelter correlation are compared with experimental heat-transfer data in Fig. 1 for air with $U_i = U_b$ and $T_i = T_b$. Equation (11) follows the data remarkably well. It should be noted that a cause for the slight overprediction of the experimental data by equation (11) is the effect on $T_i$ of molecular transfer during the flight of eddies [12]. Further, the data appear to reflect some slight inconsistency due to possible effects of property variation or experimental error.

## Acknowledgment

This investigation was partially supported by the National Science Foundation under grant GK 18815.

## References

1 Barnes, J. F., and Jackson, J. D., "Heat Transfer to Air, Carbon Dioxide and Helium Flowing Through Smooth Circular Tubes Under Conditions of Large Surface/Gas Temperature Ratio," *Journal of Mechanical Engineering Sciences*, Vol. 3, No. 19-1, p. 303.

2 Berg, P. W., and McGregor, J. L., *Elementary Partial Differential Equations*, Holden-Day, San Francisco, Calif., 1966, pp. 96–99.

3 Danckwerts, P. V., "Significance of Liquid-Film Coefficients in Gas Absorption," *Industrial and Engineering Chemistry*, Vol. 43, June 1951, pp. 1460–1467.

4 Deissler, R. G., "Analysis of Turbulent Heat Transfer, Mass Transfer and Friction in Smooth Tubes at High Prandtl and Schmidt Numbers," NACA TN 3145, May 1954.

5 Einstein, H. A., and Li, H., "The Viscous Sublayer Along a Smooth Boundary," *ASCE, Engineering Mechanics Division Journal*, 1956, Vol. 82, No. E. M., pp. 1–27.

6 Hanratty, T. J., "Turbulent Exchange of Mass and Momentum with a Boundary," *AIChE Journal*, Vol. 2, Sept. 1956, pp. 359–362.

7 Higbie, R., "The Rate of Absorption of a Pure Gas into a Still Liquid During Short Periods of Exposure," *AIChE Transactions*, Vol. 31, 1935, pp. 365–389.

8 Lawn, C. J., "Turbulent Heat Transfer at Low Reynolds Numbers," JOURNAL OF HEAT TRANSFER, TRANS. ASME, Series C, Vol. 91, No. 4, Nov. 1969, pp. 532–536.

9 Meek, R. L., and Baer, A. O., "The Periodic Viscous Sublayer in Turbulent Flow," *AIChE Journal*, Vol. 16, Sept. 1970, pp. 841–848.

10 Sams, E. W., and Desmon, L. G., "Heat Transfer from High Temperature Surfaces to Fluids," NACA Memo E9012, Jan. 1949.

11 Thomas, L. C., "Temperature Profiles for Liquid Metals and Moderate-Prandtl-Number Fluids," JOURNAL OF HEAT TRANSFER, TRANS. ASME, Series C, Vol. 92, No. 3, Aug. 1970, pp. 565–567.

12 Thomas, L. C., "A Turbulent Transport Model with Emphasis on Heat Transfer to Liquid Metals," *Canadian Journal of Chemical Engineering*, Vol. 49, June 1971, pp. 326–332.